

**B.Grynyov  
V.Ryzhikov  
Jong Kyung Kim  
Moosung Jae**

**Scintillator Crystals,  
Radiation Detectors  
&  
Instruments on Their Base**

**Editor V.Ryzhikov**

**Ukraine – Kharkiv – 2004**

This monograph deals with modern problems of scintillator materials science and advanced technologies for creation of small-sized scintillator detection systems for radiation instruments of different purpose. Principal scientific and technical aspects are considered of raw material synthesis and growth of scintillator crystals, and studies of their physico-technical, luminescent and radiation parameters are described. Data are presented on characteristics of ultra-low background spectrometric detection blocks of new generation of “scintillator-PMT” type on the basis of heavy oxide scintillators. Properties are described of a new type of integrated detectors of “scintillator-photodiode” type on the basis of ZnSe(Te) crystals. Examples are presented of practical applications of scintillators and scintielectronic detectors in medical, inspection and industrial introsopes, small-sized household and professional multi-functional and emergency dosimeters, as well as radiometric and spectrometric systems.

Editor V.Ryzhikov  
Executive Editor E.V.Sherbina

**B.Grynyov**  
**V.Ryzhikov**  
**Jong Kyung Kim**  
**Moosung Jae**

**Scintillator Crystals,  
Radiation Detectors  
&  
Instruments on Their Base**

**Ukraine – Kharkiv – 2004**

**ISBN 966-02-3314-0**

© B.Grynyov,  
V.Ryzhikov,  
Jong Kyung Kim  
Moosung Jae

# Contents

Introduction	7
Chapter 1. Alkali Halide Crystals	10
1.1. Crystal and zone structure of alkali halide crystals	10
1.2. Preparation technology of alkali halide crystals	11
1.3. Main physico-chemical properties and scintillation characteristics of alkali halide scintillators	16
1.4. The activator state and scintillation process in AHC	27
1.5. Basic concepts of the radioluminescence mechanism in AHC	31
1.6. Structure of luminescence centers and luminescence activation in AHC	33
1.7. Application fields of AHC-based scintillators: present-day state and further prospects	37
References	41
Chapter 2. Single Crystals of Complex Oxides	47
2.1. Bismuth germanate $\text{Bi}_4\text{Ge}_3\text{O}_{12}$ (BGO) and silicate $\text{Bi}_4\text{Si}_3\text{O}_{12}$ (BSO) single crystals	49
2.1.1. Crystal and electron structure of $\text{Bi}_4\text{Ge}_3\text{O}_{12}$ and $\text{Bi}_4\text{Si}_3\text{O}_{12}$	49
2.1.2. Theoretical description of thermal conditions for growth of oxide crystals of constant radius by the Czochralski method	53
2.1.3. Technological features of single crystal growth of bismuth germanate and silicate	58
2.1.4. Thermal treatment of BGO single crystals	65
2.1.5. Main physico-chemical properties and scintillation characteristics of bismuth germanate and silicate crystals	68
2.1.6. Applications of BGO and BSO single crystals.	78
2.2. Compounds of yttrium, scandium and rare-earth element silicates	80
2.2.1. Crystal structure of compounds $\text{Ln}_2\text{SiO}_5$	80
2.2.2. Technological features of $\text{Ln}_2\text{SiO}_5$ single crystal growth	83
2.2.3. Main physico-chemical properties and scintillation characteristics of yttrium, scandium and rare-earth element silicates	85
2.3. Tungstates	99

2.3.1. Crystal structure of tungstates	100
2.3.2. Technological preparation features of tungstate single crystals	103
2.3.3. Main physico-chemical properties and scintillation characteristics of tungstates	108
2.3.4. The nature of luminescence centers in tungstates and their energy diagrams	124
References	132
Chapter 3. Scintillators on the Basis of Semiconductor Compounds	143
3.1. Peculiar features of defect formation	143
3.2. Kinetics of formation processes of semiconductor scintillator crystals with isovalent dopants accounting for effects of gas media	158
3.3. Optical and electron properties of trapping centers and luminescence mechanisms in SCS	169
3.3.1. Experimental studies of spectral-kinetic characteristics	169
3.3.2. Theoretical analysis of radiative recombination center formation upon IVD introduction.	183
3.3.3. Photoluminescence decay kinetics of ZnSe(Te)-based scintillators	186
3.3.4. Parameters of emission centers in ZnSe(Te) crystals as studied by spectroscopic and thermoluminescent methods	190
3.3.5. Methods of two-photon spectroscopy for determination of parameters of deep centers in ZnSe(Te)	193
3.4. The nature of radiative recombination in $A^{II}B^{VI}$ compounds with isovalent dopants (IVD)	200
References	203
Chapter 4. Application Prospects of Oxide and Chalcogenide Crystals for Detection of Neutrons	209
4.1. Neutron flux measurements using «scintillator-photodiode-preamplifier» system and new types of scintillators	209
4.1.1. Experimental set-up: scintillators and components of the receiving electronic circuit	210
4.1.2. Experimental results	214
4.1.3. Possibilities for neutron detection: discussion and conclusions	217
4.2. Oxide and semiconductor scintillators in scintielectronic detectors for detection of neutrons	222
References	227

Chapter 5. Optimization of the Detector Size	229
References	236
Chapter 6. Detectors «Scintillator-PMT»	237
References	248
Chapter 7. Detectors of «Scintillator-photodiode» Type	249
7.1. Criteria for the optimum choice of scintillators.	
Efficiency and light collection in scintielectronic detectors	251
7.2. Photodiodes for scintielectronic detectors	254
7.3. General development principles and main properties	
of scintielectronic detectors	258
7.3.1. Energy characteristics	258
7.3.2. Noises in scintielectronic detectors	266
7.3.3. Scintielectronic detectors in the current mode: RDT noises	271
7.3.4. Pre-amplifiers for detectors operating in the current mode	273
7.3.5. Peculiar features of design and construction	
of charge-sensitive preamplifiers	276
References	281
Chapter 8. Instruments for Radiation Monitoring	284
8.1. Introduction	284
8.2. Development of radiation monitoring devices	
using “scintillator-photodiode” detectors	286
8.2.1. Measurements up from the background level	286
8.2.2. Application of scintillator-photodiode detectors	
for dosimetric monitoring in the current mode	290
8.2.3. Gamma-spectrometer on the base of a “Notebook”	
computer and detector “scintillator-photodiode”	295
8.3. New ideology of detection of $^{241}\text{Am}$ and accompanying	
radionuclides	304
8.3.1. Introduction	304
8.3.2. Composition of radioactive contaminants from NPP	305
8.3.3. A new approach to americium detection	307
8.3.4. Application fields of RK-AG-02M radiometer	311
8.2.5. Operation algorithm of RK-AG-02M radiometer	312
8.3.6. Original features of RK-AG-02 radiometer	315
8.3.7. Design features of the radiometer	316
8.3.8. Parameters and characteristics of RK-AG-02 radiometer units	318
8.4. Dosimeters for detection of solar radiation	319
8.4.1. Detector	321
8.4.2. Household UV radiation dose meter	324
8.4.3. Professional UV radiation meter	326
References	330

---

Chapter 9. Instruments and Detectors on the Base of Scintillator Crystals for Security and Customs Inspection Systems	335
9.1. Introduction	335
9.2. Experimental procedures	336
9.3. Discussion	339
9.4. Conclusion	344
References	345
Chapter 10. A Simple Method for the Calculation of Photon Dose Conversion Factors in Non-tissue Phantom as Like the PMMA Slab	346
10.1. Introduction	346
10.2. Computational model	347
10.3. Indirect method	348
10.4. Direct method	350
10.5. Results	352
10.6. Conclusions	353
References	355
Chapter 11. Dose Equivalent Per Unit Fluence Near the Surface of the ICRU Phantom by Including the Secondary Electron Transport For Photons	356
11.1. Introduction	356
11.2. Computational method	358
11.3. Results and discussions	359
11.4. Conclusions	367
References	373

## INTRODUCTION

For an average person, the beginning of each day is marked by a natural wish to know the weather forecast, comparing it with the personal observation of the surrounding world through the window. Such information about the quantity of heat, moisture and solar radiation in the environment seems to be sufficient for taking adequate measures and precautions that should protect our rather fragile organism from unfavorable external conditions.

Until recently, not much attention has been paid to the fact that, alongside the visible light and perceptible heat, the surrounding world is permeated with myriads of particles and flows of radiation that are not accessible for our sensual perception. It was assumed that this sphere of scientists' interests and activities does not come into a close touch with our personal existence. The Chernobyl catastrophe has destroyed these illusions, as death and illness of tens and hundreds of thousands of human beings were largely caused by the absence of information on the extraordinary high level of invisible penetrating radiation or the presence of local sources with high concentration of radioactive particles, found sometimes tens and hundreds of miles away from the site of the catastrophe.

This was a powerful incentive to start off the works on modernization of instruments for radiation monitoring of the environment, led to realization of the importance of these means for large masses of population. Systematic studies of radiation levels in many regions of the former Soviet Union have unexpectedly revealed a number of important factors that had no relationship to consequences of the Chernobyl catastrophe. First of all, one should note broad uncontrolled use of potassium fertilizers, which often contained high concentration of the radionuclide  $^{40}\text{K}$ , as well as the use of building materials containing fission products of transuranic elements. One should also add fuel transportation to nuclear power plants and disposal of the radioactive

wastes, uncontrolled and irrational use of radiation in medical diagnostics, radiation effects upon passengers and crew of high-altitude airlines, radiation coming from computer monitors and TV screens, not fully understood effects of the “ozone holes” in the ionosphere, etc.

It has become obvious that in the modern world, the list of common attributes of civilization, such as thermometer and barometer, should include instruments designed for detection of radiation — in the environment, technical devices, alimentary products.

The purpose of these instruments is, first of all, to establish the very fact that the level of radiation is substantially above the background level, to measure exactly the radiation dose rate, to determine the type and energy of particles or gamma-quanta. Solution of these problems would protect human beings from harmful effects of radiation, localize and eliminate its sources.

The key element of all radiation instruments is radiation detector, sensitivity and selectivity of which determine the characteristics of the whole instrument. Solid-state crystal detectors are practically the only type of sensors that can ensure both detection of the invisible radiations and determination of their type and radiation spectrum, i.e., provide us with solution of all the above-described problems. Therefore, developments in the field of nuclear instruments and methods that were observed in the recent years have been largely related to creation of new types of crystals and radiation detectors based thereon. One of the most common and efficient types of detectors are those using scintillator crystals, which transform invisible radiations into light, with subsequent recording by photoreceiving devices.

Combination of high efficiency of radiation detection, high sensitivity, and possibility to determine the energy characteristics have made scintillation detectors one of the main types of sensors used in instruments and systems for detection and monitoring of ionizing radiation.

The existing trends in the development of scintillation technologies are characterized worldwide by the following requirements to the scintillator parameters: high atomic number (above 60), high light output, fast response (down to several nanoseconds), radiation stability under powerful (up to  $10^8$  rad) radiation doses, and parameter stability under prolonged action of radiation ( $10^3$ – $10^4$  R/hour) and temperature (200°C and more). Slow luminescence components should be absent (afterglow



level below 0.01% after 3–10  $\mu\text{s}$ ), the dynamic range should be broad ( $10^6$ – $10^8$ ), and the detection system as a whole should be reliable and small-sized (which can be achieved using solid-state photoreceivers, e.g., photodiodes).

At present, the above-described complex of requirements is not fully met by any of the known scintillators. However, attention paid to the problem of radiation detection, substantial efforts and amounts of money spent for its solution allowed substantial progress in this field, leading to the development of new types of scintillators that can solve problems not realizable with conventional alkali halide crystals. Results of studies and parameters for a broad class of modern scintillators, peculiar features of their preparation technologies, description of a large class of detectors, instruments and systems for radiation detection using scintillation crystals — this is the scope of questions touched upon in the present book.

## CHAPTER 1

### ALKALI HALIDE CRYSTALS

Alkali halide crystals, in particular, crystals of alkali metal iodides are widely used as efficient scintillators and have been a subject of numerous studies. Crystals of sodium iodide doped with thallium is one of the most efficient scintillator materials. In the recent years, a large amount of experimental data has been accumulated, which show that scintillation characteristics of the materials are, in fact, not constants, but are largely determined by the obtained level of their production technology. They are closely related to structural perfection of the crystals, concentration and types of the defects formed in the course of growth and post-growth treatment. In this chapter, it is shown that the real crystal structure depends upon the state of the activator in the crystal lattice, its concentration, and crystallization conditions. Undesirable types of the activator defects are determined, which cause afterglow and worsening of the light output and intrinsic energy resolution of scintillators.

Studies of traditional scintillators based on alkali metal iodides that have been carried out in the Institute for Single Crystals of the Academy of Sciences of Ukraine provide us with evidence that the obtained scintillator characteristics are not the final limit, and in many cases can be substantially or partially improved.

#### ***1.1. Crystal and zone structure of alkali halide crystals***

Most of the alkali halide crystals (AHC) crystallize in the face-centered cubic structure of the NaCl type. CsCl, CsBr and CsI crystallize in the volume-centered cubic structure of the CsCl type. Crystals of these two groups have different structures of the first Brillouin zone (Fig.1.1). The respective band structures are also different (Fig.1.2). The most essential distinctions are observed in the conduction band structure,

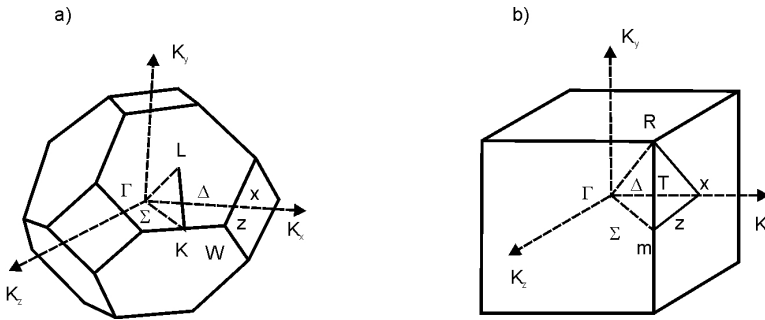


Fig.1.1.1. First Brillouin zones of AHC with structures of NaCl (a) and CsCl (b). Points and directions of higher symmetry are indicated by letters.

while the valence band structures of NaCl and CsI are largely similar. The AHC band structure is characterized by the presence of low-lying *d*-conduction bands and by a substantial distance between the alkali metal *p*-conduction bands and the valence band. This feature has been explained by mutual repulsion of the conduction and valence bands having the same symmetry [1].

## 1.2. Preparation technology of alkali halide crystals

Alkali halide scintillation crystals are most commonly obtained by two methods — those of Kyropoulos and Stockbarger, which have been known since 1920-ies [2,3]. Later, these methods were substantially developed, both in technological process and equipment design, which allowed production of large-sized crystals of controlled structural perfection and variable dopant composition, ensuring high optical and scintillation characteristics [4–6]. Harshaw [7] reported production of NaI(Tl) crystals up to 813 mm in diameter and 750 mm high.

The AHC preparation procedures, both by Kyropoulos and Stockbarger methods, consist of several stages and begin with preliminary treatment of the raw material and melt before starting the actual crystal growth process. The operation sequence in raw material treatment is essentially as follows. The most time-consuming stage is low-temperature drying (at the room temperature). At this stage, moisture present in the initial salt should be desorbed as fully as possible. Attempts to shorten this stage often lead to hydrolysis of the raw material by the residual adsorbed water. At the second stage of drying the raw material,

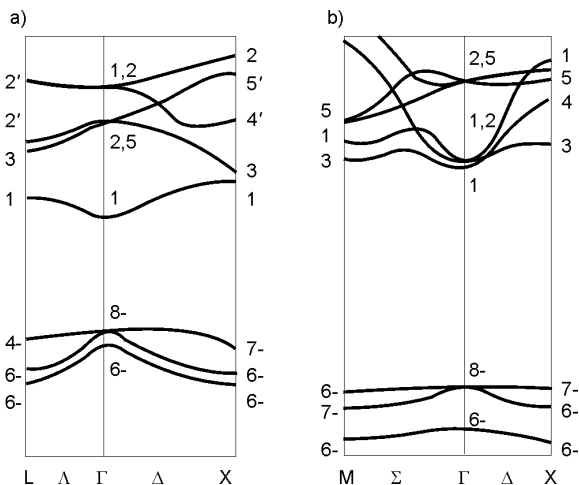


Fig.1.2. Band structure of AHC with NaCl- (a) and CsCl- (b) type lattice.

it is treated by hydrogen iodide vapor, which is formed as a result of ammonium iodide decomposition (weakly reactive atmosphere). This allows to bound traces of moisture and oxygen-containing admixtures and to remove them by subsequent heating and pumping. Sufficiently high temperature of the final stage of raw material treatment (550°C) favors desorption and final removal of the gaseous reactive treatment products from the ampoule. At this stage, all nitrogen-containing substances are removed (which, even in trace quantities, can cause substantial quenching of scintillations).

It has been known from practical experience that the main problem in production of AHC-based scintillators of high efficiency consists in removing all oxygen-containing anions from the growing crystal [8]. Among sources of such anion contamination are, firstly, components of the air atmosphere (which are actively adsorbed on the surface of each powder particle), and, secondly, oxygen-containing admixtures that remain after chemical synthesis of the initial raw material (which are located inside the powder particles). Fig.1.3 shows examples of luminescence spectra of the compacted CsI powder and single crystals grown from that raw material. Higher luminescence intensity of the compacted powder in the blue spectral region is an argument in favor

of the need for preliminary treatment to achieve additional purification of the raw material.

Having determined specific contamination sources, one can outline the ways to avoid them in preparation of the raw material. Thus, preliminary drying of the raw material (powder) and its treatment by a reactive atmosphere are aimed at the removal of adsorbed air and moisture components from the surface of the powder particles. However, this method does not help us to remove molecular anions concentrated inside the powder particles. Therefore, further manipulations are needed to achieve the required purification of the melt. If the Kyropoulos method is

used, special gas-thermal treatment of the melt in an argon, nitrogen or helium-containing medium is required, depending upon specific objectives of the growth. If the Stockbarger method is used, this role is played by graphitization of the ampoule. Advantages of the Stockbarger growth for AHC consists in the possibility of full isolation of the raw material and the melt from coming into contact with air components and other contamination sources, as well as in more convenient treatment of the raw material and the melt. Negative sides of this method include poor structural quality of the crystals obtained (extensive system of inter-grain boundaries, high dislocation density, relatively high level of the internal stresses, formation of a cellular structure, etc.). In the crystal volume, non-uniformities are often observed in the form of honeycomb-like patterns or cell networks [9]. It is assumed that cellular structure of Stockbarger-grown NaI(Tl) crystals is related to the cellular structure of the crystallization front caused by non-uniform distribution of the activator dopant. Intense forced mixing of the melt by the method of horizontal rotating am-

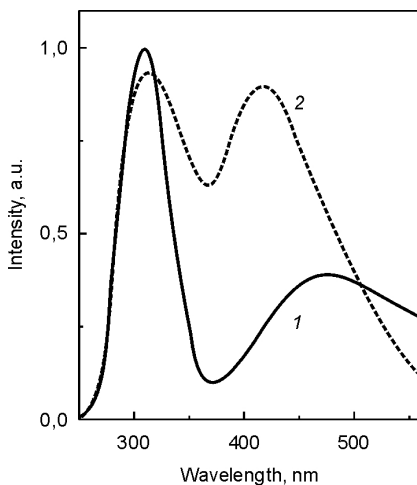


Fig.1.3. Luminescence spectra of a single crystal (1) and pressure-compacted material (2) made of the same batch of CsI raw material.

poule ensures monotonous distribution of the activator and prevents accumulation of the admixture at the crystallization front due to the absence of crystallization supercooling [10]. Non-uniform distribution of the admixtures along the AHC height leads to non-reproducibility of the scintillator properties.

Alkali halide crystals of high structural perfection and parameter uniformity can be grown by the Kyropoulos method, because in this case there is no direct contact of the growing crystal with the crucible walls, and the growing crystal can be easily moved away from the melt, thus stopping the growth process before the melt would be used completely. Generally, single crystals grown by the Kyropoulos method are of better structural perfection than those grown by the Stockbarger method. Among disadvantages of the Kyropoulos method, one should note the melt vapor contacting the heater and the furnace housing. It is also more difficult to achieve the required low pressure in the growth chamber because of large volume of the furnace.

It has been shown that, not depending upon the growth method used, the presence of admixtures in AHC, even in trace quantities, can substantially affect the character of their afterglow and radiation stability. A negative role played both by cation and anion admixtures was noted [8]. At the same time, even in salts of very high purity degree used for AHC growth, the content of  $\text{OH}^-$ ,  $\text{IO}_3^-$ ,  $\text{CO}_3^{2-}$ ,  $\text{NO}_2^-$  can reach  $10^{-3}$  mol.%. A decisive role of oxygen-containing compounds and the presence of extra vacancy type defects have been shown to be a decisive factor leading to long decay times [8,11]. Moreover, to obtain high quality NaI- and CsI-based scintillators, the activator ions should be distributed as uniformly as possible at concentration levels ensuring efficient detection of gamma-quanta, X-ray radiation and alpha particles.

Thus, achieving high scintillation parameters of AHC depends upon specific features of the growth technology used, the presence of admixtures and their concentration, as well as uniformity of the activator distribution.

The total volume of the world AHC annual production is measured in dozens of tons, and the most broadly used growth technologies are those based on the Bridgman-Stockbarger directed crystallization method. This technology, though sufficiently simple and convenient, still has some drawbacks that create problems in production of large-sized AHC of high quality.

In the Institute for Single Crystals, two methods have been developed for automated pulling of single crystals from the melt on a seed involving feeding-up of the raw charge in the course of growth [12,81]. The activator distribution non-uniformity in this case did not exceed 10% [79].

A method of crystal pulling from the melt was reported [5,6], where the melt was placed into a rotating cylindrical crucible, with feeding up by polycrystalline or granular raw charge from the feeder located outside the growth furnace. The process automation is ensured by the temperature control of the heaters using signals of a high-sensitivity electronic sensor of the melt level, thus determining either the mass speed of the growth or diameter of the growing crystal from the displacement of the melt mirror surface. This method excludes many drawbacks that are characteristic for the Bridgman-Stockbarger method, but it has its own negative sides, related to melting of the feed-up material directly in the crucible (in its peripheral part) and large free surface of the melt when large-sized crystals are to be grown.

In another method [13,14], these problems are avoided. At the radial growth stage, the crystal is pulled from the melt with the geometry of its surface being varied by means of gradual elevation of the melt level in a cone-shaped crucible. The feed-up is made with melted material from the feeder located directly under the crucible in the hermetically sealed growth furnace. This limits the maximum crystal size, but provides for additional purification of the melt, removing oxygen-containing microadmixture and mechanical inclusions. The melt level in the crucible is set by the position of the electric contacting feeler with respect to the top of the cone-shaped crucible. Information of the growth speed (or on the crystal diameter changes) comes in the form of data on the feed-up rate variation.

Both methods have been comprehensively tested in growing of large-sized NaI(Tl), CsI(Tl) [37], CsI(Na) and CsI single crystals — of 520 mm and more in diameter, of more than 500 kg in mass. High quality of scintillation detectors prepared from these crystals (in particular, detectors of large diameter for medical gamma-chambers, which should meet especially high requirements) has been confirmed by measurement of their characteristics carried out at many leading Western companies in the field of radiation instruments.

Table 1.1. Main physico-chemical properties and scintillation characteristics of NaI(Tl) [16,17,18].

Characteristic	Value
Atomic number	50
Density, g/cm <sup>3</sup>	3.67
Melting temperature, K	924
Thermal expansion coefficient, K <sup>-1</sup>	47.4·10 <sup>6</sup>
Cleavage plane	(100)
Mohs' hardness	2
Hygroscopicity	yes
Maximum of the emission spectrum, nm	415
Lower absorption band edge, nm	300
Relative light output (γ-radiation), %	100
Refraction index at the emission maximum	1.85
Scintillation decay time, μs	0.23
Afterglow after 6 ms, %	0.3–0.5

### ***1.3. Main physico-chemical properties and scintillation characteristics of alkali halide scintillators***

A substantial part of scintillation materials for detectors of ionizing radiation is based on alkali halide single crystals. At present, they represent not less than 80% of the total quantity of scintillators used in the world. In traditional application fields of AHC application, the scintillators used are based on two crystal matrices — NaI and CsI (Table 1.1 and 1.2).

**NaI(Tl).** This is one of the most efficient scintillation materials. It was reported for the first time in 1948 [15]. NaI(Tl) single crystals remain second to none among scintillator materials as for their light output, energy resolution, good matching of the radioluminescence spectrum to the maximum sensitivity region of commonly used PMT (415+5 nm) and fast response (among activated alkali metal iodides).

The luminescence spectrum of NaI(Tl) single crystals, with maximum at 415 nm, is shown in Fig.1.4.

NaI(Tl) single crystals have relatively high density and atomic number, which ensures high peak and full detection efficiency of gamma- and X-ray radiation. High transparency to the intrinsic radiation



Table 1.2. Main physico-chemical properties and scintillation characteristics of single crystals CsI(Te), Cs(Na), CsI and CsI(CO<sub>3</sub>) [16,17,18].

Characteristic	Value			
	CsI(Tl)	CsI(Na)	CsI	CsI(CO <sub>3</sub> )
Atomic number	54	54	54	54
Density, g/cm <sup>3</sup>	4.51	4.51	4.51	4.51
Melting temperature, K	894	894	894	894
Thermal expansion coefficient, K <sup>-1</sup>	54·10 <sup>6</sup>	49·10 <sup>6</sup>	49·10 <sup>6</sup>	49·10 <sup>6</sup>
Cleavage plane	No	No	No	No
Mohs' hardness	2	2	2	2
Hygroscopicity	Slight	Yes	Slight	Yes
Maximum of the emission spectrum, nm	550	420	315	405
Lower absorption band edge, nm	320	300	260	300
Relative light output with respect to NaI(Tl), %	45	85	4-6	60
Refraction index at the emission maximum	1.79	1.84	1.95	1.84
Scintillation decay time, μs	0.63–1	0.63	0.016	1.4–3.4
Afterglow after 6 ms, %	0.1–5	0.5–5	–	0.06

(absorption coefficient  $K \sim 5 \cdot 10^{-3} \text{ cm}^{-1}$ ) ensures good light absorption in large-sized single crystals.

A serious drawback of NaI(Tl) crystals is their high hygroscopicity, due to which these crystals must be placed into hermetically sealed housings. Another drawback is their phosphorescence, which causes rather high afterglow in the millisecond and minute range. The relatively high afterglow limits the application fields of NaI(Tl). In particular, this applies to computer tomography, where the afterglow level after 3 μs should not be higher than 0.4% [19]. The millisecond luminescence component, as well as the more slow components, substantially worsens counting characteristics of a detector, especially in variable radiation fields and at operation temperatures below the room temperature.

In NaI(Tl) crystals, the main luminescence component contributes 90–95% of the whole signal, and the remaining 5–10% are due to slow

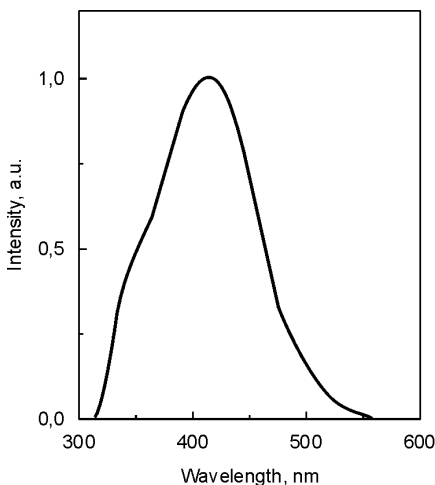


Fig.1.4. Luminescence spectrum of NaI(Tl) single crystals.

components. One more drawback of NaI(Tl) single crystals is that they are rather brittle and tend to be easily cleaved along the (100) plane. This can be slightly improved by plastic deformation at high temperatures. However, for severe operation conditions (vibration, sharp mechanical stresses, thermal shocks) NaI(Tl) as scintillation material is generally used in the form of so-called “polyscins”, which are obtained by pressure compaction and extrusion. The single crystalline ingot is recrystallized at high temperature and high pressure, resulting in a quasi-amorphous polycrystalline

material, in which the mosaic blocks are strongly disoriented. Such structure increases the polyscin hardness, not worsening their optical and scintillation properties. Mechanical properties of NaI(Tl) polyscins and single crystals are compared in Table 1.3. Brittleness and tendency to be easily cleaved is the reason why a moderate mechanical impact can produce large fissures over the crystal volume. In polyscins, an emerging small fissure is immediately blocked within a small volume and does not expand further. High mechanical hardness characteristics of NaI(Tl) polyscins allow their broad use in geology and geophysics, in outer space studies and environmental monitoring. Simpler production technology is another advantage of polyscins as compared with single crystals.

Scintillation rise time  $\tau$  and scintillation efficiency  $\eta$  of NaI(Tl) single crystals are strongly dependent upon the activator concentration (Fig.1.5). The activator concentration is chosen to ensure sufficient scintillation efficiency, keeping in mind that excess of the activator increases the number of complex thallium centers competing with the regular  $Tl^+$  luminescence centers in absorbing the excitation energy, worsening scintillation properties of the crystal [20]. Effects of the activator

Table 1.3. Mechanical properties of single crystals and polycrystals NaI(Tl) [18], CsI(Tl) and  $\text{Bi}_4\text{Ge}_3\text{O}_{12}$  [26].

Characteristic	Single crystal NaI(Tl)	Polycrystal NaI(Tl)	Single crystal CsI(Tl)	Single crystal $\text{Bi}_4\text{Ge}_3\text{O}_{12}$
Young's modulus, $10^{-10} \text{ N/m}^2$	2.02	2.02	—	10.56
Yield strength, $10^{-6} \text{ N/m}^2$	1.8–2.4	4.1–6.3	—	—
Proof strength, $10^{-6} \text{ N/m}^2$	14–20	20	—	—
Shear modulus, $10^9 \text{ N/m}^2$	7.67	—	6.8	43.6
Bulk elasticity modulus, $10^{10} \text{ N/m}^2$	1.80	—	1.26	5.66
Poisson's ratio	0.314	—	0.2	0.189
Elastooptical constants,				
$C_{11} \cdot 10^{10}, \text{ N/m}^2$	3.03	—	2.446	11.58
$C_{12} \cdot 10^{10}, \text{ N/m}^2$	0.899	—	0.661	2.70
$C_{44} \cdot 10^{10}, \text{ N/m}^2$	0.735	—	0.629	4.36
Anisotropy factor	0.69	—	0.70	0.98

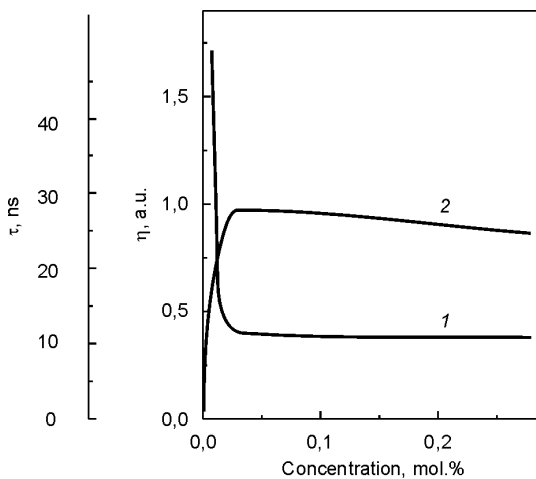


Fig.1.5. Scintillation rise time  $\tau$  (1) and scintillation efficiency  $\eta$  (2) of NaI(Tl) single crystals as function of thallium concentration.

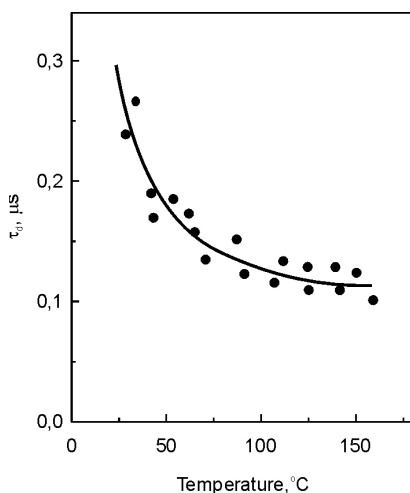


Fig.1.6. Scintillation decay time of NaI(Tl) single crystals as function of temperature.

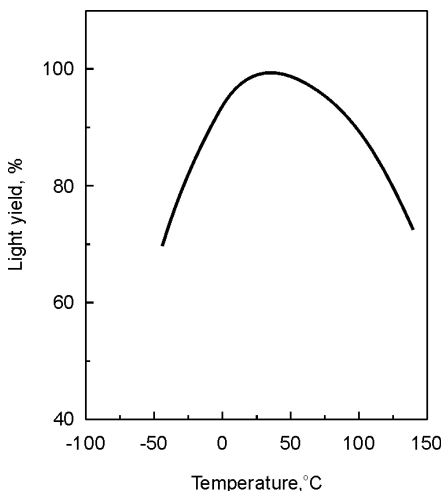


Fig.1.7. Light output of NaI(Tl) single crystals as function of temperature.

concentration upon scintillation properties of NaI(Tl) crystal will be considered in detail in Chapter 1.4. The generally used mass concentrations of the activator in NaI(Tl) crystals usually do not exceed 0.05%. An exception is scintillation detectors of X-ray radiation, where the activator concentration is purposely increased to ensure proportionality of the light output to the radiation energy [21].

The luminescence decay time and light output of NaI(Tl) single crystals are shown as functions of temperature in Figs.1.6 and 1.7, respectively.

At higher temperatures the decay time of NaI(Tl) is decreased, making it possible to use this material in radiometric equipment operating at high temperatures, e.g., in geophysical instruments. The light output of NaI(Tl) is the highest at room temperatures, the temperature coefficient is 0.22–0.5%/K, substantially depending upon the sample and radiation [22]. Below 0°C and above 60°C, the light output falls rather strongly. The temperature dependence of the intrinsic resolution of NaI(Tl) crystals depends upon concentration of the activator [23] and is related to the presence of cen-

ters that are more complex than  $Tl^+$ -centers [20]. When the temperature decreases, non-uniformities of the light output appear, worsening the intrinsic resolution of  $NaI(Tl)$  crystals. Thus, to obtain a scintillation detector with temperature-independent intrinsic resolution, one should use lower concentrations of the activator.

$NaI(Tl)$  single crystals have radiation stability that is quite satisfactory for many applications. They can be used under  $\gamma$ -radiation with flux density of up to  $10^5$  photons/(s·cm<sup>2</sup>) without any noticeable variation of their characteristics. With loads above  $10^7$  photons/(s·cm<sup>2</sup>), characteristics can change irreversibly. Studies of gamma-radiation effects upon optical and spectrometric characteristics of  $NaI(Tl)$ -based scintillation detectors at temperatures from  $-100^\circ\text{C}$  to  $+200^\circ\text{C}$  have shown that the observed worsening of scintillation parameters is mainly due to lower transparency to the intrinsic radiation [24].

At room temperatures, undoped  $NaI$  is not used, as its light output is too low. However, its cooling to liquid nitrogen temperatures leads to a substantial rise of the light output, which becomes two times higher than light output of  $NaI(Tl)$  at  $20^\circ\text{C}$  [25]. The luminescence is observed at  $\lambda_{\text{max}} = 303$  nm with the time constant of 60 ns.

**CsI(Na) and CsI(Tl).** CsI-based crystals are sufficiently stable to gamma-radiation because of their relatively high density and effective atomic number  $Z$ . CsI crystals are used as scintillators either undoped or doped with activators Na or Tl. CsI-based single crystals have high thermal stability and mechanical strength, which is primarily due to the absence of cleavage planes. Most physico-chemical properties of CsI-based crystals do not depend upon the activator used (see Table 1.2), while scintillation characteristics are essentially dependent upon the type and concentration of the dopant. CsI single crystals have higher plasticity as compared with  $NaI$ , which makes their mechanical processing easier. It is interesting to note that CsI crystals are soluble in water, but are not hygroscopic under normal conditions. However, if they are brought into contact with a material upon which water vapor is deposited, or if this material is used in an atmosphere of high humidity, surface degradation of CsI crystals can occur. For undoped CsI and for CsI(Tl), it is possible to restore their initial properties by submitting their surface to a repeated mechanical treatment. As for CsI(Na), this is a weakly hygroscopic material, and it should be hermetically packed in the same way as  $NaI(Tl)$ .

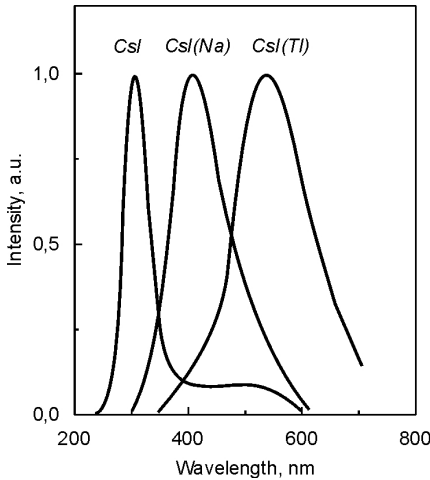


Fig.1.8. Luminescence spectra of single crystals CsI (1), CsI(Tl) (2), CsI(Na) (3).

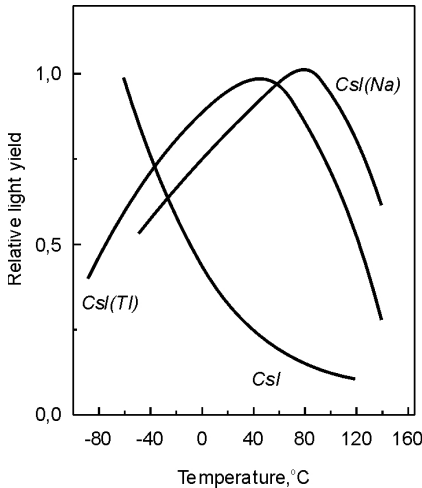


Fig.1.9. Light output of single crystals CsI (1), CsI(Tl) (2), CsI(Na) (3) as function of temperature.

On the basis of CsI matrix, the first scintillation material proposed was CsI(Tl) [26]. The light output of CsI(Tl) single crystals is one of the highest among the known inorganic scintillation materials. However, the luminescence maximum is observed at 550 nm, which does not give good matching with bi-alkali photocathodes of PMT. Consequently, the photoelectron yield for gamma-radiation is only 45% with respect to NaI(Tl). With higher photocathode sensitivity in the green region and the signal formation time constant of the order of 5  $\mu$ s, the signal amplitude rises to 85% [7]. The luminescence spectra of CsI-based single crystals are shown in Fig.1.8. Scintillation intensity of CsI, CsI(Tl) and CsI(Na) as function of temperature is shown in Fig.1.9.

CsI(Tl) is a relatively slow scintillator with average decay time of 1  $\mu$ s (for  $\gamma$ -radiation). Therefore, electronic circuitry with matching signal formation times is to be used, which limits the counting rate ensured by the detector.

The decay time of CsI(Tl) is determined by more than one component [16]. The fastest component is of the order of 0.6  $\mu$ s, and the slowest — 3.5  $\mu$ s.

Under excitation by strongly ionized particles (alpha-particles or protons), the intensity ratio of these two components varies as function of the ionizing power of the absorbed particle. A peculiar feature of scintillation in  $\text{CsI(Tl)}$  is that light emission has a finite rate of its rise, which depends both on thallium concentration and on the ionization density. This is illustrated by Fig.1.10, where data are presented for  $\alpha$ - and  $\beta$ -particles at different mass concentration  $C$  of the activator.  $\text{CsI(Tl)}$  scintillation crystals can be used for separate detection of particles by means of analyzing the pulse shape.

Radiation damage in  $\text{CsI(Tl)}$  crystals can be rather significant when the absorbed dose is higher than 10 Gy ( $10^3$  rad); however, it is at least partially reversible. As most of the radiation damages give rise to optical absorption bands that are observed mainly at lower wavelengths, the use of photodiodes for recording the scintillation light decreases the effects of radiation-induced damage upon light output and pulse height resolution [16].

If thallium is replaced by Na as activator in  $\text{CsI(Tl)}$  crystals, the result is a new scintillation material —  $\text{CsI(Na)}$  — with substantially improved characteristics (higher efficiency, shorter decay time, higher radiation stability. First detailed reports on luminescence and scintillation in  $\text{CsI(Na)}$  were made by Brinckmann in 1965 [27] and A.N.Panova with her co-workers in 1967 [28].

Luminescence spectrum of  $\text{CsI(Na)}$  single crystals has maximum at 420 nm, which is well matched to the bialkali PMT photodiode sensitivity (see Fig.1.8). The light output is up to 85% with respect to  $\text{NaI(Tl)}$  for  $\gamma$ -radiation. The decay time is reduced to 630 ns. A drawback of  $\text{CsI(Na)}$  scintillators, as well as of  $\text{CsI(Tl)}$  ones, is their rather high afterglow,

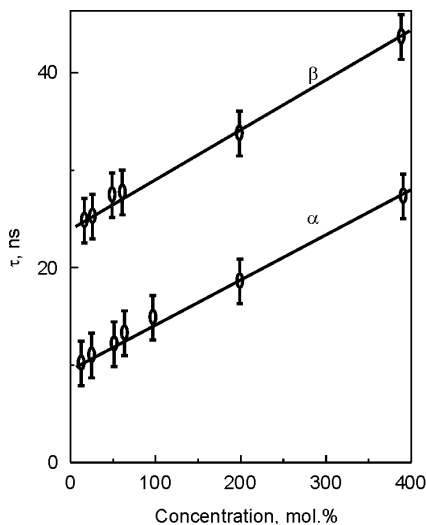


Fig.1.10. Rise time of a scintillation flash in  $\text{CsI(Tl)}$  as function of Tl concentration for  $\beta$ - and  $\alpha$ -particles.

which substantially limits the counting rate. It follows from Table 1.2 that decay time of **CsI(Na)** is shorter than of **CsI(Tl)**.

The light output temperature dependence for **CsI(Na)** single crystal suggests that maximum scintillation efficiency is obtained at  $\sim 80^\circ\text{C}$ , which makes this material suitable for application at high temperatures.

**Undoped CsI.** First reports about possible use of non-activated **CsI** crystals as fast scintillators were made in 1987 [29].

Undoped **CsI** has its luminescence maximum at 315 nm (see Fig.1.8) with intensity much lower than for both activated crystals on its base. Decay time of **CsI** is rather short — 16 ns [16]. Therefore, this material can be used in these cases when high recording speed is required. Alongside with the fast component at 315 nm, there is also a much slower component with decay time of about 1  $\mu\text{s}$ , which constitutes 15–20% of the total light output of **CsI** [16,17]. Intensity of this slow component is largely dependent upon the crystal purity, as contamination of the scintillation material by certain admixtures worsens the ratio of the fast component to the total intensity [16].

The photoelectron yield of a **CsI** scintillator in combination with alkali photocathodes is about 400 photoelectrons/MeV (for  $\gamma$ -radiation). With small **CsI** crystals, one can obtain energy resolution of the order of 17–18% (662 keV  $\gamma$ -radiation). This material finds its applications in high-energy photon spectroscopy. Undoped **CsI** can be used in combination with standard glass PMT, though better results are obtained with quartz windows. It can be seen from Fig.1.9 that scintillation intensity of **CsI** rises sharply with decreasing temperature; the same applies to the decay time [16]. Undoped **CsI** has higher radiation stability than when doped with thallium or sodium, and its properties can be largely restored after a certain time. No substantial radiation damage was observed in **CsI** up to doses of 1000 Gy (105 rad). Simultaneous presence of carbonate ( $\text{CO}_3^{2-}$ ) and hydroxyl ( $\text{OH}^-$ ) ions in **CsI** crystals substantially worsens their radiation stability [61].

**CsI(CO<sub>3</sub>).** In 1990, one more **CsI**-based scintillator was discovered at the Institute for Single Crystals — a **CsI(CO<sub>3</sub>)** single crystal was grown from the melt that additionally contained  $\text{Cs}_2\text{CO}_3$  [30]. Its optical and scintillation properties have been studied: absorption spectra, photo- and radioluminescence, luminescence excitation spectra, afterglow intensity in the millisecond range, as well as temperature dependences of the decay time and light output of  $\gamma$ -scintillations  $C_\gamma$  ( $^{137}\text{Cs}$ ,  $E_\gamma =$



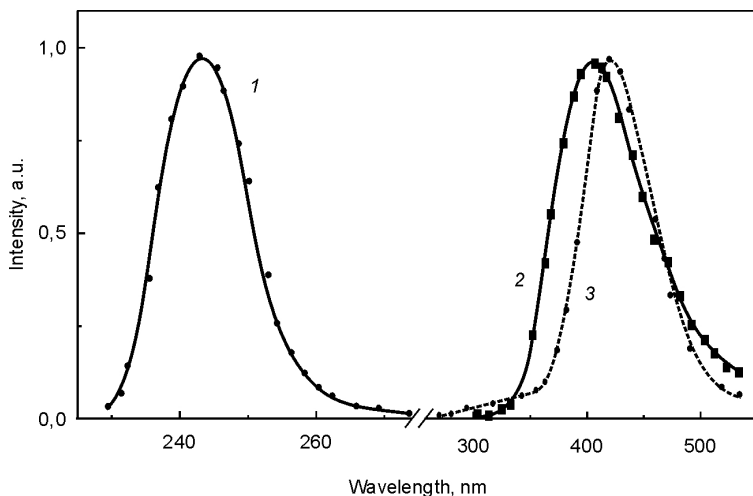


Fig.1.11. Luminescence excitation (1) and  $\gamma$ -luminescence spectra of  $\text{Cs}(\text{CO}_3)$  crystals at 300 K (2) and 80 K (3).

662 keV, and  $^{55}\text{Fe}$ ,  $E_\gamma = 5.9$  keV) and  $\alpha$ -scintillations  $C_\alpha$  ( $^{241}\text{Am}$ ,  $E_\alpha = 5.5$  MeV) in the temperature range 140–373 K. Changes in  $C_\gamma$  and  $C_\alpha$  values in the air atmosphere were also studied. In the vibrational absorption spectra of the studied crystals, bands were found that could be ascribed to  $\nu_2$ ,  $\nu_3$  and  $\nu_4$  of  $\text{CO}_3^{2-}$  ions, with their intensity increasing with higher concentration of  $\text{Cs}_2\text{CO}_3$  introduced to the melt. As it can be seen from Fig.1.11, these crystals displayed luminescence with maximum at 405 nm (300 K) and 420 nm (80 K), which could be excited both by ionizing radiation and photons from the fundamental absorption decay region in the band peaked at 243 nm. Intensity of the said luminescence increases with intensity of the absorption bands due to  $\text{CO}_3^{2-}$  ions and does not depend upon the concentration of Na (which did not exceed  $1.4 \cdot 10^{-4}$  mass % in the crystal studied).

The light output of  $\text{CsI}(\text{CO}_3)$  crystals is 60% with respect to  $\text{NaI}(\text{Tl})$  under  $\gamma$ -excitation (see Table 1.2), and the decay times of gamma- and alpha-scintillations at 300 K are  $\sim 2$   $\mu\text{s}$ . When the temperature is decreased from 375 K to 163 K, decay time rises from 1.7 to 3  $\mu\text{s}$ .  $\text{CsI}(\text{CO}_3)$  crystals are characterized by afterglow of 0.06% in 5 ms and 0.02% in 10 ms after irradiation by X-ray pulses of 10 ms duration.

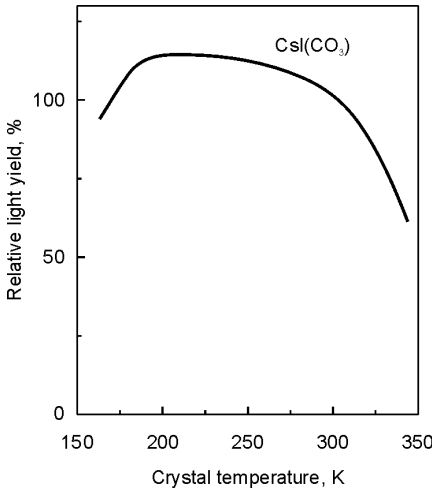


Fig.1.12. Light output of CsI(CO<sub>3</sub>) crystals as function of temperature.

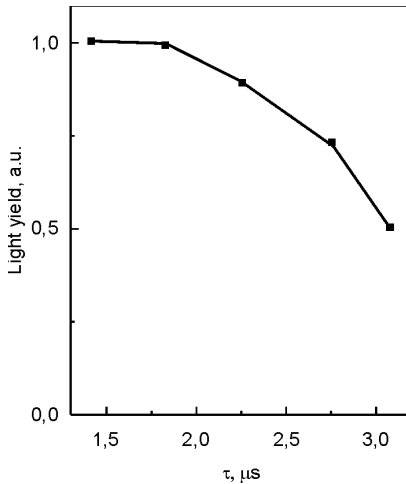


Fig.1.13. Light output and scintillation pulse duration  $\tau$  for CsI(CO<sub>3</sub>) crystals with different activator content.

The values of  $C_\gamma$  ( $^{137}\text{Cs}$ ) and  $C_\alpha$  of CsI(CO<sub>3</sub>) crystals can be as high as 130% and 200% of the respective values for industrially produced CsI crystals. The value of  $C_\gamma$  ( $^{55}\text{Fe}$ ) is 2.5 times higher as compared with CsI(Tl), though 30% lower than observed for NaI(Tl). CsI(CO<sub>3</sub>) crystals, as well as CsI(Tl) crystals, are characterized by stability of their  $C_\gamma$  and  $C_\alpha$  values in the air atmosphere.

In Fig.1.12, the light output of Cs(CO<sub>3</sub>) single crystals is shown as function of temperature. One can see that it remains constant in a rather broad temperature range. Temperature dependences of  $C_\gamma$  and  $C_\alpha$  for Cs(CO<sub>3</sub>) crystals are substantially different from similar dependences for NaI(Tl), CsI(Na) and CsI(Tl).  $C_\gamma$  and  $C_\alpha$  values for the latter crystals decrease by 40–70% upon cooling from 300 K to 213 and 163 K; for Cs(CO<sub>3</sub>), these values remain constant, and their decrease upon heating from 300 to 340 K does not exceed 20%.

In Fig.1.13, values are shown of the light yield and scintillation pulse duration  $\tau$  for Cs(CO<sub>3</sub>) crystals with different activator content. Small variations of the light output are accompanied by scintillation pulse changes from

1.4 to 2.7  $\mu\text{s}$ . The light output of  $\text{Cs}(\text{CO}_3)$  is 50–60% with respect to  $\text{NaI}(\text{Tl})$ . The intrinsic energy resolution remains at the level of 7.0–7.5%, accompanied with high transparence to the activator luminescence. Absorption coefficient at 420 nm does not exceed  $1 \cdot 10^{-2} \text{ cm}^{-1}$ , which allows fabrication of large-sized  $\text{CsI}(\text{CO}_3)$  samples.

Spectral and kinetic parameters of  $\text{CsI}(\text{CO}_3)$  crystals were reported in [80]. Depending upon the ion  $\text{CO}_3^{2-}$  position in the  $\text{CsI}$  lattice, decay time can vary from 1.8 to 3.0  $\mu\text{s}$ , and the light output with respect to  $\text{CsI}(\text{Na})$  is from 80% to 50%, respectively. Thus,  $\text{CsI}(\text{CO}_3)$  crystals appear to be a highly efficient scintillation material with low afterglow and can be successfully used for detection of hard gamma-quanta, as well as soft gamma- and X-ray radiation or alpha-particles in the temperature range from 163 to 340 K [80].  $\text{CsI}(\text{CO}_3)$  single crystals are promising for new types of combined detectors with separation of different radiation types using time characteristics.

#### 1.4. The activator state and scintillation process in AHC

Luminescent properties of inorganic compounds are related to formation of certain structure violations in their crystal lattice. Such violations in grown crystals are created artificially, either by means of partial disproportionation of the matrix and formation of defect sites its crystal lattice, or, more often, by introduction of dopant atoms — activators — into the crystal lattice. Structure defects of different nature that are present in the material give rise to luminescence centers, which take part in radiative annihilation of local electron excitations. Physico-chemical models of the luminescence centers in AHC were discussed in many papers [20, 31–34]; however, there still are many theoretical descriptions and experimental facts that are not in agreement with each other. Let us first consider the classical models of luminescence in activated AHC [31]. Such activated crystals are, in fact, solid solutions of the dopant in the matrix forming the basic lattice [35]. Fig.1.14 shows schematically possible variants of the dopant location in AHC: 1 — an isovalent dopant ion substitutes for a base cation; 2,3 — substitution for two base cations by isovalent dopant ions; 4,5,6 — an isovalent ion is located in the vicinity of a cation vacancy or a dopant anion; 7 — heterovalent substitution for a base cation; 8,9 — a heterovalent dopant ion is located in the vicinity of a cation vacancy; 10 — a cluster formed by two dopant-vacancy dipoles. By the present

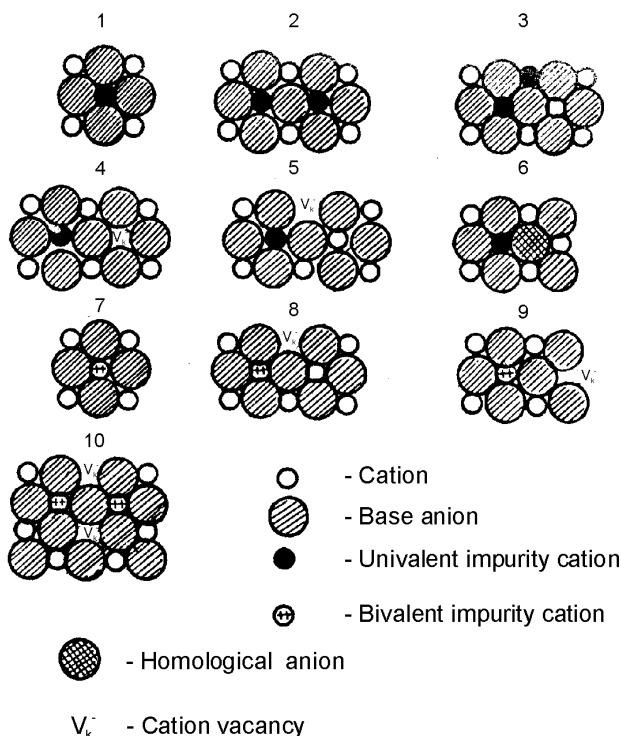


Fig.1.14. Possible location variants of dopant ions in AHC lattice.

time, experimental evidence of their presence in real crystals has been found for all types of centers shown in Fig.1.14.

Considering physico-chemical models of luminescence centers in AHC, one should account for the character of activator introduction into the matrix of the basic crystal. If basic ions and dopants that take part in the substitution process are of similar size, have equal charges and similar states of the valence electrons, as well as similar polarizability, broad range isomorphism of the initial components is possible. In this case, fitting of the dopant into the crystal is of atomic-dispersion nature. If charges are different, vacancies are formed that provide compensation for the charge; they can be located either close to the activator (local compensation) or far from it. In the case of local compensation, vacancies (or other compensating defects) can be

located close to the dopant in different positions, which makes it possible that centers of different symmetry types can exist. In the case of substantial difference between the base and dopant structure, partial isomorphic fitting of the introduced dopant is possible. The dopant is included parallel to certain planar networks of the crystal. In the case of molecular-dispersion distribution of the dopant, individual molecules or complexes are being included [31].

Numerous experimental data, first of all, spectroscopic evidence of correspondence between luminescence centers in crystals and free activator ions, show that dopant ions located on regular sites of the crystal lattice are the main luminescence centers in AHC.

The activated crystals (NaI(Tl), CsI(Tl), CsI(Na), etc.) are obviously solid solutions of the substitution type, with dopants having limited solubility in the matrix lattice [36,8]. It has been shown [36] that, for NaI(Tl), the solubility of TlI in NaI at room temperature is not less than 0.79 mol.%.

The activator content in commonly used NaI(Tl) detectors corresponds to the plateau on the light output vs. dopant concentration plot ( $L(C)$ ) and is by an order of magnitude lower than the experimentally determined solubility limit at room temperature. The  $L(C)$  dependence is the most important characteristic of scintillation systems based on activated crystals, as  $C$  is, in fact, the only controllable parameter in such systems that essentially determines the scintillator properties. Experimentally determined limiting solubility of NaI in CsI (CsI(Na) scintillators) at room temperature is  $2.2 \cdot 10^{-2}$  %.

In systems with limited dopant solubility, such as NaI(Tl), CsI(Tl), CsI(Na), as a result of non-equilibrium crystallization conditions, as well as of thermal dissolution of supersaturated solid solution, dopant microinclusions can appear. The aggregation mechanism of the dopant in AHC is essentially temperature-dependent.

The concentration quenching of the light output and worsening of the energy resolution  $R$  observed for NaI(Tl) crystals grown in vacuum (see Fig.1.15), can be explained [36] by an increase in the number of activator non-uniformities enriched with complex  $(\text{Tl}^+)_n$ -centers, which are several microns in size. For short-range particles (e.g., electrons of 5.9 keV energy) these non-uniformities are macroscopic, which leads to lowering of the detection efficiency and worsening of the “peak-to-valley” parameter. It has been shown that the reason for forma-

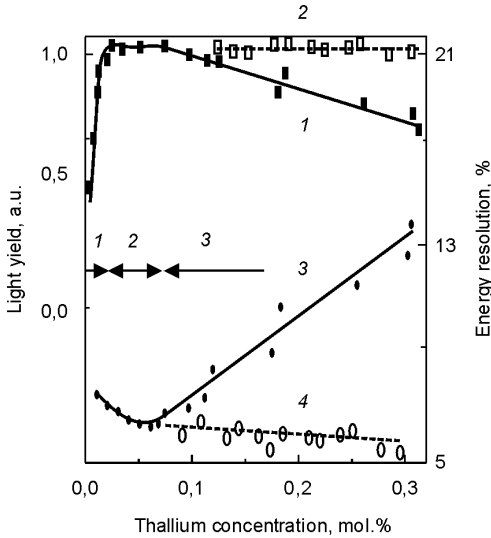


Fig.1.15. Light output (1,2) and intrinsic energy resolution (3,4) as function of TlI concentration for NaI(Tl) crystals grown in vacuum (1,3) and oxygen atmosphere (2,4).

non-uniformities is determined by the fluctuation of their number:

$$R_2 = 5.56 (1 - p)/mp,$$

where  $m = 1/Q$  is the number of non-uniformities in the track,  $p$  is probability for the track to intersect scintillating sections;  $(1 - p)$  is probability for the track to intersect sections with  $L \ll L_{\max}$ . The light output for a crystal with non-uniformities can be expressed as  $L = pL_{\max}$ .

It has been shown in [38] that for scintillation crystals with micro-non-uniformities the squared resolution value is inversely proportional to the energy of  $\gamma$ -radiation, and this dependence is much stronger than for the ideal crystals. This could explain differences in  $R(1/L)$  plots for NaI(Tl) crystals of different quality. With activator concentration increasing, the probability of its non-uniform distribution becomes higher, and effects related to worsening of scintillation parameters should become more obvious. NaI(Tl) crystals grown in oxygen atmosphere (see Fig.1.15), as distinct from those grown in vacuum, are

tion of non-uniformities is spinodal decomposition of the solid solution of TlI in NaI, and non-equilibrium crystallization conditions are a factor that further favors the decomposition process.

In [38], a theoretical description is given for effects of macro- and micro-non-uniformities in activated AHC upon changes in energy resolution. It has been shown that, when non-uniformities of size  $q$  are present in the crystal ( $q \ll e$ , where  $e$  is the ionizing particle track size) and the scintillation yield is lowered ( $L \ll L_{\max}$ ), intrinsic resolution of a crystal with

characterized by more uniform activator distribution over the crystal volume due to more efficient mixing of the melt during the crystallization process. In such NaI(Tl) crystals, no quenching of the scintillation yield (662 keV) is observed while Tl concentration is increased up to 0.3 mol.%, and the energy resolution is continuously improving. It has been established experimentally [36] that spectrometric quality of NaI(Tl) crystals is improved by increasing the activator content, because of weaker contribution to the intrinsic resolution of the part that is related to the inconstancy of specific output  $dL/dx$  [39]. This fact is of substantial significance for understanding of the reasons that limit spectrometric quality of the activated crystals. It proves that by increasing the activator concentration one can not only correct the non-linearity in the low energy region [40], but also to substantially improve the energy resolution of a scintillator.

### ***1.5. Basic concepts of the radioluminescence mechanism in AHC***

Though the history of studies and application of alkali halide scintillators has been rather long, the mechanism of scintillation pulse formation and physics of the radioluminescence process are still not clearly understood. Let us consider some classic concepts of the radioluminescence mechanisms in AHC.

It is known that when a scintillation crystal is excited by ionizing radiation, a radioluminescence pulse emerges, which is the basis of the scintillation process. The general scheme of the radioluminescence process in AHC can be summarized as follows [32,33]. An ionizing particle or quantum, getting into the crystal, does finally generate low-energy electron excitations — electron-hole pairs and excitons. Migrating over the lattice, the electron excitations transfer their energy to luminescence centers, bringing them into excited states. Transition of the luminescent center back to the ground state (relaxation) is accompanied by emission of photons. According to this scheme, the whole process can be divided into three stages: generation stage, migration stage, and intra-center stage.

The generation stage (i.e., generation of low-energy excitations in the lattice) includes energy transformation processes that start when an ionizing particle as a quantum enters the crystal and finish when electrons, holes and excitons are created. The energy of a fast charged

particle that is decelerated in the crystal is used for ionization and excitation of atoms.

If transformation of the charged particle energy in the crystal is of a cascade character, the average energy of electron excitations is lowered. The latter determines the character of the most probable physical processes occurring in the excited crystal. A peculiar feature of the generation stage is its very fast character — its duration does not exceed  $10^{-10}$  s.

The migration stage is much slower — by an order of magnitude, as compared with the generation stage. In the process of migration, electrons can get localized for a certain time on intrinsic and dopant-induced lattice defects; as for holes and excitons, they can be auto-localized at low temperatures. These intermediary localizations, not lowering the stationary radioluminescence yield, make the scintillation pulses much longer, which leads to decreases in the scintillation pulse amplitude. Thus, so-called “inertia losses” appear, which are typical for scintillators.

At present, it is generally accepted that energy transfer to luminescence centers in AHC is carried out by the electron-hole mechanism [51], though exciton mechanism is also considered [52]. Contribution of the latter is thought to be negligibly small, which is primarily due not to low transfer efficiency of the exciton energy to luminescence centers, but to a very small number of excitons generated by the ionizing radiation at room temperature. Depending upon the sequence of charge carriers falling onto a luminescence center, one can distinguish between the electron-hole and hole-electron recombination luminescence.

In Fig.1.16, electron and hole localization and recombination processes in AHC are shown schematically [33]. Recombination processes are: 1 — electron-hole recombination luminescence without an intermediary electron capture; 2 — electron-hole recombination luminescence with an intermediary electron capture; 3 — hole-electron recombination luminescence (non-relaxed holes); 4 — hole-electron recombination luminescence (relaxed holes); recombination of genetic electron-hole pairs. The capture processes are: 6 — capture on the electron activator; 7 — capture on the activator of a non-relaxed hole; 8 — hole autolocalization; 9 — capture on the autolocalized hole activator. Recombination processes 1 and 3, which are due to non-relaxed holes and electrons falling onto the luminescence center without intermediary localization



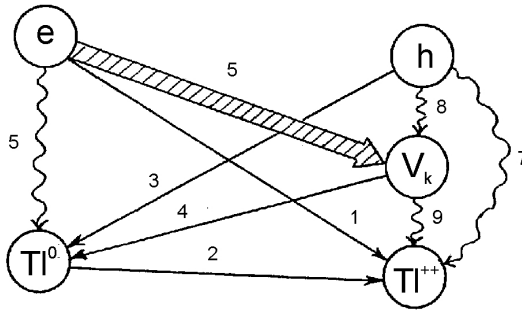


Fig.1.16. Carrier localization and recombination processes in AHC [33] (explanations given in the text).

on shallow traps, are very fast (go practically without retardation), therefore not contributing to the scintillation pulse.

Reactions 2 and 4, which are related to thermally activated processes, can in principle be too slow at room temperature or below. It has been found for NaI(Tl) crystals that both reactions (2 and 4) are sufficiently fast and do contribute to the scintillation pulse at room temperature.

The final stage of the radioluminescence processes in AHC (called also “intra-center stage”) is recombination of the charge carriers on the luminescence center, which brings the center into an excited state, and subsequent radiative transition of the center into the basic state. Thus, spectral composition of radioluminescence is determined by characteristics of the luminescence center (see Chapter 1.6).

In the region of room temperatures, quantum yield of the intra-center stage (i.e., probability of radiative transition of a center to the basic state) is close to 1. Experimentally determined values of the absolute quantum yield for the best NaI(Tl) samples can reach  $0.83 \pm 0.07$  [53].

### 1.6. Structure of luminescence centers and luminescence activation in AHC

Luminescence mechanism in AHC is commonly considered, following Kroger [42], in terms of the excitation and relaxation type luminescence that can be either “direct”, i.e., of intra-center nature, or “indirect”, i.e., activator-related.

In the case of direct activation, absorption and excitation spectra are specific for a given activator and are due to radiative transitions

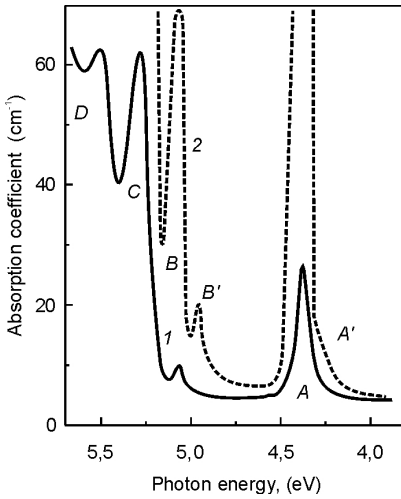


Fig.1.17. Absorption spectra of KI(Tl) crystals containing  $2 \cdot 10^{-3}$  (1) and  $4.5 \cdot 10^{-2}$  (2) mol.% Tl at 77 K.

between its energy levels. The direct activation of luminescence is observed in AHC with a broad band gap and rather small step between energy levels of the activator. Examples of systems with direct activation are AHC doped with mercury-like ions [36]. Their outer electron shell configuration is  $s^2$  (in the excited state —  $sp$ ). These configurations correspond to the basic level  $^1S_0$  and a set of excited levels:  $^1p_1$ ,  $^3p_0$ ,  $^3p_1$ ,  $^3p_2$ . In the cubic symmetry field, the transitions allowed are  $^1S_0 \rightarrow ^3p_1$  (band A) and  $^1S_0 \rightarrow ^1p_1$  (band C), and in the tetragonal symmetry field, in addition,  $^1S_0 \rightarrow ^3p_2$  (band B). The  $^1S_0 \rightarrow ^3p_0$  transition is allowed only in lower symmetry

fields. There exists a genetic relationship between absorption bands of AHC containing Hg-like ions and the corresponding transitions in the free activator ions. In absorption spectra of AHC doped with Hg-like ions, A-, B- and C-bands are observed. In the luminescence excitation spectra, in addition, a D-band is observed, located at the base exciton absorption edge (Fig.1.17).

Under excitation in A-, B-, C absorption bands, in the luminescence spectra of activated AHC at room temperature only the A-luminescence band is observed, which is due to non-radiative transitions  $^1p_1 \rightarrow ^3p_1$ ,  $^3p_2 \rightarrow ^3p_1$ . In addition, in the A absorption band at low temperatures the long-wave luminescence is also excited, which can be related to D-radiation.

With higher activator concentrations, AHC spectral characteristics are changed: additional absorption and emission bands appear, which are related to complex activator centers (pairs, trios, etc.). In NaI(Tl) single crystals, at least three types of centers exist that are created by  $Tl^+$ -ions, as well as  $(Tl^+)_2^-$  and  $(Tl^+)_n$ -forms [41]. Absorption bands of these centers are shifted to the long-wave spectral region as the

Table 1.4. Activator absorption and emission band maximums and photoscintillation times for crystals NaI(Tl).

Center type	$\lambda_m^x$ , nm	$\lambda_m^I$ , nm	$\tau_{in}$ , ns
Tl <sup>+</sup>	293	415	205, 200
		330	10 (77 K)
(Tl <sup>+</sup> ) <sub>2</sub>	260, 306	428	—
		330	7
(Tl <sup>+</sup> ) <sub>n</sub>	268	450	—
	315–320	—	—

activator composition becomes more complex. Positions of maximums of the long-wave absorption bands  $\lambda_m^x$  that are due to these centers, luminescence excited therein ( $\lambda_m^I$ ), and duration of the intra-center emission  $\tau_{in}$  are given in Table 1.4.

Later, the  $\tau_{in}$  values under excitation in absorption bands due to activator centers were measured for crystals in which the activator content corresponded to the end of the light output *vs.* TlI concentration dependence plateau ( $7 \cdot 10^{-2}$  % Tl), where complex centers were not yet formed, and in the concentration quenching range *L*, when the presence of complex centers is reflected in radioluminescence ( $5 \cdot 10^{-1}$  % TlI) (Table 1.5).

The values of  $\tau_{in}$  for Tl<sup>+</sup>, (Tl<sup>+</sup>)<sub>2</sub>, (Tl<sup>+</sup>)<sub>n</sub> as compared with  $\tau_{\gamma} = 230$ –250 ns, show, accounting for data of Table 1.4, that the scintillation process, alongside with Tl<sup>+</sup>-centers, can also involve complex (Tl<sup>+</sup>)<sub>n</sub>-centers, owing to re-absorption of the short-wave radiation emitted by Tl<sup>+</sup>-centers. The presence of (Tl<sup>+</sup>)<sub>n</sub> in the lattice leads to worsening of the energy transfer conditions from the lattice to luminescence centers, thus lowering the light output. It has been shown that long-wave luminescence is related to thallium aggregates (Tl<sup>+</sup>)<sub>n</sub> with  $2 < n < 6$  [43]. Thus, returning to Fig.1.15, we can state that, irrespective of the excitation density, the principal role in the scintillation process is played by Tl<sup>+</sup>-centers. Saturation of *L*(*C*) is ensured by sufficient concentration of Tl<sup>+</sup>-centers for a given excitation density. Concentration quenching of *L* in vacuum-grown crystals is related to spinodal decomposition of the solid solution and increased volume of the fraction containing thallium aggregates.

In the case of indirect luminescence activation, spectral characteristics of AHC are weakly dependent upon the activator dopant,

Table 1.5. Intra-center emission times  $\tau_{in}$  under excitation in activator absorption bands for  $Tl^+$ ,  $(Tl^+)_2$ ,  $(Tl^+)_n$ -centers in crystals  $NaI(Tl)$

Thallium iodide (TlI) concentration, %	$\lambda_{ex}$ , nm	$\lambda_{in}$ , ns
$7 \cdot 10^{-2}$	291	200
	260	154
	313	200
$5 \cdot 10^{-1}$	291	254
	313	250

being specific for each basic compound. Luminescence is caused by radiative annihilation of bonded or localized excitations of the halogen ( $X_2^{2-}$ ) close to lattice defects (dopant or structural). Excitation of this luminescence occurs at the falling section of the fundamental exciton absorption. Localization centers of exciton excitations can be represented by vacancies of the opposite sign — dipolons, as well as isolated (single) vacancies.

According to [44], evidence of indirect activation is observed in crystals with isovalent dopants when the dopant cation (anion) has larger ionization potential as compared with the matrix cation (anion), with the band gap width lower than in the basic material. A typical example of system with activation of indirect type is  $CsI(Na)$ , where luminescence results from radiative annihilation of excitons located close to  $Na$  [45,46]. Indirect excitation of luminescence is also characteristic for deformed [47] and not deformed [37]  $CsI$  crystals. This class of crystals should probably also include  $CsI(Ca)$  and  $CsI(CO_3)$ . In Table 1.6, luminescence characteristics are given for pure and activated  $CsI$  crystals.

A comprehensive study of the effects of  $Cs_2(CO_3)$  activator at different concentrations and high-temperature treatment upon radio-luminescence spectra, light output, scintillation pulse duration and vibrational absorption of  $CsI(CO_3)$  crystals was reported in [48]. Two types of centers were found to be responsible for scintillations. Centers I corresponded to radioluminescence at 395 nm and  $\tau = 1.4 \mu s$ , and centers II — 430 nm and  $\tau = 3.4 \mu s$ , respectively. It was assumed that Center I included the  $CO_3^{2-}$  complex — an anion vacancy, while centers II were due to cesium oxides — products of partial thermal decomposition of the activator dopant  $Cs_2(CO_3)$  in the melt of  $CsI$ .

Table 1.6. Luminescent characteristics of pure and activated crystals CsI [37]

Crystal	Luminescence				
	Photoexcitation			$\gamma$ -excitation	
	Excitation, nm	Emission, nm	Decay time, ms	Emission, nm	Decay time, ms
CsI (undoped)				307 440	0.01 3
CsI, $\epsilon = 14\%$	242	430, 460, 530		307, 440, 530	
CsI(Na)	238	425	0.4	425	0.6; 1.8
CsI(Ca)	240	415	0.53	307, 420	0.01, 1.0
CsI(Sb)	241	415		307	0.01
	262	545		420	0.98; 2.7
				550	1.6; 4.8
CsI(Bi)	240	420		307	0.011
	262	550		420	1
				550	3

It should be noted that in recent years some evidence appeared that in AHC doped with mercury-like Tl or In ions luminescence can also be caused by radiative transitions in excitons localized close to the activator [49,50].

### ***1.7. Application fields of AHC-based scintillators: present-day state and further prospects***

The scintillation method of ionizing radiation detection using AHC has been described and reviewed in a number of publications, where general information can be found on development of new AHC-based scintillation materials and current situation in their production [18,20,32,33,54–58]. The application field of AHC is so broad, and their variety is so great, that the problem of choosing the best suitable scintillation material and optimum detector design often becomes very difficult. In Chapter 1.3 we showed that each of the scintillation materials has its advantages and drawbacks and can be best suited for certain specific purposes, accounting for specific application conditions and requirements.

By the present time, a list of most common application fields of scintillation detectors based on NaI and CsI crystal matrices has been

more or less defined: high energy physics, non-destructive testing (defectoscopy), medicine, environmental monitoring, astrophysics [77,78]. Thus, NaI(Tl), CsI(Tl) and CsI(Na) crystals are widely used in scintillation counters for detection of gamma-radiation. In high energy physics, CsI(Tl), CsI(Na) and non-activated CsI are used for calorimetry of elementary particles.

Successful search for materials to be used in “fast” detectors, which would ensure not only faster radiation detection, but also time separation of scintillation pulses, resulted in creation of a new generation of instruments based on new types of detection systems.

In 1987–1988, possible uses of undoped CsI single crystals as fast scintillators were reported [59–61]. This achievement opened ways to creation of electromagnetic calorimeters for high energy physics [62,63], hodoscopic detection systems [64], positron emission tomographs [65]. Since 1991–1992, undoped CsI crystals have been used as fast scintillators in many R&D projects carried out by international high energy physics centers. Specific scintillation properties of undoped CsI make it a very promising material just for its application in electromagnetic calorimeters [63, 66–68].

Though experiments in high- and medium-energy physics are quite various, all of them are, as a rule, related to accumulation of large radiation doses during the operation period. Therefore, broader use of CsI crystals in this field requires further improvement of their radiation stability [69].

Possibilities were studied of using different types of detectors based on NaI(Tl), CsI(Tl) single crystals, as well as CsI(Tl) films, for detection of X-ray and long-wave gamma-radiation accompanying the decay of alpha-emitting  $^{239}\text{Pu}$  and  $^{241}\text{Am}$  [70].

In [71], a real time scale  $\gamma$ -telescope was reported, designed for detection, visualization and analysis (determination of intensity, spectral composition and angular coordinates) of localized areas of radioactive contamination of the environment by point and planar  $\gamma$ -emitting sources. The  $\gamma$ -telescope comprises a position-sensitive detector made of polycrystalline NaI-based scintillator. For density monitoring of light media (snow, ice, peat, plastics, etc.), a digital radioisotope density meter has been developed, in which NaI(Tl) single crystals are used as material for the stabilized scintillation detection block [72].

Table 1.7. Scintillation parameters of CsI and CsI(Na) activated by In or Tl.

Characteristics	CsI (undoped)	CsI(Na)	CsI(Tl)	CsI(In)
$\tau$ , ns	2...16	630	900	2500
$\lambda_m$ , nm	305	420	540	550

At present, combined scintillation detectors (“phoswich” detectors) [73] are among the most efficient devices for separation of radiation types over characteristic times of scintillation decay. To achieve such separation, two different scintillators are used in combination with one another.

In [8], a new approach was proposed for making a combined detector on the basis of one crystal. The idea consists in diffusion coloring of a scintillation material in the activator vapor, with the surface-adjacent layer thus formed playing the role of a second detector in combination with the initial matrix. An important advantage of the diffusion activation method is the use of one and the same material in the doped and undoped forms, which solves the problem of optical matching between different scintillator materials. For this purpose, CsI crystals were used — “pure” and doped with Na ( $\sim 0.25\%$ ). The diffusion coloring process was carried out in sealed quartz ampoules by prolonged isothermal annealing at  $550^\circ\text{C}$  under vapor of high purity metal indium. The matrix chosen allows realization of different luminescence types. Undoped CsI and CsI(Na) are widely used materials for standard “fast” scintillation detectors. Scintillation mechanisms in these crystals are based upon intrinsic (CsI) and activator-related (CsI(Na)) luminescence. Introduction of such activators as In or Tl can substantially change the scintillation characteristics (Table 1.7). The strongest effects are observed when the crystal is doped with indium ions. Maximum concentration of In in the crystal lattice is determined by the In solubility limit, and the activated zone profile — by decomposition of the supersaturated solid solution.

The optimum layer thickness is 3–4 mm. This is quite sufficient for indium-doped CsI(Na) to be an efficient material for alpha-gamma discrimination. Characteristic luminescence spectra measured for different parts of diffusion-activated crystals are presented in Fig.1.18.

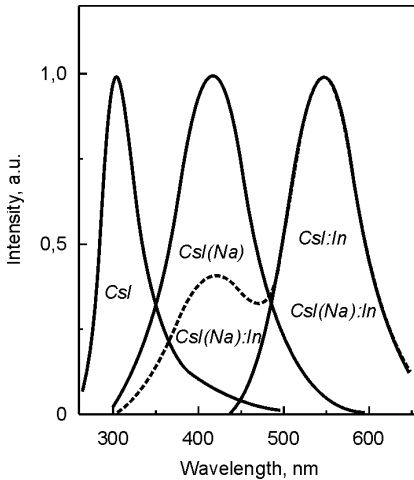


Fig.1.18. Luminescence spectra of diffusion-activated CsI and CsI(Na) crystals.

In recent years, there has been a growing interest in detecting devices that could operate under severe thermomechanical conditions, e.g., for geophysical applications (environment temperature changes from dozens below zero to hundreds above zero degrees Centigrade, vibration and shock loads, aggressive media, etc.) [54, 74–76]. Up to the present time, NaI(Tl) single crystals has been generally considered among materials suitable for these purposes [74]. The relevant parameters are: light output, energy resolution (at normal and higher temperatures), density, etc. An important drawback of NaI(Tl), which is

especially strongly felt in such applications, is its hygroscopicity. If working temperatures are not very high (not higher than 130°C), CsI(Tl) is a good alternative to NaI(Tl), ensuring higher detection efficiency of gamma-radiation and being less hygroscopic. It is known that under thermal influence scintillator crystals tend to pass over to a complex three-dimensionally stressed state, which lowers their mechanical strength. Therefore, improvement of thermal strength and shock resistance properties of activated AHC is in close connection with the growth technology, as the dopant should be uniformly distributed over the crystal volume. Further studies are needed of AHC thermophysical properties from the point of view of the activator effect upon the temperature linear expansion coefficient of the scintillator material, as non-uniformity of the activator distribution makes its value unstable, leading to high brittleness at room and lower temperatures [54]. Another important problem is caused by different materials in the detector having different thermal linear expansion coefficients, as the resulting mismatches can reach critical values making the detector partially or fully inoperable.



In the monograph [54], problems concerning scintillation detectors functioning under severe operation conditions are considered in detail. Ways are described to improve stability of AHC-based detectors, and data are reviewed on materials suitable for detectors and detection blocks with high vibration and thermal stability.

## REFERENCES

1. *Knox R.S., Teegarden K.J.* Electronic excitation of perfect alkali halide crystals // In: Physics of color centers. New York-London, Academic Press., 1968. – P.5–51.
2. *Laudise P., Parker R.* Crystal growth. Moscow: Mir, 1974. – 541 p.
3. *Wilke K.T.* Growing of crystals. Leningrad: Nedra, 1977. – 600 p.
4. *Eidelman L.G., Goriletsky V.I., Protsenko V.G.et al.* Automated pulling from the melt – an effective method for growing large halide single crystals for optical and scintillation applications // J. Cryst. Growth. –1993. – **128**. – P.1059–1061.
5. *Goriletsky V.I., Nemenov V.A., Protsenko V.G.et al.* Automated pullins of lagre alkali halide sinsle crystals. // J. Cryst. Growth. – 1981. – **52**. – P.509–519.
6. *Eidelman L.G., Goriletsky V.I., Nemenov V.A.et al.* Automated growing of large single crystals controlled by melt level sensor // J. Cryst. Res. and Technol. – 1985. – **20**. – P.167–172.
7. Harshow Radiation Detector, Filtrol Scintillation Phosphor Catalogue, 1984.
8. *Shlyakhturov V.V.* Fast scintillators on the basis of pure and doped crystals Csl. – Ph.D. (Cand.phys.-math.sci.) dissertation.- Kharkov: Inst.Single Cryst., 1996. – 192 p.
9. *Kisil' I.I., Krainov N.I., Stroilova D.L.* On cellular structure of single crystals NaI(Tl) // In: Monokristally i tehnika. - Kharkov: VNIIM, 1970. – No.2.– P.25–29.
10. *Kisil' I.I., Krainov N.I., Zolotovitskaya E.S., Fidel'man B.M.* Growth of CsI(Tl) single crystals in a horizontal rotating ampoule // In: Monokristally i tehnika. – Kharkov: VNIIM, 1971. – No.5.– P.8–11.
11. *Utts B.K., Spagno S.E.* An investigation on the characteristics of “pure” CsI // IEEE Trans. Nucl. Sci. – 1990. – **37**, No.2. – P.134–138.
12. *Zaslavskii B.G., Eidelman L.G.* State and prospects of development of automatized methods for pulling from the melt of scintillation alkali halide crystals of very large size // Abstr. Inter-State Conf. “Scintillatory-93”.– Kharkov: Inst.Single Cryst., 1993.– Part 1.– p.5–6.

13. *Zaslavskii B.G., Stadnik P.E., Danilenko E.V. e.a.* Invention No.1122014, USSR, C30B15/00.
14. *Stadnik P.E., Suzdal' V.S., Zaslavskii B.G.* On automatization of preparation processes of crystals of large sizes // *Poluchenie i svoistva kristallov*. Kharkov: VNIIM. – 1986. – No.17. – p.91–105.
15. *Hofstadter R.* Alkali halide scintillation counters // *Phys.Rev.* 1948. – **74**, No.1. – P.100–101.
16. Data sheets of Harshaw “Scintillation Detectors”. Saint-Gobain, Ceramiques Industrielles. 1992.
17. Catalogue of the Institute for Single Crystals “Scintillation. Materials. Detectors. Research, development, production”. 1994.
18. *Tsirlin Yu.A., Globus M.E., Sysoeva E.P.* Optimization of gamma-radiation detection by scintillation crystals. – Moscow: Energoatomizdat, 1991. – 152 p.
19. *Kovaleva L.V., Gurevich N.Yu., Vinograd E.L. e.a.* Scintillation detectors on the basis of CsI(Tl) for computer tomography // *Pribory i tekhnika eksperimenta*. – 1990. – **3**. – p.198–210.
20. *Panova A.N.* Inorganic scintillators // *Izv. AN SSSR, ser. Phys.* – 1985. – **49**, No.10. – p.1994–1998.
21. *Zagariy L.B., Vyday Yu.T., Tsirlin Yu.A.* Study of the concentration dependence of the light output of detectors based on NaI(Tl) scintillators in the region of X-ray and soft gamma-radiation // *Opticheskie i scintillatsionnye materialy* (Kharkov: VNIIM). – 1982. – No.9. – p.89–91.
22. *Grudskaya L.E., Tsirlin Yu.A., Serebrova N.N., Zakharin Ya.A.* On temperature dependences of the light output of alpha- and gamma-scintillations for crystals CsI(Tl), CsI(Zn), NaI(Tl) and LiI(Eu) // *Zhur.prikladnoi spektroskopii*. – 1966. – **5**, No.5. – p.655–659.
23. *Vinograd E.L., Tsirlin Yu.A., Gurevich N.Yu. e.a.* Effects of temperature upon intrinsic energy resolution of crystals NaI(Tl) // *Pribory i tekhnika eksperimenta*. 1980. – No.3. – p.67–68.
24. *Tsirlin Yu.A., Vinograd E.L., Gurevich N.Yu. e.a.* Effects of temperature on radiation coloring of detectors based on thallium-doped sodium iodide crystals // *Atomnaya energiya*. – 1978. – **45**, No.1. – p.69–71.
25. *Shamovskii L.M.* Crystallophosphors and scintillators in geology. – Moscow: Nedra, 1985.
26. *Bonanomil J., Rossel J.* Scintillation des particules dans CsI // *Helv. Phys. Acta*. – 1952. – **25**. – P.725.
27. *Brinckmann P.S.* CsI(Na) scintillation crystals // *Phys. Lett.* – 1965. – **31**, No.4. – P.305.

28. *Panova A.N., Shakhova K.V., Shiran N.V.* Optical properties of CsI crystals with admixtures of alkali metals // *Izv.AN SSSR, ser. Phys.* – 1967. – **31**, No.5. – p.859–863.
29. *Gavrilov V.V., Gektin A.V., Buravleva M.G.* Exciton-like luminescence of CsI crystals // In: *Scintillation Materials.*– Kharkov: VNIIM.– No.20.– p.22–25.
30. *Vinograd E.L., Goriletskii V.I., Panova A.N. et al.* Optical and scintillation properties of CsI crystals with addition of  $\text{Cs}_2\text{CO}_3$  // *Optika i spektroskopiya* – 1990. – **69**, No.5. – p.1185–1186.
31. *Parfianovich I.A., Penzina E.E.* Electron color centers in ionic crystals. – Irkutsk: Vostochno-Sibirskoye knizhnoe izdatel'stvo, 1977.– 208 p.
32. *Aluker E.D., Lusis Yu.Yu., Chernov S.A.* Electron excitations and radio-luminescence of alkali halide crystals. – Riga: Zinatne, 1979. – 251p.
33. *Aluker E.D., Gavrilov V.V., Deych F.G., Chernov S.A.* Fast processes in alkali halide crystals. – Riga: Zinatne, 1987. – 183p.
34. *Aluker N.L.* Processes of energy transfer to luminescence centers in alkali halide scintillators. Ph.D. (Cand.phys.-math.sci.) dissertation.-Sverdlovsk, 1985.
35. *Gurevich A.M.* Introduction of physical chemistry of crystallophosphors. – Moscow: Vysshaya shkola, 1971. – 336p.
36. *Kudin A.M.* The role of activator defects in changes of structure and scintillation properties of crystals NaI(Tl). Ph.D. (Cand.phys.-math.sci.) dissertation. – Kharkov: Inst.Single Cryst., 1996.
37. *Bondarenko S.K., Gerasimchuk L.I., Goriletsky V.I. et al.* Production of the large-scale scintillate single crystals CsI(Tl) // *Book of Abstracts (SCINT-97) inorganic scintillators and their applications.* – Shanghai: Shanghai Institute of Ceramics. – 1997. – P.73.
38. *Tsirlin Yu.A., Mokhir E.P.* Effects of micro- and macro non-uniformities upon scintillator resolution // In: *Monokristally, scintillatory i organicheskie luminofory.* Kharkov: VNIIM.– 1967.– No.1. – p.67–71.
39. *Tsirlin Yu.A.* Spectrometric scintillation detection blocks // In: *Fizika i khimiya organicheskikh i neorganicheskikh materialov.* – Kharkov: Inst.Single Cryst., 1987. – No.6. – p.8–20.
40. *Zagariy A.B., Vydai Yu.T., Tsirlin Yu.A.* Studies of concentration dependence of the light output of NaI(Tl)-based detectors in the region of X-ray and soft gamma-radiation // In: *Opticheskie i scintillacionnye materialy.* – Kharkov: VNIIM, 1982. – No.9. – p.89–90.
41. *Panova A.N., Mustafina R.H.* Studies of the effects of activator concentration upon optical and scintillation properties of NaI(Tl) crystals // In: *Monokristally i tekhnika.* – Kharkov: VNIIM, 1970. – No.1. – p.81–87.

42. *Kroger F.A.* Some aspect of the luminescence of solids // New York-Amsterdam-London-Brussel. 1948. – 419 p.
43. *Fortana M.B., Van Sciver W.I.* Energy transfer and optical properties of  $Tl^+$ -centers in  $NaI(Tl)$  crystals. // *Phys. Rev.* – 1968. – **168**, No.3. – P.960–964.
44. *Valbis Ya.A.* Luminescence of alkali halide crystals due to local annihilation of localized exciton-like excitations. – Ph.D. (Cand.phys.-math.sci.) dissertation. – Riga, 1966.
45. *Panova A.N., Shiran N.V.* Luminescence centers in  $CsI(Na)$  // *Izv. AN Latv.SSR, ser. Phys.and techn.sci.* – 1972. – No.2. – p.118–122.
46. *Panova A.N., Shakhova K.V., Shiran N.V.* Optical properties of a new scintillation material  $CsI(Na)$  // *Zhurn.prikladnoi spektroskopii.* – 1967. – **6**, No.4. – p.549–552.
47. *Gektin A.V., Shiran N.V., Serebryannyi V.Ya. e.a.* The role of vacancy defects in luminescence of  $CsI$  crystals // *Optika i spektroskopiya.* – 1992. – **72**, No.5. – p.1061–1063.
48. *Vinograd E.L., Goriletskii V.I., Panova A.N. e.a.* Optical and scintillation characteristics of  $CsI$  crystals with  $CO_3^-$  admixture // *Ibid.* – 1993. – No.5. – p.1185–1186.
49. *Nagirnyi V., Zazubovich S., Zepelin V. et al.* A new model for the visible emission of the  $CsI(Na)$  crystal. // *Chem. Phys. Lett.* – 1994. – **277**. – P.533–538.
50. *Nagirnyi V., Stolovich A., Zazubovich S. et al.* Peculiarities of the triplet relaxed excited-state structure and luminescence of  $CsI(Tl)$  crystal // *J. Phys.: Condens. Mater.* – 1995. – **7**. – P.3637–3653.
51. *Lushchik Ch.B., Soovik T.A.* Some problems in physics of inorganic scintillators // *Proc. IFA AS Est.SSR.* – 1966. – No.34. – p.68–88.
52. *Lushchik Ch.B., Liydy G.G., Soovik T.A., Yaek I.A.* On the mechanism of AHC luminescence under excitation by ultraviolet and hard radiation // *Ibid.* – 1961. – No.15. – p.103–126.
53. *Vishnevskii V.N., Pizirailo N.S.* Effects of oxygen-containing admixtures and X-ray radiation on the value of absolute quantum yield and structure of photoluminescence excitation spectra of  $NaI(Tl)$  crystals // *Ukr.Fiz.Zhurnal.* – 1967. – **12**, No.9. – p.1466–1473.
54. *Grinev B.V., Seminozhenko V.P.* Scintillation detectors of ionizing radiation for severe operation conditions. – Kharkov: Osnova, 1993. – 155 p.
55. *Tsirlin Yu.A.* Light collection in scintillation counters. – Moscow: Atomizdat, 1975. – 264 p.

56. *Lushchik I.B., Lushchik A.I.* Decay of electron excitations with formation of defects in solids. – Moscow: Nauka, 1969. – 264 p.
57. *Karas' V.R., Sysoyeva E.P.* Scintillation materials and detectors on their base. – Cherkassy: ONIITEKhim, 1989. – 25 p.
58. *Gusev E.A., Lukyanenko E.A., Chelnokov V.P.* Home-made combined and semiconductor detectors for X-ray tomography // *Defektoskopiya*. – 1992. – No.2. – p.21–32.
59. *Kubota S., Sakuragi S., Hashimoto S., Ruan J.* A new scintillation material: pure CsI with 10 ns decay time // *NIM*. – 1988. – **A268**, No.1. – P.275–277.
60. *Kubota S., Muracami H., Ruan J. et al.* A new scintillation material: CsI and its application to positron sensitive detectors // *NIM*. – 1988. – **A273**, No.2–3. – P.645–649.
61. *Shpilinskaya L.N., Kudin A.V., Mitichkin A.I., Charkina T.A.* Formation of radiation defects in CsI crystals containing hydroxyl and carbonate ions // *Book of Abstracts (SCINT-97) inorganic scintillators and their applications*. – Shanghai: Shanghai Institute of Ceramics. – 1997. – P.77.
62. *Sasao N.* A pure CsI-detector // *International Bulletin* 1988. – No.4. – P.101.
63. *Woody C.L., Levy P.W., Kierstead J.A.* Readout techniques and radiation damage of undoped cesium iodide // *IEEE Trans. Nucl. Sci.* – 1990. – **37**, No.2. – P.492–499.
64. *Gektin A.V., Gorelov A.I., Rykalin V.I. et al.* CsI-based scintillators in detector system // *NIM*. – 1990. – **A294**, No.3. – P.591–594.
65. *Tanaka E.* Recent progress on single photon and positron emission tomography from detectors to algorithms // *IEEE Trans. Nucl. Sci.* – 1987. – **34**, No.1. – P.313–320.
66. *Winstein B.* A pure CsI calorimeter for the study of Kaon decay // in: *Heavy scintillators for scientific and industrial applications*, Ed. F.De Notaristefani, P.Lecoq, M.Schneedans. Trontieres, France. 1992. – P.279–283.
67. *Roodman A.* Radiation damage and scintillation uniformity in pure CsI crystals for the KTeV electromagnetic calorimeter // In: *Heavy scintillators for scientific and industrial applications*, Ed. F.De Notaristefani, P.Lecoq, M.Schneedans. Trontieres, France. 1992. – 479–486.
68. *Aul'chenko V.M., Baibusinov B.O., Bondar' A.E. e.a.* Large electromagnetic calorimeters made in the Nuclear Physics Institute on the basis of cesium iodide crystals // *Abstr. Inter-State Conf. "Scintillatoty-93"*. – Kharkov: Inst.Single Cryst., 1993.– Part 2. – p.13–14.
69. *Woody C.L., Kierstead J.A., Levy P.W., Stoll S.* Radiation damage in undoped CsI and CsI(Tl) // *IEEE Trans. Nucl. Sci.* 1992. – **39**, No.4. – P.524–531.

70. *Vydai Yu.T., Zagariy L.B., Sysoeva E.P., Tarasov V.A.* Detectors of X-ray and long-wave gamma-radiation for determination of alpha-emitters // Abstr. Inter-State Conf. "Scintillatoty-93". – Kharkov: Inst.Single Cryst., 1993. – Part 2. – p.53.
71. *Gurov A.Yu., Per'kov A.I., Fedotov S.N., Sharak M.P.* Gamma-telescope for detection, visualization and determination of parameters of radioactive contamination zones in the environment // *Ibid.*, p.124.
72. *Anshakov M., Gurinovich V.I., Zmushko Yu.L., Chudakov V.A.* Radioisotope density meter // *Ibid.*, p.126–127.
73. *Sharma R.C., Krishnamachari G., Haridasan T.K. et al.* A large-area phoswich for measurements of low level of low-energy photon emitters // NIM. – 1975. – **130**, No.1. – P.305–311.
74. *Grinev B.V., Rogozhin A.A.* Scintillation detectors for the field nuclear-geophysical equipment: state of art and prospects // Abstr. Inter-State Conf. "Scintillatoty-93". – Kharkov: Inst.Single Cryst., 1993. – Part 2. – p.7–8.
75. *Grinev B.V., Mel'nik V.I.* Promising directions of scintillator detector improvement // *Ibid.*, p.5–6.
76. *Grinev B.V., Mel'nik V.I.* Improvement of thermal strength of scintillation detectors // *Pribory i tekhnika eksperimenta* – 1992. – No.10. – p.114–130.
77. *Kunio Tamai* Electromagnetic calorimeters for KEK B-factory detector // In: Inorganic scintillators and their applications ("SCINT-95"). – 1996. – Delft, The Netherland: Delft University press. – P.62–69.
78. *Moses W.W., Derenzo S.E.* Scintillators for positron emission tomography // In: Inorganic scintillators and their applications ("SCINT-95"). – 1996. – Delft, The Netherland: Delft University press. – P.9–16.
79. *Zaslavsky B., Grinyov B., Suzdal V. et al.* Industrial manufacturing of CsI(Tl) large diameter crystals // Book of Abstracts (SCINT-97) "Inorganic scintillators and their applications". – Shanghai: Shanghai Institute of Ceramics. – 1997. – P.136.
80. *Gorilatsky V.I., Panova A.N., Shakhova K.V. et al.* Properties and applications of a new scintillation material CsI(CO<sub>3</sub>) // *Ibid.*, P.147.
81. *Bondarenko S.K., Sumin V.I., Trofimenko V.V.* Industrial production of large alkali-halide scintillators // *Ibid.*, P.120.

## CHAPTER 2

### SINGLE CRYSTALS OF COMPLEX OXIDES

Main parameters of scintillators based on binary oxides, oxide systems, silicates of yttrium, scandium and rare-earth elements, bismuth zirconosilicates, silicates and germinates, as well as aluminates, vanadates and tungstates of metals are presented in the review [1].

Scintillation properties have been found in binary oxides  $\text{BeO}$ ,  $\text{ZnO}$ ,  $\text{Y}_2\text{O}_3$ ,  $\text{Sc}_2\text{O}_3$  [2–5]. Their scintillation characteristics, optical uniformity, radiation stability and other important properties are largely dependent upon the growth conditions and purity of the initial raw material. The above-listed two-component oxides are “fast” scintillators, with decay times  $\tau < 100$  ns. The luminescence nature in two-component oxides is largely related to the formation of excitons, as well as complex dopant centers of radiative recombination [6–10]. Applications of beryllium oxide are based on a unique combination of its thermal, mechanic, electric and optical properties, accompanied by its intense radioluminescence. For non-activated  $\text{BeO}$  samples, the light output of alpha- and beta-scintillations is 40–75% with respect to  $\text{CsI(Tl)}$ .

Kinetics of the luminescence decay of autolocalized excitons in  $\text{BeO}$  crystals was studied in [149], and the nature of point defects in cationic and anionic sublattice — in [11]. In Fig.2.1, plots are presented that characterize the decay time (“slow” component) for several scintillators as compared with  $\text{BeO}$  (using data given in [1]). Due to small size of the obtained crystals of binary oxides  $\text{BeO}$ ,  $\text{ZnO}$ ,  $\text{Y}_2\text{O}_3$  and  $\text{Sc}_2\text{O}_3$ , their use in scintillator technologies has been very limited.

The class of zirconosilicates includes such compounds as  $\text{Na}_2\text{ZrSO}_5$ ,  $\text{K}_2\text{ZrSO}_5$ ,  $\text{Na}_2\text{ZrS}_2\text{O}_7$ ,  $\text{Na}_2\text{Zr}_2\text{Si}_3\text{O}_{12}$ ,  $\text{Cs}_2\text{ZrSi}_2\text{O}_7$ , etc. The best light output was reported for  $\text{Na}_2\text{ZrSO}_5$  crystals doped with Eu and Tb (15–20% with respect to  $\text{NaI(Tl)}$ ). Zirconosilicates belong to chemically stable scintillators (in particular, they are stable to acids); however, their

efficiency is rather low, scintillations are long, and preparation technology is not adapted for large-scale production [6].

Considering the class of aluminates, attention is to be paid to scintillators based on yttrium-aluminum garnet doped with cerium, praseodymium, scandium, as well as lutetium- or gadolinium-scandium and gadolinium-gallium garnets. A sufficiently “fast” scintillator is  $\text{LiAlO}_2$  ( $\tau = 50$  ns), which is chemically and thermally stable. Cerium-doped gadolinium-scandium garnet is another “fast” scintillator ( $\tau = 100$  ns). The dopant ions (cerium, praseodymium) play the role of recombination luminescence centers in aluminates. In the excitation mechanism, the excitons are involved.

Yttrium-aluminum oxide  $\text{YAlO}_3$  (YAP) is well known in laser technologies. Its activation by cerium allows obtaining of a scintillation material. The light output of  $\text{YAlO}_3\text{-Ce}$  at  $\text{CeO}_2$  concentration of 0.2 mass % is  $\sim 40\%$ ,  $\tau = 28$  ns,  $n = 1.93$ ,  $\lambda_{\text{max}} = 347$  nm (though the value of 390 nm can also be found in literature).  $\text{YAlO}_3\text{-Ce}$  crystals are not hygroscopic, chemically stable and possess high mechanical characteristics. This allows preparation of rather thin samples (50–100  $\mu\text{m}$ ), which is required for production of low-background alpha-spectrometers. A distinctive feature of this material is that its light output is still linearly dependent on energy at high ionization densities. Its radiation resistance is very high —  $\sim 10^8$  rad [12].

Analysis of data presented in [1–12] shows that the most promising oxide scintillators can be found in the following three groups: silicates of yttrium, scandium and rare earth elements; bismuth silicate and germanate; metal tungstates, molybdates and vanadates. They are distinguished by their high thermal, chemical and radiation stability, relatively fast response, and high light output. Therefore,

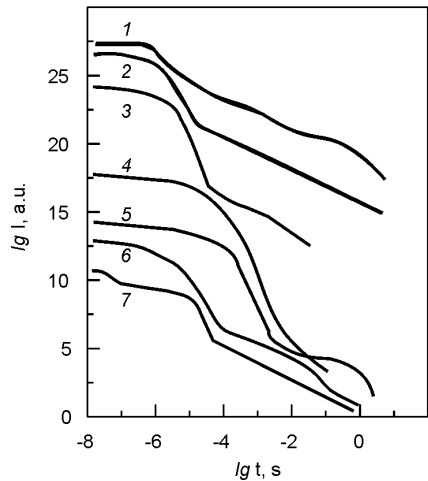


Fig.2.1. Luminescence decay time (slow component): 1 —  $\text{NaI(Tl)}$ ; 2 —  $\text{Bi}_4\text{Si}_3\text{O}_{12}$ ; 3 —  $\text{BaF}_2$ ; 4 —  $\text{CdWO}_4$ ; 5 —  $\text{ZnWO}_4$ ; 6 —  $\text{Y}_2\text{Al}_2\text{O}_{15}(\text{Ce})$ ; 7 —  $\text{BeO}$  [17].



they arouse much interest as promising materials of high efficiency and reliability of detection, good energy, spatial and time resolution. Their use in detectors of ionizing radiations opens many new practical possibilities.

Therefore, in this chapter we will consider these scintillation materials in more detail. As their preparation technologies are based on general features of crystal growth by the Czochralski method, we will also discuss (in Chapter 2.1.2) theoretical considerations for thermal conditions of the growth process that allow preparation of oxide crystals of constant radius with high structural perfection and high scintillation parameters.

## 2.1. *Bismuth germanate $\text{Bi}_4\text{Ge}_3\text{O}_{12}$ (BGO) and silicate $\text{Bi}_4\text{Si}_3\text{O}_{12}$ (BSO) single crystals*

### 2.1.1. *Crystal and electron structure of $\text{Bi}_4\text{Ge}_3\text{O}_{12}$ and $\text{Bi}_4\text{Si}_3\text{O}_{12}$*

A natural hydrothermal mineral eulytine (chemical formula  $\text{Bi}_4\text{Si}_3\text{O}_{12}$ ) is known, with its crystalline structure first determined in 1931 [13]. This mineral possesses volume-centered cubic lattice with

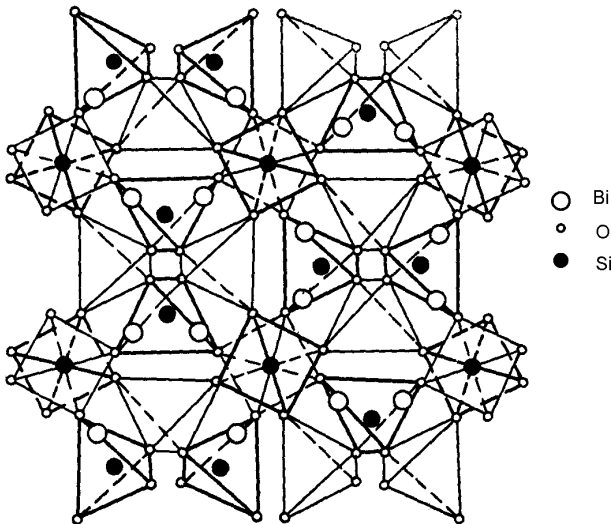


Fig.2.2. Orthogonal projections of the eulytine elementary lattice onto the (001) plane [13].

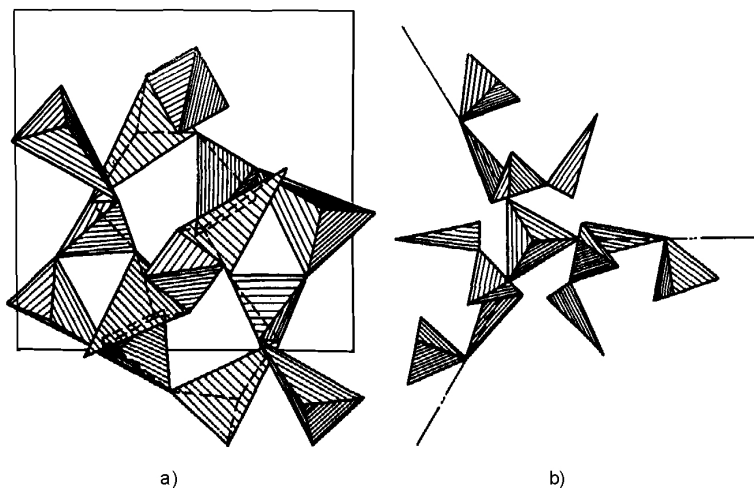


Fig.2.3. A fraction of the eulytine structure: a — projection onto the (100) plane; b — projection onto the (111) plane [14].

$a = (1.0272 + 0.0004)$  nm; its elementary cell contains four formula units. Several models have been proposed for positions of the structural elements in the eulytine lattice, which reflects difficulties of constructing graphical images of large-sized elementary cells. Fig.2.2 shows the orthogonal projection of the eulytine elementary cell onto the (001) plane according to data from [13]. A characteristic feature of such construction is the presence of clearly observed tetrahedral “cavities”, inside which localization of dopants is possible. The eulytine structure image, as interpreted by N.V.Belov [14], is shown in Fig.2.3.

According to data from [14,15], eulytine has a carcass structure composed of independent  $\text{SiO}_4$ -tetrahedrons and  $\text{BiO}_3$ -pyramids, which are interconnected by their vertexes.

In the eulytine structure, the “oxygen equality” principle is realized: each oxygen atom is bound only to two cations (silicon and bismuth); three oxygen atoms in connection to bismuth form a regular triangle with bismuth atom located over the plane. Such configuration of structural elements was called “umbrella configuration” in [14,15]. The second trio of the oxygen partners is at much greater distance from bismuth. Further studies [16] have shown, using synthetic polycrystalline samples of  $\text{Bi}_4\text{Si}_3\text{O}_{12}$ , that the bismuth octahedron is strongly distorted — tree

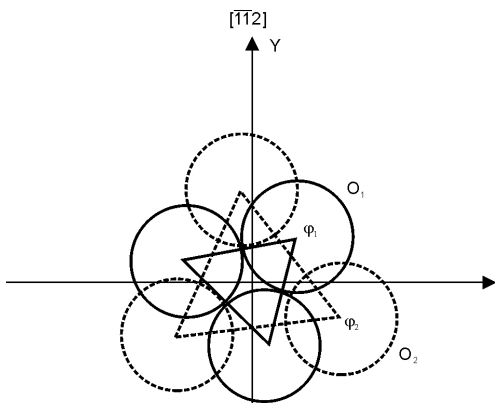


Fig.2.4. Coordination of oxygen atoms around the bismuth ion in the eulytine structure [17].

oxygen atoms are at 0.215 nm from bismuth, and the other three — at 0.265 nm. Substantial distortion of the octahedral coordination of atoms in  $\text{Bi}_4\text{Si}_3\text{O}_{12}$  was confirmed in [17] on poly- and single crystalline samples. Fig.2.4 shows the coordination of oxygen atoms around the bismuth ion in the eulytine structure: the bismuth ion is octahedrally surrounded by three “trios” of oxygen atoms with respective distances of 0.2125 nm and 0.2617 nm

[17]. Results obtained for synthetic  $\text{Bi}_4\text{Si}_3\text{O}_{12}$  crystals using neutron diffraction and ESR [17] show that, within the limits of standard deviations, both polycrystalline and single crystalline synthetic  $\text{Bi}_4\text{Si}_3\text{O}_{12}$  samples have the same structural parameters as the natural eulytine.

Single crystals of bismuth germanate  $\text{Bi}_4\text{Ge}_3\text{O}_{12}$  with eulytine structure were first synthesized in 1965 [18]. Their lattice structure and architectural design are similar to  $\text{Bi}_4\text{Si}_3\text{O}_{12}$ ; the elementary lattice parameter  $a = (1.0527 \pm 0.0003)$  nm [17–20].

The main fragments of the  $\text{Bi}_4\text{Ge}_3\text{O}_{12}$  crystal structure are isolated orthotetrahedrons of germanium and isolated octahedrons of bismuth. Fig.2.5 shows the elementary cell of  $\text{Bi}_4\text{Ge}_3\text{O}_{12}$  [17].

The coordination tetrahedrons of  $\text{GeO}_4$  and  $\text{Bi}_4\text{Ge}_3\text{O}_{12}$  are only weakly distorted, and the coordination polyhedron of bismuth atoms is a strongly distorted octahedron with two “trios” of oxygen atoms: the first — with Bi–O distance equal to 0.2605 nm, and the second — 0.2161 nm. Thus, in any crystal structure models of bismuth germanate and silicate, the bonds Ge–O or Si–O are equivalent, while Bi–O bonds are substantially different. Calculations of the local valence balance [21] showed that both types of description are acceptable — with Bi polyhedrons presented as octahedrons, and with the “umbrella” configuration for Bi.

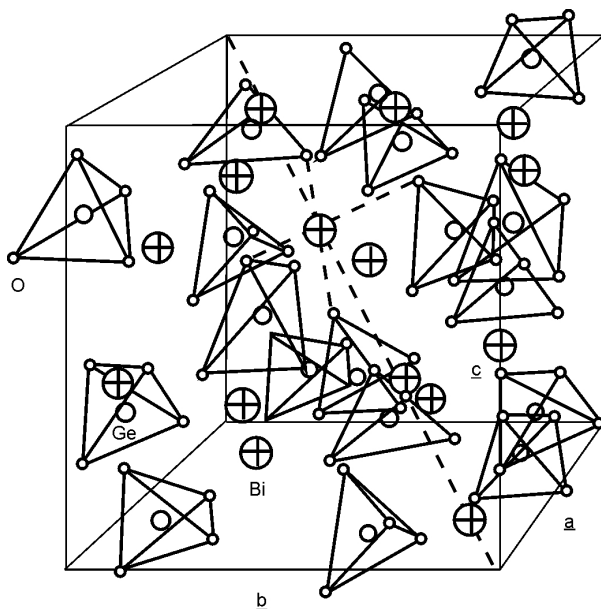


Fig.2.5. Elementary cell of  $\text{Bi}_4\text{Ge}_3\text{O}_{12}$  [17].

A detailed analysis of different electron structure models for  $\text{Bi}_4\text{Ge}_3\text{O}_{12}$  was carried out [21] in accordance with structural units of the crystal lattice. Electron structure was considered for clusters  $\text{GeO}_4^{4-}$  and  $\text{BiO}_6^{9-}$  as the smallest clusters, and for a more complex cluster  $\text{Bi}_4\text{Ge}_3\text{O}_{12}^{9-}$  proposed in [22]. In the complex cluster model, the idea of N.V.Belov of the “umbrella” crystal structure was used. The cluster was presented as a regular trigonal pyramid with Bi atom located in its vertex. Three oxygen atoms around Bi, which are located in the pyramid base, are also vertexes of the Ge tetrahedrons. The diagram of energy levels in  $\text{Bi}_4\text{Ge}_3\text{O}_{12}$  obtained as a result of calculations for the complex cluster  $\text{Bi}_4\text{Ge}_3\text{O}_{12}^{9-}$  and the minimum clusters  $\text{BiO}_6^{9-}$  and  $\text{GeO}_4^{4-}$  is shown in Fig.2.6.

In the dipole approximation, in the  $\text{Bi}_4\text{Ge}_3\text{O}_{12}^{9-}$  cluster with point symmetry  $C_{3v}$ , all transitions from the filled states to the virtual ones are permitted. The first peak *A* corresponds to the transition from the level 6s of bismuth to the conductivity band. Maximums *B*, *C* and *D* correspond to transitions from 2*p*-states of oxygen. As for maximums

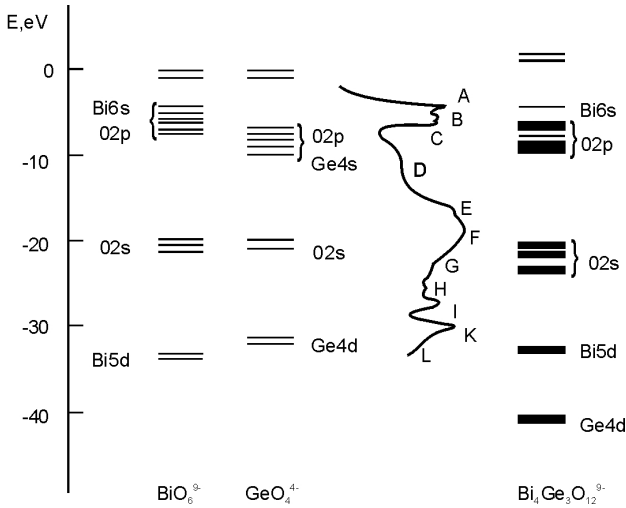


Fig.2.6. A diagram of the energy levels of the minimum ( $\text{BiO}_6^{9-}$ ), ( $\text{GeO}_4^{4-}$ ) and “umbrella” clusters in  $\text{Bi}_3\text{Ge}_4\text{O}_{12}$  [10]. The spectrum of the imaginary part of dielectric permittivity  $\epsilon_2$  is shown.

$E$ ,  $F$ ,  $G$ , they are related to transitions from  $2s$ -states of oxygen, while peaks  $K$  and  $L$  are well approximated by transitions from  $d$ -states of bismuth.

### 2.1.2. Theoretical description of thermal conditions for growth of oxide crystals of constant radius by the Czochralski method

At present, the main preparation technique of oxide scintillation crystals is their growth from the melt by the Czochralski method. To control structural perfection and scintillation characteristics of crystals, it is necessary to determine the principal factors affecting the growth conditions. The Czochralski method had been used in practice for a long time, detailed theoretical and experimental studies, clearing up the main features of the Czochralski growth process for oxide crystals [23–27].

The approach developed in [26] actually accounts for all the relevant factors, allowing an analysis of oxide crystal growth without costly experiments. One of the main growth parameters of the oxide

crystals affecting their optical quality is the crystallization rate (speed). It should be kept constant during the growth process, which is reflected in the radius of the growing crystal remaining constant. The problem of growing crystals of the constant radius is of great practical interest. Stabilization of the crystal radius in the growth process can be achieved mainly by variation of the pulling rate or by changing the heater power. In growing oxide crystals, the speed of pulling from the melt should be kept slow, as its variation can lead to changes in the effective dopant introduction coefficient. Therefore, in growing crystals of complex oxide compounds, the crystal radius is kept constant mainly by controlling the heater power. Rates of pulling and rotation of the crystal, as well as the crucible radius, should be kept constant (stabilized).

From mass and heat balance conditions during growth of a crystal with constant radius, it follows that crystal radius  $R_s$  at a constant pulling speed  $v_p$  is related to the temperature gradients in the solid  $G_s = \partial T_s / \partial z$  and liquid  $G_l = \partial T_l / \partial z = (T_m - T_l) / \delta$  phases on the crystallization front (i.e., with thermal conditions) by the following relationship [27]:

$$R_s = R_l \sqrt{\rho_l / \rho_s} \sqrt{1 - \frac{\Delta H_m \rho_s v_p}{-\lambda_s G_s + \lambda_l (T_m - T_l) \delta}}, \quad (2.1)$$

where  $T_{s,l}$  are thermal fields in the crystal (s) and melt (l), respectively,  $\rho_{s,l}$  — density,  $\lambda_{s,l}$  — thermal conductivity coefficients,  $T_m$  — melting temperature,  $\Delta H_m$  — melting enthalpy,  $R_l$  — crucible radius,  $\delta$  — thickness of the boundary layer. The values of  $G_s$  and  $G_l$  can be found from thermal conductivity equations or experimentally. It follows from (2.1) that, to ensure a constant radius of the growing crystal at a constant pulling rate, the heat flux difference at the boundary between the solid and liquid phases should be kept constant. The heat flux from the liquid phase is affected both by the temperature of the melt and by the thickness of the boundary layer. The melt temperature can be controlled by the heater power, and the boundary layer thickness  $\delta$  is determined both by thermal conductivity and by hydrodynamic properties of the melt. The value of  $\delta_h = \sqrt{\nu / \omega}$ , where  $\omega$  is the frequency of crystal rotation. During growth of oxide compound crystals  $\text{Bi}_4\text{Si}_3\text{O}_{12}$ ,  $\text{Bi}_4\text{Ge}_3\text{O}_{12}$ ,  $\text{Bi}_{12}\text{SiO}_{20}$ ,  $\text{Bi}_{12}\text{GeO}_{20}$  and  $\text{TeO}_2$ , the crystal rotation frequency should be changed as the melt level in the crucible becomes lower.

If technological parameters of the growth installation that affect the radius of the growing crystal are appropriately stabilized, changes in thermal conditions caused by the changing melt mass and crystal length become the main factor affecting the crystallization rate (and, consequently, the crystal radius).

When crystals are grown by the Czochralski method without additional “feeding-up” in the course of growth, the level of the melt and the crystallization front location with respect to the crucible walls are continuously changed. When the melt level in the crucible becomes lower, the temperature just above the melt is continuously increasing due to larger screening effects from the bare crucible walls. At low thermal conductivity of the material, this leads to worse heat removal along the crystal. In this case, to keep the crystal radius constant, the melt temperature should be lowered. At the initial stage of growth, the rate of decreasing the melt temperature should be higher than at final stages. This is explained by the increasing thickness  $\delta$  of the boundary layer caused by weakening of convection in the melt and of the thermal flux along the crystal due to the rising environment temperature. If thermal conductivity of the crystal is sufficiently high, the temperature of the melt should be increased in the course of growth. In this case, the crystal growth is strongly affected by changes in the character of heat removal from the crystal to the environment (as the top of the crystal is moving upwards from the melt surface). The heat flux from the crystallization front along the crystal is composed of the molecular  $W_m$  and radiation  $W_r$  components. The radiation component depends on the crystal transparency with respect to thermal radiation from the melt at the wavelength  $\lambda_{\max}$ , which corresponds to maximum radiation from the interface at melting temperature  $T_m$ .

Theoretical consideration of the effects of convection in the melt upon thickness of the thermal boundary layer  $\delta$  [26] have shown that it is determined both by thermal conductivity and hydrodynamics of the melt. It can be described as function of variables that are determined by thermal and hydrodynamic characteristics. In a dimensionless form, it can be expressed as

$$\frac{\delta}{R_l} = F(\delta_h / R_l, R_S / R_l, Gr, Mn, Re), \quad (2.2)$$

where  $Gr$  is the Grashof number, which characterizes the intensity of natural convection,  $Mn$  is the Marangoni number, which describes the thermocapillary convection,  $Re$  is the Reynolds number, which describes the intensity of forced convection in the melt caused by the melt entrainment by the rotating crystal and the crucible. In the course of crystal growth, relative contributions of the natural and forced convection in the melt are re-distributed, which is due to changes in thermal and geometrical growth conditions. At the initial stage, natural convection is predominant, while at the final stage forced convection becomes the most important.

One should also account for the dependence of the melt viscosity on temperature, as radial non-uniformity of the melt viscosity affects the quality of the growing crystal. To obtain crystals of high quality, it is important to choose such dimensions of the crucible and crystal that would ensure uniformity of the melt due to both natural and forced convection.

Thus, at specified values of the crucible radius  $R_g$  and crystal radius  $R_p$ , as well as of the pulling rate  $v_p$  and rotation rate  $\omega$ , initial growth conditions (the temperatures of the melt and crucible) are determined, according to (2.1), by the value of temperature gradient along the crystal pulling axis, which depends upon the design of the crystal-lizer. Experimental results show that the region of optimum thermal conditions, both for crystals with good heat removal (e.g.,  $\text{Bi}_4\text{Ge}_3\text{O}_{12}$ ,  $\text{CdWO}_4$ ) and materials with low thermal conductivity (e.g.,  $\text{LiNbO}_3$ ), is limited from both sides — from initially high melt temperatures (at temperature gradients over the melt  $> 70$  K/cm) and from low temperatures at relatively low axial temperature gradients ( $< 30$  K/cm). In the first case, undesirable negative effects can be caused by violations of the melt stoichiometry and by formation of metastable phases in the melt (and, consequently, in the grown crystal — e.g.  $\text{Bi}_4\text{Ge}_3\text{O}_{12}$ ). In the second case, there is a danger of concentration supercooling of the melt, which can cause worsening of the crystal quality and even a breakdown of the growth process.

As we had already indicated, during pulling of the growing oxide crystals stabilization of their radius is made by the appropriate variation of the melt temperature by means of controlling the heater power. Therefore, from the character of the heater power variation (which can



be easily measured) one can get information on the variation of thermal conditions in the course of growth of a crystal with constant radius.

Our studies on this question have shown that for qualitative analysis of the process in developing preparation technologies for new materials, as well as for determination of the optimum crystallizer design the following expression can be used:

$$\frac{d}{dt}(C_m m T_l) = W(t) - W_c(t) - W_f(t) - W_b(t) - W_\omega(t), \quad (2.3)$$

where the left-hand side describes the variation of the heat content of the melt in unit time,  $W$  is power coming to the melt from the heater,  $W_c$  is power removed from the melt through the crystal,  $W_f$  is power removed from the free surface of the melt to the environment,  $W_b$  is power removed from the melt through the bottom of the crucible,  $W_\omega$  is power removed through the side walls of the crucible,  $C_m$  is specific heat capacity of the melt,  $m$  is mass of the melt. A detailed analysis of (2.3) is given in [37, 38].

It can be seen from (2.3) that the power coming to the crystallizer is consumed for changing the heat content of the melt and for thermal losses indicated in (2.3). To obtain a crystal of high quality, optimum values of  $W_c(t)$ ,  $W_f(t)$ ,  $W_b(t)$ ,  $W_\omega(t)$  should be determined, as well as the best ways to achieve them, and then, on the basis of the analysis carried out, one should create a suitable crystallizer design and choose the required regimes of crystal growth.

The temperature distribution above the melt before the growth start is specified by the crystallizer design, and changes in thermal conditions in the crystallization zone during growth of a crystal with constant radius are reflected in the character of changes in the heater power. Monotonous and smooth variation of the heater power for maintaining the crystal radius constancy corresponds to monotonous variation of thermal conditions in the course of crystal growth. Such character of heater power variation guarantees high quality of the grown crystal.

In Chapters 2.1.3, 2.3.2 and 2.4.2, we have demonstrated how one can obtain, using the theory described in [26], optimum conditions for the growth process that would guarantee high structural perfection and scintillation characteristics of complex oxide crystals.

### *2.1.3. Technological features of single crystal growth of bismuth germanate and silicate*

Preparation methods of  $\text{Bi}_4\text{Ge}_3\text{O}_{12}$  (BGO) and  $\text{Bi}_4\text{Si}_3\text{O}_{12}$  (BSO) single crystals, as well as their quality, have been reviewed in detail [28]. For preparation of BGO and BSO single crystals, many of the commonly known methods of crystal growth were used. By the Bridgman-Stockbarger method, BGO crystals of 20 mm in diameter and 50–60 mm in length could be grown practically without defects. However, it is hardly possible to grow large-sized crystals by this growth method due to the difference in growth rates of the central and peripheral parts of the crystal.

The floating zone method is of simple design and high productivity. In this method, the zone of higher temperature moves along the vessel containing the seed crystal and the raw charge. However, this method also sets limits on the crystal size, primarily, on its height, because heat transfer becomes non-uniform with increasing height of the grown crystal, and temperature convection near the surface becomes stronger. BGO crystals obtained by this method tend to be ageing with time, with yellowish color appearing, which worsens their optical properties.

By the heat exchanger method, BGO crystals are grown on seed placed onto the bottom of a platinum crucible. The growth start and rate are determined by the intensity of aeration with cooling gas going through the heat exchanger. Preparation of defect-free  $40 \times 40 \times 13$  mm BGO crystals by this method has been reported [28].

The main prospects for growth of large-sized BGO single crystals are related to the development and improvement of the Czochralski method. Using a low-gradient variant of this method, BGO crystals of diameter 120–130 mm and 350 mm long could be obtained. This method could be proposed as method for industrial production of large-sized BGO crystals; however, it is worse than the conventional Chochralsky method, as there is a possibility for formation of different structure defects and coloring of single crystalline material.

At present, the most common preparation method of BGO and BSO crystals is pulling from the melt by Czochralski method (see 2.1.2).

Fundamental studies of peculiar features of the  $\text{Bi}_2\text{O}_3\text{--GeO}_2$  were carried out by V.M.Skorikov and his team [29–34]. The problem of preparation of structurally perfect BGO single crystals was considered

in works of S.F.Burachas and B.L.Timan [35–38], where technological features of growth of these crystals were discussed in detail.

Bismuth germanate  $\text{Bi}_4\text{Ge}_3\text{O}_{12}$  (BGO). Preparation of structurally perfect BGO single crystals by the Czochralski method, as it follows from Chapter 2.1.2, is related to the correct choice of crystallization conditions and regimes, which should account for physico-chemical properties of the  $\text{Bi}_2\text{O}_3\text{--GeO}_2$  system. A characteristic feature of the diagram of state of  $\text{Bi}_2\text{O}_3\text{--GeO}_2$  is a possibility of formation, depending upon specific conditions, of several stable or metastable phases of constant or variable composition. It was found that in the state of stable equilibrium, alongside with  $\text{Bi}_4\text{Ge}_3\text{O}_{12}$  of the eulytine structure, two more stable phases can be formed —  $\text{Bi}_{12}\text{GeO}_{20}$  with the sillenite structure, and  $\text{Bi}_2\text{Ge}_3\text{O}_9$  with the bentoite structure, as well as a metastable phase of  $\text{Bi}_2\text{GeO}_5$ .

The polymorphism of the initial bismuth and germanium oxides, in combination with high polarizability of Bi ion, leads to interactions of complicated nature between  $\text{Bi}_2\text{O}_3$  and  $\text{GeO}_2$ . From the review paper [28], it follows that processes of compound formation in the  $\text{Bi}_2\text{O}_3\text{--GeO}_2$  system are primarily determined by the temperature regimes of the synthesis. In Tabl.2.1, one can find the phase composition of  $\text{Bi}_2\text{O}_3\text{--GeO}_2$  samples (according to data taken from [33]) as function of the  $\text{Bi}_4\text{Ge}_3\text{O}_{12}$  synthesis temperature. At higher temperatures, the fraction of eulytine in the  $\text{Bi}_2\text{O}_3 + \text{GeO}_2$  reaction products increases.

Studies of density and viscosity polytherms indicate the presence of three temperature zones above the liquidus curve, with different melt structure in each of the zones. The upper boundary of the low-temperature zone *A* (it is also the lower boundary of zone *B*) is 30 K above the liquidus, zone *B* occupies an interval of  $\sim 100$  K, and further upwards is zone *C*. In the temperature zone *A*, the main role is played by the bond

Table 2.1. Phase composition of the  $2\text{Bi}_2\text{O}_3+3\text{GeO}_2$  reaction products

Synthesis temperature range, K	Phase composition
913–1163	$\text{Bi}_4\text{Ge}_3\text{O}_{12}$ ; $\text{Bi}_{12}\text{GeO}_{20}$ ; $\text{Bi}_2\text{Ge}_3\text{O}_5$ ; $\alpha\text{-Bi}_2\text{O}_3$ ; $\text{GeO}_2$
1213–1233	$\text{Bi}_4\text{Ge}_3\text{O}_{12}$ ; $\text{Bi}_{12}\text{GeO}_{20}$ ; $\text{Bi}_2\text{Ge}_3\text{O}_9$
1253–1273	$\text{Bi}_4\text{Ge}_3\text{O}_{12}$ ; $\text{Bi}_2\text{Ge}_3\text{O}_9$
1304	$\text{Bi}_4\text{Ge}_3\text{O}_{12}$

$\text{Bi}^{3+}\text{--GeO}_4^{4-}$ , which is broken when the temperature is raised. When the melt is heated to temperatures corresponding to zone *B*, polymer structures are formed from  $\text{GeO}_4^{4-}$  tetrahedrons and  $\text{Bi}_2\text{O}_3^{2+}$  covalent complexes. Modification of the melt structure under heating is accompanied by abrupt changes in its properties, especially in viscosity.

The metastable phase  $\text{Bi}_2\text{GeO}_5$  is crystallized from the metastable melt upon cooling from the temperature zone *B*. Therefore, if during the growth process the temperature remains more than 30 K higher than the melting temperature of the stable phase for a long time, formation of the metastable phase occurs. This phase accompanies the main (eulytine) phase during crystallization, thus worsening optical quality of the grown crystal. Otherwise, substantial overcooling of the melt also negatively affects the crystal quality. Accounting for peculiar features of the  $\text{Bi}_2\text{O}_3\text{--GeO}_2$  system and the results of detailed studies of  $\text{Bi}_4\text{Ge}_3\text{O}_{12}$  crystal growth that had been carried out in the Institute for Single Crystals, we have developed a scientific base for production technology of these crystals. This technology allows preparation of structurally perfect bismuth germanate crystals of large size. These crystals have practically no defects, are of the color of pure water droplet, and are suitable for application in high energy physics.

$\text{Bi}_4\text{Ge}_3\text{O}_{12}$  crystals 55 mm in diameter and 250 mm long were obtained using the Czochralski method by pulling from the melt at 1.5 mm/hour; crystal rotation speed was 40 rpm. A platinum crucible of 100 mm diameter was used; above the crucible, a platinum screen of the same diameter was installed coaxially. For heating of the crucible and the screen, high frequency currents were used. An automatic control system maintained the crystal diameter constant within  $\pm 0.5$  mm.

Charge for the crystal growth was prepared by solid-phase synthesis. Accounting for crystallochemical properties of the system  $\text{Bi}_2\text{O}_3\text{--GeO}_2$ , as well as effects of the atmosphere moisture, possibility of formation of carbon-containing compounds, purity of the reagents and the container material on the quality of BGO crystals, optimum regimes were proposed for synthesis of bismuth germanate charge.

Annealing of  $\text{Bi}_2\text{O}_3$  was carried out at the temperature of  $440\pm 10^\circ\text{C}$ , at which moisture and volatile admixtures should be completely removed, thus making the powder mass to be constant. When  $\text{GeO}_2$  is annealed at  $965\pm 15^\circ\text{C}$ , alongside with establishment of the powder mass constancy, the oxide is transformed into a stable hexagonal

modification. This is a necessary condition for the reaction of eulytine-structured bismuth germanate formation to be fully completed.

A new method of melt preparation had been proposed, which consisted in the following. A homogenized mixture of pre-calcinated germanium and bismuth oxides, taken in the stoichiometric ratio, are placed into a crucible in the crystallization unit of the growth installation. Oxides are heated in a platinum crucible at a rate of 100–150 K/min up to  $940\pm 10^\circ\text{C}$ ; this temperature is higher than the melting temperature of the metastable phases. So, the oxide mixture remains inside the temperature range of the metastable phases (and of high corrosion activity of  $\text{Bi}_2\text{O}_3$  to platinum) for only 1.5–3 min, which is 10–20 times less than in other known methods.

Under these conditions, the solid-phase reaction of  $\text{Bi}_4\text{Ge}_3\text{O}_{12}$  formation goes with high speed, which correspondingly decreases the corrosion rate of the platinum crucible by 10–20 times. When the temperature reaches  $940\pm 10^\circ\text{C}$ , the heating rate is lowered to 15–20 K/min, and the oxide mixture is further heated until melting. The melted mixture is further heated up to  $1075\pm 10^\circ\text{C}$  and kept at this temperature for 1–3 hours. The melt is fully homogenized, metastable phases fully decomposed, and bismuth germanate is synthesized in the liquid phase. Because of high heating rate, absence of cyclic cooling and shorter high-temperature isothermal stage, the total duration of the technological process is reduced by about 2 times. Chemical analysis shows that platinum content in the melt and in the grown BGO crystal is not higher than  $10^{-4}$  mass % (as compared with  $10^{-2}$ – $10^{-1}$  %, typical for other known methods of BGO synthesis).

One of the ways used to achieve high scintillation parameters and optical uniformity of BGO crystals is application of double crystallization, which is intended to minimize the content of admixtures. However, even the highest possible purity of the initial components used for BGO synthesis cannot guarantee that the grown large-sized crystals will have satisfactory optical and scintillation properties, because various microphases tend to be formed at the growth stage in an uncontrolled way [29,39].

Effects of non-stoichiometry and phase composition of the initial charge and the melt upon quality of BGO crystals were reported in [36]. In the bottom part of grown BGO crystals, often high concentration of

micropores and inclusions is observed (up to  $8 \cdot 10^3 \text{ cm}^3$ ), which makes the absorption coefficient in the intrinsic luminescence region as high as  $(1-2) \cdot 10^{-1} \text{ cm}^{-1}$ . Scintillation characteristics are also worsened (light output  $< 12\%$  and energy resolution  $> 16\%$ ). The main phase that negatively affects the process of  $\text{Bi}_4\text{Ge}_3\text{O}_{12}$  crystallization at the final stage of synthesis is that of  $\text{Bi}_2\text{Ge}_3\text{O}_9$  with the benitoite structure. When concentration of this phase in the melt increases, it can be captured into the crystallization zone, resulting in drastic changes in the thermophysical conditions of BGO growth, which can even lead to a complete disruption of the growth process because of substantial crystallographic differences between the two phases (cubic  $\text{Bi}_4\text{Ge}_3\text{O}_{12}$  and hexagonal  $\text{Bi}_2\text{Ge}_3\text{O}_9$ ). If in the course of BGO crystal growth the melt stoichiometry is violated (e.g., because of evaporation of  $\text{Bi}_2\text{O}_3$  or due to non-stoichiometry of the charge used), formation of the  $\text{Bi}_{12}\text{GeO}_{20}$  phase is possible. However, its effects upon structural perfection and scintillation parameters of BGO crystals are much weaker than those of  $\text{Bi}_2\text{Ge}_3\text{O}_9$ .

As we have already noted (Chapter 2.1.2), in the Czochralski growth of BGO the melt homogeneity and crystal quality are substantially affected by the dimensions ratio of the growing crystal and the crucible. It has been shown [37] that if melt viscosity is strongly temperature-dependent, growth of defect-free crystals is possible only in a certain range of values of the crucible and crystal diameter. Expressions have been obtained [37] that allow a qualitative evaluation of radial temperature gradients required for the melt to be homogeneous. It was shown that, in order to obtain structurally perfect BGO crystals of eulytine structure with diameter of 50–60 mm, the optimum crucible diameter should be about 100 mm. When larger crucibles are used, additional heaters should be applied in the BGO growth installation.

Conditions of heat removal from the growing BGO crystal and their influence upon its side shape were considered in [38]. The problem is related to relatively high conductivity of  $\text{Bi}_4\text{Ge}_3\text{O}_{12}$  crystals; consequently, large fraction of heat is removed from the melt through the crystal. This is confirmed by direct measurements of the melt temperature upon removal of the crystal from the crucible. Thus, with crucible diameter 100 mm, crucible height 100 mm, crystal diameter 50 mm, crystal length 200 mm, when the crystal was torn away from

the melt, the melt temperature, at the same heater power, increased by about 30 K.

As for temperature distribution in the melt, it was shown to substantially affect the possible faceting of the side surface of the growing crystal [38]. Such faceting is related to the integral thermal effect, which depends upon thermal conditions both in the melt and in the growing crystal, determining the shape of the crystallization front. No faceting is observed when the crystallization front is convex with respect to the melt, and the axial temperature gradient is large.

Another important result of these studies has been a discovery of the temperature range of the melt in which there is no defect formation – neither defects due to overheating, nor those caused by supercooling [35]. This temperature range is ensured by correctly chosen regimes and conditions of BGO crystal growth accounting for peculiar features of the  $\text{Bi}_2\text{O}_3\text{--GeO}_2$  system.

Bismuth silicate  $\text{Bi}_4\text{Si}_3\text{O}_{12}$  (BSO). Single crystals of bismuth silicate are grown using the Czochralski method by pulling from the melt. As charge, a mixture of silicon dioxide  $\text{SiO}_2$  and bismuth oxide  $\text{Bi}_2\text{O}_3$  is generally used. Interaction of the initial components in the  $\text{Bi}_2\text{O}_3\text{--SiO}_2$  system is much more complex than in the  $\text{Bi}_2\text{O}_3\text{--GeO}_2$  system. Phase diagram of the  $\text{Bi}_2\text{O}_3\text{--SiO}_2$  system was presented in [147], with the existence of three compounds noted. Stable compounds  $\text{Bi}_{12}\text{SiO}_{20}$  and  $\text{Bi}_4\text{Si}_3\text{O}_{12}$  have melting points at 900°C and 1032°C, respectively. The metastable phase  $\text{Bi}_2\text{SiO}_5$  is crystallized above 845°C. Between the two stable compounds  $\text{Bi}_{12}\text{SiO}_{20}$  and  $\text{Bi}_4\text{Si}_3\text{O}_{12}$  an eutectic reaction occurs at 887°C, with the eutectic point close to 25 mol.%  $\text{SiO}_2$ . When  $\text{SiO}_2$  concentration is increased from 20% to 100%, the following reactions proceed one after another:  $\delta\text{-Bi}_2\text{O}_3$  (20–30 mol.%  $\text{SiO}_2$ )  $\rightarrow$   $\delta\text{-Bi}_2\text{O}_3$  +  $\text{Bi}_2\text{SiO}_5$  (30–45 mol.%  $\text{SiO}_2$ )  $\rightarrow$   $\text{Bi}_2\text{SiO}_5$  (about 50 mol.%  $\text{SiO}_2$ )  $\rightarrow$   $\text{Bi}_2\text{SiO}_5$  +  $\text{SiO}_2$  (50–60 mol.%  $\text{SiO}_2$ )  $\rightarrow$   $\text{Bi}_4\text{Si}_3\text{O}_{12}$  (> 60 mol.%  $\text{SiO}_2$ ). If  $\delta\text{-Bi}_2\text{O}_3$  and  $\text{Bi}_2\text{SiO}_5$  crystallize simultaneously, the  $\delta$ -phase is transformed into  $\text{Bi}_2\text{SiO}_5$  at 720°C.

Complex physico-chemical nature of the interaction of crystal-forming oxides of the  $\text{Bi}_2\text{O}_3\text{--SiO}_2$  system makes it difficult to look for optimum technological regimes of BSO crystal growth, especially of large-sized BSO crystals. Alongside with the main substance of the eulytine structure, other substances can be formed, such as

$\text{Bi}_{12}\text{SiO}_{20}$  (sillenite structure),  $\text{Bi}_4\text{Si}_3\text{O}_{12}$  (benitoite structure), as well as metastable phases like  $\text{Bi}_2\text{SiO}_5$ , formation probability of which depends upon time and temperature conditions of the synthesis [40]. From the viewpoint of preparation of high-quality crystals, the most important is to obtain the eulytine monophasic structure, which can be ensured by an appropriate control of melt overheating (accounting for its thermal instability) and supercooling.

Some peculiar problems emerge in preparation of a homogeneous melt in the  $\text{Bi}_2\text{O}_3\text{--SiO}_2$  system, because, under certain conditions, a glass-like film is formed on the melt surface. This process is rather stable, which largely hinders formation of nuclei of the main phase during BSO crystal growth. This film can be melted only by undesirable substantial overheating of the melt above the melting point of the main eulytine phase. In addition, silicate melts have much higher viscosity and density as compared with germanate melts.

In [41], a method has been proposed for growth of  $\text{Bi}_4\text{Si}_3\text{O}_{12}$  single crystals, in which higher crystal quality is ensured by homogenization of the melt at lower growth temperatures and more efficient use of the charge.

Bismuth silicate crystals 35 mm in diameter and 150–200 mm long were grown by the Czochralski method using high-frequency heating in a platinum crucible. Diameter of the growing crystal was kept constant by a specially designed automatic control system with a mass sensor. An important feature of this method is the use of non-stoichiometric charge — the concentration of  $\text{Bi}_2\text{O}_3$  deviated from stoichiometric value by 1–5% and was subsequently added to the obtained mixture only at the temperature of 1100–1130°C. Addition of the appropriate quantity of bismuth oxide in the form of powder directly onto the surface of a hardened melt before the crystal growth leads to disappearance of the glass-formed film and formation of a homogeneous melt suitable for single crystal growth. The content of the main phase —  $\text{Bi}_4\text{Si}_3\text{O}_{12}$  — in the single crystals obtained was 99.8%, and the content of compound  $\text{Bi}_{12}\text{SiO}_{20}$  with sillenite structure did not exceed 0.2%. These crystals were characterized by nearly total absence of light scattering centers.

In [148], growth of BSO crystals was reported (diameter 35 mm, length 220 mm) by the Bridgman method in a platinum crucible at a



speed of 0.5 mm/hour. The crystals were of good quality, with energy resolution at the level of 22% at 662 keV.

#### *2.1.4. Thermal treatment of BGO single crystals*

Bismuth germanate single crystals grown from the melt by the Czochralski method in non-uniform thermal fields are usually characterized by substantial thermoelastic residual stresses, which are, with other conditions equal, proportional to the crystal diameter squared. For large-sized BGO crystals ( $D \geq 50$  mm and  $L \geq 150$  mm), the residual stress values approach the strength limit of the material, and sometimes even surpass it. This can cause fissuring and cracking of the crystal — either just after the growth or later, during their optical-mechanical treatment.

Some of the grown BGO crystals appear to have rather poor structural perfection. They can be optically non-uniform, contain admixtures and inclusions of metastable phases captured from the melt, agglomerations of pores, color centers. In many BGO samples small-angle micro-block boundaries are observed, with disorientation from 5 to 60 angular seconds. It has been shown [42] that optical transmission coefficient of BGO single crystals is correlated to the degree of its structural perfection. The above-mentioned structural defects lead to increases in optical absorption in the intrinsic radioluminescence bands, they can cause worsening of such important scintillation parameters as light output and energy resolution. Directly after the growth, many BGO crystals have energy resolution  $R > 20\%$  and light output less than 8%, which substantially limits their application in high energy physics and nuclear instruments.

It is known that thermal treatment is an efficient way to improve the crystal quality and increase the production yield of good pieces. For BGO crystals, studies on improvement of their optical and scintillation characteristics by means of thermal treatment have been reported [43,44]. This problem becomes especially important because of the growing demand for large-sized BGO single crystals with high scintillation parameters.

One of the variants of thermal treatment allowing substantial increases in light output and improvement of energy resolution of BGO scintillators is their annealing in an oxygen-containing medium by heating at a rate of 75–200 K/hour up to 950–1030°C, keeping the

crystals at this temperature for 0.5–2 hours, then cooling down to 960–900°C at 50–100 K/hour, and finally cooling to the room temperature at 100–200 K/hour. The presence of an oxygen-containing atmosphere favors healing of the oxygen vacancies in the crystal matrix and suppresses diffusion of bismuth from the crystal. A distinctive feature of the thermal treatment regime proposed in [43] for BGO crystals is passing of 0.05–0.25 mA/cm<sup>2</sup> DC through the crystal (along the growth axis) during the stage of keeping at the highest annealing temperature. Introduction of this new stage can be explained in the following way.

It was established experimentally that, to accelerate the chemical decay of the inclusions of  $\text{Bi}_2\text{GeO}_5$  and  $\text{Bi}_{12}\text{GeO}_9$  metastable phases and their transformation to the main phase of  $\text{Bi}_4\text{Ge}_3\text{O}_{12}$ , as well as to achieve compensation of the charged defects and ordering of the crystal structure, thermodiffusion and thermodissociation, characteristic for the conventional annealing, should be accompanied by electrodiffusion (transfer of charges) and electrodisassociation (electrolysis), induced by the direct current passing through the crystal. In Fig.2.7, relative changes in optical transmission of BGO crystals occurring after carrying out the heat treatment are shown, and in Table 2.2, changes in scintillation parameters are shown that were observed after thermal treatment of different regimes. Numbering of crystals in Fig.2.7 and table 2.2 is identical.

For BGO scintillators of 40–55 mm diameter and the same length, after annealing the absolute value of light output increased by 3–3.9%, and the energy resolution value improved by 2–7.3%. The relative light output increase was 20–60%, and the energy resolution improvement — 10–30% with respect to the values before annealing. Passing

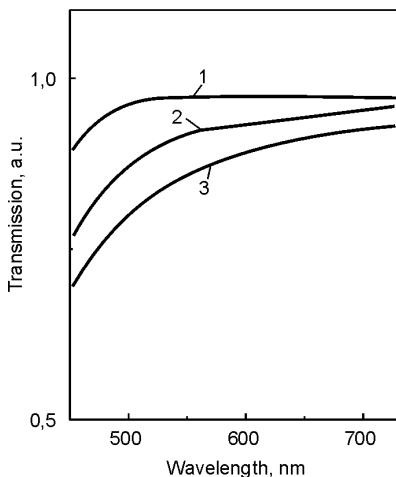


Fig.2.7. Relative changes in optical transmission of BGO crystals as a result of thermal treatment.

Table 2.2. Scintillation parameters of BGO crystals at different thermal treatment (TT) regimes

Characteristic	Crystal No.		
	1	2	3
Heating rate, K/hour	100	150	100
Temperature, °C	1010	1015	1000
Current density, mA/cm <sup>2</sup>	—	0.15	0.15
Oxygen content, %	100	20	20
Light output with respect to NaI(Tl) %			
Initial	5.0	6.6	7.5
After TT	8.5	10.5	10.6
$\Delta C$	3.5	3.9	3.1
Energy resolution $R$ , ( $E_\gamma=0,662$ MeV), %			
Initial	24.0	19.2	18.2
After TT	16.7	14.9	16.2
$\Delta R$	7.3	4.3	2.0
Outer appearance after TT	No fissures	No fissures	No fissures

the electric current through the crystal leads to a further increase in light output by 15–20%

Higher oxygen content in the annealing atmosphere (up to 100% — annealing in an ampoule) favors further improvement of scintillation parameters by 5–10%. The effects of oxygen annealing are due to thermal dissociation of oxides and further diffusion of the free oxygen into the crystal.

A similar effect is achieved by annealing BGO crystals in  $\text{Bi}_2\text{O}_3$  vapor ( $T=970\text{--}1030^\circ\text{C}$ ,  $t=0.5\text{--}1$  hour) or  $\text{Sb}_2\text{O}_5$  ( $T=900\text{--}1030^\circ\text{C}$ ,  $t=2\text{--}8$  hours) in a sealed ampoule. The effect of thermal treatment in  $\text{BiO}_3$  or  $\text{Sb}_2\text{O}_5$  vapor is comparable to annealing in the oxygen atmosphere and is explained in similar terms — thermal dissociation of these oxides with liberation and subsequent diffusion of free oxygen into the crystal.

Annealing in  $\text{Bi}_2\text{O}_3$  or  $\text{Sb}_2\text{O}_5$  atmosphere leads to the crystal structure ordering not only due to thermal diffusion and thermal dissociation

of the irregular oxide phases, but also because of healing of the oxygen vacancies. The thermally less stable  $\text{Sb}_2\text{O}_5$ , starting from 630 K, begins to lose oxygen, being transformed stage by stage to  $\text{Sb}_6\text{O}_{12}$ ,  $\text{Sb}_2\text{O}_6$ ,  $\text{Sb}_2\text{O}_3$ . The liberated oxygen atoms, even during short time of their existence, substantially increase the annealing efficiency. When BGO crystals are annealed in  $\text{Bi}_2\text{O}_3$  vapor, the average light output values increased from the initial 14.8% (with respect to  $\text{NaI(Tl)}$ ) to 17.8%. The energy resolution changed from 14.4% to 12.9%. Annealing in  $\text{Sb}_2\text{O}_5$  leads to even better results — the light output reaches 18.8%, and the energy resolution is improved to 12.5% [28].

Thus, it can be concluded that thermal treatment of large-sized BGO crystals is an essential stage of their production technology. Optimum annealing procedures ensure high production yields of scintillators with high functional parameters.

#### *2.1.5. Main physico-chemical properties and scintillation characteristics of bismuth germanate and silicate crystals*

Main physico-chemical properties of  $\text{Bi}_4\text{GeO}_3$  and  $\text{Bi}_4\text{Si}_3\text{O}_{12}$  are presented in Table 2.3. Their scintillation characteristics are given in table 2.4.

As compared with alkali halides, main advantages of BGO are high atomic number and high density, which ensures much higher detection efficiency for scintillators of similar size. In Fig.2.8, the peak efficiency is shown for BGO- and  $\text{NaI(Tl)}$ -based scintillation detectors of equal size.

Linear total absorption coefficients of the medium-range gamma-radiation are 2.1–2.5 times larger for BGO crystals than for  $\text{NaI(Tl)}$ . Therefore, to achieve similar detection efficiency one should use  $\text{NaI(Tl)}$  crystals of 9–16 times larger volume as compared with BGO, depending on the energy of the detected particles. The energy dependence of the total absorption coefficients of  $\text{NaI(Tl)}$  and BGO crystals is shown in Fig.2.9.

Considering different classes of inorganic crystals, one can see that complex oxide single crystals are somewhat inferior to AHC as for their scintillation parameters, but they also have many advantages such as their fast response, radiation and thermal stability, mechanical strength. The decay time of BGO at the room temperature is  $\sim 300$  ns, i.e., only slightly worse than with  $\text{NaI(Tl)}$ . However,

Table 2.3. Main physico-chemical properties of bismuth germanate and silicate crystals

Characteristic	$\text{Bi}_4\text{Ge}_3\text{O}_{12}$	$\text{Bi}_4\text{Si}_3\text{O}_{12}$
Lattice constant, nm	1.0497	1.0240
Density, $\text{kg/m}^3$	7120	6800
Melting temperature, K	1317	1293
Specific heat capacity, $\text{J}/(\text{kg}\cdot\text{K})$	300	
Molecular heat capacity, $\text{cal}/(\text{mol}\cdot\text{K})$	40.39	39.90
Debye temperature, K	236	271
Grueneisen constant	1.18	1.88
Linear thermal expansion coefficient at $20^\circ\text{C}$ , $10^{-6}\text{K}^{-1}$	2.69	10.65
Latent heat of crystallization, Kcal/mole	44.6	
Thermal conductivity, $\text{W}/(\text{m}\cdot\text{K})$	2	6
Mohs' hardness	5–6	6
Microhardness, $\text{kG/mm}^2$	315	
Young's module, $10^{10}\text{N/m}^2$	10.56	
Conductivity, $10^{-13}\text{Ohm}\cdot\text{m}^{-1}$	8.4	

unlike  $\text{NaI}(\text{Tl})$ , the afterglow of BGO in the millisecond range (after 3–6 ms) is only 0.005–0.1%. Therefore, BGO crystals, as a whole, are considered more fast than  $\text{NaI}(\text{Tl})$ , which makes BGO scintillators the most suitable for their use in tomography. The scintillation time  $\tau$  and light output of BGO are temperature-dependent; in Fig.2.10, the light output and decay time of BGO single crystals are shown as functions of temperature.

Due to its lower light output, BGO generally has somewhat worse energy resolution as compared with  $\text{NaI}(\text{Tl})$ . However, this largely depends upon the crystal quality. It has been shown that, using raw materials of the highest purity, BGO single crystals can be grown that show the energy resolution of 9.3% ( $^{137}\text{Cs}$   $\gamma$ -radiation). At a constant crystal diameter, the crystal length increase by 4 times changes the energy resolution by 1.3 times (from 10.5% to 13.3%), and the light output becomes two times lower (12% and 6% with respect to  $\text{NaI}(\text{Tl})$ , respectively). This is caused by insufficient transparency to

Table 2.4. Main scintillation characteristics of single crystals  $\text{Bi}_4\text{Ge}_3\text{O}_{12}$  [45]

Characteristic	
Effective atomic number	74
Radiation length, cm	1,13
Relative light output, % with respect to NaI(Tl)	12–16
Energy resolution for $E_\gamma=662$ keV, %	9–13
Decay time, ns	0.3
Luminescence maximum, nm	480–500
Refraction index at the emission maximum излучения	2,15
Absorption coefficient at the emission maximum, $\text{cm}^{-1}$	0,07–0,2
Afterglow level (after 20 ms), %	0,05

the intrinsic radiation, which is characteristic for large-sized BGO crystals.

Increasing temperatures affect scintillation parameters of BGO rather strongly (as compared with AHC). Thus, when the temperature rises from  $70^\circ\text{C}$  to  $100^\circ\text{C}$ , the light yield of BGO decreases by 10 times, and the decay time is decreased logarithmically. Though scintillation characteristics of BGO are strongly temperature-dependent, high detection efficiency and high stability to the influence of mechanical and climatic factors make it possible to use BGO-based instruments for detection of  $\gamma$ -radiation in geophysical studies, ore pits, etc.

It can be seen in Tables 1.1 and 2.4 that spectrometric characteristics of BGO single crystals are lower than those of AHC due to their low light output. Different authors gave the BGO light output values in the range from 8% to

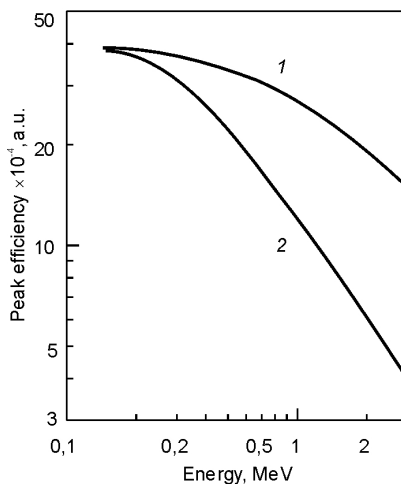


Fig.2.8. Peak efficiency of scintillation detectors based on BGO (1) and NaI(Tl) (2) single crystals of dimensions  $\varnothing 76.2 \times 76.2$  mm.

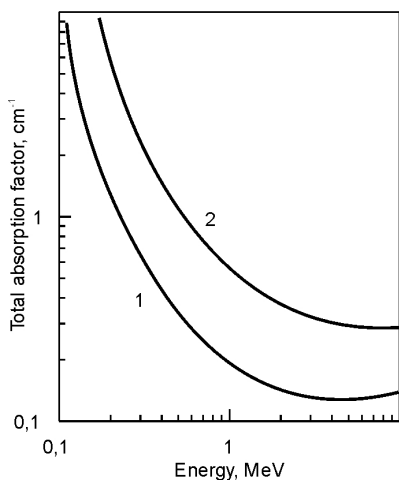


Fig.2.9. Energy dependence of the total absorption coefficient for NaI(Tl) (1) and BGO (2) crystals.

20% with respect to NaI(Tl). The absolute value of this parameter, as it follows from the analysis of literature data, depends upon specific features of the growth technology, such as purity of the initial raw material, presence of impurities in the crystal, its optical transparency. A BGO crystal, 25 mm in diameter and 25 mm long, produced by Harshaw, which was grown from a twice-recrystallized raw material, showed the resolution of 9.3% ( $^{137}\text{Cs}$   $\gamma$ -radiation), while BGO crystals of similar sizes obtained from Hitachi, produced from twice- and thrice-recrystallized raw material, had these values as 11.6% and 9.5–10%, respectively [21].

BGO single crystals display photo- and radioluminescence in the visible spectral range. In these scintillators, the role of luminescence centers is played by Bi ions; therefore, BGO crystals do not require doping with activators. Their excitation and luminescence spectra at room temperature are shown in Fig.2.11. The luminescence maximum at 505 nm is slightly shifted towards the long-wave region, and attempts were made to use BGO-based scintillation detectors in combination with photodiodes for spectrometry of  $\gamma$ -radiation. However, because of low light output of BGO, photodiode noises impose substantial limitations on spectrometric properties of such devices. Better resolution can be achieved when the whole device is cooled down to  $-15^\circ\text{C}$ . In Table 2.5, luminescent-optical characteristics of  $\text{Bi}_4\text{Ge}_3\text{O}_{12}$  and  $\text{Bi}_4\text{Si}_3\text{O}_{12}$  crystals are presented [46].

Model descriptions of the luminescence in BGO have been summed up in [21], with many contradictory experimental and theoretical data available in the literature.

The configurational model of intra-center luminescence is based upon ideas developed for crystals possessing  $\text{Bi}^{3+}$  ions as activators.

The energy level structure of  $\text{Bi}^{3+}$  ion corresponds to the general picture of the hydrogen-like atom terms [47]. Optical properties of such crystals are, as a rule, determined by electron transitions between states  $6s^2$  and  $6s6p$  of the trivalent bismuth ion. A characteristic feature of the luminescence of bismuth-containing crystals in the hydrogen-like ions model is the presence of an excited metastable level  $^3p_0$ , which plays the role of an electron trap in the intra-center processes, thus determining the decay time at low temperatures. Considering  $\text{Bi}^{3+}$ -centers as parts of  $\text{BiO}_6^{9-}$  clusters, one should note that excitation relaxation processes in  $\text{BiO}_6^{9-}$  ions are similar to excitation relaxation processes of  $\text{WO}_4^{2-}$  ions in calcium tungstate.

The cluster models of BGO luminescence are based on considering  $\text{BiO}_6^{9-}$  and  $\text{Ge}_4^{4-}$  type clusters as absorption centers [48]. Absorption is considered as transitions from the occupied molecular orbitals  $6s$  (bismuth) or  $2p$  (oxygen) to the free molecular orbitals  $6p$  (bismuth) and  $4s$  (germanium). Absorption (excitation) can go by different ways. In [48], the exciton excitation model is described. The role of Frenkel excitons is played by

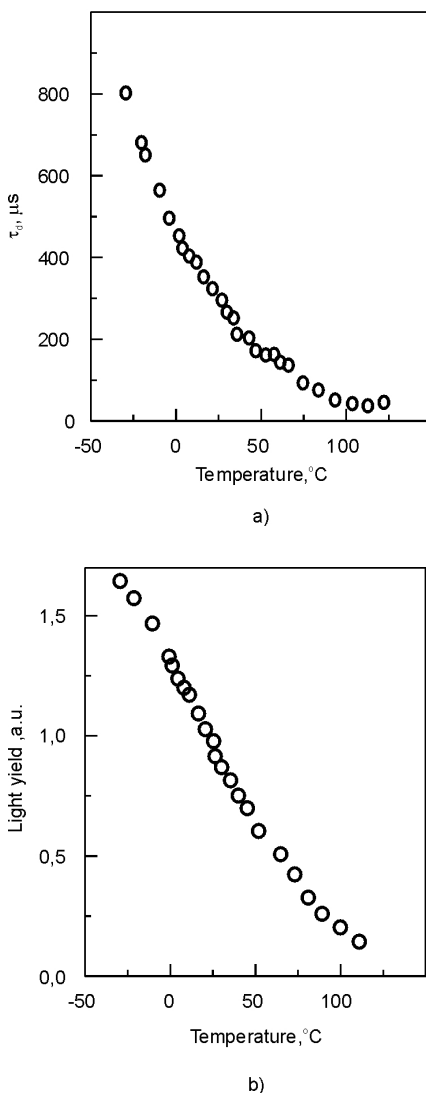


Fig.2.10. Decay time  $\tau_d$  (a) and light output (b) as function of temperature for BGO single crystals.



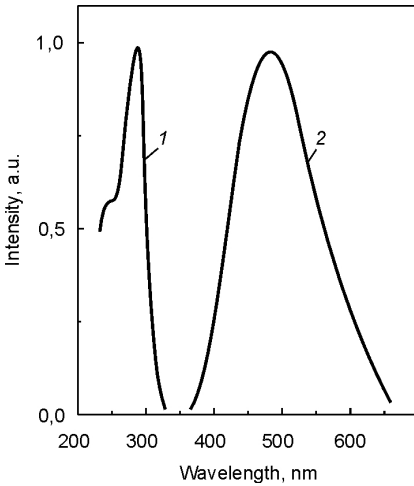


Fig.2.11. Excitation (1) and luminescence (2) spectra of  $\text{Bi}_4\text{Ge}_3\text{O}_{12}$  at the room temperature.

tals with blocks of up to  $1\text{ cm}^3$  volume and disorientation between them not more than  $5'$  have scintillation parameters practically identical with those of crystals without blocks grown from the same charge under the same conditions. As for admixtures and inclusions, their influence

Table 2.5. Luminescent-optical characteristics of crystals  $\text{Bi}_4\text{Ge}_3\text{O}_{12}$  and  $\text{Bi}_4\text{Si}_3\text{O}_{12}$ .

Crystal	$\text{Bi}_4\text{Ge}_3\text{O}_{12}$	$\text{Bi}_4\text{Si}_3\text{O}_{12}$
Band gap, eV	5.0	5.4
Low-energy peak in reflection spectra, eV		
300 K	4.68	5.1
80 K	4.8	5.2
4.2 K	4.8	—
Emission maximum, eV	2.45	2.5
Quantum yield of luminescence at $T$ , K		
295	0.13	0.027
80	0.44	0.3

excited ion-clusters  $\text{BiO}_6^{9-}$  and  $\text{Ge}_4^{4-}$  (in analogy with the situation in  $\text{CaWO}_4$ , where the Frenkel exciton is represented by an excited quasi-molecule  $\text{WO}_4^{2-}$ ). The energy transfer from excitons to dopant centers in BGO can be realized by two mechanisms [49] — non-radiative sensibilization transfer and migration of the mobile excitons interacting with the dopant centers.

Let us now consider how the defects of different nature can affect scintillation parameters of BGO crystals.

Effects of dislocations and the block structure upon scintillation properties of BGO crystals are practically not known. BGO crystals

Table 2.6. Effects of structure imperfectness in BGO crystals upon their energy resolution.

Sample No.	Sample characteristics		Energy resolution, %
	Coloring	Presence of in- clusions	
1	Yellow	Yes	14.6
2	Yellow	No	13.2
3	Colorless	Yes	10.0
4	Colorless	No	34.5

upon optical and scintillation parameters can be rather significant. In Table 2.6, results are presented showing how structural imperfections of  $\varnothing 25 \times 25$  mm BGO crystals affect their energy resolution [50].

As it is seen from the Table, coloring of the BGO crystal and the presence of inclusions in its volume substantially worsen one of the most important scintillation characteristics — the energy resolution. Statistical processing of the results obtained for BGO crystals with low values of the main scintillation parameters has shown that these low values are generally due to macro- and microdefects, as well as admixtures. Thus, for a batch of BGO crystals with light output from 10.3% to 17.5% and energy resolution from 12.8% to 18.3%, the following variation limits were established for the impurity content (in mol.%): **Cu** — from  $3 \cdot 10^{-6}$  to  $1 \cdot 10^{-5}$ ; **Fe** — from  $1.1 \cdot 10^{-4}$  to  $2 \cdot 10^{-4}$ ; **Al** — from  $6 \cdot 10^{-5}$  to  $1.1 \cdot 10^{-4}$ ; **Mg** — from  $2.5 \cdot 10^{-5}$  to  $1 \cdot 10^{-4}$ ; **Pb** — from  $< 2.5 \cdot 10^{-5}$  to  $< 2.5 \cdot 10^{-4}$ ; **C** — from  $3.5 \cdot 10^{-3}$  to  $4.4 \cdot 10^{-2}$ , with Si content nearly constant. Some crystals were uncolored, the color of others varied from light yellow to dark yellow. The number of inclusions in these crystals was substantially different.

Coloring of a crystal can be caused both by an admixture introduced into the crystal in quantities more than  $10^{-4}$  and by the presence of improper phases in the crystal, such as compounds **Bi<sub>2</sub>GeO<sub>5</sub>** and **Bi<sub>12</sub>GeO<sub>20</sub>**. The coloring can be avoided by using charge of higher purity or growing the crystal from a recrystallized raw material. In the latter case, there is a danger of the metastable phase formation and violation of the melt stoichiometry due to evaporation of one of the components — **Bi<sub>2</sub>O<sub>3</sub>**.

Among macro- and microdefects that can be found in BGO crystals even by visual observation, one should note chaotic bands of inclusions, periodic bands of inclusions, inclusions due to concentrational supercooling of the melt, isolated small-sized inclusions. Practically all the defects of this type can be avoided by optimizing the crystal growth conditions, specifically, by using an automatic growth control system.

Inclusions of different nature in BGO crystals may lead to appearance of absorption bands in the visible spectral range and increased absorption in the near-UV range. They also affect the shape of the fundamental absorption band edge. In yellow BGO crystals, an absorption band was recorded close to 400 nm, with its nature still unclear. The best optical transmission values were obtained for totally colorless crystals grown from high-purity charge that had been submitted to triple recrystallization.

For applications of BGO crystals in high-energy physics, one of the requirements is stability with respect to ionizing radiation. BGO single crystals have satisfactory radiation stability (this term means that BGO crystals preserve their main parameters and functional abilities both directly under irradiation and after irradiation had been stopped). Radiation stability of BGO crystals depends both on the crystal quality and on properties of the radiation – its type, dose rate, exposure time, etc. In analyzing the radiation stability of BGO crystals, attention should be paid to deterioration of the crystal transparency (emergence of coloring centers), crystal degradation due to radiation-induced structure violations and formation of defects in the bulk crystal and on its surface, increased noise of the scintillation detector, etc. Radiation stability of BGO single crystals is strongly affected by the presence of such admixtures as Pb, Fe, Mn, and oxygen, which is the most harmful. Depending upon the crystal size and purity, in powerful radiation fields the main scintillation characteristics of BGO crystals are either practically unchanged or are changed with a possibility of subsequent restoration.

Restoration of the initial optical transparency can occur spontaneously under influence of thermal factors or can be stimulated by laser irradiation of the crystal. In [51], kinetics of the de-coloring after irradiation was explained in terms of a Frenkel pair model, the formation of which involves the admixture atoms. This pair is unstable, as its dissociation requires only 30 MeV. The de-coloring

time of BGO crystals can be from 1 to 30 days. Analyzing results obtained by various researchers, one could note that both the process of radiation-induced damaging and the process of restoration of the irradiated samples are largely specific for each individual crystal, depending upon purity of the raw material, presence of admixtures and various microstructure defects, crystal size, radiation energy, dose and dose rate.

Under similar radiation conditions, radiation-induced changes in such parameters as light output and optical transmission are much smaller for crystals of relatively short length, and greater for crystals of large dimensions. The main type of radiation-stimulated defects formed in BGO crystals under  $\gamma$ -irradiation are coloring centers, which affect the crystal transparency. It should be noted that in the high-energy physics applications of BGO crystals, the degradation of the transmission coefficient, and not variation of the scintillation properties, is the most important factor.

When BGO crystals are affected by neutrons and protons, substantial degradation of the transmission spectra and loss of transparency are observed. Restoration of optical transparency of BGO crystals that had been irradiated by neutrons or protons goes more slowly than after  $\gamma$ -irradiation. As for electron radiation ( $E \sim 200$  keV), it can cause radiation-stimulated point defects or their aggregates in BGO crystals.

When BGO crystals are irradiated by neutrons, protons or electrons, thermally stable luminescent radiation defects can also be formed. Annealing of BGO crystals up to 670–870 K favors destruction of the absorbing centers in the visible range of the spectrum that are associated with admixture or intrinsic pre-radiation defects, and, at the same time, formation of new luminescent radiation defects. Analysis of experimental and theoretically calculated values of the threshold energy  $E_d$  for the impact displacement mechanism [21] has shown that luminescent radiation defects can be formed in BGO by the said mechanism ensuring breaking of inter-atomic bonds and formation of Frenkel pairs. Electrons with energies  $E < E_d$  do not create such defects. If there are admixture defects, or pre-radiation defects of other types, formation of radiation-stimulated defects that would be optically active, but not luminescent, is possible even by electrons with energies  $E < E_d$ , as well as by low-energy  $\gamma$ -radiation. In the same paper, possible models of luminescent radiation defects

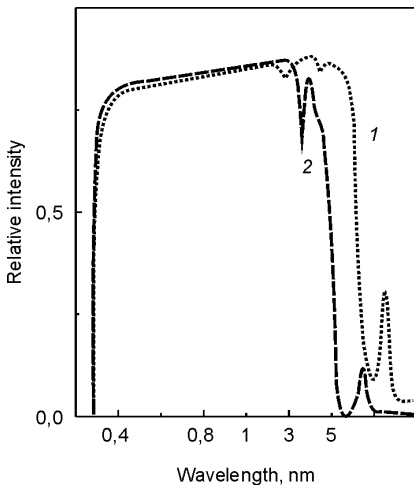


Fig.2.12. Transmission spectra of BGO (1) and BSO (2) crystals.

crystals grown in similar conditions. The luminescence spectrum had maximum at 480 nm, and the decay time was 0.1  $\mu$ s. The energy resolution was reported as 30% ( $^{137}\text{Co}$   $\gamma$ -radiation). It is clear that BSO is inferior as compared to BGO by nearly all parameters. The only exception is the decay time, which is 3 times shorter as compared with BGO. The transparency range of BSO is narrower, but the level of transparency is similar (Fig.2.12). Reflection and absorption spectra of both crystals are largely similar.

It has been noted [46] that in BSO crystals the absorption edge and the low-energy maximum of the reflection spectrum are shifted towards higher energies. Scintillation parameters of  $\text{Bi}_4\text{Si}_3\text{O}_{12}$  single crystals reported in [53] were similar to the above-described: light output of 18% (with respect to BGO), X-ray luminescence maximum at 500 nm, decay time  $\tau = 0.1 \mu$ s.

In general, scintillation parameters of  $\text{Bi}_4\text{Si}_3\text{O}_{12}$  single crystals are not very high, but still they can be used for detection of  $\gamma$ -radiation. However, due to their low light output, BSO can hardly be considered as a promising scintillation material, even accounting for its being relatively cheap.

in irradiated BGO crystals are discussed.

Thus, radiation-stimulated defects in BGO crystals generally worsen their scintillation characteristics. The induced absorption has been shown to lower the scintillator transparency to the intrinsic radiation; luminescence that is due to radiation defects can make the scintillation pulse substantially longer, especially at low temperatures.

Single crystals of  $\text{Bi}_4\text{Si}_3\text{O}_{12}$  have been studied much less than those of  $\text{Bi}_4\text{Ge}_3\text{O}_{12}$ .  $\text{Bi}_4\text{Si}_3\text{O}_{12}$  single crystals reported in [52] had their light output at the level of just 20% with respect to  $\text{Bi}_4\text{Ge}_3\text{O}_{12}$

### *2.1.6. Applications of BGO and BSO single crystals.*

Possible application fields of BGO and BSO single crystals are determined by their physico-chemical properties and scintillation characteristics. At present, BGO is considered as the most promising material for high energy physics — the field where disadvantages of such commonly used scintillation materials as NaI(Tl) and CsI(Tl) are especially obvious. These disadvantages include relatively high radiation length, which implies the use of large-sized detectors, hygroscopicity, which makes continuous problems with appropriate housing and containers for scintillator crystals, etc. For efficient experiments using accelerators of charged particles, small-sized electromagnetic calorimeters are needed with high spatial, energy and time resolution, which would ensure high detection efficiency and reliability. Large density of BGO and its high effective atomic number ensure small radiation length, and relatively short decay times ensure sufficiently fast response of BGO-based detectors. Lower light output of BGO as compared with alkali halide scintillators is not so important at high energies of elementary particles, where at  $E > 10$  MeV BGO has much better energy resolution than AHC. BGO crystals are also suitable for spectrometry and radiometry of  $\gamma$ -radiation.

Because of their substantial advantages in afterglow (it is by two orders of magnitude lower as compared with NaI(Tl)), BGO crystals are very promising for application in computer tomography, as they ensure substantially lower dynamical errors of the measurements.

Recently, there has been much interest in BGO single crystals as scintillation materials for positron emission tomography (PET) [54,56,57,64].

In [54,56], a position-sensitive detector of gamma-quanta is described, which is used in a positron emission tomograph based on hodoscopic PMT in combination with BGO and GSO scintillators. Intrinsic spatial resolution was measured for the tomograph elements: with a  $\text{Bi}_4\text{Ge}_3\text{O}_{12}$  scintillator, it was 3.6 mm, and with  $\text{Gd}_2\text{SiO}_5\text{:Ce}$  — 1.75 mm.

Fig.2.13 shows time and spatial resolution of a position-sensitive detector using GSO (a) and BGO (b) crystals, which means that nearly complete separation of events coming from the neighboring scintillation plates had been achieved.

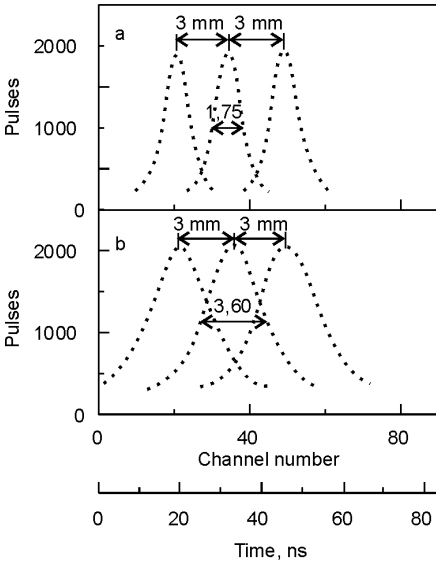


Fig.2.13. Time and spatial resolution of positional-sensitive detectors using GSO (a) and BGO (b) crystals. The values were obtained at three positions of the scintillation plate along the hodoscopic PMT photocathode:  $-3.0$  mm and  $+3.0$  mm. The source used is  $^{22}\text{Na}$ .

interaction cross-sections with BGO and  $\text{NaI(Tl)}$  are practically the same). Disadvantages of BGO scintillators: light output is only 10–20% with respect to  $\text{NaI(Tl)}$ ; optical refraction index is high ( $n_d = 2.15$ ), which causes additional light losses at the boundary between the crystal and the photoreceiver. In [55], BGO scintillation crystals with good spectrometric parameters were reported (high energy resolution and uniformity of the light output), which could be used in a high-resolution spectrometer of neutral particles.

In [147, 148], BSO crystals were presented as promising materials for experiments in high-energy physics as a fast and heavy scintillator. Though light output of BSO is only 20% of the light output of BGO, the decay time is three times shorter (just 100 ns) [148].

BGO scintillation crystals are characterized by many properties that make them also promising for applications in the medium-energy physics, especially for detection of neutral particles ( $\pi^0$ ,  $\eta$ -mesons,  $\gamma$ -quanta). The most important parameters of the detectors of neutral particles are high energy resolution, high spatial resolution in determining the  $\gamma$ -quanta interaction coordinates in the detector, low sensitivity to background neutrons. In this connection, advantages of BGO crystals are obvious: high effective atomic number and high density ensuring short radiation length and good localization of the electromagnetic showers inside the crystal, low sensitivity to thermal neutrons ( $\sim 0.1$  with respect to  $\text{NaI(Tl)}$ ; at  $E_n \sim 10$  MeV, the neutron interaction cross-sections with BGO and  $\text{NaI(Tl)}$  are practically the same).

## 2.2. *Compounds of yttrium, scandium and rare-earth element silicates*

### 2.2.1. *Crystal structure of compounds $\text{Ln}_2\text{SiO}_5$*

It is known that in  $\text{Ln}_2\text{O}_3\text{--SiO}_2$  binary systems (here Ln denotes a lanthanide element) at  $\text{Ln}_2$  to  $\text{SiO}_5$  ratio 1:1 for all Ln, as well as for Y and Sc, there exist compounds of formula  $\text{Ln}_2\text{SiO}_5$  (lanthanide orthosilicates  $\text{Ln}_2\text{O}[\text{SiO}_4]$ ) that are congruently melting and stable in a broad temperature range. Lanthanide orthosilicates are characterized by their high mechanical strength, high thermal and chemical stability, as well as good transparency in a broad optical range. It has been noted [58] that yttrium, scandium and rare-earth element silicates are highly efficient for detection of radiation of different types; with their relatively short scintillation time ( $\sim 15\text{--}60$  ms), they can ensure efficient loading of scintillation detector circuits. The crystal structure of  $\text{Ln}_2\text{SiO}_5$  allows introduction of activator ions in rather high concentrations for purposeful variation of scintillation characteristics. X-ray studies of  $\text{Ln}_2\text{SiO}_5$  crystals have shown [59] that, depending upon their crystal structure, they can be sub-divided into three types. The first type includes lanthanide orthosilicates from Lu to Tb (monoclinic lattice,  $P2_1/c$ ,  $z = 4$ ), the second type — those from Tb to Nd (monoclinic lattice,  $B2/b$ ,  $z = 8$ ), and the third type —  $\text{La}_2\text{SiO}_5$ , the structure of which had not been determined. In a later publication [60], all  $\text{Ln}_2\text{SiO}_5$  crystals studied were subdivided into only two types (Table 2.7).

For  $\text{Dy}_2\text{SiO}_5$ , dimorphism is observed. Spectroscopic studies also confirmed the existence of two crystalline modifications of  $\text{Dy}_2\text{SiO}_5$  — their absorption spectra are markedly different both in number of Dy lines and their position.

Recent data [61] indicate that  $\text{Ln}_2(\text{SiO}_4)\text{O}$  orthosilicates, where Ln can be yttrium, scandium or one of 14 lanthanides, can belong to two structural types, depending upon the size of the rare-earth element ion (Table 2.8). Table 2.8 includes data on six compounds that were not present in Table 2.7.

Let us consider in more detail some features of the crystal structure of  $\text{Gd}_2\text{SiO}_5$  (GSO), which is an optimally suited matrix for such activators as cerium and europium. The diagram of state for the system  $\text{Gd}_2\text{O}_3\text{--SiO}_2$  was presented in [62]. In this system, three compounds exist of the following composition:  $\text{Gd}_2\text{O}_3 \cdot \text{SiO}_2$ ,  $2\text{Gd}_2\text{O}_3 \cdot 3\text{SiO}_2$  and  $\text{Gd}_2\text{O}_3 \cdot 2\text{SiO}_2$ . The first two (50%  $\text{SiO}_2$  and 60%  $\text{SiO}_2$ ) have congru-



Table 2.7. Structural properties of lanthanide oxyorthosilicates [60]

Compound	Structural type	Elementary lattice parameters				V, Å <sup>3</sup>
		a, Å	b, Å	c, Å	β, deg	
Gd <sub>2</sub> SiO <sub>5</sub>	<i>P</i> 2 <sub>1</sub> / <i>c</i> (Type I)	9.6 (2)	7.09 (2)	6.83 (1)	107.58 (20)	422.9
Tb <sub>2</sub> SiO <sub>5</sub>	I	9.14 (2)	7.08 (3)	6.76 (2)	107.64 (28)	416.8
Dy <sub>2</sub> SiO <sub>5</sub>	I	9.11 (3)	7.05 (3)	6.70 (3)	107.25 (38)	411.0
Dy <sub>2</sub> SiO <sub>5</sub>	<i>B</i> 2/ <i>b</i> (Type II)	14.56 (2)	10.51 (2)	6.789 (7)	122.36 (15)	877.7
Ho <sub>2</sub> SiO <sub>5</sub>	II	14.48 (1)	10.47 (1)	6.761 (4)	122.23 (7)	867.9
Er <sub>2</sub> SiO <sub>5</sub>	II	14.42 (2)	10.40 (2)	6.729 (9)	122.16 (18)	854.4
Tm <sub>2</sub> SiO <sub>5</sub>	II	14.41 (2)	10.37 (2)	6.721 (7)	122.12 (13)	850.5
Yb <sub>2</sub> SiO <sub>5</sub>	II	14.37 (1)	10.34 (1)	6.693 (4)	122.28 (10)	840.5
Lu <sub>2</sub> SiO <sub>5</sub>	II	14.33 (2)	10.32 (2)	6.671 (6)	122.30 (13)	833.8
Y <sub>2</sub> SiO <sub>5</sub>	II	14.43 (2)	10.41 (2)	6.733 (8)	122.13 (13)	856.1

ent melting points, and the third compound (66% SiO<sub>2</sub>) is formed by a peritectic reaction. The compound Gd<sub>2</sub>SiO<sub>5</sub> melts at 1900°C and is stable in a broad temperature range, including room temperature. As compared with other compounds that are possible in the Gd<sub>2</sub>O<sub>3</sub>–SiO<sub>2</sub> system, the crystallization temperature of Gd<sub>2</sub>SiO<sub>5</sub> is relatively low.

The structure of Gd<sub>2</sub>SiO<sub>5</sub> (according to [63]) is shown in Fig.2.14. It was constructed by superposition of the electron density cross-sections over the (001) plane.

Gadolinium atoms are located in alternating layers parallel to the (100) plane. In one of these layers (Gd<sub>1</sub> in the picture) gadolinium atoms are surrounded by nine nuclei — eight oxygens from Si-tetrahedrons, and one “free” oxygen. In another layer, gadolinium atoms are in sevenfold coordination (Gd<sub>2</sub> in the picture). Their coordination polyhedron is formed by four oxygens from tetrahedrons and three “free” oxygens. Each oxygen atom in the tetrahedrons is bonded to silicon and three gadolinium atoms. The “free” oxygen is bonded to four gadolinium atoms.

Table 2.8. Crystal structure of yttrium, scandium and rare-earth element oxyorthosilicates.

Compound	Crystal structure	Compound	Crystal structure
Sc <sub>2</sub> (SiO <sub>4</sub> )O	<i>B2/b</i>	Tb <sub>2</sub> (SiO <sub>4</sub> )O	<i>P2<sub>1</sub>/c</i>
Y <sub>2</sub> (SiO <sub>4</sub> )O	<i>B2/b</i>	Dy <sub>2</sub> (SiO <sub>4</sub> )O	<i>P2<sub>1</sub>/c</i>
La <sub>2</sub> (SiO <sub>4</sub> )O	<i>P2<sub>1</sub>/c</i>	Dy <sub>2</sub> (SiO <sub>4</sub> )O	<i>B2/b</i>
Ce <sub>2</sub> (SiO <sub>4</sub> )O	<i>P2<sub>1</sub>/c</i>	Ho <sub>2</sub> (SiO <sub>4</sub> )O	<i>B2/b</i>
Nd(SiO <sub>4</sub> )O	<i>P2<sub>1</sub>/c</i>	Er <sub>2</sub> (SiO <sub>4</sub> )O	<i>B2/b</i>
Sm <sub>2</sub> (SiO <sub>4</sub> )O	<i>P2<sub>1</sub>/c</i>	Tm <sub>2</sub> (SiO <sub>4</sub> )O	<i>B2/b</i>
Eu <sub>2</sub> (SiO <sub>4</sub> )O	<i>P2<sub>1</sub>/c</i>	Yb <sub>2</sub> (SiO <sub>4</sub> )O	<i>B2/b</i>
Gd <sub>2</sub> (SiO <sub>4</sub> )O	<i>P2<sub>1</sub>/c</i>	Lu <sub>2</sub> (SiO <sub>4</sub> )O	<i>B2/b</i>

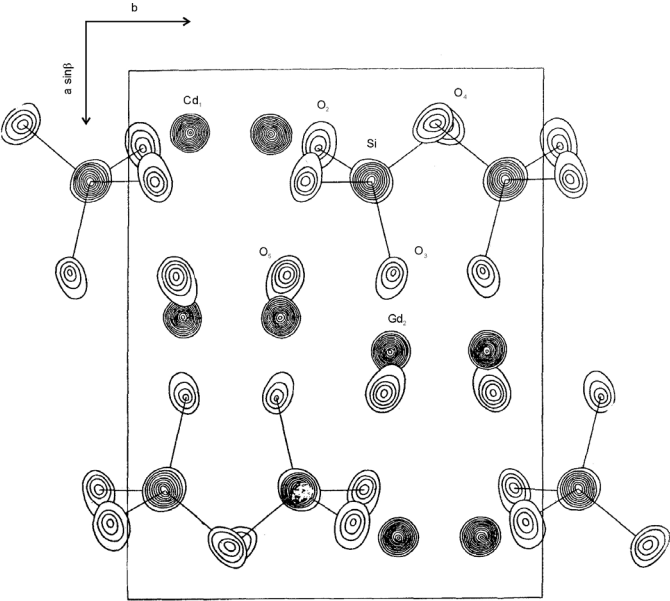


Fig.2.14. Projection of the electron density cross-section onto the (001) plane of Gd<sub>2</sub>SiO<sub>5</sub>. Isolines are drawn with step 50 electrons/Å<sup>3</sup> for heavy atoms and 10 electrons/ Å<sup>3</sup> — for light atoms.

A rather clear relationship between the Si–O bond length in the tetrahedrons and the average bond length between the corresponding oxygen and cations was noted [63]. An increase in the interatomic distance Gd–O is accompanied by shortening of the corresponding O–Si distance. This relationship between the distances Gd–O, O–Si allows one to assume that Gd–O bonds are largely covalent in character, and decreasing the Gd–O distance increases the O–Si bond order, and vice versa.

### *2.2.2. Technological features of $\text{Ln}_2\text{SiO}_5$ single crystal growth*

Czochralski growth of lanthanide oxyorthosilicate crystals was first reported in the mid-seventies of the 20<sup>th</sup> century [65,66]. All the crystals listed in Table 2.7 could be successfully obtained by this method. The initial charge for single crystal growth was synthesized by the solid-phase method. Pre-annealed oxides  $\text{Ln}_2\text{O}_3$  and  $\text{SiO}_2$ , taken in stoichiometric ratio 1:1, were powdered in an agate mortar and thoroughly mixed, after which the powder was annealed sequentially at 1270 K, 1470 K and 1720 K. Melt crystallization was carried out in an inert atmosphere (Ar). Because of high melting temperature of  $\text{Ln}_2\text{SiO}_5$ , iridium crucibles had to be used. In growing the crystals, iridium wires or plates cut from already grown samples were used as seeds. Growth speed was 3–10 mm/hour, and rotation speed was 20–30 rpm. The grown crystals were annealed in the same installation for 4–6 hours, and the temperature was lowered by a programmed decreasing of the generator power. Using this method, optically uniform single crystals of  $(\text{Gd-Lu})_2\text{O}[\text{SiO}_4]$  and  $\text{Y}_2\text{O}[\text{SiO}_4]$  could be obtained, 10–15 mm in diameter and up to 100 mm long [65,66].

A single crystal of composition  $\text{Ce}_{0.01}\text{Gd}_{1.99}\text{SiO}_5$  was grown by the Czochralski method [67] in a nitrogen atmosphere (growth speed 3 mm/hour, rotation speed 40 rpm, iridium crucibles). No evaporation or decomposition of the melt was observed. About 80–90% of cerium initially contained in the melt was introduced into the grown crystal, showing that the distribution coefficient of Ce was close to 1. Grown  $\text{Gd}_2\text{SiO}_5\text{:Ce}$  single crystals were uniform all over the crystal volume as for their composition and scintillation parameters.

As cerium oxide and silicates are unstable, the Czochralski growth of  $\text{Gd}_2\text{SiO}_5\text{:Ce}$  single crystals normally requires an inert atmosphere.

However, oxidation medium could also be used [68]. Annealing of the oxide mixture (1500°C), melting in an iridium crucible (1900°C) and crystal growth itself were carried out in air. As for reduction of the activator oxidized to  $\text{Ce}^{4+}$ , it was made by a subsequent thermal treatment at 1200°C in hydrogen atmosphere. A single crystal sample obtained by this procedure was characterized by improved scintillation characteristics; the luminescence decay time did not exceed 30 ns.

In [69,70] some crystallographic features of  $\text{Gd}_2\text{SiO}_5$  single crystal growth were noted. These crystals belong to the monoclinic syngony, which implies not only marked anisotropy of their physical properties, but also crystallochemical non-equivalence of growth shapes taking part in the crystal formation in the course of its growth. For GSO crystal growth, two crystallographic directions are the most important: [001] (cleavage plane along the growth direction), and [010], when the cleavage plane is normal to the growth direction.

It has been noted that  $\text{Gd}_2\text{SiO}_5$  crystals grown along the [001] direction show much less tendency of block structure formation. This should be accounted for in choosing the optimum crystallographic direction of their growing.

In [69], GSO crystals 25–55 mm in diameter and 90–180 mm long were grown in iridium crucibles by the Czochralski method at pulling speed of 1.3 to 3.5 mm/hour. Thermal conditions were chosen accounting for the need of substantial overheating. The grown GSO crystals had no inclusions of other phases, were colorless and showed sufficiently high scintillation characteristics. The crystals were annealed directly in the crystallization chamber after separation of the grown crystal from the melt.

The most difficult problem in GSO production is its preservation after growth. Anisotropy of mechanical strength and the presence of two cleavage planes cause cracking of the grown crystals at the stages of thermal and mechanical treatment. This kind of defectness is the most important for Czochralski-grown GSO single crystals.

In Table 2.9, typical parameters are given for the growth process, as well as typical dimensions of YSO, GSO and LSO crystals [61]. These crystals were prepared by the Czochralski method in iridium crucibles from the components  $\text{Ln}_2\text{O}_3$ ,  $\text{SiO}_2$  and  $\text{CeO}_2$  (purity not less than 99.99%) taken in stoichiometric proportions. The atmosphere used was either inert ( $\text{N}_2$ ) or oxygen-containing ( $\text{N}_2+\text{O}_2$ ).

Table 2.9. Typical parameters of crystal growth

Parameter	YSO	GSO	LSO
Rotation speed, rpm	6–30	6–60	20–65
Pulling rate, mm/hour	0.5–2.0	0.5–2.0	0.5–5.0
Maximum diameter, mm	25	62	35
Maximum length, mm	60	300	100

YSO and LSO crystals were grown in different crystallographic directions, while GSO crystals were oriented in such a way as to minimize the possibility of fissure formation and cracking along the cleavage plane.

*2.2.3. Main physico-chemical properties and scintillation characteristics of yttrium, scandium and rare-earth element silicates*

Physico-chemical properties of lanthanide oxyorthosilicates are presented in Table 2.10.

$\text{Ln}_2\text{SiO}_5$  crystals are biaxial and optically positive. They are characterized by high melting temperatures, and most of them — also by their high density. Crystals with monoclinic lattice  $P2_1/c$  (Type I) are characterized by their perfect cleavage plane (100) and another clear cleavage plane (010), while those with monoclinic lattice  $B2/b$  (Type II) — by non-perfect cleavage planes (001) and (011). Especially easily cleaved along the (100) plane are  $\text{Gd}_2\text{SiO}_5$  crystals.  $\text{Gd}_2\text{SiO}_5$  single crystals are also characterized by high anisotropy of heat conduction: in the [010] direction, it is 2–3 times higher than in the directions [001] or [100].

Studies of optical properties of  $\text{Ln}_2\text{SiO}_5$  crystals have shown that Gd, Yb, Lu and Y orthosilicates are transparent in a broad spectral range — from 0.2 to 5.0  $\mu\text{m}$ . The character of absorption spectra of colored  $\text{Ln}_2\text{SiO}_5$  crystals in the UV, visible and near-IR ranges is determined by absorption due to  $\text{Tb}^{3+}$ ,  $\text{Dy}^{3+}$ ,  $\text{Ho}^{3+}$ ,  $\text{Er}^{3+}$ ,  $\text{Tm}^{3+}$  ions. In the 5–6  $\mu\text{m}$  region, absorption spectra of  $\text{Ln}_2\text{SiO}_5$  crystals are determined by combinations of valence vibration frequencies due to  $[\text{SiO}_4]$  tetrahedral groups, with clearly noted differences in the band structure noted for crystals of structural types I and II.

Table 2.10. Physico-chemical properties of lanthanide oxyorthosilicates [60]

Compound	Structural type	$T_{melt}$ , K	$\rho$ , g/cm <sup>3</sup>	Refraction index			Optical sign	Cleavage plane
				$n_g$	$n_m$	$n_p$		
Gd <sub>2</sub> SiO <sub>5</sub>	I	2170	6.77	1.910	1.884	1.871	+	(100), (010)
Tb <sub>2</sub> SiO <sub>5</sub>	I	2180	6.93	1.912	1.888	1.870	+	(100), (010)
Dy <sub>2</sub> SiO <sub>5</sub>	I	2190	7.20	1.908	1.885	1.869	+	(100), (010)
Dy <sub>2</sub> SiO <sub>5</sub>	II	2190	6.66	1.848	1.822	1.820	+	(001), (011)
Ho <sub>2</sub> SiO <sub>5</sub>	II	2190	6.80	1.847	1.818	1.813	+	(001)
Er <sub>2</sub> SiO <sub>5</sub>	II	2250	6.96	1.838	1.812	1.809	+	(001)
Tm <sub>2</sub> SiO <sub>5</sub>	II	2230	7.07	1.836	1.812	1.809	+	(001)
Yb <sub>2</sub> SiO <sub>5</sub>	II	2250	7.28	1.834	1.811	1.805	+	(001), (011)
Lu <sub>2</sub> SiO <sub>5</sub>	II	2320	7.41	1.825	1.803	1.797	+	(001)
Y <sub>2</sub> SiO <sub>5</sub>	II	2200	4.45	1.811	1.784	1.780	+	(001), (011)

In [61], some data are given on other orthosilicates not mentioned in [60]. These data are presented in Table 2.11.

Scintillation properties of yttrium, scandium and rare-earth element silicate crystals are given in Table 2.12 [58].

X-ray luminescence spectra for these crystals [58] are shown in Fig.2.15. It should be noted that concentration of Tb in Y<sub>2</sub>SiO<sub>5</sub> was 3 at.%, Eu in Y<sub>2</sub>SiO<sub>5</sub> — 4 at.%, Dy in Gd<sub>2</sub>SiO<sub>5</sub> — 10<sup>-4</sup> at.%. Y<sub>2</sub>SiO<sub>5</sub> samples contained cerium (< 10<sup>-3</sup> mass %).

The relative light output values for crystals studied in [58], measured in the pulse mode, is presented in Table 2.12, and those measured in the current mode — in Table 2.13.

Single crystals Y<sub>2</sub>SiO<sub>5</sub>-Tb,  $\Sigma$ TR, as follows from data of Tables 2.12 and 2.13, possess a whole set of scintillation characteristics that allows us to consider them as promising materials for detection of  $\beta$ -particles, electron beams and  $\beta$ -radiation. They have high light yield of  $\beta$ - and  $\gamma$ -scintillations, satisfactory energy resolution and scintillation time,

Table 2.11. Physical properties of some orthosilicates of rare-earth elements [61]

Compound	Melting point, K	Density, g/cm <sup>3</sup>
Sc <sub>2</sub> (SiO <sub>4</sub> )O	2220	3,49
La <sub>2</sub> (SiO <sub>4</sub> )O	2220	5,49
Ce <sub>2</sub> (SiO <sub>4</sub> )O	—	6,11
Nd <sub>2</sub> (SiO <sub>4</sub> )O	2250	6,00
Sm <sub>2</sub> (SiO <sub>4</sub> )O	2210	6,38
Eu <sub>2</sub> (SiO <sub>4</sub> )O	2250	6,51

high thermal stability, etc. In the integral current mode, this material is also highly efficient for detection of X-ray radiation. It should be also noted that Y<sub>2</sub>SiO<sub>5</sub>-Tb and Gd<sub>2</sub>SiO<sub>5</sub>-Dy crystals have rather short scintillation time, and the first of them has rather low  $\alpha/\beta$  ratio equal to 0.02. Sc<sub>2</sub>SiO<sub>5</sub> crystals have very different times of  $\alpha$ - and  $\beta$ -scintillations, which allows signal selection from different sources not only by amplitude, but also by time.

Y<sub>2</sub>SiO<sub>5</sub> crystals that are simultaneously doped by terbium and cerium are the most efficient cathodo- and radioluminophores in this class of materials [71]. Analysis of the luminescence kinetics carried out in [71] shows that, in the case of pulse cathodoluminescence, at the initial stages (up to 15 ns) only bands due to Tb<sup>3+</sup> ions are observed in the luminescence spectra. The luminescence band due to Ce<sup>3+</sup> (~405 nm) appears only in 15–20 ns after the appearance of terbium bands. Both Tb<sup>3+</sup> and Ce<sup>3+</sup> bands reach their maximum intensity after 50 ns. These bands are also visible at the decay stage, up to 150 ns. A peculiar feature of the cathodoluminescence spectra of Y<sub>2</sub>SiO<sub>5</sub>-Tb,Ce crystals (as distinct from the known spectra for the case of stationary excitation) is that Ce<sup>3+</sup> and Tb<sup>3+</sup> bands, which are ideally overlapping in the 380–480 nm region, are much more intense than for Y<sub>2</sub>SiO<sub>5</sub> doped just by Tb or Ce. It can be assumed that under pulse excitation of Y<sub>2</sub>SiO<sub>5</sub>-Tb,Ce crystals efficient channels are opened for exchange energy transfer Tb<sup>3+</sup> ↔ Ce<sup>3+</sup>, resulting in the increased cathodoluminescence yield. This can also explain high scintillation efficiency of Y<sub>2</sub>SiO<sub>5</sub>-Tb,Ce crystals in the nanosecond range as compared with monoactivated samples.





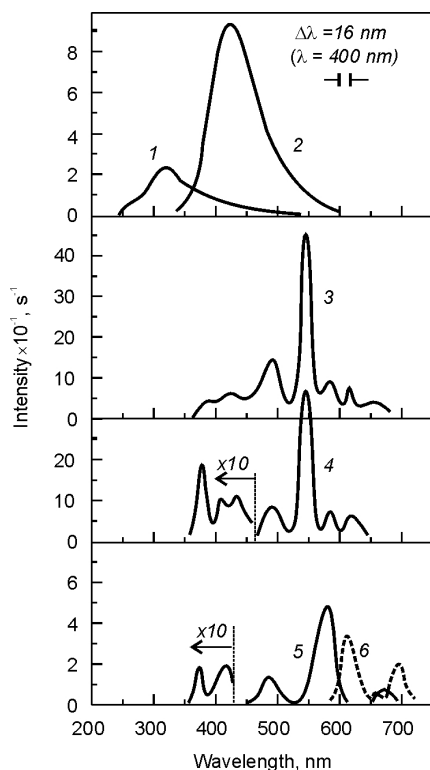


Fig.2.15. X-ray luminescence spectra at 300 K: 1 —  $\text{Sc}_2\text{SiO}_5$ ; 2 —  $\text{Y}_2\text{SiO}_5$ ; 3 —  $\text{Y}_2\text{SiO}_5\text{-Tb}$ ,  $\Sigma\text{TR}$ ; 4 —  $\text{Y}_2\text{SiO}_5\text{-Tb}$ ; 5 —  $\text{Gd}_2\text{SiO}_5\text{-Dy}$ ; 6 —  $\text{Y}_2\text{SiO}_5\text{-Eu}$  [3].

location of the activator. As for GSO, its luminescence peak is in the more long-wave region, according to its monoclinic crystal lattice  $P2_1/c$ .

Among lanthanide oxyorthosilicates, the most important is  $\text{Gd}_2(\text{SiO}_4)\text{O}:\text{Ce}$ , which is widely used as fast scintillator for detection of gamma-quanta and for positron emission tomography [54].

Trivalent cerium is an efficient scintillation center, which is primarily due to fast electron transitions  $4f-5d$ . The most efficient matrix for Ce from the standpoint of high quantum yield is  $\text{Gd}_2\text{SiO}_5$  [72].

Table 2.13. Relative scintillation light output of crystals (scintillation block operation in the current mode)

Crystal	Light output (current mode)
$\text{Y}_2\text{SiO}_5\text{-Tb}$ , $\Sigma\text{TR}$	100
$\text{Y}_2\text{SiO}_5\text{-Eu}$	3.8
$\text{Y}_2\text{SiO}_5$	5.6
$\text{Gd}_2\text{SiO}_5\text{-Dy}$	10.1
$\text{Sc}_2\text{SiO}_5$	25.8
$\text{Y}_2\text{SiO}_5\text{-Tb}$	70.5
$\text{CsI(Tl)}$	182

Thus, yttrium, scandium and rare-earth element silicates are a promising class of fast, efficient, thermally and chemically stable scintillators.

Main scintillation properties of single crystals  $\text{Y}_2(\text{SiO}_4)\text{O}:\text{Ce}$  (YSO) and  $\text{Lu}_2(\text{SiO}_4)\text{O}:\text{Ce}$  (LSO), as well as of  $\text{Gd}_2(\text{SiO}_4)\text{O}:\text{Ce}$  (GSO), which will be considered in detail, are presented in Figs.2.16–2.19 according to data given in [61].

Luminescence spectra of YSO and LSO are largely similar, as they have the same monoclinic crystal lattice  $B2/b$  and similar

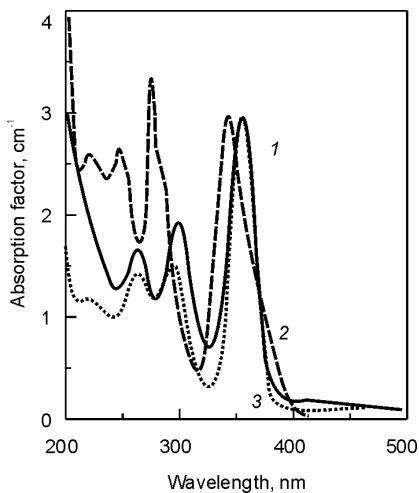


Fig.2.16. Absorption spectra of Ce-doped crystals YSO (1), GSO (2), LSO (3).

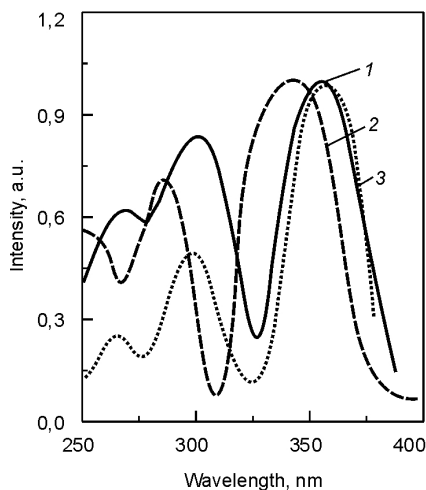


Fig.2.17. Excitation spectra of Ce-doped crystals YSO (1), GSO (2), LSO (3).

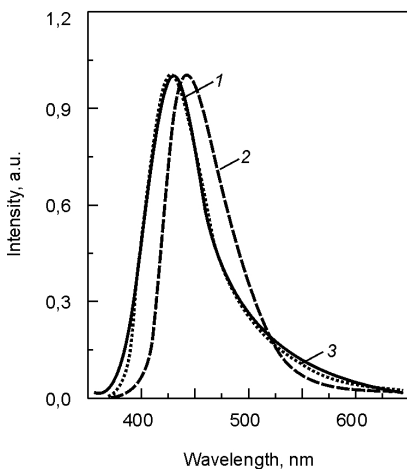


Fig.2.18. Luminescence spectra of Ce-doped crystals YSO (1), GSO (2), LSO (3).

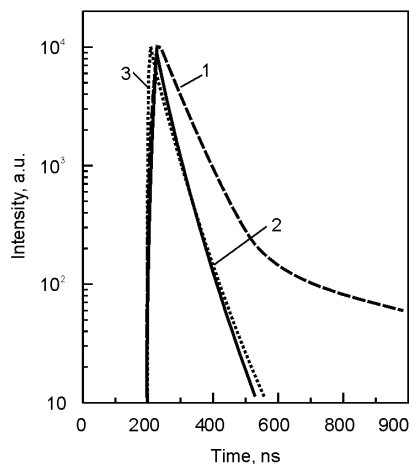


Fig.2.19. Decay times of Ce-doped single crystals YSO (1), GSO (2), LSO (3) under γ-irradiation.

Single crystals of gadolinium oxyorthosilicate  $\text{Gd}_2(\text{SiO}_4)\text{O}:\text{Ce}$ , as for combination of their qualities, are superior to all other known scintillation materials for uses in positron computer tomography and certain fields of nuclear physics. In particular, as compared with another promising and already popular bismuth germanate, it has slightly lower density and effective atomic number, but its decay time is 5 times shorter, light output is more than two times higher, and energy resolution is better. This allows sufficient improvement of fastness and sensitivity of scintillation detectors using gadolinium oxyorthosilicate. Among drawbacks of this material, one could note high cost of gadolinium oxide as raw material and the use of iridium crucibles for crystal growth. Development of the production technology of GSO single crystals meets with many problems because of high melting point of  $\text{Gd}_2\text{SiO}_5$  and difficulties of mechanical treatment due to the presence of cleavage planes.

Main physico-chemical properties and scintillation characteristics of  $\text{Gd}_2\text{SiO}_5:\text{Ce}$  single crystals are presented in Table 2.14. GSO, as a promising material with short decay time, has been extensively studied [61, 75–77].

Undoped  $\text{Gd}_2\text{SiO}_5$  single crystals, though they show scintillation properties, have very low light output. In [78], the optimum concentration of cerium, which ensured the highest light output with decay time of 60 ns, was indicated as 0.5 mol.%. With larger cerium concentrations, crystals become brownish in color. The light output of undoped  $\text{Gd}_2\text{SiO}_5$  crystals is only 5% of the light output of  $\text{Gd}_2\text{SiO}_5$  doped with optimum amount of cerium. As compared with  $\text{Bi}_4\text{Ge}_3\text{O}_{12}$  crystals, the main advantage of  $\text{Gd}_2\text{SiO}_5:\text{Ce}$  is their fastness, which, in combination with high effective atomic number and absence of hygroscopicity, makes this material an optimum choice for positron tomography, experiments in nuclear physics, geology. The emission peak of  $\text{Gd}_2\text{SiO}_5:\text{Ce}$  is observed at 440 nm, i.e., in the range of maximum sensitivity of many commonly used PMT.

In Fig.2.20, transmission spectra in the 380–550 nm region are presented for  $\text{Gd}_2\text{SiO}_5:\text{Ce}$  crystals with different cerium content. X-ray luminescence spectra for the same samples are shown in Fig.2.21. They appear as unstructured bands with maximums around 440 nm.

Similarly to the absorption band edge, the short-wave part of the luminescence band is also shifted depending upon the activator

Table 2.14. Principal physico-chemical properties and scintillation characteristics of cerium-doped  $\text{Gd}_2\text{SiO}_5$  scintillators [73].

Characteristics	Value
Density, $\text{g/cm}^3$	6.71
Effective atomic number	59
Radiation length, cm	1.38
Mohs' hardness	6
Hygroscopicity	no
Emission maximum wavelength, nm	440
Emission band edge, nm	395
Refraction index at the emission maximum	1.85
Absorption coefficient in the emission maximum, $\text{cm}^{-1}$	0.005–0.008
Photoelectron yield for $\gamma$ -radiation (% with respect to $\text{NaI(Tl)}$ )	15–25
Decay time, ns	30–60
Light yield (photons/MeV) for $\gamma$ -radiation	$(8\text{--}10)\cdot 10^3$

concentration. It should be noted that the peak emission intensity is the highest for Ce concentration of 0.8 mol.%. At liquid nitrogen temperatures, the absorption band edge (Fig.2.20, curve 4) is shifted to the short-wave spectral region by  $\sim 10$  nm, and the emission band (Fig.2.21, curve 4) — to higher wavelengths.

In [78], the optimum concentration of cerium, which ensured the highest light output with decay time of 60 ns, was indicated as 0.5 mol.%. With larger cerium concentrations, crystals become brownish in color. The light output of undoped  $\text{Gd}_2\text{SiO}_5$  crystals is only 5% of the light output of  $\text{Gd}_2\text{SiO}_5$  doped with optimum amount of cerium. As compared with  $\text{Bi}_4\text{Ge}_3\text{O}_{12}$  crystals, the main advantage of  $\text{Gd}_2\text{SiO}_5\text{:Ce}$  is their fastness, which, in combination with high effective atomic number and absence of hygroscopicity, makes this material an optimum choice for positron tomography, experiments in nuclear physics, geology. The emission peak of  $\text{Gd}_2\text{SiO}_5\text{:Ce}$  is observed at 440 nm, i.e., in the range of maximum sensitivity of many commonly used PMT.

In Fig.2.20, transmission spectra in the 380–550 nm region are presented for  $\text{Gd}_2\text{SiO}_5\text{:Ce}$  crystals with different cerium content. X-ray luminescence spectra for the same samples are shown in Fig.2.21. They appear as unstructured bands with maximums around 440 nm.

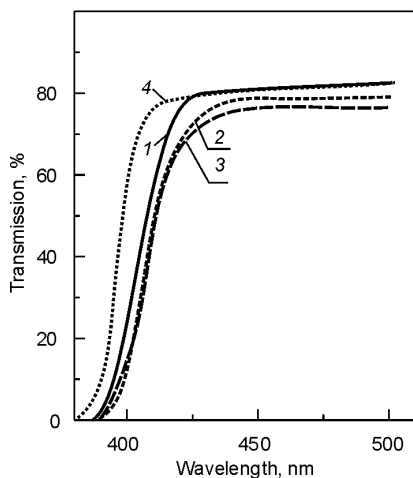


Fig.2.20. Transmission spectra of  $\text{Gd}_2\text{SiO}_5:\text{Ce}$  crystals with different activator concentration: 1 — 0.8 mol.% (300 K), 2 — 1.3 mol.% (300 K), 3 — 1.45 mol.% (300 K), 4 — 0.8 mol.% (80 K).

band is located at close energies, this results in self-absorption of the emitted light, which becomes more significant with higher Ce content in the crystal. Moreover, transparency of  $\text{Gd}_2\text{SiO}_5$  crystals in the emission range worsens at higher Ce concentrations. Both these factors directly affect the light output values of the crystals. The highest light output is observed for crystals with Ce content of  $\sim 0.8$  mol.%, which is related with reaching the conditions for the best optical quality of the scintillator. The light output of tomographic elements based on Ce-activated  $\text{Gd}_2\text{SiO}_5$  crystals under excitation by 662 keV  $\gamma$ -quanta ( $^{137}\text{Cs}$ ) was 21–26% with respect to  $\text{NaI}(\text{Tl})$  crystals, depending upon shape and size. The energy resolution at optimum cerium concentrations was 10–12%, and the decay time — 50–60 ns.

To study possible effects of excitation intensity upon luminescence of  $\text{Gd}_2\text{SiO}_5:\text{Ce}$  crystals, luminescence spectra were measured at different excitation levels [67]. Two spectra measured after excitation of

Similarly to the absorption band edge, the short-wave part of the emission band is also shifted depending on the activator concentration. It should be noted that emission in the maximum acquires the largest values for samples with Ce concentration of 0.8 mol.%. At liquid nitrogen temperatures, the absorption band edge (Fig.2.20, curve 4) is shifted by  $\sim 10$  nm to the short-wave spectral region, and the emission band (Fig.2.21, curve 4) — towards larger wavelengths.

The results obtained show that increased Ce content in  $\text{Gd}_2\text{SiO}_5$  crystals results in a shift of the 3.62 eV absorption band edge towards longer wavelengths due to its broadening related with higher Ce concentration. As the short-wave side of the emission

the third harmonics (energy of the quanta — 3.494 eV) and the fourth harmonics (4.569 eV) of a Nd laser are shown in Fig.2.22. The only difference between these spectra was a slight broadening (by 15 MeV) of the band under excitation by the fourth harmonics. Actually, these differences appear to be more significant if one accounts for re-absorption.

Fig.2.23 shows the luminescence spectrum of  $\text{Gd}_2\text{SiO}_5\text{:Ce}$  crystals at 4.2 K. No significant differences were noted in comparison with similar spectra recorded at room temperature. The only distinction is that in the low-temperature spectra the structure in the band maximum region is more clearly defined, while the total band width is only slightly reduced. This can be possibly explained by narrowing of the band components.

The experiments carried out have shown that the broad luminescence band peaked at 2.85–2.92 eV is predominant in the emission spectrum in a wide range of excitation intensities. The observed invariance of the spectrum shape under temperature changes indicates that two strongly overlapping components of the total band are observed as a result of optical transitions from one excited level to two different levels. Such explanation is in good agreement with the energy structure of  $\text{Ce}^{3+}$  ion and is confirmed by luminescence studies with time resolution, as well as by luminescence excitation spectra [79].

As for their radiation stability,  $\text{Gd}_2\text{SiO}_5\text{:Ce}$  crystals are superior to all other oxide scintillators [83]. They can function at least up to the doses of 108 rad. However, it should be noted that  $\text{Gd}_2\text{SiO}_5\text{:Ce}$  crystals are a very expensive material. Its cost is twice as high as that of BGO [80].

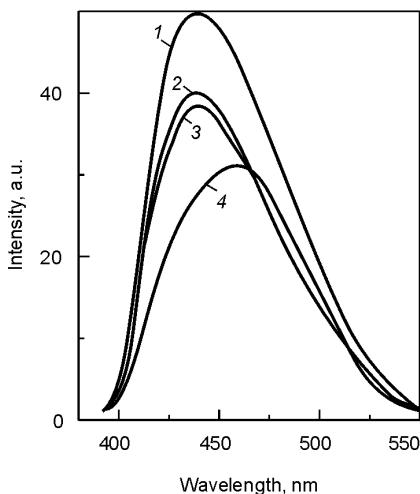


Fig.2.21. X-ray luminescence spectra of  $\text{Gd}_2\text{SiO}_5\text{:Ce}$  crystals with different activator concentration: 1 — 0.8 mol.% (300 K), 2 — 1.3 mol.% (300 K), 3 — 1.45 mol.% (300 K), 4 — 0.8 mol.% (80 K).

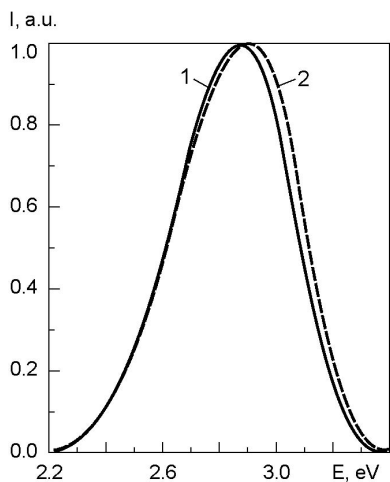


Fig.2.22. Luminescence spectra of  $\text{Gd}_2\text{SiO}_5\text{:Ce}$  single crystals: 1 — excitation by 3.494 eV quanta; 2 — excitation by 4.659 eV quanta.

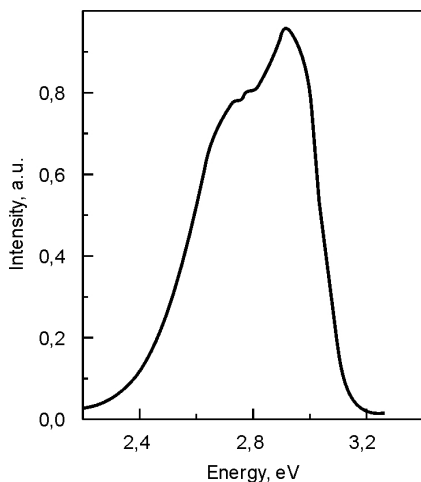


Fig.2.23. Luminescence spectrum of  $\text{Gd}_2\text{SiO}_5\text{:Ce}$  single crystals at 4.2 K.

Scintillation properties of Eu-activated gadolinium silicate were reported in [81,82]. Property modeling for these crystals was carried out using pressure-compacted powder-like products of solid-phase synthesis. As dopants for europium silicate, oxides of Gd, Yb, Lu, Er and Nd were also used (0.5 mol.%).

Samples of  $\text{Eu}_2\text{SiO}_5$ , both nominally pure and doped with 0.5%  $\text{Ln}_2\text{O}_3$ , are monophasic. For these samples, a characteristic band series is observed in X-ray luminescence spectra (Fig.2.24), with the highest intensity at 613.5 nm, which is related to  $^5D_0 - ^7D_2$  transition of the  $\text{Eu}^{3+}$  ion. Maximums of the  $\text{Eu}_2\text{SiO}_5$  luminescence spectra retain their locations under doping with lanthanides, which is an evidence of similar symmetry of the  $\text{Eu}^{3+}$  ion position in the crystal structure. The height of the main bands of the X-ray luminescence spectra of  $\text{Eu}_2\text{SiO}_5$  is decreased in the presence of other lanthanides in the order  $\text{Gd} > \text{Yb} > \text{Lu} > \text{Er} > \text{Nd}$ .

The light output concentration dependence for polycrystalline samples of the  $\text{Gd}_2\text{SiO}_5 - \text{Eu}_2\text{SiO}_5$  system is shown in Fig.2.25. Increases in the  $\text{Gd}_2\text{O}_3 \cdot \text{SiO}_2$  content above 0.05 mole up to composition  $0.2\text{Gd}_2\text{O}_3 \cdot \text{SiO}_2 : 0.8\text{Eu}_2\text{O}_3 \cdot \text{SiO}_2$

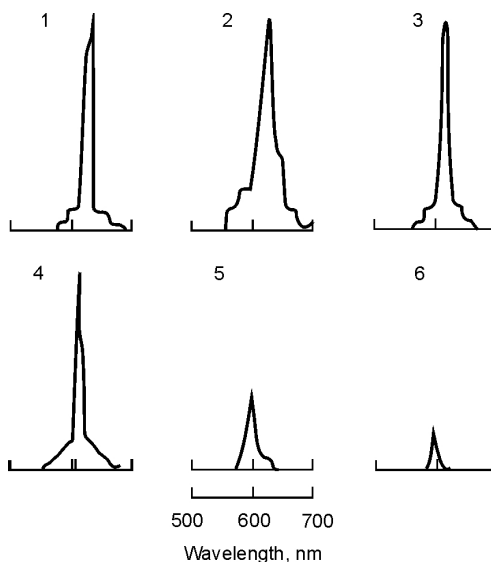


Fig.2.24. X-ray luminescence spectra of polycrystalline  $\text{Eu}_2\text{SiO}_5$ : pure (1) and containing 0.5 mol.%  $\text{Gd}_2\text{O}_3$  (2),  $\text{Y}_2\text{O}_3$  (3),  $\text{Lu}_2\text{O}_3$  (4),  $\text{Er}_2\text{O}_3$  (5) and  $\text{Nd}_2\text{O}_3$  (6).

resulted in lowering of the luminescence intensity. Further enrichment of the material with gadolinium oxide is accompanied with the light output rising, with its maximum value (20.2% with respect to  $\text{CsI(Tl)}$ ) obtained for the composition  $0.9\text{Gd}_2\text{O}_3 \cdot \text{SiO}_2 : 0.1\text{Eu}_2\text{O}_3 \cdot \text{SiO}_2$ . Colorless  $\text{Gd}_2\text{SiO}_5$  crystals containing 0.5 mol.%  $\text{Eu}_2\text{O}_3$ , 100 mm long and 40 mm in diameter, were obtained in [81,82]. A practically uniform europium distribution over the single crystal volume ensured their optical and scintillation uniformity. The light output in single crystalline samples was  $13 \pm 0.5\%$ , which is two times higher than the light output values for polycrystalline samples of the same composition. Luminescence spectra of these single crystals and polycrystalline samples are presented in Fig.2.26. It can be seen that  $\text{Eu}^{3+}$  luminescence spectra are different in these two cases. Formation of the crystalline field symmetry by the nearest neighbors of  $\text{Eu}^{3+}$  ions depends upon preparation conditions of the  $\text{Gd}_2\text{SiO}_5\text{:Eu}$  phase. Decay times of  $\text{Gd}_2\text{SiO}_5\text{:Eu}$  single crystals do not exceed 15 ns. Their absorption band edge is in the region of  $440 \pm 3$  nm.



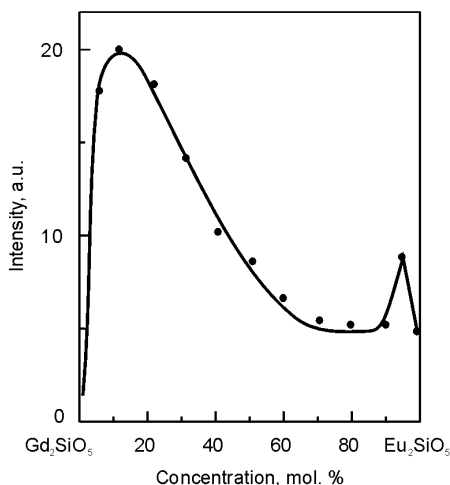


Fig.2.25. Concentration dependence of the light yield for polycrystalline samples  $\text{Gd}_2\text{SiO}_5\text{--Eu}_2\text{SiO}_5$ .

Thus, due to their optical and scintillation uniformity, satisfactory light output, short decay times in the red-orange spectral region, the  $\text{Gd}_2\text{SiO}_5\text{--Eu}_2\text{SiO}_5$  solid solutions can find their applications as scintillators. The most efficient X-ray luminescence has been noted for single crystals containing 10% of  $\text{Eu}_2\text{SiO}_5$  in  $\text{Gd}_2\text{SiO}_5$ .

In the recent years, much attention was paid to a new scintillation material — LSO single crystals [84–88], which are promising for their application in positron emission tomography. The crystal structure of  $\text{Lu}_2(\text{SiO}_4)\text{O}$  contains

two trivalent cation sites that can be occupied by  $\text{Ce}^{3+}$ , forming the luminescence centers.

In Table 2.15, some physical characteristics are presented for cerium-doped lutetium orthosilicate crystals in comparison with properties of well-known scintillators  $\text{NaI}(\text{Tl})$  and BGO.

LSO crystals have rather good detection efficiency to gamma-radiation due to their high density and rather high effective atomic number. The radiation path in LSO is only slightly longer than in BGO. The refractivity index of LSO is somewhat smaller as compared with other materials listed in the Table. The absence of hygroscopicity and relative mechanical strength of LSO crystals makes their mechanical treatment relatively simple.

Fig.2.27 shows emission spectra of LSO crystals under gamma-excitation in comparison with  $\text{NaI}(\text{Tl})$  and BGO. The intensity of LSO luminescence is about 5 times higher as compared with BGO and is ~75% of the  $\text{NaI}(\text{Tl})$  values. The decay time data for LSO under gamma-excitation can be presented as a sum of two exponential contributions with time constants of 12 ns and 42 ns [84].

It has been shown [87] that the light output of LSO:Ce crystals depends upon the dopant concentration in the melt. Ce concentration in LSO crystals was shown to be proportional to its concentration in the melt.

The data presented above show both advantages and drawbacks of LSO crystals as compared with NaI(Tl) and BGO. Main advantages of LSO crystals are their rather high emission intensity and short decay time. Moreover, LSO crystals show no after-

glow, they are non-hygroscopic, of sufficient mechanical strength, and show radiation stability up to  $10^6$  rad. These crystals can be relatively easily grown by the Czochralski method. Their drawbacks include the following points. LSO crystals are temperature-sensitive. As for emission intensity variation with temperature, they are in an intermediate position between NaI(Tl) and BGO. A negative moment is also the presence of a radioactive isotope  $^{71}\text{Lu-176}$  (2.6%) in the raw material for the growth charge, which remains in the grown crystals [85,86]. One more drawback of LSO is rather low energy resolution (7.9%). And one should remember the high cost of the raw material  $\text{Lu}_2\text{O}_3$ .

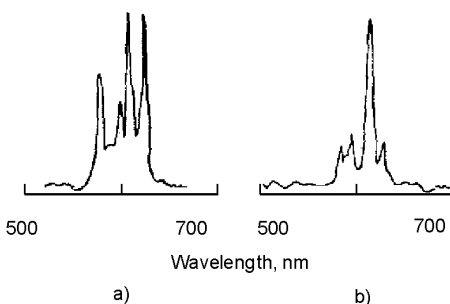


Fig.2.26. X-ray luminescence spectra of  $\text{Gd}_2\text{SiO}_5$  (0.5 mol.%  $\text{Eu}_2\text{O}_3$ ) for a single crystalline sample (a) and a polycrystalline sample prepared by solid-phase synthesis (b).

Table 2.15. Main characteristics of crystals NaI(Tl), BGO and LSO [84]

Characteristics	NaI(Tl)	BGO	LSO
Density, $\text{g/cm}^3$	3.67	7.13	7.41
Effective atomic number	51	75	66
Radiation length, cm	2.56	1.12	1.14
Refraction index	1.85	2.15	1.82
Hygroscopicity	Yes	No	No
Mechanical strength	Bad	Good	Good

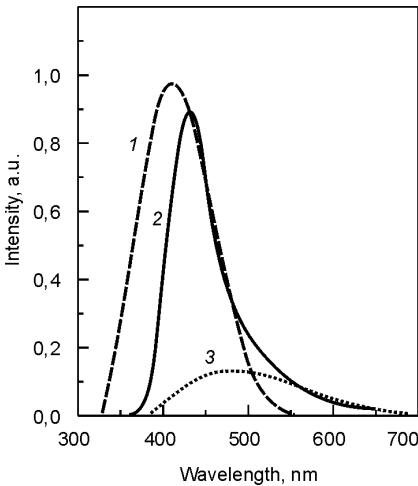


Fig.2.27. Emission spectra of crystals NaI(Tl) (1), LSO (2), BGO (3) [84].

### 2.3. Tungstates

Scintillation properties of tungstates of the general formula  $AWO_4$ , where A — Ca, Cd, Zn, Pb, Mo, Co, have been known for a long time. However, because of long delay time (characteristic for many of them) and difficulties in preparation of high quality crystals, they were not widely used. In recent times, there has been renewed interest in tungstate scintillators caused by requirements of high-energy physics and computer tomography [89–98]. Advantages of tungstates are their relatively high atomic number and density,

which ensures good detection efficiency with small-sized crystals, and their low afterglow, which is

Table 2.16. Physical properties and main scintillation characteristics of crystals LSO:Ce, LSO:Pr and GSO:Ce [85]

Characteristics	LSO:Ce	LSO:Pr	GSO:Ce
Density, g/cm <sup>3</sup>	7.4	7.4	6.7
Melting point, °C	2150	2150	1950
Hygroscopicity	No	No	No
Phase uniformity	Good	Good	Good
Cleavage tendency	No	No	No
Structure	$C2/c$	$C2/c$	$P2_1/c$
Emission maximum wavelength, nm	420	280/315	430
Decay time, ns	12/40	~10	60
Light output, % with respect to NaI(Tl)	75		20
Light yield, photons/MeV, 662 keV	23,000		9,300
Light yield, photons/MeV, X-rays	15,000		
Energy resolution (%) at 662 keV	7.9		7.8

comparable to BGO. If loads are not high, tungstates are successfully used for spectrometry of  $\gamma$ -radiation with pulse formation time of 12–20  $\mu$ s [102]. The most common scintillator crystals of this group are  $\text{PbWO}_4$  (PWO),  $\text{CdWO}_4$  (CWO),  $\text{ZnWO}_4$  and  $\text{CaWO}_4$ .

### 2.3.1. Crystal structure of tungstates

Tungstates belong to two structural types.  $\text{CdWO}_4$  and  $\text{ZnWO}_4$  are characterized by monoclinic syngony (spatial group  $P2/c$ ) — the wolframite structural type, while  $\text{PbWO}_4$  and  $\text{CaWO}_4$  are of tetragonal syngony (spatial group  $14_1/a$  — the scheelite structural type). It has been shown that when the radius of the bivalent cation  $r < 10^{-10}$  m, the wolframite structure is formed, and the scheelite structure appears at  $r \geq 10^{-10}$  m. In Table 2.17, data are given on the crystal structure and lattice parameters of some  $\text{AWO}_4$  compounds [99].

New type fast oxide scintillators described in [85] and full reveiew [86]. The quest for inorganic scintillator for future represented in [87]. At last very promising Scintillator on base  $\text{LaCl}$  with energy resolution 3.2% (662 keV) represented in [88].

The wolframite elementary lattice includes two formula units. Fig.2.28 shows an image of the elementary lattice of  $\text{CdWO}_4$  [100]. Each atom of cadmium and tungsten is surrounded by a distorted octahedron of oxygen atoms. The degree of this distortion is different for different  $\text{AWO}_4$  compounds.

Table 2.17. Crystal structure and lattice parameters of tungstates.

Cation	Bivalent cation radius, $10^{-10}$ m	Spatial group	Lattice parameters				Volume per oxygen atom, $\times 10^{-10}$ m
			$a$ , Å	$b$ , Å	$c$ , Å	$\beta$	
Cu	0.72	$P$	—	—	—	—	
Co	0.72	$P2/c$	4.66	5.69	4.98	90°00'	16,5
Fe	0.74	$P2/c$	4.70	5.69	4.93	90°00'	16,5
Zn	0.74	$P2/c$	4.68	5.73	4.95	89°30'	16,6
Cd	0.97	$P2/c$	5.02	5.85	5.07	91°29'	18,7
Ca	0.99	$14_1/a$	5.242		11.372		19,5
Pb	1.20	$14_1/a$	5,462		12.046		23,7

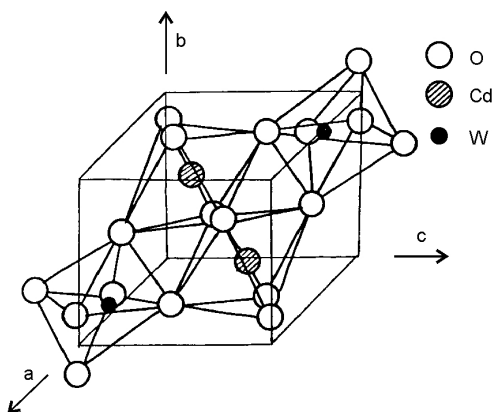


Fig.2.28. Elementary lattice of  $\text{CdWO}_4$  crystal.

The structure of  $\text{CdWO}_4$  and  $\text{ZnWO}_4$  can be presented as a somewhat deformed hexagonal packing of oxygen atoms, where Cd, Zn and W atoms fill a half of octahedron vacancies. Similar cations are located in planes parallel to (100). Oxygen anions, located between these planes, do not lie in one plane, but rather form a layer of  $0.2 \cdot 10^{-10}$  m. Such structure type creates open channels along direction C.

Thus, wolframite structure

can be described as a system of zig-zag-like chains of octahedrons, with each chain (consisting of octahedrons of only one sort of metals) directed along C axis.

In Fig.2.29, a characteristic zig-zag-like structure is shown, formed by octahedrons around Zn atoms in  $\text{ZnWO}_4$  lattice [101]. It was noted that oxygen octahedrons in the  $\text{ZnWO}_4$  structure are more isometric than octahedrons around Cd atoms in  $\text{CdWO}_4$ . Each octahedron of W is connected by two edges with two W octahedrons, and by four angles — with four Cd or Zn octahedrons belonging to different chains.

It can be seen from Table 2.17 that, if the cell volume per one oxygen atom is larger than  $19.5 \cdot 10^{-10}$  m, "loosening" of the densest anion packing upon increasing cation radius leads to a change of the structural type — instead of wolframite, the scheelite structure is observed in  $\text{PbWO}_4$  and  $\text{CaWO}_4$ . The crystal structure of  $\text{CaWO}_4$  is shown in Fig.2.30. The scheelite

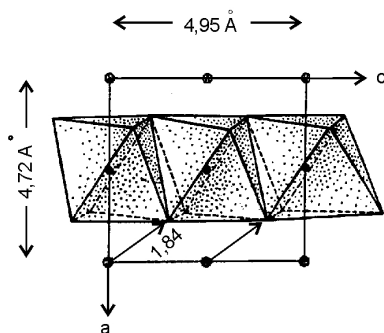


Fig.2.29. A zig-zag structure formed by Zn octahedrons in  $\text{ZnWO}_4$ .

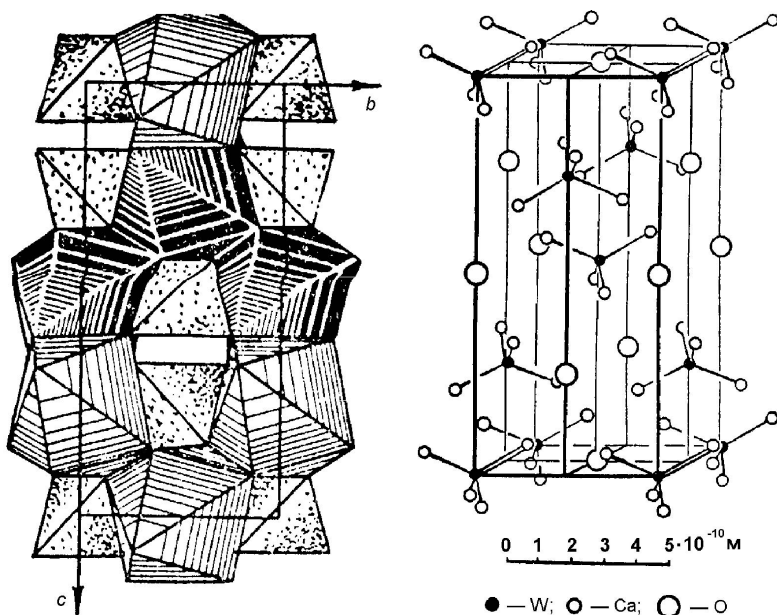


Fig.2.30. Structure of  $\text{CdWO}_4$  crystal.

structure is based on a three-dimensional frame formed by infinite zig-zag-like chains of metal  $\text{Me}^{\text{II}}$  polyhedrons. Ca or Pb eight-vertex structures are connected by their side edges into spirals around quadruple helix axes parallel to  $[001]$ . Between polyhedron pairs, singular (not connected to each other)  $\text{WO}_4$  orthotetrahedrons are located. It was noted [99] that the wolframite-scheelite structural transformation is not clearly marked; the wolframite structure can be considered as a kind of distorted scheelite. The presence of isolated  $\text{WO}_4$  complexes is the most important feature of the scheelite structure as compared with wolframite, where  $\text{WO}_6$  complexes form continuous chains. It should be noted that the bond between  $\text{Me}^{\text{II}}$  cation and  $\text{WO}_4^{2-}$  anion is ionic, and bonds W—O within the  $\text{WO}_4$  complex in scheelites are largely covalent. The  $\text{WO}_4^{2-}$  complex in  $\text{CaWO}_4$  persists up to the melting temperature and even higher, i.e.,  $\text{WO}_4$  polyhedrons in the scheelite structure can be considered as stable molecular complexes. Probably the  $\text{WO}_6$  complexes in the wolframite structure should have similar properties.

### 2.3.2. Technological preparation features of tungstate single crystals

For preparation of tungstate crystals of  $\text{AWO}_4$  type, many different growth methods have been tested: growth from the melt, Stockbarger, Verneuil, hydrothermal, preparation from gas phase, etc. Analysis of these methods [99] has shown that none of these methods, though yielding crystals of relatively high quality, can solve the problem of producing large-sized tungstate crystals with high scintillation parameters.

Technological recommendations on growing tungstate crystals of sufficiently large sizes using the Czochralski method were given in works by M.V.Pashkovsky and his team (see, e.g., [99]). The main points related to the tungstate preparation technology could be noted as follows.

An essential moment in preparation of structurally perfect  $\text{AWO}_4$  crystals is the choice of the container material. The best suited for tungstate melts are crucibles made of platinum, platinum-rhodium alloy or iridium, characterized by high stability towards oxidation and low vapor pressure. A necessary condition for  $\text{AWO}_4$  crystal growth is large temperature gradient in the vertical direction. Using high-frequency heating of the crucible with charge and choosing an optimum growth regime for each of the  $\text{AWO}_4$  compounds, one can obtain tungstate single crystals that are optically uniform and structurally perfect. Their size is limited, in principle, only by the crucible size and the design of the lifting mechanism used.

For preparation of  $\text{ZnWO}_4$  and  $\text{CdWO}_4$  crystals with low dislocation density ( $\sim 10^2 \text{ cm}^{-2}$ ), it is desirable to have the following conditions fulfilled [99]:

1. Vacuum melting of the charge;
2. Low growth speed at high rotation rates for maximum possible removal of gas inclusions, thus avoiding low optical quality and high dislocation density;
3. Single crystal growth in the direction [100]; the cleavage plane (010) is oriented parallel to the growth direction, which in most cases excludes twinning.
4. Crystal growth in isothermal conditions to decrease the radial temperature gradient, thus weakening thermal stresses and prevents cracking of crystals, which is especially important for large-sized crystals.

5. The temperature gradient in the vertical direction should be sufficiently large.
6. Seeds with orientation [100] should be used for crystal growth, free from small-angle boundaries, with low dislocation density.
7. Careful synthesis of raw material to be used as charge for crystal growth.

Experiments on  $\text{ZnWO}_4$  growth under conditions of stoichiometry violation (extra  $\text{ZnO}$  or  $\text{WO}_3$ ) have shown that coloring acquired by the crystal in the course of growth is due to the presence of admixtures. Even higher requirements are made to raw material for high quality  $\text{CdWO}_4$  crystals, as volatility of  $\text{CdO}$  is another problem for growing crystals of stoichiometric composition.

In [103],  $\text{CdWO}_4$  crystals were grown from cadmium tungstate charge of the strictly stoichiometric composition or with specified excess quantities of cadmium oxide. The charge preparation process is based on solid-phase synthesis by reaction between cadmium and tungsten oxides. The charge was prepared from specially purified raw material with concentration of the iron group elements not higher than  $2 \cdot 10^{-4}\%$  (mass), and of alkali metal elements — not more than  $5 \cdot 10^{-4}\%$ . Growth of  $\text{CdWO}_4$  and  $\text{ZnWO}_4$  of diameter up to 30 mm was carried out by the Czochralski method in a platinum crucible using high-frequency heating [103]. For studies of the defect formation in  $\text{CdWO}_4$  crystals, charge with different admixture content and different  $K$  ( $K$  is the quantity of  $\text{CdO}$  to quantity of  $\text{WO}_3$  ratio) was used. At  $K \leq 1.0022$ , the presence of  $\text{WO}_3$  phase in a non-uniform part of the crystal was found by X-ray structure studies. At  $K > 1.01$ , precipitation of  $\text{CdO}$  phase is observed. The optimum charge composition is at intermediate values —  $K = 1.009$ , when no precipitation of either  $\text{CdO}$  or  $\text{WO}_3$  should occur. At such  $K$  values, deviations from stoichiometry will be minimized. One should note that  $K$  is not equal to unity because of predominant evaporation of  $\text{CdO}$  in the course of growth process.

In numerous experiments on  $\text{CdWO}_4$  growth, it was established that formation of pores in the crystals is favored both by strong deviation of the  $K$  value of the charge used from the optimum values and by the presence of uncontrolled admixtures in the charge. Another reason for pore formation are temperature instabilities, which lead to overheating and decomposition of the melt in the vicinity of crucible walls.



Formation of structure defects in  $\text{CdWO}_4$  crystals grown by the Czochralski method was studied in [104]. It was shown that the most efficient way to avoid visible defects, block structure and scattering centers in  $\text{CdWO}_4$  crystals is to prevent supercooling of the melt at the initial stage of growth. As a matter of fact, the defect formation mechanism is chiefly related to the lack of correspondence between growth shapes and internal symmetry of the melt that had been supercooled. Removing the melt supercooling allows one to avoid macroinclusions, suppress block structure features down to disorientation angles not larger than 5 minutes, as well as substantially reduce the number of scattering centers. At the same time, “blue-gray” color centers can appear in  $\text{CdWO}_4$  crystals. It can be seen from the transmission spectra (Fig.2.31) that such color centers give rise to a non-selective absorption band in the 400–700 nm range, with absorption coefficient reaching  $2\text{--}3\text{ cm}^{-1}$  at 700 nm. The presence of color centers substantially worsens functional characteristics of scintillators. It has been established [104] that color center formation mechanism is primarily related to the oxygen deficiency and formation of anion vacancies. Predominant role of oxygen in the formation of color centers is proved by the fact that color centers are removed under thermal treatment in oxygen-containing atmosphere (Fig.2.31, curve 3'). From the other side, anisotropy of the crystal structure of  $\text{CdWO}_4$  leads to non-uniform oxygen diffusion in the course of thermal treatment of the crystals. In  $\text{CdWO}_4$ , diffusion is slower in the directions [010] and [100]. Therefore, crystals grown in the [001] direction are “closed” to diffusion, which makes removal of color centers by thermal treatment substantially more difficult. On the basis of studies carried out in [104] and the results presented in [26, 105], thermal conditions and growth regimes have been chosen that ensure preparation of structurally perfect  $\text{CdWO}_4$  single crystals up to 55 mm in diameter and 200 mm long.

The use of  $\text{PbWO}_4$  as detectors of total absorption in electromagnetic calorimeters started after large-sized (diameter — 34 mm, height — 200 mm) optically transparent  $\text{PbWO}_4$  single crystals and scintillation elements on their base had been produced, for the first time in the world, at the Institute for Single Crystals. Problems of  $\text{PbWO}_4$  crystal preparation are related to many technological difficulties, starting from the stage of charge synthesis and finishing with thermal treatment of ready scintillators.

The diagram of state of the  $\text{PbO}-\text{WO}_3$  system indicates at the existence of two congruently melting compounds: lead oxytungstate  $\text{Pb}_2\text{WO}_5$  ( $T_m=935^\circ\text{C}$ ) and lead tungstate  $\text{PbWO}_4$  ( $T_m=1123^\circ\text{C}$ ) [106]. Both compounds can undergo polymorphic transitions. The high-temperature modification  $\beta\text{-PbWO}_4$  is transformed into a low-temperature monoclinic -modification at  $887^\circ\text{C}$ . It has been shown that formation of the low-temperature phase is possible only when a special cooling regime is applied, in which the melt is being kept in the super-

cooled state for a long time. In such melt, structural transformations occur, which are accompanied by increasing coordination of tungsten and formation of its octahedral complexes, making the melt structurally similar to the monoclinic  $\beta\text{-PbWO}_4$ . Accounting for peculiar features of the  $\text{PbO}-\text{WO}_3$  system, it can be assumed that light scattering centers in  $\text{PbWO}_4$  crystals are due primarily to capturing of the compound  $\text{Pb}_2\text{WO}_5$  when optimum growth conditions are violated. This is a serious problem that hinders preparation of optically uniform and structurally perfect  $\text{PbWO}_4$  single crystals. Problems also emerge as a result of a certain stoichiometry violation in the overheated melt due to evaporation of crystal-forming components with high partial pressure. Account of factors affecting thermal stability of the melt lays down severe requirements to the growth thermal condition ensuring preparation of  $\text{PbWO}_4$  crystals with minimum concentration of scattering centers. To develop an optimum technology of  $\text{PbWO}_4$  crystal growth, the region of thermal stability of the melt should be determined, in the same way as it had been done for  $\text{Bi}_4\text{Ge}_3\text{O}_{12}$  crystals [35].

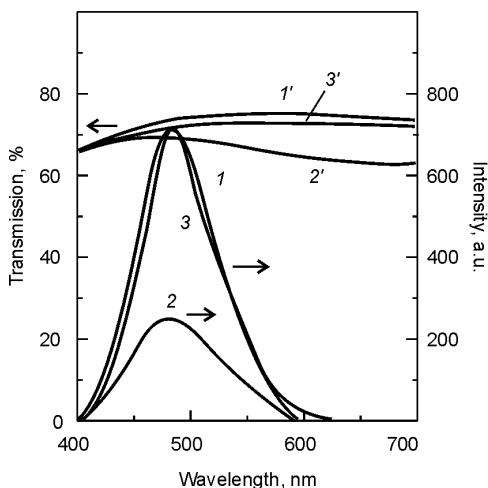


Fig.2.31. X-ray luminescence spectra  $I(\lambda)$  (1–3) and transmission spectra  $T(\lambda)$  (1'–3') of  $\text{CdWO}_4$ : 1 — uncolored, 2 — “blue-gray”, 3 — “blue-gray” after thermal treatment.

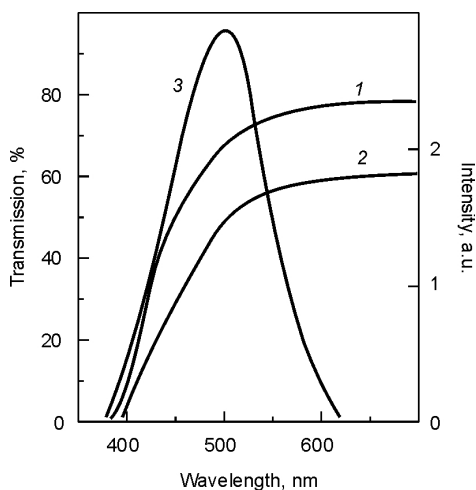


Fig.2.32. Transmission (1,2) and emission (3) spectra of  $\text{PbWO}_4$  single crystals: 1 — growth in an inert atmosphere; 2 — growth in an oxygen-containing atmosphere.

Basing on the knowledge on this important temperature region, a crystallizator design has been developed, ensuring such thermal conditions that the melt temperature never leaved the region of its thermal stability. The heater power is monotonously increased as the crystal grows, thus automatically maintaining the diameter of the growing crystal at a constant value. The developed crystallizer design and the optimized growth regimes (pulling speed — 4–6 mm/ hour; rotation rate — 15–30 rpm) ensured preparation of uniform colorless transparent  $\text{PbWO}_4$  single crystals, up to

34 mm in diameter and 300 mm long [144].

Another important point is the influence of the gas medium upon structure-sensitive properties of  $\text{PbWO}_4$  single crystals. It has been established that the shorter is the time of post-growth thermal treatment in an oxygen-containing atmosphere, the higher is the light output. Such crystals are characterized by their less pronounced coloring and absence of absorption in the region of 430 nm. For those  $\text{PbWO}_4$  crystals which showed the absorption bands in the 430 nm region a green-yellow coloring was observed, due to surplus oxygen content. Controlling the composition and pressure of the gas medium at the stages of charge melting, crystal growth and annealing, it is possible to obtain  $\text{PbWO}_4$  crystals with 75–80% transparence at 50 mm thickness in the 500–600 nm region. Comparison of the transparence values of  $\text{PbWO}_4$  crystals grown in different media (sample size 20×20×160 mm) can be made from data shown in Fig.2.32 [107]. Much higher transparence and better uniformity was obtained when the crystals were grown in an inert medium ( $\text{Ar}$ ,  $\text{N}_2$ ). Depending upon the oxygen content in the gas medium,

with other conditions equal at the stages of growth and annealing, three groups of  $\text{PbWO}_4$  crystals can be obtained: colorless, gray and yellow-green, which are distinguished by their transmission spectra and the luminescence maximum wavelength.

The preferable direction along which a  $\text{PbWO}_4$  crystal should be grown is [001]. It is the best suited to the actual distribution of temperature fields in a crystallizer typical for the Czochralski method. However, the presence of a cleavage plane (001) impedes preparation of large-sized scintillators from the whole ingots, because the grown ingots tend to be cracked along the cleavage plane during mechanical treatment. When  $\text{PbWO}_4$  crystals are grown along the [100] direction, it is possible to minimize the risk of their damage at the stages of post-growth thermal and mechanical treatment.

### *2.3.3. Main physico-chemical properties and scintillation characteristics of tungstates*

Cadmium tungstate  $\text{CdWO}_4$  and zinc tungstate  $\text{ZnWO}_4$ . Luminescence of  $\text{CdWO}_4$  crystals was described for the first time in 1948 [108], and their application as scintillators — in 1950. Since then, scintillation, optical and mechanical properties of  $\text{CdWO}_4$  have been extensively studied [109–114]. Main physico-chemical properties and scintillation characteristics of  $\text{CdWO}_4$  are presented in Table 2.18. The most important advantages of  $\text{CdWO}_4$  scintillators are their high light output (up to 40% with respect to  $\text{NaI(Tl)}$  in measurements with sufficient time for signal formation or in the current mode), as well as high radiation stability.

The emission spectrum has its intensity maximum in the region from 480 nm to 540 nm (Fig.2.33), which allows the use of  $\text{CdWO}_4$  both with PMT and photodiodes. The value of 540 nm is related to measurements on thick samples with low transparency to the intrinsic radiation, as self-absorption shifts the emission maximum towards longer wavelengths.

A possibility of obtaining satisfactory resolution, high detection efficiency, stability towards climatic and mechanical factors allows the use of  $\text{CdWO}_4$  scintillator crystals in geophysics and geology. A unique property of  $\text{CdWO}_4$  as scintillation material is that its light output is nearly independent on temperature in a broad temperature range (Fig.2.34, a, b) [102]. It follows from Fig.2.35 that the light yield of BGO

Table 2.18. Main physico-chemical properties and scintillation characteristics of tungstates

Characteristics	CdWO <sub>4</sub>	PbWO <sub>4</sub>	ZnWO <sub>4</sub>	CaWO <sub>4</sub>
Density, g/cm <sup>3</sup>	7.9 [152] 7.99 [151]	8.28 [151]	7.87 [153]	6.06 [153]
Effective atomic number	66 [151]	73 [151]	61 [153]	62 [153]
Radiation length, cm	1.06 [151]	0.85 [151]	1.19 [1]	
Mohs' hardness	6 [151]	6 [151]		4,5–5 [1]
Hygroscopicity	No [151]	No [151]	No [153]	No [153]
Luminescence maximum, nm	490 [151] 540 [152]	420 [121] 430–520 [151] 370–500 [119]	480 [152] 490 [153]	430 [153]
Refraction index at the emission maximum	2.25 [151] 2.30 [1]	2.20 [151]	2.20 [1]	1.94 [1]
Melting temperature, °C	1325 [1]	1123 [106]	1200 [1]	1576 [1]
Chemical activity	Inert	Inert	Inert	Inert
Light output, % with respect to NaI(Tl)	35–40 [151]	1 [151]	28 [153]	32–50 [153]
Decay time, ns	5000 [151] 10.5 and 19.5 μs [1]	2/10/30 [151] <10 [121] 5–10 [1]	21.8 [153] 20000 [152] 20/3.3/ ~0.1 μs [1]	3,8 [153] 25/500/ 1100/3200 [1]
Energy resolution at 662 keV, %	7.97 [152] 8.0 [150] 12.0 [1]		7.97 [152] 15–18 [1] 13 [118]	12.0– 20.0 [1]
Scintillation efficiency, %	3.8 [152]		4.3 [152]	
Light yield, photons/MeV	12220 [152]	70 [90]	9300 [152]	1400 [118]
Phosphorescence, %/3 ms	0.1 [152]		<0.05 [152]	
Afterglow after 3 ms and 20 ms (in parentheses)	(<0.02)		(0.23) [153]	1–5 [153]

crystals falls by 10 times in the temperature range 200–373 K. At 273 K, the light yield of NaI(Tl) crystals is reduced by more than 50% as compared with its value at 300 K. For  $\text{CdWO}_4$  crystals, this decrease is not more than by 15–20% [150]. Fig.2.34, b shows the decay time of  $\text{CdWO}_4$  scintillators as function of temperature. According to Fig.2.34, these crystals are especially suited for temperatures just below 70°C, when light yield changes are still small, and the decay time is significantly decreased; this allows detection of large radiation fluxes.

Detection efficiency of  $\text{CdWO}_4$  is practically the same as that of bismuth germanate. Therefore, when there are no high loads,  $\text{CdWO}_4$  crystals can successfully compete with bismuth germanate. One more important property of these scintillation crystals is their low afterglow. It is less than 0.02% in 20 ms after irradiation. Low afterglow and a possibility of functioning in combination with photodiodes make  $\text{CdWO}_4$  a very promising material for application in tomography.

The light output of  $\text{CdWO}_4$  is proportional to the energy of gamma-radiation [115], and, provided its transparence to the intrinsic radiation is high, its intrinsic resolution can be very small as compared with intrinsic resolution of the photoreceiver used, making it possible to use  $\text{CdWO}_4$  crystals for spectrometry of gamma-radiation. The energy resolution of detectors with  $\text{CdWO}_4$  crystals and PMT is 8–12% ( $^{137}\text{Cs}$   $\gamma$ -radiation); the best value — 7.9% — was obtained for a crystal of 10×10×20 mm size [102].

In [150], spectrometric characteristics (energy resolution  $R$  and light output  $C$ ) are presented for detectors based on  $\text{CdWO}_4$  crystals of different size (Table 2.19).

As for its spectrometric characteristics, detectors based on  $\text{CdWO}_4$  crystals are comparable to doped CsI crystals and are only slightly

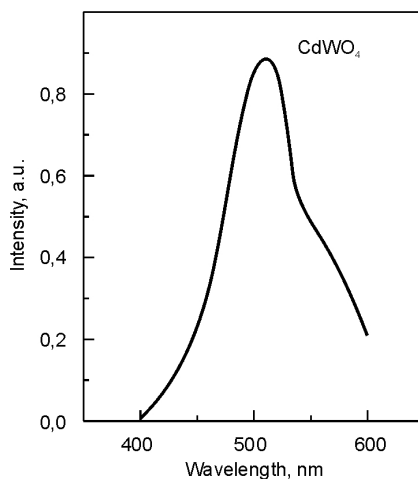


Fig.2.33. Emission spectrum of  $\text{CdWO}_4$  single crystals.

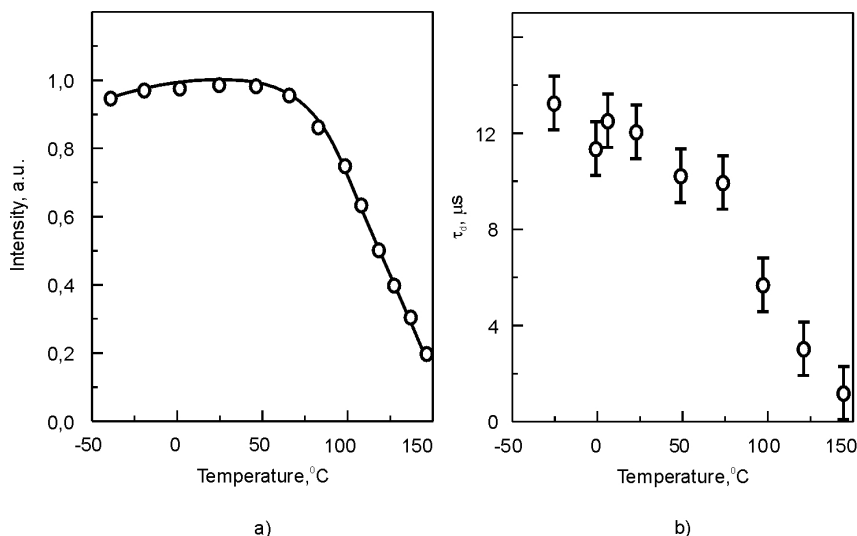


Fig.2.34. Light output (a) and decay time (b) of CdWO<sub>4</sub> single crystals as function of temperature.

worse than NaI(Tl). Due to high effective atomic number and density of CdWO<sub>4</sub>, detectors on their base ensure high detection efficiency in small volumes.

Spectrograms obtained using NaI(Tl)- and CWO-based detectors under excitation by <sup>137</sup>Cs  $\gamma$ -quanta are shown in Fig.2.36. It can be seen that peak efficiency of  $\gamma$ -quanta detection is practically the same for NaI(Tl) detectors (scintillator size 60×60 mm) and CWO detectors (40×40 mm). For CWO detectors, the efficiency peak of gamma-quanta in the energy range 0.5–1 MeV is 2–2.5 times higher, and in the energy range 1.4–3 MeV — about 3 times higher as compared with NaI(Tl). CWO detectors, like NaI(Tl) detectors, have nearly linear energy dependence in the 0.06–4.4 MeV range.

Among the drawbacks of CdWO<sub>4</sub>, one should note its high decay time — 5–7  $\mu$ s, which sets limits to those applications of this scintillators that require high counting rates. However, this drawback is not important for such application fields as measurement of low levels of radioactive contamination in environment objects or monitoring of ore pits. It has been noted [109] that CdWO<sub>4</sub> has very low level of radioac-

tive contamination, which allows the use of this material in fundamental studies in search for unusual or forbidden processes or decays. For further progress in such experiments, as well as for improvement of procedures for measurements of low radioactivity levels,  $\text{CdWO}_4$  crystals of much larger sizes are needed that would preserve good energy resolution obtained with small samples [145]. High light output of cadmium tungstate crystals makes it possible in principle to achieve resolution values close to characteristics of  $\text{NaI(Tl)}$ .

The following possible reasons for worsening of the energy resolution of  $\text{CdWO}_4$  crystals upon increasing their size have been noted [109]: self-absorption, and crystal defects causing formation of scattering centers (optical non-uniformities). The main reasons for formation of these defects are: deviations of the charge composition from the optimum; the presence of uncontrolled admixtures in the charge; temperature instabilities emerging in the course of growth. Such  $\text{CdWO}_4$  crystals have insufficient transparency, are of yellowish color and contain certain amounts of  $\text{CdO}$  or  $\text{WO}_3$  extra phase [103].

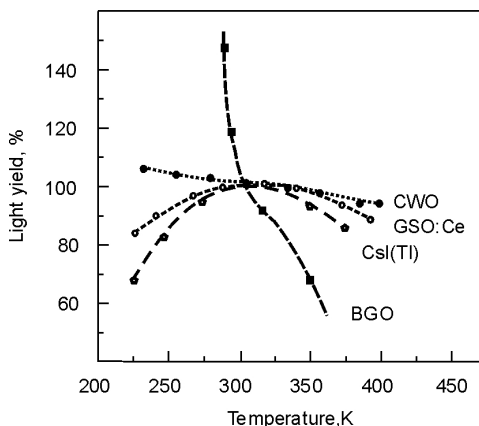


Fig.2.35. Light output of oxide scintillators as function of temperature.

Table 2.19. Spectrometric characteristics of  $\text{CdWO}_4$

$D$ , mm	$H$ , mm	$C$ , %	$R$ (% for $\gamma$ -quanta)		
			$^{137}\text{Cs}$ (662 KэВ)	$^{22}\text{Na}$ (1.275 MeV)	$^{232}\text{Th}$ (2.61 MeV)
40	30	45	8.0	6.1	5.0
40	40	36	9.0	6.8	5.3
40	50	32	10.0	7.3	6.0
40	70	21.9	11.5	8.8	7.8



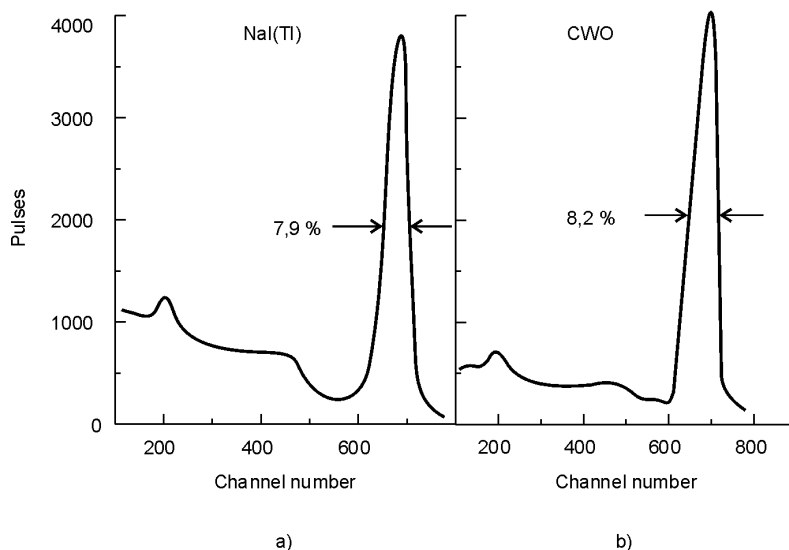


Fig.2.36. Spectrograms of NaI(Tl) (1) and  $\text{CdWO}_4$  (2) scintillators ( $^{137}\text{Cs}$ ,  $E_\gamma = 662 \text{ keV}$ ).

Analysis of the absorption coefficient changes upon concentration of cation admixtures from groups I–V shows that isovalent dopants Ca, Ba, Zn do not significantly affect the transparency of  $\text{CdWO}_4$  crystals, even if their concentration in the melt is as high as 0.1%. Dopants with non-compensated charges ( $\text{Bi}^{3+}$ ,  $\text{Y}^{3+}$ ,  $\text{Gd}^{3+}$  and especially  $\text{Fe}^{3+}$ ) substantially worsen the crystal transparence even at concentrations of  $10^{-3} \%$  and less. Their influence decreases when a charge compensator is introduced. The best transparence ( $K = 0.02 \text{ cm}^{-1}$ ) is observed in nominally pure  $\text{CdWO}_4$  crystals of the stoichiometric composition. When extra Cd content in the charge increases up to 0.2%, transparence is worsened by 2 times ( $K = 0.04 \text{ cm}^{-1}$ ). In Table 2.20, comparative results are shown for transparence of  $\text{CdWO}_4$  crystals and their light output  $C$  (with respect to NaI(Tl)) and reduced resolution  $R$  at  $^{137}\text{Cs}$   $\gamma$ -line [116].

The light output and afterglow values for  $\text{CdWO}_4$  with different degree of deviation from the stoichiometric composition in cadmium concentration are shown in Tabl.2.21 [103].

Table 2.20. Characteristics of  $\text{CdWO}_4$  single crystals of different transparence ( $D=40\text{--}50$  mm;  $H=40\text{--}70$  mm).

$K, \text{cm}^{-1}$	$H/D$ ratio					
	1		2		0.5	
	$C, \%$	$R, \%$	$C, \%$	$R, \%$	$C, \%$	$R, \%$
0.02	21.6	10.0	17.8	11.5	25.7	9.8
0.03	18.5	11.2	14.0	12.8	21.3	10.7
0.05	14.8	16.5	10.6	21.8	19.0	18.2

Table 2.21. Light output and afterglow of  $\text{CdWO}_4$  with different deviations from stoichiometry

Deviation of cadmium concentration from stoichiometry, mol. %	Light output with respect to $\text{CsI(Tl)}$ , %	Afterglow after 5 ms, %
Stoichiometry	50	<0.0005
0.05	50	<0.0005
0.10	47	0.0010
0.25	42	0.0015
0.50	37	0.0050

It can be seen that deviations larger than 0.05% decrease the light output and increase the afterglow. The presence of admixtures does also affect main characteristics of  $\text{CdWO}_4$  scintillators (Table 2.22) [103].

Doping the crystals with iron induces the largest effects not only upon the light output of  $\text{CdWO}_4$  crystals, but also upon their color — absorption in the 470–800 nm range substantially increases with increased Fe concentration. In the most transparent crystals, Fe content does not exceed  $2 \cdot 10^{-4} \%$ , and concentration of other admixtures (Ni, Co, Cr) is less than  $10^{-4} \%$ . The absorption coefficient within the intrinsic luminescence band ( $\sim 500$  nm) is  $\sim 0.05 \text{ cm}^{-1}$  for such crystals. When Fe concentration is  $> 5 \cdot 10^{-4} \%$ ,  $\text{CdWO}_4$  crystals acquire a yellowish color, and at  $\sim 5 \cdot 10^{-3} \%$  Fe they become reddish-brown. With higher coloring intensity, the light yield is decreasing — due both to passive absorption and non-radiative de-activation of electrons captured on  $\text{Fe}^{3+}$  (or due to resonance energy transfer by the iron ions activated by luminescence centers. In the lattice crystal

Table 2.22. Effects of admixtures upon light output and afterglow of  $\text{CdWO}_4$  crystals.

Admixture	Concentration, mass %	Light output with respect to $\text{CsI(Tl)}$ , %	Afterglow after 5 ms, %
Pb	$1.5 \cdot 10^{-4}$	50	<0.0005
Pb	$2 \cdot 10^{-4}$	49	<0.0005
Pb	$6 \cdot 10^{-4}$	40	<0.0005
Pb	$3 \cdot 10^{-3}$	32	0.005
Na	$2 \cdot 10^{-4}$	50	<0.0005
Na	$2 \cdot 10^{-4}$	50	<0.0005
Na	$10^{-3}$	48	<0.0005
Na	$4 \cdot 10^{-3}$	45	0.001
Ni	$3 \cdot 10^{-5}$	50	<0.0005
Ni	$2 \cdot 10^{-4}$	49	<0.0005
Ni	$10^{-3}$	30	<0.0005
Fe	$2 \cdot 10^{-4}$	50	<0.0005
Fe	$2 \cdot 10^{-4}$	41	<0.0005
Fe	$3.5 \cdot 10^{-4}$	23	<0.0005

field,  $\text{Fe}^{3+}$  ions have several closely located levels over which non-radiative transitions to the basic levels are proceeding.

Thus, a large discrepancy in the light yield and energy resolution values that is observed experimentally for  $\text{CdWO}_4$  crystals is related to the presence of defects (which cause coloring) and scattering centers. High quality  $\text{CdWO}_4$  crystals with high light output can be obtained only if charge with optimum ratio of tungsten and cadmium oxides is used, with concentration of Fe and other admixtures less than  $10^{-4}$  % [115].

Effects of dopant and structure defects upon optical and scintillation properties of  $\text{CdWO}_4$  crystals have been comprehensively studied in the Institute for Single Crystals. Basing on the results obtained, procedures have been developed for production of large-sized optically uniform  $\text{CdWO}_4$  crystals (50 mm in diameter and 100–120 mm long). These crystals showed sufficiently high transparence in the intrinsic luminescence region ( $K = 0.02\text{--}0.03 \text{ cm}^{-1}$ ) [150].

Zinc tungstate ( $\text{ZnWO}_4$ ) single crystals, like  $\text{CdWO}_4$ , have relatively high light output (Table 2.18), which is 28% with respect to  $\text{NaI(Tl)}$ , and

long decay time, which is due to a combination of three components ( $\tau_1 = 20 \mu\text{s}$ ,  $\tau_2 = 3.3 \mu\text{s}$ ,  $\tau_3 = 0.1 \mu\text{s}$ ). The amplitude ratio for the first two components is 0.25, and the third component covers about 5% of all scintillations. The luminescence spectrum of  $\text{ZnWO}_4$  has maximum at 490 nm, which allows its use both with PMT or photodiodes.

$\text{ZnWO}_4$  single crystals display high radiation stability. According to [117], after  $\text{ZnWO}_4$  crystals of dimensions  $1.5 \times 1.5 \times 1.5 \text{ mm}$  had been submitted to  $^{60}\text{Co}$   $\gamma$ -irradiation ( $5 \cdot 10^3 \text{ Gy}$ ), their parameters practically did not change. After  $\gamma$ -irradiation (1 MeV) by an accelerator, the light yield fell by 40%; however, in several months it was restored to 90% of the initial value.

Scintillation properties of  $13 \times 13 \times 6 \text{ mm}$   $\text{ZnWO}_4$  crystals, which were covered with a  $\text{MgO}$  light reflector and had an optical contact to a PMT with a quartz window, were reported in [118]. Their energy resolution was 13% for  $E_\gamma = 662 \text{ keV}$ , photoelectron yield —  $1400 \text{ MeV}^{-1}$ . 5% of the emitted light had the decay time constant 100 ns, and 95% — 25  $\mu\text{s}$ . Time resolution of the scintillator was 960 ns.

Lead tungstate  $\text{PbWO}_4$  and calcium tungstate  $\text{CaWO}_4$ .  $\text{PbWO}_4$  crystals have been studied since 1948 [108], being considered at first as just a luminescent material with a very low light output at room temperature — about 1% with respect to  $\text{CsI(Tl)}$ . Their applications are thus mostly limited to the field of high energy physics. They have the shortest radiation length ( $\chi_0 = 0.85 \text{ cm}$ ) and the smallest Moliere radius ( $R_m = 2.19 \text{ cm}$ ) among the known scintillators. Lead tungstate is a heavy ( $\rho = 8.28 \text{ g/cm}^3$ ,  $Z = 73$ ) and fast ( $\tau_d = 3\text{--}5 \text{ ns}$ ) scintillation material. Main physico-chemical properties and scintillation characteristics of  $\text{PbWO}_4$  are presented in Table 2.18.

Studies of  $\text{PbWO}_4$  luminescent properties, which were analyzed in [92], show substantial inconsistencies in interpretation of the experimental results. This could reflect high sensitivity of  $\text{PbWO}_4$  luminescence characteristics to specific conditions of the crystal preparation. Even minor differences in the growth technology may lead to substantial differences in absorption and emission spectra of  $\text{PbWO}_4$  crystals. Under  $\gamma$ -excitation,  $\text{PbWO}_4$  luminescence spectrum is a broad and complex emission band from 370 nm to 500 nm, the shape of which is strongly dependent upon W concentration in the melt. This fact is explained [92] by considering the observed emission as superposition of

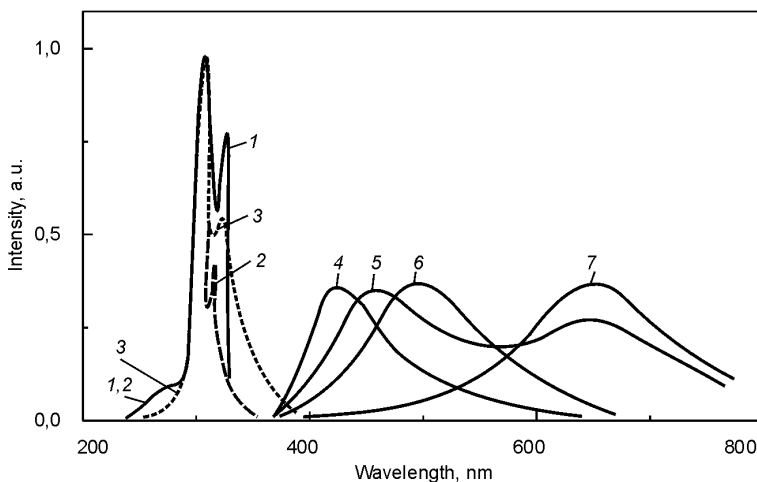


Fig.2.37. Excitation and luminescence spectra of  $\text{PbWO}_4$  at 300 K. Excitation: 1 —  $\lambda_l = 420$  nm; 2 —  $\lambda_l = 500$  nm; 3 —  $\lambda_l = 650$  nm. Luminescence: 4 —  $\lambda_{\text{exc}} = 275$  nm; 5 —  $\lambda_{\text{exc}} = 308$  nm; 6 —  $\lambda_{\text{exc}} = 325$  nm; 7 —  $\lambda_{\text{exc}} = 350$  nm.

several luminescence bands, with their relative contribution depending upon the ratio of stoichiometric defects in the crystal.

Intensity and shape of the luminescence bands were found to be different for the upper and lower part of a single crystalline ingot of  $\text{PbWO}_4$  [120]. This was attributed to stoichiometry variation along the crystal length, leading to non-uniform distribution of the emission centers. Luminescence spectra of  $\text{PbWO}_4$  crystals are shown in Fig.2.37 (according to [92]).

It has been also noted [121] that optical, scintillation and kinetic characteristics of  $\text{PbWO}_4$  are strongly dependent upon crystallization conditions, purity and stoichiometric composition of the crystals. Especially important are the defects formed both in anionic and cationic sublattice. Nominally pure  $\text{PbWO}_4$  crystals of the stoichiometric composition are characterized by their luminescence spectrum with maximum at 420 nm. The decay time constant (85% of the intensity) is less than 10 ns.

Detailed studies of transparency for  $\text{PbWO}_4$  crystals of different length allowed making a correlation between their spectral characteristics and growth conditions (Fig.2.38) [94]. The crystals

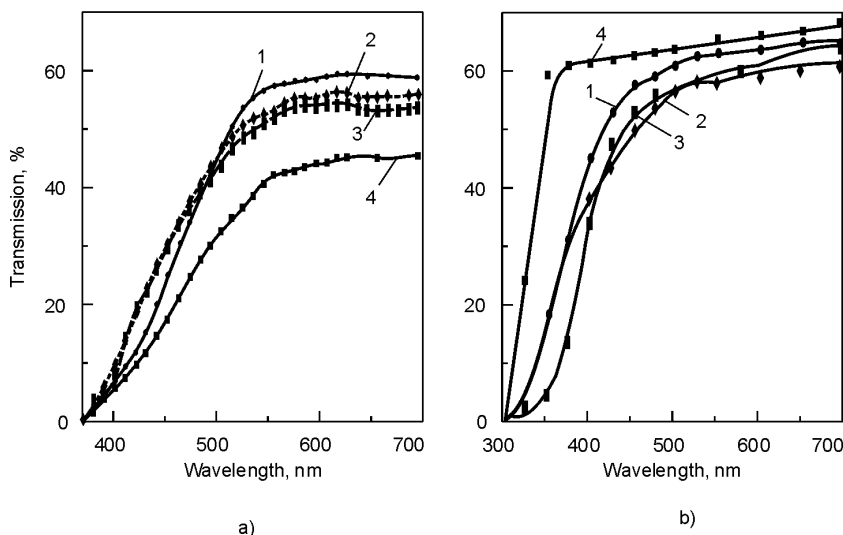


Fig.2.38. Transmission spectra of PbWO<sub>4</sub> crystals: a — crystals of different length: 1 — 180 mm, 2 — 180 mm, 3 — 180 mm, 4 — 220 mm; b — crystals with different defects: 1 — stoichiometric crystal; 2 — stoichiometric crystal grown from a recycled melt; 3 — crystal with excess Pb; 4 — crystal grown in a controlled oxygen-containing atmosphere.

prepared in oxygen-containing media (with exception of yellow-colored crystals) were distinguished by their high transparency above 400 nm. Yellow-colored PbWO<sub>4</sub> crystals have an absorption band at 430 nm. As a rule, yellow-colored crystals are obtained when grown from the recurrently used (recycled) melt. Growing the crystals in a medium with controlled (reduced) oxygen concentration results in an increased transparency, especially in UV spectral region. The crystal transparency is also strongly affected by stoichiometric and dopant defects, especially heterovalent admixtures.

In [122], two broad absorption bands were reported for PbWO<sub>4</sub> crystals, peaked at 350 nm and 420 nm. They affected substantially the scintillation properties of large-sized crystal elements, decreasing the light output and worsening its uniformity over the crystal length.

Worsening of PbWO<sub>4</sub> scintillation properties is also caused by admixtures of Mo, Fe and some other trivalent and bivalent admixtures

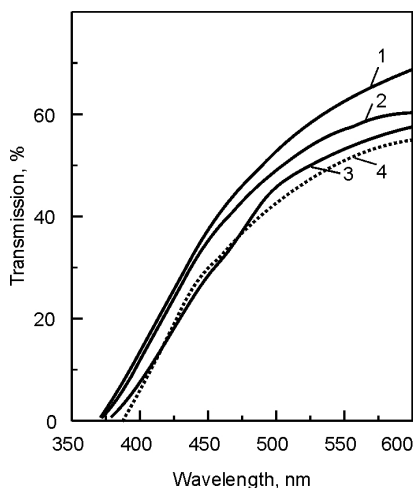


Fig.2.39. Transmission spectra of  $\text{PbWO}_4$  samples ( $20 \times 20 \times 160$  mm): 1 — crystal grown in an inert atmosphere with composition close to stoichiometry; 2 — crystal with excess oxygen in the anion sublattice, grown in an inert atmosphere; 3 — crystal grown in oxygen-depleted atmosphere; 4 — crystal grown on air.

band at 430 nm is observed and, correspondingly, the yellow coloring does not appear. In the visible range, the best transparency is observed for  $\text{PbWO}_4$  crystals grown in an inert medium (Fig.2.39, curve 1).

2. Crystals grown in an inert atmosphere have higher uniformity over the ingot length. Absorption coefficient values in the intrinsic emission region for best  $\text{PbWO}_4$  crystals are scattered no more than within 3–4% (Fig.2.40). This is also in agreement with light output data measured for six different crystals over their length (Fig.2.41) [121].
3. Crystals grown in conditions that ensure their composition to be close to stoichiometry have their integral emission plot with maximum in the 2.9 eV region (Fig.2.42, curve 1). When defects are formed

that can be present in the raw material charge. An absorption band around 420 nm is partially overlapped with the luminescence spectrum. Typical values of the absorption coefficient in this case are  $\sim 0.05 \text{ cm}^{-1}$ . A relative light output decrease by about two times is observed for  $\text{PbWO}_4$  scintillation elements of  $>200$  mm length [122].

The available data on the effects of technological growth conditions upon quality of  $\text{PbWO}_4$  single crystals and their scintillation characteristics can be summarized as follows.

1. Crystals grown in an inert atmosphere have higher transparency, both in UV region (close to the absorption edge) and in the intrinsic emission region, than those grown in an oxygen-containing atmosphere (Fig.2.39). In such  $\text{PbWO}_4$  crystals, no absorption

in the anionic sublattice, this maximum is shifted to longer wavelengths (2.5–2.61 eV, Fig.2.42, curve 2).

Light output of  $\text{PbWO}_4$  scintillators is rather strongly dependent on temperature, which is related to the nature of luminescence centers and temperature quenching [123]. The temperature dependence of  $\text{PbWO}_4$  light output in the  $-193^\circ\text{C} - +50^\circ\text{C}$  range is shown in Fig.2.43.

The calculated value of the light output temperature coefficient at  $20^\circ\text{C}$  is  $1.98\%/\text{K}$ . A typical picture of scintillation decay in undoped  $\text{PbWO}_4$  is shown in Fig.2.44. More than 90% of light is emitted less than in 100 ns. For Nb-doped  $\text{PbWO}_4$  crystals, which show only blue and green emission, the scintillation decay is shorter and is well described by two exponents with time constants of 3 ns and 14 ns, contributing 55% and 45%, respectively. The temperature dependence of the average decay time for  $\text{PbWO}_4$  in the  $-193^\circ\text{C} - +50^\circ\text{C}$  range is shown in Fig.2.45.

An interesting fact has been noted, related to the effects of anisotropy of  $\text{PbWO}_4$  crystal structure upon its luminescence characteristics. In [96], the maximum luminescence yield was observed when the crystal surface was irradiated in directions “[001]” or “[104]”. The difference in the light output values for different orientations of the crystal was more marked at lower excitation energies. At the excitation energy of  $\sim 30$  keV, this

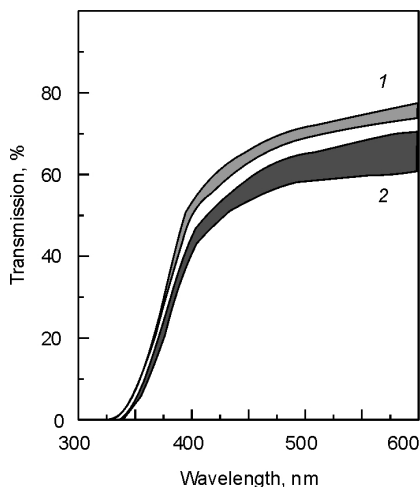


Fig.2.40. Spectral distribution of  $\text{PbWO}_4$  transmission over crystal length: 1 — crystal grown in an inert atmosphere; 2 — crystal grown on air.

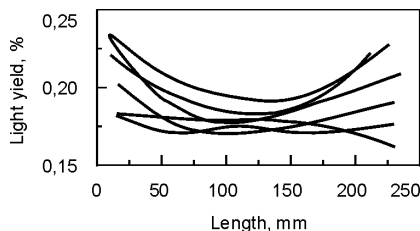


Fig.2.41. Light output variation over  $\text{PbWO}_4$  crystal length.



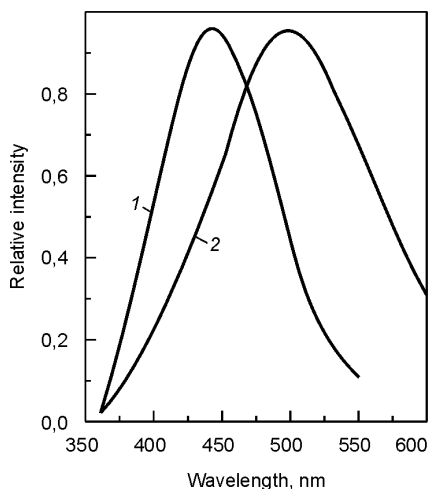


Fig.2.42. X-ray luminescence spectra of  $\text{PbWO}_4$  crystals: 1 — crystals close to stoichiometry; 2 — crystals with defects in the anion sublattice.

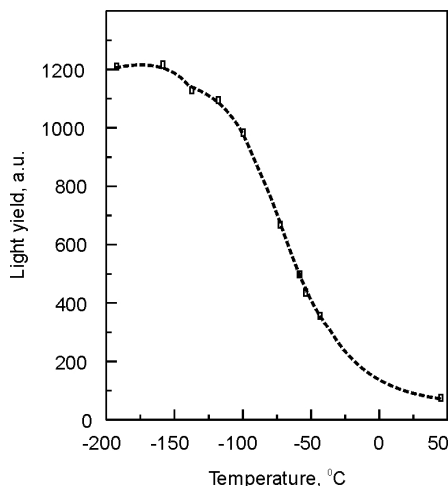


Fig.2.43. Light output of  $\text{PbWO}_4$  crystals as function of temperature.

difference was 40% larger. This can be explained by different density of luminescence centers in different crystallographic directions.

The radiation stability of  $\text{PbWO}_4$  crystals is sufficiently high. Irreversible radiation damages appear at doses above  $10^5$  Gy. Under irradiation,  $\text{PbWO}_4$  crystals grown in different conditions show worsening of their transparence. Usually an additional absorption band appears at 620 nm [30] (or 600 nm [92]), which is due to  $\text{Pb}^{3+}$ -type defects. Therefore, niobium-doped  $\text{PbWO}_4$  crystals (0.1% Nb) have higher radiation stability because of compensation of  $\text{Pb}^{3+}$  defects. Doping of  $\text{PbWO}_4$  with niobium, alongside with improvement of radiation stability, favors also better uniformity of the material along the crystal ingot. Fig.2.46 shows non-uniformities of radiation damage caused by induced absorption at 420 nm along the crystal length of Nb-doped and undoped  $\text{PbWO}_4$ .

Negative effects of radiation can be seen also in an increase in afterglow. Parameters of this afterglow in each specific case are related to certain coloring centers emerging under irradiation [122].

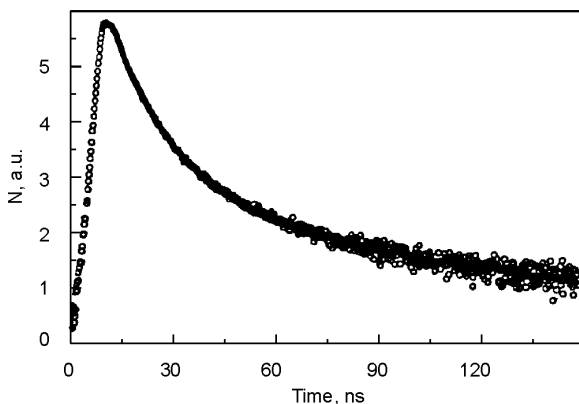


Fig.2.44. A typical scintillation decay plot for undoped  $\text{PbWO}_4$ .

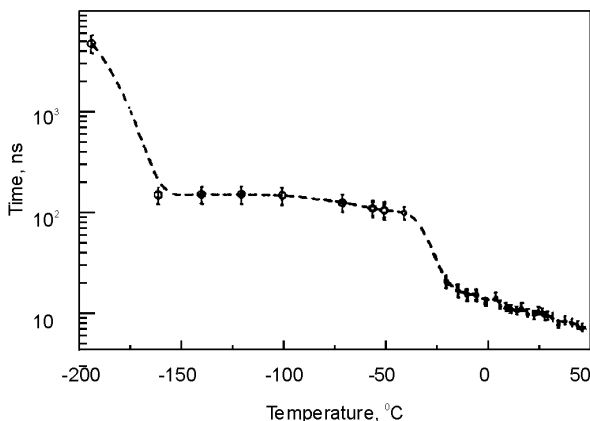


Fig.2.45. Average decay time for  $\text{PbWO}_4$  as function of temperature.

In [146], a substantial improvement of  $\text{PbWO}_4$  scintillation characteristics was achieved by its doping with lanthanum. This improvement involved optical transparency in the short-wave region between 320 nm and 450 nm, decay time and radiation stability. Under  $\gamma$ -irradiation of the doped crystals, the absorption coefficient remained as low as for the non-irradiated material up to the doses of  $10^8$  rad.

The mechanical strength of  $\text{PbWO}_4$  single crystals can be substantially improved. To achieve this, fissure formation after growth and

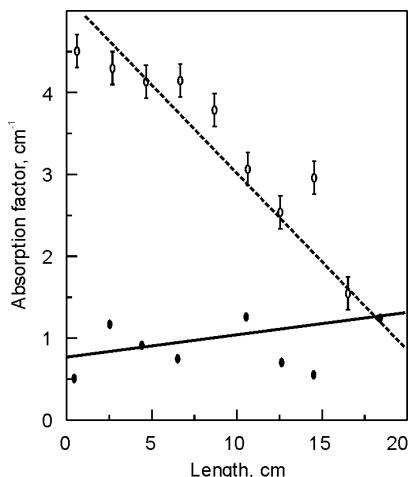


Fig.2.46. Non-uniformity of radiation damage along large  $\text{PbWO}_4$  crystals without dopants (1) and doped with Nb (2).

annealing should be prevented. At present, brittleness of these crystals results in less than 70% yield of good products after mechanical treatment [122].

Among alkali earth metal tungstates, the highest light output is observed for calcium tungstate  $\text{CaWO}_4$  (see Table 2.18). It reaches 50% with respect to  $\text{NaI(Tl)}$ . The emission maximum is at 430 nm, making it possible to use  $\text{CaWO}_4$  for spectrometry of  $\gamma$ -radiation. For  $\text{CaWO}_4$  detectors of dimensions  $\varnothing 10 \times 10$  mm in combination with PMT, resolution of 13.6% was obtained for  $^{137}\text{Cs}$   $\gamma$ -radiation, and of 12.5% — with a  $\text{HgI}_2$ -based photodiode. However, applications of this crystal are substantially

limited by its slow response (decay time of 0.5–20  $\mu\text{s}$ ) [102].

The main application field of  $\text{CaWO}_4$  single crystals is computer tomography.

The luminescence kinetics of  $\text{ZnWO}_4$  and  $\text{CdWO}_4$  crystals has been studied in detail by V.D.Ryzhikov, G.Tamulaitis e.a. [89], and of  $\text{PbWO}_4$  crystals — in [90,143].

In [143], luminescence kinetics was studied for  $\text{PbWO}_4$  crystals excited by synchrotron radiation and selective photoexcitation of the intrinsic luminescence. The excitation dynamics is treated in terms of thermally activated depletion of the emission centers and their renewed occupation from the adhesion centers, which gives rise to slow components of the luminescence decay. The relative intensities of the blue and green luminescence were found to be strongly dependent on temperature. Changes in the luminescence spectra with increasing temperature are shown in Fig.2.47. It can be seen that blue luminescence is quenched quicker than the green.

The luminescence kinetics of  $\text{PbWO}_4$  crystals at 3.02 eV (the blue luminescence band maximum) is illustrated in Fig.2.48 for different

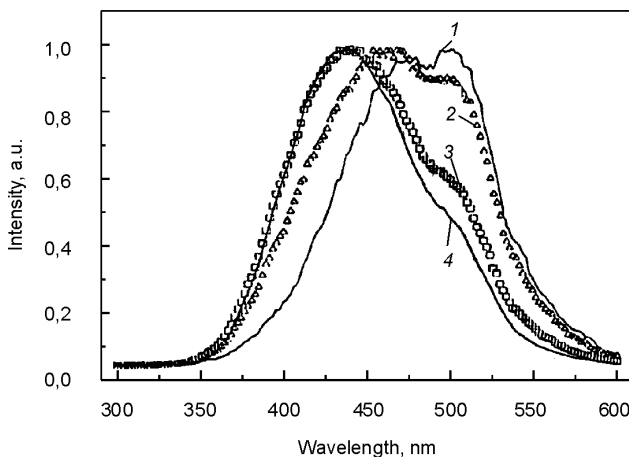


Fig.2.47. Evolution of the luminescence spectrum of  $\text{PbWO}_4$  crystals with temperature: 250 K (1), 200 K (2), 175 K (3), 150 K (4).

temperatures. Detailed studies of  $\text{PbWO}_4$  luminescence kinetics in the 200–295 K would be interesting, according to [143], from the standpoint of promising applications of this scintillation material.

In [57], the luminescence decay time was presented as sum of three exponents with different decay time constants and weight factors. This approximation has physical meaning if the complex character of decay at a specified wavelength results from superposition of three different bands that are subject to exponential decay with different speeds. In fact, the luminescence decay in  $\text{PbWO}_4$  is even more complex than just superposition of three exponentially decaying luminescence bands.

In [89], luminescence and photoexcitation spectra of  $\text{ZnWO}_4$  and  $\text{CdWO}_4$  crystals of wolframite structure were studied in a broad temperature range (from 4.2 to 300 K). Decay kinetics in different spectral ranges was determined, and for the first time bands of red luminescence and of fastly decaying violet luminescence were reported.

#### *2.3.4. The nature of luminescence centers in tungstates and their energy diagrams*

Questions on the nature of luminescent centers in tungstates and their relationship with crystal structure defects of specified types have not yet been fully cleared up, and discussions on these

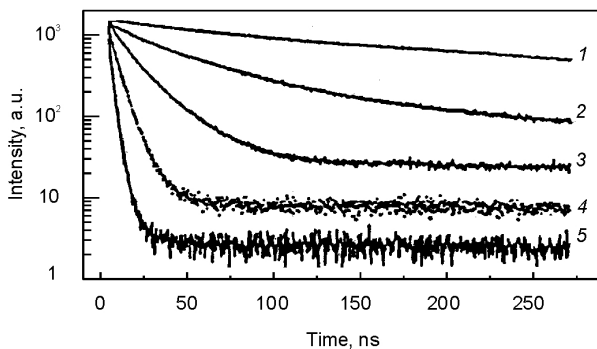


Fig.2.48. Luminescence decay time in  $\text{PbWO}_4$  at 3.02 eV and different temperatures: 200 K (1), 225 K (2), 247 K (3), 270 K (4), 295 K (5) [143].

points are still under way. Several different models of luminescence centers have been used for interpretation of luminescent properties of tungstates. The most commonly used is the model that relates the emission to transitions inside the  $\text{WO}_6^{6-}$  complex for wolframites, and  $\text{WO}_4^{6-}$  complex — for scheelites [124–126]. Proceeding from the crystal structure features of tungstates described in Chapter 2.3.1, these complexes can be considered as multi-atom molecules or complex oxyanions.

Most authors [125,127,128] attribute the luminescence to transitions  $5dW - 2pO$  inside a  $\text{WO}_6^{6-}$  or  $\text{WO}_4^{6-}$  complex; however, there were also assumptions [129] that only isolated complexes do luminesce. This conclusion can be reached if one considers effects of raw material composition and growth conditions upon the luminescence intensity of tungstates. An assumption was also made that luminescence due to ideal  $\text{WO}_4^{6-}$  complexes could be observed only at low temperatures ( $<10$  K).

According to another model of luminescence centers in tungstates, in particular, in  $\text{PbWO}_4$ , luminescence can be due to the  $\text{Pb}^{3+}-\text{WO}_4^{3-}$  complex, i.e., complex composed of an electron localized on the oxyanion and a hole on the nearest cation [130]. The complex pattern of the luminescence center levels is explained in this paper by tetragonal distortion of  $\text{WO}_4$ , spin-orbital interaction and the presence of different isotopes in the lattice:  $^{207}\text{Pb}$  with nuclear spin  $I = 1/2$  and  $^{204}\text{Pb}$ ,

$^{206}\text{Pb}$ ,  $^{208}\text{Pb}$  with  $I = 0$ . This picture is considered as adequate for the yellow-green luminescence [130].

A substantially different luminescence center model was proposed in [131], which assumes that tungsten can exist in a partially reduced state, i.e. in the form of  $\text{W}^{5+}$  (and not  $\text{W}^{6+}$ ). The absorption and luminescence spectra can then be described as  $d-d$  transitions in  $\text{W}^{5+}$ , the energy of which depends upon distortions of the tetrahedral oxygen complex. However, large intensity of the UV absorption bands and large breadth of the distorted luminescence bands raise doubts that these bands can be ascribed to the  $d-d$  transitions.

In [129,133,134], the authors proposed a luminescence center model, which satisfactorily described the experimental results. The model considers an isolated  $\text{WO}_6$  complex, the existence of which in the wolframite structure is ensured by a break in the  $\text{WO}_6^{6-}-\text{WO}_6$  chain of complexes along the  $C$  axis, i.e., by defects of  $\text{O}_{\text{WO}_4}^{2-}$  and  $\text{V}_0^{2+}$  type. Concentration of such centers in  $\text{CdWO}_4$  and  $\text{ZnWO}_4$  is  $\sim 10^{18} \text{ cm}^{-3}$ . However, the estimate of the number of luminescence centers made in [126] from an intensity characteristic under powerful excitation, gives 2.6% of the total number of particles. The presence of defects in such a great number is highly improbable. Moreover, no intensity increase was reported for the main luminescence band after annealing the crystals in vacuum, which led to an increase in number of these defects. On the contrary, an opposite effect was observed — the light output increased after annealing in an oxygen atmosphere [103], which could lead only to curing of the oxygen sublattice defects, i.e., to decrease in  $\text{V}_0^{2+}$  concentration.

As the highest occupied and the lowest vacant state in tungstates are formed by molecular orbitals of  $\text{WO}_6^{6-}$  and  $\text{WO}_4^{2-}$ , knowledge of the energy structure of such clusters is necessary for understanding of the processes related to luminescence and absorption in these crystals.

An energy pattern of luminescence centers in cadmium and zinc tungstate was proposed in [111,135,136]. Potential functions of  $\text{WO}_6^{6-}$  complex are shown in Fig.2.49 according to data of [136]. The transition energy values (for  $\text{CdWO}_4$ ) are shown by arrows. Slight differences in the band maximums are noted for  $\text{CdWO}_4$  and  $\text{ZnWO}_4$ : 2.50 eV – 2.55 eV, 2.17 eV – 2.14 eV, 3.40 eV – 3.49 eV, 3.84 eV – 3.90 eV, respectively. These differences reflect changes in position of terms of the  $\text{WO}_6^{6-}$  complexes due to changes in the crystal field.

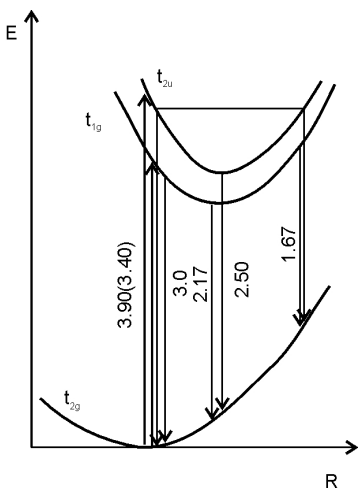


Fig.2.49. A diagram of potential curves for  $\text{WO}_6^{6-}$  complex [136].

Most experimental data evidence that luminescence in  $\text{CdWO}_4$  and  $\text{ZnWO}_4$  crystals is intrinsic in character and is determined by  $\text{WO}_6^{6-}$  complexes. The luminescence spectrum consists of broad, nearly symmetrical structureless bands  $E_l = 2.50$  eV ( $\text{CdWO}_4$ ) and 2.55 eV ( $\text{ZnWO}_4$ ), 2.17 eV ( $\text{CdWO}_4$ ) and 2.14 eV ( $\text{ZnWO}_4$ ). This implies that radiative transitions originate from the lowest relaxed vibrational states of the  $\text{WO}_6^{6-}$  complexes. These states can be considered as autolocalized excitons [137]. The autolocalized excitons model was applied to luminescence of  $\text{ABO}_4$  crystals with scheelite structure ( $\text{CdWO}_4$  and  $\text{ZnWO}_4$ ) in [127]. At low temperatures (4.2–10 K) the 2.14 eV luminescence band is readily excited

in  $\text{ZnWO}_4$ , while the 2.55 eV band is practically not excited (as well as 2.50 eV and 2.17 eV bands in  $\text{CdWO}_4$ ). This implies that autolocalization to state  $t_{1g}$  in  $\text{ZnWO}_4$  encounters no barrier, while that to state  $t_{2u}$  in  $\text{CdWO}_4$  — a barrier of  $8 \cdot 10^{-4}$  eV.

In [136], it was assumed that the structure of luminescence centers in  $\text{CdWO}_4$  and  $\text{ZnWO}_4$  is determined by crystal defects related to deviations of the composition from stoichiometry. These defects take part in formation of the luminescence and capture centers, determining main spectral and kinetic properties. The greatest role in shaping the spectra is played by cadmium, zinc and oxygen defects. Luminescence and photoexcitation spectra, crystal structure features, as well as theoretical calculations of the electron structure indicate that luminescence and absorption spectra of tungstates are determined by transitions in  $\text{WO}_6^{6-}$ -involving complexes [103]. A detailed picture of the luminescence centers can be obtained from effects of different kinds of thermal treatment upon spectral-kinetic characteristics of  $\text{CdWO}_4$  and  $\text{ZnWO}_4$  crystals. Absorption bands  $E_a = 3.40$  eV; 2.80 eV for  $\text{CdWO}_4$  and  $E_a = 3.49$  eV; 2.90 eV for  $\text{ZnWO}_4$  are related to the complex of  $\text{WO}_6^{6-}$  plus zinc (cadmium) vacancy. The presence of two bands

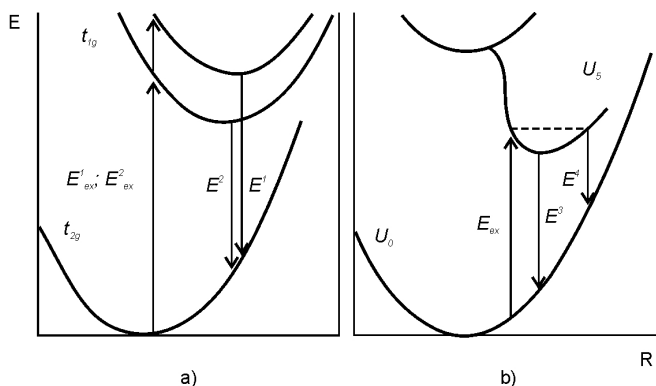


Fig.2.50. A model of configuration plots for  $\text{WO}_6^{6-}$  complex (a), and autolocalized exciton (b) in  $\text{ZnWO}_4$  and  $\text{CdWO}_4$  crystals of wolframite structure [89].

determined by one type of defects can be related, firstly, to different charge states of cadmium (zinc) vacancies, and secondly, with two different positions of cadmium (zinc) in the elementary cell with respect to tungsten, causing formation of non-equivalent cadmium (zinc) vacancies. The luminescence bands  $E_l=2.17$  eV ( $\text{CdWO}_4$ ) and  $E_l=2.14$  eV ( $\text{ZnWO}_4$ ) are also related with the said complex. Thus, the luminescence center appears to be a complex of composite structure, comprising three coordination spheres, which at the same time is also a capture center. The absorption band  $E_a=2.48$  eV and the slow emission band  $E_l=1.8$  eV, which is related to it, are both due to defects in the oxygen sublattice. The emission within this band is of recombination nature.

Similarity in emission characteristics noted in [89] for  $\text{CdWO}_4$  and  $\text{ZnWO}_4$  has allowed explaining luminescence in these crystals of wolframite structure using configuration plot models for a self-activated emission center and autolocalized exciton (Fig.2.50).

For  $\text{CaWO}_4$  crystals of scheelite structure, structural defects do also substantially affect their spectral-kinetic characteristics [138]. Luminescence of  $\text{CaWO}_4$  is generally related to radiative surexcitation of the  $\text{WO}_4^{2-}$  anionic complex. This model is confirmed by calculations of the excited states of  $\text{WO}_4^{2-}$  complex, which are in good agreement with experimental results. For emission of such luminophores, it is characteristic that the influence of the central ion of the anionic complex is predominant, and practically no effects related to the cation are noted.



Luminescence in  $\text{CaWO}_4$  is created not by all  $\text{WO}_4^{2-}$  anions, but only a part of them located in irregular lattice cells, i.e., in distorted parts of the anionic sublattice; however, peculiar features of the distortions have not yet been fully cleared up. According to one of the hypotheses forwarded, such distortions can be created by distortions of the crystal field around separate  $\text{WO}_4^{2-}$  complexes caused by point defects and dislocations [139]. According to another model, distortions in  $\text{CaWO}_4$  are related to lowering of the valence of some fraction of tungsten ions ( $\sim 2 \cdot 10^{-4}$  g/atom/mol) [132]. In [138], a fast weak UV band was noted in  $\text{CaWO}_4$  spectra at 225 nm. Low emission intensity and low duration ( $\tau < 25$  ns) suggest a relationship between this luminescence and the luminescence due to autolocalized excitons that had been observed in  $\text{CaWO}_4$  [52]. Still another model of UV-emission in  $\text{CaWO}_4$  is possible, related to “hot” luminescence of  $\text{WO}_4^{2-}$  complexes [140].

Relationship between luminescence bands in  $\text{PbWO}_4$  and possible luminescence centers in these crystals has been comprehensively analyzed in [141], accounting for practically all known publications on this subject. Comparison of experimental data from [141] and those obtained by other authors for  $\text{PbWO}_4$  crystals grown in different conditions have shown that the blue luminescence band at 420 nm is always present in all tungstates. This observation confirms that these bands are related to the emission of regular  $\text{WO}_4^{2-}$  centers in these scintillation materials. It was noted [142] that, alongside with the “blue” luminescence, there exist at least two “green” and one “red” emission band. Studies carried out on samples cut from different parts of one and the same crystal have established relationship of the green and red luminescence to point defects of different nature. Two green luminescence bands in  $\text{PbWO}_4$  are ascribed to  $(\text{WO}_3 + \text{F})$  centers. These centers are based on anion vacancies in the first coordination sphere of the  $\text{WO}_6^{6+}$  ion and are similar in structure to admixture centers. They are of high radiation stability, and stable in time. On the contrary, the red luminescence is related to a set of defects emerging as a result of tungsten deficiency in the crystal. These centers are not stable under irradiation, which makes them a potential source of radiation damage in these crystals.

Summing up the above described, it can be concluded that scintillations in  $\text{PbWO}_4$  are related to  $\text{WO}_4^{2-}$  and  $(\text{WO}_3 + \text{F})$  luminescence centers through  $\text{Pb}^{2+}$  ions. A diagram showing energy transitions in  $\text{PbWO}_4$  according to data from [141] is presented in Fig.2.51. It fol-

lows from this diagram that there exists a limitation for obtaining very high light output in  $\text{PbWO}_4$ . All the emitting centers show large Stokes' shift and strong thermal quenching of the luminescence. The main part of the absorbed energy is transferred from  $\text{Pb}^{2+}$  ions to regular  $\text{WO}_4^{2-}$  centers. This cannot ensure substantial contributions to the light output because of overlapping of wave functions, which leads to migration of excitations and quenching of the luminescence. Though  $(\text{WO}_3 + \text{F})$  centers compete with  $\text{WO}_4^{2-}$  complexes in the energy transfer from

lead ions and contribute to the scintillation significantly, they cannot substantially contribute to the light output because of their low concentration in the crystal. Their influence is counter-balanced by the presence of uncontrolled admixtures, which can compete with  $(\text{WO}_3 + \text{F})$  centers in transferring the energy from  $\text{Pb}^{2+}$  ions. An important conclusion follows: the use of materials of higher purity can lead to more efficient energy transfer to  $\text{WO}_4^{2-}$  and  $(\text{WO}_3 + \text{F})$  luminescence centers. Optimization of  $\text{PbWO}_4$  crystal growth technology makes it possible to achieve higher light output of scintillators on their base, improves their radiation stability and ensures uniformity of scintillator parameters. In [141], improvement of  $\text{PbWO}_4$  scintillation characteristics was achieved by introduction of Nb dopant, which prevented formation of  $\text{Pb}^{3+}$ -type defects.  $\text{Nb}^{5+}$  ions replace the  $\text{W}^{6+}$  ions and compensate for the W ions deficiency. In these crystals no red luminescence is observed, which is related to  $\text{Pb}^{3+}$ -type defects.

In [90], two types of centers were noted and described, which appeared responsible for short-wave emission in  $\text{PbWO}_4$  crystals of scheelite structure. Centers of the first type can be presented as regular  $\text{WO}_4^{2-}$ -complexes, while those of the second type can be described within the autolocalized exciton model. In Fig.2.52, a model

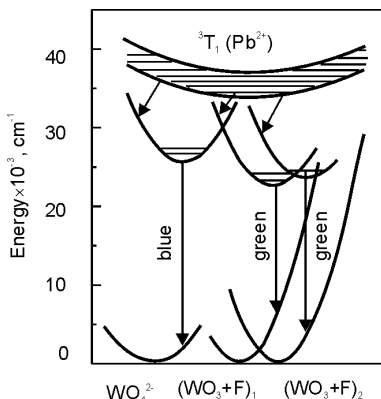


Fig.2.51. A diagram of energy transitions in  $\text{PbWO}_4$  scintillator.

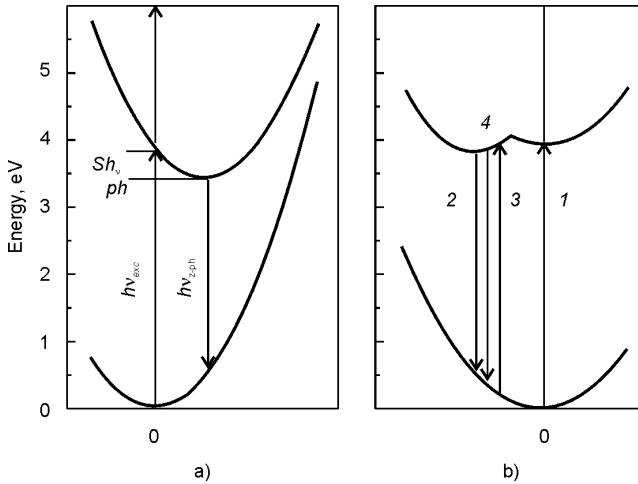


Fig.2.52. A model of configuration plots in  $\text{PbWO}_4$  for: a —  $\text{WO}_4^{2-}$  complex; b — autolocalized exciton. The arrows in Fig. b indicate: 1 — absorption of excitons in the free state; 2 — recombination of thermalized autolocalized excitons; 3 — direct excitation of autolocalized excitons; 4 — “hot” luminescence due to autolocalized excitons [90].

configuration of plots for  $\text{PbWO}_4$  is given according to data of [90] for the  $\text{WO}_4^{2-}$  complex and the autolocalized exciton. Results of this work indicate also that excitation transfer between different centers plays an important role.

## REFERENCES

1. *Viktorov L.V., Skorikov V.M., Zhukov V.M., Shul'gin B.V.* Inorganic scintillation materials // *Izv. AN SSSR, ser. "Inorganic materials"*. – 1991. – **27**, No.10. – p.2005–2020.
2. *Shul'gin B.V., Viktorov L.V., Volkov A.R. e.a.* Scintillation properties of some oxide and fluoride systems. Sverdlovsk: Ed. Ural Polytechnical Institute, 1990. – Dep. VINITI, 1990, No.3570, 13p.
3. *Shul'gin B.V., Kruzhalov A.V., Ogorodnikov I.M. e.a.* Scintillation properties of single crystals BeO // *Zhurn. prikladnoi spektroskopii*. – 1988. – **49**, No.2., p.286–291.
4. *Batsch T., Bengtson B., Moszinsky M.* Timing properties of ZnO–Ca scintillator // *Phys.Rev.*. – 1975. – **125**, No.3, P.443–446.
5. *Viktorov L.V., Ershov V.A., Kruzhalov A.V., Shul'gin B.V.* Scintillation effects in oxide crystallophosphors // In: *Khimiya tverdogo tela*. Sverdlovsk: Ed. Ural Polytechnical Institute, 1982, p.87–95.
6. *Shul'gin B.V., Gavrilov F.F., Parshin V.K., Chukhlantsev V.G.* Radioluminescence of zirconosilicates // *Izv. vuzov. Ser. Physics*. – 1967. – No.7. – p.122–124.
7. *Keda O.A., Vasilenko M.V., Viktorov L.V. e.a.* Dosimetric and scintillation properties of crystals with garnet structure // *Zhurn.prikladnoi spektroskopii*. – 1984. – **41** – p.867–869.
8. *Ogorodnikov I.N., Kruzhalov A.V., Ivanov V.Yu.* Mechanism of fast UV-scintillations in oxide crystals with self-trapped excitons // In: *Inorganic scintillators and their applications. "Scint-95"*, 1995, Delft, The Netherland: Delft University Press. – P.216– 19.
9. *Murk V.* Self-shrunked excitons in complex oxides. // In: *Inorganic scintillators and their applications. "Scint-95"*, 1995, Delft, The Netherland: Delft University Press. – P.223–226.
10. *Murk V., Svinarenko O.* Relaxation processes in  $Y_2O_3$  and  $Sc_2O_3$  // In: *Inorganic scintillators and their applications. "Scint-95"*, 1995, Delft, The Netherland: Delft University Press. – P.227–229.
11. *Ogorodnikov I.N., Ivanov V.Yu., Kruzhalov A.V.* Point defects and radiative decay of low-energy electron excitations in BeO // *Fiz.tverdogo tela*. – 1994. – **36**, No.11. – p.3287–3298.
12. *Akimov Yu.A.* Detectors of nuclear radiations on the basis of inorganic scintillators // *Fizika elementarnykh chastits i atomnogo yadra*. – 1994. – **25**, No.1. – p.229–283.
13. *Menzer G.* Die kristallstruktur von Eulytin // *Z.Kristallog.* – 1931. – **Bd.78**, N 11–25. – P.136–63.

14. *Belov N.V.* Essays on structural mineralogy // Mineral.sb.Lvovsk.geol. obshch. – 1950. – No 4. – p.21–34.
15. *Belov N.V.* Essays on structural mineralogy // Moscow: Nedra.– 1976.– 344 p.
16. *Segal D.T., Santoro R.P., Newnham R.E.* Neutrodiffraction study of  $\text{Bi}_4\text{Si}_3\text{O}_{12}$  // Z. Kristallogr. – 1966. – **Bd.123**, N 1. – P.73–76.
17. *Fisher P., Walder F.* Comparison of neutron diffraction and EPR results on the cubic crystal structures of piezoelectric  $\text{Bi}_4\text{X}_3\text{O}_{12}$  (X = Ge, Si) // Solid State Commun. – 1982 – **44**, No.5. – P.657–661.
18. *Nitsche R.* Crystal growth and electro-optic effect of vismuth germanate  $\text{Bi}_4(\text{GeO}_4)_3$  // J.Appl.Phys. – 1965 – **35**, No.8. – P.2358–2360.
19. *Liebertz Y.* Einkristallzuchtung von wismutgermanat  $\text{Bi}_4(\text{GeO}_4)_3$  // J.Cryst.Growth. – 1969. – **5**. – P.150.
20. *Durif A., Averbuch-Pouchot M.T.* Affinement de la structure cristalline du germanate de vismuth  $\text{Bi}_4(\text{GeO}_4)_3$  // C.R.Seances Acad.Sci.Ser. – 1982. – **295**, No.5. – P.555–556.
21. *Shul'gin B.V., Polupanova T.I., Kruzhalov A.V., Skorikov V.M.* Bismuth orthogermanate // Ekaterinburg: Vneshtorgizdat. – 1992. – 170 p.
22. *Pustovarov V.A., Kruzhalov A.V., Kalinkin N.M. et al.* The electronic structure of vismuth germanate // Nucl.Inst. and Meth.Phys.Rev. – 1989. – **A263**. – P.595–596.
23. *Burachas S.F.* Studies and automatization of the growth process of lithium niobate crystals. Ph.D. (Cand. tech. sci.) dissertation. Institute for Single Crystals, 1981.
24. *Timan B.L., Burachas S.F.* Analysis of crystal growth conditions by the Czochralski method // In: Fizika i khimiya kristallov. – Kharkov: VNIIM.– 1977. – p.1–4.
25. *Timan B.L., Burachas S.F.* Effects of crystal growth conditions from the melt upon its radius // Kristallografiya. – 1978. – **23**, No.6 – p.1262 – 1263.
26. *Burachas S.F., Kolotiy O.D., Timan B.L.* Thermal conditions of the growth process of oxide crystals of constant radius by the Czochralsky method // Functional Materials. – 1996. – **3**, No.1. – p.29–36.
27. *Timan B.L., Burachas S.F.* Growth of crystals of constant diameter by a method of melt level control // Kristallografiya, 1981, **26**, p.892–896.
28. *Burachas S.F., Gerasimckuk L.I., Kukhtina N.N. et al.* Physico-chemical principles of germanoeulitine single crystals synthesis and groth // Functional Materials – 1996. – **3**, No.3. – p.373–388.

29. *Pustovarov V.A., Kruzhalov A.V., Skorikov V.M. e.a.* Effects of crystal structure defects on luminescent properties of crystals  $\text{Bi}_4\text{Ge}_3\text{O}_{12}$  // *Zhurn. prikladnoi spektroskopii.* – 1987. – **48**, No.6. – p.1009–1012.
30. *Suleimanova G.S., Skorikov V.M.* Phase transformations in system  $\text{Bi}-\text{Bi}_2\text{O}_3-\text{GeO}_2$  // *Izv.AN SSSR, ser. Inorganic Materials.*– 1990. – **26**, No.9. – p.1986–1987.
31. *Kargin Yu.F., Kargin V.F., Skorikov M.V. e.a.* Synthesis and studies of scintillation properties of bismuth germanate single crystals // *Izv.AN SSSR, ser. Inorganic Materials.* – 1984. – **20**, No.5. – p.815–817.
32. *Tananaev I.V., Skorikov V.M., Kutvitski V.K. e.a.* Solubility of Pt in melts of systems  $\text{Bi}_2\text{O}_3-\text{X}_2\text{O}_y$ , or  $\text{X} = \text{Si, Ti, Ge, Zn, Cd}$  // *Izv.AN SSSR, ser. Inorganic Materials.* – 1981. – **17**, No.4. – p.663–668.
33. *Kargin Yu.F., Endrzhevskaya V.Yu., Skorikov V.M.* Interaction of bismuth and germanium (silicon) oxide in the solid phase // *Izv.AN SSSR, ser. Inorganic Materials.* – 1991. – **27**, No.3. – p.530–533.
34. *Suleimanova G.S., Skorikov V.M.* Thermodynamic properties of compounds in system  $\text{Bi}-\text{Bi}_2\text{O}_3-\text{GeO}_2$  // *Izv.AN SSSR, ser. Inorganic Materials.* – 1991. – **27**, No.3. – p.634 – 636.
35. *Burachas S.F., Timan B.L., Bondarenko S.K. e.a.* Conditions of growth of bismuth germanate  $\text{Bi}_4\text{Ge}_3\text{O}_{12}$  crystals by the Czochralsky method // *Kristallografiya.* – 1994. – **39**, No.3. – p.544 – 546.
36. *Burachas S.F., Starzhinskiy N.G., Bondar' V.G. e.a.* Effects of dopants upon scintillation parameters and perfectness of germanoeulytine crystals // *Inorganic Materials.* – 1991. – **27**, No. 9. – p.1895–1898.
37. *Burachas S.F., Timan B.L., Kolotiy O.D. e.a.* Effect of the crucible radius upon quality of bismuth germanate crystals grown by the Czochralsky method // *Kristallografiya.* – 1996. – **41**, No.3. – p.574–576.
38. *Burachas S.F., Timan B.L., Bondar' V.G. e.a.* Influence of the character of heat removal from the crystal upon shape of its side surface in bismuth germanate growth by the Czochralsky method // *Kristallografiya.* – 1990. – **35**, No.1. – p.181–184.
39. *Tokagi K., Fukuzawa T.* Improvement in the scintillation conversion efficiency of  $\text{Bi}_4\text{Ge}_3\text{O}_{12}$  single crystals // *J.Crysth.Growth.* – 1981. – **52**, No.4. – P.584–587.
40. *Tananaev N.V., Skorikov V.M., Kargin Yu.F. e.a.* Studies of formation of metastable phases in the system  $\text{Bi}_2\text{O}_3-\text{SiO}_2(\text{GeO}_2)$  // *Izv.AN SSSR, ser. Inorganic Materials.* – 1978. – **14**, No.11. – p.2024–2028.
41. *Burachas S.F., Bondar' V.G., Martynov V.P. e.a.* Method for growth of bismuth orthosilicate single crystals // *Patent of Ukraine No. 94076246, C30B33/00, 15.07.94.*

42. Tkachenko V.F., Rom M.A., Borodenko Yu.A., Burachas S.F. Structural perfection of large-sized single crystals of bismuth germanate // Abstr. 8<sup>th</sup> FSU Conference on crystal growth. – Kharkov, 1992. – v.3, part 2. – p.374–375.
43. Pirogov E.N., Burachas S.F., Ryzhikov V.D. e.a. Method of thermal treatment of scintillation single crystals // Patent of Russia No.1609211, Bulletin No.15, 23.04.1993
44. Kukhtina N.N., Pirogov E.N., Ryzhikov V.D. Method of thermal treatment of bismuth germanate single crystals // Patent of Russia No.1784669, Bulletin No.48, 30.12.1992.
45. Kovalenko A.V., Bochkova T.M. Detectors of ionizing radiation upon the structure scintillator (substrate) – planar photoreceiver  $\text{ZnSe}_{1-x}\text{Te}_x$ – $\text{ZnSe}$  // Fizika i tekhnika poluprovodnikov. – 1993. – **27**, No.8. – p.1335–1339.
46. Ivanov V.Y., Kruzhalov A.V., Pustovarov V.A., Petrov V.L. Electron excitation and luminescence in  $\text{Bi}_4\text{Ge}_3\text{O}_{12}$  and  $\text{Bi}_4\text{Si}_3\text{O}_{12}$  crystals // Nucl. Instrum. and Meth.Phys.Res.. – 1987. – **A261**. – P.150–152.
47. Lushchik N.E., Lushchik Ch.B. Models of luminescence centers in alkali halide crystals // Proc. Institute of Physics and Astronomy of AS of Estonia. – 1957. – No.6. – P.5–62.
48. Moncorge R., Jacquier B., Boulon G. Temperature dependent luminescence of  $\text{Bi}_4\text{Ge}_3\text{O}_{12}$ : Discussion on possible models // J.Lum. – 1976. – **14**. – P.337 – 348.
49. Aluker E.D., Lutsis D.Yu., Chernov S.A. Electronic excitations and radio-luminescence of alkali halide crystals. – Riga: Zinatne. – 1979. – 252 p.
50. Horovitz A., Kramer G. The nature of imperfections in Bismuth germanate (BGO) crystals // J.Cryst.Growth. – 1986. – **78**, No.1. – P.121–128.
51. Laviron C., Lecog P. Radiation damage of bismuth germanate crystals // Nucl.Instrum.and Meth.Phys.Res. – 1984. – **227**, No.1. – P.45–53.
52. Kobayashi M., Kondo K. et al. Radiation damage of BGO crystals due to low energy g-rays, high energy photons and fast neutrons // Nucl.Instrum.and Meth.Phys.Res. – 1983. – **206**, No.1–2. – P.107–117.
53. Burachas S.F., Bondar' V.G., Dol'chin T.N. e.a. Bismuth orthosilicate – a prospective material for high energy physics // Abstr. Conf. “Physics of Ukraine”. – Kiev. – 1993. – p.18.
54. Abrashov A.A., Alekseeva E.L., Burachas S.F. e.a. Position-sensitive detector of gamma-quanta for a position emission tomograph // Priboiry i tekhnika eksperimenta. – 1990. – No.5. – p.78–83.
55. Ivashkin A.P., Kudenko Yu.G., Lobashev V.M. e.a. Scintillation crystals BGO for detectors of  $^0$ ,  $\eta$ -mesons and  $\gamma$ -quanta // Preprint 709 Inst.Nucl. Stud. AS USSR. – 1991. – 10 p.

56. Abramov A.A., Alekseeva E.A., Burachas S.F. et al. Position-sensitive detector for  $\gamma$ -quanta for PET // Nucl.Instrum.and Meth.Phys.Res. – 1991. – **A302**. – P.529–534.
57. Morel C., Tavernier S., Ziegler S. Development of a high performance European positron tomograph. // Book of Abstracts (SCINT-97) inorganic scintillators and their applications. – Shanghai: Shanghai Institute of Ceramics. – 1997. – P.11.
58. Kulesskiy A.R., Korovkin A.M., Kruzhanov A.V. e.a. Radioluminescent and scintillation properties of single crystals of yttrium and rare-earth element silicates // Zhurn.prikladnoi spektroskopii. – 1988. – **48**, No.4. – p.650–653.
59. Toropov N.A., Bondar' I.A., Lazarev A.N., Smolin Yu.I. Silicates of rare-earth elements and their analogs. Leningrad: Nauka, 1971, 193 p.
60. Ananyeva G.V., Korovkin A.M., Merkulyaeva T.I. e.a. Growth of single crystals of lanthanide orthosilicates and their structural and optical characteristics // Izv.AS USSR, ser. Inorganic Materials. – 1981. – **17**, No.6. – p.1037–1042.
61. Melcher C.L., Schweitzer J.S. Peterson C.A. et al. Crystal growth and scintillation properties of the rare earth oxyorthosilicates // In: Inorganic scintillators and their applications (“SCINT-95”). – 1996. – Delft, The Netherlands: Delft University press. – P.309–316.
62. Toropov N.A., Barzakovskii V.P., Lapin V.P., Kurtseva N.N. Diagrams of state for silicate systems: a handbook. – Leningrad: Nauka. – 1965. – 86 p.
63. Smolin Yu.I., Tkachev S.P. Determination of gadolinium orthosilicate  $\text{Gd}_2\text{O} \cdot \text{SiO}_2$  // Kristallografiya. – 1969. – **14**, No.1. – p.22–24.
64. Moses W., Derenzo S., Budinger T. PET detector modules based on novel detector technologies // Nucl.Instrum.and Meth.Phys.Res. – 1994. – **A353**. – P.189–194.
65. Morozov A.M., Petrov M.V., Stratsev V.R. e.a. Luminescence and induced radiation of holmium in single crystals of yttrium and erbium orthosilicates // Optika i spektroskopiya. – 1976. – **41**, No.6 – p.1086.
66. Ananyeva G.V., Korovkin A.M., Merkumaeva T.I. e.a. Growth, structural and crystal-optic characteristics of single crystals of rare-earth element oxyorthosilicates // Abstr. 5<sup>th</sup> All-Union Conference on crystal growth. – Tbilisi. – 1977. – **v.2**. – p.131.
67. Kazumasu Takagi, Tokuumi Fukazawa Cerium activated  $\text{Gd}_2\text{SiO}_5$  single crystal scintillators // Phys.Appl.Lett.. – 1983. – **42**, No.1. – P.43–45.
68. Patent No.2620236, France. – 1988.



69. *Burachas S.F., Bondar' V.G., Katrunov K.A. e.a.* Some peculiar features of preparation of gadolinium silicate and cadmium tungstate scintillation crystals // *Inorg. Mater.* – 1996. – **32**, No.12, p.1525–1527.
70. *Burachas S.F., Kukhtina N.N., Martynov V.P. e.a.* X-ray luminescence of materials on the basis of gadolinium and europium silicates // *Inorg. Materials.* – 1993. – **29**, No.8. – p.1133–1135.
71. *Shul'gin B.V., Kulesskii A.R., Korovkin A.M. e.a.* Spectra and kinetics of pulse cathodoluminescence of  $\text{Y}_2\text{SiO}_5\text{--Te}$ ,  $\text{Ce}$  // *Optika i spektroskopiya.* – 1990. – **68**, No.4. – p.841–843.
72. *Burachas S.F., Martynov V.P., Ryzhikov V.D.* Photoluminescence of gadolinium silicate doped with cerium // *Abstr. Inter-State Conf. "Scintillators-93"*. – Kharkov: Inst. Single Cryst. – part 2. – p.171.
73. Каталог фирмы Harshow "Scintillation Detectors" Saint-Gobain.
74. *Burachas S.F., Bondar' V.G., Katrunov K.A. e.a.* Some peculiar features of preparation of gadolinium silicate and cadmium tungstate scintillation crystals // *Inorg. Mater.* – 1996. – **32**, No.12, p.1525–1527.
75. *Blasse B.* Quenching mechanism of  $\text{Ce}^{3+}$  luminescence // In: *Inorganic scintillators and their applications "SCINT-95"*. – 1996. – Delft, The Netherlands: Delft University press. – P.114–117.
76. *Moszynski M, Ludziejewski T., Wolski D. et al.* Timing properties of GSO and LSO scintillators // *Ibid.* – P.372–375.
77. *Rossner W., Breu R.* Luminescence properties of cerium-doped gadolinium oxyorthosilicate ceramic scintillators // *Ibid.* – P.376–379.
78. *Ishibashi H., Shimizu K., Susa K., Kubota S.* Cerium-doped GSO scintillators and Its application in position sensitive detector // *IEEE Trans.Nucl.Sci.* – 1989. – **36**, No.1. – P.170–172.
79. *Jekita M., Iyazawa Y., Akarane T. et al.,* Optical studies of Ce-doped  $\text{Gd}_2\text{SiO}_5$  single crystals // *J.Appl.Phys.* – 1989. – **66**, No.1. – P.373–378.
80. *Akimov Yu.K.* Detectors of nuclear radiations on the basis of inorganic scintillators // *Fiz. Elementarn. Chastits i Atomn. Yadra.* – 1994. – **25**, No.1. – p.229–283.
81. *Kukhtina N.N., Burachas S.F., Martynov V.P. e.a.* Scintillation properties of gadolinium silicate doped with europium // *Abstr. Inter-State Conf. "Scintillators-93"*. – Kharkov, Inst.Single Cryst.– part 2. – 1993. – p.100–101.
82. *Burachas S.F., Kukhtina N.N., Martynov V.P. e.a.* X-ray luminescence of materials based on gadolinium and europium silicates // *Inorg. Materials.* – 1993. – **29**, No.8. – p.1133–1135.

83. *Tanaka M., Mara K., Kim S. et al.* Stability of Ce-doped  $\text{Gd}_2\text{SiO}_5$  (GSO) scintillator under irradiation // Book at Abstracts.International Conference on Inorganic Scintillators and their applications (SINT-97). – 1997. – Shanghai: Shanghai Institute of Ceramics. – P.61.
84. *Melcher C.L., Schweitzer J.S.* A promising new scintillator: cerium-doped lutetium oxyorthosilicate // Nucl.Instr. and Meth. in Phys.Res. – 1992.– **A314**.– p.212–214.
85. *Kuntner C., Aiginger H., Auffray E., et al.* Scintillation properties and mechanism in  $\text{LuAlO}_3\text{:Ce}$  // Nucl.Instrum.and Meth.A. – 2002. – **486**, P.176–180.
86. *Globus M., Grinyov B.* Inorganic scintillators. Kharkov, 2000, Acta. – P.402.
87. *Derenzo S., Weber M., Klintonberg M.* The quest for the ideal inorganic Scintillator // Nucl.Instrum.and Meth.A. – 2003. – **505**, P. 111–117.
88. *Shah K., Clodo J., Klugerman M., et al.*  $\text{LaCl}_3\text{:Ce}$  Scintillator for  $\gamma$ -ray detection // Nucl.Instrum.and Meth.A. – 2003. – **505**, P. 76–81.
89. *Ovechkin A.E., Ryzhikov V.D., Tamulaitis G., Zukauskas A.* Luminescence of  $\text{ZnWO}_4$  and  $\text{CdWO}_4$  crystals // Phys.Stat.Sol.(a). – 1987. – **103**. – P.285–290.
90. *Tamulaitis G., Burachas S., Martinov V. et al.* Photoluminescence of  $\text{PbWO}_4$  single crystals // Phys.Stat.Sol.(a). – 1996. – **157**. – P.187–198.
91. *Nagornaya L., Ryzhikov V.* Fast scintillators based on large heavy tungstate single crystals // Proceedings of the “Crystal 2000” International Workshop, Chamonix, France. – 1992. – P.367–374.
92. *Lecoq P., Dafinei I., Auffray E. et al.* Lead tungstate ( $\text{PbWO}_4$ ) scintillators for LHC EM-calorimetry // NIM. – 1995. – **A365**. – P.291.
93. *Kobayashi M., Ishii M., Usuki Y et al.*  $\text{PbWO}_4$  scintillator at room temperature // Proceedings of the “Crystal 2000” International Workshop, Chamonix, France. – 1992. – P.375–379.
94. *Nagornaya L.L., Ryzhikov V.D., Tupitsina I.A. et al.* Development of lardge heavy fast  $\text{PbWO}_4$  scintillator // IEEE Trans.Nucl.Sci.. – 1995. – **42**. – P.337–340.
95. *Nagornaya L., Apanasenko A., Tupotsina I.* Spectralkinetic and thermostimulated studies of  $\text{MeWO}_4$  single crystals // In: Inorganic.scintillators and their applications “SCINT –95”. – 1996. – Delft, The Netherland: Delft University press. – P.299–302.
96. *Borodenko Yu., Burachas S. et al.* Lead tungstate crystals for calorimetry at LHC // Там же. – P.260–262.

97. *Nagornaya L., Apanasenko A., Ryzhikov V.* Luminescence and radiation damage of the single crystals  $\text{PbWO}_4$  // Nuclear Science Symposium IEEE. – 1996. – Anaheim, California. – **2**. – P.890–893.
98. *Kachanov V., Baryshevsky V., Nagornaya L.* Single crystals of tungston compounds promising materials for the tatlle absorption detector of the EM-calorimeters // NIM. – 1992. – **A322**. – P.231–234.
99. *Limarenko L.N., Nosenko A.E., Pashkovskii M.V. e.a.* Influence of structural defects upon physical properties of tungstates. – Lvov: Vyshcha shkola, 1978.– 160 p.
100. *Morell D.I., Cantrell I.S., Chang L.I.* Phase relation and crystal structures of Zn and Cd tungstates // J.Amer.Ceram.Soc.. – 1980. – **63**, No.5–6. – P.261–264.
101. *Burochas S., Ryzhikov V., Manko V., et al.* Photochromic Effect and its influence upon scintillation CWO, PWO crystals // Nucl.Instrum.and Meth.A. – 1998. – **372**, P. 251–259
102. *Tsirlin Yu.A., Globus M.E., Sysoeva E.P.* Optimization of detection of gamma-radiation by scintillation crystals. – Moscow: Energoatomizdat, 1991. – 152 p.
103. *Ovechkin A.E.* Influence of non-stoichiometry defects upon spectral-kinetic properties of tungstates. Ph.D. (Cand. Phys.-math. Sci.) Dissertation – Kharkov: Inst. Single Cryst. – 1988.
104. *Burachas S.F., Bondar' V.G., Katrunov K.A. e.a.* Some preparation features of gadolinium silicate and cadmium tungstate // Inorg. Materials. – 1996. – **32**, No.1. – p.1525–1527.
105. *Burachas S.F., Timan B.L., Bondar' V.G. e.a.* Peculiar features of growth of crystals of complex oxide compounds // Abstr. 7<sup>th</sup> All-Union Conf. on crystal growth. – Moscow: Nauka. – 1988. – p.234–235.
106. *Toporov N.F., Barzakovskii V.P., Lapin V.V.* Diagrams of state for silicate systems: a handbook. Moscow-Leningrad: Nauka. – 1965.
107. *Borodenko Yu., Burachas S., Katrunov K. et al.* Lead tungstate crystals for calorimetry at LHC // In: Inorganic.scintillators and their applications “SCINT –95”. – 1996. – Delft, The Netherlands: Delft University press. – P.260–262.
108. *Kroger F.A.* Some aspects of the luminescence of solids. – Elsevier Publ. Co, Amsterdam, 1948.
109. *Georgadze A.Sh., Danilevich F.A., Zdesenko Yu.T. e.a.* Scintillators  $\text{CdWO}_4$  of large volume // Priboiy i tekhnika eksperimenta. – 1996. – No.3. – p.48–52.

110. *Pashkovskii M.V., Ovechkin A.E., Nagornaya L.L. e.a.* Effects of  $\gamma$ -radiation upon scintillation characteristics of single crystals  $\text{CdWO}_4$  // *Zhurnal prikladnoi spektroskopii* – 1987. – **47**, No.1. – p.81–84.
111. *Ovechkin A.E., Nagornaya L.L., Maistrenko V.I.* Luminescence studies of crystals  $\text{CdWO}_4$  and  $\text{ZnWO}_4$  // *Abstr. 30<sup>th</sup> Conference on luminescence.* – Rovno, 1984. – p.134.
112. *Ovechkin A.E., Poltoratskii Yu.B., Nagornaya L.L. e.a.* Formation of defects and color centers in crystals  $\text{CdWO}_4$  and  $\text{ZnWO}_4$  // *In: Scintillation materials.* – Kharkov: VNIIM, 1987. – No.20. – p.4–8.
113. *Krylov A.O., Konopleva O.V.* High-temperature electric transfer in  $\text{CdWO}_4$  // *Izv.AN SSSR, ser. Inorganic Materials.* – 1986. – **22**, No.7, p.193–198.
114. *Spitkovskii I.M., Pashkovskii M.V.* Some peculiar features of defects in single crystals  $\text{ZnWO}_4$  and  $\text{CdWO}_4$  // *Kristallografiya.* – 1971. – **16**, No.4. – p.837–840.
115. *Nagornaya L.L., Ovechkin A.E., Vostretsov Yu.Ya. e.a.* Spectrometric characteristics of defects in single crystals of cadmium tungstate // *In: Problemy polucheniya i issledovaniya monokristallov.* – Kharkov: VNIIM, 1988. – No.21. – p.54–59.
116. *Nagornaya L.L., Vostretsov Yu.A., Globus M.E. e.a.* Large-sized optically uniform single crystals  $\text{CdWO}_4$  // *Abstr. 8<sup>th</sup> FSU Conference on crystal growth, v.3, part 2.* – Kharkov: Inst.Single Cryst., 1992. – p.362–363.
117. *Valbis Ya.A., Rachko Z.A., Yansons Yu.A.* Vacuum ultraviolet cathodoluminescence of crystals  $\text{KF}$ ,  $\text{KMgF}_3$  and  $\text{KCaF}_3$  (cross-luminescence) // *Optika i spektroskopiya.* – 1988. – **64**, No.5. – p.1196–1198.
118. *Zhu Y.C., Lu J.G., Shao Y.Y. et al.* Measurements of the scintillation properties of  $\text{WNO}_4$  crystals // *Nucl.Instrum.and Meth.Phys.Res.* – 1986. – **A244**, No.3. – P.579–581.
119. *Dafinei J.* Lead tungstate for high energy calorimetry // *14<sup>th</sup> crystal Clear Collaborations Meeting, CERN, March 1994.* – CERN – Geneva.
120. *Korzhik M.N.* Recent results on  $\text{PbWO}_4$  // *Там же.*
121. *Britwisch G., Burachas S., Vostretsov Yu. et al.* Scintillation and kinetic parameters of  $\text{PbWO}_4$  scintillators // *Nuclear science Symposium IEEE 1996.* – Anaheim, California. – v.2. – P.763–767.
122. *Korzhik M.N.*  $\text{PbWO}_4$  scintillator. Carrent status of RSD // *In: Inorganic scintillators and their applications (“SCINT-95”).* – 1996. – Delft, The Netherland: Delft University press. – P.241–248.
123. *Dafinei J et al.* Load tungstate for high energy calorimetry // *MRS Spring Meeting’94.* – San-Francisco, April, 1994.

124. *Lammers M.J., Blasse G., Robertson D.S.* The luminescence of cadmium tungstate // *Phys.Stat.Solidi (A)*. – 1981. – **63**, No.2. – P.569–572.
125. *Blasse G., Rokkers G.* Low temperature decay time measurement on the luminescence of  $\text{CaWO}_4$  // *J.Solid State Chem.*. – 1983. – **49**, No.1. – P.126–128.
126. *Reut E.G.* Optical and electric properties of crystals with scheelite structure // *Izv. AN SSSR, ser. Phys.* – 1985. – **49**, No.10. – p.2032–2038.
127. *Reut E.G.* Manifestation of a stochastic Ian-Teller effect in intrinsic luminescence of crystals with scheelite structure // *Izv. AN SSSR, ser. Phys.* – 1979. – **43**, No.10. – p.1186–1193.
128. *Hofstaetter A., Oeder R., Scharmann A., Schwaba D.* Polarization of thermoluminescence of various scheelits // *J.Luminescence*. – 1981. – **22**, No.4. – P.419–428.
129. *Batenchuk M.M.* The red emission component in  $\text{CdWO}_4$  and  $\text{ZnWO}_4$  // *Fizicheskaya elektronika*. – 1985. – **30**. – p.111–113.
130. *Kochler H.A., Kikuchi C.* Identification of three trapping centers in Calcium Tungstate // *Phys.Stat.Solidi (b)*. – 1971. – **43**. – P.423–432.
131. *Kononov O.V.* The nature and structural types of scheelite stationary luminescence centers // *Zhurn.prikladnoi spektroskopii*. – 1974. – **21**, No.4, p.644–648.
132. *Gurvich A.N., Gutan V.B., Mikhalev A.A.* The nature of luminescence, capture, quenching centers of calcium-tungstate luminophore // In: *Luminescentnye materialy i osobo chistye veshchestva*. – Stavropol': VNILuminoforov, 1975. – No.12. – p.30–40.
133. *Batenchuk M.M., Moroz Z.T., Nagornaya L.L. e.a.* Spectral-kinetic characteristics of luminescence and a possible model for emission centers in  $\text{CdWO}_4$  and  $\text{ZnWO}_4$  // *Abstr. 30<sup>th</sup> Conference on luminescence*. – Rovno, 1984. – p.133.
134. *Batenchuk M.M.* Effects of luminescence defects and scintillation properties of tungstates. – Ph.D. (Cand,phys.-math.sci.) dissertation. – Lvov, 1985.
135. *Pashkovskii M.V., Ovechkin A.E., Nagornaya L.L.* Luminescence centers of cadmium tungstate // *Fiz.elektronika*. – 1986. – **32**. – C.18–22.
136. *Ovechkin A.E., Viktorov L.V., Nagornaya L.L.* Pulse luminescence of crystals  $\text{CdWO}_4$  and  $\text{ZnWO}_4$  // *Zhurn.prikladnoi spektroskopii*. – 1988. – **48**, No.3. – p.336–340.
137. *Rebane K.K., Saari P.M.* Hot luminescence and relaxation processes // *Izv. AN SSSR, ser. Phys.* – 1976. – **40**, No.9. – p.1778–1785.
138. *Viktorov L.V., Veselova N.A., Ershov V.A., Shul'gin B.V.* Radioluminescence kinetics of calcium tungstate // *Zhurn.prikladnoi spektroskopii*. – 1982. – **37**, No.3. – p.391–396.

139. *Krongauz V.G.* X-ray luminescence and mechanisms of energy migration in oxygen-containing luminophores // In: *Luminescentnye materialy i osobo chistye veshchestva*. – Stavropol': VNIILuminoforov, 1975. – No.12. – p.12–20.
140. *Kuusman I.L., Lushchik Ch.B.* Intrinsic luminescence of ionic crystals // *Izv. AN SSSR, ser. Phys.* – 1976. – **40**, No.2. – p.1785–1782.
141. *Lecoq P., Dafinei I., Auffray et al.* Lead tungstate ( $\text{PbWO}_4$ ) scintillators for LHC EM-calorimetry // CERN – PPE. – 1994. – P.225.
142. *Korzhik M.V., Pavenko V.B., Timoschenko T.N. et al.* Spectroscopy and origin of radiating centers in  $\text{PbWO}_4$  single crystals // LAPP–EXP. – 1994.
143. *Tamulaitis G., Burachas S., Martinov V.P. et al.* Luminescence kinetics of  $\text{PbWO}_4$  scintillator crystals // *Phys.Stat.Solidi (a)*. – 1997. – **161**. – P.538–541.
144. *Burachas S., Martinov V., Ryzhikov V. et al.* Peculiarities of growth  $\text{PbWO}_4$  scintillator crystals for application in energy physics // *Cryst. growth*. – 1998. – **186**, No.1–2. – P.175–180.
145. *Burachas S., Danevich F., Georgadze A. et al.* Large volume  $\text{CdWO}_4$  crystal scintillators // *Nucl.Inst. and Meth.Phys.Res.(A)*. – 1996. – **369**. – P.164–168.
146. *Kobayashi M., Usuki Y., Izhii M. et al.* Improvement in scintillation characteristics of  $\text{PbWO}_4$  scintillating crystals by La-doping // *Book of Abstracts (SCINT-97) inorganic scintillators and their applications*. – Shanghai: Shanghai Institute of Ceramics. – 1997. – P.6.
147. *Fei Yiting, Fan Shiji, San Renuing* Phase relation and crystallization behaviour of  $\text{Bi}_2\text{O}_3$  –  $\text{SiO}_2$  systems // *Book of Abstracts (SCINT-97) inorganic scintillators and their applications*. – Shanghai: Shanghai Institute of Ceramics. – 1997. – P.145.
148. *Ijhii M., Mirose Y., Harada K. et al.* Growth and characterization of large BSO ( $\text{Bi}_4\text{Si}_3\text{O}_{12}$ ) crystals for radiation detectors // *Book of Abstracts (SCINT-97) inorganic scintillators and their applications*. – Shanghai: Shanghai Institute of Ceramics. – 1997. – P.66.
149. *Pustovarov V.A., Ivanov V.Yu., Kruzhalov A.V., Zinin E.I.* Kinetics of autolocalized exciton luminescence quenching in BeO crystals // *Fizika tverdogo tela*. – 1994. – **36**, No.5. – p.1523–1526.
150. *Nagornaya L.L.* Scintillators based on compound oxides for detection of ionic radiation // *Nucl.Tracks.Radiat.Meas.* – 1993. – **21**, No.1. – P.15–18.
151. Institute for Single Crystals Catalogue “Scintillation.Materials. Detector Reseach. Development, Production”. – 1994.
152. Data sheets “Quartz et silice”. – France. – 1990.
153. *Panova A.M.* Inorganic scintillators // *Izv. AN SSSR, ser. Phys.* – 1985. – **49**, No.10. – p.1194–1198.

## CHAPTER 3

### SCINTILLATORS ON THE BASIS OF SEMICONDUCTOR COMPOUNDS

Development of semiconductor scintillators (SCS) on the basis of  $A^{II}B^{VI}$  compounds has bridged the gap in a series of “scintillator-photodiode” detectors used in modern multi-channel low-energy devices for visualization of hidden images (tomographs, introsopes). In accordance with the requirements of eventual applications, such SCS materials as  $ZnSe(Te)$ ,  $CdS(Te)$  show the best matching of intrinsic radiation spectra to photosensitivity spectra of silicon photodiodes (PD) among the materials of similar kind. They are characterized by high radiation and thermal stability of their output parameters, as well as by high conversion efficiency. In this chapter, a thermodynamic model is described for interaction of isovalent dopants (IVD) with intrinsic point defects of  $A^{II}B^{VI}$  semiconductor structures at different ratios of their charges, a decisive role of IVD is shown in formation of the luminescence centers, kinetics of solid-phase reactions and the role of a gas medium are considered under real preparation conditions of  $ZnSe(Te)$  and  $CdS(Te)$  scintillation crystals, and luminescence mechanisms in IVD-doped SCS are discussed.

#### ***3.1. Peculiar features of defect formation***

in semiconductor scintillators with isovalent dopants.

It has been generally accepted that parameters of  $A^{II}B^{VI}$  crystals are largely determined by the ensemble of intrinsic point defects (IPD) of the crystal lattice. Numerous fundamental studies related to this problem (among which classic works of Watkins, Taguchi and Ray, Fistul' and Bazhenov, etc. can be noted [1–3], as well as works of the authors of the present book [4–6]) have substantially contributed to our understanding of IPD effects upon principal characteristics of binary

semiconductor crystals. It has been shown that, alongside with traditional methods of introducing IPD into the crystal lattice by controlled stoichiometry violation and radiation damaging, a powerful way to form IVD is doping semiconductor compounds with isovalent admixtures.

IVD, which has the same formal valence as the substituted lattice atom, has different ionization energy, electric negativity, degree of ionic/covalent bond with atoms of the neighboring sublattice, values of ionic and covalent radius. Bond energies of charge carriers with IVD are by an order of magnitude lower than with a donor (D) or acceptor (A) dopant; at the same time, charge localization on IVD is much stronger. Combination of these features results in a possibility that introduction of IVD would give rise to singular local states with their energy levels playing the role of quenching centers (QC) inside the band gap (IVD of the 1<sup>st</sup> kind), or it would lead to changes in the zone spectrum of the valence and conductivity bands (IVD of the 2<sup>nd</sup> kind). The discriminating factor allowing formation of local levels inside the band gap is the difference between potential energies of the IVD atom and the substituted atom:

$$\Delta U = U_{\text{IVD}} - U_{\text{QC}} = \Delta E_g - \frac{\partial E_g}{\partial \ln V} \frac{\Delta V}{V}, \quad (3.1)$$

where  $\Delta E_g = E_g|_{x=0} - E_g|_{x=1}$  for compound  $A_{1-x}A'_xB(AB_{1-x}B'_x)$ ,  $\Delta V/V$  is the relative change of the elementary cell volume from  $x = 0$  to  $x = 1$ .

In the approximation of the atom pseudopotentials model, one should expect new local levels inside the band gap for crystals CdS(Te), CdSe(Te), ZnSe(Te), ZnTe(Cd) and some others according to the condition

$$(2\Delta U/E_V) \gg 1, \quad (3.2)$$

where  $E_V$  is the valence band width.

In general, the following factors should be accounted for in determination of the localized energy value due to IVD introduction: 1) contribution from ionic admixture potential due to different electric negativity of the IVD and the substituted atom; 2) electron polarization, which leads to shielding of the difference in atomic pseudopotentials; 3) local lattice distortions, as well as elastic and electron-phonon interactions; 4) spin-orbital interaction.

Accounting for all these factors requires using a multi-zone theory that has not yet been developed. Even calculations in the Koster-Slater



one-zone one-site model, accounting just for ionic admixture potential effects, meet with substantial difficulties because of multi-factor character of the interactions.

Calculations carried out by Thomas e.a. [7–9] for semiconductor compounds of  $A^{III}B^V$  group (GaAs, GaP) upon their P and N isovalent doping predicted formation of efficient radiative recombination centers, in a good agreement with experiment.

The same authors made attempts to extrapolate this calculation method to  $A^{II}B^VI$  compounds — ZnSe(Te) и CdS(Te). However, broad smeared emission bands in these crystals do not agree with the proposed mechanism of exciton emission. There are also other inconsistencies that appear in comparison of theory and experiment.

Alongside with isovalent doping, IPD in the crystal lattice can be due to radiation damage and stoichiometry violations occurring when the crystals are prepared in atmosphere containing some excess of one of the components. Experiments of Kulp and Detweiler on bombardment of cadmium sulfide and zinc selenide by fast electrons [10,11] are generally considered as classic examples of inducing radiation damage.

ESR and ODMR (optically detected magnetic resonance) experiments of Lee, Cavennett, Watkins e.a. [12–14] have shown that in zinc selenide under bombardment defects are formed only in the cation sublattice. Thus, the luminescence band L-730 could be related to the double-charged zinc vacancy  $V_{Zn}^{--}$ , and L-640 — to the  $[V_{Zn}D_i^+]$  complex. The donor nature could not be established by direct observations; the most known early interpretation was  $[V_{Zn}Cu_i^+]$  [15], though more recent studies proved its inconsistency [16–18].

Introduction of defects into crystals (e.g., cadmium sulfide) by means of annealing stimulates formation of  $V_{Cd}$  and  $S_i$  after annealing in sulfur,  $V_S$  and  $Cd_i$  after annealing in cadmium. Results of these experiments, which were first carried out by Vlasenko, Vitrikhovski e.a. [19] and later — by Susa, Watanabe and Wada [20], are in agreement with experiments on radiation damaging of these crystals.

Main parameters of the emission bands L-600, L-730 (first observed by Thomas and Cuthbert in CdS(Te) crystals) are in an obvious relationship with the emission due to intrinsic defects in undoped cadmium sulfide crystals. However, luminescence in CdS(Te) was generally

described as exciton emission due to isoelectron traps, similar to that observed in  $\text{GaN(P)}$ ,  $\text{GaAs(N)}$ . This interpretation had been generally accepted until the works of Ryzhikov e.a. [21–23].

We were the first to note a correlation between emission features of isovalently doped cadmium sulfide crystals and the effects of radiation damage and structure non-stoichiometry. We had predicted that in  $\text{CdS(Te)}$  crystals, prepared using an appropriate technology, an infrared emission band L-1020 should be observed. It has also been postulated that on the basis of  $\text{A}^{\text{II}}\text{B}^{\text{VI}}$  crystals one can obtain scintillators of high efficiency with predictable emission spectrum, provided conditions are met of substantial difference of ionic radius and electric negativity values of IVD and the substituted atom. Taking into account that parameters of emission centers in crystals with IVD are determined by the predominant type of crystal lattice IPD, in accordance with theoretical predictions a new scintillator  $\text{CdS(Hg)}$  was obtained with its luminescence spectrum similar to that of  $\text{CdS(Te)}$ , but with somewhat different kinetics [4,16–18, 21–23].

In  $\text{ZnSe(Te)}$  crystals, directly after growth (from raw material of stoichiometric composition) luminescence in IR-bands is observed, and after annealing in zinc — emission with maximum at 640 nm (L-640), or at even shorter wavelengths (depending on thermal treatment conditions [24]). A similar evolution is observed in crystals with radiation damage or in non-stoichiometric crystals [6]. The regularities in SCS luminescence spectra changes, as shown below for  $\text{ZnSe(Te)}$  taken as an example, are caused by re-structuring of the defect structure of crystals.

Introduction of tellurium IVD into zinc selenide, due to substantial differences in atomic and ionic radii of Se and Te, is accompanied by local deformation of the lattice

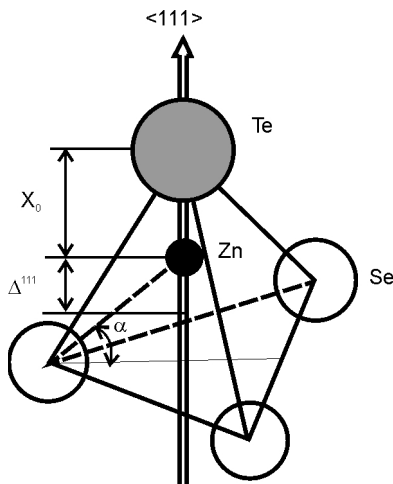


Fig.3.1. Displacement of Zn atom in  $\text{ZnSe}$  structure under isovalent doping.

and localization of the hole in a vicinity of the substituted atom due to interactions [1, 18, 25] described by Coulomb potential of the point charges [26] with effective charges of the corresponding bonds of MX ions  $e_{\text{ZnSe}}^*$  и  $e_{\text{ZnTe}}^*$ , as well as by deformation forces.

Interaction of the first type results in shifting the metal atom towards Te atom in the direction (111) by the distance  $\Delta$  (Fig.3.1).

From the equilibrium condition for Zn atom written down in the form

$$\frac{(e_{\text{ZnTe}}^*)^2}{\left(\frac{\sqrt{3}}{4} - \frac{\Delta}{a}\right)^2} = \frac{3(e_{\text{ZnSe}}^*)^2 \left(\frac{\sqrt{2}}{4} + \sqrt{6} \frac{\Delta}{a}\right)}{\frac{1}{6} \left[1 + \left(\frac{\sqrt{2}}{4} + \sqrt{6} \frac{\Delta}{a}\right)^2\right]^{3/2}}, \quad (3.3)$$

one can estimate the displacement of  $\Delta$  if  $e^*$  is known. The effective charge is defined in [28] by the expression

$$e^* = \frac{N\lambda^2 - (8 - N)}{1 + \lambda^2}, \quad (3.4)$$

where  $N$  is the valence,  $\lambda = 1 - \exp\{-0.25(x_x - x_m)\}$  is the degree of density. Using the electronegativity values  $x_{\text{Zn}} = 1,5$ ;  $x_{\text{Te}} = 2,1$ ;  $x_{\text{Se}} = 2,4$  [25], we obtain the ratio  $e_{\text{ZnTe}}^*/e_{\text{ZnSe}}^* = 0,973$ , which makes  $\Delta$  equal to  $0,24 \text{ \AA}$ . When two or three chalcogen atoms are substituted, causing the metal atom to be shifted in the direction (001) [27], similar considerations give, respectively,  $\Delta^{001} = 0.61 \text{ \AA}$  and  $\Delta^{111} = 0.12 \text{ \AA}$ .

If elastic interactions are accounted for, interaction of atoms is described by the Born-Maier repulsion potential [26]

$$U_r = A \exp\left(-\frac{\rho}{r}\right), \quad (3.5)$$

where  $A$  and  $\rho$  are interaction potential constants. When one selenium atom is substituted by tellurium, the equilibrium condition has the form

$$\frac{\partial U_{\text{ZnTe}}}{\partial r} - 3 \frac{\partial U_{\text{ZnSe}}}{\partial r} \sin \alpha = 0. \quad (3.6)$$

Solution of this equation, accounting for the interaction radius  $\rho$  expressed in terms of first ionization potentials of the lattice components [27, 29]:  $\rho^{-1} = 0,54(\sqrt{I_m} + \sqrt{I_x})$ , leads to the following expression:

$$U_{\text{ZnSe}}(r) = 1.34 \cdot 10^4 \exp(-0.298/r) \quad (3.7)$$

$$U_{\text{ZnTe}}(r) = 1.55 \cdot 10^4 \exp(-0.301/r) \quad (3.8)$$

Substituting these into (3.6), we obtain the value for non-equilibrium distance between Zn and Te equal to 1,46 Å, i.e.  $\Delta = 1,0$  Å.

As in the elastic model the shift of Zn atom towards Te (1 Å) is larger than in the Coulomb model (0,24 Å), for our estimates we can assume that  $\Delta$  is in the range  $0,24 \text{ Å} < \Delta < 1,0 \text{ Å}$ .

An important result of these calculations is the very fact that the atom is shifted from the tetrahedron center irrespective of the interaction potential form.

From considerations of the crystal electric neutrality, we can write down

$$n_A^i + n_B^V + \left(1 - \frac{e_{AC}^*}{e_{AB}^*}\right) n_c = n_A^V + n_B^i, \quad (3.9)$$

where  $n_A^i$ ,  $n_B^V$  is the number of interstitial atoms of types A and B, respectively;  $n_A^V$ ,  $n_B^i$  is the corresponding number of vacancies;  $n_c$  is the number of isovalent atoms in the anion sublattice. As mobility of the interstitial metal atoms is much higher than the mobility of its vacancies [30], we have  $n_A^i \ll n_A^V$ . Accounting for the condition  $n_B^i \cong n_B^V$  that is valid for interstitial anions [31], from (3.9) we get the expression

$$n_A^V = \left(1 - \frac{e_{AC}^*}{e_{AB}^*}\right) n_c. \quad (3.10)$$

This relationship, under assumption of  $e_{AB}^* > e_{AC}^*$ , shows that isoelectron doping results in formation of additional vacancies in the metal sublattice, with their concentration proportional to the concentration of IVD [18].

The main conclusions from these considerations are the following. Doping by IVD–Te of ZnSe crystals ( $C_{\text{Te}} \approx 0,015\text{--}0,005$ ) results in local

distortions of the lattice due to shifting of the metal atom from the tetrahedron center, and is accompanied by generation of vacancies in the cation sublattice  $C_{Zn}^V = 2 \cdot 10^{-5}$ , which exceeds by several orders of magnitude the equilibrium concentration of  $n_B^V$  in undoped ZnSe crystals [18, 23].

Contributions from other admixtures affect the behavior of the IPD ensemble in SCS with IVD, which can be described by the model representation method of the thermodynamic state of the system using perturbing potentials [32–35]. This leads to analytical expressions for concentrations of IPD of different types, accounting for electrochemical constants of the materials and calculated values of parameters that determine the predominant defect formation type in  $A^{II}B^{VI}$  compounds [18]. In this case, variation of the free energy  $\Delta F$  of the crystal volume unit upon introduction of IVD is

$$\Delta F = n_A^V E_A^V + n_A^i E_A^i + n_B^V E_B^V + n_B^i E_B^i + n_c W - T \Delta S, \quad (3.11)$$

where  $n_{A(B)}^V$ ,  $n_{A(B)}^i$  are numbers of vacancies and interstitial atoms in the respective sublattices;  $n_c$  is the number of IVD atoms;  $E_{A(B)}^V$ ,  $E_{A(B)}^i$  are formation energies of vacancies and interstitial atoms in the cation (A) and anion (B) sublattices;  $W$  is the elastic energy of an IVD atom substitution for a lattice atom;  $T$  is the temperature;  $\Delta S$  is the entropy change of the crystal (only the configurational entropy is accounted for, neglecting its changes due to lattice distortions emerging because atoms of the main substance and the dopant are different). Now we write down the free energy extremum conditions of the doped crystals, which involve indefinite Lagrange factors  $\lambda_1$ ,  $\lambda_2$  [36] and correspond to the thermodynamic state of the system:

$$\begin{cases} \frac{\partial \Delta \tilde{F}}{\partial n_A^V} = \frac{\partial \Delta \tilde{F}}{\partial n_A^i} = \frac{\partial \Delta \tilde{F}}{\partial n_B^V} = \frac{\partial \Delta \tilde{F}}{\partial n_B^i} = \frac{\partial \Delta \tilde{F}}{\partial n_c} = 0, \\ n_A^V - \delta n_A^i - n_B^V + \delta n_B^i + \beta^* n_c = 0, \\ \gamma(1 - n_B^V + n_B^i) - (1 + \gamma)n_c = 0, \end{cases} \quad (3.12)$$

$$\begin{aligned} \Delta \tilde{F} = \Delta F + \lambda_1 (n_A^V - \delta n_A^i - n_B^V + \delta n_B^i + \beta^* n_c) + \\ + \lambda_2 \{ \gamma(1 - n_B^V + n_B^i) - (1 + \gamma)n_c \}, \end{aligned}$$

$\lambda_1, \lambda_2$  are indefinite Lagrange factors,  $\beta^* = 1 - e_{AC}^*/e_{AB}^*$ ). From here, we can see that the increase in the equilibrium concentrations of cation vacancies and interstitial anions is proportional to the IVD concentration:

$$C_A^V/C_{AO}^V = \beta^* C_c/C_{AO}^V; C_B^i/C_{BO}^i = f\beta^* C_c/C_{AO}^V \quad (3.13)$$

The physical meaning of expressions (3.13) is in agreement with conclusions made in [37] for solid solutions AB–AC formed by the anion substitution type. In Table 3.1, calculation results are presented under conditions of (3.12) for defect formation in  $A^{II}B^{VI}$  compounds with IVD (anion and cation doping). Hence it is clear that:

1) both anion and cation isovalent doping lead to re-distribution of equilibrium point defects in the doped crystal as compared with the undoped state. Depending upon the ratio of effective charges of the crystal matrix atom and the dopant atom, both cation and anion IVD can lead to predominance of one and the same type of defects in the doped crystal. Thus, doping with mercury and tellurium results in additional generation of cation vacancies and interstitial anions, while doping with Cd and O — to cation interstitials ( $I_A$ ) in the anion sublattice ( $V_B$ );

2) one and the same IVD introduced to different crystals can, depending of the ratio of effective charges, shift the equilibrium concentration of point defects either to their excess ( $I_A$  и  $I_B$ ) or ( $V_A, I_B$ ); e.g., doping of cadmium and mercury compounds with Zn (cationic substitution); at the same time, doping with sulfur and selenium (anionic substitution) leads to different character of the point defect ensemble even for compounds with one and the same metal (Zn, Cd, Hg);

3) multi-component doping (i.e., more than one dopant) allows purposeful control of the point defect composition in the crystal.

Let us consider this point in more detail. Let  $C_{Cl}$  be the concentration of the  $l$ -th isovalent dopant introduced to the anion sublattice, where  $l = 1, 2 \dots$ ,  $e_{AC_l}^*$  is the effective charge of its bond with the crystal matrix cation. Similarly, for the  $j$ -th component of the cation doping we introduce  $C_{D_j}$  and  $e_{D_jB}^*$ . Then concentrations of intrinsic defects in such multi-doped IVD crystal are

Table 3.1. Calculated data predicting predominant point defect formation in isovalent doping of  $A^{II}B^{VI}$  compounds.

Compound	Electro- negativity $\chi_O, \Delta\chi_{AB}$	Degree of ionicity, $I_{AB}$ [41]	Isovalent dopant						
			Zn	Cd	Hg	O	S	Se	Te
			Electronegativity						
			1.5	1.4	1.9	3.5	2.5	2.4	2.1
			$\beta^* = (1 - e_{AC}^*/e_{AB}^*) \text{ or } (1 - e_{DC}^*/e_{AB}^*)$						
ZnO	2.0	0.632		-0.06	+0.25		+0.65	+0.71	+0.86
ZnS	1.0	0.0221 (0.635)		-0.18	+1.57	-1.86		+0.17	+0.61
ZnSe	0.9	0.183 (0.630)		-0.21	+2.00	-2.45	-0.21		+0.53
ZnTe	0.6	0.086 (0.608)		-0.34	+7.60	-6.35	-1.57	-1.13	
CdO	2.1	0.668	+0.05		+0.29		+0.39	+0.67	+0.83
CdS	1.1	0.261	+0.15		+0.67	-1.56		+0.15	+0.56
CdSe	1.0	0.221	+0.17		+0.72	-2.02	-0.18		+0.48
CdTe	0.7	0.115 (0.669)	+0.25		+0.91	-4.81	-1.27	-0.92	
HgO	1.6	0.473	-0.34	-0.41			+0.82	+0.87	+0.98
HgS	0.6	0.086	-1.57	-2.04		-4.50		+0.29	+0.88
HgSe	0.5	0.061	-2.00	-2.62		-6.75	-0.41		+0.84
HgTe	0.2	0.070	-7.60	-10.50		-46.3	-7.60	-5.10	

Note:  $\langle\leftrightarrow\rangle - C_A^V, C_B^i; \langle\leftrightarrow\rangle - C_A^i, C_B^V$

$$C_A^V = \sum_l \left(1 - e_{AC_l}^* / e_{AB}^*\right) C_{C_l} + \sum_j \left(1 - e_{D_lB}^* / e_{AB}^*\right) C_{D_l} \quad (3.14)$$

$$C_B^i = f \left\{ \sum_l \left(1 - e_{AC_l}^* / e_{AB}^*\right) C_{C_l} + \sum_j \left(1 - e_{D_lB}^* / e_{AB}^*\right) C_{D_l} \right\} \frac{C_{BO}^i}{C_{AO}^V}$$

Here it is taken into account that simultaneous generation of Frenkel pair defects, e.g.,  $V_A - I_A$ , does not lead to formation of a stable defect. Hence it follows that simultaneous IVD doping with effective charges larger and smaller than effective charges of the crystal bonds can lead to compensation of the effective charges [3], and additional defect formation due to differences in effective charges will be thermodynamically not favorable. Differences in crystallochemical size between IVD and the substituted lattice atom become a predominant factor in the defect generation.

As an example, we consider zinc selenide doped with oxygen and tellurium. Their respective concentrations and effective charges are  $C_O$ ,  $e_{ZnTe}^*$  and  $C_{Te}$ ,  $e_{ZnO}^*$ . Then it follows from (3.14) that

$$C_{Zn}^V = \left(1 - e_{ZnTe}^* / e_{ZnSe}^*\right) C_{Te} + \left(1 - e_{ZnO}^* / e_{ZnSe}^*\right) C_O, \quad (3.15)$$

and additional generation of zinc vacancies is observed (as shown in Table 3.1, doping with **Te** results in generation of zinc vacancies, while doping with oxygen favors formation of interstitial **Zn**) upon conditions:

$$\frac{C_O}{C_{Te}} << - \frac{1 - e_{ZnTe}^* / e_{ZnSe}^*}{1 - e_{ZnO}^* / e_{ZnSe}^*} \quad (3.16)$$

Using the Pauling's definition of the degree of ionicity and the expression (3.16), we obtain

$$\frac{C_O}{C_{Te}} << \frac{\exp(-0,25\Delta X_{ZnSe}^2) - \exp(-0,25\Delta X_{ZnTe}^2)}{\exp(-0,25\Delta X_{ZnO}^2) - \exp(-0,25\Delta X_{ZnSe}^2)}. \quad (3.17)$$

Then from data of Table 3.1 and (3.17) we obtain  $C_O/C_{Te} << 0,21$ , i.e. oxygen concentration in **ZnSe(Te)** crystals of about one-fifth of the



Table 3.2. Effects of thermal treatment upon activation energy of evaporation of ZnSe(Te) crystal components.

Thermal treatment regime			Temperature interval, K	Activation energy of evaporation process, eV		
Medium $P, \text{Pa}$	$T_{\text{ann}}, \text{K}$	$t_{\text{ann}}, \text{hours}$		Zn	Se <sub>2</sub>	Te
$\text{без TO}$			873–1073 873–1173 973–1173	1,14±0,34	0,97±0,29	0,60±0,18
$P_{\text{Zn}} = 10^5$	1273	24	858–938 938–1053	1,10±0,33 0,78±0,23	2,41±0,72 0,85±0,26	
$P_{\text{Te}} = 10^5$	1273	46	823–898 898–1023 873–923 923–1053	0,78±0,23 0,55±0,17	2,41±0,72 0,85±0,26	
$P_{\text{Te}} = 10^5$	1273	46	823–1073 873–923	0,88±,26	2,41±0,72	
$P_{\text{Zn}} = 10^5$		24	923–923		0,85±0,26	
$P \approx 10^{-1}$	1273	24	858–938 938–1053 923–973 973–1053	1,10±0,33 0,78±0,23	2,41±0,72 2,41±0,26	

tellurium concentration prevents generation of additional vacancies in the zinc sublattice; consequently,  $V_{\text{Zn}} + \text{Te}$  complexes are not formed.

These theoretical considerations have been confirmed experimentally (with tellurium-doped zinc selenide taken as an example) by our studies of thermodesorption kinetics [23]. These studies have also provided further information on specific features of the dopant introduction into the crystal lattice and effects of the dopant upon defect formation processes in ZnSe(Te) crystals.

Evaporation of ZnSe(Te) crystals was studied using a MCX–4 mass-spectrometer. Before the measurements, the samples were annealed in different conditions (sample characteristics and results obtained are presented in Table 3.2 and Figs. 3.2–3.4).

Zinc selenide crystals belong to congruently evaporating substances with dissociative character of evaporation (dissociation degree  $\alpha = 1$ ):

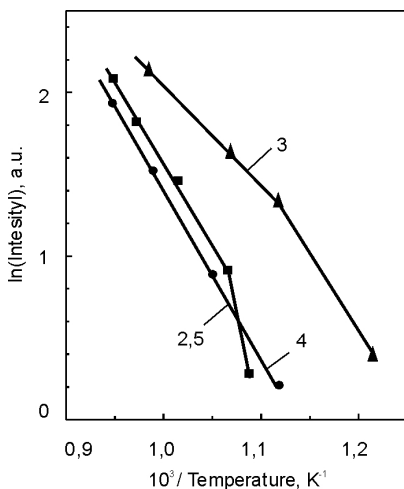


Fig.3.2. Logarithm of zinc thermodesorption peak intensity as function of inverse temperature. Plot numbers correspond to crystal numbers in Table 3.2.

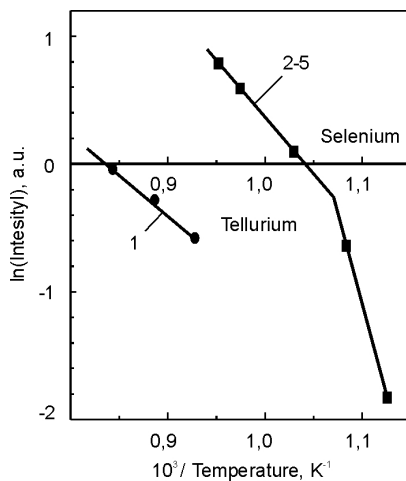


Fig.3.3. Thermodesorption peak intensity for selenium and tellurium. Plot numbers correspond to crystal numbers in Table 3.2.

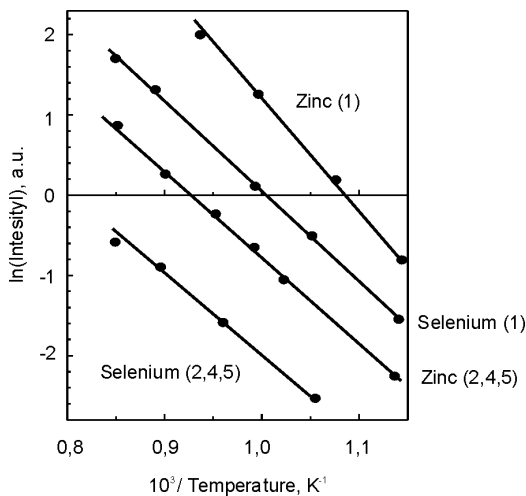
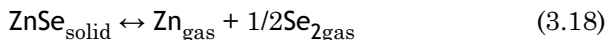


Fig.3.4. Thermodesorption peak intensity for selenium and tellurium. Numbers in parentheses correspond to crystal numbers in Table 3.2.



Analysis of thermodesorption peaks (TDP) shows that at one and the same temperature TDP amplitudes for the initial crystals are much higher (both for zinc and selenium) than TDP amplitudes for the same crystal elements after annealing. E.g., at 973 K  $I_{\text{Zn}}^{\text{I}}/I_{\text{Zn}}^{\text{TA}} = 10$ ,  $I_{\text{Se}}^{\text{I}}/I_{\text{Se}}^{\text{TA}} = 11$ , and these ratios are the same for crystals thermally treated in vacuum, zinc vapor or tellurium vapor ( $I^{\text{I}}$ ,  $I^{\text{TA}}$  is the TDP intensity for the initial and thermally treated crystal, respectively).

Due to the congruent character of evaporation, the ratio  $I_{\text{Zn}}/I_{\text{Se}}$  should be of the order of 1, which is confirmed in our experiments at  $T \geq 973$  K. At lower temperatures this ratio is shifted towards excess of zinc, reaching the values of 1.4–1.6 at  $T \leq 873$  K. Annealing conditions ( $T$ , atmosphere) mostly affect  $I_{\text{Zn}}$  and less significantly —  $I_{\text{Se}}$ . After thermal treatment in Te atmosphere TDP  $I_{\text{Zn}}$  is observed at  $T \leq 773$  K, while under other conditions of thermal treatment — only at  $T \geq 873$  K. Higher stability of selenium sublattice as compared with the zinc sublattice implies lower defect formation energy in the latter (and, consequently, larger defect formation probability in the zinc sublattice). This conclusion is in agreement with known interpretation of data on the radiation damage. Predominant evaporation of zinc, which is due to higher Zn mobility, results in increased concentration of the defects of  $V_{\text{Zn}}$  type; this process is the most obvious in crystals doped by tellurium or thermally treated in tellurium atmosphere, which can be explained by formation of stable associates  $V_{\text{Zn}}\text{Te}_{\text{Se}}\text{Zn}_i$ . This result is in essential agreement with the concept of vacancy generation in the neighboring sublattice upon introduction of an atom that has much higher ionic radius than the substituted atom.

Thus, studies of the evaporation process of zinc selenide have shown that: 1) thermodynamics of the process depends upon degree of crystal defectness; 2) introduction of Te IVD favors generation of additional vacancies in the cationic sublattice and shifts the stoichiometry towards zinc deficiency; 3) upon introduction of Te IVD, stable associates  $V_{\text{Zn}} + \text{Te}$  of low mobility are formed.

An important consequence of generation of additional defects under isovalent doping is an increase in radiation stability of the doped crystals as compared with undoped ones. It has been shown [38] that the following condition is necessary and sufficient for high radiation

stability of non-metal crystals: the free path length of a dynamic crowdion ( $l_f^{hkl}$ ) should be less than the instability zone radius ( $r_0^{hkl}$ ) in any given crystallographic direction:  $l_f^{hkl} < r_0^{hkl}$ .

In crystals of sphalerite type (to which zinc selenide also belongs) [38, 39], symmetric triangular lenses were observed around the [111] direction (Fig.3.1), which cause additional focusing of an atom knocked out of the site along this direction and its driving outside the instability zone with formation of a stable radiation defect. This result was observed in numerous experiments on different crystals of sphalerite structure (see, e.g., [40]).

At the same time, radiation stability of ZnSe crystals in comparison with Ge (lattice of diamond — “monoatomic” sphalerite) and GaAs under influence of different types of ionizing radiation (electrons, neutrons,  $\gamma$ -quanta) was noted in [41]. Irradiation by  $\gamma$ -quanta ( $^{60}\text{Co}$ ,  $I_\gamma = 3800$  R/s) at  $T = 300$  K at doses up to  $10^8$  rad and fast electrons ( $E = 1$  MeV) does not lead to changes in IR absorption spectra for all substances studied. Irradiation by fast neutrons substantially increases IR absorption of Ge and GaAs. Thermal treatment does not lead to restoration of the optical properties of germanium, which is related by the authors to formation of disordered regions as a result of irradiation.

Irradiation of zinc selenide results in transmittance changes only in the visible spectral range. The authors of [41] conclude that ZnSe has the highest radiation stability among the materials studied.

Pulse irradiation of zinc selenide by electrons ( $E = 5$  MeV,  $\tau_{\text{pulse}} = 2,3$   $\mu\text{s}$ ) gives rise to short-living optical absorption in the 450–1000 nm region, which is quickly removed by annealing (50% of the radiation-induced absorption in 50–60  $\mu\text{s}$ ) already at 473 K. The 465 nm band is related to formation of unstable pairs zinc vacancy ( $V_{\text{Zn}}$ ) — interstitial zinc atom ( $\text{Zn}_i$ ). Above 1000 nm, no absorption is observed [41].

In [42, 43], cathodoluminescence spectra (CL) spectra of zinc selenide were studied under pulse irradiation by electrons ( $E = 6$  MeV,  $\tau_{\text{pulse}} = 10$  ns,  $I = 10$  A). The 580 nm emission center was related to an unstable Frenkel pair ( $V_{\text{Zn}} - \text{Zn}_i$ ) absorbing at 465 nm; also observed were CL bands at 630, 680, 720, 780, 820 nm. The 630 nm band was related with admixture of copper, and the 830 nm band, according to [43] — with selenium vacancies.

Thus, a whole set of experimental results is available demonstrating relatively high radiation stability of zinc selenide.

Higher radiation stability of ZnSe as compared with GaAs and Ge described in [41] can be related to a significant difference in atomic mass values of the lattice components of ZnSe ( $m_{\text{Se}}:m_{\text{Zn}} = 1,21$ ;  $m_{\text{As}}:m_{\text{Ga}} = 1,08$ ;  $m_{\text{Ge}}:m_{\text{Ge}} = 1,00$ ), which lowers the energy transmitted in collisions of the knocked-out atoms [26], thus decreasing the dynamic crowdion free path length  $l_f^{hkl}$ , as well as to substantial difference of dielectric permittivities of these crystals ( $\epsilon_{\text{ZnSe}} = 5,9$ ;  $\epsilon_{\text{GaAs}} = 10,9$ ;  $\epsilon_{\text{Ge}} = 16,2$  [44]), which, with other conditions equal, (as  $r_0^{hkl} \sim \epsilon^{-1/2}$  [44]), gives larger size of instability zone in zinc selenide:  $r_0^{\text{ZnSe}} > r_0^{\text{GaAs}} > r_0^{\text{Ge}}$ .

Therefore, ZnSe has shorter free path length of the knocked-out atom, and also larger size of instability zone. This, according to the structural criterion of [33] should result in higher radiation stability of physical properties of this material as compared with germanium and gallium arsenide.

As shown above, IVD introduction leads to redistribution of the equilibrium concentration of point defects; in particular (see Tabl. 3.1), doping of zinc selenide by tellurium results in formation of equilibrium zinc vacancies:

$$C_{\text{Zn}}^V = \left( 1 - \frac{e_{\text{ZnTe}}^*}{e_{\text{ZnSe}}^*} \right) C_{\text{Te}},$$

i.e., isovalent doping leads to formation of additional (as compared with pure crystal) vacancies in the metal sublattice, with their concentration comparable to the concentration of the introduced dopant.

According to data of [38], additional vacancies exert de-focusing influence upon atoms knocked out from their sites: primarily, because the vacancies are located in the [111] direction and shorten the free path length of the knocked-out zinc atom [18], and, secondly, they destroy the focusing lenses for knocked-out chalcogene atoms in this direction, i.e., dynamic crowdions are scattered on these defects.

Thus, accounting for numerous data indicating that the emission character of isovalently doped  $A^{\text{II}}B^{\text{VI}}$  crystals [4–6, 21–23] is correlated with luminescence of non-stoichiometric or radiation-damaged structures. [12–14, 19, 20], and basing upon thermodynamic analysis of the system state using the method of disturbing potentials and the concept of efficient atom charge, it has been established that on the basis of  $A^{\text{II}}B^{\text{VI}}$  crystals, provided the conditions are met of difference in ionic

radius and electronegativity values of IVD and substituted atoms, it is possible to obtain highly efficient scintillators with predictable luminescence spectrum. This is due to the fact that parameters of luminescence centers that include complexes of  $[V_A Te_B]$  type in IVD-doped crystals are determined by the predominant type of IPD of the crystal lattice [16–18, 21–23], defining optoelectronic, radiation and thermal characteristics of a specified semiconductor crystal. For many practically important cases, purposeful forming of IPD ensembles in IVD-doped SCS is considered in Chapter 3.3.

### ***3.2. Kinetics of formation processes of semiconductor scintillator crystals with isovalent dopants accounting for effects of gas media***

Crystals of  $A^{II}B^{VI}$  compounds are prepared by two principal methods – from the melt and from the gas phase, and each of them has several modifications [4, 45, 46].

When crystals are grown from a solution in melt, crystallization temperature is substantially lowered, which allows, in principle, obtaining structurally perfect samples; however, the crystal obtained is doped by the solvent material (In, Bi, Pb, Sn, etc.), so, this method can hardly be used to obtain SCS. Methods such as XTP, which combine, at relatively low temperatures, the processes of component synthesis and crystal growth, are also not suitable for SCS preparation because of crystal doping by the transport material and limited size of the obtained samples. The use of sublimation methods, when the initial substance is placed into a sealed container under vacuum and is crystallized upon heating in the cool gradient zone, results in single crystals of high purity, but of small size (up to 10–15 g). Therefore, this method can be useful only for research purposes. Large-sized (hundreds of cubic centimeters) undoped  $A^{II}B^{VI}$  polycrystals can be obtained by condensation from the gas phase (CVD), but growth of scintillation crystals by this method is only at the stage of development.

One of the most widely used preparation methods of crystals of binary and multicomponent  $A^{II}B^{VI}$  systems is growth by melt crystallization under inert gas pressure — the Bridgman-Stockbarger method. This method allows preparation of crystals up to 100 mm in diameter and up to 10 kg mass in a relatively short time (several days). High (up to  $10^7$  Pa) inert gas pressure lowers mass transfer of

the initial substance from the crystallization zone to the cool zone. This process is due to high pressure of the components that dissociate in the liquid phase.

In the growth process, the temperature is increased up to values 50–100 K above melting point (see Table 3.3, where main characteristics of  $A^{II}B^{VI}$  compounds are presented). After this, the crucible with initial charge is moved (usually in vertical direction) at a speed of 2.5–25 mm/hour through this zone. After going through the maximum temperature zone, the melt is crystallized in the zone of 30–100 K/cm temperature gradient. This method ensures the highest productivity and requires relatively simple equipment, at the same time ensuring sufficient reproducibility of scintillation parameters of IVD-doped  $A^{II}B^{VI}$  crystals.

However, this method has also some drawbacks. The use of high (up to 2000°C) temperatures and pressures results in certain technological difficulties and puts special requirements to labor safety. For some  $A^{II}B^{VI}$  compounds, this method does not allow preparation of single crystalline structures of high perfection [46]. In the case of ZnSe(Te), the situation is as follows. The system ZnSe–ZnTe at  $T < 1290^{\circ}\text{C}$  forms a continuous series of solid solutions with sphalerite type cubic lattice; no other phases have been observed by X-ray analysis [46]. Studies of  $\text{ZnSe}_{1-x}\text{Te}_x$  crystals at  $x = 0.002\text{--}0.02$  by methods of differential thermal analysis and X-ray analysis have shown that in the temperature region of  $\sim 1400^{\circ}\text{C}$  (heating) and  $1370 \pm 10^{\circ}\text{C}$  (cooling) a polymorphic transition occurs, corresponding to the wurtzite-sphalerite phase transition, which was earlier observed for undoped zinc selenide crystals [47]. On the surface of grown ZnSe(Te) crystals, macroscopic twinning is observed with band width up to several millimeters, as well as angular disorientation of crystallographic planes. Depending upon the cooling speed (6–30 K/min), a single crystalline sample can be transformed into a large-crystalline block ingot, or twinning structures can be redistributed in the single crystal. At slow cooling speed, the polymorphic transition in ZnSe(Te) goes according to the diffusion mechanism, and at higher speed — by the martensite mechanism. Therefore, in this growth method the temperature gradient in the phase transition region, as well as crystal cooling (movement) speed, should be chosen and maintained very accurately, as the temperature profile in this zone substantially affects formation of the lattice defect

Table 3.3.

Parameter	Compound					
	CdS	ZnSe	CdSe	ZnS	ZnO	
1	2	3	4	5	6	
Structure (W — wurtzite, S — sphalerite)	W S (unstable)	S (probably) W	W S (unstable)	S W (stable at high temp.)	W (probably) S	
Lattice constant, Å	S 5.82- 5. 83 W 4.13-4.14 6.71- 6.75	S 5.667 W 7.01;4.30	S 5.83-6.05 W 7.01;4.30	S 5.42 W 6.26	S 1.95 W 5.2; 4.27	
Atomic number, Z	48 16	30 34	48 34	30 16	30 8	
Density $\rho$ , g/cm <sup>3</sup>	4.82	5.13 (W) 5.30 (S)	5.84 (W) 5.68 (S)	4.102(W) 4.087—4.09(S)	5.64 (W) 4 (S)	
Refraction index, n	2.3→≥2.25 (100-800 nm)	2.55 (640 nm)	2.65→≤2.5 (700-1000 nm)	2.564 →2.303 (400-1000nm)	2.24→ >1.9435 (400-1000 nm)	
Band gap $E_g$ , eV	2.52-2.58	2.7-2.8	1.48-1.8	3.6-3.91	3.3-3.44	
Electronegativity X, eV (M — Millican, P — Pauling, O-R — Older-Rokhov)	A 1.4-1.5 (M); 1.7(P); 1.46 (O-R)	1.5-1.6 (M); 1.5-1.6(P); 1, 61-1,66(O-R)	1.4-1, 5 (M); 1, 7 (P); 1, 46 (O-R)	1.5-1, 6 (M); 1, 5-1. 6 (P); 1, 61-1, 66 (O-R)	1.5-1, 6 (M); 1, 5-1.6(P); 1, 61-1, 66 (O-R)	
Ion (atom) radius, Å	B 2, 5-2.6 (M); 2.5 (P); 2.44 (O-R)	2, 2-2, 4 (M); 2, 4(P); 2.48 (O-R)	2, 2-2, 4 (M); 2, 4 (P); 2, 48 (O-R)	2, 5-2, 6 (M); 2, 5(P); 2, 44 (O-R)	3.5(M); 3.5 (P); 3.5 (O-R)	
	A 0.95 (1.49) 1.84 (1.04)	0.74(1,32) 1.98(1.17)	0.95 (1.49) 1, 98(1,17)	0.74 (1,33) 1, 84 (1.04)	0.74 (1.33) 1.4 (0.66)	



Table 3.3. (continued)

1	2	3	4	5	6
Distance between adjacent atoms, Å observed calculated (covalent) calculated (ionic)	2,52	2,45	2,62	2,34	-
	2,52	2,45	2,62	2,35	
	2,66	2,58	2,81	2,43	
Atom binding energy $E_0$ , eV A B	2,4; 2,7	8–10	6; 8,1	9,9	14; 57
	8,7; 9,6	6,2–8	8,6; 11,6	20,2	57; 230
Atom shift threshold energy $E_c$ , keV A B	285	195–200	250 320 (5K)	240	310 900
	290	240 (85 K)	322	185	900 310
	125–115	240 195–200	320 250		
Melting temperature ( $T_m$ ), °C	115	(10–35 K)	(77K)		
	1475–1500	1515–1520	1239–1350	S1800–1830	1670
Melting temperature of the components, °C	321	420	321	W1900	1870, 1875
	94–119	217–219	217–219	420	420
Boiling temperature of the components, °C	767; 765	907	767; 765	94–119	–218,65 (14 atm. O <sub>2</sub> )
	545; 445	737; 657; 685 (ev.)	685 (ev.)	907	907
Dielectric constant $\epsilon$ : high-frequency $\epsilon_\infty$ residual $\epsilon_s$	5,2–5,24	5,9	6–7,9	545; 445	–183 (O <sub>2</sub> )
	9,3–8,9	8,1–8,8	9,63–8,75	5,13	8,5
				S 8,1–8,32 W 8,3–8,65	S 8,8–8,3

Table 3.3. (continued)

Parameter	Compound				
	Zr i Te	CdTe	HgTe	HgSe	HgS
1	2	3	4	5	6
Structure (W — wurtzite, S- sphalerite)	S	W low probab.	S	S	W (unstable)
Lattice constant, Å	6.08–6.104 4.27–4.31 6.99– 7.09	6.48–6.482 4.57 7.47	6.46–6.482	6.08–6.084	5.841–5.851 4.149–4.15 9.495
Atomic number, Z	A B	48 52	80 52	80 34	80 16
Density ρ, g/cm <sup>3</sup>	6.34	5.85;6.20	8.12	8.25	7. 73; 8.1
Refraction index n	2.68–3.56	2.67–2.85	3.7–4.2	2.5–2.85	-
Band gap $E_g$ , eV	2.12-2.34	1.5-1.6	0.08-0.115	0.2-0.22	1.4-2
Electronegativity X, eV (M — Millican, P — Pauling, O-R — Older-Rokhov)	A	1.4–1.5 (M); 1.7 (P); 1.46 (O-R)	2.0–1. 9 (M); 1.8–1.9 (P); 1,44 (O-R)	2, 0–1,9 (M); 1,8–1, 9 (P); 1,44 (O-R)	2.0–1,9 (M); 1.8–1.9 (P); 1.44 (O-R)
	B	(O-R) 2.1 (M); 2.1 (P); 2.01 (O-R)	2.1 (M); 2.1 (P); 2.01 (O-R)	2,1 (M); 2Д (II); 2,01 (O-R)	2.2–2,4 (M); 2.4 (P) 2.48 (O-R)
Ionic (atomic) radius, Å	A	0.74(1.33) 2.21	0.97 (1.1)	0.97 (1.1)	0.97 (1.1)
	B	(1.37)	2.21(1.37)	1.98(1.17)	1.84 (1.04)

Table 3.3. (continued)

1	2	3	4	5	6
Distance between adjacent atoms, Å	observed calculated (covalent) calculated (ionic)	2.64	2.53	2.63	2.80
		2.63	2.52	2.62	2.80
		2.81	2.80	2.95	3.18
Atom binding energy $E_0$ , eV	A	4–13	–	–	–
	B	2–6.7	–	–	–
Atom shift threshold energy $E_c$ , keV	A	110 185 (77 K)	–	–	–
	B	235 300 (77 K)	–	–	–
Melting temperature ( $T_m$ ), °C		1285	670	794	S 1477 W 583.5
Melting temperature of the components, °C	A	420	–38.9	–38.9	–38.9
	B	450	450	217–219	94–119
Boiling temperature of the components, °C	A	907	357	357	357
	B	1087; 990; 1390 (ev.)	1087; 990; 1390 (ev.)	737; 657; 685 (ev.)	545; 445
Dielectric constant $\epsilon$ : high-frequency $\epsilon_\infty$ residual $\epsilon_s$		72.8	–	7.5	–
		9.7–10.1	–	2.5	–

structure and output parameters of A<sup>II</sup>B<sup>VI</sup>-based SCS. Also, when A<sup>II</sup>B<sup>VI</sup> crystals are doped by a dopant with distribution coefficient  $K \ll 1$  (for tellurium in zinc selenide  $K \approx 0.1$ ), non-uniform dopant distribution over the grown ingot volume is observed. Accounting for high temperatures and aggressive growth medium, the only material that is stable to these factors is graphite. Its purity (as well as dopant composition and stoichiometry of the initial charge) must meet special requirements, especially concerning the presence of oxygen-containing components.

While concentration of other admixtures can be made acceptable at the stages of component preparation and charge synthesis, the removal of oxygen is a special problem. As follows from thermodynamics of ZnSe-ZnTe system (see Chapter 3.1), oxygen in concentration of about one-fifth of tellurium concentration suppresses generation of additional vacancies in the zinc sublattice. This is an obstacle to formation of  $V_{Zn} + Te_{Se}$  complexes, which are responsible for the main luminescence band. Furthermore, oxide films on the grain surfaces of the initial mixtures ZnSe-ZnTe and CdS-CdTe hinder formation of homogeneous solid solutions used as starting material for growth of SCS [48, 49].

Reagent interaction in the ZnSe-O<sub>2</sub> system can lead to formation of a large variety of compounds (ZnSeO<sub>3</sub>, ZnSeO<sub>4</sub>, SeO<sub>2</sub>, ZnO); in fact, at  $T > 800$  K the principal stable end product is zinc oxide, i.e., reaction goes as  $ZnSe \rightarrow ZnO$  and, consequently, the quantity of matter ( $\mu_0$ ) in the solid phase should remain constant before and after the reaction:  $\mu_0 = \text{const}$ ,  $\mu_0 = m_0/M_{ZnSe} = m_{ZnSe}/M_{ZnSe} + m_{ZnO}/M_{ZnO} = \text{const}$ , where  $m_0$  is the mass of initial zinc selenide sample;  $m_{ZnSe}$ ,  $m_{ZnO}$  are masses of ZnSe and ZnO formed as a result of oxidation after a given time;  $M_{ZnSe}$  и  $M_{ZnO}$  are molar masses of zinc selenide and zinc oxide. If the mass loss of the sample after oxidation is  $\Delta m$ , mass concentration of zinc oxide  $C_{ZnO} = m_{ZnO}/m_0 - \Delta m$  can be expressed as function of the relative mass of the oxidized sample  $\Delta m/m_0$ :

$$C_{ZnO} = \{[\Delta m/m_0 - 1][(M_{ZnSe}/M_{ZnO}) - 1]\}^{-1}. \quad (3.19)$$

A satisfactory agreement of experimental and calculated data (Fig.3.5) confirms that under real conditions, close to 900 K, zinc oxide is the main stable reaction product. Its physico-chemical state in ZnSe can be determined from the character of the dependence of film thickness  $x$  upon interaction time  $\tau$  in the ZnSe-O<sub>2</sub> system.

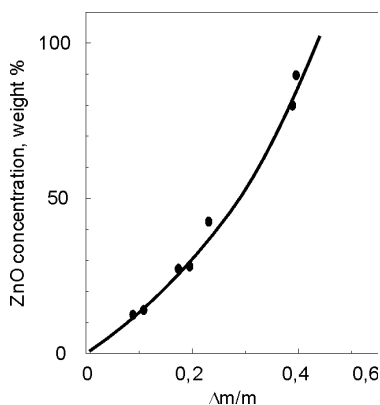


Fig.3.5. Concentration of zinc oxide formed ( $C_{\text{ZnO}}$ , mass %) as function of the relative sample mass (Solid line: calculated; points: experimental).

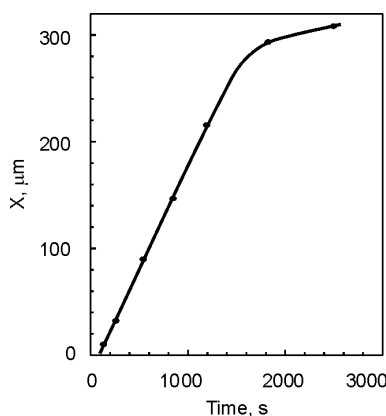


Fig.3.6. Thickness of ZnO layer as function of thermal treatment time.

A linear plot  $x(\tau)$  obtained experimentally (from  $C_{\text{ZnO}}$  measurements), shown in Fig.3.6, confirms the assumption that at 990 K oxidation rate of ZnSe is determined by the reaction kinetics at the phase boundary. Deviations from linearity at  $\tau > 1800$  s are probably related to an increased diffusion resistivity of the ZnO layer to oxygen and  $\text{SeO}_2$ , as well as with slowing down of the reaction, as zinc oxide concentration after 1800 s is 0.8 mass %, and after 5400 s — 0.92 mass %.

The negative effect of ZnO film upon formation of  $\text{ZnSe}_{1-x}\text{Te}_x$  solid solution becomes obvious when results for sintering of the initial mixture in neutral and reduction media are compared.

Sintering of initial powder mixtures in hydrogen after thermal treatment time  $< 4$  h, as well as sintering in argon after any thermal treatment time, results in mass losses both of ZnSe and ZnTe not exceeding 3–4 %. Thermal treatment in hydrogen for more than 4 hours lead to a strong increase in losses of ZnTe only. As shown in Fig.3.7, a, mass losses of ZnTe at  $x > 0,1$  are 30–50 % at  $\tau = 4,5$  hours, while at low ZnTe concentrations ( $x < 0,05$ ) mass losses of zinc telluride are insignificant and decrease with smaller  $x$ .

It follows from Fig.3.7, b that thermal treatment in  $\text{H}_2$  includes a certain “incubation” period of less than 4 hours when there are practically no ZnTe losses related to sub-

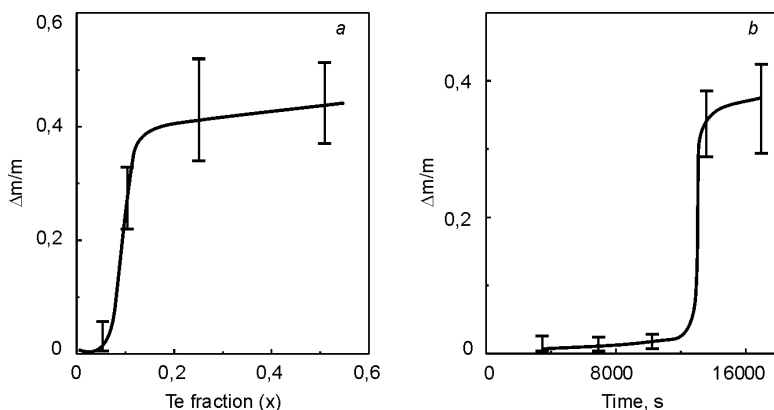


Fig.3.7. ZnTe mass losses: a — as function of composition (thermal treatment in hydrogen for 4.5 hours); b — as function of thermal treatment time in hydrogen at  $x = 0.2$ ).

limination or a reaction with hydrogen. Samples thermally treated in hydrogen appeared to be ceramics with density noticeably increasing at longer thermal treatment times and higher ZnTe concentration. At the same time, thermal treatment in argon resulted in poorly sintered, brittle samples of low mechanical strength.

These results can be explained assuming that the sintering process is affected by oxide phases formed on the surface of ZnSe and ZnTe grains as a result of their oxidation.

The ZnO layer limits the rates of sintering, sublimation and interactions of ZnSe and ZnTe with each other and with the annealing atmosphere. The rates of these processes, as shown in Fig.3.7,b, are strongly increased in the hydrogen atmosphere after chemical and thermal etching of the ZnO layer. When thermal treatment is carried out in argon, i.e., when the atmosphere does not interact with the oxide film, it can be destroyed only due to thermal evaporation; such processes, as noted above, are stationary and rather slow.

Thus, efficiency of the formation process of  $\text{ZnSe}_{1-x}\text{Te}_x$  solid solutions, as well as the actual phase composition after sintering of ZnSe and ZnTe powders are essentially dependent upon the presence of a ZnO layer, its interaction with  $\text{H}_2$ , interaction of zinc telluride and selenide with hydrogen, and the rate of their dissociative sublimation.

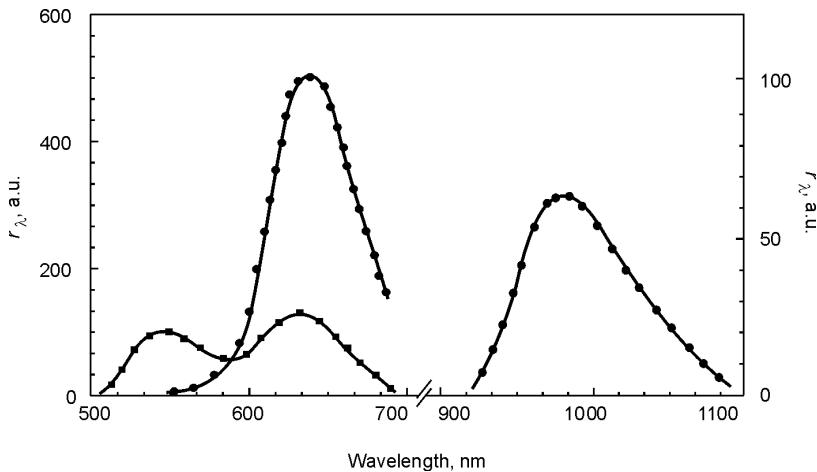


Fig.3.8. Luminescence spectra of crystals ZnSe:Zn (1) and ZnSe(Te):Zn (2).

An important stage of the preparation process of ZnSe(Te)-type SCS, when luminescence centers are finally formed and possible non-radiative recombination channels, as well as levels causing the afterglow, are suppressed, is after-growth thermal treatment of the crystals [24].

To optimize the activator concentration and thermal treatment regimes ensuring high quantum yield in the L-640 band, photoluminescence (PL) spectra of zinc selenide samples were studied. In these samples, lattice defect formation was induced by annealing of stoichiometric crystals in Zn vapor, as well as by introduction of an isovalent activator Te (the corresponding samples are referred to as ZnSe:Zn and ZnSe(Te), respectively).

For luminescence excitation, we used lasers LGN-402 ( $\lambda_B = 488$  nm,  $h\nu = 2.54$  eV) at  $T = 4.5$  K, LG-70 ( $\lambda_B = 440$  nm,  $h\nu = 2.82$  eV) at  $T = 300$  K. As the band gap of ZnSe is  $E_g = 2.80$  eV at  $T = 0$  K and  $E_g = 2.58$  eV at  $T = 300$  K [24], in the first case PL was excited in the crystal volume, and in the second case — in a surface-adjacent layer.

The results obtained are presented in Table 3.4. In PL spectra of the studied zinc selenide samples, from one (“red”) to three (“green”, “red”, “infrared”) bands could be observed. In Fig.3.8, all three luminescence bands can be seen for Sample 2. The maximum intensities of L-540, L-640 and L-980 bands for Sample 2 were taken as reference

Table 3.4. Parameters of PL spectra for zinc selenide samples.

Sample No.	Material	Activator concentration, %	Luminescence intensity, relative units			
			L-540	L-980	L-640	L-640
1	ZnSe	—	0,2	0,5	4	5–15
2	ZnSe:Zn	—	1	1	1	1
3	ZnSe:Te	—	1	0,6	0,9	1
4	ZnSe(Te)	1	—	0,6	3	5
5	ZnSe(Te):Zn	1	3	0,5	1,5	12
6	ZnSe(Te):Te	1	0,3	0,6	4	145
7	ZnSe(Te):Zn*	1	—	—	9	200
8	ZnSe(Te):Zn**	1	0,6	—	17	204
9	ZnSe(Te)	3	—	1	9	48
10	ZnSe(Te):Zn	3	—	1	20	400
11	ZnSe(Te):Te	3	—	1	8	77
12	ZnSe(Te):Zn*	3	—	1	16	263
13	ZnSe(Te):Zn**	3	—	1	16	314
			$T=4.5\text{ K}$	$T=4.5\text{ K}$	$T=4.5\text{ K}$	$T=300\text{ K}$

*Note:* Annealing of the samples was carried out for 24 hours at  $T = 980\text{--}1000^\circ\text{C}$  and vapor pressure of the corresponding component  $P = 10\text{ Pa}$ . \* — before annealing in Zn, samples were treated in Te vapor; \*\* — cyclic thermal treatment Zn – Te – Zn. Each thermal treatment stage was carried out as described above.

units in the respective spectral ranges. For other samples, relative PL intensity values are presented with respect to the corresponding bands of Sample 2 at the same values of the excitation radiation power.

ZnSe crystals used as elements of radiation detectors should show intense luminescence in the “red” PL band L-640, with luminescence in other bands as low as possible. Data of Table 3.4 show that the best suited are Samples 10, 12, 13, where there is no PL band L-540, L-980 band is negligibly weak, and intensities in the maximums of L-640 band are 20, 16 and 16 relative units, respectively (at  $T = 4.5\text{ K}$ ). PL spectrum of Sample 10 is shown in Fig.3.8. Samples 10, 12, 13 contain 3 % of Te and were thermally treated in Zn vapor.

Thus, analysis of “red” luminescence of zinc selenide crystals depending upon dopant concentration and thermal treatment regimes



show that higher intensity of L-640 band is related to removal of the non-radiative centers of surface recombination, which is efficiently achieved by introduction of Te activator with subsequent annealing in Zn vapor.

It should be specially noted that controlled variation of the luminescence intensity within three orders of magnitude and shifting of the luminescence maximums within the 500–1000 nm range can be efficiently achieved just by variation of the IVD-doped zinc selenide crystal composition without introduction of any other admixtures.

### ***3.3. Optical and electron properties of trapping centers and luminescence mechanisms in SCS***

In the previous chapter, we have shown that introduction of isovalent dopants (IVD) to  $A^{II}B^{VI}$  crystals and/or ratio variation of the initial lattice components by choosing an appropriate thermal treatment regime (annealing in an appropriate atmosphere, over-stoichiometric raw material composition, or a combination of these) can be a decisive factor in formation of the intrinsic point defect (IPD) ensemble determining luminescent properties of SCS; the basic structural defect are vacancies in the cation sublattice. Now we will consider additional theoretical and experimental data to give a more detailed description of the nature of luminescence centers and physics of luminescence of this class of scintillators.

#### ***3.3.1. Experimental studies of spectral-kinetic characteristics***

Kinetic characteristics of scintillators based on IVD-doped  $A^{II}B^{VI}$  compounds were studied in the time range from several nanoseconds to tens of milliseconds under photoexcitation by a pulse laser, irradiation by electron beams (energies from 1.5 to 5 MeV, beam current up to 5 kA/cm<sup>2</sup>, X-ray and gamma-irradiation with energies of 0.05–4 MeV. The measurements were carried out in the temperature range 4.2–400 K [50,51].

Analysis of kinetic characteristics of CdS(Te) crystals [52] show that  $\tau$  — the decay time (at the 1/e level) in the luminescence band L-600 is 50–70 ns, and L-730 — about 0.3  $\mu$ s. In the newly obtained scintillators CdS(Hg) (Fig.3.9, curve 1), the predominant decay time is  $\tau = 7$ –10  $\mu$ s both for L-730 and L-980 bands. In infrared scintillators (L-1020) based on CdS(Te)  $\tau = 5$ –7  $\mu$ s [50] (Fig.3.9, curve 2).

In ZnSe(Te) crystals just after the growth, predominant are the components with decay times 0.3–0.5 and 8–10  $\mu\text{s}$ , and the crystals can be divided into two groups in which one or another component is predominant [50] (Fig. 3.10, curves 1,2). After thermal treatment in Zn vapor, the slower component is predominant ( $\tau = 50\text{--}70\ \mu\text{s}$ ). Analysis of the decay character in semi-logarithmical coordinates show that decay plots contain sets of 3–5 components (for different groups of crystals). Characteristic decay times  $\tau_e$  are determined from the expression:

$$\tau_e = \frac{t_2 - t_1}{\ln(I_1/I_2)}. \quad (3.20)$$

From the linear regions (in semi-logarithmical coordinates), the decay times can be found as (Fig.3.11) 0,8  $\mu\text{s}$ ; 4  $\mu\text{s}$ ; 8–10  $\mu\text{s}$ ; 30–50  $\mu\text{s}$ . In (3.20), and correspond to the luminescence intensity at the boundaries of the linear regions; and are the decay times at these points. As luminescence spectra of ZnSe(Te) crystals are of complex character and contain bands L-560-580, L-600, L-640, L-730, it can be assumed that different decay times correspond to different spectral components. Analysis of

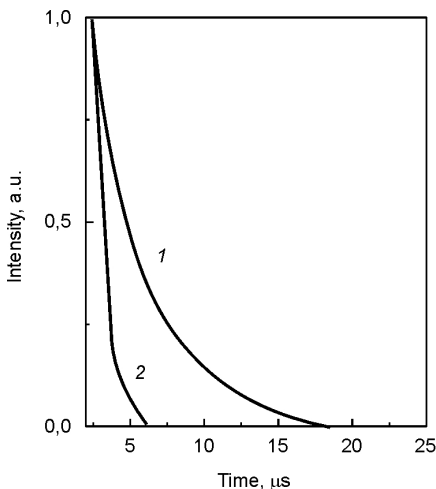


Fig.3.9. Luminescence intensity of CdS(Hg) and CdS(Te) crystals [17] as function of time: 1 — L-1020; 2 — L-730.

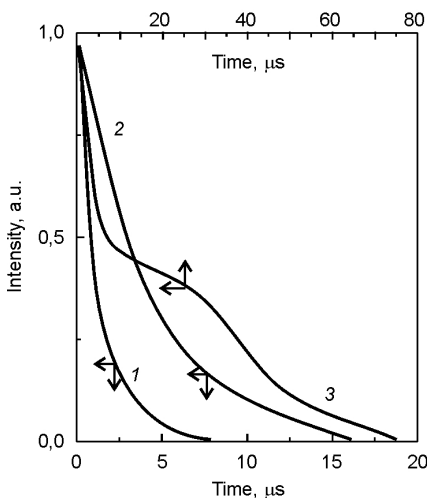


Fig.3.10. Luminescence intensity as function of time for ZnSe(Te) crystals: as-grown (1,2) and after thermal treatment in Zn vapor (3).

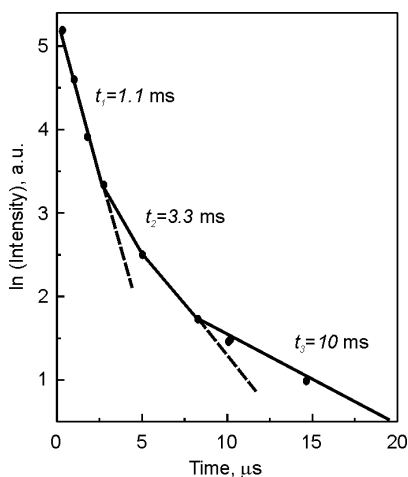


Fig.3.11. Characteristic decay times of ZnSe(Te):  $t_1 = 1 \mu\text{s}$ ,  $t_2 = 3 \mu\text{s}$ ,  $t_3 = 8\text{--}10 \mu\text{s}$ .

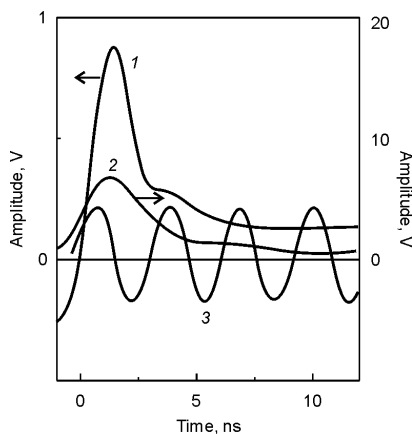


Fig.3.12. Decay time oscillograms: ZnSe(Te) crystal (1), plastic scintillator of SDP type (relative light output = 0.4) (2), and a reference 400 MHz generator (3).

luminescence kinetics in different spectral regions will be presented in Chapter 3.3.3.

Studies of the luminescence components of ZnSe(Te) and CdS(Te) crystals using a Sigma installation has shown the presence of a super-fast component in the nanosecond range (Fig. 3.12 and 3.13). Hence follows that each crystal has at least two luminescence components in the analyzed time range. The fast component in ZnSe(Te) is shorter than 2 ns, and in CdS(Te) — about 20 ns. The slow components are 0.05  $\mu\text{s}$  and 0.2–0.3  $\mu\text{s}$ , respectively. The relative technical light output of the fast component in zinc-selenide based crystals was 0.01, and in cadmium sulfide-based crystals — 0.1 with respect to a reference plastic scintillator (light output of 0.4 universal light output units). Fig.3.14 shows the photosensitivity spectrum of a multi-alkali cathode used in the experiments (curve 1) and luminescence spectra of the plastic scintillator (curve 2) and of ZnSe(Te) crystals (curve 3). It can be seen that spectral matching coefficients of the PMT cathode to the plastic scintillator, ZnSe(Te) and CdS(Te) are, respectively, close to unity, less than 0.2 and about 0.05. Hence it follows that the light flux intensity of the fast component of CdS(Te) is approximately at

the level of plastic scintillators, while for  $\text{ZnSe}(\text{Te})$  this value is by an order of magnitude lower.

Analysis of the fast component of kinetic characteristics of semiconductor scintillators under excitation by radionuclides (Table 3.5, Fig.3.15) has also shown the presence of several time components[50]. With this kind of excitation and data processing procedures [51], the presence of a fast and a slow component of the decay time are observed, and it is possible to observe a fine structure of the “slow” component — (tens, hundreds of nanoseconds) — filled by rapid fluctuations with a period corresponding to the pulse rise front — several nanoseconds (Table 3.5). With other methods of excitation, this structure could not be resolved, probably due to high pumping density. A distinct feature of zinc selenide crystals was the presence of shorter (less than 1 ns, which was comparable to parameters of the measurement circuit) constituents of the fast component. The full decay time of zinc selenide-based crystals is by several orders higher than a similar parameter of cadmium sulfide crystals, which suggests that in  $\text{ZnSe}(\text{Te})$  there are deep carrier trapping centers with large capture cross-section.

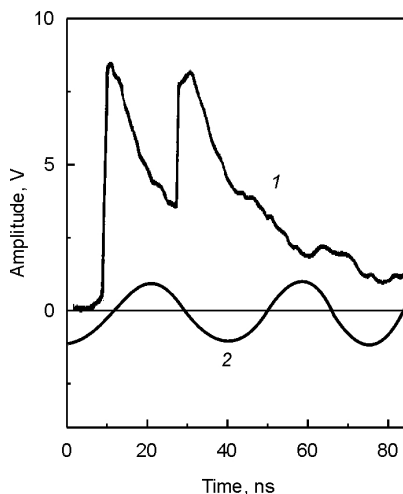


Fig.3.13. Decay time oscillograms:  $\text{ZnSe}(\text{Te})$  crystal (1) and a reference generator 25 MHz (40 ns period) (2).

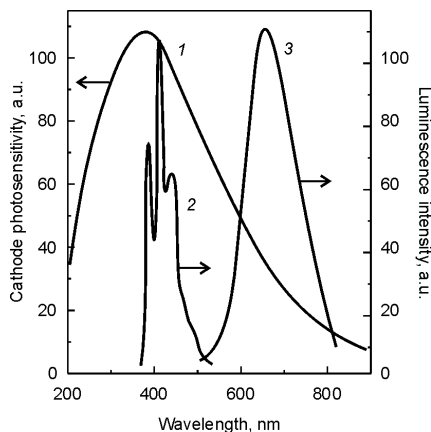


Fig.3.14. Photosensitivity spectrum of a SNFT-8 PMT photocathode (1) and emission spectra of scintillators SDP (2),  $\text{ZnSe}(\text{Te})$  (3).

Table 3.5. Kinetic characteristics of semiconductor scintillators under excitation by radionuclides.

Scintillator	Excitation source, type of particles	Energy, MeV	Characteristic time		
			rise, ns	decay, ns	full decay, $\mu$ s
CdS(Te)	$^{239}\text{Pu-}$	5.15	1.5–2	40–45	1.5–2
	$^{207}\text{Bi-}\beta$	0.975		220–250	4–6
	$^{137}\text{Cs-}\gamma$	0.662	1.5–2		
	$^{60}\text{Co-}\gamma$	1.25			
ZnSe(Te)	$^{239}\text{Pu-}$	5.15	$\leq 1$	$(8-10) \cdot 10^4$	$(4-8) \cdot 10^2$
	$^{207}\text{Bi-}\beta$	0.975	$\leq 1$	$(1.5-2) \cdot 10^5$	$(1-2) \cdot 10^3$
	$^{137}\text{Cs-}\gamma$	0.662			
	$^{60}\text{Co-}\gamma$	1.25			

This will be considered in detail in Chapter 3.3.5 in relationship with experiments on non-linear light absorption.

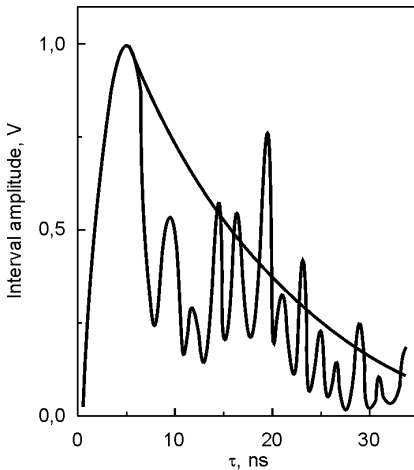


Fig.3.15. Decay time oscillogram for CdS(Te) crystals under excitation by  $^{239}\text{Pu}$  (alpha-particles, energy 5.15 MeV).

As the emission spectrum transformation with time for CdS(Te) crystals has been sufficiently well studied, here we will consider the processes in ZnSe(Te) crystals.

When ZnSe(Te):Zn crystals are excited by fast electrons with pre-threshold energy of 150 keV (pulse current about 1 A /cm<sup>2</sup>,  $\tau = 15$  ns), in the first 20–30 ns an intense peak of cathodoluminescence (CL) is observed, with emission in the “blue” region (maximum at 460–490 nm) with a tail into the 600–640 nm region. This maximum is intensified after 0.5–1  $\mu$ s, and after 10  $\mu$ s the emission energy is transferred to the long-wave (750–830 nm) band. In

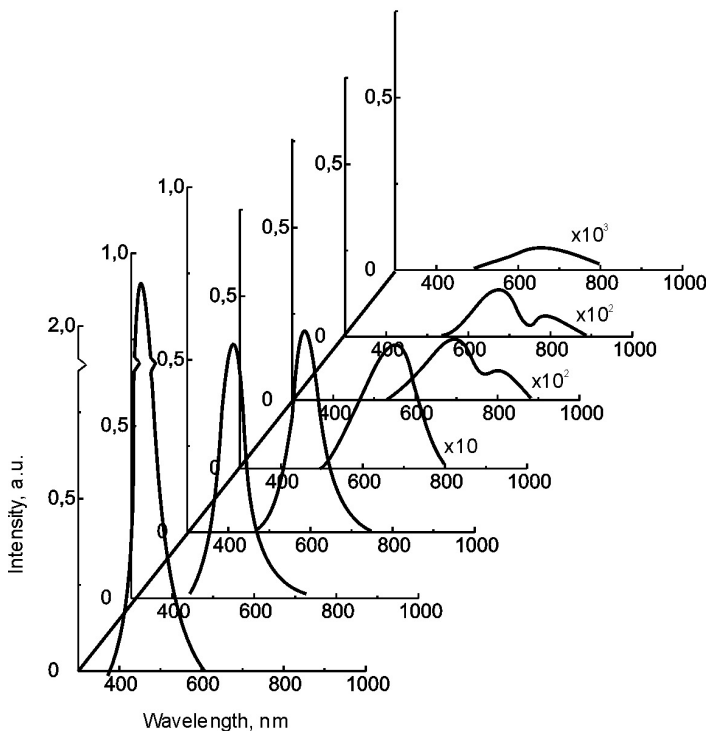


Fig.3.16. Transformation in time of cathodoluminescence spectra (electrode energy 150 keV) of crystals  $\text{ZnSe(Te):Zn}$ : 1 — spectrum at the moment of excitation; 2–7 — delays of 10 ns, 300 ns, 1  $\mu\text{s}$ , 10  $\mu\text{s}$ , 100  $\mu\text{s}$ , 1 ms.

a similar way the photoluminescence spectrum is changed under laser excitation (3.49 eV) (Fig.3.17).

Excitation at room temperature by over-threshold electrons at substantially higher pumping density (250 keV, pulse current 1.5 kA/cm<sup>2</sup>) also leads to a bright “blue” emission (L-477 — 480 nm) with a subsequent shift to the long-wave region (Fig.3.18) [53]. The shifting effect is not observed for undoped zinc selenide crystals. Main parameters of the emission spectra under pulse and stationary excitation are presented in Tables 3.6, 3.7.

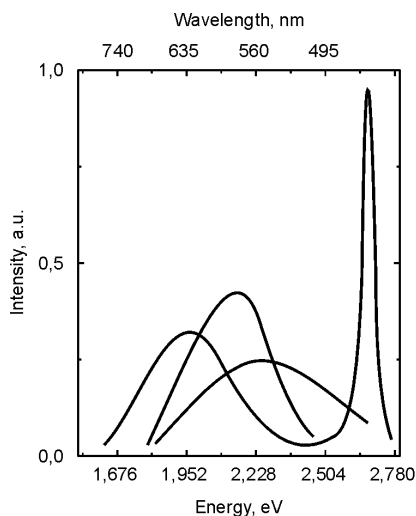


Fig.3.17. Photoluminescence spectra of crystals ZnSe(Te):Zn — delays of 1  $\mu$ s (1) and 10  $\mu$ s (2). Excitation 2.8 eV, 10 ns (3) — stationary excitation (300 K).

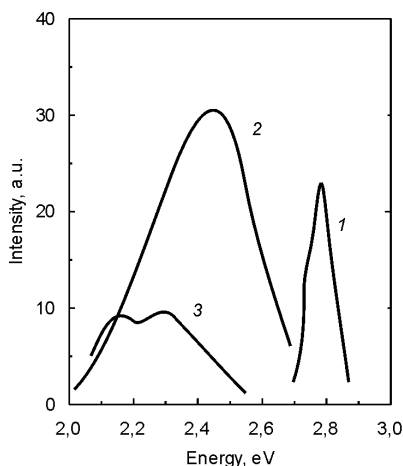


Fig.3.18. Cathodoluminescence spectra of ZnSe(Te) crystals under above-threshold excitation (300 keV): without delay (1), with delay of 60 ns (2) and 450 ns (3).

In Fig. 3.16–3.18 one can see the following characteristic features of ZnSe(Te) emission spectra, which confirm the data of Table 3.6. Under pulse excitation, the half-width is 1.5–2 times larger than under the stationary excitation. For all excitation types with high pumping density, at the moment of excitation predominant is the edge luminescence L-460–490 nm. Its maximum is somewhat shifted depending upon the crystal quality, activator concentration and the type of excitation. In 20–60 ns, the luminescence maximum is shifted to L-600–640, and after 5–10  $\mu$ s — to L-730–840, with intensity decreasing by 2–4 orders of magnitude. The long-wave luminescence bands (L-640 and L-730) are predominant under normal conditions (300 K) and low excitation intensity. They are the main “working” ranges of zinc selenide crystals for detection of isolated particles and gamma-quanta and radiation flux rates from the background level ( $10^{-2}$  mR/hour) to the levels  $10^6$ – $10^8$  times higher. For more detailed studies of kinetics for these bands, we have used intra-zone excitation (energy of 2.33 eV), which excluded the edge luminescence and effects

Table 3.6. Characteristics of luminescence centers under pulse excitation of ZnSe(Te).

Excitation conditions				Decay time at level $I/e$	Emission maximum, nm	Spectrum halfwidth, eV
Type	Energy	Pulse duration	Delay after ex-			
Photo–Nd-laser	3,49	2–3	10 $10^2$ $10^3$	0.27 mon. < 1 $\mu$ s 6	470 564 600	0.14 0.6 0.38
X-ray MIRA-2D	150 keV	10–15	—	60 ns 300 ns 0.6 $\mu$ s 3 $\mu$ s	600 640 720–740	0.21–0.23 0.36–0.4
Cathodo 1 A/cm <sup>2</sup>	150 keV	15	0 10 300 $10^3$ > 5·10 <sup>3</sup>	10 ns 30–50 ns 1–3 $\mu$ s 7–10 $\mu$ s 50–70 $\mu$ s	480 500–540 640 640 740	0.14 0.36 0.3 0.35 > 0.4
1,5 kA/cm <sup>2</sup>	250–300 keV	30	0 60	25–30 ns 450 ns	510–520 580–600	0.20–0.25 0.3
Fast electrons 20 A/cm <sup>2</sup> “Sigma”	450 keV	0.4	< 1 ns	2 ns 0.5 ns	470 640	— —
<sup>207</sup> Bi	975 keV		< 1 ns	1 ns 100 $\mu$ s	470 650–700	— —
Alpha-particles <sup>239</sup> Pu	5.15 MeV		< 1 ns	1 ns 70 $\mu$ s	470 650–700	— —

related to the surface-adjacent layers. As an excitation source, we used the second harmonics of a neodymium laser (532 nm). Fig.3.19 shows luminescence spectra (at 300 K) of crystals ZnSe(Te) after growth, ZnSe(Te):Te (annealed in tellurium) and ZnSe(Te):Zn (annealed in zinc), measured in the moment of excitation and after delays of 1  $\mu$ s and 10  $\mu$ s (curves 1–3, respectively). For better convenience, the



Table 3.7. Characteristics of emission centers under continuous excitation of ZnSe(Te).

Excitation conditions		Temperature, K	Wavelength at the emission maximum, nm	Spectrum half-width, eV
Type	Energy			
Photo-He-Cd laser	2.8 eV	300	467	0.14
			640	0.38
X-ray source REIS-I	20 keV	300	630	0.21–0.29
			730	0.33
	20 keV	80	560	0.18
			630	0.19–0.21
Cathodo-	120–150 keV	300	640	0.19–0.21

spectra have been normalized by amplitude. In Fig.3.20, luminescence spectra are shown for ZnSe(Te):Te and ZnSe(Te):Zn crystals after different time delays normalized to the non-delayed spectrum.

In all the samples studied, predominant is the L-600–630 emission band, with its maximum location in ZnSe(Te):Zn crystals ( $E_m = 1.95\text{--}1.98$  eV) not changing with the delays. In the crystals annealed in anion vapor after growth (in all cases the intrinsic component vapor pressure in annealing was  $(0.5\text{--}1)\cdot 10^5$  Pa, annealing temperature  $950\text{--}1100^\circ\text{C}$ ), the maximum of this band was found at  $2.05\text{--}2.1$  eV, and the delay shifted it to the long-wave region; such behavior is characteristic for the donor-acceptor mechanism [52]. However, in this case there could be a superposition of different components of the L-630 band having different decay times. Crystals ZnSe(Te), ZnSe(Te):Se, ZnSe(Te):Te are also characterized by fast decay with a luminescence delay (Fig.3.20,a), while with ZnSe(Te):Zn crystals the emission intensity increases by 1.5 times after  $1\text{ }\mu\text{s}$  (Fig.3.20, b), returning back to the initial values after  $10\text{ }\mu\text{s}$ . This effect is observed only under intra-zone excitation.

Our studies of the luminescence amplitude time dependence (Fig.3.21) have shown that in ZnSe(Te) crystals there are two predomi-

nant components of the decay time, which can be linearly approximated in a semi-logarithmic scale with characteristic times of 0.3  $\mu\text{s}$  and 8  $\mu\text{s}$ . For ZnSe(Te):Se crystals, a “long” component with  $\tau_c = 120 \mu\text{s}$  is also observed, with its amplitude less than 1% of the initial value. In ZnSe(Te):Zn crystals, the decay constant after the initial rise is 60–80  $\mu\text{s}$ .

A distinguishing feature of the luminescence spectra at 80 K for all these crystals, with exception of ZnSe(Te):Zn, is that the L-540–560 band is predominant, which was also noted in the previous chapter. In ZnSe(Te):Zn crystals no changes are noted at 80 K as compared with the room temperature, except a slight shift (by 0.05 eV) of the maximum of this band in accordance with the band edge shift.

At 4.2 K, the luminescence maximum of the initial sample is shifted from 2.1 eV (L-590) to 1.98 eV (L-630), which is possibly related to a change in intensity ratio of the bands 2.1 eV, 2.05 eV and 1.95 eV (the resulting band is a superposition of these). The decay time for L-605 (2.05 eV) is 0.5  $\mu\text{s}$ , and for L-630 — several microseconds. The luminescence spectrum of all crystals at 4.2 K is slightly shifted in time to the long-wave region (Fig.3.22, a,b)

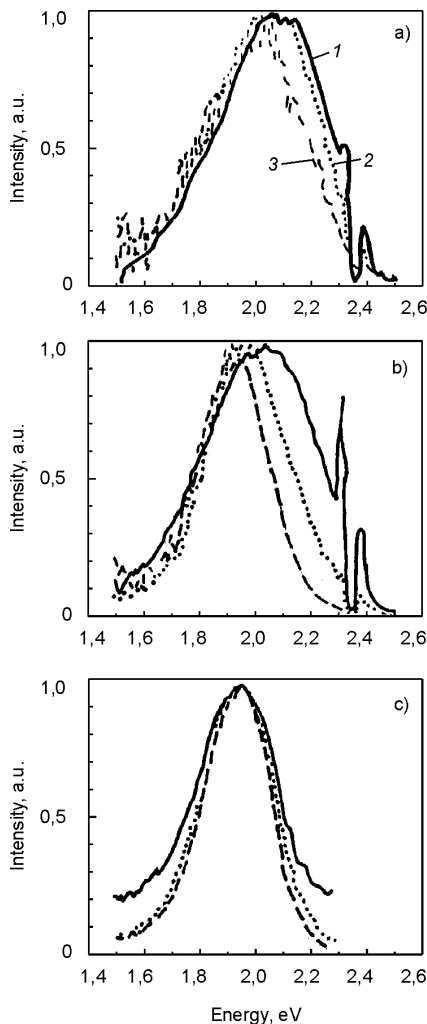


Fig.3.19. Photoluminescence spectra of crystals ZnSe(Te) (a), ZnSe(Te):Te (b) and ZnSe(Te):Zn (c) without delay (1), with delay of 1  $\mu\text{s}$  (2) and with delay of 10  $\mu\text{s}$  (3) with respect to the excitation pulse ( $E_{exc} = 2.33 \text{ eV}$ , 300 K).

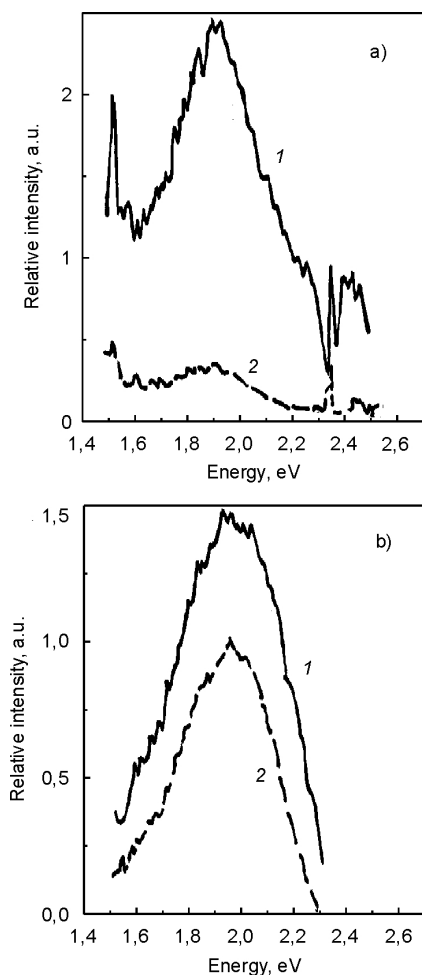


Fig.3.20. Photoluminescence spectra of crystals ZnSe(Te):Te (a) and ZnSe(Te):Zn (b) with delays of 1  $\mu$ s (1) and 10  $\mu$ s (2) normalized to the undelayed spectrum (300 K) ( $E_{exc} = 2.33$  eV).

from 2.00 eV to 1.95–1.98 eV. At 4.2 K, the luminescence kinetics of all annealed samples (Fig.3.23) is almost similar, as well as photoluminescence intensity changes in time. For all annealed samples, after 1  $\mu$ s it becomes 0.8–1.0 with respect to the initial values, while with samples that were not thermally treated it falls by an order of magnitude starting from  $\tau_c \cong 0.5$   $\mu$ s, and with a 50  $\mu$ s delay it is 120–130  $\mu$ s both in initial and annealed samples.

Thus, analysis of the luminescence decay kinetics (4.2 K) for IVP-doped ZnSe crystals shows that under intra-zone excitation (2.33 eV) spectral-kinetic characteristics of all annealed samples are practically similar and are only slightly different from parameters of the initial crystals. At higher temperatures substantial differences are noted for crystals thermally treated in metal or chalcogen vapor. For ZnSe(Te):Zn crystals, photoluminescence kinetics (as well as spectral characteristics) remain essentially unchanged (62  $\mu$ s; 120  $\mu$ s), the other crystals show a predominance of ‘short’ components 0.3  $\mu$ s, 8  $\mu$ s (Fig.3.21). Analysis of the decay kinetics under intra-zone excitation implies that the longest decay time and the highest afterglow level should

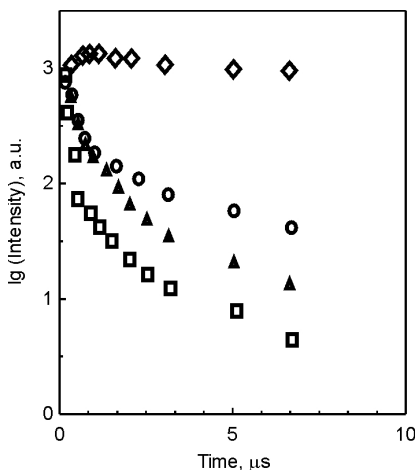


Fig.3.21. Luminescence decay kinetics for crystals ZnSe(Te) (1), ZnSe(Te):Se (2), ZnSe(Te):Te (3), ZnSe(Te):Zn (4) at 300 K ( $E_{exc} = 2.33$  eV).

be observed with ZnSe(Te):Zn, and the minimum values – with the initial crystals. In fact, under excitation beyond the band edge, quite an opposite picture is observed. The afterglow level of the initial ZnSe(Te) crystals and those annealed in chalcogen vapor is 5–15% after 20 ms, while for ZnSe(Te):Zn crystals this value is less than 0.05%, limited only by the accuracy of our measurements. Such difference in kinetics under intra-zone and high-energy excitation is explained by the structure of luminescence centers in zinc selenide-based crystals and by peculiar features of the ra-

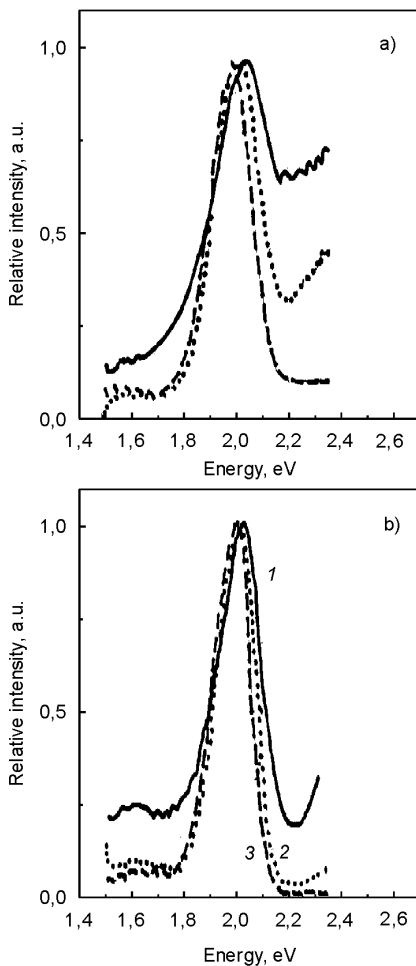


Fig.3.22. Luminescence spectra of crystals ZnSe(Te):Te (a) and ZnSe(Te):Zn (b) without delay (1), with delays of 1  $\mu$ s (2) and 10  $\mu$ s (3) with respect to the excitation pulse (4.2 K) ( $E_{exc} = 2.33$  eV).

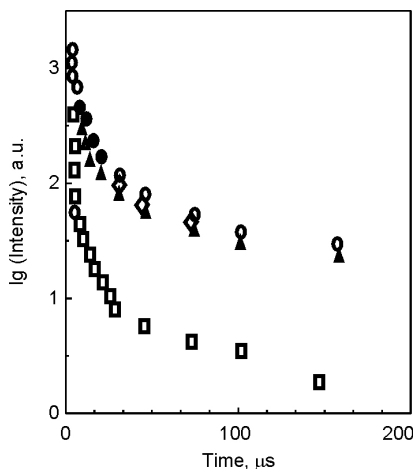


Fig.3.23. Luminescence decay kinetics for crystals ZnSe(Te) (1), ZnSe(Te):Se (2), ZnSe(Te):Te (3), ZnSe(Te):Zn (4) at 4.2 K ( $E_{exc} = 2.33$  eV).

diative recombination mechanism in these crystals.

The above-noted differences in emission spectra upon changes in the flux density of incident particles can be of practical importance in certain application fields, e.g., in uses of X-ray microanalyzers. One of the main conditions for reliable operation of a microanalyzer is correct setting and adjustment of the electron probe (check-up of its position and cross-section shape). For electron probe visualization in X-ray spectral studies, fluorescent properties of the crystal used should ensure a quality image of the probe with clearly outlined boundaries, and its electrical properties (conductivity), which

affect localization of the electron beam on the crystal surface, should guarantee high current stability on the surface, ensuring constant brightness and configuration of the light spot.

Good luminescent properties were found experimentally for zinc selenide activated with isovalent dopants — tellurium or magnesium. In these studies, a MAP-2 X-ray analyzer was used at accelerating voltage of 25 kV and current of  $10^{-6}$  A.

In Table 3.8, the averaged data are presented on cathodoluminescence intensity for zinc selenide crystals doped with isovalent admixtures (Te, Mg), fluorite crystals with an applied film, and ZnS(Ag) crystals, which are generally considered among the best cathodoluminophores for fluorescent screens.

It can be seen that cathodoluminophores based on isovalently doped zinc selenide are markedly different, as for their fluorescent properties, from commonly used luminophores of the fluorite type, as well as from cathodoluminophores based on zinc sulfide (ZnS(Ag)). The cathodoluminescence intensity of ZnSe(Te, Mg) crystals is by several orders higher as compared with fluorite and ZnS(Ag).

Table 3.8. Output parameters of luminophores on the basis of  $A^{II}B^VI$  compounds.

Parameter	Sample			
	Fluorite (with film)	ZnS(Ag)	ZnSe(Mg)	ZnSe(Te)
Activator concentration, mass %	—	0.1	0.5	0.3
Cathodoluminescence intensity, pulses/s	90	5000	60000	250000
Cathodoluminescence intensity normalized to the flux of incident particles, pulses/s	$2.0 \cdot 10^{-11}$	$1.5 \cdot 10^{-9}$	$1.7 \cdot 10^{-8}$	$7.0 \cdot 10^{-8}$
Electron current through the sample, $\mu A$	0.64	0.52	0.55	0.56

This effect could be explained in the following way. It is known that luminescence centers in  $A^{II}B^VI$  compounds are mostly complexes involving point lattice defects. Depending upon their structure, these complexes can serve as centers of both radiative and non-radiative recombination. A peculiar feature of zinc selenide is its ability to quick “self-curing” of the lattice defects formed under bombardment by fast electrons. As a consequence, the effects that accompany the formation of such defects (e.g., cathodoluminescence) are observed only at low temperatures and disappear above 150 K. Under normal conditions (300 K), generation and annihilation of defects proceed simultaneously, and the rate of the latter process can be on the scale of several nanoseconds. It can be assumed that introduction of an isovalent activator to ZnSe ensures formation of stable complexes playing the role of emission centers; effects of the quenching centers are negligibly small due to their short lifetime in the isovalently doped ZnSe.

The highest cathodoluminescence intensity is observed at isovalent dopant concentrations of  $5 \cdot 10^{-2} - 5 \cdot 10^{-1}$  mass %.

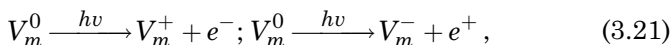
At dopant concentrations outside these limits, the cathodoluminescence intensity becomes comparable to that observed with other cathodoluminophores (Table 3.8).

Thus, the use of zinc selenide activated with isovalent dopants (tellurium or magnesium) allows substantial improvement of the screen brightness as compared with ZnS(Ag), as well as the instrument adjustment, due to clear fixation of the spot and good conductivity. This is

important when working with low currents (analysis of low-melting compounds, studies of chemical shifts of X-ray lines), i.e. in all cases where higher accuracy is required. Moreover, the use of such screens simplifies the experimental procedure and reduces the required time. Such fluorescent screens are multi-purpose, relatively easy in manufacturing (wastes of industrial zinc selenide production can be used as raw material) and can be successfully used in X-ray spectral studies.

### ***3.3.2. Theoretical analysis of radiative recombination center formation upon IVD introduction.***

A neutral vacancy in a semiconductor compound can be considered as a certain quasi-atom of the same valence as the substituted lattice atom, i.e., as a special kind of isoelectronic defects [3,54]. Its ionization can be described by reactions that accompany the radiative recombination:



where  $V_m^0$ ,  $V_m^+$ ,  $V_m^-$  are neutral and charged states of the center;  $e^-$  and  $e^+$  are free electron and hole, respectively.

As the main role in formation of radiative recombination centers in SCS is played by IPD of the crystal lattice [4–6, 55–56], amphoteric nature of the luminescent centers (i.e., donor-acceptor properties of the IVD multi-charge character) is an obvious consequence of (3.21) [6, 54]. Re-charging described by (3.21) can occur for IVD atoms in general and, what is important, for complex centers as a whole, which are, in fact, donor-acceptor pairs. Such pairs in, e.g., ZnSe(Te) crystals are complexes that include  $V_{Zn}$  located (according to ESR and ODMR data [1,8]), in the vicinity of tellurium atom, and a shallow donor  $D_1$  (captured from electrocompensation considerations), which can be in different crystallographic positions with respect to  $[TeV_{Zn}]$  [18, 54]. The  $[V_{Zn}Te D_1]$  complex ( $M$ -center [3]), in which the role of donor is most probably played by  $Zn_1$ , was considered by many authors [1–4]. It has been generally accepted that it is a highly efficient center of radiative recombination; recent studies have shown that this center forms the working “red” luminescence band L-640 in zinc selenide [4, 57, 58], with emission efficiency comparable or superior (at room temperature) to the conversion efficiency of conventional alkali halide scintillators [4, 59].

We continue our theoretical consideration of luminescent properties of IVD-doped SCS taking ZnSe(Te) crystals as an example, as for this material substantial amount of experimental and calculation data is available. Multi-charge character of amphoteric centers is essential in all phenomena that are accompanied by re-charging of the center. In particular, it plays a decisive role in formation of spectral-kinetic characteristics of radiative recombination centers.

Let us consider a scheme describing electron transitions in a broad-gap ZnSe with an amphoteric dopant forming two levels in the band gap – a donor level and an acceptor level (Fig.3.24) [60]. Kinetics of charge carrier recombination can be described by an equation system:

$$dn/dt = g - C_{n0}N^0n - C_{n1}N^+n - \gamma np, \quad (3.22)$$

$$dN^-/dt = C_{n0}N^0n - C_{p1}N^-p + rN^0 + f_2N^0, \quad (3.23)$$

$$dN^+/dt = C_{p0}N^0p - C_{p1}N^+n - (gN^+ + f_1N^+), \quad (3.24)$$

$$N^- + n = N^+ + p, \quad (3.25)$$

$$N = N^0 + N^- + N^+, \quad (3.26)$$

where  $N^0$ ,  $N^-$ ,  $N^+$  are concentrations of neutral, negatively and positively charged admixture centers, respectively;  $N$  is the total concentration of amphoteric centers;  $n$  is concentration of free electrons, and  $p$  — of free holes;  $g$  is generation rate of electron-hole pairs;  $C_{n0}$ ,  $C_{n1}$  are recombination coefficients of free electrons on neutral and positively charged centers, respectively;  $r$ ,  $f_1$  are probabilities of thermal and infra-red (IR) neutralization of a  $N^+$ -center due to electron transitions from the valence band to the donor level of the amphoteric center, respectively;  $r$ ,  $f_2$  are probabilities of thermal and IR excitation of electrons from the valence band to the acceptor level of the amphoteric center, respectively;  $\gamma$  is coefficient of electron-hole recombination.

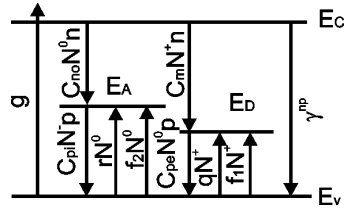


Fig.3.24. A scheme of electron transitions in the presence of an amphoteric center. Recombinations at intrinsic excitation.



Let us introduce dimensionless values  $X_1 = n/N$ ,  $X_2 = N^-/N$ ,  $X_3 = N^+/N$ ,  $A = C_{n1}/C_{n0}$ ,  $B = C_{p0}/C_{n0}$ ,  $D = C_{p1}/C_{n0}$ ,  $G = g/C_{n0}N$ ,  $T = C_{n0}Nt$ ,  $Q = g/C_{n0}$ ,  $R = r/C_{n0}N$ ,  $\Gamma = \gamma/C_{n0}N$ ,  $F_1 = f_1/C_{n0}N$ ,  $F_2 = f_2/C_{n0}N$ .

Then, accounting for (3.35) and (3.36), we obtain the following system of kinetic equations:

$$dX_1/dT = G - X_1(1 - X_2 - X_3) - AX_1X_3 - \Gamma X_1(X_1 + X_2 - X_3), \quad (3.27)$$

$$dX_2/dT = X_1(1 - X_2 - X_3) - DX_2(X_1 + X_2 - X_3) + (R + F_2)(1 - X_2 - X_3), \quad (3.28)$$

$$dX_3/dT = B_1(1 - X_2 - X_3)(X_1 + X_2 - X_3) - AX_1X_3 - (Q + F_1)X_3. \quad (3.29)$$

This equation system was solved numerically [54, 55, 56] by the method of steepest descent. Now we will consider some results of these calculations.

The luminescence decay kinetics, with intensity proportional to  $X_1(1 - X_2 - X_3)$ , is described by equations (3.27)–(3.29) upon conditions

of  $\Gamma = P = F_1 = F_2 = 0$ . A peculiar feature is intensification of the afterglow after switching off the illumination, which is possible if there is a substantial disbalance between the number of admixture centers in positively and negatively charged states. For this disbalance, we assumed  $C_{p0} \gg C_{n0}$  (positively charged centers are predominant).

In Fig.3.25, results of numerical calculations are presented of relaxation  $X_1(T)$ ,  $X_2(T)$ ,  $X_3(T)$  upon removal of parameter  $G$  (excitation switched off). It can be seen that relative concentrations of free electrons  $X_1$  (curves 1, 4) and bonded holes  $X_3$  (curves 3, 6) are monotonously decreasing with time, while in the case of bonded electrons  $X_2$  (curves 2,5) show a maximum.

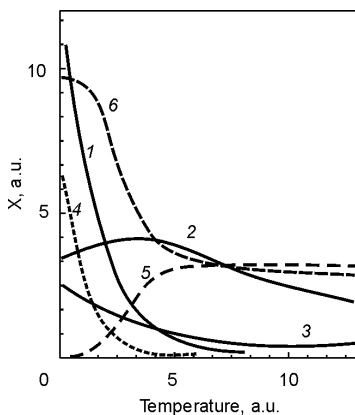


Fig.3.25. Relaxation of parameter  $x_i$  at  $G = 0$  from stationary values ( $G = 8$ ,  $Q = 6.2$ ). Curves 1 and 4 show  $x_1(T)$ , 2 and 5 —  $x_2(T)$ , 3 and 6 —  $x_3(T)$ . Solid lines obtained at  $A=B=D=1$ , dashed lines — at  $A=D=1$ ,  $B=150$ .

Curves  $X_1$  for different values of  $B$  are qualitatively similar, while pairs of other curves ( $X_2, X_3$ ) have substantial differences reflecting anomalies in the luminescence decays (Fig.3.26). Such character of the decay kinetics under intra-zone excitation ( $T = 300$  K) is observed for ZnSe(Te):Zn crystals (Fig.3.21), where luminescence intensity in  $1\ \mu\text{s}$  after stopping the excitation is increased by 1.5 times, and returns to the initial state only in  $10\ \mu\text{s}$  with subsequent monotonous decreasing. At  $4.2$  K (Fig.3.23) and under inter-zone excitation such anomalies are not observed for all types of ZnSe(Te) crystals. In many cases, upon switching off the excitation ( $G = 0$ ) luminescence intensity falls, then increases again, and then falls out finally. When higher excitation  $G$  is switched off, these processes are expanded in time. When parameter  $Q$  rises, the luminescence decay anomalies are smoothened (curve 1,  $Q = 30$ ), so, at  $Q > 100$  the decay is monotonous.

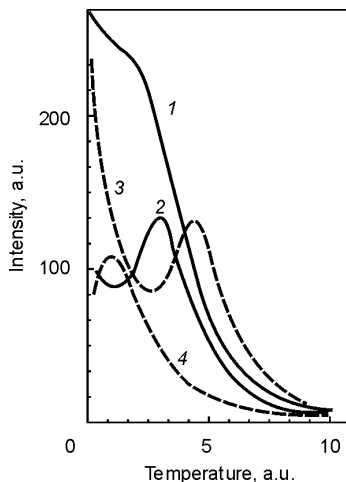


Fig.3.26. Luminescence decay kinetics  $I_{lum} = x_1(1-x_2-x_3)$  at  $A=D=1$ ,  $B=150$  for different levels of initial excitation and thermal neutralization probability of the donor state of an amphoteric center: 1 —  $G=8$ ,  $Q=30$ ; 2 —  $G=8$ ,  $Q=6.2$ ; 3 —  $G=30$ ,  $Q=6.2$ ; 4 —  $G=1$ ,  $Q=6.2$ .

### 3.3.3. Photoluminescence decay kinetics of ZnSe(Te)-based scintillators

The anomalies considered in Chapter 3.3.2 were observed in radioluminescence kinetics studies at high excitation levels. In [4], such radioluminescence kinetics was explained in terms of not less three decay processes characterized by the times  $\tau_{0.5}$ : 1–1.5, 7–10, and  $>50\ \mu\text{s}$ . It was noted that the nature of luminescence centers responsible for these components required further studies. In [56], the observed features of zinc selenide radioluminescence were explained by amphoteric properties of radiative recombination centers  $[V_{Zn}TeD_l]$ , characteristics of which could be determined by the amphoteric nature of  $V_{Zn}$  as a

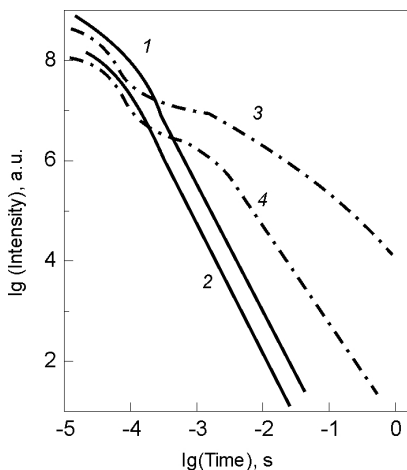


Fig.3.27. X-ray luminescence decay kinetics for crystals ZnSe(Te):Zn: 1 — L-630, 2 — L-730, and crystals ZnSe(Te): 3 — L-630, 4 — L-730 ( $E_{exc} = 150$  eV).

multi-charge center ( $V_{Zn}^+$ ,  $V_{Zn}^0$ ,  $V_{Zn}^-$ ) with two levels: the acceptor level ( $0, -e$ ) and donor level ( $0, +e$ ), as it was assumed in our calculations.

Under inter-zone excitation, time dependences of the decay for ZnSe(Te):Zn crystals are of similar hyperbolic character with the exponents close to 2 and are distinguished only by the scaling factor (Fig.3.27) [6, 61]. Similarity in the decay character of curves 1,2 suggests a predominant contribution of one emission center. A bimolecular decay kinetics implies, accounting for the time stability of spectra, a recombination mechanism of radioluminescence ( $E_{exc} = 150$  keV), i.e., recombination of a carrier localized on the luminescence center with a free carrier of

another sign [4–6,62].

In ZnSe(Te) crystals after growth or thermal treatment in chalcogen vapor, the decay time range in different spectral regions (inter-zone excitation,  $E_e = 150$  keV) is 0.1–10 ms, and radioluminescence decay follows a complex law described by a sum of several exponents and hyperboles. The decay character (Fig.3.27, curves 3,4) in different spectral ranges is essentially different, which is in agreement with thermoluminescence and temperature quenching data suggesting that in these crystals several types of deep traps can be present, and radiative recombination centers can be of different nature.

Depending on the experiment conditions, one and the same radiative recombination center can affect the measured characteristics in different ways. E.g., under excitation with energy higher than the band gap width ( $E_e = 3.68$  eV) of ZnSe(Te):Zn crystals, the decay kinetics is of hyperbolic character (Fig.3.28) [6], and predominant is the component of several microseconds. In the same crystals, under inter-zone photoexcitation ( $E_e = 2.34$  eV) decay is exponential with decay times of 100–120  $\mu$ s (general-

ized characteristics of luminescent properties of ZnSe(Te) are presented in Tables 3.6, 3.7).

The observed changes in spectral-kinetic characteristics of ZnSe(Te) crystals are in agreement with specific conditions (3.22)–(3.26) and re-charging kinetics of the amphoteric centers (Fig.3.24).

In the absence of strong excitation, in semiconductors of  $n$ -type  $N \cong N^-$  predominant is the radiative recombination channel due to acceptor centers, and the “red” luminescence intensity has the form

$$I_A = C_{n0} N_n^0. \quad (3.30)$$

Under strong excitation, concentration of non-equilibrium carriers is much higher than that of equilibrium ones. Accounting for differences in the electron and hole capture cross-sections, this lead to predominance of  $N^+$  centers and, consequently, of radiation recombination due to donor centers (“blue” luminescence):

$$I_D = C_{n1} N_n^+. \quad (3.31)$$

In our case, such centers are isovalent tellurium atoms.

Neglecting other recombination channels, the quantum yield of channel I (“red” luminescence) is:

$$\eta_k = I_A / (I_A + I_D) = (1 + C_{n1} N_n^+ / C_{n0} N_n^0)^{-1}, \quad (3.42)$$

whence the  $\eta_k$  dependence upon pumping intensity is linear provided  $C_{n1} N_n^+ \ll C_{n0} N_n^0$ . A criterion of strong excitation is violation of this inequality. It is clear from Fig.3.29 that deviation of L-640 from linearity is observed when pumping intensity  $\Phi \geq 2 \cdot 10^{24}$  photons/cm<sup>2</sup>, and in this intensity range “blue” luminescence becomes predominant. The decay kinetics is determined by  $N^0(t)$ . At the first

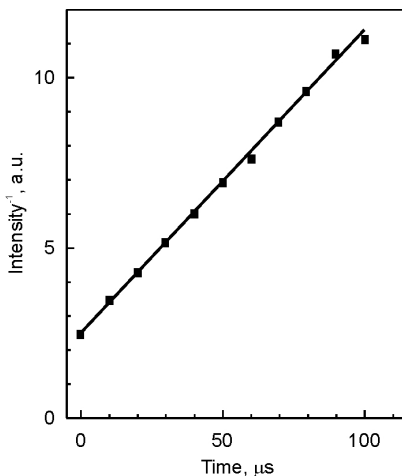


Fig.3.28. Kinetics of L-640 photoluminescence ( $E_{exc} = 3.68$  eV) for crystals ZnSe(Te):Zn at 300 K.

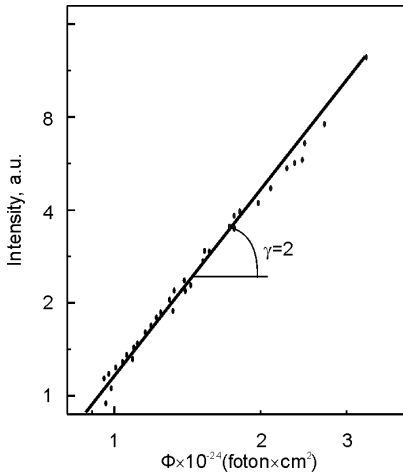


Fig.3.29. L-630 intensity as function of excitation intensity ( $E_{exc} = 2.34$  eV).

stage  $n(t) \cong p(t)$ , and the degree of re-charging of the centers does not depend on time; luminescence decays exponentially, and decay time changes as

$$\tau_1 = (C_{n0}N_{\infty}^0 + C_{n1}N_{\infty}^+)^{-1}. \quad (3.33)$$

At the second stage,  $n = (n_0 + n(t)) > p(t)$ , where  $n_0$  is the concentration of equilibrium carriers,  $N^0$  is increased due to  $(N_n^+)$  recombination,  $\eta$  is decreased, and  $I_A(t)$  dependence has a complex character,  $\tau_2 > \tau_1$ .

At the third stage  $n \cong n_0$ ,  $N^+ \ll N^0$ , and decay is exponential:

$$\tau_3 \cong (C_{n0}n_0)^{-1}. \quad (3.34)$$

As follows from (3.33), (3.34), relaxation times  $\tau$  for ZnSe(Te) should be substantially decreased at higher  $n_0$ . However, as shown by our studies, these conditions for the L-640 band are fulfilled only up to concentrations  $n_0 \leq 2 \cdot 10^{13} - 5 \cdot 10^{14} \text{ cm}^{-3}$ , while at  $n_0 \sim 10^{15} - 10^{16} \text{ cm}^{-3}$  experimentally measured L-640 decay times are 50–100  $\mu\text{s}$ , which is by an order of magnitude higher than the calculated values. (It should be noted, however, that low-resistivity crystals show the lowest afterglow levels among different kinds of ZnSe(Te) crystals). Such ambiguity of  $\tau(n_0)$  dependence had been observed for other low-resistivity  $A^{II}B^{VI}$  crystals [8, 9] and is explained by changes in the charged state  $r$  of a center (which, in principle, can be a double-charged acceptor —  $V_M$ ) from  $r^-$  to  $r^{2-}$  when the Fermi level is moved sufficiently close to the conductivity band edge. In this case, recombination of non-equilibrium electrons (after the capture of a hole) will occur to the  $r^-$  center, i.e., in a repulsive Coulomb field, leading to a sharp increase in  $\tau$ . Because of this, as well as because of specifics of mutual position of shallow levels with  $E_a^i = 0.02 - 0.13$  eV ( $Zn_i$ ) and the adjacent (but lower) Fermi level (which creates optimum conditions for “freezing” of non-equilibrium carriers), it seems essentially impossible to reach  $\tau < 50 - 100 \mu\text{s}$  values for the L-640 band.

Experimental verification of these assumptions have demonstrated one more interesting property of **ZnSe(Te)**: provided the concentrations  $n_0 > 10^{17} - 10^{18} \text{ cm}^{-3}$  are reached ( $n_0$  estimates for different **ZnSe(Te)** samples were made from the values of absorption due to carriers in the IR range), it is possible to obtain a scintillator with  $c \tau \approx 1 - 3 \mu\text{s}$  with the working band maximum shifted from L-640 to L-590 and somewhat lower conversion efficiency. The change of the relaxation channel is possibly related to formation of an admixture sub-band (merging of  $\text{Zn}_i$  levels, very high concentration due to overlapping of wave functions). In this case, the Fermi level is not below  $E_a^i$  (i.e., the “freezing” mechanism is not effective), and kinetics in **ZnSe(Te)** crystals of ultra-low resistivity with L-590 as the main band (as well as samples of high resistivity) is determined only by concentration dependence  $\tau \sim n_0^{-1}$  (as distinct from the latter, they are characterized by very low afterglow level).

### 3.3.4. *Parameters of emission centers in ZnSe(Te) crystals as studied by spectroscopic and thermoluminescent methods*

Behavior of the main L-640 band of a **ZnSe(Te)** scintillator in terms of parameters  $R$  and  $Q$  (3.27)–(3.29) can be expressed as

$$R = R_0 \exp(-\varepsilon_1/KT), \quad (3.35)$$

$$Q = Q_0 \exp(-\varepsilon_{21}/KT). \quad (3.36)$$

We put the depth of the acceptor and donor levels as  $\varepsilon_1 = E_a - E_v = 0.5 \text{ eV}$  and  $\varepsilon_2 = E_d - E_v = 0.1 \text{ eV}$ , respectively. Solving the system (3.37)–(3.39) for the stationary case ( $dx_i/dT = 0$ ) at  $F_1 = F_2 = 0$  [55], we determine the kinetic parameters from temperature plots of the stationary luminescence intensity for different excitation levels  $G$ . Results for  $B = 1$  are shown in Fig.3.30. It can be seen that all the plots have maximums, which are smoothened with higher  $G$ .

Certain features characteristic for the discussed theoretical plots were found experimentally. E.g., in [63] a temperature dependence was obtained for the intensity of “blue” and “red” luminescence of **ZnSe:Co**. In the temperature range  $270 \leq T \leq 300$  the “red” luminescence is intensified, and the “blue” luminescence is quenched. After a maximum close to 880 K, the “red” luminescence intensity is decreased.

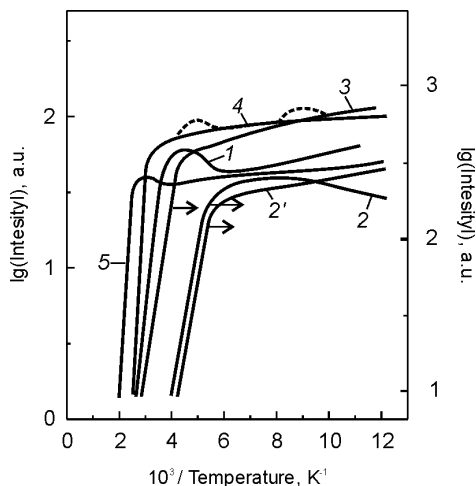


Fig.3.30. Temperature dependences of the stationary luminescence intensity at  $A=B=D=1$ ,  $\Gamma=0.5$  and different excitation levels  $G$ : 1 – 1; 2 – 5; 3 – 50.

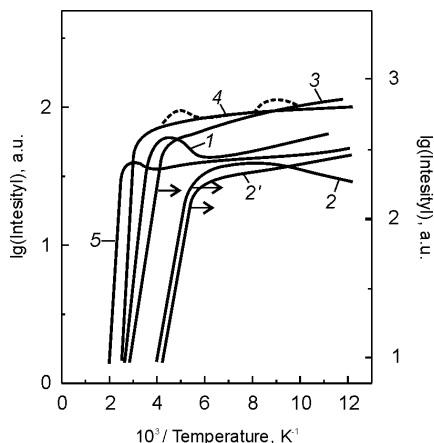


Fig.3.31. Radioluminescence thermal quenching curves for crystals ZnSe (1,2), ZnSe:Zn (2'), ZnSe(Te) (3,4), ZnSe(Te):Zn (5). Curves 1,3,5 correspond to L-630, 2,2' — L-560, 4 — L-730.

We have also observed similar features on the luminescence thermal quenching (LTQ) plots for ZnSe and ZnSe(Te) crystals (Fig.3.31). The intensity and temperature position of the local maximums on LTQ plots are dependent upon the presence of IVD, post-growth treatment regime and the level of excitation [4, 6]. L-630 band plots (1,3,5) in the inflection region show local maximums; in the case of ZnSe(Te):Zn crystals, both temperature position of the ascents on LTQ plots and the character of its final decay in the high-temperature region ( $T > 350$  K) are an evidence of higher thermal stability of radiative recombination centers in this material as compared with other modifications of the crystals studied. Such luminescent properties of ZnSe(Te):Zn are in agreement with data presented in Chapter 3.1 on high physico-chemical thermal stability of  $[V_{Zn}TeZn_i]$  centers. In addition to qualitative results, from the slope of LTQ plots in high-temperature regions the values were calculated of thermal activation energy  $E_T$  of the corresponding in-

intermediary trapping levels: for the L-560 band — 0.24 eV; L-630 (L-640) — 0.62–0.65 eV for ZnSe and 0.65–0.70 eV for ZnSe(Te):Zn;  $E_T$  for L-730 was 0.8–1 eV.

Similar results were obtained for activation energies  $E_a$  of the intermediary trapping centers in zinc selenide crystals from experimental thermoluminescence plots [6]. As it is clear from Figs.3.32, 3.33, upon similar conditions of preliminary annealing in vapor of intrinsic components and the excitation dose, the presence of IVD increases the concentration of IPD of different types by several orders

of magnitude. Data on activation energies  $E_a$  of traps and intensity ratio of thermoluminescence peaks for different ZnSe-based crystals

Table 3.9. Relative luminescence intensity at thermoluminescence (TL) peaks in ZnSe-based crystals

Material	Activation energy for TL peaks, eV			
	0.13	0.29	0.41	$\geq 0.6$
	Luminescence intensity, relative units*			
ZnSe	0,1	0,55	0,2	—
ZnSe:Zn	1	—	5	$\sim 1$
ZnSe:Se	0,1	0,3	—	0,1*
ZnSe(Te):Zn	—	—	—	—
ZnSe(Te):Se	3,5	2	2*	1,5*
ZnSe(Te):Te	7	2.5	0.5*	
ZnSe(Te)	40	5	30*	3*

\* TL peaks marked by \* are in L-730 band; the others – in L-640.

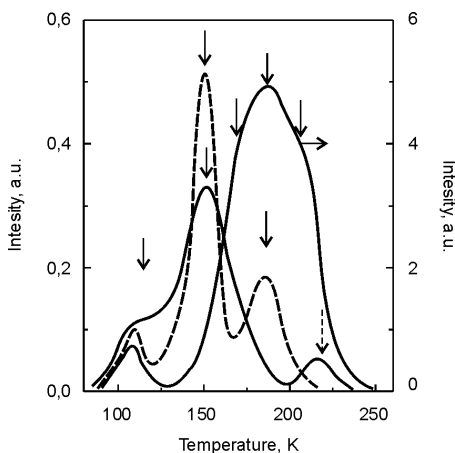


Fig.3.32. Thermoluminescence curves for crystals ZnSe (1), ZnSe:Zn (2), ZnSe:Se (3). The exposure dose of X-ray radiation is  $3 \cdot 10^{-3}$  A/kg. Solid lines: L-630; dashed lines — L-730.



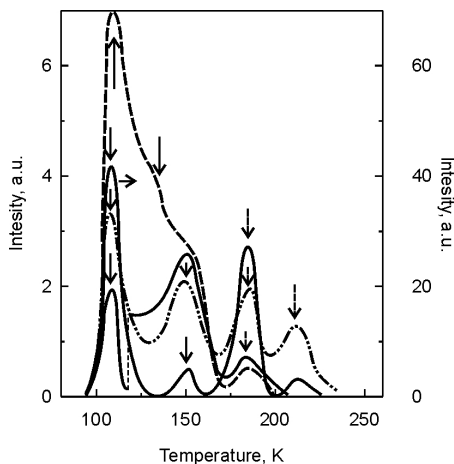


Fig.3.33. Thermoluminescence curves for crystals ZnSe(Te) (1); ZnSe(Te) after annealing in vacuum (2), in Se vapor (3) and in Te vapor (4). Intensity peaks ratio on thermoluminescence curves in Figs.3.32 and 3.33 is the same; solid lines – L-630, dashed lines — L-730.

are presented in Table 3.9. Thermal ionization of traps leads to thermoluminescence peaks with two main channels of radiative recombination: at  $E_a < 0.3$  eV, the predominant band in thermoluminescence spectra is L-640, at  $E_a > 0.4$ – $0.5$  eV — L-730. For ZnSe(Te) crystals annealed in zinc, no thermoluminescence peaks were observed at X-ray exposition doses up to  $8 \cdot 10^{-2}$  A/kg ( $U_a \leq 40$  kV). Accounting for the highest (for this type of crystals) intensity of the main band L-640 and low afterglow level ( $< 0.05\%$  after 1–5 ms), it could be concluded that  $[V_{Zn}TeZn_i]$  centers were predominant, and other intermediary trapping centers were largely degraded in this

scintillator.

It should be specially noted that, because of practically complete suppression by  $[V_{Zn}TeZn_i]$  complex of other radiative recombination centers, only ZnSe(Te):Zn crystals showed time stability of the L-640 band maximum position, and slight evolution of its shape is mainly due to a more prolonged kinetics as compared with other bands (Tables 3.6, 3.7).

### 3.3.5. Methods of two-photon spectroscopy for determination of parameters of deep centers in ZnSe(Te)

Considering possible relaxation channels of excited channels in ZnSe(Te) crystals, we accounted for both donor and acceptor nature of the amphoteric intermediary trapping centers. However, the question of their localization inside the band and energy of the unperturbed state remained not fully understood. Information on

the type of predominant emission centers (donor, acceptor), especially of those controlling the main L-640 band, as well as data on characteristic parameters (energy position  $E_M$ , concentration  $N_M$ , cross-section of photoionization  $\sigma_{pi}$  and photoneutralization  $\sigma_{pn}$ , photoneutralization edge energy  $E_{pn} \approx E_d - E_{pi}$ , etc.) were obtained from studies of photoinduced absorption (PIA) of light through deep centers (the method of laser modulation of two-stage absorption was used) [17, 64]. As a result of studies of kinetic light-intensity dependences of the non-linear absorption coefficient, energy processes of two-stage absorption in ZnSe(Te) crystals with variable composition of predominant IPD (by annealing in Zn, Se, Te and other media, growth of non-stoichiometric samples with properties as given in Table 3.4), we have determined the roles and parameters of many centers (complexes). Among those, for IVD-doped zinc selenide the most characteristic are deep centers (DC) based on  $V_{Zn}$  with the depth of the non-excited state  $E_M$ : 1.1–1.2 eV ( $E_{pn} = 1.45$  eV;  $\sigma_{pi} = 0.2 \cdot 10^{-15}$  cm<sup>2</sup>;  $N_M = 10^{14}$  cm<sup>-3</sup>); 0.6–0.7 eV ( $E_{pn} = 2.15$  eV;  $\sigma_{pi} = (0.6-1) \cdot 10^{-16}$  cm<sup>2</sup>;  $\sigma_{pi} \approx 3 \cdot 10^{-16}$  cm<sup>2</sup>;  $N_M > 10^{15}$  cm<sup>-3</sup> (in this case,  $N_M$  is essentially dependent upon Te concentration in ZnSe and thermal treatment regimes); 0.3–0.4 eV ( $E_{pn} = 2.21-2.25$  eV;  $\sigma_{pi} = (6-8) \cdot 10^{-17}$  cm<sup>2</sup>;  $N_M \approx 8 \cdot 10^{15}$  cm<sup>-3</sup>). It will be shown below that radiative recombination centers in ZnSe(Te) are of predominantly acceptor nature and are located in the lower part of the band gap, which is in agreement with data of LTQ, TSL and physico-chemical studies of this material [4–6].

The deep centers under study are formed by the introduced Te atoms, which gives rise to short-range forces localized at inter-atom distances. These forces are related to decreased dielectric permittivity in the vicinity of an admixture center and different charge of the dopant atom nucleus. Such a model (so-called Lukovski model) [64] involves the Schroedinger equation with attracting  $d$ -potential values determining the depth of the ground state  $E_i$ . In this case

$$\sigma(\hbar\omega) \sim \frac{(\hbar\omega - E_D)^{3/2}}{(\hbar\omega)^3}. \quad (3.37)$$

Account for Coulomb interaction reflecting the charge state of the dopant center [65] leads to the expression

$$\sigma \sim \frac{2[e^4]\eta^3(\eta^2 + \beta)(1 + \beta)}{\left[1 - \exp\left(-\frac{2\pi\eta}{\sqrt{\beta}}\right)\right]}, \quad (3.38)$$

$\eta = Z_e \sqrt{E_0/E_i}$ , where  $Z_e$  is the admixture center charge after ionization,  $E_0 = -\frac{me^4}{2\varepsilon^2\eta^2}$  is the bond energy of a single-charged hydrogen-like admixture center,  $m$  is the effective mass,  $\beta = \left(\frac{\hbar\omega}{E_1} - 1\right)$ ,  $e$  is the base of natural logarithms.

In the Lukovski model approximation [17], we made calculations of the spectral dependence of the induced absorption coefficient  $\Delta\alpha$  in comparison with experimental data (Fig.3.34, curve 1). The results

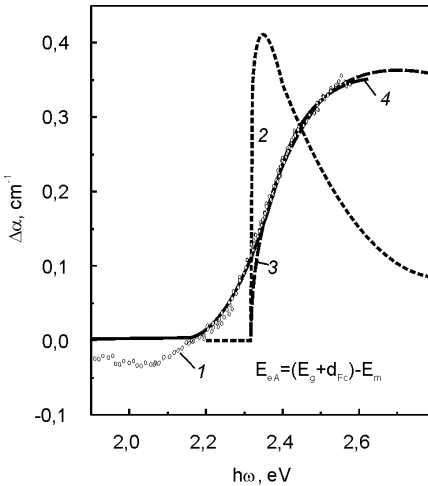


Fig.3.34. Experimental (at 80 K, 1, points) and theoretically calculated plots for induced absorption coefficient: 2,3 – Lukovsky model for donor and acceptor dopants, respectively; 4 – model accounting for electron-phonon interaction for acceptor centers [17].

obtained show that that the acceptor center model (Fig.3.34, curve 3) in the high-energy region correlates with the experiment, while the donor center model (Fig.3.34, curve 2) yield essentially different results. Thus, our assumption that DC in ZnSe(Te) are predominantly of acceptor nature has been confirmed. Differences between theoretical and experimental results in the low-energy range can be due to limitations of the Lukovski model, which does not account for electron-phonon interaction processes.

It was noted in [3, 4] that introduction of IVD substantially affects the formation of the lattice point defect ensemble, which, in turn, requires accounting for electron-phonon

interaction with atoms of the nearest surroundings. Account for such interaction for DC was made in [66]: the Kopylov-Pikhtin formula describing these processes has the form

$$\sigma(\hbar\omega) = \frac{const}{\hbar\omega} \frac{1}{(\pi\theta_1)^{1/2}} \int_1^\infty e^{-\frac{(x-y_1)^2}{\theta_1}} \frac{(x-1)^{1/2}}{x^2} dx, \quad (3.39)$$

where  $y_1 = \frac{\hbar\omega - E_0 + \varepsilon}{\varepsilon}$ ,  $\varepsilon = \frac{m_1^*}{m^*} E_1$ ,  $\theta_1 = \left( \frac{a\hbar\Omega}{\varepsilon} \right)^2 \text{cth} \frac{\hbar\Omega}{2KT}$ ,  $\hbar\omega$  is the energy of absorbed photons,  $\Omega$  is the frequency of vibration localized on the complex involving point defects,  $a$  is a dimensionless electron-photon interaction constant,  $E_0$  — ionization (neutralization) energy of the center,  $E_1$  — minimum energy gap between the admixture level and the band forming this level,  $m^*$  is the corresponding effective mass,  $m$  is the effective mass of carriers in the band participating in electron transitions.

It can be seen from Fig.3.34 (curve 4) that the theoretical dependence calculated according to (3.39) shows small deviations from experiment in the low-energy range, while in its larger part the calculated  $\Delta\alpha(\hbar\omega)$  dependence is in good agreement with experiment. In calculating the theoretical curve that accounted for electron-phonon interaction, the energy of vibrations localized on point defects was subject to variation. The electron-phonon interaction constant was determined from the relationship [67]:

$$m_p^* = m_e^*(1 - a/6), \quad (3.40)$$

where  $m_p^*$ ,  $m_e^*$  are effective polaron and electron masses. For known values of  $m_p^*$ ,  $m_e^*$ ,  $a = 3,2$  in our case. From the known relationship [68], the Frank-Condon shift is

$$d_{FC} = 1/2 a^2 \hbar\Omega. \quad (3.41)$$

Accounting for the energy of DC local vibrations  $\hbar\omega_{L0} = 33$  meV, the obtained value is 150 meV; thus, atom displacement  $\delta$  under excitation is determined from the expression:

$$\delta = a\sqrt{\hbar/M\Omega} \cong 0,016 \text{ \AA}, \quad (3.42)$$

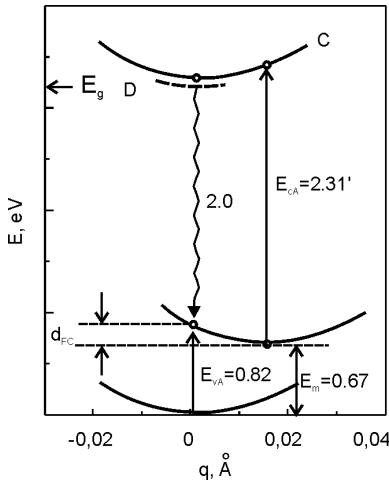


Fig.3.35. Configurational model I for a deep center studied by the method of laser modulation of two-stage absorption ( $E_{pi} =$

where  $M$  is the mass of the displaced atom. Using calculated values of  $d_{FC}$ ,  $q$ ,  $E_M$ , we can construct a configurational model of DC responsible for the L-640 band (Fig.3.35) (the unperturbed state energy  $E_M = 0.67$  eV). According to this model, radiative recombination goes by trapping non-equilibrium electrons onto the  $[V_{Zn}Te_{Se}Zn_i]$  center. As already noted, for all kinds of ZnSe(Te) crystals kinetics and spectral composition of the L-640 band are not elementary (see Tables 3.6, 3.7), they are transformed with time and temperature, and only for ZnSe(Te):Zn crystals high stability of these parameters can be observed, which indicates that the radiative recombination channel considered in the model is predominant.

The configurational model for acceptors (Fig.3.36) with  $E_M \approx 1.1$  eV ( $E_{pn} = 1.45$  eV) is constructed in a similar way (here  $\hbar\omega_{L0} = 30$  meV;  $\alpha = 6.5$ ;  $d_{FC} = 0.68$  eV), and the average atom displacement upon re-charging for a given center is  $\delta = 0.031$  Å. Such large shift of  $d_{FC}$  implies strong localization and strong electron-phonon interaction for this center, which is characteristic for non-radiative trapping centers with phonon energy dissipation. These defects can be characterized as recombination centers that weaken emission properties of ZnSe(Te) in the visible spectral region.

The center in question has practically no thermal barrier for trapping of free holes (Fig.3.36), which corresponds to equally efficient manifestation of DC both at 300 K and at 80 K. According to Fig.3.36, there is a barrier for electron capture, however, there exists a possibility of radiative trapping with emission in the 1.28 eV region (960 nm). Such IR-luminescence was observed in our experiments on ZnSe(Te) crystals after thermal treatment (Table 3.4). The 950 nm luminescence was observed in electron-irradiated ZnSe crystals; it was related

to selenium vacancies  $V_{Se}$  [11]. Probably it corresponds to photoluminescence in the initial crystal, while IR luminescence at 960 nm is related to other centers, as, according to our data, the  $E_{VA} = 1,45$  eV levels are formed upon annealing in Se and Te and are destroyed upon subsequent annealing in Zn, which can hardly be explained by the presence of  $V_{Se}$ .

Technological evidence suggests that these defects can include zinc vacancies or interstitial  $Se_i$ . This is also supported by the fact that after growth from the melt the crystals show over-stoichiometric excess of selenium [32–34], and annealing in a chalcogen does not favor its rejection from the crystal. The absence of such recombination

centers in initial ZnSe(Te) crystals indicate that for their formation, a certain after-growth transformation of the defect ensemble is needed, e.g., for association of  $V_{Zn}$  or  $(Se_i)$  defects. Upon annealing in Zn, zinc atoms of high mobility are subject to diffusion over the volume, destructing such centers and hindering their formation, which gives rise to photoluminescence. In this relation, and accounting for the fact that annealing in Te, as well as in Se, leads to worsening of radiative properties and formation of centers of the same type, we conclude that these defects should be of vacancy nature. It is not excluded that, due to their amphoteric nature,  $V_{Zn}$  defects, depending upon the conductivity type in ZnSe(Te) samples, are responsible for both L-630 and L-960 bands [24]. In the first case (annealing in Zn,  $n$ -type conductivity)  $V_{Zn}^-$  defects are formed in thermoionization occurring under this  $V_{Zn}^{2-}$  defect thermal treatment regime as  $V_{Zn}^{2-} \rightarrow V_{Zn}^- + e^-$ , where  $e^-$  is the free electron. In the second case (annealing in Se, Te,  $p$ -type conductivity), defects are formed as  $V_{Zn}^0 \rightarrow V_{Zn}^- + h^+$ , where  $h^+$  is the free hole. When the conductivity type is changed (this change

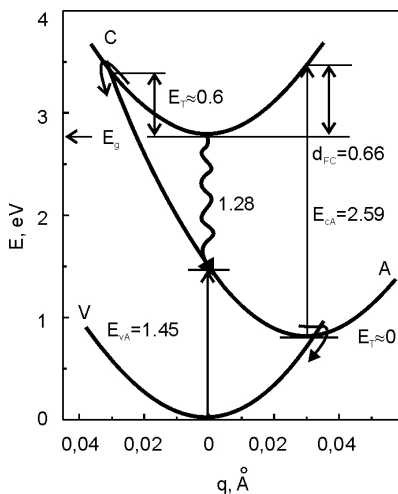


Fig.3.36. Configurational model for a deep center studied by the method of laser modulation of two-stage absorption ( $E_{pi} = 2.59$  eV) [17].

can be due to non-stoichiometry of the initial charge or to post-growth thermal treatment), the Fermi levels and  $V_{Zn}$  are gradually moved in the opposite directions [4–6]. Then, for  $n$ -type crystals the level will be closer to the valence band ( $E_T = 0.7$  eV, radiative transition valence band —  $V_{Zn}$ , L-640 band) than for  $p$ -type samples ( $E_T \approx 1$  eV, the same radiative transition, L-960 band). The possibility of this mechanism is supported by a very close genetic connection between the “red” and IR bands — in the initial crystal they can still be observed together, but, after thermal treatment of this or that kind, one of the bands becomes clearly predominant (it is especially obvious after annealing of ZnSe(Te) crystals in zinc — the L-640 band intensity increases by several orders, while the L-960 band disappears completely).

Thus, it can be concluded that both theoretical and experimental studies of  $A^{II}B^{VI}$ -based SCS show that their optical and electron properties are essentially determined by IPD, and introduction of IVD allows purposeful variation of their scintillation characteristics. In the case of ZnSe(Te), tellurium atoms, due to specific crystallographic properties of the ZnSe-ZnTe system, lead to generation of  $V_{Zn}$ , manifesting their amphoteric character and associating with IPD of other types. Uniform introduction of the ZnTe phase into ZnSe lattice at preliminary stages of SCS preparation is favored by appropriate choice of optimum thermal treatment conditions — composition, pressure and temperature of the annealing atmosphere.

The final formation of centers responsible for the main L-640 band occurs by conglomeration of  $\{V_{Zn}^- + D_1^+\}$  centers with Te atoms. The latter, compensating for the local deformation around them, ensure high stability of new M-centers  $\{V_{Zn}^- Te_{Se} D_1^+\}$ . The recombination flux is then re-distributed to M-centers with high decay times and large photoionization cross-sections; destruction of these by  $Zn_i$  trapping is hindered by a compensating deformation interaction of  $V_{Zn}$  and  $Te_{Se}$ .

The above-described results and conclusions has formed a base for the development of a complete technological cycle of SCS ZnSe(Te) preparation, including the following stages: 1) synthesis of initial raw material of required composition; 2) thermal treatment — raw material purification, preliminary formation of ZnSe-ZnTe solid solution; 3) growth of ZnSe(Te) single crystals; 4) post-growth thermal treatment — formation of amplitude-spectral and kinetic characteristics of SCS that would be optimum for their specific applications. At present,

SCS ZnSe(Te) crystals are produced on an industrial scale, several tens of cm<sup>3</sup> in size, with light output of 150–170% with respect to CsI(Tl) ( $E_\gamma < 150$  keV, photodiode receiver), decay time of 50–100 (3–5)  $\mu$ s, and afterglow level of  $\leq 0.05$  % after 3 ms. Their application fields are described in subsequent chapters.

### **3.4. The nature of radiative recombination in A<sup>II</sup>B<sup>VI</sup> compounds with isovalent dopants (IVD)**

Development of new scintillation materials is aimed at obtaining crystals with high light output and good energy resolution. These parameters are not in a direct functional relationship, though are in a certain correlation with each other [70]. As for character of radiative recombination, scintillators can be divided into 2 groups. One of them are activated (doped) crystals, in which luminescence centers are due to the introduced activator dopant, e.g., CsI(Tl), NaI(Tl), Gd<sub>2</sub>SiO<sub>5</sub>(Ce), etc. The other group includes crystals with intrinsic luminescence, such as Bi<sub>4</sub>Ge<sub>3</sub>O<sub>12</sub>, CdWO<sub>4</sub>, etc. It seems that full understanding of luminescence processes in AII BVI compounds can be achieved only if both mechanisms are taken into account.

In early publications on the emission mechanism in crystals with isovalent dopants, exciton luminescence on isoelectronic traps (IET) was considered assuming the following mechanism [71]:

A dopant atom replaces an atom of the similar element in the crystal lattice, forming an IET. This trap attracts a hole or an electron, which, in turn, captures a carrier of the opposite sign, forming a bonded exciton. When the hole and electron recombine, light is emitted. Under irradiation, holes and electrons are continuously generated, which is accompanied by the processes of recombination and light generation.

The exciton mechanism of luminescent centers supposes formation of narrow luminescence peaks with short decay times (tens of nanoseconds and less) in the region close to the intrinsic absorption edge. Such luminescence was observed in GaP(N), ZnTe(O) [72]. However, in CdS(Te) [9,73,74] and ZnSe(Te) [74,75] broad luminescence bands are predominant, with decay times from hundreds of nanoseconds to tens of milliseconds, which is not typical for emission due to excitons.

Explanation of the mechanism describing the actually observed luminescence in crystals of A<sup>II</sup>B<sup>VI</sup> compounds is possible only if crystal defect formation caused by introduction of IVD is accounted for. In 1977,



J. Watkins [1,77] showed, using ESR, that introduction of IVD of tellurium to zinc selenide leads to generation of  $V_{Zn}$  vacancies in the cation sublattice and formation of a stable complex  $(Te_{Se}V_{Zn})Zn_i$  involving the interstitial zinc. Further studies [10, 78] of bonding energies in the sublattices of CdS and ZnSe crystals have shown the following. When these crystals are bombarded by electrons with energies above the threshold required for atom displacement from the lattice site, vacancies and interstitial atoms are formed, both of metal and of chalcogen. This process is accompanied by formation of radiative recombination centers with luminescence maximums in CdS — 600 nm ( $Cd_i$ ), 730 nm ( $V_S$ ), 1020 nm ( $V_{Cd}$ ), and in ZnSe — 560, 600 и 640 nm. Identification of bands in zinc selenide is hindered by fast recombination of radiation defects. Comparison of the main parameters of radiative recombination centers in IVD-doped crystals and in crystals with radiation-induced defects shows their almost complete similarity [75–78].

In principle, in doping of semiconductor crystals, one can distinguish between isovalent dopants of the 1st and the 2nd kind [3]. An IVD of the 1st kind, with its atomic radius, ion radius and electronegativity not much different from the substituted atom, can form a continuous series of solid solutions. The band gap width is changed linearly according to Vegard's law, and no local centers are formed inside the gap. Introduction of an IVD of the 2nd kind, with its parameters differing strongly from the substituted atom, leads to formation of local levels playing the role of radiative recombination centers. Criteria of such difference for  $A^I B^{VI}$  compounds are formulated in [74], and in [61] a theoretical explanation is given for radiation, temperature and time stability of  $(Te_{Zn}V_{Zn})Zn_i$  complexes in ZnSe(Te) crystals.

Our studies of spectral-kinetic luminescence parameters in a broad temperature and time ranges [61,76] have shown that in CdS(Te) and ZnSe(Te) crystals edge-adjacent exciton luminescence with decay times of several nanoseconds is observed, which can be described by the IET mechanism [9,71–73] (Fig. 3.15, 3.16). As the process is developing in time, the main “working” luminescence bands due to intrinsic defects can be observed. Under weak excitation, exciton bands due to IET are observed only at low temperatures (below 100 K). However, under intense excitation by a laser or a focused electron beam the edge-adjacent “blue” luminescence in ZnSe(Te) is more than by 3 orders of magnitude stronger than the conventional “red” luminescence, which

can find its practical application [79]. High radiation stability makes **ZnSe(Te)**-based scintillators promising as radiation detectors in mixed  $n\text{-}\gamma$  fields. They are stable under gamma-radiation up to 108 rad and neutron fluence up to  $10^{13}$  [80].

Summing up, we can conclude that, among chalcogenide scintillators, the most widely used and promising are **ZnSe(Te)** crystals, which are produced by an exclusive technology at the Institute for Single Crystals, Kharkov, Ukraine. Their advantages — non-hygroscopicity, radiation and thermal stability, high light output, low afterglow — makes these crystals the best choice for detectors of low-energy (up to 80–100 keV) X-ray radiation, as well as for detection of short-range alpha- and beta-particles. Drawbacks of this material are low transparency and relatively low atomic number. Therefore, their most promising application fields are low-energy detector arrays for scanning X-ray imaging systems for customs & security inspection of loads and luggage, which are produced in Ukraine and Germany (Heimann).

## REFERENCES

1. *Watkins G.D.* Radiation effects in semiconductors, 1976, The Institute of Physics, Bristol and London, 1977.
2. *Taguchi T., Ray B.* Point defects in II-VI compounds // *Prog. Crystal Growth and Charact.* – 1983. – **6**, No.2. – P.103–162.
3. *Bazhenov V.K., Fistul' V.I.* Isoelectron admixtures in semiconductors. State of the problem // *Fizika i tekhnika poluprovodnikov.* – 1984. – **18**, No.8. – p.1345–1362.
4. *Ryzhikov V.D.* Scintillation crystals of semiconductor compounds AI-IBVI. Preparation, properties, applications // *Moscow: NIITEKhim.* – 1989. – 127 p.
5. *Ryzhikov V.D.* High efficiency semiconductor scintillators on the basis of AIBVI compounds // *Moscow: NIITEKhim.* – 1984. – 35 p.
6. *Ryzhikov V., Tomulaitis G., Starzhinskiy N.,* Luminescence. – 2002. – **101**. – P.45–53.
7. *Thomas D.G.* A review of radiative recombination at isoelectronic donors and acceptors // *J.Phys.Jap. (Suppl.).* – 1966. – **21**. – p.265–271.
8. *Hopfield J.J., Thomas D.G., Lynch R.T.* Isoelectronic donors and acceptors // *Phys.Rev.Lett.* – 1966. – **17**, No.6. – p.312–315.
9. *Guthbert D.G., Thomas D.G.* Optical properties of tellurium as an isoelectronic trap in cadmium sulphide // *J.Appl.Phys.* – 1968. – **39**, No.3. – p.1573–1580.
10. *Kulp B.A.* Displacement of cadmium atoms in single crystal CdS by electron bombardment // *Phys.Rev.* – 1962. – **125**, No.4. – p.1865–1869.
11. *Detweiler R.M., Kulp B.A.* Annealing of radiation damage in ZnSe // *Phys.Rev.* – 1966. – **146**, No.2. – p.513–516.
12. *Dunstan D.J., Nicholes J.E., Carenett B.C. et al.* Optically detected magnetic resonance of the V-centre in ZnSe // *Solid State Commun.* – 1977. – **24**, No.9. – p.677–690.
13. *Lee K.M., Le Si Dang, Watkins J.D.* Optically detected magnetic resonance of zinc vacancy in ZnSe // *Ibid.* – 1980. – **35**, No.8. – p.5127–5130.
14. *Cavennett B.C.* Optically detected magnetic resonance (ODMR) investigations of recombination process in semiconductors // *Adv. Phys.* – 1981. – **30**, No.4. – p.475–538.
15. *Godlewski M., Lamb W.E., Cavenett B.C.* ODMR investigations of recombination process in ZnSe(Cu) // *Solid State Commun.* – 1981. – **39**, No.4. – p.596–599.

16. *Vakulenko O.V., Ryzhikov V.D., Shutov B.M.* The nature of the long-wave luminescence of  $\text{ZnSe}(\text{Te}):\text{Zn}$  // *Zhurn.prikladnoi spektroskopii*. – 1988. – **49**, No.3. – p.440–444.
17. *Baltramejunas R., Gavryushin V., Ryzhikov V. e.a.* Spectroscopy of deep centers in single crystals  $\text{ZnSe}(\text{Te}):\text{Zn}$  by the method of laser modulation of two-stage absorption // *Fizika i tekhnika poluprovodnikov*. – 1988. – **22**, No.7. – p.1163–1170.
18. *Dmitriev Yu.N., Ryzhikov V.D., Gal'chinetskii L.P.* Thermodynamics of isovalent doping of crystals of semiconductor compounds  $\text{A}^{\text{II}}\text{B}^{\text{VI}}$ . Kharkov: VNIIM, 1990. – 50 p.
19. *Vlasenko N.A., Vitrikhovskii N.I., Denisova Z.L. e.a.* On the nature of luminescence centers in pure cadmium silfide // *Optika i spektroskopiya*. – 1966. – **21**, No.4. – p.466–475.
20. *Susa N., Watanabe H., Wada M.* Effects of annealing in Cd or S vapour on photoelectric properties of Cds single crystals // *Jap. J. Appl. Phys.* – 1976. – **15**, No.12. – p.2365–2370.
21. *Ryzhikov V.D., Chaikovskii E.F.* Development of new scintillation materials on the basis of compounds  $\text{A}^{\text{II}}\text{B}^{\text{VI}}$  with isovalent activators // *Izv.AN SSSR, ser. Phys.* – 1979. – **43**, No.6. – p.1150–1154.
22. *Ryzhikov V., Starzhinskiy N., Galchinetskiy L.* Luminescence properties of isovalent doped  $\text{ZnSe}$  crystals // *Functional materials*. – 2003. – **10**, No 2. – P.207–211.
23. *Gal'chinetskii L.P., Dmitriev Yu.N., Ryzhikov V.D. e.a.* Peculiar features of evaporation of zinc selenide crystals with isovalent dopants // *Izv.AN SSSR, ser. Inorganic Materials*. – 1989. – **25**, No.10. – p.1632–1636.
24. *Vakulenko O.V., Lysyi V.S., Ryzhikov V.D. e.a.* Effects of thermal treatment and doping with tellurium upon intensity of the admixture luminescence in single crystals of zinc selenide // *Zhurn.prikladnoi spektroskopii*. – 1990. – **53**, No.4. – p.673–675.
25. *Dmitriev Yu.N., Ryzhikov V.D.* On radiation stability of crystals  $\text{ZnSe}(\text{Te})$  // *Atomnaya energiya*. – 1991. – **70**, No.2. – p.119–121.
26. *Thompson M.* Defects and radiation damage in metals. – Moscow: Mir, 1971. – 367 p.
27. *Urusov V.S.* Energetic crystallochemistry. – Moscow: Nauka, 1975. – 335 p.
28. *Pauling L.* The nature of chemical bond. – Moscow: Nauka, 1973. – 375 p.
29. *Urusov V.S.* Effective parameters of electron shells of atoms and ions // *Zhurn.strukturnoi khimii*. – 1962. – **3**, No.4. – p.437–447.

30. Vavilov V.S., Kiv A.B., Niyazova O.R. Mechanisms of formation and migration of defects in semiconductors. – Moscow: Nauka, 1981. – 368p.
31. Gurvich A.M. Introduction to physical chemistry of crystallophosphors. – Moscow: Vysshaya shkola, 1982. – 376 p.
32. Solovyeva E.V., Mil'vidskii M.G. Peculiar features of defect formation in semiconductors under isovalent doping // Fizika i tekhnika poluprovodnikov. – 1983. – **17**, No.11. – p.2022–2024.
33. Rytova N.S., Solovyeva E.V. Effects of isovalent dopants of elastic stress sources in the crystal upon behavior of point defects // Ibid. – 1986. – **20**, No.8. – p.1380–1387.
34. Rytova N.S. Equilibrium concentration of vacancies in a semiconductor compound under its doping by isovalent admixtures // Ibid. – p.1514–1517.
35. Levin A.A., Syrkin Ya.K., Dyatkina M.E. The problem of single-atom multi-charge ions and the chemical bond character in inorganic crystals // Uspekhi khimii. – 1969. – **38**, No.2. – p.193–221.
36. Lanneau M., Bourgoin J. Point defects in semiconductors. Theory. Moscow: Mir, 1984. – 264 p.
37. Fistul' V.I. Distribution of an amphoteric admixture over sublattices of multicomponent solid solutions  $A^{IV}B^{VI}$  // Fizika i tekhnika poluprovodnikov. – 1983. – **17**, No.6. – p.1107–1110.
38. Koshkin V.M., Dmitriev Yu.N., Zabrodskii Yu.R. e.a. Radiation stability of loose crystalline structures // Ibid. – 1984. – **18**, No.8. – p.1373–1378.
39. Akilov Yu.Z., Lenchenko V.M. Displacement chains of atoms in Ge and Si (computer modeling) // Ibid. – 1974. – **8**, No.1. – p.30–35.
40. Vavilov V.S. Effects of radiation upon semiconductors. – Moscow: Fizmatgiz, 1963. – 264 p.
41. Spitsyn V.I., Ryabov A.I., Stel'makh N.S., Pirogova G.N. Effects of radiation upon optical properties of high-resistivity single crystals of Ge, GaAs and ZnSe // Izv.AN SSSR, ser. Inorganic Materials. – 1977. – **13**, No.1. – p.27–31.
42. Stel'makh N.S., Pirogova G.N., Glazunov P.Ya. e.a. Luminescence spectra of zinc selenide under pulse irradiation by electrons // Ibid. – 1983. – **19**, No.8. – p.1265–1269.
43. Brant F.J., Manning P.S. Displacement of selenium and IR cathodoluminescence of ZnSe // J.Phys.C. – 1972. – **5**, No.14. – p.1914–1920.
44. Goryunova N.A. Complex diamond-like semiconductors. Moscow: Sov.radio, 1968. – 268 p.
45. Schefer G. Chemical transport reactions. – Moscow: Mir, 1964. – 190 p.

46. *Mizetskaya I.B., Oleinik G.S., Budennaya L.D. e.a.* Physico-chemical foundations of synthesis of single crystals of solid solutions of AIBVI compounds // Kiev: Naukova dumka, 1986. – 159 p.
47. *Lakin E.E., Fedorenko O.A.* Effects of the phase transformation upon the structure of ZnSe single crystals // Materialy dlya opticheskikh ustroystv i scintillatorov. - Kharkov: VNIIM, 1985. – No.14. – p.89–95.
48. *Ryzhikov V.D., Galkin S.N., Gal'chinskii L.P.* Study of the solid solution formation process in sintering of ZnSe and ZnTe powders // Zhurnal neorganicheskoi khimii. – 1990. – **35**, No.8. – p.3178–3182.
49. *Morozova N.K., Kuznetsov V.A., Ryzhikov V.D. e.a.* Zinc selenide. Preparation and optical properties. – Moscow: Nauka, 1992. – 98 p.
50. *Ryzhikov V.D., Silin V.I., Verbitskii O.P. e.a.* Kinetics of luminescence and light accumulation in crystals of cadmium sulfide and zinc selenide // Fizika i khimiya opticheskikh i scintillacionnykh materialov. – Kharkov: VNIIM. – 1985. – No.14. – p.89–95.
51. *Zdesenko Yu.G., Nikolayko A.S., Ryzhikov V.D. e.a.* Spectrometric characteristics of scintillators on the basis of cadmium sulfide // Pribory i tekhnika eksperimenta. – 1985. – No.3. – p.80–82.
52. *Cuthberg I.D., Thomas D.G.* Optical properties of tellurium as isoelectronic traps in cadmium sulphide // J.Appl.Phys. – 1968. – **39**, No.3. – p.1573–1580.
53. *Ryzhikov V.D., Gal'chinskii L.P., Lisitsyn V.M.* Studies of binary semiconductors under influence of intense beams of fast electrons // Vyrashchivanie, issledovanie i primeneniye monokristallov. - Kharkov: VNIIM, 1985. – No.5. – p.56–60.
54. *Vakulenko O.V., Suprunenko V.N., Ryzhikov V.D.* Kinetics of admixture luminescence in semiconductors in the presence of amphoteric recombination centers // Ukr.fiz.zhurnal. – 1990. – **35**, No.10. – p.1485–1489.
55. *Vakulenko O.V., Suprunenko V.N., Ryzhikov V.D.* Temperature dependence of the admixture luminescence intensity in semiconductors with amphoteric recombination centers // Fizika i tekhnika poluprovodnikov. – 1991. – **25**, No.6. – p.1053–1057.
56. *Vakulenko O.V., Veretennikov A.N., Ryzhikov V.D.* Peculiar features of X-ray luminescence kinetics of ZnSe:Te at high excitation levels // Zhurnal tekhnicheskoi fiziki. – 1988. – **58**, No.3. – p.632–635.
57. *Baltramejunas R., Gavryushin V., Rachiukaitis R. e.a.* Effects of fundamental edge deformations by the defects in two-photon spectroscopy of semiconductors // Fizika tverdogo tela. – 1991. – **33**, No.3. – p.944–946.

58. *Vakulenko O.V., Lysyi V.S., Ryzhikov V.D.* Kinetics of “red” luminescence in single crystals of zinc selenide // *Ukr.fiz.zhurnal.* – 1990. – **35**, No.11. – p.1628–1631.
59. *Gal’chinetskii L.P., Katrunov K.A., Ryzhikov V.D.* Determination of scintillation efficiency and photometric characteristics of X-ray luminophores // *Pribory i tekhnika eksperimenta.* – 1991. – No.1. – p.173–178.
60. *Vakulenko O.V., Suprunenko V.M.* Influence of infra-red irradiation upon luminescence of semiconductors with amphoteric recombination centers // *Visnyk Kyiv.Univ., Phys.-math.sci.* – 1991. – No.1. – p.70–73.
61. *Ryzhikov V.D.* D.Sc. (Doctor of Phys.-Math.Sci.) Dissertation. – Kharkov. – 1989. – 440 p.
62. *Lawrence R., Bube R.H.* Photothermoelectric analysis of thermally stimulated thermoelectronic effect: techniques in photoelectronic analysis // *Jap. J. Appl. Phys.* – 1968. – **39**, No.3. – p.1807–1813.
63. *Tolstoi N.A.* On mutual relationship of the blue and red emission bands in the phosphor  $\text{ZnSe:Co}$  // *Optika i spektroskopiya.* – 1957. – **3**, No.1. – p.73–75.
64. *Ryzhikov V.D., Baltramejunas R., Gavryushin V. e.a.* Luminescence and nonlinear spectroscopy of recombination centers in isovalently doped  $\text{ZnSe:Te}$  crystals // *J. Luminescence.* – 1992. – **52**. – p.71–81.
65. *Baltramejunas R., Gavryushin V., Ryzhikov V.D. e.a.* Centers of radiative and non-radiative recombination in isoelectronically doped  $\text{ZnSe:Te}$  crystals // *Phys.B.* – 1993. – **185**. – p.245–249.
66. *Grinberg A.A.* Photoionization of deep admixture centers in semiconductors // *Fizika i tekhnika poluprovodnikov.* – 1976. – **10**, No.10. – p.1872–1877.
67. *Kopylov A.A., Pikhtin A.N.* On determination of ionization energy of deep centers from optical absorption spectra // *Ibid.* – 1976. – **10**, No.1. – p.15–21.
68. *Rode D.L.* Electron mobility in II-VI semiconductors // *Phys.Rev.* – 1970. – **2**, No.10. – p.4036–4043.
69. *Valakh M.Ya., Lisitsa M.P.* Phonons in semiconductors  $\text{A}^{\text{II}}\text{B}^{\text{VI}}$  // *Kvantovaya elektronika.* – 1982. – No.22. – p.16.
70. *Naidenov S.V., Ryzhikov V.D.* Prospects for creation of a scintielectronic detector with improved energy resolution // *Izvestiya VUZov, Ser. Mater. Electron.Tech.* – 2001.– No.2. – p.65–70.
71. *Brown W.L., Heights D., Madden T.C. e.a.* Radiation detector using isoelectronic trap material // 1971, pat USA N 3586856.
72. *Madden T.C., Merz J.L., Miller G.L., Thomas D.G.* The use of semiconductors doped with isoelectronic traps in scintillation counting // *IEEE Trans Nucl Sci.* – 1968. – **NS-15**. – p. 47–57.

73. *Merz J.L., Lynch R.T.* Isoelectronic traps in II-VI compounds. In: II-VI semiconducting compounds. Ed. D.G. Thomas, 1967, Benjamin, N.J., p.731–742.
74. *Ryzhikov V.D., Verbitskii O.P., Nosachev B.G.* A semiconductor scintillation material. – Pat.USSR, No. 826769, 1978.
75. *Ryzhikov V.D., Chaikovskii E.F.* New scintillation materials based on AIIIBVI compounds with an isovalent activator // *Izvestiya AN SSSR, ser.phys.* – 1979. – **43**, No.6. – p.1150–1154.
76. *Baltramejunas R., Ryzhikov V., Gavryushin V. e.a.* Luminescent and nonlinear spectroscopy of recombination centers in isovalent doped ZnSe(Te) crystals // *J. Lum.* – 1992. – **52**. – p.71–81.
77. *Watkins J.* Lattice defects in II–VI compounds // *Inst. Phys. Cont. Ser.* No.31, 1977. Chapter 1, p.95–111.
78. *Detweiler R., Kulp B.* Annealing of radiation damage in ZnSe // *Phys. Rev.* – 1966. – **146**, No.2. – p.513–516.
79. *Zaytseva Yu., Tarasenko L., Ryzhikov V., Silin V.* A fluorescent screen for visualization of an electron probe // 1989. – USSR Patent No. 497940.
80. *Litovchenko P., Rozenfeld A., Zhivrich V., Ryzhikov V.* Compensator for reduction of sensitivity of a scintielectronic detector // 1990. – USSR Patent No.1774740.



## CHAPTER 4

# APPLICATION PROSPECTS OF OXIDE AND CHALCOGENIDE CRYSTALS FOR DETECTION OF NEUTRONS

### *4.1. Neutron flux measurements using «scintillator- photodiode-preamplifier» system and new types of scintillators*

After the Chernobyl catastrophe among the problems of current concern a question arose of detection of “hot” particles formed from plutonium alloys with carbon, nitrogen, silicon, etc. For this purpose, the instruments are needed, which would be able to detect not only alpha-particles and low energy gamma-radiation, but also neutrons and high energy gamma-quanta from ( $\alpha$ ,  $n\gamma$ )-reactions. At present for each kind of radiation detectors of different types are used (e.g., proportional counters, ionization chambers, scintillation detectors based on organic, alkali halide, semiconductor crystals, etc.). A general drawback of all these instruments is their narrow dynamic range of dose rates and energies, and especially impossibility to registrate  $n$ -flux in condition large background activity  $\gamma$ -rays nuclei, which makes each of them applicable only under certain specific conditions. For detection of “hot” particles, oxide and semiconductor scintillators were used [1–3], which contained elements with large capture cross section for thermal neutrons. In this chapter, we try to determine possibilities and limitations of solid-state neutron detectors based on CdS(Te), ZnSe(Te), CdWO<sub>4</sub> (CWO), Gd<sub>2</sub>SiO<sub>5</sub> (GSO) scintillators developed and produced by the Science and Technology Center for Radiation Instruments of the Institute for Single Crystals (STC RI ISC). The instruments developed by Center are based preferable on a very promising system

Table 4.1. Characteristics of oxide and semiconductor scintillators in comparison with CsI(Tl) and LiI(Eu).

Crystal	$\rho$ , g/cm <sup>3</sup>	$Z_{eff}$	$\lambda_{peak}$ , nm	Light yield, Ph/MeV	$\alpha/\beta$	Shaping time, $\mu$ s	p.e.yield/ MeV $\gamma$ in Si photodiode
CsJ(Tl)	4.5	52	560	51800	0.5	0.9( $\gamma$ ) 0.6( $\alpha$ )	$3.9 \times 10^4$
CsJ(Tl)						4–12	$4.0 \times 10^4 - 4.6 \times 10^4$
LiJ(Eu) <sup>a)</sup>	4.08	50	470	11000	1.0– 1.1 <sup>b)</sup>	1.4	
BGO	7.13	74	480	8200		0.3	$6.15 \times 10^3$
CWO	7.9	66	470/540	11000		4–12	$6.15 \times 10^3$
GSO(Ce) <sup>c)</sup>	6.7	59	430	11500	0.25 <sup>d)</sup>	0.043( $\gamma$ ) 0.045( $\alpha$ )	$6.32 \times 10^3$
GSO(Eu) <sup>e)</sup>	6.7	59	613.5	7800		<0.015	
CdS(Te)	4.8	48	730	17000	0.72– 0.76 <sup>f)</sup>	4–12	$1.2 \times 10^4 - 1.3 \times 10^4$
ZnSe(Te)	5.42	30	645	55000	$1 \pm 0.1$ <sup>g)</sup>	4–12	$4.7 \times 10^3 - 1.2 \times 10^4$

<sup>a)</sup> See Ref.[5]; <sup>b)</sup> See Ref.[6]; <sup>c)</sup> See Ref.[7]; <sup>d)</sup> See Ref.[8]; <sup>e)</sup> See Ref.[9]; <sup>f)</sup> See Ref.[2]; <sup>g)</sup> See Ref.[10].

“scintillator-photodiode-preamplifier” (S-PD-PA) matched with modern computer data processing techniques.

#### *4.1.1. Experimental set-up: scintillators and components of the receiving electronic circuit*

**Scintillators.** Principal characteristics of scintillator crystals used in our study (in comparison with more conventional CsI(Tl) and LiI(Eu)) are presented in Table 4.1.

It is clear from the data presented that most of these scintillators, as it has been already shown [11,12], can be used, in combination with PIN-photodiodes, for detection of thermal neutrons by  $\gamma$ -quanta of the radiation capture and the secondary charged particles, and, in

Table 4.2. Thermal neutrons capture cross-section by nuclei of cadmium, gadolinium, lithium and boron.

Reaction	Reaction threshold, MeV	Cross-section for the isotope, measured at neutron energy 0.0253 eV, barn	Relative isotope content in the natural mixture, %
$^{106}\text{Cd}(n,\gamma)^{107}\text{Cd}$		$1.0\pm 0.5$	1.24
$^{108}\text{Cd}(n,\gamma)^{109}\text{Cd}$		1.1	0.87
$^{110}\text{Cd}(n,\gamma)^{111}\text{Cd}$		$1.2\pm 0.1$	12.32
$^{112}\text{Cd}(n,\gamma)^{113}\text{Cd}$		$0.03\pm 0.015$	24.15
$^{113}\text{Cd}(n,\gamma)^{114}\text{Cd}$		$20000\pm 300$	12.21
$^{114}\text{Cd}(n,\gamma)^{115}\text{Cd}$		$0.14\pm 0.03$	28.93
$^{116}\text{Cd}(n,\gamma)^{117}\text{Cd}$		1.5	7.61
		$2450\pm 50$	natural mixture
$^{155}\text{Gd}(n,\gamma)^{156}\text{Gd}$		$61000\pm 5000$	15.10
$^{157}\text{Gd}(n,\gamma)^{158}\text{Gd}$		$240000\pm 12000$	15.70
$^6\text{Li}(n,\alpha)\text{T}$	4.785	$936\pm 6$	$1.42\dots 7.52$
$^{10}\text{B}(n,\alpha)^7\text{Li}^*$	2.781	3813	$18.83\dots 19.61$

combination with avalanche photodiodes — for detection of thermal neutrons by instantaneous internal conversion electrons (ICE) with  $E_e \cong 100$  keV.

High detection efficiency for thermal neutrons is expected with cadmium- and gadolinium-containing materials due to high cross-section values of their nuclei. (Table 4.2). As for lithium- and boron-containing scintillators, high detection efficiency is generally due to the high degree of enrichment (up to 80–90%) with Li-6 and B-10 isotopes.

Lil(Eu) single crystals enriched in Li-6 have large capture cross-section of thermal neutrons by iodine-127 ( $\sigma = 6.2$  barn), with radioactive iodine-128 ( $T_{1/2} = 25$  min,  $E_{\beta\text{max}} = 2$  MeV) being formed. This causes a significant intensification of the background during long-term continuous measurements in the fields of thermal neutrons.

As for boron compounds possessing radioluminescent properties, the best known are yttrium and indium borates doped with lanthanide activators. It has been shown [13] that intensity of the principal lumi-

Table 4.3.

ICE lines of  $^{114}\text{Cd}$  [14]

$E_e, \text{keV}$	69.0	91.9	96.1	531	553	625	1280	1304
Intensity, r.u. ( $I_{531}=100$ )	~956	~296	~33	100	17.1	16.1	133	20.1

ICE lines of  $^{156}\text{Gd}$  [15]

$E_e, \text{keV}$	39	81	88	149	191	198	247	289	991	1016
Intensity, r.u. ( $I_{1016}=1$ )	~6800	~8900	~1200	250	110	28	4.80	1.42	2.16	1.00

ICE lines of  $^{158}\text{Gd}$  [15]

$E_e, \text{keV}$	29.1	34.9	41.4	71.5	78	132	174	180	205	277	1059	1137
Intensity, r.u. ( $I_{1016}=1$ )	~5500	~110	~60	~6500	~1150	~280	~90	~25	1.67	5.9	1.0	1.69

nescence band of terbium-activated yttrium borate is comparable to that of such scintillators as GSO, CWO or BGO; however, spectral-kinetic characteristics of the borate scintillators have not yet been studied in detail and for that time this scintillator research only as ceramic.

Let us estimate the possibilities of thermal neutron detection by cadmium- and gadolinium-obtaining scintillators using ICE's formed as a result of radiation capture reaction on the  $^{113}\text{Cd}$ ,  $^{115}\text{Cd}$  and  $^{157}\text{Gd}$  nuclei [14–15] (Table 4.3).

It is clear that conversion coefficient is lower with higher energies; thus, the scintillator thickness should be increased proportionally with energy. As high-energy  $\gamma$ -quanta are also present together with the neutrons, and emission cross-section of the secondary electrons is the smallest at  $180^\circ$ , it is natural to select the ICE's going just in this direction.

Receiving electronic circuits. A Pu-Be( $\alpha$ ,  $n\gamma$ ) neutron source was studied using a spectrometric gamma-beta detector of the S-PD-PA system [12]. S-3590-01 photodiodes (Hamamatsu, Japan) were used as photoreceivers, parallel to "Porog" photodiodes produced by CCB "Ritm" (Chernovtsy, Ukraine). Their comparative characteristics are presented in Table 4.4.

Table 4.4. Parameters of PIN-photodiodes.

Parameters	S-3590-01	“Porog”
Light-sensitive area, mm <sup>2</sup>	10·10	10·10
Dark current $I_m$ , nA	1.5	1.6
Bias voltage, V	30	30
Capacitance, pF	70	67
Sensitivity for $\lambda$ nm, A/W	0.31	0.26

Spectral sensitivity maximum of the silicon photodiodes is about 850–900 nm, which is matched only by 30% with CsI(Tl) scintillators; this leads to a certain lowering of the signal. Hence, especially important is the role of the preamplifier. It comprises the charge-sensitive section with a field transistor at the input and the detector power supply elements.

The main element determining the signal to noise ratio of the system is the input field transistor (FT). Our studies have shown that, among FT used in nuclear spectrometry (such as KP 303 G, KP307 Zh, KP 31 P, ZN 4416), the lowest level of intrinsic noise (770 e with PD capacitance of 70 pF) is obtained with KP 314 A. Using this FT, the spectrometric preamplifier developed by STC RI and produced in hybrid technology by PC “Kommunar” showed the following characteristics (Table 4.5).

After the preamplifier, further amplification and formation of the signal was performed using a 1101 type filter-amplifier modified for formation times up to 40  $\mu$ s. Formation times used for the studies reported were 5  $\mu$ s for CdS(Te), and 20  $\mu$ s for CWO crystals.

Spectrometric data were processed using an IBM PC/AT 486 notebook with the built-in original analogo-digital transformer, which ensured small size and low energy consumption of the instrument as a whole.

Detection efficiency of the thermal neutrons was determined using the method of cadmium counting rate difference of the detector over equal time intervals from a <sup>239</sup>Pu-Be ( $\alpha$ ,  $n\gamma$ ) source of neutrons (input — 10<sup>5</sup> neutron/s) placed in the center of a polyethylene sphere 150 mm in diameter; the yield of thermal neutrons on the surface was 0.09.

Table 4.5. Technical characteristics of the hybrid spectrometric preamplifier KVANT-PU-1-01

Detector capacitance, pF	40–200
Pulse rise time, $\mu$ s	2
Pulse decay time, $\mu$ s	100
Load resistance, not less than, kOhm	1
Load capacitance, not more than, pF	1000
Power supply voltage, V	+(7.5...16)
Specified power voltage, V	9
Consuminy current, mA	0.9
Max. output positive amplitude, V	5.5
Noise value, normalized over output with $C_d = 70$ pF and $\tau_f = 5$ $\mu$ s, electrons, not more than	450

Table 4.6. Spectrometric parameters of the “Porog” photodiode.

Souse of $\gamma$ -quanta	ICE souse	Energy resolution, %
$^{241}\text{Am}$ $E_\gamma = 59.6$ keV		6.5
	$^{109}\text{Cd}$ $E_e = 61.5$ keV	14
	$^{207}\text{Bi}$ $E_e = 482$ keV	1.8
	$E_e = 976$ keV	0.9

4.1.2. Experimental results

Accounting for the fact that silicon PD was successfully used as a detector of X-ray and low-energy  $\gamma$ -radiation (and, without a protective layer on the input window, for detection of electrons), we have tested a possible detector design used without the scintillator. The results are presented in Table 4.6 and in Fig.4.1.

The gamma-spectrum of a plutonium-beryllium source (Fig.4.1), apart from the  $^{239}\text{Pu}$  (14 keV, 39 keV and 52 keV)  $\gamma$ -lines, has a distinct  $\gamma$ -line of  $^{241}\text{Am}$  (59.6 keV) overlapping with the two

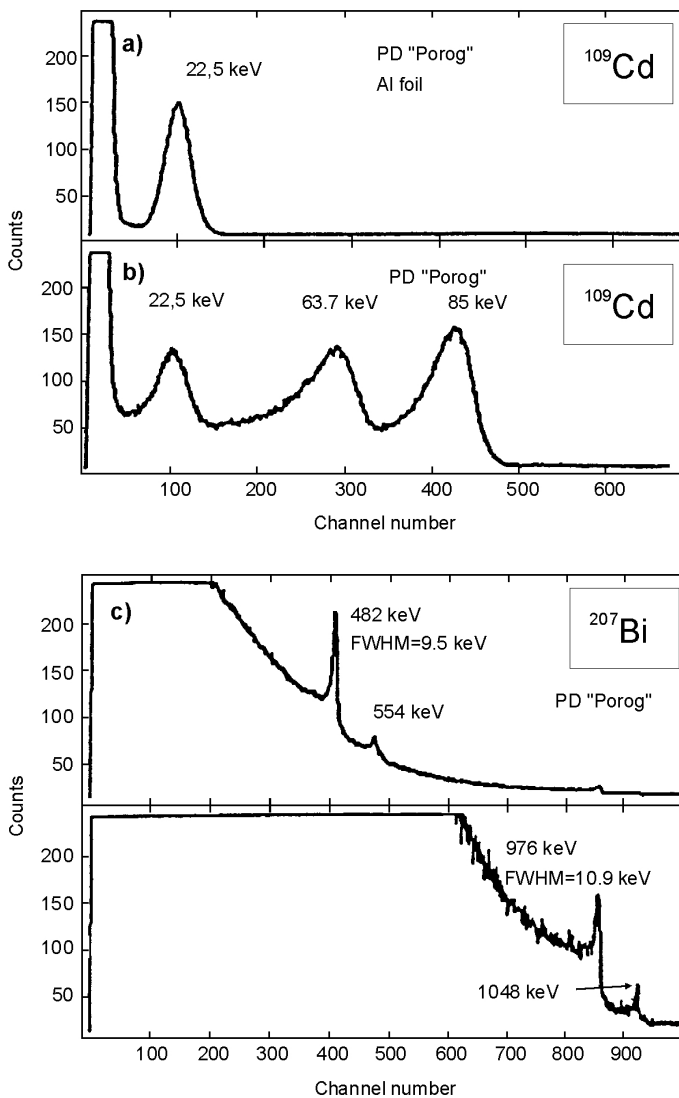


Fig. 4.1. Pulse amplitude spectra of a "Porog" type silicon photodiodes: a)  $^{109}\text{Cd}$  source with and without a aluminum foil, b)  $^{207}\text{Bi}$  source, c) Pu-Be ( $\alpha$ ,  $n\gamma$ ) source, d)  $^{241}\text{Am}$  source.

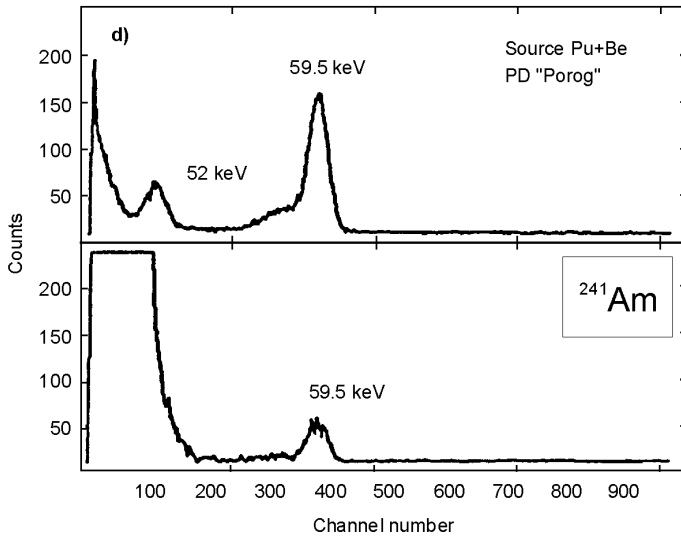


Fig. 4.1. (Continued).

latter  $^{239}\text{Pu}$  lines. The  $^{241}\text{Am}$  radionuclide is accumulated in the  $^{239}\text{Pu}$ -Be ( $\alpha, n$ )-source as a result of  $\beta$ -decay of  $^{241}\text{Pu}$  ( $T_{1/2} = 13$  years), which can be present in this source as a dopant [16]. The spectrograms shown in Figs.1,2 show that ICE from the ( $n, \gamma$ ) reaction can, in fact, be detected using thin gadolinium and cadmium converters and “Porog” type photodiodes. It can be noted for comparison that spectrometric parameters of the corresponding windowless PIN-photodiodes (S 1723-06N, Hamamatsu) used for ICE detection ( $^{156}\text{Gd}$ ,  $^{158}\text{Gd}$ ) made of gadolinium foil are (for  $E_\gamma = 122$  keV) 9 keV (FWHM);  $R_\gamma = 7.4\%$  [17].

Detectors of this type can be used for indirect spectrometry of neutrons in the active zone of a reactor provided a set is available of neutron-activation and fissionable reference samples.

Testing results of the second modification of the detector (using CWO and CdS(Te) scintillators and S 3590 type PD) are presented in Table 4.7 and in Fig.4.2.

Such a version of the S-PD-PA detector (CsI(Tl)-PIN-PD) with a neutron-gamma converter based on cadmium or samarium foil has been used for neutron dosimetry [18]. With a cadmium foil, the



Table 4.7. Spectrometric and radiometric parameters of the S-PD-PA system using a S 3590 type photodiode.

Scintillator	Measurement source	Detection efficiency	Energy resolution, %
$\text{CdWO}_4$ $10 \times 10 \times 5 \text{ mm}^3$	thermal neutrons $^{137}\text{Cs}$ $E_\gamma = 0.662 \text{ MeV}$	0.2	24
$\text{CdS}(\text{Te})$ $7 \times 7 \times 2.5 \text{ mm}^3$	$^{137}\text{Cs}$ $E_\gamma = 0.662 \text{ MeV}$		11.7
	$^{226}\text{Ra}$ $E_\alpha = 7.69 \text{ MeV}$		4.6

558.6 keV gamma-line was used from the  $^{113}\text{Cd} (n, \gamma) ^{114}\text{Cd}$  reaction. In our version, the cadmium-containing scintillator plays the role of a neutron-gamma converter. A  $\text{ZnSe}(\text{Te})$ -based S-PD-PA detector can be used as the compensation detector with lower sensitivity towards the thermal neutrons [3]. One should note high radiation stability of  $\text{ZnSe}(\text{Te})$ ,  $\text{CdS}(\text{Te})$  and tungstate scintillators in the mixed fields of neutron-gamma radiation (Fig.4.3). The intensity of  $\gamma$ -luminescence *vs.* dose rate was practically linear up to  $1.8 \cdot 10^5 \text{ R/h}$  ( $^{60}\text{Co}$  source).

#### 4.1.3. Possibilities for neutron detection: discussion and conclusions

In mixed gamma-neutron fields luminescence intensity of  $\text{ZnSe}(\text{Te})$  scintillators increases after neutron irradiation with the fluency  $\Phi_n > 4 \times 10^{12} \text{ neutrons/cm}^2$  (Fig.4.4). This is related to the reconstruction of the defect structures according to the model proposed in [1, 2]: zinc vacancies are being generated (due to low bonding energy); the complexes formed ( $V_{\text{Zn}} + \text{Zn}_i + \text{Te}$ ) are stable and play the role of the recombination centers.

As it is shown by the results of our studies, parameters of the silicon PD are worsened after irradiation by  $10^6 \text{ rad}$  ( $\gamma$ ) or by the neutron fluency of  $10^{10}$ – $10^{11} \text{ neutrons/cm}^2$ ; these values determine the limits of their radiation stability. However, the use of  $\text{ZnSe}(\text{Te})$  scintillators in combination with silicon photodiodes does compensate to a certain extent the post-irradiation effect of sensitivity decrease. (Fig.4.5).

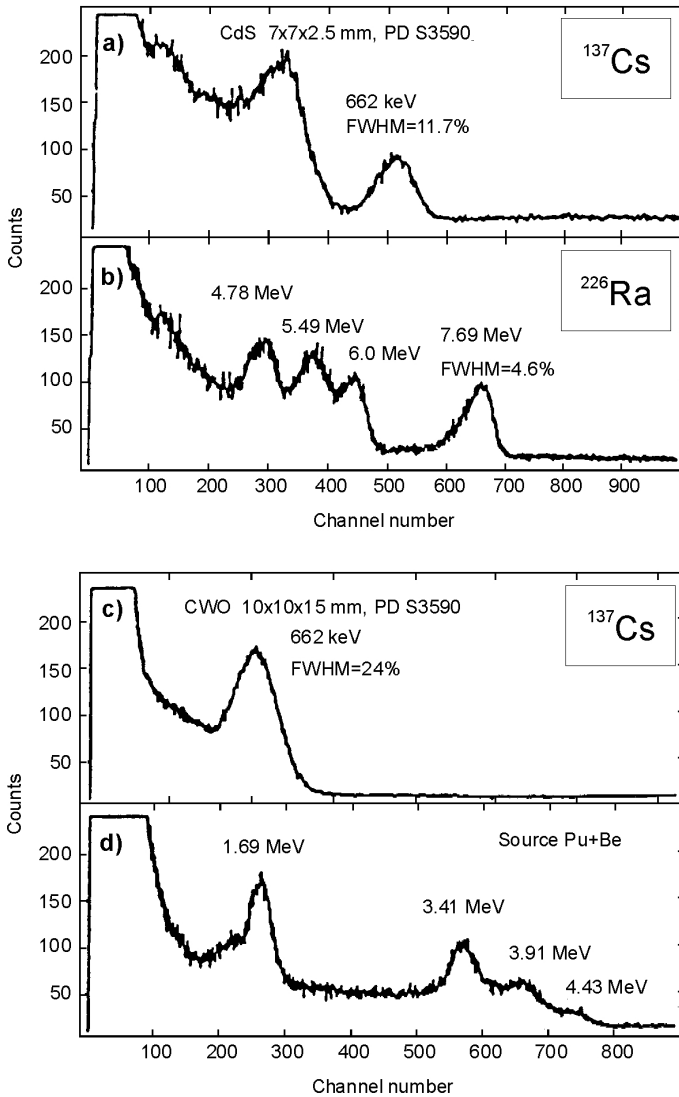


Fig. 4.2. Pulse amplitude spectra of the scintillator-photodiode-preamplifier system: CdS(Te) crystal on  $^{137}\text{Cs}$   $\gamma$ -quanta (a) and  $^{226}\text{Ra}$   $\alpha$ -particles (b); CWO crystal on  $^{137}\text{Cs}$   $\gamma$ -quanta (c) and Pu-Be ( $\alpha$ ,  $n\gamma$ )-source with  $E_\gamma=4.43\text{MeV}$  (d).

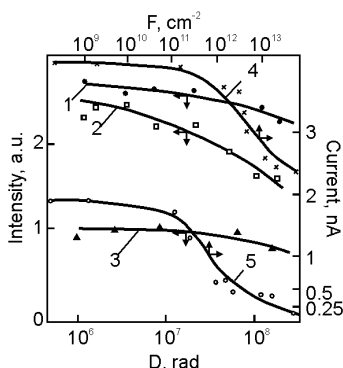


Fig.4.3. Radiation stability of  $\text{AlBVI}$  and tungstate scintillators and “scintillator-photodiode” detectors based on them [3]: 1,2,3 — intensity of  $\gamma$ -luminescence ( $I_{\text{lum}}$ ) vs. dose  $D$  of  $\gamma$ -irradiation for  $\text{ZnSe}(\text{Te})$ ,  $\text{CdWO}_4$ ,  $\text{ZnWO}_4$  respectively ( $^{60}\text{Co}$  source, dose rate  $18 \times 10^4$  R/h; 4,5 — detector current ( $I_{\text{det}}$ ) vs. neutron fluence  $F$  ( $^{137}\text{Cs}$  source, dose rate 210 R/h) for  $\text{ZnSe}(\text{Te})$  and  $\text{CdS}(\text{Te})$ -based scintillator-photodiode detectors.

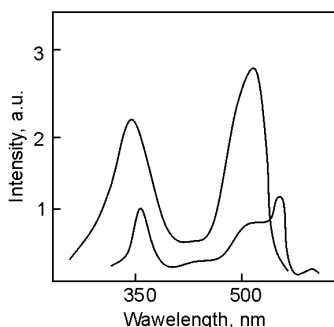


Fig.4.4. Intensity of  $\text{ZnSe}(\text{Te})$  radioluminescence as function of neutron fluency.

To increase the area of input windows, scintillator detection blocks were constructed which comprised CWO- or GSO-based scintillators and photoelectronic multipliers. Parameters of these scintillation blocks are presented in Table 4.8, Figs.4.6, 4.7.

Figs.4.6, 4.7 show the pulse amplitude spectra of the detection blocks based on CWO and GSO crystals in the fields of thermal neutrons.  $^{156}\text{Gd}$  and  $^{158}\text{Gd}$  ICE peaks ( $E_\gamma = 71.5$ , 78, 81 and 88 keV) are presented in Fig.4.6. Despite a noticeable non-linearity of scintillator characteristics, the low-energy region considered is the most efficient for selective detection of neutrons. Further increase of the selectivity of GSO crystals can be obtained by a decrease in the scintillator thickness (up to several dozens of microns).

On the pulse amplitude spectrum of the CWO-based detection block (crystal size  $40 \times 40$  mm) ICE peaks from  $^{114}\text{Cd}$  are practically not resolved (Fig.4.7, a). This can be related to the fact that the scintillator is too thick — 1–2 mm thickness would be sufficient for the total absorption of thermal neutrons, and the rest of crystal volume is used, in fact, as a light transducer. This is indirectly confirmed by the data presented in Fig.7b, where, apart from the peaks due to ICE,  $\gamma$ -quantum ( $E_\gamma = 558$  keV) due to radiation capture of thermal neutrons is clearly seen (as in [18]).

With thin (1 mm) CWO crystals the peaks due to ICE are more clear than with the thick (40 mm) ones (Fig.7c). Scintillators of this type (as the GSO-based ones) can also be used for detection of fast neutrons with external hydrogen-containing delay elements.

Thus, complex studies of semiconductor and oxide single crystals CdS(Te), ZnSe(Te), CdWO<sub>4</sub>, GSO and BGO have shown a possibility to use them in "SELDI" detectors for detection of neutrons in mixed gamma-neutron fields. The selectivity is realized using instantaneous low-energy internal conversion electrons and gamma-quanta from the reactions of radiation capture of thermal neutrons on cadmium and gadolinium nuclei.

Scintillators CdS(Te) and ZnSe(Te), due to their unique features of radiation-induced defect formation were especially suitable for control of large doses of neutrons. Good matching of these crystals with photodiodes makes possible to produce detectors of small size.

Complex oxide scintillators have been successfully tested together with a photomultiplier also for  $\alpha$ -activation detection of light nuclei, e.g., beryllium, in the environment and measurement <sup>241</sup>Am mixed with great quantity  $\gamma$ -rays nuclei.

The results presented are preliminary, but they clearly show that the scintillation materials studied can successfully compete with conventional lithium- and boron silicate glasses. Further studies are under way, aimed at improving fabrication technology of detectors and instruments based on these crystals.

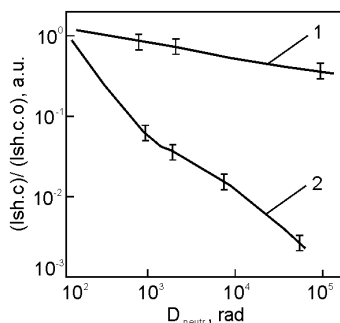


Fig.4.5. Relative response of scintillator-photodiode-preamplifier systems to  $\gamma$ -quanta from <sup>137</sup>Cs (100 R/h) after irradiation by fast neutrons with dose  $D_n$ : 1 — ZnSe(Te); 2 — CdS(Te). ( $I_{sh.c.}$  — shot circuit current after irradiation,  $I_{sh.c.0}$  — before irradiation).

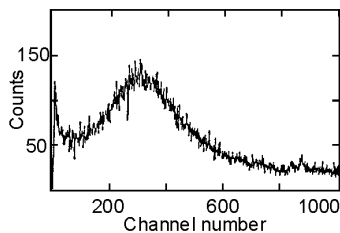


Fig.4.6. Pulse amplitude spectra of GSO-based scintillator-photoelectric multiplier system in the field of thermal neutrons.

Table 4.8. Basic parameters of spectrometric detection blocks.

Parameters	Radionuclide	BGO	CWO		GSO*
Overall dimension, mm		40×40	40×40	40×1	40×1
Photoelectric multiplier		PM-176, Russian	PM-176, Russian	PM-176, Russian	PM-176, Russian
Amplitude resolution $R$ , %	$^{137}\text{Cs}$ $E_{\gamma}=0.662\text{ MeV}$ $^{239}\text{Pu-Be}(\alpha, n\gamma)$ $E_{\gamma}=4.43\text{ MeV}$ $^{241}\text{Am}$ $E_{\gamma}=59.6\text{ MeV}$ $E_{\alpha}=5.49\text{ MeV}$	11.9–12.0  4–5	10–10.6  6–7	   24	   27 13
Sensitivity, pulsed/Bk×s pulsed×s/R×h <sup>-1</sup> μg/m <sup>3</sup>	$^{137}\text{Cs}$ $^{40}\text{K}$  $^9\text{B}(\alpha, n\gamma)^{12}\text{C}^*$	0.0046 0.0014 $7.97\times 10^6$ 5.0	0.0041 0.0013		
Intrinsic background in the nuclide windows, s <sup>-1</sup>  a) without protection  b) with passive protection	  $^{241}\text{Am}$ $^{137}\text{Cs}$ $^{40}\text{K}$  $^{241}\text{Am}$ $^{137}\text{Cs}$ $^{40}\text{K}$	  5.6 2.35  0.55 0.23	  5.2 2.0  0.52 0.20		  1.15  0.6
Minimum detectable activity, Bk/kg (with protection, $T_{exp}=1\text{ h}$ )	$^{137}\text{Cs}$ $^{241}\text{Am}$	5.4	5.3		4.5
Exposure dose rate measurement range, R/h		from $13\cdot 10^{-6}$ to $10^{-2}$			
Specific activity measurement range, Bk/kg					from $A_{min}$ to 9999
Overall dimension diameter × $L$ , mm		63×345	63×345		78×345**
Mass of the detection block, kg		1.5	1.52	0.04	1.5
Power	200V, 50 Hz; or storage-battery 12 V, 10 W				

\*See Ref. [19]; \*\* with passive protection

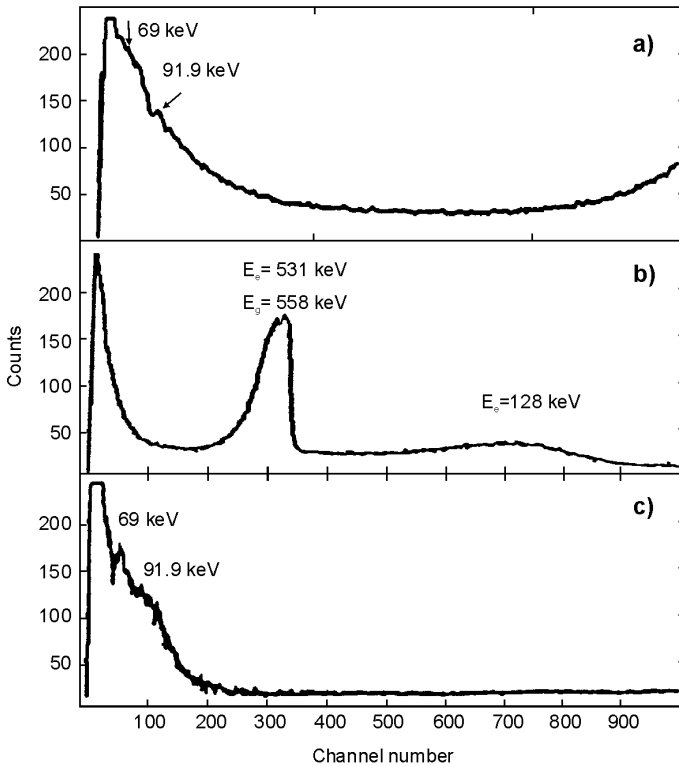


Fig.4.7. Pulse amplitude spectra of scintillator- photomultiplier systems based on CWO crystals of different size:  $40 \times 40 \text{ mm}^3$  (a,b). and  $40 \times 1 \text{ mm}^3$  (c).

#### 4.2. *Oxide and semiconductor scintillators in scintielectronic detectors for detection of neutrons*

The method of neutronography is one of the most informative and promising for nondestructive testing. At present, there is a clear tendency to be the use, alongside with gas discharge devices, solid-state scintillation detectors and dosimeters based on materials with high capture cross-section, such as  $^6\text{Li}$ ,  $^{155,157}\text{Gd}$ , etc. The aim of this work was to continue our studies of different possibilities of high efficiency oxide scintillators applications for neutron detection.

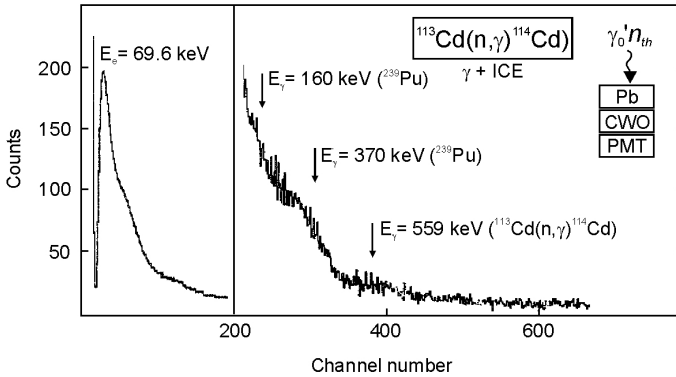


Fig.4.8. Pulse amplitude spectrum of CWO crystal in thermal neutron field. Between the source and the crystal — 50 mm thick Pb shield.

Reder [20], as well as Ryzhikov and Nagornaya [21, 22] have demonstrated a principal possibility to detect thermal neutrons using oxide scintillators  $\text{Gd}_2\text{SiO}_5(\text{Ce})$  (GSO) and  $\text{CdWO}_4$  (CWO).

Fig.4.8 presents the spectrum of gamma-quanta from the reaction  $^{113}\text{Cd}(n,\gamma)^{114}\text{Cd}$ , obtained by the internal counting method for thermal neutrons captured by cadmium nuclei. The presented amplitude and pulse spectra show that, alongside with the above-mentioned gamma-quanta, there are also intrinsic gamma-quanta of a Pu-Be source that are observed.

To exclude more completely the influence of the Pu-Be source gamma-background, we used, in addition to the lead filter, a LiF filter of 10 mm thickness. This crystal does not absorb hard gamma-quanta of the neutron source, though absorbs thermal neutrons quite well (up to 92%). Thus, using the two filters, we obtain a spectrogram of the residual gamma-background and neutrons. The difference between the spectrograms measured with and without the LiF screen using a CWO crystal of  $\varnothing 40 \times 40 \text{ mm}^3$  size allows to obtain a spectrogram due to thermal neutron capture, eliminating the gamma-background more completely (the “lithium difference” method, Fig.4.9).

Another efficient way to eliminate the noise due to gamma-background of the neutron source is comparison of source spectra obtained using BGO and CWO crystals. These crystals are of comparable sensitivity to gamma-quanta, but they differ considerably in their sensitivity

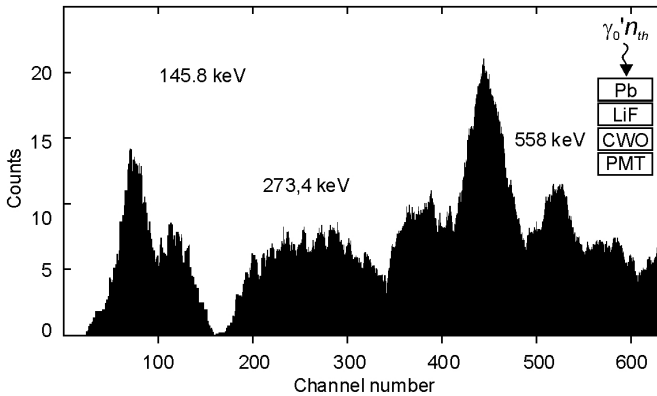


Fig.4.9. Pulse amplitude spectrum of CWO crystal in thermal neutron field. Between the source and the crystal — Pb and LiF shield.

to thermal neutrons (the sensitivity of BGO is much lower). Our studies have shown (Fig.4.10) that on the difference spectrum obtained using computer analysis more clearly seen are the gamma-peaks due to radiation capture reaction on  $^{186}\text{W}$  (peaks at 145.8 keV and 273.4 keV) and on  $^{113}\text{Cd}$  (the 558 keV peak).

In addition to the detection of internal conversion electrons and gamma-quanta due to radiation capture of thermal neutrons on W and Cd nuclei (energies up to 1 MeV), gamma-lines appear at 2.22 MeV and 4.43 MeV in the high energy region of the gamma-spectrum. The 2.22 MeV line is due to the thermal neutron capture on the moderator hydrogen nuclei. The 4.43 line emerges from the reaction  $(\alpha, n\gamma)$  on berillium nuclei. Both these lines are, in fact, caused by inefficiency of the lead protection. Fig.4.11 shows characteristic spectrograms of the high-energy region of the pulse spectrum.

The results obtained suggest that the use of massive CWO-based scintillators can be promising not only for efficient detection of thermal neutrons, but also for detection of fast neutrons, provided the CWO crystals are used with an external hydrogen-containing converter.

In the pulse amplitude spectrum, one should expect, alongside with gamma-quanta resulting from capture of thermalized fast neutrons on the hydrogen nuclei ( $E_\gamma = 2.2 \text{ MeV}$ ), gamma-quanta of lower energy due to neutron capture on tungsten and cadmium nuclei.



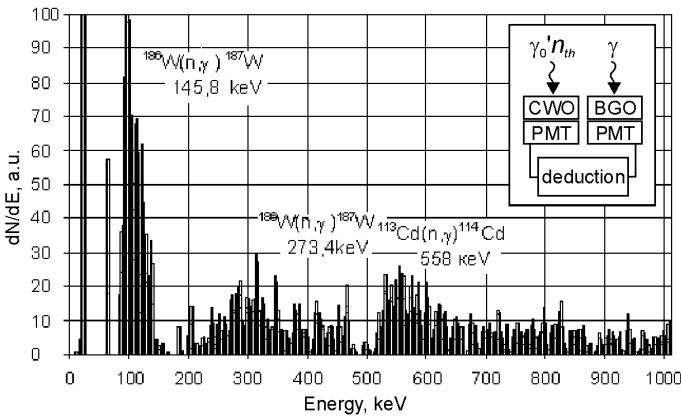


Fig.4.10. Pulse amplitude spectrum of CWO-BGO crystal in the radiation field of  $^{239}\text{Pu}\text{-Be}(\alpha,n)$ -source.

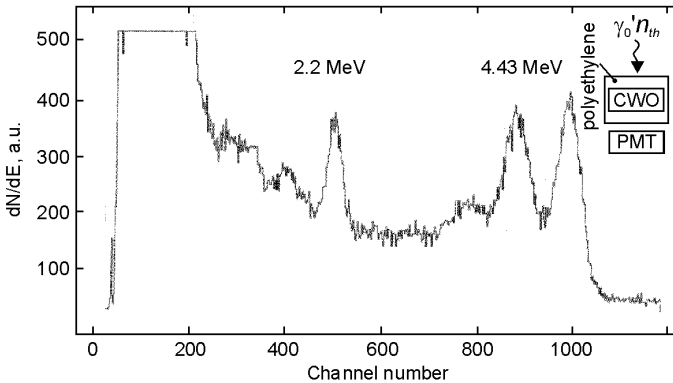


Fig.4.11. Pulse amplitude spectrum of CWO crystal with an external hydrogen-containing converter-moderator.

CWO crystals can be also used, as it has been shown by our studies, for direct detection of thermal and resonance neutrons, as well as for simultaneous detection of fast neutrons by deceleration and capture of the thermalized fast neutrons on hydrogen nuclei with subsequent detection of high energy radiation capture quanta by a scintillator.

Efficiency was measured for detection of thermal neutrons by crystals of cadmium tungstate and gadolinium silicate, and comparison was

Table 4.9. Efficiency of thermal neutron detection.

Scintillator	Detecting element	Detector size, mm	Energy range of detection of secondary particles or quanta, keV	Instrumental efficiency of detection, $E_{t.n.}, \%$
${}^6\text{LiJ}(\text{Eu})$	Single crystal	25×2	(p.c.a.) from particles from reaction ${}^6\text{Li}(n, \alpha)\text{T}$	87
GSO	Small crystalline	63×3	30–1000	67
CWO	Short crystal	80×2	20–100 30–1000	3,4 11,8
CWO	Single crystal	40×40	30–1000	14,3

made with similar data obtained with detectors based on  ${}^6\text{LiI}(\text{Eu})$  single crystals. Detection efficiency for “thin” detectors (i.e., those non-sensitive to gamma-radiation) was evaluated by the cadmium difference method. The results obtained are presented in Table 4.9. As follows from these data, detection efficiency of thermal neutrons with  ${}^6\text{LiI}(\text{Eu})$  detectors is 87%, and it is 67% for detectors made of small-crystalline GSO. This value is just 3.4% for detectors made of small-crystalline crumb powder of CWO on the energy range of gamma-quanta 20...100 keV, and 11.8% in the 30...1000 keV range. The efficiency of the crystals used is of the same order of magnitude. Comparative characteristics of detectors on the basis of complex oxides and  ${}^6\text{LiI}(\text{Eu})$  are given in Table 4.9.

The following conclusions can be made from these results:

- A possibility is shown of detection of different groups of thermal and resonance neutrons by the internal counting method using an array of heavy nuclei with large neutron capture cross-section.
- Combined detectors have been developed and tested on the basis of different oxide scintillators or semiconductor scintillators for detection of different groups of thermal and resonance neutrons, as well as for simultaneous and separate detection of neutrons, gamma-quanta and heavy charged particles.
- Methods and equipment have been proposed to account for the gamma-background of the environment and the neutron source during spectrometry of thermal and resonance neutrons.

- A small-sized disperse detector for detection of fast neutrons has been developed and tested.
- Possibility is shown to detect fast neutrons by means of their deceleration and capture of the thermalized fast neutrons on hydrogen nuclei with subsequent detection of high energy gamma-quanta of the radiation capture by CWO scintillators.

## REFERENCES

1. *Ryzhikov V.D.* Highly efficient semiconductor scintillation detectors based on compounds  $A^{II}B^{IV}$ , Monocrystally i osobo chistyyi veshchestva. – Moskva, 1984. – 36 p.
2. *Ryzhikov V.D.* Scintillation crystals of semiconductor compounds  $A^{II}B^{IV}$ . Preperation, properties, applications, Monocrystally i scyntillacionnyji materialy. – Moskva, 1989. 126 p.
3. *Harrison M.* Digital radiography – a review of detector design // Nucl. Instrum. and Meth. A. – 1991. – **310**, P.24–34
4. *Atroshchenko L., Gryneov V., Ryzhikov V. et al.* Scintillator crystals and detectors of ionization radiation on their base. – Kiev: Naukova Dumka. – 1998. – 311 p.
5. *Globus M., Grinyov B.* Inorganic scintillators. Kharkov: Acta, – 2000. – 408 p.
6. *Schotanus P.* Readout of inorganic scintillation crystals with semiconductor devices // Proceedings of the “CRYSTAL 200” international workshop. – September 22–26, 1992. – Chamonix, France: Editions Frontiers. – 1993. – P.533–538.
7. *Moszynski M., Ludziejewski T., Wolski D. et al.* Properties of the YAG:Ce scintillator // Nucl. Instrum. Meth. in Phys. Res. – 1994. – **A345**. – P.461–467.
8. *Burachas S.F., Zdesenko Yu.Y., Ryzhikov V.D.* On a possibility of  $^{160}\text{Gd}$   $2\beta$ -decay detection using GSO scintillators. – Kiev. – 1993. – 12 p.
9. *Burachas S.F., Kughtina N.N., Ryzhikov V.D. et al.* Radio-luminescence of materials based on gadolinium and europium silicate // Neorganicheskiye materialy. – 1993. – **29**, No.8. – P.1133–1135.
10. *Zdesenko Yu.Y., Burachas S.F., Ryzhikov V.D. et al.*  $\text{CdWO}_4$ ,  $\text{ZnSe}$  and  $\text{ZnWO}_4$  scintillators in studies of  $2\beta$ -processes // Pribory i tehnika experimenta. – 1989. – No.5. – P.80–94.

11. *Ryzhikov V.D., Selegenev Ye.M., Danshin Ye.A. et al.* Uses of avalanche photoreceivers for detection of nuclear radiation // Proceedings of the 2-th Soviet Union conference on avalanche photoreceivers instruments. – Rostov-Jaroslavskiy. – 1988. – P.37.
12. *Reeder P.L.* Thin GSO scintillator for neutron detection // Nucl. Instrum. Meth. in Phys.Res. – 1994. – **A353**. – P.134–136.
13. *Ryzhikov V.D., Burachas S.F., Dolgikh T.N.* Scintillation characteristics of yttrium borate ceramics // Proc. Symposium F: Advances in Solidification Process E MRS 1993 Spring Meeting. – Strasbourg, France. – May 4–7, 1993.
14. *Groshev L.V., Demidov A.M., Lucenko V.N. et al.* Spectra of  $\gamma$ -rays and internal conversion electrons from the reaction  $^{113}\text{Cd}(n, \gamma)^{114}\text{Cd}$  // Izvestiya AN SSSR, Ser.Phys. – 1962. – **26**, No.8. – P.979–992.
15. *Groshev L.V., Demidov A.M., Ivanov V.A. et al.* Gamma-ray and internal conversion electrons spectra encerging from the reaction  $(n, \gamma)$  on gadolinium isotopes // Izvestiya AN SSSR, Ser.Phys. – 1962. – **26**, No.9. – P.1119–1133.
16. *Fominykh V.L.* Studies of stability and angular distribution of neutron flux of standard neutron sources, Issledovaniya v oblasti ioniziruyshchih isluchenij // Trudy metrologicheskikh institutov SSSR. – 1974. – No.166(226). – P.35–414.
17. *Takahiko Ayama, Yasushi Oka, Kiyonari Honda et al.* A neutron detector using silicon PIN photodiodes for personal neutron dosimetry // Nucl.Instrum. and Meth. in Rhys. Res. – 1992. – A314. – P.590–594.
18. *Norikazu Horiuchi, Tadashi and Eiji Kobayashi* A High-Sensitivity Neutron Dosimeter Using the Coherent Demodulation Technique // IEEE Trans. on Nucl. Sci. – 1995. – **42**, No.6. – P.2203–2208.
19. *Burachas S.F., Piven' L.A., Ryzhikov V.D. et al.* Spectrometric scintillation detection block for selective detection of  $^{241}\text{Am}$   $\gamma$ -radiation of transuranic elements // Pribory i tehnika experimenta. – 1996. – No.3. – Pp.1–5.
20. *Reder P.L.* Neutron detection using GSO scintillator // Nucl. Instr. and Meth. – 1994. – **A340**, No.2. – P.371–378.
21. *Ryzhikov V., Nagornaya L., Volkov V. et al.* Studies of cadmium tungstate single crystals for detection of thermal neutrons // Book of Abstracts (SCINT-97) inorganic scintillators and their applications. – Shanghai: Shanghai Institute of Ceramics. – 1997. – P.157–160.
22. *Ryzhikov V., Nagornaya L., Burachas S. et al.* Detection of thermal and resonance neutrons using oxide scintillators // IEEE Transaction on Nuclear Science. – 2000. – **47**, No.6. – P.2061–2064.

## CHAPTER 5

### OPTIMIZATION OF THE DETECTOR SIZE

Main requirements to scintillators used for different application include high light output, density and effective atomic number, as well as low afterglow level. These requirements are met by such scintillators as  $\text{CdWO}_4$  (CWO),  $\text{Bi}_4\text{Ge}_3\text{O}_{12}$  (BGO),  $\text{ZnSe}$ , which are replacing traditional  $\text{CsI}(\text{Tl})$  in modern tomographs digital radiography nuclear measurmant, ect. [1–5].

Alongside with advantages, these scintillators have also some drawbacks. BGO and CWO have lower light output than  $\text{CsI}(\text{Tl})$  — about 15% and 40%, respectively. These materials have relatively low transparence to intrinsic radiation. E.g., experimentally measured values of the light attenuation coefficient  $K$  in the intrinsic radiation wavelength range is  $0.1\text{ cm}^{-1}$  for  $\text{CsI}(\text{Tl})$ ,  $0.3\text{--}0.4\text{ cm}^{-1}$  for BGO,  $0.6\text{ cm}^{-1}$  for CWO,  $0.2\text{--}0.7\text{ cm}^{-1}$  for  $\text{ZnSe}$ . With broadening of the energy range for different application, thickness of the detecting element increases, with corresponding attenuation of the emission of detecting elements. Our analysis, which is presented below, allows making an optimum choice of type and thickness of scintillation material in a specified interval of the energy range embracing all possible application fields of medical and technical tomography. The calculations took into account such factors as absorption in the material, scintillator light output, light attenuation coefficient in the intrinsic radiation range, light flux intensity in the scintillator output window, spectral matching between the scintillator emission and photoreceiver sensitivity.

Theoretical analysis. A generally accepted criterion for choosing thickness  $L$  of a detecting element is 90% absorption of the photon energy flux in the material. Table 5.1 presents these  $L$  values calculated for some typical scintillators materials at different photon energies. The calculation methods used are described in [6] (energies up to 100 MeV)

Table 5.1. Thickness of scintillator material layer ensuring 90% absorption of the photon radiation energy flux as function of the radiation energy  $E_{ph}$  for different scintillators.

$E_{ph}$ , MeV	Thickness of 90% absorption layer, mm			
	CsI(Tl)	ZnSe	CWO	BGO
0.01	0.03	0.03	0.03	0.03
0.02	0.19	0.1	0.07	0.05
0.05	0.4	1.2	0.48	0.53
0.08	1.4	4.4	0.6	1.7
0.1	2.5	7.5	1.1	0.82
0.12	4.0	11	1.7	1.3
0.15	6.9	17	2.9	2.2
0.2	13	25	5.7	4.4
0.3	28	37	13	10
0.5	52	52	26	24
1	88	74	46	48
3	140	120	76	81
5	140	130	79	84
10	130	130	74	78
50	83	98	49	50
100	72	86	42	43
1000	60	78	34	34
10000	60	78	34	34

and [7] (for higher energies). The mass attenuation coefficient of lead was taken from [8], and the effective atomic number was calculated as described in [9].

The lowest values of the linear attenuation coefficient  $M$  (correspondingly, the highest values of  $L$ ) for BGO, CWO and CsI(Tl) were obtained for  $\sim 5$  MeV photons ( $\sim 80$  mm and 140 mm), and for ZnSe — 10 MeV (130 mm, Table 5.1). This is due to re-distribution of relative contributions from the Compton scattering and pair generation mechanisms.

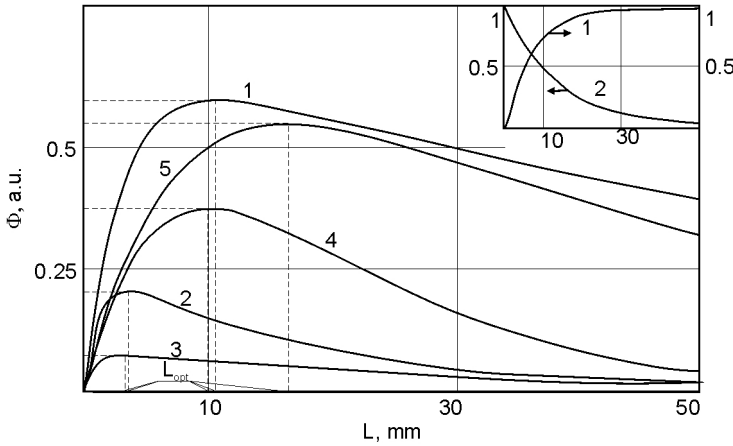


Fig.5.1. Light flux intensity as function of crystal thickness under excitation by photon radiation of 0.15 MeV for scintillators: 1 — CsI(Tl); 2 — CWO; 3 — BGO; 4 — ZnSe ( $K_{eff}=0.7 \text{ cm}^{-1}$ ), 5 — ZnSe ( $K_{eff}=0.2 \text{ cm}^{-1}$ ). In the Insert: 1 — attenuation of the photon radiation over crystal thickness (ZnSe, 0.15 MeV); 2 — attenuation of optical radiation over ZnSe crystal thickness ( $K_{eff}=0.7 \text{ cm}^{-1}$ ).

Absorption of the photon radiation energy  $I_{ph}$  inside the crystal varies according to the law (Fig.5.1, curve 1 in the Insert)

$$I_{ph} = I_0(1 - e^{-ML}), \quad (5.1)$$

where  $I_0$  is the photon radiation flux density over the input plane of the crystal, and  $L$  is the crystal thickness.

Intensity  $\Phi$  of the optical radiation propagating along the crystal from its input plane ( $\Phi = \Phi_0$ ) changes, accounting for the light attenuation coefficient  $K_\lambda$  for a specified wavelength  $\lambda$ , as shown in Fig.5.1 (curve 2 in the Insert).  $\Phi(L, \lambda)$  plots calculated accounting for non-linear attenuation  $I_{ph}(L)$  at the photon radiation energy  $E_{ph} = 150 \text{ keV}$  are shown in Fig.5.1.

The values of  $K_\lambda$  variation at the half-height boundaries of the emission band were  $0.16\text{--}0.075 \text{ cm}^{-1}$  for CsI(Tl),  $0.62\text{--}0.28 \text{ cm}^{-1}$  for BGO,  $0.86\text{--}0.48 \text{ cm}^{-1}$  for CWO, and  $0.9\text{--}0.55 \text{ cm}^{-1}$  for ZnSe. If we substitute an averaged value  $K_{eff}$  for  $K_\lambda$  values in the range under consideration, the expression for calculations is simplified:

$$\Phi(L) = \frac{SM_\alpha}{K_{eff} - M} (e^{-ML} - e^{-K_{eff}L}), \quad (5.2)$$

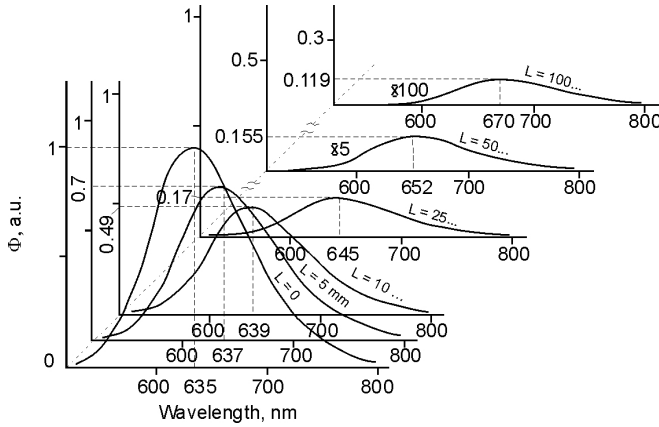


Fig.5.2. Changes in luminescence spectra of ZnSe crystals ( $K_{eff} = 0.7 \text{ cm}^{-1}$ ) as light passes through crystals of thickness 0, 5, 10, 25, 50 and 100 mm.

where  $S$  is an efficiency factor for transformation of the exciting photon radiation into light,  $M_0$  is the linear photon radiation absorption coefficient determined according to [6] in the energy range 0.01–100 MeV. From (5.3), an approximate expression can be obtained for the optimum thickness  $L_{opt}$ , at which the light flux through the output plane of the crystal would have the highest intensity:

$$L_{opt} = \frac{\ln(M/K_{eff})}{M - K_{eff}}, \quad (5.3)$$

At this thickness, the output light flux density is

$$\Phi(L_{opt}) = S \frac{M_0}{M} e^{-K_{eff} L_{opt}} \quad (5.4)$$

Comparison of results obtained using expressions (5.2)–(5.4) and by numerical calculations shows that nearly in all the relevant energy range the errors do not exceed 12–15%.

**Discussion.** Because the short wavelength edge of the emission spectrum is superimposed over the fundamental absorption edge, the intrinsic radiation attenuation coefficient  $K_\lambda$  can vary by an order of magnitude and more. This means that the emission spectrum can be transformed on the way of the light flux from the input to the output plane of the crystals. In Fig.5.2, such transformation is shown for ZnSe



Table 5.2. Optimum scintillator crystal thickness  $L_{opt}$  and attenuation of the exciting photon radiation  $\alpha$  at the optimum thickness.

$E_{ph}$ , MeV	CsI(Tl)		CWO		BGO		ZnSe $K_{eff}=0.7 \text{ cm}^{-1}$		ZnSe $K_{eff}=0.2 \text{ cm}^{-1}$	
	$L_{opt}$ , mm	$\alpha$ , %	$L_{opt}$ , mm	$\alpha$ , %	$L_{opt}$ , mm	$\alpha$ , %	$L_{opt}$ , mm	$\alpha$ , %	$L_{opt}$ , mm	$\alpha$ , %
0.05	1.1	100	0.92	99	1.1	99	1.8	96	2.5	99
0.075	2.5	99	0.97	99	2.4	98	3.9	91	5.7	97
0.1	4.9	99	1.7	97	1.5	99	6.2	85	9.5	95
0.15	11	97	3.5	94	3.2	97	9.8	74	16	90
0.2	17	95	5.5	89	5.3	94	12	67	21	86
0.3	28	90	9.1	81	9.3	87	15	60	27	81
0.5	42	84	14	70	15	77	18	54	33	77
1	57	77	18	60	22	66	21	47	40	71
5	74	70	24	50	30	56	26	36	54	60
10	70	72	23	51	29	57	26	36	54	60
50	55	78	19	59	23	65	23	42	46	66

crystals with  $K_{eff}=0.7 \text{ cm}^{-1}$ . The following features can be noted. Maximum of the emission spectrum is shifted to longer wavelengths — in this case, by 35 nm at 100 mm crystal thickness. The attenuation coefficient is decreased by 3–8% for crystals of <50 mm thickness.

Account for intrinsic light attenuation in scintillators shows that the optimum thickness values can be lower than  $L$  values calculated for 90% absorption. In Table 5.2 and Fig.5.3  $L_{opt}$  values are listed for different scintillators in a broad energy range. Comparison of these data with those in Table 5.1 show that the difference  $\Delta L = L(90\%) - L_{opt}$  becomes larger at higher energies and worse crystal transparency. Our measurements on CsI(Tl), CWO and ZnSe crystals in the 10 keV — 1 MeV energy range have shown good correlation of the experimental data with calculated values of  $L_{opt}$ .

For the highest optimum thickness values at 5–10 MeV, attenuation of photon radiation (Table 5.2) varies from 36% for ZnSe of aver-

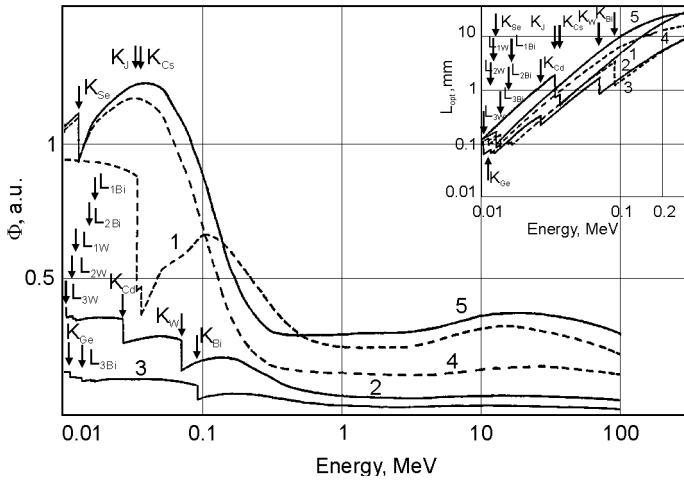


Fig.5.3. Luminescence intensity (accounting for spectral matching with photoreceiver [10]) at optimum thickness as function of the photon radiation energy. In the Insert: optimum scintillator thickness as function of the photon radiation energy. 1 — CsI(Tl); 2 — CWO; 3 — BGO; 4 — ZnSe ( $K_{eff} = 0.7 \text{ cm}^{-1}$ ), 5 — ZnSe ( $K_{eff} = 0.2 \text{ cm}^{-1}$ ). Arrows indicate the energies of K- and L-jumps of photon radiation absorption by the respective elements.

age transparency to 70% for highly transparent CsI(Tl).  $L_{opt}$  becomes smaller than  $L$  (90%), beginning from energies of 0.08–0.3 MeV.

To choose an optimum material for a specified energy range, difference in the light output should be accounted for. In Fig.5.3, luminescence intensity  $\Phi$  is shown as function of energy at the optimum sample thickness. For all crystals, except ZnSe, a FEU-79 PMT was used, with its maximum sensitivity range at 400–600 nm. As ZnSe scintillators were intended for application with photodiode, this photoreceiver was used in this case. The luminescence intensity was compared with CsI(Tl) studied under the same conditions. It follows from Fig.5.3 that ZnSe (both of medium and improved transparency) in the energy range from several keV to 100–120 keV are superior to other materials. At higher energies, it is preferable to use ZnSe of high transparency and CsI(Tl), but in this case CWO and BGO are even more advantageous due to much lower optimum thickness, making dimensions of the the whole receiving system smaller.

Thus, choosing the type and thickness of scintillator for detection of photon radiation in a specified energy range, one should account not only for attenuation of the detected photon beam, but also for attenuation of the intrinsic radiation of the scintillator [10]. This results in smaller optimum thickness (as compared with generally accepted thickness of 90% absorption). This effect is already felt (see Tables 5.1 and 5.2) at  $>0.2\text{--}0.3$  MeV, and at energies above 5 MeV the optimum thickness is 2–3 times smaller than the 90% absorption value. Accounting for different light output of CWO, BGO and ZnSe scintillators, as well as existing technological possibilities for growing crystals of required dimensions, ZnSe crystals should be recommended as the most suited for radiation detection in the 0.3–0.5 MeV range, while CWO and BGO scintillators would be preferable at higher energies.

---

REFERENCES

1. *Farakhi M.R.* // IEEE Trans. – 1982. – **NS-29**, No.3. – p.1237.
2. *Grabmaier B.C.* // IEEE Trans. – 1984. – **NS31**, No.1. – p.372.
3. *Ryzhikov V.D., Shapiro O.S., Ignatov S.M., Silin V.I.* // Pribory i tekhnika eksperimenta. – 1986. – No.4. – p.155.
4. *Farukhi M.R.* Radiation detectors for CT instrumentation. Lecture Notes Medicine Information. – 1984. – No.23. – p.62.
5. *Sidorin I.V., Mukhin V.I.* // Preprint ITEF, No.96. – Moscow: TsNI-IAtominform, 1987.
6. *Nemets O.S., Gofman Yu.V.* Handbook on nuclear physics. – Kiev: Naukova Dumka, 1975.
7. *Umanskii Ya.S.* Roentgenography of metals and semiconductors. – Moscow: Metallurgiya, 1969.
8. *Noskov B.M.* Nuclear physics. Interaction of nuclear radiations with substance. Methods of detection of nuclear radiations. – Gor'kii: Ed. Gor'kii Univ., 1972.
9. *Ivanov V.I.* Course of dosimetry. – Moscow: Atomizdat, 1978.
10. *Ryzhikov V.D., Stadnik P.E., Yakovlev Yu.A.* // Pribory i tekhnika eksperimenta. – 1982. – No.4. – P.57.

## CHAPTER 6

### DETECTORS «SCINTILLATOR-PMT»

The scintillation method of radiation studies, initially based on the visual counting of scintillations, has found broad applications in studies of ionizing radiation thanks to invention of a “scintillator-PMT” type detector in 1946. Specific characteristics of such detectors - internal signal amplification by  $10^4$ – $10^8$ , input window area of hundreds of  $\text{cm}^2$ , good spectral matching of the PMT sensitivity region (Fig.6.1) to “blue-green” emission of many efficient scintillators (NaI(Tl), CsI(Tl), BGO, PWO, CWO, etc.) — allow their wide use in nuclear physics and high energy physics for detection of charged and neutral particles, in biology and medicine, in outer space, technical and other fields related to studies and applications of ionizing radiations [1–3].

Principal characteristics of “scintillator-PMT” (S-PMT) detectors are: detection efficiency  $P$ , energy (amplitude) resolution  $R$ , maximum statistical load for pulse counting  $N_M$ , integral non-linearity of the output signal, stability with respect to mechanical and climatic factors, parameters of mass and size.

Efficiency  $P$  of a S-PMT detector can be expressed as a product of physical efficiency (proportional to the probability of interaction of the falling radiation and the detector scintillation element) and “instrument” efficiency, dependent upon the recording probability of the emerged scintillation [4]. If the response (discrimination) threshold of a recording system is  $V_B$ , the detection efficiency is

$$P(V_B) = P_d \frac{\int_{V_B}^{V_{\max}} G(E_\gamma, V) dV}{\int_{V_B}^{V_{\max}} G(E_\gamma, V) dV},$$

where  $P_d = f(\mu, l, \theta)$  is the scintillator efficiency depending only on its full linear attenuation coefficient  $\mu$  (i.e., atomic number and other physical

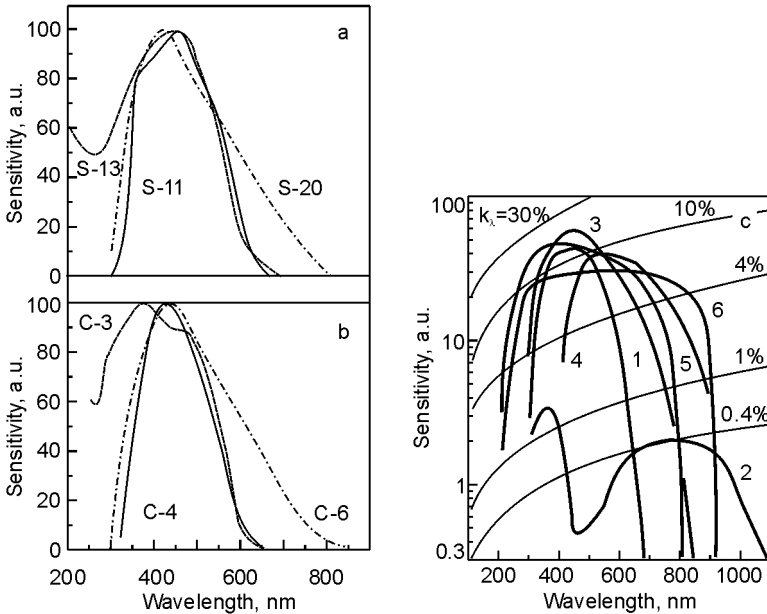


Fig. 6.1. Some types of PMT spectral characteristics: a — according to classification adopted in the USA and Great Britain (S-11 — SbCs; S-13 — SbCs with a quartz window; S-20 — SbKNaCs); b — according to classification adopted in CIS (S-4 — semi-transparent photocathode SbCs; S-3 — the same in a flask of uviol glass; S-8 — multi-alkali photocathode); c — spectral characteristics of photocathodes produced by RCA, USA: 1 — Sb<sub>3</sub>Cs; 2 — AgOS<sub>3</sub>; 3 — SbNaKC; 4 — ERMA; 5 — GaAsP; 6 — GaAs.

properties of the scintillator), scintillator dimensions  $l$ , angle  $\theta$ , at which the radiation comes to the scintillator;  $G(E_\gamma, V)$  is the kind of a counting dependence. For S-PMT detectors,  $P$  is much higher than for SCD and ionization chambers; with NaI(Tl) scintillators of 40 mm in diameter and height, for a parallel beam with  $E_\gamma = 5$  MeV  $P \approx 0,35$ , and at  $E_\gamma = 0,5$  MeV  $P \approx 0,7$ . The ratio  $S_p/S$  ( $S_p$  — the area under the photopeak,  $S$  — the total area under the counting characteristic curve) for such detector at  $E_\gamma = 4.5$  MeV is 0.2, and at  $E_\gamma = 0.66$  MeV — about 0,5 [5].

Accounting for the energy transformation mechanisms, light collection conditions and internal signal amplification in the detector, charge  $Q$  at the detector output is [4, 6]:

$$Q = \frac{e}{h\nu} E_\gamma \eta_{SC} K_A \Sigma_k M = \frac{e}{h\nu} E_\gamma \eta_{SC} K_c \Sigma_a \quad , \quad (6.1)$$

where  $e$  is the electron charge,  $h\nu$  is the mean energy of scintillation photons,  $E_\gamma$  is the incident radiation energy,  $\eta_{SC}$  is conversion efficiency of the scintillator,  $K_c$  — light collection coefficient,  $\Sigma_k$  — PMT photocathode quantum sensitivity (including photoelectron collection coefficient on the first dynode),  $M$  — PMT amplification (multiplication) coefficient,  $\Sigma_a$  — PMT anode sensitivity. Correspondingly, the voltage pulse  $V_a$  on the anode load  $R_a$  is

$$V_a = \frac{Q}{C_a} \Gamma = \frac{e}{h\nu C_a} E_\gamma \eta_{SC} K_c \Sigma_k M \Gamma \quad , \quad (6.2)$$

where  $C_a$  is the PMT anode stray capacitance,  $\Gamma$  is a function of  $R_a C_a / \tau_{SC} = \gamma_{ph}$  ratio ( $\tau_{SC}$  is the scintillator decay time); commonly used are  $\gamma_{ph}$  values leading to  $\Gamma \approx 0,5-0,8$  [6]. Estimates of  $V_a$  from (6.1, 6.2) for a NaI(Tl)-PMT detector at  $E_\gamma = 1$  MeV;  $C_a \approx 10$  pF;  $\tau_{SC} = 0,15$ ;  $h\nu \approx 3$  eV,  $\Sigma_k \approx 0,05-0,1$ ;  $M = 5 \cdot 10^5$ ;  $\Gamma = 0,5$  lead to signal amplitude values at the detector output about 4–7 V, with duration of several microseconds (we did not account for leakage of luminescence photoelectrons and other processes affecting the output detector signal) [4,5].

The relative value of the pulse amplitude dispersion  $\Delta V_a^2 / V_a^2$  at the S-PMT detector output determines its energy resolution  $R = \Delta E_\gamma / E_\gamma$ . In the first approximation (accounting for the fact that in (6.2) the largest statistical fluctuations are for the values of  $\Sigma_k$  [46]), the expression for  $R$  is

$$R^2 = \left( \frac{\Delta E_\gamma}{E_\gamma} \right)^2 = (2,36)^2 \frac{\Delta V_a^2}{V_a^2} = (2,36)^2 \left[ \frac{D_\rho}{\rho^2} + \frac{1 + \rho(\sigma - 1)}{N\rho(\sigma - 1)} \right], \quad (6.3)$$

where  $\rho$  is the probability that the photon formed in the scintillator would give rise to an electron appearing at the first PMT dynode;  $D_\rho$  is the dispersion;  $\sigma$  is the secondary electron emission coefficient (usually  $\sigma \approx 5$ ). Denoting the first term in (4.3) as  $\delta^2$  and accounting for the relationship of  $N$  and  $E_\gamma$ , we obtain

$$R^2 = \delta^2 + C_1 / E_\gamma, \quad (6.4)$$

where  $C_1 = (2.36)^2 \bar{h\nu} [1 + \rho(\sigma - 1)] / [C_{ef}(\sigma - 1)\rho]$ ;  $\bar{h\nu}/C_{ef}$  is the energy of a charged particle in the scintillator required for creation of one photon. It follows from (6.4) that  $R \sim 1/\sqrt{E}$ . An estimate of  $R$  from (6.3), (6.4) for a NaI(Tl)–PMT detector at  $E_\gamma = 1$  MeV;  $\bar{h\nu}/C_{ef} \approx 30\text{--}50$  eV;  $\rho \approx 0,05$ ;  $C_1 = 10^{-3}$  MeV;  $\delta^2 \approx 2 \cdot 10^{-4}$  gives the values of about 4.5%, and at  $E_\gamma = 0.15$  MeV  $R \approx 14\%$  [6].

From the general expression (6.3) for  $R$ , it follows that the energy resolution of a detector is determined both by PMT and scintillator properties, with

$$R^2 = R_{PMT}^2 + R_{SC}^2, \quad (6.5)$$

where  $R_{PMT}$ ,  $R_{SC}$  are, respectively, the PMT amplitude resolution and intrinsic resolution of the scintillator. The PMT amplitude resolution is essentially determined (provided the power supply is of high stability, etc.), by non-uniformity of the photocathode sensitivity, counting characteristics of noise (dark) pulses  $N_N$  and their amplitude  $V_N$ . The energy equivalent of PMT noises will be [3,4].

$$E_N = (V_N/V_a) \cdot E_\gamma \text{ [keV]}.$$

The measurements of  $R$  for NaI(Tl)–PMT detectors at  $E_\gamma = 0.66$  MeV have shown that at  $R = 8.2\text{--}9\%$   $R_{PMT} = 4.3\text{--}6\%$ , and, according to (6.5),  $R_{SC} \approx 5\text{--}8\%$ , which is substantially worse as compared with SCD.

Temperature variations of  $P$  and  $R$  are also determined by both PMT and scintillator properties: the conversion efficiency  $\eta_{SC}$  (light output) is, for most scintillators, monotonously decreasing at  $T > 200\text{--}300$  K, and PMT dark currents become substantially higher (Fig.6.2) [3].

Counting and time characteristics ( $N_M$ , front steepness, etc.) of S-PMT detectors comprising inorganic crystals are essentially determined, in each specific case, by amplitude-kinetic characteristics of the scintillator used, as even for the “fastest” scintillators like PWO, GSO their decay times are comparable or much slower than time parameters of PMT (which are normally of several nanoseconds or lower) [3,7]. When S-PMT detectors are used in coincidence circuits, one of the main parameters is the resolution time characterized by the dispersion  $D_t$  of the time interval  $t$  distribution from the moment when the particle comes to the crystal to the moment when  $V_a(t) = V_{amax}$ . For inorganic scintillators ( $\tau_{SC} > 10^{-10}$  s), the following condition holds [4]:



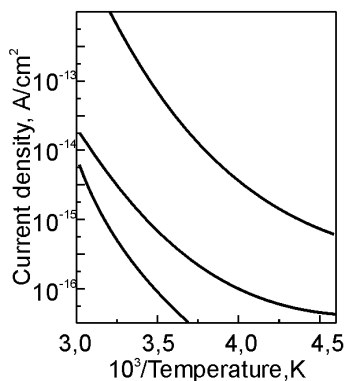


Fig. 6.2. Photocathode thermoemission current density ( $\text{A}/\text{cm}^2$ ) as function of temperature: 1 — SbNaKCs; 2 — SbCs; 3 — SbCs(O).

Especially severe requirements are imposed on the PMT high voltage power supply stability  $U_n$ , because relative changes in the PMT amplification coefficient  $\Delta M/M$  and voltage  $\Delta U_n/U_n$  are related as [3]:

$$\Delta M/M = (0.7-1.0)n_p \Delta U_n/U_n$$

( $n_p$  is the number of PMT multiplication stages). Thus, to ensure stability of the output signal  $V_a$  in (4.2) within 1 %, fluctuations of  $U_n$  should not exceed 0.05–1 %, and pulsation coefficient of  $U_n$  should be less than 0.001 %.

For the most common alkali halide detectors (NaI(Tl), CsI(Na) etc.), as these crystals are hygroscopic, hermetic sealing of the appropriate housing is required, and the use of large-sized (of tens and thousands of cubic centimeters) scintillation elements requires account for non-uniformity of thermal and mechanical parameters of all the AHC-PMT detector components, which makes their design rather complex (Fig.6.3 (a); only the scintillator packing is shown, without PMT) [1].

Design of new type detectors based on “heavy” oxide scintillators is much simpler (in Fig.6.3, a scintillation block “BGO-PMT-preamplifier” is shown) thanks to non-hygroscopicity, large  $Z_{eff}$  and other advantages of such scintillators [8].

$$(D_t)_{\min} \geq 2(\tau_{SC}/N_e),$$

where  $N_e$  is the number of primary photoelectrons broken away from the PMT photocathode. For NaI(Tl)–PMT detectors, the resolution time is  $\sim 2 \cdot 10^{-8}$  s (at  $P = 1$  for all detectors of the system).

Output signal  $V_a$  linearity (proportionality) as function of  $E_\gamma$  (or the flux density) of particles is determined, for S-PD detectors, both by non-linearity of PMT light characteristics (which can reach 5–15 % and is partially compensated for by optimization of the power supply voltage  $U_n$  and its distribution between PMT dynodes [3]) and by the energy leakage from the scintillator (reaching several per cent at  $E_\gamma > 1-5$  MeV due to longer path length of Compton electrons [4,5]).

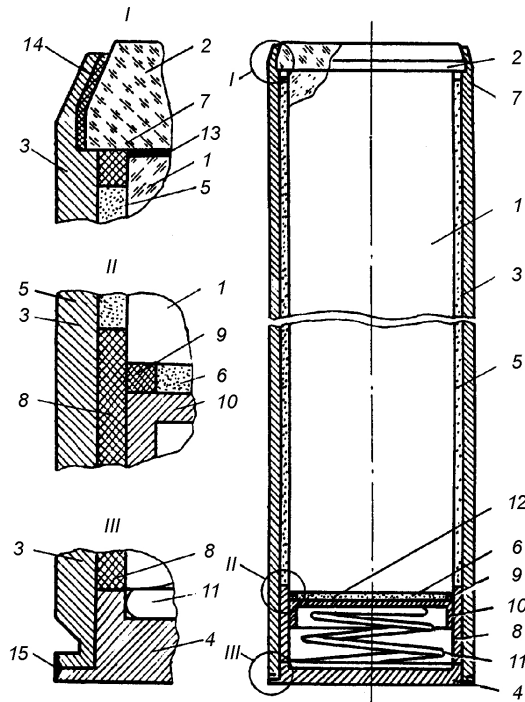


Fig. 6.3. Thermo-proof scintillation detection block: 1 — scintillator; 2 — output window; 3 — container; 4 — output window lid; 5 — light-reflecting cover; 6 — powder-like reflector; 7 — centering ring; 8 — centering guide plug; 9 — stopping ring; 10 — pusher; 11 — spring; 12 — pusher-powder interface; 13 — adhesive; 14,15 — hermetization units [2].

Such “heavy” oxide scintillators as CWO, BGO, PWO, GSO (their properties were considered in Chapter 2) have recently aroused great interest of producers and consumers of S-PMT detectors. In addition to the above-mentioned advantages, they are characterized by larger (as compared with AHC) efficiency  $P$ , faster response (especially for PWO and GSO [7,9]), very low intrinsic background level (CWO), which is important for recording of infrequent events, e.g.,  $2\beta$ -decay [10–13]. Detectors based on oxide scintillators at  $E \geq 0.15$  MeV have also larger (as compared with AHC)  $N_{pp}/N_{\Sigma}$  ratio ( $N_{pp}$  is the number of photons in the photopeak,  $N_{\Sigma}$  is the total number of photons emerging in the scintillator under irradiation) [14].

Table 6.1. Characteristics of S-PD detectors on the base of NaI(Tl) and BGO crystals.

Parameter /Detector	BDEG–22 NaI(Tl) Ø40×40 mm	BDEG–40T BGO Ø40×40 mm
Amplitude resolution, %	9.0–11.0	12.4–13.1
Sensitivity, cm <sup>2</sup>	1.0	≥5
Intrinsic background level in <sup>137</sup> Cs window, s <sup>-1</sup>	3.4	5.7
Integral non-linearity, %	2.0–2.4	0.25

For detectors based on BGO crystals and FEU-183 PMT, the resolution  $R$  is about 10 % (typical comparative characteristics of detectors based on BGO (BDEG-40T) and NaI(Tl) (BDEG-22) are presented in Table 6.1 and Figs.6.4, 6.5). BDEG-40T detectors are slightly inferior to BDEG-22 ones as for their energy resolution (see Fig.6.4), but they are definitely better in detection efficiency (especially in the Marinelli vessel geometry), integral non-linearity and functional reliability [8].

Detectors on the basis of GSO crystals, in addition to other excellent characteristics (see Chapter 2), are also distinguished by their high sensitivity to low-energy (0.03–0.2 MeV)  $\gamma$ - and  $\alpha$ -radiation ( $E_\alpha = 0.51$ –0.55 eV), which is characteristic, for example, for <sup>241</sup>Am (monitoring of <sup>241</sup>Am is very important, as its quantity in the Chernobyl catastrophe zone, due to specific transformations of isotopes emerged from the Chernobyl nuclear power plant, will increase till the year 2060, and only after that it will begin to decrease with  $T_{1/2} = 433$  years).

Detection blocks of “GSO-PMT-preamplifier” type developed at STC RI are superior, as for their selective detection efficiency of <sup>241</sup>Am  $\alpha$ -,  $\beta$ -,  $\gamma$ -radiation, to other known detection systems (comparative characteristics of detectors based on GSO and NaI(Tl) (BDEG 4–31–01A standard detector) are presented in Table 6.2; Fig.6.5 illustrates the detection ability of GSO-PMT detectors) [9]. The detection block has two low-resistance outputs: the first one, with the output pulse signal after the pre-amplifier, can be used with a PC, the second one, with output after a four-level signal formation device singling out the <sup>241</sup>Am  $\gamma$ -line ( $E_\gamma \sim 60$  keV) and  $\alpha$ -radiation of main transuranic radionuclides ( $E_\alpha \sim 5.5$  MeV) in the controlled windows — in combination with a

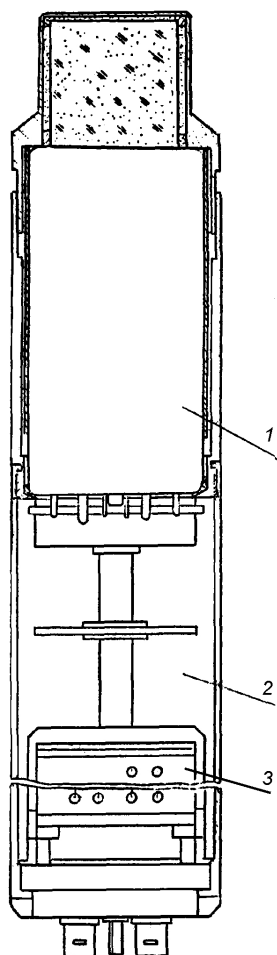


Fig. 6.4. Multi-purpose scintillation detection block BDEG-40T: 1 — scintillation block BGO-PMT; 2,3 — electronic subblock BDS-1.

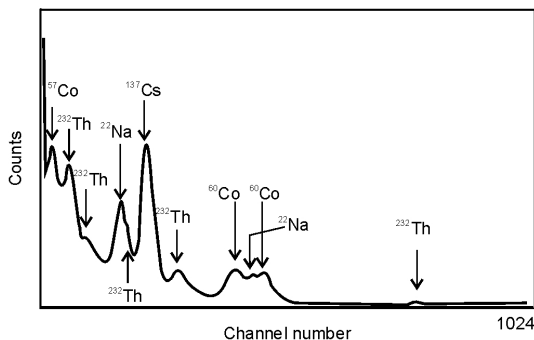


Fig. 6.5.  $^{137}\text{Cs}$   $\gamma$ -radiation spectrum on the background of  $\gamma$ -radiation from  $^{241}\text{Am}$ ,  $^{57}\text{Co}$ ,  $^{22}\text{Na}$ ,  $^{60}\text{Co}$ ,  $^{65}\text{Zn}$ ,  $^{54}\text{Mn}$ ,  $^{88}\text{Y}$  and  $^{223}\text{Th}$  (similar to the natural background accounting for contamination after Chernobyl catastrophe).

specialized data processing block of a  $\gamma$ - $\alpha$ -radiometer. Our measurements have shown that  $\gamma$ -radiation detection efficiency ratio for Am-241 and Co-57 with detection blocks based on GSO and NaI(Tl) is  $\sim 3.9$  and  $0.14$ , respectively, i.e., the selectivity for Am-241  $\gamma$ -line is much higher with GSO-PMT as compared with NaI(Tl)-PMT. For GSO-PMT detector,  $\alpha/\beta$ -ratio is  $\sim 0.41$ , and the minimum detectable activity for Am-241 is  $4.5 \text{ Bq/kg}$ .

Ultra-low background detectors based on CWO scintillators of several hundreds  $\text{cm}^3$  volume and very high (as for this type of sensors) energy resolution have been developed by STC RI using the latest achievements in crystal growth technology, optimization of light collection and electronic circuitry in the “detector-preamplifier-spectrometer (radiometer)” chain [10–13].

In combining a CWO-PMT pair, the best output parameters ( $S$ ,  $R$ , signal to noise ratio) were obtained using

Table 6.2. Detection efficiency  $P$  and energy resolution  $R$  of detection blocks based on GSO and NaI(Tl) for  $\gamma$ - and  $\alpha$ -radiation from different radionuclides.

Source (radio-nuclide)	Energy of $\gamma$ -quanta or $\alpha$ -particles, keV	Kind of radiation	Detection efficiency, abs. units		Energy resolution, %	
			GSO	NaI(Tl)	GSO	NaI(Tl)
$^{241}\text{Am}$	59,5	$\gamma$	0,270	0,069	26,5	33,2
$^{57}\text{Co}$	122	$\gamma$	0,016	0,117	19,0	22,5
$^{137}\text{Cs}$	662	$\gamma$	0,011	0,051	7,5	8,8
$^{241}\text{Am}$	5490	$\alpha$	0,30	—	13,0	—
$^{239}\text{Pu}$	5155	$\alpha$	0,31	—	13,0	—

Table 6.3. Energy resolution of CWO–XP2412 detectors with scintillators of different volume.

Crystals $\text{CdWO}_4$		Energy resolution (%) at given energies, keV		
Size (volume)	Mass, kg	570	662	1063
$\varnothing 40 \times 30$ mm ( $37.5 \text{ cm}^3$ )	0.3	9.7	8.5	6.7
$\varnothing 50 \times 37$ mm ( $73 \text{ cm}^3$ )	0.6	11.1	9.8	7.6
$\varnothing 54 \times 65$ mm ( $149 \text{ cm}^3$ )	1.1	13.2	11.4	9.3
$\varnothing 54 \times 95$ mm ( $217 \text{ cm}^3$ )	1.7	14.9	13.8	11.1
$\varnothing 25 \times 20$ mm ( $10 \text{ cm}^3$ )	0.08	8.8	7.5	6.4

Philips XP2412 PMT, as well as FEU-39 PMT in certain cases. The optimum light collection (for cylindrical scintillator shape) was ensured by the diffuse reflection coefficient of the scintillator surfaces monotonously changed with height [6,12] (the best diffuse reflection was expected from the input plane and adjacent side surface areas of a cylindrical scintillator, which, for a scintillation element with length to diameter ratio  $> 1$  results in 1.2 times higher  $R$  values, with light output decreasing by 10 %).

Data on the measured resolution  $R$  values for detectors with scintillators of different volume are presented in Table 6.3, and spectra in Fig.6.6 demonstrate excellent resolution and photopeak/Compton

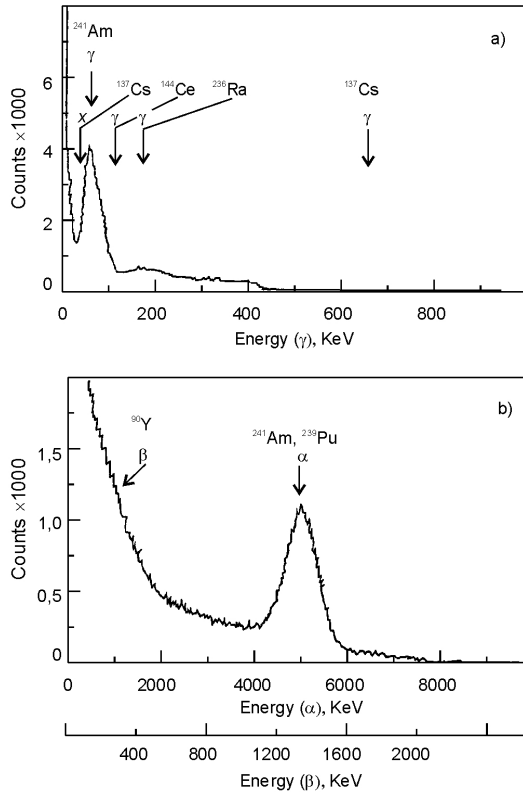


Fig. 6.6.  $\gamma$ - and X-ray radiation spectra from several radionuclides (a) and spectra of  $\alpha$ - ( $^{241}\text{Am}$ ,  $^{239}\text{Pu}$ ) and  $\beta$ - ( $^{90}\text{Y}$ ) radiation (b) obtained using a GSO-based detection block.

ratio values for a “reference” detector with scintillator volume  $10 \text{ cm}^3$  (a) and a large-sized detector (mass of  $1.1 \text{ kg}$ ) (b).

The background index of CWO-PMT detectors of new generation in the  $E_\gamma = 2\text{--}3 \text{ MeV}$  range is  $\sim 5 \text{ counts}/(\text{year} \cdot \text{keV} \cdot \text{kg})$ , which is close to background characteristics of ultra-low background HPGe-semiconductor detectors ( $F = 2 \text{ counts}/(\text{year} \cdot \text{keV} \cdot \text{kg})$ ) that are used in installations for Ge-76  $2\beta$ -decay studies [10,11]. Sensitivity of CWO-detectors with scintillator volume of  $149 \text{ cm}^3$ , e.g., for  $^{40}\text{K}$  and  $^{208}\text{Tl}$ , in measurements of the activity of a standard soil sample of  $1 \text{ kg}$  mass with  $24 \text{ h}$

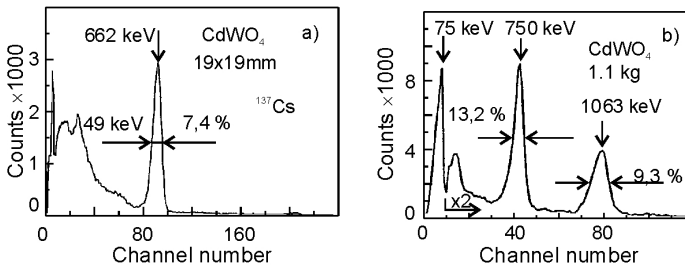


Fig. 6.7.  $\gamma$ -radiation spectra from  $^{137}\text{Cs}$  (a) and  $^{207}\text{Bi}$  (b) measured using CWO-based detectors.

exposure, is  $1.2 \cdot 10^{-12}$  Ci/kg and  $1,2 \cdot 10^{-2}$  Ci/kg, respectively, which is also close to characteristics of ultra-low background HPGe-detectors. Having worse spectrometric characteristics, CWO-PMT detectors are clearly superior in detection efficiency (sensitivity) and operational characteristics, which is especially important for measurements of low radioactivity levels and determination of isotope composition of samples in non-stationary conditions.

Further developments of new S-PMT detectors are now under way. New types and geometries of scintillators are used, detector design is improved by choosing optimally matched “scintillator-PMT” pairs. Functional parameters of S-PMT detectors are improved by using channel-type PMT, hybrid semiconductor and ceramic microchannel integrated PMT matrices with  $M = 10^6$ – $10^7$ , ensuring high mechanical strength, fast response, multiplication channel density up to 250, etc. This allows creation of small-sized detectors with improved spatial and time resolution ( $\sim 1.5$  mm and 5 ns, respectively,  $R = 30$  % and  $P = 10$  % with BGO crystal) [3,15].

## REFERENCES

1. *Grinev B.V., Seminozhenko V.P.* Scintillation detectors of ionizing radiations for severe operation conditions. – Kharkov: Osnova. – 1993. – 156 p.
2. *Kleuknecht K.* Detectors of corpuscular radiations. – Moscow: Mir. – 1990. – 200 p.
3. *Anisimova I.I., Glukhovskii B.M.* Photoelectronic multipliers. – Moscow: Sov.Radio. – 1974. – 64 p.
4. *Abramov A.I., Kazanskii Yu.A., Matusevich E.S.* Foundations of experimental methods in nuclear physics. – Moscow: Atomizdat. – 1977. – 528 p.
5. *Lyapidevskii V.K.* Methods for detection of radiations. – Moscow: Energoatomizdat. – 1987. – 408 p.
6. *Tsirlin Yu.A.* Light collection in scintillation counters. – Moscow: Atomizdat. – 1975. – 204 p.
7. *Kochanov V.F., Prokoshkin Yu.D. e.a.* Properties and beam tests of  $\text{PbWO}_4$  crystals. – Cern Libraries: Lapp. – Exp. – 93.08. – 1993.
8. *Burachas S.F., Borodenko Yu.A., Pirogov E.N. e.a.* Spectrometric scintillation blocks on the basis of bismuth germanate crystals // *Pribery i tekhnika eksperimenta*. – 1993. – No.4. – p.60–65.
9. *Bondar'kov M.D., Burachas S.F., Govorova R.A. e.a.* A spectrometric scintillation block on the basis of gadolinium silicate single crystal for selective detection of  $^{241}\text{Am}$  gamma-radiation and alpha-radiation of transuranic radionuclides // *Pribery i tekhnika eksperimenta*. – 1996. – No.3. – p.1–5.
10. *Burachas S.F., Panevich F.A., Georgadze A.Sh. e.a.* Large volume  $\text{CdWO}_4$  crystal scintillators // *Nucl. Instrum. and Meth. in Phys.* – 1996. – **A369**. – p.164–168.
11. *Danilevich F.A., Zdesenko Yu.G., Nikolaiko A.S. e.a.* Scintillators  $\text{CdWO}_4$ ,  $\text{ZnSe}$ ,  $\text{ZnWO}_4$  in studies of  $2\beta$ -processes. – Kiev: Inst. Nuclear Studies. – 1988. – 52 p.
12. *Nagornaya L.L., Zelenskaya O.V., Vostretsov Yu.Ya. e.a.* Spectrometric detectors on the basis of  $\text{CdWO}_4$  crystals // *Pribery i tekhnika eksperimenta*. – 1991. – No.2. – p.66–69.
13. *Georgadze A.Sh., Danevich F.A., Zdesenko Yu.G. e.a.* Scintillators of  $\text{CdWO}_4$  of large volume // *Pribery i tekhnika eksperimenta*. – 1996. – No.3. – p.48–52.
14. *Ryzhikov V.D., Sokhin V.P.* Spectrometric properties of crystals  $\text{CsI}(\text{Tl})$ ,  $\text{CdWO}_4$  and  $\text{Bi}_4\text{Ge}_3\text{O}_{12}$  in detection of gamma-radiation of energies from 0.1 to 10 MeV // *Pribery i tekhnika eksperimenta*. – 1996. – No.5. – p.62–66.
15. *Comby G., Karolak M.* Performances of multi channel ceramic photomultipliers // *Abstr. Int. Conf. "Inorganic scintillators and their applications"*. – Delft, Netherlands. – 1995. – p.45.



## CHAPTER 7

### DETECTORS OF «SCINTILLATOR-PHOTODIODE» TYPE

“Scintillator-PMT” (S-PMT) detectors have many drawbacks. They are mainly related to such PMT properties as strong dependence of the output signal upon changes in the average current value (“fatigability”), sensitivity to magnetic field (including that of Earth) and temperature changes, relatively small ( $10^2$ – $10^3$ ) region of the dynamic range linearity, the need for high voltage power supply of high stability, etc. [1–5]. In addition, in many application fields of radiation instruments, such as matrix introscopy, tomography, individual dosimetry, a limiting factor for the use of S-PMT detectors is their relatively large size, which puts obstacles to creation of introscopic systems with high spatial resolution. An alternative to S-PMT detectors in many cases is the use of systems of “scintillator-photodiode” (S-PD) type systems [6–9].

Combined radiation detectors of S-PD type have many advantages over traditional S-PMT systems. They are small-sized, do not require high voltage power supply, they are not sensitive to magnetic fields. One should also note high stability and reproducibility of their characteristics, as well as their broad ( $10^8$ – $10^{10}$ ) dynamic range. As for their parameters and functional characteristics, S-PD detectors are in an intermediate position between S-PMT and semiconductor detectors (SCD).

With size and weight of the same order as SCD, S-PD detectors ensure much higher detection efficiency, as scintillators of high density and atomic number can be used [10]. A drawback of S-PD, as compared with SCD, is its worse energy resolution. This is due to double transformation of the radiation energy — firstly into light, and only then to electric energy, as distinct from SCD with a direct energy transformation.

As compared with S-PMT, a drawback of S-PD detectors is that industrially produced photodiodes are of small area (1–4 cm<sup>2</sup>), and no amplification is available. Small charges on PD output terminals (10<sup>-12</sup>–10<sup>-16</sup> K) put high requirements to parameters of a pre-amplifier (PA), making the whole design rather complex and expensive.

Thus, the combination S-PD-PA, though not always the best choice for radiation detection, occupies its own place in radiation technologies and is extensively used in systems and instruments where its advantages are the most essential.

S-PD detectors produced by STC RI, Kharkov, bear the trade mark SELDI (an abbreviation from “scintielectronic radiation detectors”). These S-PD detectors have practically all the advantages of S-PMT, including (if an avalanche photodiode is used) realization of the internal amplification effect [8] in the radiation detector. Like SCD, SELDI detectors provide broad possibilities for miniaturization of the receiving-detecting circuit, and they show better functional characteristics as compared with S-PMT (low power voltage and consumption, low sensitivity of output parameters to mechanical, thermal and magnetic factors, broader — by 2–3 orders of magnitude — dynamic range of optoelectronic characteristics linearity). In addition, radiation energy transformation efficiency in S-PD detectors is by an order of magnitude higher than in S-PMT ones. This becomes clear if one compares the number of charge carriers  $N_d$  at the PD output with the number of electrons  $N_f$  that reach the first PMT dynode under equal irradiation and light collection conditions in both detectors [3]:

$$N_d/N_f = (\eta_d \cdot \eta_q)/(\eta_f \cdot \eta_e), \quad (7.1)$$

where  $\eta_d$  is PD quantum efficiency,  $\eta_f$  — quantum efficiency of the PMT photocathode,  $\eta_q$  — charge collection efficiency,  $\eta_e$  — electron collection efficiency onto the first PMT dynode. At  $\eta_q \approx \eta_e$ ,  $\eta_d \approx 10\eta_f$  we obtain that  $N_d$  is by an order of magnitude higher than  $N_f$ . Correspondingly higher is the energy transformation efficiency by S-PD detectors as compared with S-PMT. The highest possible energy resolution of S-PD is higher, because the detector signal fluctuations are proportional to  $1/N_d^{1/2}$ ,  $1/N_f^{1/2}$ .

Accounting for the factors considered, to ensure such qualities of S-PD detector as sufficiently small size, maximum sensitivity, good

energy resolution, high dynamic range and stability to external factors, its components should meet the following requirements:

- a) large effective atomic number  $Z_{eff}$  of the scintillator material;
- b) high quantum yield of the scintillator luminescence;
- c) intrinsic emission spectrum of the scintillator should be matched to spectral sensitivity of PD;
- d) low optical absorption coefficient of the scintillator;
- e) luminescence intensity should be independent or weakly dependent on temperature;
- f) high radiation stability of both scintillator and PD;
- g) satisfactory kinetic characteristics of both scintillator and PD;
- h) small  $I_T$  (large  $R_0$ ) and  $C_0$  values of the photoreceiver;
- i) appropriate photosensitive area  $S_{pd}$  of PD;
- j) high thermal stability, moisture stability, optical efficiency of light-reflecting, protective and adhesive compositions.

These requirements are often contradictory, so the scintillator material, type of PD and general design of a scintielectronic (SELDI) detector are chosen according to its specific purposes.

Dosimeters with S-PD detectors were tested for the first time in 1988 under real emergency conditions (at the 4<sup>th</sup> block of Chernobyl nuclear power station) [11]. These tests confirmed high reliability and radiation stability of S-PD detectors, with operator safety ensured by remote control. These detectors, functioning in the current mode, are promising for instruments designed for operation under heavy radiation loads — from 10 mR/hour to  $10^3$ – $10^4$  R/hour.

Combination of the counting and current modes of S-PD detector operation allows broadening of its dynamic range, carrying out measurements from the background level [12].

### ***7.1. Criteria for the optimum choice of scintillators. Efficiency and light collection in scintielectronic detectors***

Scintillators intended for their use in scintielectronic detectors should meet the following requirements:

- a) high light output, which is primarily determined by the conversion efficiency of the scintillator,

$$\eta_{SC} = E_{ph}/E_{\gamma} = N_{ph} \cdot h\nu/E_{\gamma};$$

- b) short decay time  $t_{SC}$  ( $t_{SC}$  is generally defined as the time in which the scintillation amplitude is reduced by  $e$  times);
- c) low afterglow level  $\delta$  after a specified time interval (the ratio of X-ray or  $\gamma$ -luminescence amplitudes measured during the stationary irradiation ( $A_0$ ) and at the time  $t$  after the irradiation ( $A_t$ )):

$$\delta = A_t/A_0;$$

- d) high energy resolution  $R_{SC}$ , which is related to physico-chemical uniformity of the scintillator (surface uniformity — for detection of short-range particles, and spatial (bulk) uniformity — for detection of penetrating radiation).  $R_{SC}$  is characterized by the relationship [13]:

$$R_{SC}^2 = R_a^2 + R_{kc}^2,$$

where  $R_a$  is determined by scintillator properties, and  $R_{kc}$  depends upon  $K_c$  and, in the approximation of Gaussian light collection non-uniformity, is determined from the relationship

$$R_{kc} \approx 2.36 \cdot \left( \overline{K_c^2} - K_c^2 \right)^{1/2}$$

where  $\overline{K_c}$  is the averaged value over the scintillator volume;

- e) the effective atomic number  $Z_{SC}$ , which determines the probability of interaction of the ionizing radiation with the scintillator material, should be as high as possible;
- f) high transparency of the scintillator material to the intrinsic radiation;
- g) the best possible matching of the scintillator luminescence spectrum to the sensitivity region of the photodiode used, which ensures optimum values of the spectral matching coefficient  $K_m$  and detection efficiency of the detector as a whole;
- h) high radiation stability and temperature stability of luminescent characteristics.

From the viewpoint of production technology and applications, the scintillator material should also be of high mechanical strength and show stability to moisture.

Among the known scintillators, not many of them can meet specific requirements for application in S-PD detectors. Many well-known efficient scintillators (e.g., NaI(Tl), CsI(Na), ZnS(Ag), plastic scintilla-

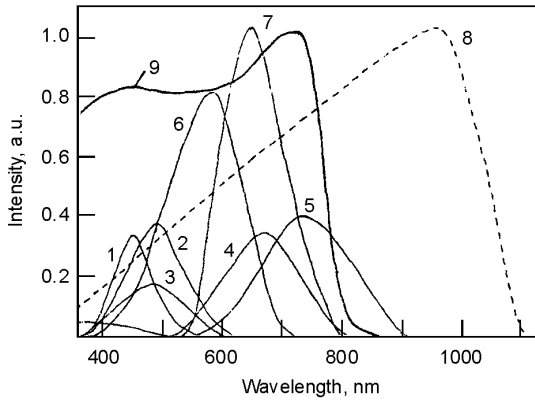


Fig.7.1. Spectral characteristics of scintillators: 1 —  $\text{Cd}_2\text{SiO}_5$ ; 2 —  $\text{CdWO}_4$ ; 3 —  $\text{Bi}_2\text{Ge}_3\text{O}_{12}$ ; 4 —  $\text{Al}_2\text{O}_3(\text{Ti})$ ; 5 —  $\text{CdS}(\text{Te})$ ; 6 —  $\text{CsI}(\text{Tl})$ ; 7 —  $\text{ZnSe}(\text{Te})$ ; 8 — Si-PD sensitivity; 9 —  $\text{AlGaAs}$ -PD sensitivity.

tors, etc.) can hardly be used in scintielectronic detectors because of their specific properties like high hygroscopicity, brittleness, too low values of  $\mu$ ,  $\eta_{\text{SC}}$ ,  $K_m$  in combination with Si-photodiodes, high afterglow level, etc.

The scintillator conversion efficiency largely determines the output parameters  $C$  and  $R$  of detectors used for various applications. Because of substantial discrepancies in the literature data (e.g., for  $\text{Cs}(\text{Tl})$   $\eta_{\text{SC}}$  was given as 11.9 % [13] or 22 % [14], for  $\text{CdWO}_4$  — 3.1 % [15] or 10,6% [14]; no reliable data at all could be found for  $\text{ZnSe}(\text{Te})$ ,  $\text{CdS}(\text{Te})$ , etc.), we have developed and systematically used our own procedure for determination of scintillation parameters accounting for inertia (decay) losses [16]. This procedure is based on experimental determination of the technical light output  $C_T$  and light collection coefficient  $K_c$  under excitation of scintillator samples (with grinded surfaces) by continuous X-ray radiation:

$$\eta_c = C_T / K_c \cdot K_m, \quad (7.2)$$

where  $K_m = \int_0^\infty I(\lambda) S_\lambda(\lambda) d\lambda / \int_0^\infty I(\lambda) d\lambda$ ,  $I(\lambda)$  is the spectral distribution of the scintillator emission intensity, — spectral monochromatic sensitivity of the photodiode (plots for  $I(\lambda)$ ,  $S_\lambda(\lambda)$  are shown in Fig. 7.1);

Table 7.1. Conversion efficiency  $\eta_{SC}$  и coefficients  $K_m, K_c$  of S-PD detector components

Parameter	Scintillator					
	CsI(Tl)	ZnSe(Te)	BGO	CWO	CdS(Te)	GSO
Spectral matching coefficient $K_m$	0.30	0.49	0.26	0.27	0.55	0.24
Light collection coefficient $K_c$	0.48	0.31	0.46	0.45	0.31	0.43
Conversion efficiency $\eta_{SC}$ , %	15.0	19.4–22.2	1.45	3.5	4.85	2.8

$$K_c = \left[ (1 - \overline{R_{gr}})(1 + \overline{R_{gr}}) \cdot e^{\alpha l_{ave}} \right] / \left[ 1 - \overline{R_{gr}^2} e^{2\alpha l_{ave}} \right], \quad (7.3)$$

$\overline{R_{gr}}$  — the reflection coefficient from the grinded scintillator surface,

$l_{ave} = \frac{1}{\varphi_{\max}} \int_0^{\varphi_{\max}} dc \cos^{-1} \varphi d\varphi$  — an averaged light path length from the scintillation site to the scintillator output surface,  $\varphi_{\max}$  — the angle between the light beam not subject to the total internal reflection and a normal to the output scintillator surface. The values of  $\eta_{SC}$ ,  $K_m$ ,  $K_c$  for some scintillators are listed in Table 7.1.

## 7.2. Photodiodes for scintielectronic detectors

Main characteristics of photodiodes used in scintielectronic detectors are given in Table 7.2.

In practical applications, requirements to such PD parameters as monochromatic sensitivity,  $\eta_{PD}$ ,  $\eta_e$ ,  $I_T$ ,  $R_D$ ,  $C_D$ ,  $S_{PD}$ , shape of the photosensitive area, temperature dependences,  $I_T(T)$ , radiation stability are determined by the design of the conversion-amplification circuit, as well as by purpose and operation conditions of the detector. Thus, for dosimetry of weak radiation fluxes, spectrometry and tomography PD should have high and  $R_D$  in combination with low  $C_D$  and  $I_T$ ; for dosimetry of powerful radiation and industrial introscopy, important factors are radiation stability and minimum changes in,  $I_T(T)$ .

Table 7.2.Characteristics of photodiodes used in scintielectronic detectors.

PD type	Parameter				
	$\Delta\lambda, \mu\text{m}$	$S_\lambda(\lambda), \text{A/W}$	$I_m, \text{A}$	$C_{PD}, \text{pF}$	$S, \text{mm}^2$
FD-263	0.4–1.1	0.3 ( $\lambda=0.55$ )	$5 \cdot 10^{-9}$	<30	16
FD321-M	0.3–1.1	0.38 ( $\lambda=0.63$ )	$3 \cdot 10^{-10}$	150	$4.8 \times 16$ pcs.
FD-327	0.3–1.1	0.38 ( $\lambda=0.63$ )	$10^{-8}$	150	$24 \times 2$ pcs.
FD-288	0.2–1.1	0.24 ( $\lambda=0.55$ )	$1.5 \cdot 10^{-7}$	$7 \cdot 10^2$	100
FD-337	0.4–1.4	0.3 ( $\lambda=0.63$ )	$5 \cdot 10^{-9}$	200 ( $U=10 \text{ V}$ )	100
FD-307	0.3–1.1	0.4 ( $\lambda=0.55$ )	$3 \cdot 10^{-9}$	—	35
S3590-01	0.32–1.1	0.56 ( $\lambda=0.92$ )	$1.5 \cdot 10^{-9}$	75 ( $U=30 \text{ V}$ )	100

Quantum efficiency for Si-PD in the 500-900 nm range is very high, reaching 0.8–0.98; for GaAs-PD, it is substantially lower [17]. Sensitivity  $S_\lambda(\lambda)$  of any PD can be expressed as

$$S_\lambda(\lambda) = \left( 1 - R_{PD} \eta_e \cdot \frac{\lambda(\mu\text{m})}{1.239852} \right), \quad (7.4)$$

where  $R_{PD}$  is the reflection coefficient of PD,  $\lambda$  — wavelength of the light flux, and  $\eta_e \sim 0.5$ –1 and is determined by the PD structure, diffusion path of the secondary charge carriers, light absorption coefficient, band gap width of the PD material, and the value of  $U_{bias}$ . The PD sensitivity limit calculated according to (7.4.) at  $\eta_e = 1$  and the absence of reflection at  $\lambda = 500 \text{ nm}$  is 0.4 A/W,  $\lambda = 600 \text{ nm}$  — 0.48 A/W,  $\lambda = 900 \text{ nm}$  — 0.725 A/W. In real conditions, it is possible to approach the limiting values by application of antireflecting coatings onto PD, increasing  $U_{bias}$  etc. However, this can lead to an increase in  $I_T$  and lowering of the output signal because of a partial loss of photocarriers as a result of more rapid surface recombination.

In a general case, the voltage-current characteristic of PD under illumination can be written down as  $I = I_{sat} \left( e^{eU_{bias}/kT} \right) - I_p$ , where  $I_{sat}$  is the current of saturation due to thermal generation of carriers,  $I_p$  is the photocurrent; consequently, in order to broaden the dynamic range of scintielectronic detectors, one should use PD with minimum values of  $I_{sat}$  (and  $I_T$ ).

Intrinsic PD capacity  $C_D$ , which forms, together with  $R_D$ , the total impedance  $Z_D = Z_D(\omega)$ , is determined as

$$C_D = S_{PD} \{ \varepsilon_{PD} \varepsilon_0 [2m\xi(U_k - U_{bias})] \}^{1/2} \quad (7.5)$$

where  $\varepsilon_{PD}$ ,  $\varepsilon_0$  are dielectric permittivities of the PD material and vacuum,  $\xi$  is the resistivity of the initial material of PD,  $U_k$  is the contact potential difference. This puts the requirement of optimum choice of  $S_{PD}$  and  $U_{bias}$  to reach the highest photocurrent ( $I_p \sim S_{PD}$ ) and minimum noise ( $I_n \sim U_{bias} \sim I_T$ ) at the required  $Z_D$  of PD. The use of Si-PD with dark currents of 1–10 nA allows one to create a scintielectronic detector with dynamic range of  $10^8$  and linearity of output characteristics.

Radiation stability of PD is mainly determined by the material and the production technology. Testing of photoreceivers have shown that at radiation loads up to 1.6 Mrad (source: Co-gun, dose rate 216 R/s) voltage-current characteristics of standard PD (of FD-263 type) are changed by more than 25%, while with FD-288 and FD-327 PD (used in our scintielectronic detectors for emergence dosimetry and industrial introscopy, respectively) these changes do not exceed 4%. To evaluate the radiation resource (a measure of service time under irradiation)  $D_\gamma$  (in rad/year) of detectors (e.g., designed for an industrial introscope for customs inspection of railway containers) we use the expression

$$D_\gamma = \nu^{-1} P \lambda n N, \quad (7.6)$$

where  $\nu$  is the frequency of probing  $\gamma$ -pulses,  $P_\gamma$  — required dose rate of the pulse,  $n$  — number of pulses required for inspection of one container,  $N$  — number of containers per year. At  $\nu = 10$  pulses/s,  $P_\gamma = 10$  R/min,  $n = 3 \cdot 10^3$  pulses/container,  $N = 5 \cdot 10^4$  containers/year, we obtain the value of  $D_\gamma = 1.5$  Mrad/year (not accounting for partial absorption of the probing radiation in the containers). This shows that scintielectronic detectors can be used for such applications.

Temperature variations of Si-PD do not exceed 0.4–0.6%/K, and temperature variations of the detector signal/noise ratio are determined by decreasing  $R_T(T)$ , which is lowered with Si-PD by about 10 times in the 25–60°C region, and increasing  $I_T(T)$  (Fig.7.2). The main contribution to sensitivity variation of Si-PD based detectors (Fig.7.3) comes from the temperature dependence of the scintillator light output. For GaAs-PD, optoelectronic characteristics are less dependent



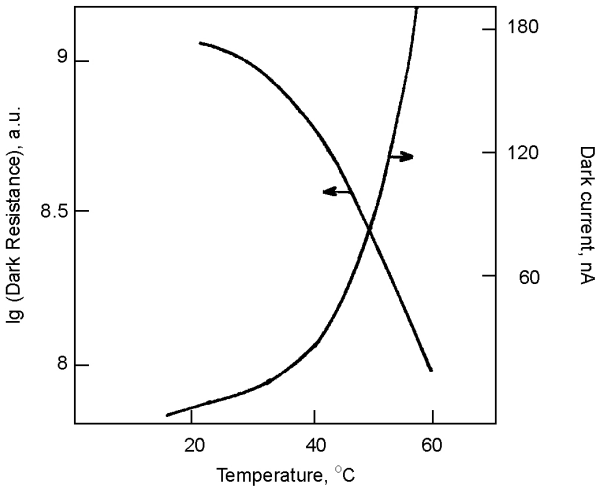


Fig.7.2. Temperature dependences of dark resistance  $R_T$  (1) and dark current (2) of Si-PD.

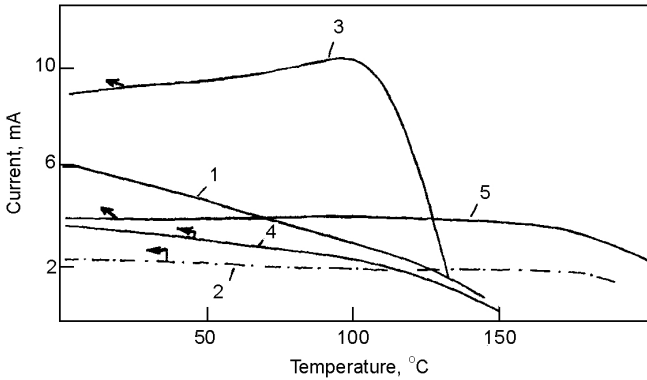


Fig.7.3. Temperature dependences of sensitivity of Si-PD-263 (1), GaAs-P1743 (2) and detectors on their base: SDK-15 (3), ZnSe(Te)-PD-288 (4), GaAs-PD-GSO (5).

on temperature because of wider band gap (Fig.7.2); in combination with thermally stable scintillators (like GSO) such detectors could be promising for radiation monitoring under extreme thermal and radiation conditions.

In property studies and industrial production of scintielectronic detectors, PD of different types are used (see Table 7.2), both home-made and imported. In collaboration with STC RI, development and production of photodiodes is carried out by PO Kvarts, Chernovtsy, Ukraine. Their products include PD for dosimetric detectors (FD-263, FD-337A, FD-288A, B), for medical and industrial introspecty, tomography, including multi-channel PD (FD-327, FD-321M1), for spectrometry (PD of “Zond” type, with improved sensitivity and uniformity over PD surface), etc. These photodiodes, as for many essential characteristic, are not inferior to the best world analogs. Further developments are under way with the aim of improvement of the existing PD types and creation of new ones for their use in scintielectronic detectors of different types.

In Fig. 7.4, the general design of scintielectronic detectors is shown, with their main parameters given in Table 7.3.

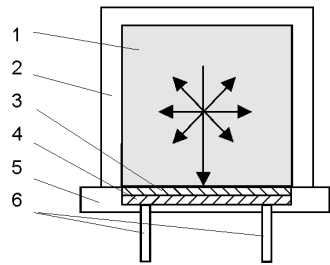


Fig.7.4. General design of an S-PD scintillation detector: 1 — scintillator; 2 — light-reflecting coating; 3 — optical contact; 4 — PD *p-i-n*-structure; 5 — sial substrate; 6 — outputs.

### 7.3. General development principles and main properties of scintielectronic detectors

#### 7.3.1. Energy characteristics

Transformation of the ionizing radiation energy  $E_\gamma$  into an output signal of a scintielectronic detector is occurring stage by stage a result of the following processes:

1. Absorption of the incident radiation by the scintillator. The absorbed radiation fraction is  $\alpha_\gamma = (\mu_a/\mu)(1 - e^{-\mu d})$ , where  $\mu$  is the linear absorption coefficient, which characterizes that fraction of  $E_\gamma$  which is transferred to the scintillator [24], and  $d$  is the scintillator thickness.
2. Transformation of the absorbed energy into a light scintillation  $h\nu N_c = \eta_{SC} E_\gamma$ , where  $N_c$  is the total number of scintillation photons, and  $\eta_{SC}$  is the conversion efficiency, or physical light output of the scintillator.

Table 7.3. Parameters of S-PD type scintillation detectors produced by STC RL.

Detector type	Scintillator; dimensions, mm	Radiation sensitivity, nA min/ R cm <sup>2</sup>	Dark resistance, Ohm	Energy range, MeV (radiation)	Input window dimensions, mm	Number of channels (step)	Overall dimensions, mm	Applications
1	2	3	4	5	6	7	8	9
SDK-15	CWO, ZnSe 5×5×7	10; 30	>10 <sup>9</sup>	0.05–0.2 (X-ray)	5×5	1	6×7×10	Introscopy
SELDI-M.01	CWO, ZnSe	10; 30	>2·10 <sup>8</sup>	0.03–0.2	4.0×1.4	16 (1.7)	27.2×20×15	Inspection
SELDI-M.02	CsI(Tl)	30	>1·10 <sup>8</sup>	(X-ray)				Customs
SELDI-M.01A	ZnSe, CWO 16 (4×4×1.4)		>2·10 <sup>8</sup>					Inspection
SDN-131A	CWO, ZnSe	10; 30	>2·10 <sup>8</sup>	0.03–0.2 (X-ray)	4.0×1.2	16 (1.6)	26×20×15	
SDN-131B	CsI(Tl) 16 (4×4×1.2)	30	>1·10 <sup>8</sup>					
SDN-127A	CWO, ZnSe	10; 30	>2·10 <sup>8</sup>	0.03–0.2 (X-ray)	2.0×1.4	16 (1.7)	27.2×20×10	Non-destructive testing
SDN-127B	CsI(Tl) 16 (4×4×1.4)		>1·10 <sup>8</sup>	(X-ray)				

Table 7.3. (continued).

1	2	3	4	5	6	7	8	9
SDN-126-01	CWO, ZnSe 2 (20×1.4×4)	10; 30	>10 <sup>8</sup>	0.15–10 (gamma)	4.0×1.4	2(1.7)	5×12×35	Tomography
SDN-126-02	2 (20×1.4×8)				8×1.4		5×8×35	
SDN-128-01	Cs(Tl) 10×10×10	10 <sup>−5</sup> P/q	>10 <sup>9</sup>	0.05–3 (gamma)	10×10	1	19.5×29.5×20	Dosimetry
SDN-128-02	10×10×4						6.5×14.5×15.5	
SDN-128-01A	10×10×2.5						5×14.5×15.5	
SDN-130	ZnSe ø15×0.15	0.05 pulses cm <sup>2</sup> Bq s	>10 <sup>8</sup>	0.05–1.5 (beta)	ø15	1	ø30×15	Dosimetry
SND-129	CWO, ZnSe 10×10×10 ø11×10	10; 30	>10 <sup>7</sup>	0.01–10 (gamma)	10×10 ø10	1	ø23×25	Dosimetry

3. Collection of the light quanta on the photodiode (PD); its efficiency is determined by the light collection coefficient  $K_c = N_{ph}/N_c$ , where  $N_{ph}$  is the number of light quanta reaching PD.
4. Transformation of the light energy absorbed by PD into the energy of charge carriers, which is determined by the PD quantum efficiency and spectral matching coefficient  $K_m$  of the scintillator luminescence spectrum and the PD spectral sensitivity.
5. Separation of the charge carriers in the  $p$ - $n$  junction and their accumulation on the PD electrodes, which is determined by the charge carrier collection efficiency  $\eta_e$ .

As a result, the signal value  $Q$  at the scintielectronic detector output is:

$$Q = (\alpha_\gamma e E_\gamma / h\nu) (\eta_{SC} \eta_{PD} \eta_e K_m K_c), \quad (7.7)$$

and the radiation sensitivity  $C$  is

$$C = Q/E_\gamma \text{ [Coulombs/eV]}. \quad (7.8)$$

In radiation technologies, another measurement unit for radiation sensitivity is also widely used — [A min/R] ( $1 \cdot 10^{-21}$  C/eV  $\approx$  30 nA·min/R). An estimate of  $C$  according to (2) and (3) at  $E_\gamma = 100$  KeV for scintielectronic detectors on the basis of CsI(Tl) and silicon PD ( $\eta_{SC} = 0.15$ ,  $\eta_{PD} = 0.9$ ,  $\eta_e = 0.8$ ,  $K_m = 0.77$ ,  $K_c = 0.47$ ,  $h\nu = 2.2$  eV) gives a value of  $2.5 \cdot 10^{-21}$  C/eV (upon conditions of 100% absorption of the detected radiation in the detector volume, i.e.  $\alpha_\gamma = 1$ ). In the real situation, e.g., at the scintillator dimensions  $10 \times 10 \times 10$  mm<sup>3</sup> and silicon PD photosensitive area 100 mm<sup>2</sup> and  $E_\gamma = 0.1 \div 1$  MeV,  $(1.1 \div 5.5) \cdot 10^3$  charge carriers are formed in the photodiode, and radiation sensitivity of this type of scintielectronic detectors will be  $(1.75 \div 0.88) \cdot 10^{-21}$  C/eV, or 52.5–26.4 nA min/R cm<sup>2</sup>.

The conversion efficiency  $\eta$  of an S-PD detector is a number of charge carriers that are transformed in PD per unit initial radiation energy absorbed in the scintillator, i.e.

$$\eta = Q/eE_\gamma. \quad (7.9)$$

For S-PD detectors with crystals CsI(Tl) and ZnSe(Te) in the  $E_\gamma \leq 0.1$  MeV range at the above-given parameter values used in (2), (3) (for ZnSe(Te)  $K_u = 0.92$ ,  $h\nu = 1.95$  eV),  $\eta$  will be  $1.1 \cdot 10^3$  and  $1.48 \cdot 10^3$ , respectively. At higher  $E_\gamma$ , advantages of ZnSe(Te)-PD detectors as

compared with CsI(Tl)-PD will be largely lost because of lower values of  $\mu$  and  $\mu_\alpha$ .

The energy resolution  $R$  is determined by the relationship

$$R = 2.36\Delta E_n / \varepsilon \eta E_\gamma, \quad (7.10)$$

where  $\Delta E_n$  is the mean squared value of noises from the S-PD detector and amplification devices,  $\varepsilon$  is the average energy required for formation of a charge carrier pair in the semiconductor (for silicon  $\varepsilon \approx 3.6$  eV [21]). The  $R$  value for the detector as a whole is determined by the respective energy resolution values  $R_{SC}$  and  $R_{PD}$  of the scintillator and photodiode:

$$R^2 = R_{SC}^2 + R_{PD}^2. \quad (7.11)$$

Spectrometric characteristics of the detectors, in addition to factors accounted for in (2–5), are largely dependent upon the scintillator transparency to its intrinsic radiation, because scintillation intensity fluctuations vary as  $\Delta(h\nu \cdot N_\gamma) \sim (\alpha d)^{1/2}$ . E.g., in a simple case the relative difference in scintillation amplitudes near input and output sides of the scintillator will be  $I/I_{out} \approx (I_{out} - I_{in})/I_{out} = (1 - e^{-\alpha d})$ ; for crystals ZnSe(Te), at  $d = 1$  cm and  $\alpha = 0.1$ – $0.7$  cm,  $I/I_{out}$  will be about 10–50%, substantially worsening the energy resolution of the detector.

Alongside with parameters  $C$ ,  $\eta$ ,  $R$ , an important characteristic of scintielectronic detectors is the dependence of their sensitivity upon energy  $C(E_\gamma)$ , which can vary by more than an order of magnitude for solid-state detectors in a broad energy range. Thus, with ZnSe(Te) scintillator thickness  $L = 15$  mm (corresponding to 90% absorption of photons with  $E_\gamma \approx 0.14$  MeV) the detector sensitivity will be varied by  $\sim 4.2$  times in the energy range  $E_\gamma = 0.1$ – $1$  MeV (Fig. 7.5., curve 1). Leveling of the detector sensitivity is possible when long-wave radiation filters of a specified thickness are used. E.g., for a given detector type, when a copper plate of thickness  $L_{Cu} = 4.2$  mm is used as filter,  $C(E_\gamma)$  of such sandwich structure is changed by not more than 54% in the same  $E_\gamma$  range (Fig. 7.5, curve 2), with detector sensitivity decreased by 20% at  $E_\gamma = 1$  MeV. Even more efficient is the structure composed of a ZnSe-based scintillator and a complex filter of tin and lead layers. These materials have been chosen because they have substantially different density and atomic number (6.5 g/cm<sup>3</sup> and 50 for Sn, 11.35 g/cm<sup>3</sup> and 82 for Pb). Accounting for substantial attenuation of the low-energy radiation by the filter, a part of the input scintillator

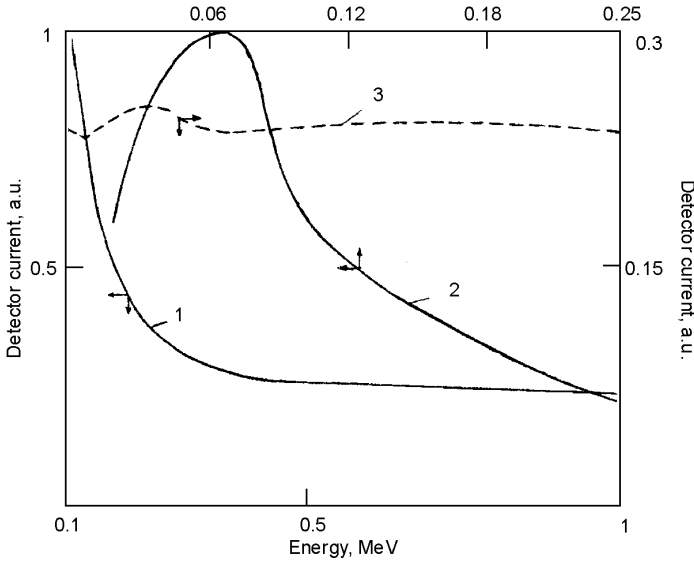


Fig.7.5. Energy dependence of ZnSe(Te)-PD detector sensitivity: 1 — without filter; 2 — with Cu-filter; 3 — with Sn,Pd filters.

window is left open. Thickness of the filter elements was calculated for four energy values  $E_\gamma = 0.1; 0.15; 0.4; 1$  MeV by the method of parameter variation in a system of three equations of the following type:

$$\begin{aligned} \Phi_i &= \eta \frac{\mu_\alpha}{\mu} [1 - \exp(-\mu L)] \approx \\ &\approx 1 + [\exp(-\mu_f L_{f1}) + \exp(-\mu_f L_{f2}) - 2] S_f, \end{aligned} \quad (7.12)$$

where  $\Phi_i$  is the scintillation light flux,  $\mu, \mu_\alpha$  are linear and actual absorption coefficient,  $\mu_f = 0.3\mu_{\text{Sn}} + 0.7\mu_{\text{Pb}}$ ;  $L_{f1}, L_{f2}$  — filter thickness before the 1<sup>st</sup> and 2<sup>nd</sup> scintillator, respectively,  $S_f$  is the fraction under the filter of the total input window area of the detector. Solving the system, we obtain values  $S_f = 0.395$ ;  $L_{f1} = 1.71$  mm;  $L_{f2} = 0.75$  mm; thickness of Sn and Pb is 0.513 mm and 1.197 mm, and 0.225 mm and 0.525 mm for the 1<sup>st</sup> and 2<sup>nd</sup> scintillator, respectively. The values of  $\Phi$  calculated according to (7.12.) (Fig.7.5, curve 3) are practically not energy-dependent (maximum deviation does not exceed 8%), with 6.5 and 7.8 % of radiation with  $E_\gamma = 1$  and 0.1 MeV absorbed by the filters.

In practice,  $C(E_\gamma)$  was determined by the pulse counting method ( $N_i$ ) using radionuclides  $^{57}\text{Co}$ ,  $^{137}\text{Cs}$ ,  $^{241}\text{Am}$ ,  $^{54}\text{Mn}$ ,  $^{60}\text{Co}$  from the OSGI set in the same measurement conditions at a standard distance from the source to the detector (1 cm). The results for  $N_i$  are given for one and the same exposure dose rate (EDR) for different radionuclides with respect to  $^{137}\text{Cs}$ :

$$\bar{N}_i = N_i \cdot K_i$$

( $K_i = P_{cs}/P_i = K_{\gamma cs} A_{cs}/K_{\gamma i} A_i$ ;  $P_{cs}$ ,  $P_i$  — EDR of  $^{137}\text{Cs}$  and the  $i$ -th isotope, respectively;  $K_{\gamma i}$ ,  $A_i$  is the total gamma-constant of the  $i$ -th radionuclide of activity  $A_i$  (using reference data for the radionuclide activity, the half-life time is accounted for)). Basing on data on  $N_i$ , the  $C(E_\gamma)$  dependence is obtained. The error of EDR determination, depending upon the radiation energy, is calculated according to the expression

$$\Delta M_\gamma[\%] = [(N_{cs} - N_i \cdot K_i)/N_{cs}] \cdot 100\%.$$

The values of  $K_{\gamma i}$  parameters that are required for calculations of  $C(E_\gamma)$  are given in Table 7.4.

Thus, we may conclude that S-PD type detectors are characterized by the following parameters:

- radiation sensitivity  $C$ ,
  - conversion efficiency  $\eta$ ,
  - sensitivity-energy dependence  $C(E_\gamma)$ ,
  - energy resolution  $R$ ,
- as described by (7.8–7.11).

In (7.11)  $R_{PD}$  depends upon non-uniformity of the sensitivity of PD active surface and intrinsic noises of the “PD- electronic amplification circuit” system.

In addition to smaller dimensions and better functional characteristics, S-PD detectors ensure much higher transformation efficiency of the radiation energy as compared with S-PMT detectors. PMT quantum efficiency is 10–20% in the 400–420 nm range, while for PD its value can be as high as 70% in the 420–500 nm range (reaching nearly 100% with the best PD specimens). Therefore, it is possible in principle to obtain S-PD detectors with better energy resolution as compared with S-PMT ones. However, as S-PD detectors use double transformation of the ionizing radiation energy, and PD has



Table 7.4. Values of  $K_\gamma$  for radionuclides from the OSGI (reference standard calibration sources) set.

Radionuclide	$K_\gamma$	Energy, keV	% output
$\text{Am}^{241*}$	0.63	20.345	2.5
		59.537	35.75
		16.7	38.2
$\text{Co}^{57}$	0.574	122	85.7
		136	10.6
$\text{Cs}^{137}$	3.1	661.66	85.08
$\text{Mn}^{54}$	4.69	834.8	99.97
$\text{Co}^{60}$	12.93	1173	99.89
		1337	99.98

\*) — for energy 59.5 keV,  $K_\gamma = 0.13$ .

no intrinsic amplification, high requirements are put to electronic amplification circuits.

At present, S-PD detectors are widely used in medical and industrial tomographs, in introsopes with tens, hundreds and thousands of detectors arranged in one- or two-dimensional arrays [18–24], in dosimetry [25–27] and spectrometry of ionizing radiations [28–32].

Dimensions of the scintillation element, orientation of its input window with respect to the PD photosensitive area, the use of various materials for elements of optical communication, light-protecting and light-reflecting coatings, as well as general design of a detector is determined by its purpose. For detectors of high-energy  $\gamma$ -radiation, large scintillator thickness is needed, therefore its input window is located perpendicularly to the PD surface (scintielectronic detector of SDN-126 type). For detection of  $\alpha$ - and  $\beta$ -radiation, very thin (0.1 mm) scintillators are used, often with specific light reflective coatings. For tomography and introscopy of high spatial resolution, two- or 16-channel PD are used (SDN-126, SDN-127, SELDI-M), etc.

### 7.3.2. Noises in scintielectronic detectors

Noises that emerge in scintielectronic detectors and put limits to the sensitivity and energy resolution of the measuring-detecting circuit, are proportional to quantum fluctuations of the fraction of the detected radiation absorbed by the scintillator  $\Delta E_{ns}$  ( $\Delta E_{ns} \sim (\mu N_c)^{-1/2} = (h\nu/(\mu E_\gamma \eta_c)^{1/2}$ , fluctuations of light collection and quantum efficiency of the photoreceiver  $E_{ne}$  ( $E_{ne} \approx (h\nu/E_\gamma \eta_c \eta_{ph} K_c)^{1/2}$ , as well as fluctuations of scintillation efficiency  $h\nu N_c$  due to light absorption in the scintillator; i.e.,  $N_c = f(\alpha, l, \mu)$ , where  $\alpha$  is the optical absorption coefficient,  $l$  is the optical path length from the scintillation flash site inside the scintillator to PD. E.g., for a NaI(Tl)-PMT, with  $\alpha$  changing from  $0.01 \text{ cm}^{-1}$  to  $0.027 \text{ cm}^{-1}$ ,  $R$  is worsened from  $\sim 6 \%$  to  $10 \%$  [13–15]. Estimates show that noises of a scintillation block  $\Delta E_{ns} + \Delta E_{ne}$  limit the resolution of CsI(Tl)-PD detectors at  $E_\gamma = 0.1\text{--}1 \text{ MeV}$  by the values of  $1\div 3 \%$ . The limiting values of  $C$  and  $R$  are strongly affected by the PD intrinsic noises — fractional ( $\sim (I_T \Delta f)^{1/2}$ ;  $I_T$  — dark current of PD,  $\Delta f$  — frequency band), thermal ( $\sim (TR_g)^{1/2}$ ;  $T$ ,  $R_g$  — temperature and inverse resistance of PD) and surplus noises ( $1/f$ ), as well as the total impedance value  $Z = Z(\omega)$  (including  $R_g$  and intrinsic capacity  $C_g$  of the photoreceiver), affecting proportionally the dynamic range of linear detector sensitivity and the value of the signal/noise ratio of the receiving-detecting circuit (RDC) as a whole [14–19]. Further limitations upon RDC output parameters are imposed by the detection method of detector signals (modes using measurements of charge, voltage or current), as well as circuitry of the electronic amplification circuit (EAC), the impedance and amplitude-frequency characteristics of which, in combination with corresponding parameters of the detector, determine the signal shape and noise properties of the RDC as a whole.

PD, unlike PMT, have no intrinsic amplification, and electron-hole pairs formed by crystal scintillations at the PD p-n transition, create a charge signal (for CsI(Tl) —  $\sim 3 \cdot 10^4$  electron-hole pairs per 1 MeV energy of gamma-quanta). The charge signal is amplified by a low-noise charge-sensitive pre-amplifier up to a level required for further processing. The spectral sensitivity maximum of silicon PD is in the 850–900 nm range, scintillation maximum of CsI(Tl) is at 550 nm, which determines spectral matching of the scintillator and PD within 30% and further lowers the useful signal level.

This implies that high requirements are put to all parts of the spectrometric circuit, in particular, to the pre-amplifier.

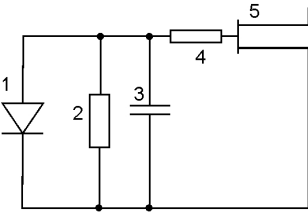


Fig.7.6. Equivalent diagram of the detector and input circuit of the charge-sensitive preamplifier: 1 — PD — photodiode; 2 —  $R_{par}$  — equivalent noise resistance switched in parallel to PD; 3 —  $C$  — total capacitance of the input circuit, including  $C_{pd}$  — PD capacitance,  $C_{FT}$  — input capacity of the field transistor,  $C_{PD}$  — assembling capacitance; 4 —  $R_s$  — equivalent noise resistance switched sequentially with PD; 5 — FT — input field transistor.

Radiometric and dosimetric monitoring devices are normally expected to ensure operability up from the natural background level, i.e., detection of isolated gamma-quanta in the energy range of 0.1–1 MeV. Accounting for the conversion efficiency of modern scintillators (12–15%), formation energy of a carrier pair in semiconductor scintillators (up to 10 eV), phototransformation efficiency of silicon PD (30–40%), it follows that the electric charge  $Q$  accumulated by the photodiode for a given energy range is  $3 \cdot 10^{-17}$ – $10^{-15}$  Coulombs, which corresponds, with a charge detection scheme used (Fig.7.6), to the e.m.f. values at PD output from  $5 \cdot 10^{-7}$  V.

Let us consider input characteristics of a RDT in the charge-sensitive variant, assuming (as an example) that the EAC input circuit comprises a field transistor (an equivalent diagram of the input part of such RDT is shown in Fig.7.6). A generally accepted reliability condition for detection of an event by EAC is  $U_c/U_n > 1$ , where  $U_c$ ,  $U_n$  are voltages at the EAC output due to signal and noise, respectively.

The signal value obtained at the scintielectronic detector output  $U_c = U(t)$  is approximated by the functions:

$$U(t) |_{0 \leq t \leq \tau} = U_{\tau_m} e^{-\alpha t} \quad (7.13)$$

$$U(t) |_{t > \tau, t < 0} = 0$$

where  $\tau$  is the scintillator decay time, and  $\alpha = 2.3/\tau$ .

The spectrum is described by the expression

$$S(\omega) = \frac{U_m \tau}{4.6 \pi \sqrt{1 + 0.189 \tau^2 \omega^2}} \quad (7.14)$$

$$\psi = \arctg(0.435 \omega \tau),$$

where  $S(\omega)$  is the signal spectral density module, and  $\psi$  is its argument. The spectrum width  $\Delta F_c$  and effective width  $\Delta F_{cef}$  are equal:

$$\Delta F_c = 3.64/\tau ; \Delta F_{cef} = 1.13/\tau.$$

For gamma quantum energy of 1 MeV,  $Q = 10^{-15}$  C, accounting for PD capacity  $C = 100$  pF at  $U_m = 10^{-5}$  V

$$\Delta F_{cef} = 100 \text{ kHz}.$$

Optimum conditions for filtration of the useful signal with a specified frequency characteristics require an amplifier frequency characteristic that should be complex-conjugated to the signal pulse envelope:  $K(\omega) = K_0 U^* S(\omega)$ , where  $K(\omega)$  is the amplifier transmission coefficient in a given frequency range. коэффициент передачи усилителя в диапазоне частот.

In a simplified model

$$K(\omega) = \begin{cases} 1 & \text{at } 0.006 < f < 0.1 \text{ MHz} \\ 0 & \text{at } f < 0.006, f > 0.1 \text{ MHz} \end{cases}$$

i.e., a rectangular filter in the frequency range specified.

The source of noise in the considered switching scheme (Fig.7.3) is the equivalent noise resistance  $R_{par}$ , which is due to the PD inverse current  $I_{pd}$ , input current of the field transistor  $I_{FT}$ , and feedback leakage. The frequency dependence of this “white” noise is determined by the ratio of  $R_n$  and the EAC input capacity  $C$

$$\overline{U_{nFT}^2} = 4kT \frac{1}{R_{par}} \frac{1}{(\omega C)^2} \Delta f, \quad (7.15)$$

where  $k$  is the Boltzmann constant, and  $T$  is the absolute temperature. The  $R_s$  value includes the sequentially switched resistance of the field transistor of the input circuit  $R_s = 1/S$ , where  $S$  is the transistor steepness, with its noise voltage

$$\overline{U_{SPP}^2} = 4kT_s \Delta f,$$

The frequency component of the field transistor noise is

$$U_n^2 = \frac{A_f}{f} \Delta f$$

where  $A_f$  is a coefficient that is constant for a given FT type.

The total noise voltage at the EAC input is written down as

$$\overline{U_n^2} = \left[ \frac{2qI_{PD}}{\omega^2 C^2} + \frac{2qI_{FT}}{\omega^2 C^2} + \frac{4kT}{R_{par}\omega^2 C^2} + 4kTR_s + \frac{A_f}{f} \right] \Delta f = N(\omega)\Delta f \quad (7.16)$$

where:

1.  $\overline{U_n^2} = \frac{2qI_{PD}}{\omega^2 C^2} \Delta f = U_{nPD}^2 = 0.81I_{PD} \frac{\Delta f}{f^2}$  — the noise voltage created by the “dark” photodiode current  $I_{PD}$  due to “fractional” effect,  $q$  is the charge of an electron.

2.  $\overline{U_n^2} = \frac{2qI_{FT}}{\omega^2 C^2} \Delta f = U_{nFT}^2 = 0.81I_{FT} \frac{\Delta f}{f^2}$  — the noise voltage created by the “dark” current  $I_{FT}$  due to the field transistor gate.

3.  $\overline{U_n^2} = \frac{2qI_{PD}}{R_{par}\omega^2 C^2} \Delta f = U_{npar}^2 = 0.42 \frac{1}{R_{par}} \frac{\Delta f}{f^2}$  — the noise voltage created by the parallel resistance  $R_{par}$  composed of the leakage resistances of the photodiode  $R_{PD}$  and field transistor  $R_{FT}$ , as well as of the amplifier feedback resistor  $R_{oc}$ , where

$$\frac{1}{R_{par}} = \frac{1}{R_{PD}} + \frac{1}{R_{FT}} + \frac{1}{R_{oc}}$$

4.  $\overline{U_S^2} = 4kTR_s \Delta f = U_{nFT}^2 = 1.165 \cdot 10^{-21} R_S \Delta f$  — the noise voltage created by the “thermal channel” of the field transistor.

5.  $\overline{U_n^2} = \frac{A_f}{f}$  — the noise constituent dependent upon transistor manufacturing technology.

The expression  $N(\omega)$  represents the spectral density of the input noises.

The noise level at the amplifier output with transmission band  $\Delta f$  is determined by an integral expression

$$\overline{U_{na}^2} = \frac{1}{2\pi} \int_{f_H}^{f_G} |N(\omega)| |K(\omega)|^2 d\omega U_{na}^2 = \frac{1}{2\pi} \int_{f_H}^{f_G} |N(\omega)| |K(\omega)|^2 d\omega \quad (7.17)$$

where  $K(\omega)$  is the frequency characteristic of the amplifier,  $f_G$  is the upper edge of the amplifier transmission band, and  $f_H$  is the respective lower edge.

From (7.16; 7.17), accounting for parameters of a FD-142 photo-diode (for individual samples)  $I_{PD} = 10^{-8}$  A,  $R_{lk} = 1 \cdot 10^{10}$  Ohm, and for KP307Zh  $S = 4 \cdot 10^{-3}$  A/V,  $R_s = 0.25 \cdot 10^{-3}$  Ohm,  $I_{lk} = 10^{-10}$  A,  $T = 300$  K, mean-squared noise voltage values from different noise-contributing components:

$$\begin{aligned}\sqrt{U_{PD}^2} &= 1.16 \cdot 10^{-6} \text{ V} \text{ — PD current} \\ \sqrt{U_{FT}^2} &= 1.16 \cdot 10^{-7} \text{ V} \text{ — FT leakage current} \\ \sqrt{U_T^2} &= 6.43 \cdot 10^{-7} \text{ V} \text{ — FT thermal noise} \\ \sqrt{U^2} &= 1.27 \cdot 10^{-7} \text{ V} \text{ — PD, FT leakage resistance,}\end{aligned}\tag{7.18}$$

whence the numerical value of the noise voltage for the actually used elements of the EAC input circuit is

$$\sqrt{U_n^2} = \sqrt{\sum_i U_{n_i}^2} = 1.34 \cdot 10^{-6} \text{ V}$$

and is mainly determined by the values of  $I_{PD}$  of PD and  $S$  of FT.

Comparing (7.18) with the previously calculated value of the useful signal, we obtain, using the optimized filters (7.14), as well as KP307Zh and carefully chosen FD-142 in the input circuit, the signal to noise ratio at  $E_\gamma = 1$  MeV

$$U_c / U_n = 5\tag{18}$$

This ratio is close to unity for  $E_\gamma = 0.1$  MeV.

When in the input circuit one uses a FD-337 ( $R_{lk} = 1 \cdot 10^{10}$  Ohm,  $I_{PD} = 5 \cdot 10^{-10}$  A) and a FT of KP341 type ( $S = 26 \cdot 10^{-3}$  A/V,  $R_s = 0.04 \cdot 10^3$  Ohm,  $I_{lk} = 10^{-9}$  A), similarly to (7.18) the following noise voltages will result:

$$\begin{aligned}\sqrt{U_{PD}^2} &= 2.59 \cdot 10^{-7} \text{ V} \text{ — PD current} \\ \sqrt{U_{FT}^2} &= 3.6 \cdot 10^{-7} \text{ V} \text{ — FT leakage current} \\ \sqrt{U_T^2} &= 2.4 \cdot 10^{-7} \text{ V} \text{ — FT thermal noise}\end{aligned}\tag{7.18a}$$

$$\sqrt{U^2} = 3.72 \cdot 10^{-8} \text{ V} \text{ — PD, FT leakage resistance,}$$

whence the numerical value of the noise voltage for the actually used elements of the EAC input circuit is

$$\sqrt{U_n^2} = \sqrt{\sum_i U_{n_i}^2} = 5 \cdot 10^{-7} \text{ V}$$

and is mainly determined by the values of  $I_{PD}$  of PD and  $S$  of FT. Comparing (7.18a) and the useful signal values, we obtain the signal to noise ratio for  $E_\gamma = 1 \text{ MeV}$  as  $U_c/U_n = 13$ , and for  $E_\gamma = 0.1 \text{ MeV}$  —  $U_c/U_n \geq 1$ .

### 7.3.3. Scintielectronic detectors in the current mode:

#### RDT noises

Let us consider output characteristics of the receiving-detecting circuit (RDC) for the case when a scintielectronic detector is used in the current mode. As an example, we take one of the most commonly

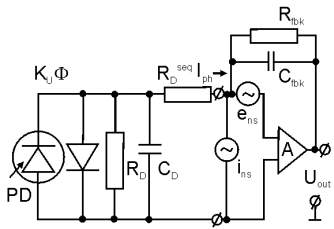


Fig. 7.7. Equivalent diagram of detector with operational amplifier:  $\Phi$  — light flux power;  $K_u$  — spectral matching coefficient of the scintillator and PD;  $R_D$  and  $C_D$  — shunt resistance and capacity of PD;  $i_{ph}$  — photo current;  $R_D^{seq}$  — equivalent sequential resistance of PD;  $R_{fb}$ ,  $C_{fb}$  — feedback resistance and capacity;  $i_{ns}$ ,  $e_{ns}$  — generators of the noise current and e.m.f.;  $A$  — amplification coefficient of the operational amplifier with feedback circuit disconnected.

used EAC designs (Fig. 7.7) with an operational amplifier (OA). In this case, the equivalent input resistance of the measurement circuit, the value of which determines how closely this circuit approximates the short circuit mode, can be evaluated as  $Z_{in}^{eq}(w) = 1/A(w) \cdot Z_{oc}(w)$ , where  $A(w)$  is the OA amplification coefficient,  $Z_{oc}(w) = (R_{oc}/wC_{oc})/(R_{oc} + 1/wC_{oc})$ ; for the direct current,  $R_{in}^{eq} = 1/A R_{oc}$ .

The output voltage  $U_{out}$ , which is an output parameter of RDC, depends upon the photocurrent  $I_p$  as  $U_{out} \approx R_{oc} I_p$ , implying that in order to increase the RDC output signal,  $R_{oc}$  should be made as high as possible.

One of important RDC characteristics is its linearity in the dynamic range of radiation detection. The current in the load is here related with the  $K_m \Phi$  value as

$$I_p = K_m \Phi \left[ 1 + \frac{R'}{R_D} + \frac{I_0}{I_p} \left( \exp \frac{I_p R'}{A \cdot V_t} - 1 \right) \right] - 1 = \beta \{K_m \Phi\} \quad (7.19)$$

where  $R' = R_D^{seq} + R_{in}^{eq}$  ( $R_D^{seq}$  — sequential resistance of PD),  $I_0$  is the PD saturation current,  $V_t = kT/l \approx 0.025$  V at room temperature. A quantitative estimate of the deviation from linearity  $\xi$  for function  $I_p = \beta \{K_m \Phi\}$  can be presented as

$$\xi = \frac{\beta - \beta_1}{\beta^1} = I_0 \cdot \frac{\frac{R'}{AV_t} - \frac{\exp(I_p R' / AV_t) - 1}{I_p}}{1 + \frac{R'}{R_D} + \frac{I_0}{I_p} [\exp(I_p R' / AV_t) - 1]} \quad (7.20)$$

As it is seen from (7.19) and (7.20), relationship between the load current and the light flux power due to scintillations can be made linear if  $\beta = \text{const}$ . This, in turn, can occur if the third term in the denominator of (7.20) is negligibly small as compared with the first and the second, or is a constant, i.e., when

$$I_p(R_{in}^{eq} + R_D^{seq}) \ll AV_t \approx 0.0025 \text{ V}, \quad (7.21)$$

it is possible, using (7.19)–(7.21), to determine the dynamic range of linearity of the RDC as a whole for specified  $R_D$ ,  $C_D$ ,  $I_p$  values of a scintielectronic detector and EAC parameters.

The noise characteristics of a “current mode” RDC are largely determined by PD thermal noises, as well as generators of the noise e.m.f.  $e_n$  and noise current  $i_n$  (see Fig. 7.7), connected, respectively, sequentially and in parallel to the EAC input. According to the scheme of Fig.7.7 and the expression (7.18a), the contribution from thermal noises is

$$U_{out}^n(4kTR) = R_{oc}(4kT/R_D)^{1/2}, \quad (7.22)$$

and for  $R_{oc} \geq 10^6$  Ohm and  $R_D \approx 10^6$  Ohm this gives:

$$\begin{aligned} \text{at } \Delta f = 10^3 \text{ Hz } U_{out}^n(4kTR) &= 4 \cdot 10^{-6} \text{ V;} \\ \text{at } \Delta f = 10^4 \text{ Hz } U_{out}^n(4kTR) &= 1.25 \cdot 10^{-5} \text{ V.} \end{aligned}$$

For  $R_{oc} \geq 10^6$  Ohm and  $R_D \approx 10^5$  Ohm,

$$\begin{aligned} \text{at } \Delta f = 10^3 \text{ Hz } U_{out}^n(4kTR) &= 1.25 \cdot 10^{-5} \text{ V;} \\ \text{at } \Delta f = 10^4 \text{ Hz } U_{out}^n(4kTR) &= 4 \cdot 10^{-5} \text{ V.} \end{aligned}$$



Typical spectral density values for  $e_n$  and  $i_n$  for the case when a 544UD1A type OA is used are:  $e_n \approx 10^{-7}$  V/Hz<sup>1/2</sup> and  $i_n \approx 10^{-14}$  A/Hz<sup>1/2</sup>. For the case under consideration, noise values at the RDC output are expressed as

$$U_{out}^n(e_n) = e_n \left( 1 + \frac{R_{oc}}{R_D} \right) \Delta f^{1/2} \quad (7.23)$$

and

$$U_{out}^n(i_n) = i_n R_{oc} \Delta f^{1/2}. \quad (7.24)$$

Numerical estimates for  $U_{out}^n(e_n)$  at  $R_{oc} \geq 10^6$  Ohm and  $R_D = 10^6$  Ohm give:

$$\text{at } \Delta f = 10^3 \text{ Hz } U_{out}^n(e_n) = 6.6 \cdot 10^{-6} \text{ V};$$

$$\text{at } \Delta f = 10^4 \text{ Hz } U_{out}^n(e_n) = 2 \cdot 10^{-5} \text{ V}.$$

For  $U_{out}^n(i_n)$ , similar estimates yield

$$\text{at } \Delta f = 10^3 \text{ Hz } U_{out}^n(i_n) = 3 \cdot 10^{-7} \text{ V};$$

$$\text{at } \Delta f = 10^4 \text{ Hz } U_{out}^n(i_n) = 10^{-6} \text{ V}.$$

The signal to noise ratio, accounting for (7.18a), (7.22–7.24), can be presented in the form

$$\frac{U_c}{U_n} = \frac{I_p R_{oc}}{\left[ \frac{4kT}{R_D} + \frac{e_n^2}{R_{oc}^2} \left( 1 + \frac{R_{oc}}{R_D} \right) + i_n^2 \right]^{1/2} R_{oc} (\Delta f)^{1/2}} \quad (7.25)$$

Analysis of the expression (7.25) shows that signal to noise ratio values are directly proportional to  $R_D$ . In the general case, when varying signals are detected, the signal to noise ratio is affected by capacitance values  $C_D$  and  $C_{oc}$ , and keeping the signal/noise ratio constant requires the condition  $R_D C_D = R_{oc} C_{oc}$ . Moreover, according to (7.23) and (7.25) the value of  $R_{oc}$  is limited from the viewpoint of requirements to linearity of the measurement circuit.

#### 7.3.4. Pre-amplifiers for detectors operating in the current mode

The systems and receiving-detecting circuits (RDC) designed for detection of ionizing radiation can belong, depending on the operation mode, to one of the two types — the pulse type and integration type. In the pulse operation mode, there is a set of separate time-resolved

signals at the detector output. Each signal corresponds to a particle passing through the scintillator volume. In systems of the other type, a certain averaged effect is measured, caused by a large number of particles that enter the scintillator volume.

The process of averaging of the effects produced by a great number of nuclear particles is going on directly in the detector. Interaction acts of individual particles with the detectors are not resolved in time, but each particle contributes to the output signal [1]. Such systems are used for measurements of the average radiation level, and RDC are functioning in the mode of measuring the electric current (the current mode).

The current mode of RDC operation is used in combination with S-PD detectors in dosimetry and introscopy when it is necessary to measure slowly changing ionizing radiation fluxes in a broad dynamic range (5–6 orders of magnitude). In this case, PD is functioning in the photo-e.m.f. generation mode (valve), is used as a source of current, can operate without bias voltage and is connected directly to the input of the current amplifier.

Here we consider RDC characteristics in the current mode for an EAC design with an operational amplifier (OA) (Fig.7.8). The equivalent input resistance of the measurement circuit (which is a measure of how closely is the PD short circuit mode approximated) can be evaluated as  $R_{in}^{eq} = 1/A R_{oc}$ , where  $A$  is the amplification coefficient of OA.

The output voltage  $U_{out}$  is an output parameter of RDC; it depends upon the photocurrent value  $I_p$  as  $U_{out} \approx R_{oc} I_p$ , which implies that increasing RDC output signals requires as high  $R_{oc}$  values as possible.  $R_{oc}$  increase is possible by using OA with low input currents (Table 7.5).

Noise characteristics of RDC are largely determined by thermal noises of PD, as well as generators of noise e.m.f.  $e_n$  and noise current  $i_n$  (see Fig.7.7) in sequential or parallel connection (respectively) to the EAC input. Typical values of  $e_n$  and  $i_n$  density with a 544UD1A type OA (see Table 7.5) are  $e_n \approx 10^{-7}$  V/Hz<sup>1/2</sup> and  $i_n \approx 10^{-14}$  A/Hz<sup>1/2</sup>.

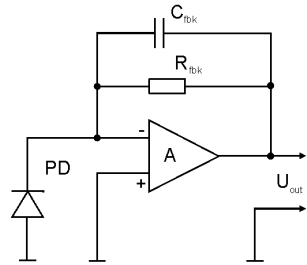


Fig. 7.8. Circuit diagram of pre-amplifier for operation in combination with S-PD detector in the current mode:  $A$  — operation amplifier,  $C_{fb}$  and  $R_{fb}$  — feedback circuit elements.

Table 7.5. Parameters of operational amplifiers with low input currents.

OA type	Parameters					
	Power supply voltage, V	$K_D \times 10^3$	$I_p$ , mA	$TKU_{bias}$ , $\mu\text{V/K}$	$I_1$ , nA	$f_1$ , MHz
KR140UD8	$\pm 15$	50	5	50	50	1
KR544UD1	$\pm 15$	50	3,5	50	0.1	1
KR574UD1	$\pm 15$	50	8	50	0.5	10
KR574UD2	$\pm 15$	25	10	30	1	2
KR574UD3	$\pm 15$	20	7	5	0,5	15
K1409UD1	$\pm 15$	20	6	—	0.05	1
OPA 627 AM	$\pm(4.5 \div 18)$	900	7	0.8	0.005	16
OPA 134 PA	$\pm(2.5 \div 18)$	1000	4	2	0.005	8
AD 743 K	$\pm(4.8 \div 18)$	1000	8	2.5	0.25	4.5
AD 8551	+5	1000	0.65	0.03	0.02	1.5

Notation in the Table:  $K_D$  – minimum amplification coefficient;  $I_n$  – consumed current;  $TKU_{bias}$  – temperature coefficient of the bias voltage;  $I_1$  – input current;  $f_1$  – frequency of unit amplification.

For low scintillation levels, amplifiers with differential input are used (Fig.7.9). Output voltage of such amplifier is

$$U_{out} = 2U_{in} \cdot R_2 / R_1 \cdot R_5 / R_3. \quad (7.26)$$

Suppression coefficient of synphasic noise  $K_{sp} = -20 \lg \delta$  is determined by the relative error  $\delta$  in fulfilling the condition  $R_4 \cdot R_6 = R_3 \cdot R_5$  and can reach 80 dB (10,000 times). The amplifiers have low temperature coefficient of zero bias at the output, especially if the input stage involves doubled OA mounted on one microchip crystal, e.g., K574UD2 (Table 7.5).

Higher sensitivity can be obtained with low current amplifiers designed under the modulator-demodulator pattern. A simplified diagram of one of such amplifiers is presented in Fig.7.10. The circuit includes an OA-based repeater  $A_1$ , a modulator based on field transistors  $T_1$ – $T_4$  and a synchronous differential amplifier based on OA  $A_2$  and  $A_3$ . In the

amplifier, it becomes possible (by lowering the power supply voltage of the first OA to  $\pm 4$  B and choosing K574UD2A microchips) to obtain the leakage current in the input stage of 20 fA.

The need to choose an appropriate OA for the first amplifier stage and complex character of the circuit hinder large-scale production of such amplifiers. Therefore, they are used mainly in experimental physics.

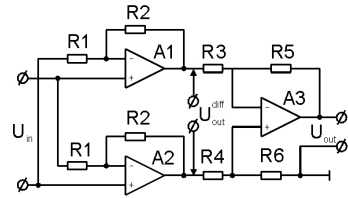


Fig.7.9. Schematic diagram of a DC amplifier with differential input.

### 7.3.5. Peculiar features of design and construction of charge-sensitive preamplifiers

A signal from a semiconductor detector is a pulse of electric charge collected between the detector electrodes. The charge created by a particle of 1 MeV energy in a depleted silicon layer is about  $5 \cdot 10^{-14}$  C. If the intrinsic capacity of the detector is about 100 pF, the voltage pulse formed is of  $\sim 0.5$  mV.

In S-PD detectors, as *p-i-n*-PD provides no intrinsic amplification, the electron-hole pairs formed by crystal scintillations at the *p-n* transition create a charge signal (with CsI(Tl), about  $3 \cdot 10^4$  electron-hole pairs per 1 MeV energy of gamma-quanta  $E_\gamma$  [35,36]). According to (26), a charge of  $Q \sim 5 \cdot 10^{-15}$  C is taken from PD. Amplification of the charge signals from the first and second detectors can be made using pulse amplifiers. The output voltage will be

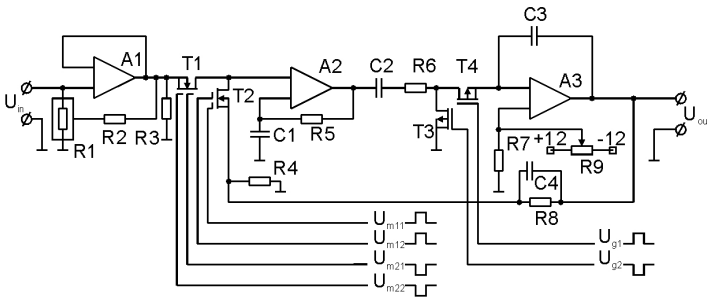


Fig. 7.10. Schematic diagram of the low current amplifier.

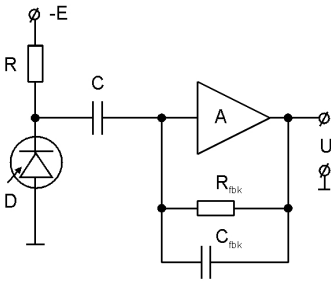


Fig. 7.11. Connection of the detector to a charge-sensitive preamplifier.

$$V_o = Q / C_{PD} \beta \quad (7.27)$$

where  $\beta$  is the preamplifier feedback parameter,  $C_{PD}$  is PD capacity.

In this case, strong dependence is observed of the output voltage of the detector-preamplifier system upon the detector capacity, which substantially depends upon the detector bias voltage and the environment temperature. Therefore pulse amplifiers are used when detectors operate in the counting mode and are absolutely not suitable for the spectrometric mode. For amplification of signals from

spectrometric detectors, it is necessary to use charge-sensitive preamplifiers (CSPA). The voltage at the CSPA output upon connecting the detector (Fig.7.11) is:

$$V_o = Q / C_{PD} \quad (7.28)$$

i.e., it is determined by the charge that is taken off the detector and by  $C_{oc}$  value of the feedback capacitor, which is usually chosen to be up to several pF. A CSPA scheme was first proposed by Cottini e.a. for work with ionization chambers.

Among distinctive features of CSPA, one should note the following:

- 1) the presence of feedback capacity  $C_{oc}$  from the output to input that determines the sensitivity to charge;
- 2) high input resistance (hundreds of Mohm);
- 3) low input capacity (several pF);
- 4) low level of intrinsic noises (several thousand eV);
- 5) high stability (time and temperature);
- 6) large amplification coefficient (2–3 orders with feedback circuit disconnected);
- 7) fast response.

Though CSPA design schemes are very different, three components can be always singled out (Fig. 7.12):

1. An input stage, which determines noise properties of the preamplifier as a whole. Comprises a field transistor and ensures the signal inversion.

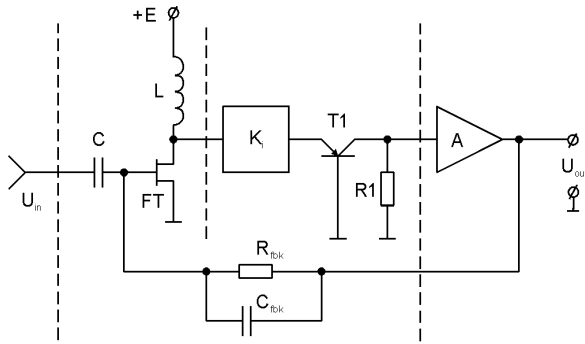


Рис. 7.12. Block diagram of a charge-sensitive preamplifier.

2. A stage for amplification without phase rotation. Such stage has low input resistance and high output resistance, i.e., works as current amplifier. The low input resistance, being a load for the field transistor, lowers the effects of the transistor transient capacity. The output resistor in combination with the high-resistance input resistor of the next stage forms a high-resistance load required to obtain high amplification coefficient of the whole charge-sensitive circuit. In the simplest case, the role of such amplifier is played by a stage with the common base with a bipolar transistor.
3. An output stage of CSPA matches the high-resistance load of the current amplifier to the input resistors of the next stages. This can be a voltage repeater.

Some more information can be given on the purpose of the main elements of CSPA and requirements put to them.

Requirements to FT of the input stage (Fig. 7.12):

- high steepness of the characteristic (more than 10 mA/V);
- low input capacity (several pF);
- low leakage current (less than  $10^{-8}$  A);
- low level of noises;
- minimum size.

Presently, many types of silicon FT are industrially produced which can be used in the CSPA outer stage. The choice of FT type and operation regime determine, in fact, such detector parameters as minimum detectable radiation energy and energy resolution.

The feedback resistor  $R_{oc}$  fulfills two functions:

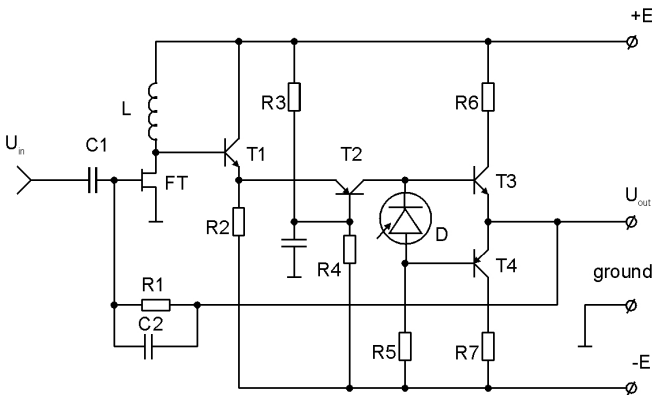


Fig. 7.13. A simplified schematic diagram of a charge-sensitive preamplifier.

- 1) ensures DC feedback and maintains the regimes of all transistors of the circuit;
- 2) discharges the capacitor  $C_{oc}$  with time constant  $\tau_{oc} = R_{oc} C_{oc}$  after each separate pulse or a group of input pulses, tends to restore the initial level of the output potential, thus determining the loading capability of the amplifier.

Resistor  $R_{oc}$  is connected to CSPA input and is an additional source of noise. Usually it is a high-resistance resistor (hundreds of MOhm) of the same type as resistor  $R$  in the circuit for detector bias voltage supply (see Fig. 7.12). These resistors should meet high requirements as for their noise characteristics and stability, and their dimensions should be minimal to reduce parasitic capacity.

The dividing capacitor  $C_p$  at the CSPA input, as well as the capacitor  $C_{oc}$  in the feedback circuit, should possess low leakage currents, minimum size and minimum intrinsic inductivity.

The second CSPA stage contributes to some extent to noise characteristics of the amplifier. Therefore, the most suitable are silicon low-noise transistors with large  $\beta$  and low transient capacity; the switching-on circuit is made with a common base [37].

No special requirements are put to other CSPA circuit elements. In Fig. 7.13, a simplified diagram is presented of one of CSPA variants. In designing CSPA, much attention should be paid to mounting of the elements on the board to minimize mutual interference of dif-

ferent elements. Materials with good insulating properties should be used (resistivity  $\rho = 2 \cdot 10^5 \div 10 \cdot 10^6$  Ohm cm) to lower leakage currents between elements of input circuits and earth. As such materials, glass textolite, fluoroplastics, sithal etc. can be recommended.

Analyzing CSPA designs described in literature, the following drawbacks can be noted:

- input stages show high levels of noise;
- inductive outflow load  $L$  of the input FT (Fig.7.13) is of large size and is affected by electromagnetic noises, requires careful screening and is not applicable when hybrid technologies are used;
- bipolar power supply and substantial power consumption hinder application of such circuits in small-sized instruments with independent power sources;
- low loading ability due to long decay times (hundreds of  $\mu$ s) of the signals determined by the feedback time constant  $\tau_{oc} = C_{oc} R_{oc}$ ;
- limited application field, i.e., connection of a specified detector type with appropriate parameters.



## REFERENCES

1. *Abramov A.I., Kazanskii Yu.A., Matusevich E.S.* Foundations of experimental methods of nuclear physics. – Moscow: Atomizdat, 1997. – 525 p.
2. *Globus M., Grinyov B.* Inorganic scintillators. Kharkov: Acta, – 2000, – 408 p.
3. *Lyapidevskii V.K.* Methods for detection of radiations. – Moscow: Energoatomizdat, 1987. – 408 p.
4. *Anisimova I.I., Glukhovskii B.M.* Photoelectronic multipliers. – Moscow: Sov.Radio, 1974. – 56 p.
5. *Ivanov V.I.* A course of dosimetry. – Moscow: Atomizdat, 1978. – 392 p.
6. *Karpenko V.P., Matveev O.A.* Studies of CdTe-detectors for computer X-ray tomography // *Fizika i tekhnika poluprovodnikov*. – 1993. – **27**, No.11–12. – P.1904–1908.
7. *Naydenov S., Ryzhikov V.* Prospects for creation of a scintielectronic detector with improved energy resolution. *Izvestia Vuzov. Materialy elektronnoy tekhniki*. – 2001. – **2**, P.65–70.
8. *Kishimoto S.* High time resolution X-ray measurement with an avalanche photodiode detector // *Rev. Sci. Instrum.* – 1992. – **63**, No.1, pt.2A. – p.824–827.
9. *Ryzhikov V.D., Stadnik P.E., Yakovlev Yu.A.* Prospects of development of the system scintillator-photodiode // *Pribory i tekhnika eksperiments*. – 1984. – No.5. – p.6–16.
10. *L.V.Atroshchenko, B.V.Grinev, V.D.Ryzhikov e.a.* Scintillator crystals and detectors of ionizing radiations on their base. – Kiev: Naukova Dumka, 1998. – 311 p.
11. *Ryzhikov V.D., Yakovlev Yu.A.* Application of S-PD detectors for dosimetric monitoring // *Atomnaya energiya*. – 1990. – **66**, No.6. – p.392–394.
12. *Ryzhikov V., Volkov V., Grinyov.* Miniaturize scintillation detector ionization rays on base ZnSe(Te), *Pribory i tekhnika eksperimenta*, – 1999, No 1, P.37–42.
13. *Holl I., Lorens E., Mageras G.A.* Measurements of the light yield of common inorganic scintillators // *IEEE Trans.Nucl.Sci.* – 1988. – **35**, No.1. – P.105–109.
14. *Viktorov L.V., Volkov A.P., Kruzhalov A.B. e.a.* Absolute scintillation efficiency of inorganic crystals // *Atomnaya energiya*. – 1991. – **1**, No.1. – p.64–67.
15. *Sakai E.* Recent measurements on scintillator-photodetector systems // *IEEE Trans.Nucl.Sci.* – 1987. – **34**, No.1. – p.418–422.

16. *Gal'chinetskii L.P., Zelenskaya O.N., Katrunov K.A., Ryzhikov V.D.* Determination of conversion efficiency of X-ray luminophores by measurements of radiation power // *Atomnaya energiya*. – 1994. – **76**, No.5. – p.428–431.
17. *Anisimova I.D., Vikulin I.M., Zaitov F.A., Kurmashev Sh.D.* Semiconductor photoreceivers. Ultraviolet, visible and near-infrared spectrum ranges. – Moscow: Radio i svyaz', 1984. – 252 p.
18. *Ignatov S.M., Grinev S.I., Lisurenko V.A. et al.* Energy resolution of gamma-detectors made on the basis of scintillator CsI(Tl)-Si photodiode // *Pribory i tekhnika eksperimenta*. – 1994. – No.2. – p.38–42.
19. *Kudenko Yu., Imazato T.* Performance of high-resolution CsJ(Tl)-PIN readout detector // *KEK Report*. – 1992. – No.92-15. p.1–18.
20. *Ryzhikov V., Naydenov S., Grynyov B., et al.* Multienergy radiography on basis of “Scintillator-photodiode” detectors // *Nucl.Instrum.and Meth.A*. – 2003. – **505**, P.549–551.
21. *Ryzhikov V., Kozin D., Grynyov B., Lisetskaya E.* “Scintillator-photodiode” detectors for scanning microscopy with high – spatial resolution // *Nucl. Instrum.and Meth.A*. – 2003. – **505**, P.58–62.
22. *Ryzhikov V., Chernikov V., Gal'chinetskii L. et al.* The use of semiconductor scintillation crystals  $A^{\text{II}}B^{\text{VI}}$  in radiation instruments // *Journal of Crystal Growth*. – 1999. – V.197. – p.655–658.
23. *Makino M.Q., Kawakami K., Kanaya K. et al.* Characteristics of miniature CsI Photodiode detectors for gamma ray and their clinical applications // *Nucl. Instr. and Meth. Phys. Res.* – 1994. – **A353**. – P.453–456.
24. *Tsirlin Yu.A., Globus M.E., Sysoeva E.P.* Optimization of gamma-radiation detection by scintillation crystals. – Moscow: Energoatomizdat, – 1991. – 152 p.
25. Schotanus P. Miniature radiation detection instruments readout of scintillation crystals with semiconductor devices. // *Int. Symp. Luminescence Detect. and Transformers of Ionising Radiation*. – LUMDETR'94. – Tallinn. – 1994. – P.98.
26. *Ryzhikov V.D., Piven L.A., Opolonin A.D. et al.* Dosimeters based on “scintillator-photodiode” detectors – a new generation of radiation control instrument // *Int. Symp. Luminescence Detect. and Transformers of Ionising Radiation*. – LUMDETR'94. – Tallinn. – 1994. – P.96.
27. *Slapa M., Traczyk M.* A new concept dosimeter with silicon photodiodes // *IEEE Trans. Nucl. Sci.* – 1996. – **43**. – P.1855–1859.
28. *Ryzhikov V., Starzhinskiy N., Chernikov V., et al.* Detectors for selective registration of charged particles and gamma-quanta. *Voprosy atomnoy nauki i tekhniki*, – 2002, v. 81, No 3, P. 130–132.

29. *Novikov V.M.* A method for monitoring of Gd concentration in Gd-loaded scintillators. // Nucl. Instr. and Meth. Phys. Res. – 1995. – **A366**. – P.413–414.
30. *Schotanus P., Dorenbos P., Ryzhikov V.D.* Detection of CdS(Te) and ZnSe(Te) scintillation light with silicon photodiodes // IEEE Trans. Nucl. Sci.. – 1992. – **39**, No.4. – P.546–550.
31. *Moszynski M., Wolski D., Ludziejewski T. et al.* Particle identification by digital charge comparison method applied to CsI(Tl) crystal coupled to photodiode // Nucl. Instr. and Meth. Phys. Res. – 1993. – **A336**. – P.587–590.
32. *Adeva B. et al.* The construction of the L3 experiment // Nucl. Instr. and Meth Phys. Res A. – 1990. – **A289**, No. 1,2. - P.23–109.
33. Handbook on semiconductor electronics. Ed. Lloyd, P.Hunter. – Moscow: Mashinostroenie, 1975. – 504 p.
34. *Scherbakov V.I., Grezdov G.I.* Electron circuits on operational amplifiers. Kiev: Tekhnika, 1983. – 213 p.
35. *Stolyarova E.L., Drygin V.N., Zhezlov A.M., Samedov V.V.* Amplitude characteristics of the system scintillator-photodiode // Prikladnaya yadernaya spektrometriya. – 1977. – No.7. – p.C. 135–144.
36. *Kurchaninov L.L., Sushkov V.V., Shuvalov R.S.* Electrometric amplifier // Pribory i tekhnika eksperimenta. – 1990. – No.1. – p.138–139.
37. *Krasnokutskii R.N. e.a.* Low-noise transistors for applications in nuclear electronics // Pribory i tekhnika eksperimenta. – 1988. – No.5. – p.118–120.
38. *Matveev V.V., Murin I.D., Polenov B.V. e.a.* Instruments for individual and group dosimetric monitoring of external radiation and radiometric measurements // Voprosy atomnoi nauki i tekhniki, Ser. Nuclear Instruments. – 1987. – No.3. – p.80–91.
39. Semiconductor detectors in dosimetry of ionizing radiation. Ed. V.K.Lyapidevskii. – Moscow: Atomizdat, 1973. – p.104–106.
40. *Ryzhikov V.D., Sokhin V.P.* Optimization of scintillator thickness in detection of X-ray and gamma-radiation in a broad energy range // Pribory i tekhnika eksperimenta. – 1988. – No.5. – p.177–181.
41. Radiation stability in optoelectronics. Ed.V.G.Sredin. – Moscow: Voenizdat, 1987. – 168 p.
42. *Nirhl J.* Photodiode scintillation detector for radiation instrumentation // Nucl. Instrum. Methods. – 1984. – **226**. – p. 487–495.

## CHAPTER 8

# INSTRUMENTS FOR RADIATION MONITORING

### *8.1. Introduction*

In recent years, development of dosimetry was aimed at creation of high sensitivity devices for radiation detection at dose rates from the natural radioactivity level to levels exceeding the natural background by  $10^5$ – $10^7$  times. As a result, dosimeters were created with sensitive elements on the basis of gas discharge detectors, in some cases with parameters allowing their use as individual dosimeters.

Development of radiation technology and nuclear power production brought up the need for similarly small-sized and reliable devices for detection of more powerful radiation — with dose rates  $10^5$ – $10^{10}$  times higher than the natural background, i.e., from 1 to  $10^5$  R/h. Ionization detectors allow detection of dose rates not higher than  $10^3$  R/h, when the limiting frequency of pulses in the counting mode is reached; for operation in the current mode, an ionization detector should be of very large size (up to  $1000\text{ cm}^3$  volume). Another drawback of ionization detectors is that they require high voltage power supply (300–1100 V).

The use of “scintillator-PMT” type detectors in dosimetry is limited, first of all, by the drawbacks of PMT. As for semiconductor detectors (SCD), their use is limited by insufficiently high absolute sensitivity, which is related to difficulties in obtaining high thickness (above 10 mm) of their sensitive region. Overall dimensions comparable to SCD, but much higher sensitivity (especially in the energy range that is the most important for dosimetry — 0.1–1.2 MeV) are provided by the “scintillator-photodiode” (S-PD) system. This is confirmed by  $\gamma$ -radiation detection efficiency data for SCD and S-PD detectors given in Tables 8.1, 8.2.

Table 8.1. Gamma-radiation detection efficiency for semiconductor detectors and S-PD detectors (1 mm SCD working layer thickness and optimized scintillator thickness).

Energy, MeV	Absorption efficiency , %						
	Semiconductor detectors, material			Scintillator-photodiode detectors, scintillator material			
	CdTe	HgI <sub>2</sub>	Si	CsI(Tl)	CdWO <sub>4</sub>	CdS(Te)	ZnSe(Te)
0.01	100	100	100	100	100	100	100
0.02	100	100	65	100	100	100	100
0.05	99.9	99.8	10	100	100	100	100
0.1	64	87	4.3	99	100	98	97
0.2	18	31	3	95	98	94	92
0.5	5.6	7	2	85	91	85	85
1.0	3.5	3.7	1.5	79	86	80	81

Table 8.2 Sensitivity of scintillation detectors.

Photoreceiver, material	Sensitive area, mm <sup>2</sup>	Detector current with scintillator CsI(Tl), nA	Relative detector sensitivity, %, for different scintillator materials				
			CsI(Tl)	ZnSe(Te)	CdS(Te)	CdWO <sub>4</sub>	BGO
FD-146, Si	175	125	100	438	82	30	5
FD-263, Si	9	10	100	134	85	25	4
FD-295, Si	100	100	100	135	83	60	12
FD-288, Si	150	125	100	150	90	35	8
«Alpha», Si	87	90	100	140	85	30	9
«Solntse», CuSe-CuS	100	130	100	110	55	50	12
FEU-79	—	—	100	46	5	1.5	12

From the standpoint of their application in dosimetry, S-PD detectors have also certain drawbacks:

- strong dependence of sensitivity and noise level of S-PD detectors upon temperature. In the temperature range from  $-50^{\circ}\text{C}$  to  $+50^{\circ}\text{C}$  these parameters are changed by nearly two orders of magnitude;
- when S-PD detectors are used in the current mode, the lower sensitivity limit of dosimeters on their base is 5–10 mR/hour, which is by 3 orders of magnitude higher than the background level.
- measurements in the counting mode up from the background level are possible for dosimeters with a “detector-preamplifier” circuit, including measurements on the real time scale. However, high sensitivity of a charge-sensitive preamplifier can result in a false response of the dosimeter caused, e.g., by vibration (which is also characteristic for SCD-based dosimeters).

Thus, dosimeters based on S-PD detectors can find their application among nuclear instruments, provided their advantages are used reasonably, and their drawbacks are not decisive for this or that specific application.

## **8.2. Development of radiation monitoring devices using “scintillator-photodiode” detectors**

### *8.2.1. Measurements up from the background level*

The main problem of successful application of S-PD detectors at low dose rates, i.e., for detection of isolated  $\gamma$ -quanta, is the problem of detection and subsequent amplification of charges of  $10^{-15}$ – $10^{-16}$  C. These values are obtained for energies in the 0.1–1 MeV range, taking into account the energy of a carrier pair formation in the photodiode ( $<10$  eV), scintillation efficiency (12–15%) and efficiency of phototransformation ( $\sim 40\%$ ) [1].

For recording of such small charges, the most suited would be the use of a charge-sensitive preamplifier (CSPA). Its limiting possibilities are determined by steepness of the field transistor characteristic, values of capacitance and leakage current of the photodiode, thermal noises of the preamplifier. Accounting for available world experience in application of S-PD systems for spectrometry of nuclear radiations, parameters of the best available photodiodes (FDK-142, Ukraine, and S-1790, Hamamatsu, Japan) are presented in Table 8.3.

Table 8.3. Results of laboratory tests of “scintillator-photodiode” detectors.

Detector No.	Scintillator		Photodiode		Measurement results, R/h, Radiation sources		
	material	size, mm	type	sensitive area, mm <sup>2</sup> are	<sup>137</sup> Cs	<sup>60</sup> Co	Mixture
157	ZnSe(Te)	12×10	PD-288	150	3.3	2.5	2.5
158	CdWO <sub>4</sub>	12×10	»	150	3	1.6	1.8
159	Al <sub>2</sub> O <sub>3</sub>	12×10	»	150	0.75	0.5	0.75
137	ZnSe(Te)	5×20×3	PD-295	100	1	0.95	1
140	»	3×2\i×5	“Alpha”	35	0.3	0.3	0.6
164	»	J×2(,)×1 0	»	35	0.9	0.9	0.86
156	»	5×5×7	PD-263	9	0.28	0.21	0.16
353	»	»	»	9	0.3	0.3	0.5
355	»	»	»	9	0.4	0.3	0.2

Analysis of the main parameters of these photodiodes, as well as of field transistors for CSPA input circuits (KP303G, KP307Zh, Russia; 2SK147, 2SK316, USA) shows advantages of the Western element base. However, the known results on the use of S-PD systems in dosimetry (detection threshold of 1 mR/h) [2] suggested that performance of the system could be substantially improved by optimum selection and matching of high-quality components of the S-PD-CSPA chain. In STC RI, a small-sized dosimetric device was developed, ensuring  $\gamma$ -radiation detection up from the background level (20–40  $\mu$ R/hour).

Fig.8.1 and 8.2 show diagrams of the input and output circuits of CSPA. The input circuit comprises a KP307Zh field transistor with a p-n transition-based shutter and KP312B as a dynamic load in the leakage chain [3]. An emitter repeating unit based on a KT328A transistor ensures matching of the first and subsequent circuits, thus substantially increasing the total amplification coefficient of CSPA [4]. The subsequent circuit (with a joint base on KP3109A) is made as recommended in [5].

The presence of the emitter repeating unit based on KT328A transistor and efficient negative feedback in the shutter chain  $T_2$  makes

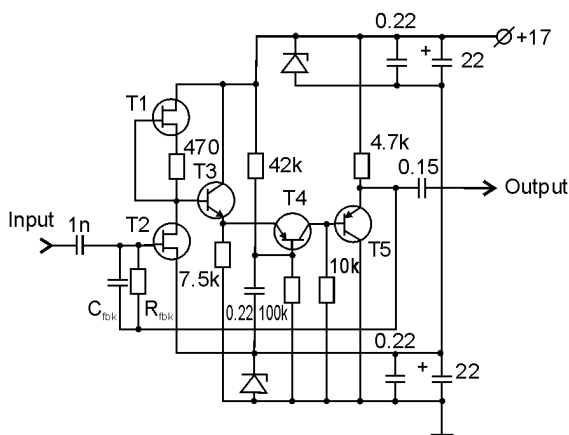


Fig.8.1. CSPA input circuit: T1 – KP312, T2 – KP307Zh, T3 – KT382, T4, T5 – KT3109; diodes – KS191.

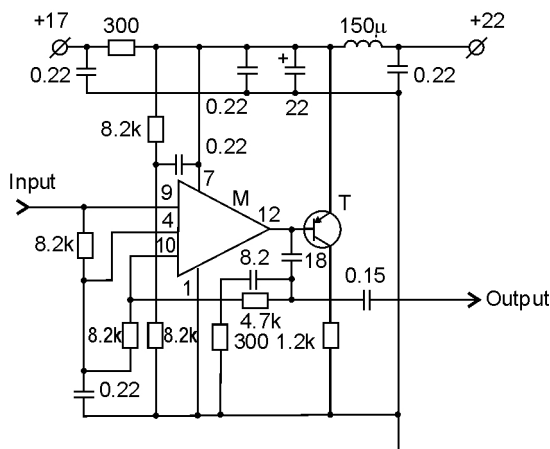


Fig.8.2. CSPA output circuit: M – K140UD1B; T – KT326.

the design weakly sensitive to parameter scatter of the constituent elements. Amplification coefficient of the input CSPA is 65–67 dB, pulse front duration — 30 ns, mean square level of output noises — 2–4 mV, output signal amplitude 1 V.



The output circuit of CSPA, comprising a K140UD1B operational amplifier and a KT326B transistor, amplifies the useful signal to the amplitude of 18–20 V, which is sufficient for its recording by standard digital pulse counters. The use of high-frequency transistors ensures fast response of the circuit. Its main parameters are the following: front duration 30 ns, amplification coefficient 27 dB, load resistance 1 k $\Omega$ . Power supply voltage of CSPA is 22–24 V, current  $\leq 30$  mA.

Fig.8.3 shows the number of detected pulses as function of radiation dose rate. The plots are close to

linearity in the range from 40  $\mu$ R/hour to 10 R/hour. A FDK-142 photodiode was used in combination with CsI(Tl), CdWO<sub>4</sub> or ZnSe(Te) scintillators. The highest sensitivity in the counting mode was noted for CsI(Tl), and the highest efficiency — for CdWO<sub>4</sub>.

Basing on the above-described technical solutions, a dosimeter has been developed which is small-sized and easy to use.

This instrument — a household dosimeter-clock with combined functions — is designed for indication of current time (alarm clock), measurement of the absorbed dose and dose rate of gamma-radiation.

Sound signalization is provided for indication the dose rate to have gone over a preset threshold limit.

The dosimeter is designed for a wide field of applications, primarily:

- by the personnel of atomic power stations;
- by the inhabitants of areas contaminated with radionuclides;
- by customs officers;
- for environmental control;
- for medical purposes.

The use of a small-sized scintielelectronic detector of a new generation (SELDI) and a liquid crystal display have allowed to obtain sufficiently high technical characteristics of the dosimeter.

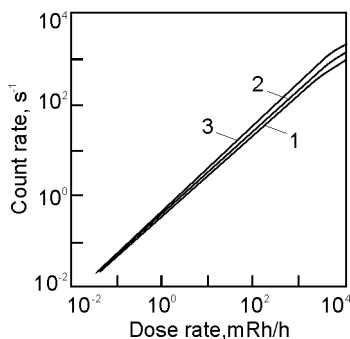


Fig.8.3. Pulse counter readings as function of dose rate (662 keV  $\gamma$ -source): 1 — scintillator ZnSe, 2 — CdWO<sub>4</sub>, 3 — CsI(Tl).

### Technical characteristics

Detected gamma-rays dose rate (R/h)	$10^{-5}$ – $10^{-2}$
Detected energy range (MeV)	0.05–3
Energy dependence in the 0.06 to 3 MeV energy range (%)	$\pm 10$
Error of the dose rate measurement (%)	$\pm 15$
Preset dose rate threshold range ( $\mu$ R/h)	0–990
Exposure dose measurement range (mR)	0–999.9
Accumulation time of the exposure dose (days)	1–7
Operation time with one set of power elements (SC-32 or similar)	not less than 6 month
Overall dimensions (mm)	$6 \times 52 \times 13$
Mass (g)	30

The use of a massive — about  $10 \text{ cm}^3$  — scintillator CsI(Tl) increases the instrument dimensions, but allows detection of radiation from the background level on the real time scale. This has been achieved in a RM-1401 dosimeter produced by Polimaster, Minsk, Belarus.

The main purpose of this instrument is looking for and localization of gamma-radiation sources. A high-sensitivity CsI-based detector, an original microprocessor, signalization with signal sequence frequency changing with approaching the source ensure efficient detection of relatively small activity sources (at the distance of 1 m, the instrument detects  $25 \mu\text{Ci}$  of  $^{137}\text{Cs}$ , and at 20 cm —  $1 \mu\text{Ci}$ ; when used in search for special nuclear materials, RM-1401 detects 4.3 g  $^{239}\text{Pu}$  at the distance of 2.4 m).

The instrument is relatively small-sized and is equipped with a wrist-watch type vibration signaling device, which allows its use by, e.g., secret service agents in search for radioactive materials in prevention of smuggling and terrorism.

A hermetic housing of high mechanical strength, the absence of a high-voltage block, up to 1000 hours operation time using one set of electric power cells — these features that allow this instrument to be widely used in emergency situations related to radiation-related accidents, under conditions of fire and explosion danger.

#### *8.2.2. Application of scintillator-photodiode detectors for dosimetric monitoring in the current mode*

Studies of various combinations of scintillators and photodiodes (Table 8.2) allowed us to make optimum choices for the developed de-

tectors. The photodiode current was measured in detecting radiation of standard sources. The data obtained were normalized with respect to the detector current with a CsI(Tl) scintillator taken as 100%. For comparison, similar data obtained with a FEU-79 PMT are also presented.

One should especially note a very high radiation stability of ZnSe(Te), CdS(Te) and tungstate scintillators. This was confirmed by testing carried out at the Institute of Nuclear Physics of the Academy of Sciences of Uzbekistan and the Institute for Nuclear Studies of NAS of Ukraine (Fig. 8.4). These results, as well as account for the fact that worsening of functionability and working parameters of silicon photodiodes occur under  $\gamma$ -irradiation of  $10^6$  rad or more and under neutron flux of  $10^{10}$ – $10^{11}$  cm $^{-2}$ , the radiation stability threshold for detectors with these scintillators and silicon photodiodes is not less than 106 rad under  $\gamma$ -radiation and neutron fluence of  $10^{10}$  cm $^{-2}$ .

For further studies, we have chosen detectors with scintillators ZnSe(Te) and CdWO $_4$  in combination with different photodiodes, aiming at high sensitivity and high radiation stability at small dimensions.

For amplification and detection of the detector photocurrent, a detection block was developed and constructed, distinguished by the use of a current-voltage converter based on a hybrid operation amplifier with extra low input current ( $< 10$  nA) and bias voltage ( $< 10$   $\mu$ V). The block output signal was proportional to the dose rate. The measurement range was 0.01–1000 R/hour, dimensions — 100×200×240 mm, mass — not more than 1.2 kg.

A rational choice of the feedback circuit parameters of the input operational amplifier allowed us to connect the detector to the electron block by a standard coaxial cable up to 25 mm long. The instrument was calibrated by measuring the detector current (scintillator ZnSe(Te), photodiode FD-295, radiation of 60 keV energy from  $^{241}\text{Am}$  of 2 Ci activity) in a standard geometry for the point source. Similar measurements were also carried out for a detector ZnSe(Te) — FD-288 photodiode with  $^{60}\text{Co}$  source of 63 Ci activity (Fig. 8.4). In the same figure, a similar dependence is shown for a detector consisting of a CdWO $_4$  scintillator (10×10×3 mm) and a Hamamatsu silicon photodiode of 98 mm $^2$  light sensitive area in detection of  $^{137}\text{Cs}$   $\gamma$ -radiation. These data show much higher (by about 5 times) sensitivity of ZnSe(Te) detector as compared with CdWO $_4$ .

Further studies were carried out using experimental facilities of the Complex Expedition of the Kurchatov Atomic Energy Institute

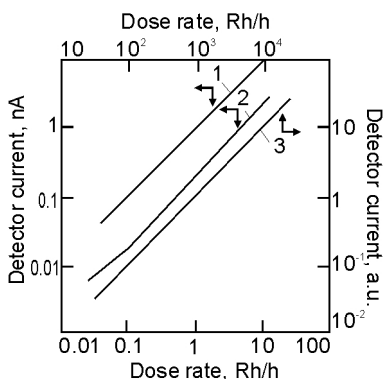


Fig.8.4. Photocurrent of “scintillator-photodiode” detectors as function of  $\gamma$ -radiation dose: 1,2,3 — detectors with scintillators ZnSe(Te),  $\text{CdWO}_4$ , ZnSe(Te) and sources  $^{241}\text{Am}$ ,  $^{137}\text{Cs}$ ,  $^{60}\text{Co}$ , respectively.

in Chernobyl. At first, to select the best detectors, measurements were carried out of radiation from  $^{137}\text{Cs}$ ,  $^{60}\text{Co}$  of 0.1 Ci and from a source composed of radionuclides imitating the composition of radioactive elements in the reactor pit of the 4<sup>th</sup> block of the Chernobyl nuclear power plant.

The detectors were located at such a distance from each of the sources that the dose rate measured by a reference dosimeter DP-5 was 5 R/hour. Basing on the results of the measurements (Tabl.8.3), detectors Nos.137 and 157 had been chosen. In December 1988, these detectors were used for measurements of the radiation profile (radiation dose rate) of the Hole No.24a in the

reactor pit of the 4<sup>th</sup> block. In all Chernobyl experiments, detectors were connected to the electronics block by a 25 m long cable, which allowed measurements at a safe distance (Fig.8.5).

The leadership of the Kurchatov Institute Complex Expedition gave their official conclusion on the results of these experiments, which included the following:

SELDI type detectors are suitable for control and analysis of radiation situation under conditions of medium and large dose rates (from 0.1 to  $10^3$  R/hour), including the vicinity of radiation source (nuclear reactor, nuclear fuel). Zinc selenide single crystals is the most promising scintillation material possessing high sensitivity, radiation and thermal stability.

The design of the device for amplification and recording of the detector signals is found to fully match SELDI type detectors in monitoring a radiation situation. It can be used as a basic version while developing dosimeters for recording of intense radiation fluxes.

It has to be specially noted that such dosimeters can work with remote detectors at significant distances (tens of meters). This is

necessary for the use of such units in local high-activity radiation fields, e.g., in real emergency situations or at the maintenance servicing of high-activity radiation sources.

At present, an experimental batch of such instruments has been produced and certified. They are successfully used at nuclear sites in Ukraine and are highly evaluated by specialists.

Combining the current mode and the counting mode allows a substantial broadening of the dynamic range of the instruments. This technical solution has been realized in the instrument “Uran” (Fig. 8.6.).

This instrument, in which detectors of SDN-128, SDN-129 types are used, is designed for radiation monitoring and recording of exposition dose rate of X-ray and  $\gamma$ -radiation and has the following characteristics:

Measurement range:

- at cable length 30–250 m –  $1 - 10^4$  R/hour;
- with a rod or a built-in detector –  $10^{-5} - 1$  R/hour;

Electric power supply voltage:

- AC (mains) — 220 V;
- DC (5 accumulators D-0.26) — 5.0–6.5 V;

Measurement time:

- in the  $1-10^4$  R/hour range  $\leq 10$  s;
- in the  $10^{-5}-1$  R/hour range  $\leq 30$  s;

Continuous operation time:

- from mains — not less than 10 hours;
- from D-0.26 accumulators — not less than 1 hour.

Testing carried out in Zaporozhye nuclear power plant showed high accuracy of exposure dose determination using this instrument both in the counting and current mode (Fig.8.6).

A principal distinctive feature of the dosimeter is the use of one-crystal microcontroller 1830BE31, which allows substantial widening

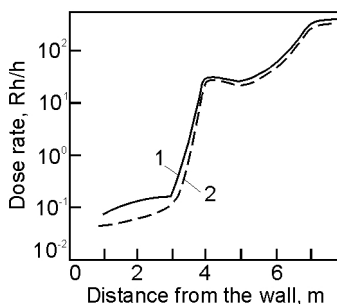


Fig.8.5. Radiation profile of the 24a pit of the 4th block of the Chernobyl power station measured using detectors No.137 (1) and 157 (2).

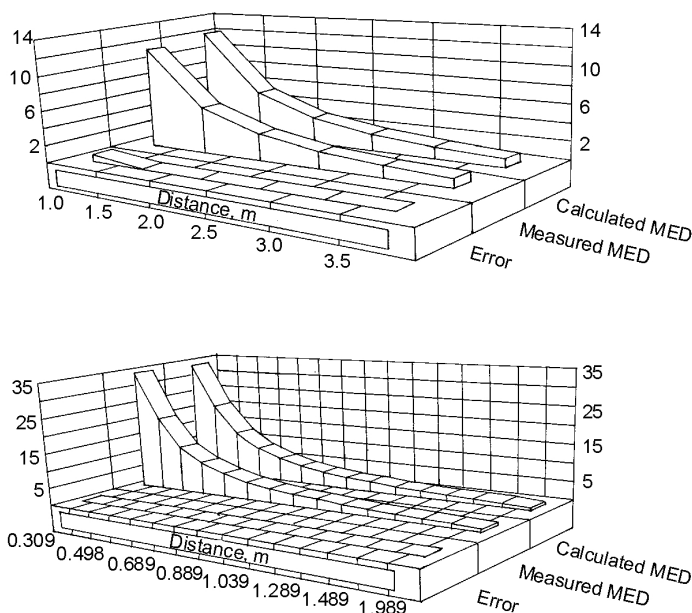


Fig.8.6. Readings from an instrument “Uran” (in relative units) at different distances between SELDI detectors and a  $^{60}\text{Co}$   $\gamma$ -source in the counting (a) and current (b) modes.

of service possibilities, application of mathematical processing (e.g., sliding averages) and connection of the two measurement ranges (from  $10^{-5}$  to 1 R/hour and from 1 to  $10^4$  R/hour) with minimum modification of the element base of the instrument.

For measurements in the whole dose rate range, two similar detectors are to be used, one of which functions in the counting mode (for low dose rates), and the other — in the current mode (for high dose rates). In measurements of low dose rates, an original hybrid low-noise broadband amplifier is used. High dose rates are measured by a remote detector with maximum cable length up to 250 m.

The instrument can be used at nuclear power stations in check-up and repair of technological equipment, at experimental reactors, accelerators, medical and industrial irradiation installations, radioactive waste storages, nuclear testing sites, nuclear industry plants, etc.

SDN-130 detector consists of a FD-337B photodiode and a ZnSe(Te) scintillator of 100–150 mm thickness. Its sensitivity is 0.05 pulses  $\text{m}^2/(\text{Bq s})$ , and it is designed for detection of  $\beta$ -radiation as a professional dosimeter. As light protection for the output window, beryllium foil of 0.1 mm thickness is used, and a metal housing ensures protection of the detector from electric fields.

Recently, combined detectors have been developed for detection of neutron radiation on the converter-photodiode or scintillator-photodiode basis. Thus, using a windowless silicon pin-PD and a converter of 25  $\mu\text{m}$  gadolinium foil, detection efficiency and lower detection limit for neutrons with  $E_n \leq 10$  keV are 5.6% and  $3.1 \cdot 10^2 \text{ cm}^{-2} \text{ s}^{-1}$ , respectively, with discrimination of  $\gamma$ -background up to 25  $\mu\text{Sv/hour}$  [6]. Using a CsI(Tl)-pin-PD detector with cadmium and samarium foils, neutron detection efficiency is 4.4% at  $\gamma$ -background of 6.4 mR [7], and in the pulse amplitude spectra peaks can be discerned from the radiation capture of neutrons with  $E_\gamma = 558.6$  keV (cadmium converter) or 333.4 and 439.4 keV (samarium converter).

In [8], the possibility has been shown in principle to use a cadmium-containing scintillator as a neutron-gamma converter. Detectors based on CWO-PD (of S3590 type) and CdS(Te)-PD have detection efficiency of thermal neutrons 0.2, as well as energy resolution of 24% and 11.7%, respectively, for  $E_\gamma = 662$  keV.

### *8.2.3. Gamma-spectrometer on the base of a “Notebook” computer and detector “scintillator-photodiode”*

A portable spectrometer SEG-04 has been developed, basing on a gamma-radiation detector of the scintillator-photodiode-preamplifier system and a computer of the “Notebook” class, used as a multichannel amplitude analyzer.

In the described gamma radiation detector a Hamamatsu S3590 silicon photodiode with active surface of  $10 \times 10 \text{ mm}^2$  is used as light sensor, and CsI(Tl) scintillator is used. Quantum yield is 65–69%. An original technology of light collection is used in scintillator packing. This allowed us to increase the conversion efficiency for  $1 \text{ cm}^2$  crystals to  $3.9 \times 10^4$  electron-hole pairs per 1 MeV of energy in comparison with the value presented in [9]. A hybrid amplifying section to be used with the detector has been developed and prepared for commercial

production. The preamplifier is constructed using the charge-sensitive scheme with a low noise field effect transistor in the input and has the equivalent noise charge of 450 electrons with the detector hooked up [10]. Shaping time constant of the hybrid forming amplifier is 5  $\mu$ s. Basing on these devices, a miniature detection unit has been developed with low energy consumption (22 mW), comprising also a bias voltage transformer of the photodiode (30 V). Power supply voltage of the detecting unit is 6÷9 V.

A possibility is studied to use in the detector scintillators of cubic and cylindrical shape with the volume of 1 to 16 cm<sup>3</sup>. For the experiment all scintillators were prepared from one and the same crystal. Dependence of the energetic resolution of the detecting unit over the <sup>137</sup>Cs line (662 keV) and <sup>60</sup>Co line (1.33 MeV) upon volume and shape of scintillator is shown in Fig. 8.7. Dependence of the relative efficiency of the detector upon scintillator volume and shape is presented in Table 8.4.

Multichannel amplitude analyzers traditionally used in nuclear spectrometry are either functionally self-contained devices or specialized moduli built in to a personal computer. The second variant is preferable due to high operating characteristics and possibilities of on-line processing of the spectra.

Using a computer of the “notebook” class and the above-described separable detection block a portable 1024-channel gamma radiation spectrometer has been developed and produced (Figs. 8.8, 8.9)

Development of the amplitude analyzer had to ensure a simplification of the apparatus hardware by the more sophisticated use of the computer facilities, which has been realized using special programs for data processing. The analyzer is made as a detachable interface modulus compatible with the computer. It can be produced as a built-in part inside the computer not affecting its functional possibilities, energy consumption and outside appearance. MS-Windows software environments can be used. A built-in power source ensures self-sufficient operation of the spectrometer for not less than 3 hours.

An experimental spectrometer SEG-04 has been successfully used for radiation monitoring in the Chernobyl exclusion zone. Many advantages of this instruments have been noted in official reports issued by the General Director of the Object “Ukrytie”, which include:



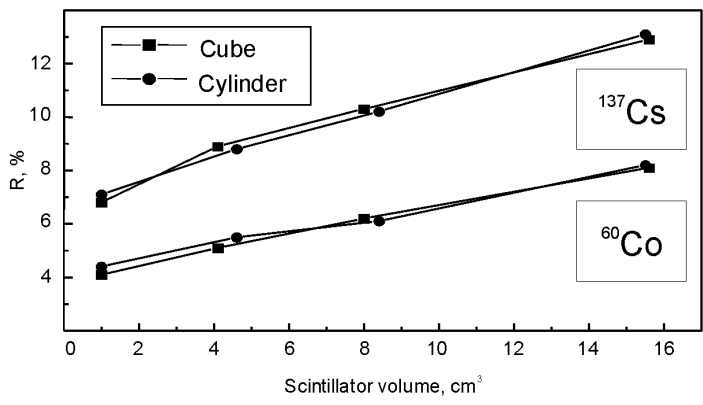


Fig.8.7. Dependence of the energetic resolution of the detecting block upon volume and shape of scintillator.

- small size and weight, making it suitable for operation in field conditions;
- the use of a “scintillator-photodiode” assembly allowed substantial reduction in size of the detection block, which, in turn, was very important for operation in severe radiation conditions requiring powerful shielding from the background radiation. The instrument with appropriate shielding remained small-sized and portable;
- the instrument can be easily moved without the need to switch it off, which reduces the time required for entering the functioning state, thus reducing the radiation dose received by the personnel;

Table 8.4. Dependence of the relative efficiency of the detector upon scintillator volume and shape.

Scintillator volume, cm <sup>3</sup>	Detector efficiency, relative units	
	Cube	Cylinder
1	1	1.1
4	4.7	4.9
8	10.6	10.7
16	22.3	23.4



Fig.8.8. A portable gamma-spectrometer SEG-04

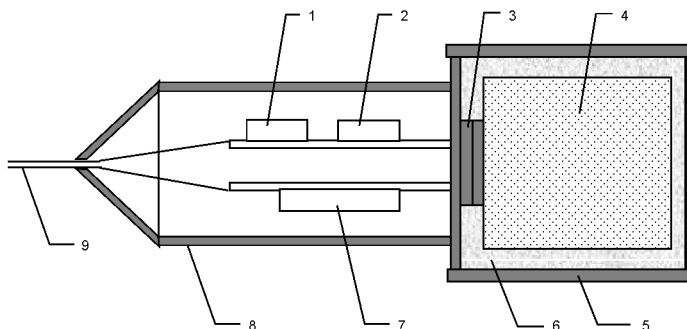


Fig.8.9. General design of the spectrometric detection block:

1 — amplifier-shaper; 2 — charge-sensitive preamplifier; 3 — photodiode;  
4 — scintillator; 5 — housing lid; 6 — reflective coating; 7 — voltage converter;  
8 — housing; 9 — cable

- availability of the controlling software not only for the measurement process, but also for preliminary processing of the acquired data, which makes working with the instrument sufficiently easy and convenient.

Fig.8.10–8.14 show spectra obtained using this spectrometer with different detection blocks, involving CsI(Tl) scintillators of different size (Fig.8.10, 8.11), ZnSe(Te) scintillator crystals (Fig.8.12, 8.13), and photodiodes.

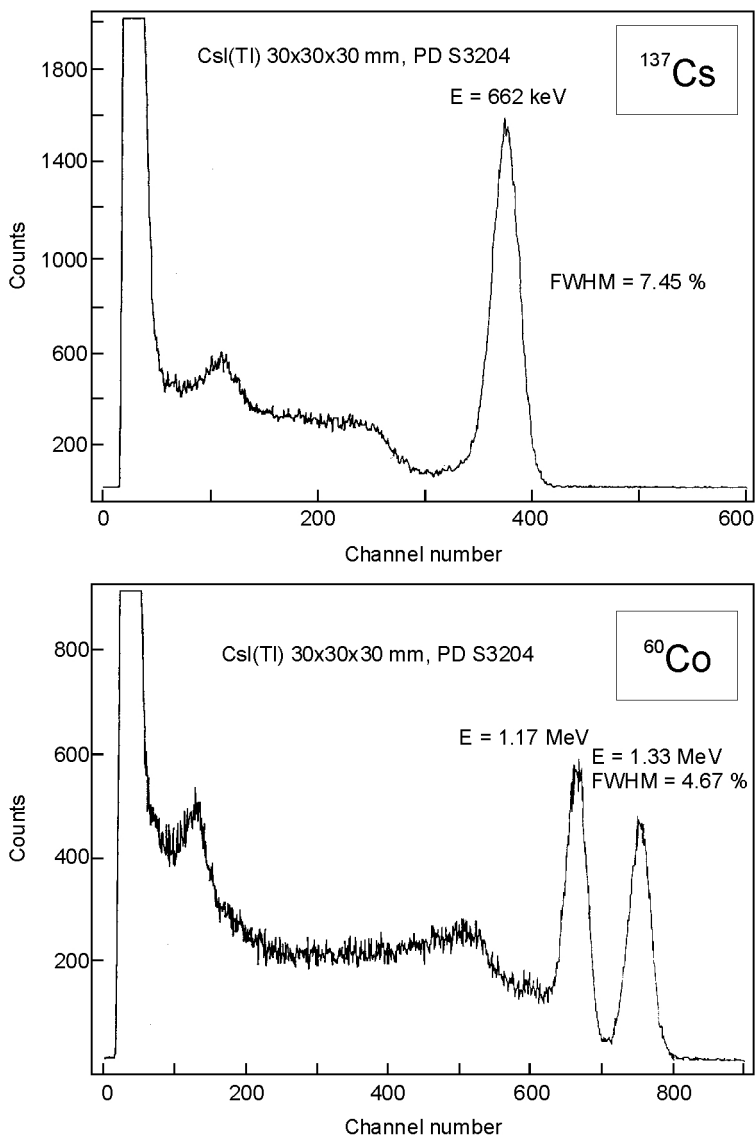


Fig.8.10.

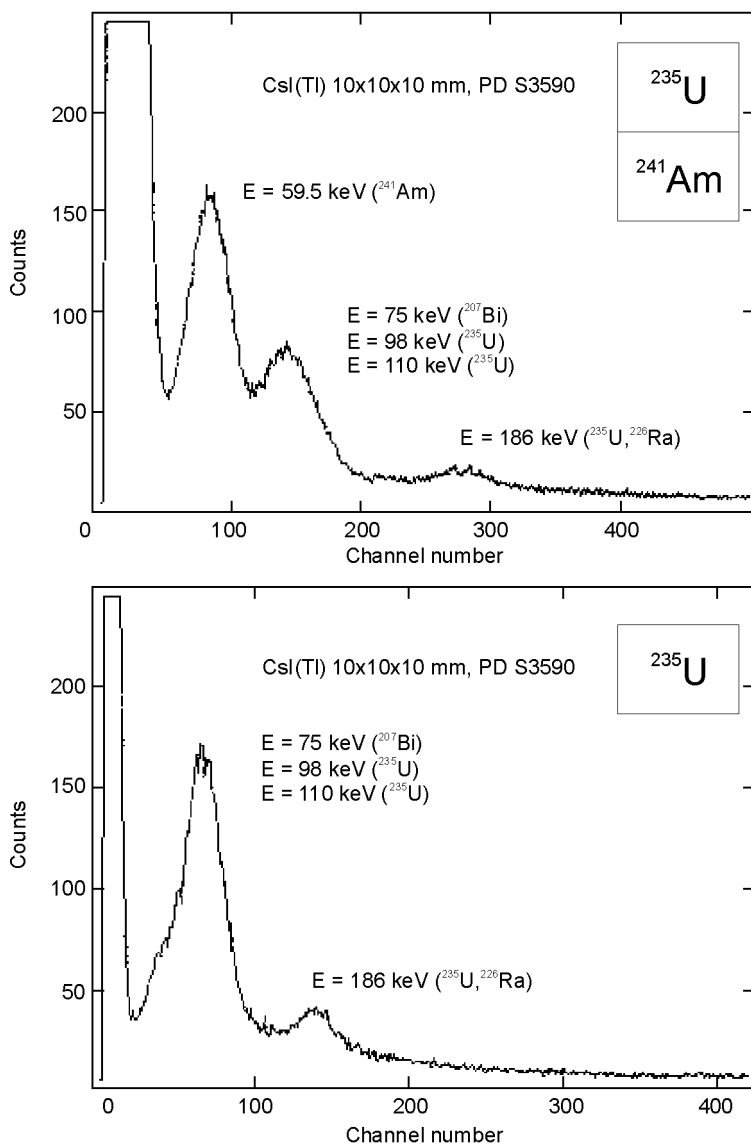


Fig.8.11.

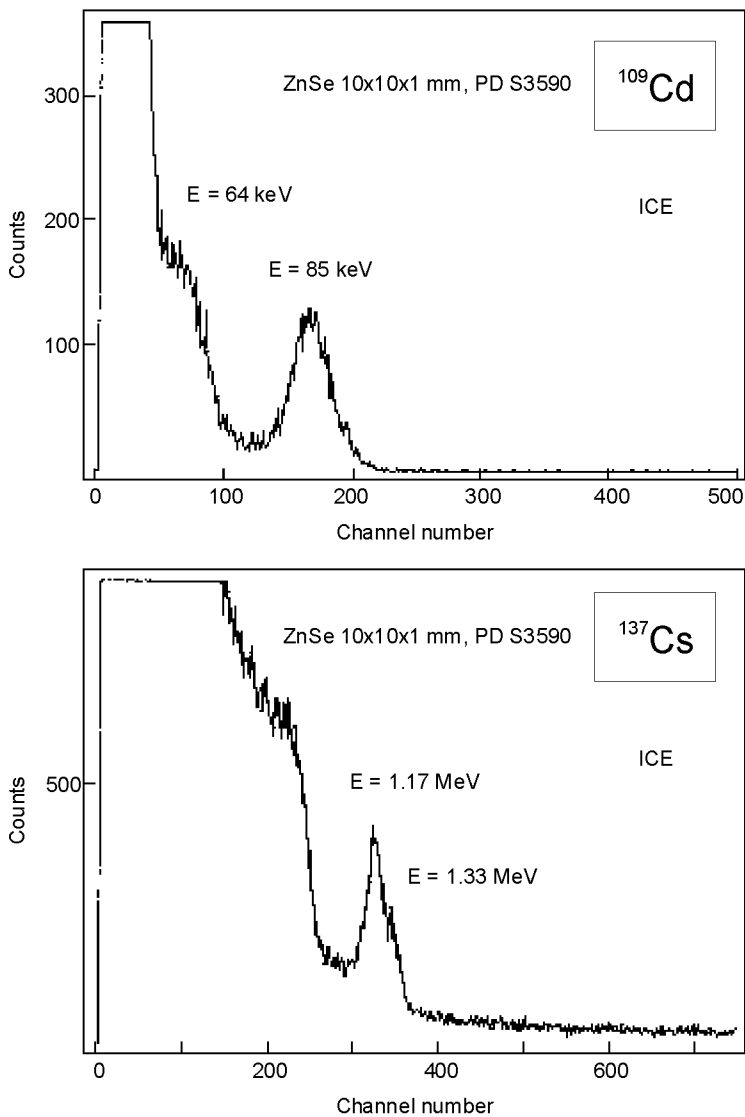


Fig.8.12.

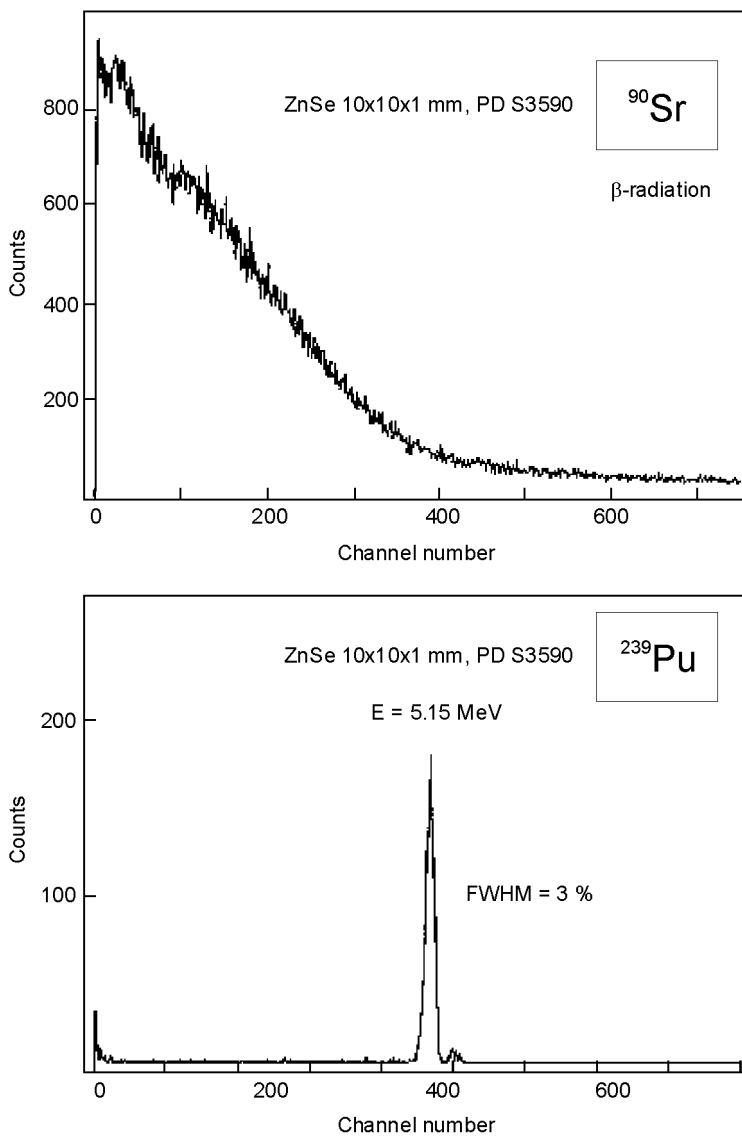


Fig.8.13.

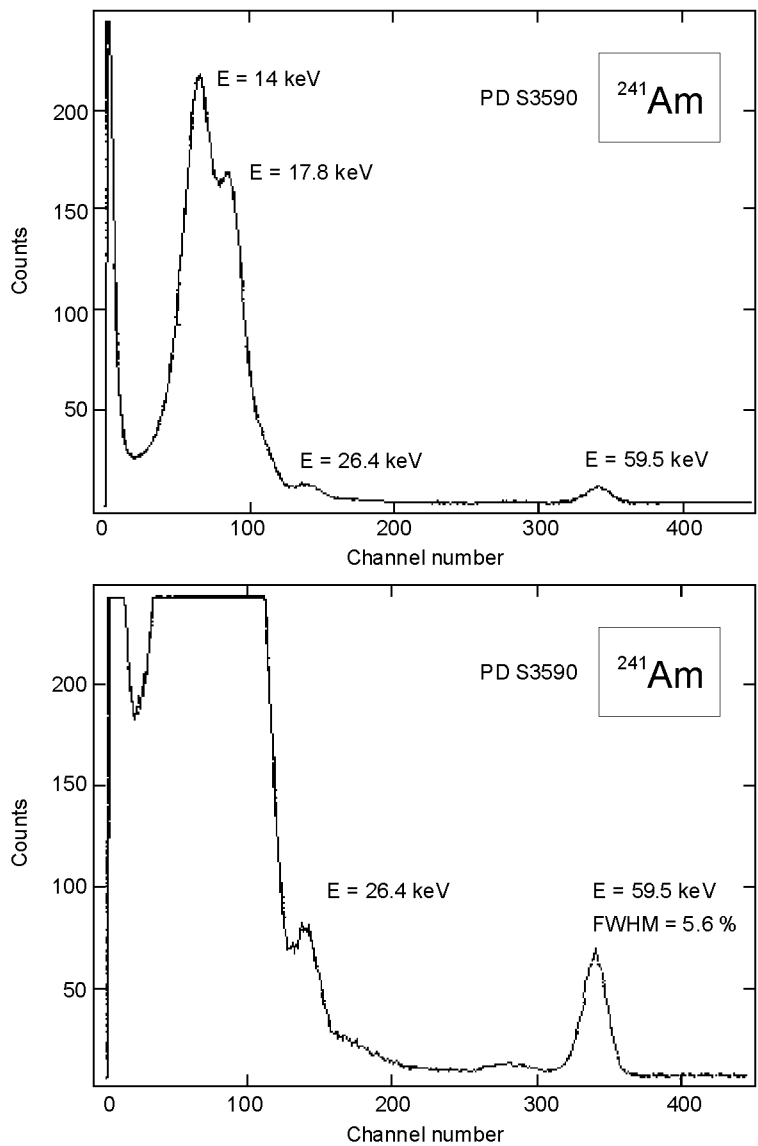


Fig.8.14.

### ***8.3. New ideology of detection of $^{241}\text{Am}$ and accompanying radionuclides***

#### ***8.3.1. Introduction***

Analysis of accidents at nuclear power plants (NPP) and radiochemical production plants that occurred in the last decades shows that some of these accidents were accompanied by substantial emission of radioactive substances to the environment. Such accidents occurred at a plant in Krasnoyarsk-26 (USSR, 70-ies, 80-ies), Leningrad NPP (USSR, 1974, 1975), Brunsbüttel (West Germany, 1977), Three-Mile Island (USA, 1979), Tsuruga (Japan, 1981), 1<sup>st</sup> block of Chernobyl NPP (Ukraine, 1982), Sellafert (Great Britain, 1986), and, the most known of all, 4<sup>th</sup> block of Chernobyl NPP (Ukraine, 1986). In addition to pollution due to nuclear industry, radioactive contamination can also come from technical nuclear explosions. The most known have been underground explosions called “Kristall” near Nadezhny village and “Kraton-3” near Aikhal village in Yakutia, USSR, in the 70-ies; these explosions obtained the status of emergencies. Though these explosions were intended to be underground, much of radioactivity burst outside.

After NPP, the most dangerous in this respect are radiochemical plants. Ecological harmfulness of these plants is due to their continuous release into the environment (even under normal operation conditions) of radionuclides that had not occurred in the nature before. Thus, in the vicinity of NPP and radiochemical plants artificial radionuclides are accumulating, including such long-living and dangerous radionuclides as plutonium, americium, tritium,  $^{14}\text{C}$  and many others. Most of the radioactive traces on Earth (excluding those due to nuclear weapons tests) have been formed by radiochemical plants – as a result of accidents or during normal operation. E.g., the Ural (Kyshtym) trace of north-eastern direction, several hundred kilometers long, is a result of an explosion of a liquid radioactive waste storage in 1957; the Chelyabinsk trace along the Techa river, coming to the Ob basin, had been formed by continuous radioactive waste discharge by the “Mayak” radiochemical plant; the Tomsk trace of north-eastern direction was formed in 1993 after a chemical explosion of technological equipment; the trace along the Enisei river up to the Karsk sea was formed by wastes of a radiochemical plant.



Among causes of such accidents, in most cases “mistakes of personnel” are considered among the most important. An IAEA international consulting group on nuclear safety has concluded that the main cause of such accidents is the lack of safety culture. This notion is much wider than just technical safety and includes all kinds of activities that can affect safety, including lawmaking and executive activities of government bodies. This implies that similar accidents can also occur in the future.

The main factor of efficient radiation protection is carrying out of continuous, timely and reliable radiometric monitoring of the environment. This requires a great variety of portable spectrometers and specialized radiometers.

### *8.3.2. Composition of radioactive contaminants from NPP*

In small local NPP accidents, alongside fission products in gaseous and aerosol form (volatile radionuclides Kr, Xe, I, Cs, Tl), “large” fuel particles do also emerge in the form of finely dispersed powder with particle size of tens and hundreds of microns (Mo, Zr, Ce, Pu, Sr). In the active stage of the accident, nuclear fuel is oxidized, and small fuel particles of up to 5  $\mu\text{m}$  are formed. After the Chernobyl explosion, such particles were blown away together with hot air flows to distances of tens of kilometers [11].

The Chernobyl catastrophe stressed the importance of continuous monitoring of radioactive contamination of the environment by highly toxic  $\alpha$ -emitting transuranic radionuclides (TUR) that had been thrown out from the damaged reactor as nuclear fuel components. The danger is related to a possibility of internal irradiation of the human organism by so-called ‘hot’ particles, i.e., finest particles of the active nuclear fuel dispersed in the environment. Analyses carried out using  $\gamma$ - and  $\alpha$ -spectrometers have shown that, alongside with long-living  $\gamma$ -emitting nuclides ( $^{137}\text{Cs}$ ,  $^{60}\text{Co}$ ,  $^{152}\text{Eu}$ ,  $^{154}\text{Eu}$ ,  $^{155}\text{Eu}$ ), these “hot” particles include isotopes of uranium ( $^{238}\text{U}$ ,  $^{234}\text{U}$ ,  $^{236}\text{U}$ ) and transuranic elements ( $^{239,240}\text{Pu}$ ,  $^{238}\text{Pu}$ ,  $^{243}\text{Am}$ ,  $^{241}\text{Am}$ , etc.).

Fig. 8.15 shows a typical spectrum of soil samples taken in the vicinity of Chernobyl NPP (measured by a scintillation detector).

The danger of such particles is that they are  $\alpha$ -emitters, which makes their detection rather difficult (as compared with  $\gamma$ -emitters). Moreover,  $\alpha$ -emitters are extremely harmful in the case of internal emission because of very high specific ionization losses. It is also known

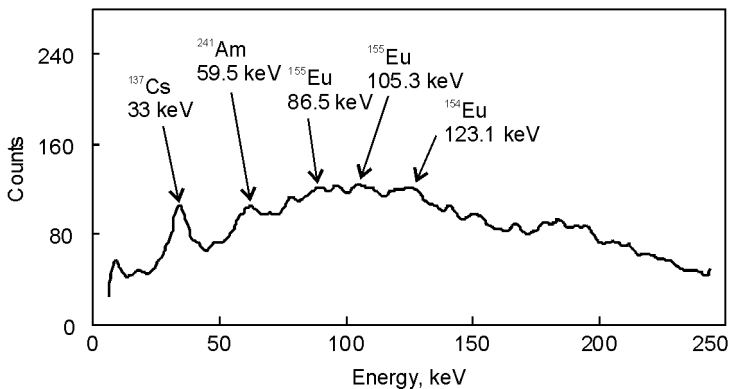


Fig.8.15. A typical spectrum of soil samples taken in the Chernobyl exclusion zone.

that uranic and transuranic elements are also dangerous because of their high chemical toxicity. The lower limit of specific  $\alpha$ -activity due to  $^{241}\text{Am}$  and  $^{239,240}\text{Pu}$ , estimated from determination of particle sizes and radionuclide content therein, can reach  $10^8$  Bq/kg, making them extremely dangerous pollutants. The presence of just several such particles inside a human organism (e.g., when inhaled into the respiratory system) can lead to tragic consequences.

At present, the Chernobyl exclusion zone is abundant in  $\alpha$ -emitting nuclides (energy of  $\alpha$ -particles —  $\sim 4\text{--}6$  MeV) — uranium isotopes,  $^{238}\text{Pu}$ ,  $^{239}\text{Pu}$ ,  $^{240}\text{Pu}$ ,  $^{242}\text{Pu}$ ,  $^{237}\text{Np}$ ,  $^{244}\text{Cm}$ , as well as  $^{241}\text{Am}$ , which is genetically related to them and is, in fact, the most dangerous [12,13].

$^{241}\text{Am}$  is formed in fuel elements of the reactor both during reactor operation:  $^{238}\text{U} \rightarrow (n, \gamma) \rightarrow ^{239}\text{U} \rightarrow (\beta, 23 \text{ min}) \rightarrow ^{239}\text{Np} \rightarrow (\beta, 2.3 \text{ days}) \rightarrow ^{239}\text{Pu}$  (weapon-grade)  $\rightarrow (n, \gamma, \text{ intra-reactor irradiation}) \rightarrow ^{240}\text{Pu} \rightarrow (n, \gamma, \text{ intra-reactor irradiation}) \rightarrow ^{241}\text{Pu} \rightarrow (\beta, 13.2 \text{ years}, E_{\beta\text{ave}} = 5 \text{ keV}) \rightarrow ^{241}\text{Am}$  ( $E_\alpha = 13.9 \text{ keV}$ ,  $E_\gamma = 59.537 \text{ keV}$ ), and in the after-explosion period — as a result of beta-decay of large quantities ( $\sim 0.14 \text{ MCi}$ ) of  $^{241}\text{Pu}$  thrown out to the environment, which makes  $\sim 84\%$  of the total TUR activity. Because of a relatively short half-life time of  $^{241}\text{Pu}$  ( $T_{1/2} = 13.2$  years), the content of highly radiotoxic  $^{241}\text{Am}$  in the environment will increase up to the year 2059, and only after that will begin to slowly ( $T_{1/2} = 433$  years) decrease. Presently,  $\sim 50\%$  of the total activity of  $\alpha$ -emitting radionuclides is due to  $^{241}\text{Am}$  [14]. Therefore,

by measuring the  $^{241}\text{Am}$  activity and accounting for a pre-determined activity ratio of TUR and  $^{241}\text{Am}$ , which is essentially constant in the Chernobyl exclusion zone, it is possible to determine activities of other transuranic elements, i.e., to solve the problem of TUR monitoring.

At present, TUR are intensively migrating from their initial fallout locations. This migration is carried out by rain and soil waters, air, over alimentary chains, including external contamination of agricultural products by dust etc. TUR can get inside the human organism by peroral (with food and water) or inhalatory (with air) way [14,15,16]. Therefore, continuous monitoring of radioactive contamination by TUR and  $^{241}\text{Am}$  in areas inside and around the Chernobyl exclusion zone is a task of primary importance. Monitoring of TUR migration requires regular carrying out of numerous measurements in soil samples of different density, in aerosol filter-samples, etc. It should be noted that  $^{241}\text{Am}$  detection in soil samples is additionally hindered by the presence of a strong background from accompanying radionuclides ( $^{137}\text{Cs}$  and others).

### 8.3.3. A new approach to americium detection

The radiochemical enrichment method (RCE) is a traditional way used in  $^{241}\text{Am}$  detection in samples. It has many drawbacks — the samples are to be preliminarily concentrated, which requires much time (analysis of a sample usually takes from 7 to 10 days); expensive chemical reagents are to be used (amounting to hundreds of dollars), and the accuracy is rather low — about 25–30%. This makes RCE not suitable for continuous large-scale radiation monitoring.

As the energies of common  $\alpha$ -emitters are in the  $\sim 4\text{--}9$  MeV range, the use of semiconductor  $\alpha$ -radiation detectors for determination of specific activity of  $\alpha$ -emitters in bulky soil samples cannot be used without RCE because of strong self-absorption of  $\alpha$ -particles in the sample matter. This method is useful only for preliminary estimates of the sample surface contamination.

Thus, rapid and efficient determination of  $^{241}\text{Am}$  and TUR specific activity in the environment using RCE methods and semiconductor radiation detectors is practically impossible [17].

However, in some cases radiation monitoring of  $\alpha$ -emitting TUR can be carried out by the accompanying  $\gamma$ - or X-ray radiation:  $E_\gamma = 59.5$  keV,  $E_x = 13.9$  keV [8]. This principle has been used in a new

portable radiometer RK-AG-02, designed for efficient detection of  $^{241}\text{Am}$  by the accompanying low-energy  $\gamma$ -radiation [19–43].

In developing the radiometer, main requirements were formulated to the design of specialized selective X-ray radiometers of high sensitivity, with special attention paid to stability of the PMT power supply source, parameters of the built-in spectrometric amplifier, temperature stability of the amplitude circuit amplification coefficient and thresholds of differential discriminators, electromagnetic compatibility of the scintillation block units, accounting for effects of geomagnetic field variation upon PMT amplification coefficient, etc.

In Fig. 8.16–8.18,  $\gamma$ -emission spectra of  $^{241}\text{Am}$  and  $^{137}\text{Cs}$  are shown as detected using a GSO scintillator.

Possessing a sufficiently high charge,  $\alpha$ -particles are efficiently decelerated in a substance (in air, path length of  $\alpha$ -particles is 3...5 cm, in soil — up to 50  $\mu\text{m}$ ). Due to self-absorption of  $\alpha$ -particles, it is practically impossible to determine specific activity of thick samples by measuring the surface  $\alpha$ -radiation without radiochemical separation of radionuclides, because distribution of “hot” particles in a sample is essentially non-uniform. However, in some cases information on the surface activity can also be useful, e.g., for checking the presence of  $\beta$ -radiation noises.

The  $\gamma$ -line  $E_x = 13.9$  keV is of high quantum yield, but it is practically adjacent to the PMT noise boundary. Therefore, the most suitable for  $^{241}\text{Am}$  activity measurements is  $\gamma$ -radiation with the quanta energy of 59.54 keV.

A conventional “windows” method used for determination of radionuclide activity from  $\gamma$ -radiation measurements [1] comprises measurement of  $\gamma$ -radiation by a detector, analysis of the obtained spectrum by an amplitude-to-digit converter (ADC) or a differential discriminator, measurement of the average pulse counting rate in the channels corresponding to  $\gamma$ -radiation photopeak regions of the analyzed radionuclide and continuous “background” distribution on both sides of the photopeak (with and without sample — background measurements), determination of noises from accompanying radionuclides (a “base” under the photopeak), and calculation, using these measurement results, of specific activity of the analyzed radionuclide, accounting for radiometer sensitivity and sample mass. This method

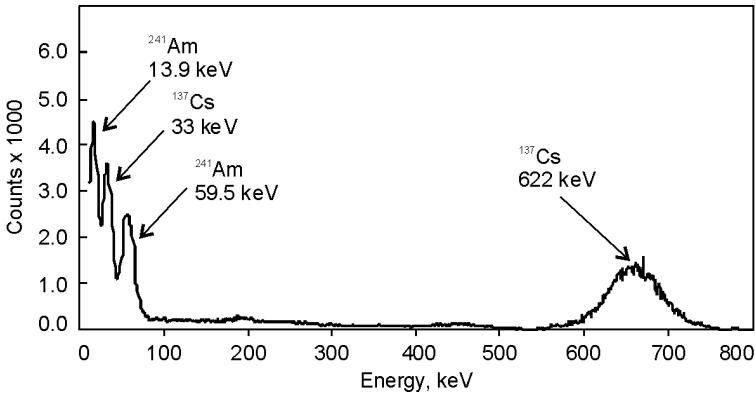


Fig.8.16.  $^{241}\text{Am}$  +  $^{137}\text{Cs}$  gamma-radiation spectrum. Scintillator — GSO.

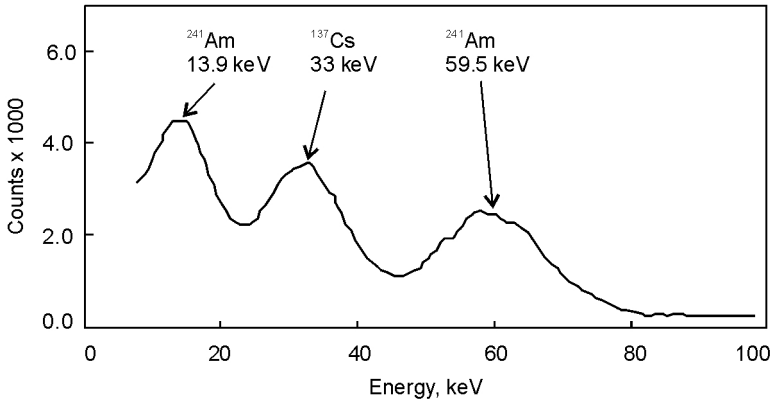


Fig.8.17. Low-energy region of the  $^{241}\text{Am}$  +  $^{137}\text{Cs}$  gamma-radiation spectrum. Scintillator — GSO.

gives satisfactory results when activity of the accompanying radionuclides is relatively low.

However, in soil or other environment objects activity of  $^{137}\text{Cs}$  can be 2–3 orders of magnitude higher than activity of  $^{241}\text{Am}$ . The most essential hindrance in measurement of  $^{241}\text{Am}$  activity by the 59.5 keV  $\gamma$ -line is an X-ray line of  $E_x = 33$  keV, which is due to an isomeric state of  $^{137}\text{Ba}$  ( $^{137}\text{Cs} \rightarrow ^{137}\text{Ba}$ ). Energy resolution of scintillation detectors

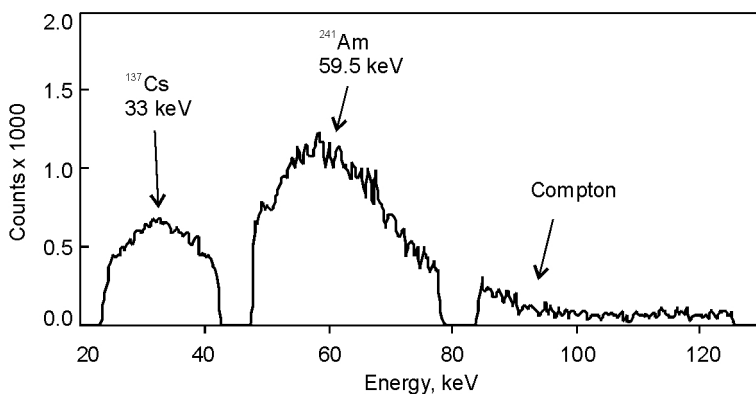


Fig.8.18. Low-energy region of the  $^{241}\text{Am} + ^{137}\text{Cs}$  gamma-radiation spectrum as measured by RK-AG-02. Scintillator – GSO.

is low in this spectral region, and the photopeak of this 33 keV line partially gets to the americium (59.5 keV) working window. If alkali halide scintillators are used, their advantage in higher resolution is lost because of the presence of an escape peak at  $\sim 30$  keV, accounting for which is very difficult when the signal/noise ratio is low. This peak makes impossible to account for  $^{137}\text{Cs}$  noise, and alkali halide crystals were not used in this radiometer.

In Fig.8.19, a typical spectrum is shown of a soil sample with low  $^{241}\text{Am}$  activity (about 35 Bq/kg) and high  $^{137}\text{Cs}$  activity (about 5 thousand Bq/kg), recorded by a selective radiometer. The signal-to-noise ratio is  $\sim 1:150$ . The  $^{241}\text{Am}$  photopeak is nearly completely eclipsed by the noises.

As it can be seen, when activity of a sample with low  $^{241}\text{Am}$  content is measured, it is not possible to visually estimate the tuning quality of discriminator windows to the  $^{241}\text{Am}$  photopeak. The windows tuning procedure should be carried out only with reference sources when the radiometer is calibrated.

Thus, main advantage of the developed instrument as compared with other radiometers is its higher sensitivity in detection of  $^{241}\text{Am}$  and genetically related TUR. Testing in the Chernobyl exclusion zone confirmed the validity of the method for TUR detection by accompanying  $^{241}\text{Am}$   $\gamma$ -radiation. Using GSO scintillators in combination with

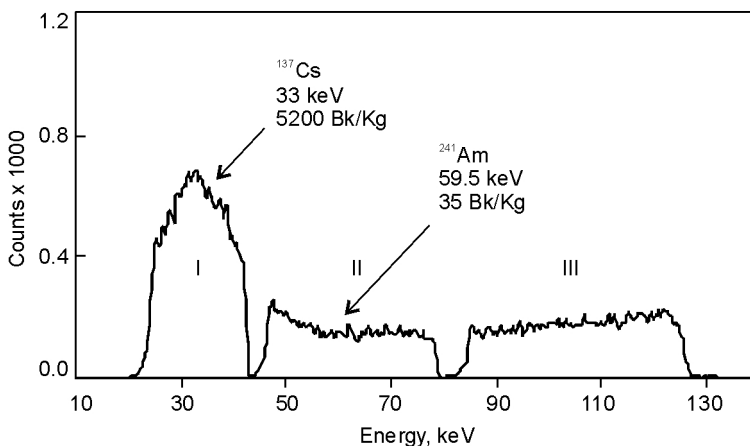


Fig.8.19. A typical soil sample in the working windows of RK-AG-02 radiometer.  
 $^{241}\text{Am}$  — 35 Bq/kg  
 $^{137}\text{Cs}$  — 5200 Bq/kg.

a modified algorithm for measurement “windows” and subtraction of noises due to  $\gamma$ -radiation from accompanying radionuclides allows measurements on a real time scale of  $^{241}\text{Am}$  specific activity in bulky soil samples of different density ( $\rho \sim 0.5\text{--}2.5 \text{ g/cm}^3$ ) under real radiation conditions at  $^{241}\text{Am}/^{137}\text{Cs}$  activity ratio  $\sim 1:100\text{...}1:500$ . This allows us to recommend this instrument as an efficient instrumental alternative to RCE methods.

#### 8.3.4. Application fields of RK-AG-02M radiometer

The portable radiometer RK-AG-02M is designed for continuous rapid measurements in field conditions of  $^{241}\text{Am}$  specific activity by accompanying  $\gamma$ -radiation ( $E_\gamma = 59.54 \text{ keV}$ ). The minimum detected activity is  $\sim 30 \text{ Bq/kg}$  at sample volume  $50 \text{ cm}^3$  and measurement time 40 min without outer protection. It can be also used for evaluation of TUR content in bulky soil samples and aerosol filters over substantial ( $\sim 1:100\text{--}1:500$  and more) accompanying background of  $^{137}\text{Cs}$  in real radiation conditions of the Chernobyl exclusion zone, for measurements of  $\alpha$ -particle flux density from the sample surface. It can be used for efficient radiation monitoring of agricultural products, soil, and aerosol filters in field conditions.

### 8.2.5. Operation algorithm of RK-AG-02M radiometer

The operation algorithm of the RK-AG-02M radiometer is based on the windows method. Three differential channels (windows) ensure amplitude selection of signals in a broad pulse load range. A modification of the method [25], which was proposed by us for  $^{241}\text{Am}$  activity measurements, takes into account interference noises both from  $\gamma$ -radiation of  $^{137}\text{Cs}$  ( $E_x = 33$  keV) and from continuous distribution of  $^{137}\text{Cs}$  and other radionuclides.

$^{241}\text{Am}$  activity values are determined by solving an equation system:

$$K_{11}A_1 + K_{12}A_2 + K_{13}A_3 = n_1^*$$

$$K_{21}A_1 + K_{22}A_2 + K_{23}A_3 = n_2^*$$

$$K_{31}A_1 + K_{32}A_2 + K_{33}A_3 = n_3^*$$

where  $K_{ij}$  is the sensitivity of the  $i$ -th differential measurement channel to the  $j$ -th radionuclide;  $A_j$  — activity of a reference source of the  $j$ -th radionuclide;  $j = 1, 2, 3$  ( $^{137}\text{Cs}$ ,  $^{241}\text{Am}$  and  $^{22}\text{Na}$ , respectively — the latter as a “Compton generator”;  $n_i^* = n_i - n_{ib}$ ;  $n_i$  and  $n_{ib}$  — total averaged counting rates in the  $i$ -th measurement window in the presence of a source or without it (background).

In a general case, solution of this equation system requires measurements (with appropriate accuracy) of nine coefficients  $K_{ij}$  using three special reference sources  $^{137}\text{Cs}$ ,  $^{241}\text{Am}$  and  $^{22}\text{Na}$ . However, by an optimum choice of the measurement channel boundaries, the required measurements can be reduced just to three spectrum shape coefficients.

The method comprises the following stages: simultaneous measurement of the average pulse counting rate  $n_i = N_i/t_e$  (where  $N_i$  is the total number of recorded pulses in the  $i$ -th channel during the measurement time  $t_e$ ;  $i$  – channels: “1” —  $E_x = 33$  keV; “2” —  $E = 59.5$  keV; “3” — continuous distribution (“Compton”); preliminary processing using a microcontroller (in the data processing block); further calculations using a built-in PC and visualization of the results on its monitor. Energy ranges of the measurement channels Nos. 1, 2 and 3 are, respectively,  $\sim 25 \dots 40$  keV,  $45 \dots 70$  keV,  $80 \dots 140$  keV. A sample of  $V = 50 \text{ cm}^3$  volume is placed into a measurement cell connected to the detection block from the side of a GSO scintillator covered by a protection membrane. Analysis of the amplitude spectrum of the scintillation detection block



in recording  $\gamma$ -radiation in this range, as well as appropriate calculations, show that the pulse counting rate of the useful signal (i.e., minus background and noises from the accompanying radionuclides) in the  $^{241}\text{Am}$  channel  $n_{2c}$  is

$$n_{2c} = \frac{n_2 - n_{2a} - q_{21}[(n_1 - n_{1a}) - q_{13}(n_3 - n_{3a})] - q_{23}(n_3 - n_{3a})}{1 + q_{21}q_{13}q_{32} - q_{21}q_{12} - q_{23}q_{32}}, [\text{s}^{-1}]$$

where the  $q_{21}$  term in the numerator is the interference noise in the  $^{241}\text{Am}$  channel from  $^{137}\text{Cs}$  photopeak with  $E_x = 33$  keV, the  $q_{13}$  term — the noise in the  $^{137}\text{Cs}$  channel with  $E_x = 33$  keV from the “Compton”, the  $q_{23}$  term — noise in  $^{241}\text{Am}$  channel from “Compton”,  $n_i$  — average pulse counting rate  $[\text{s}^{-1}]$ , recorded by the instrument in the  $i$ -th ( $i=1, 2, 3$ ) channel in the presence of a sample,  $n_{ia}$  — the average pulse counting rate recorded in the  $i$ -th channel without a sample (background),  $q_{ik}$  — spectrum shape coefficient of the interference noise from the  $k$ -th channel in the  $i$ -th channel

$$q_{ik} = \frac{n_i - n_{iD}}{n_k - n_{kD}} = \frac{\sum_{j=1}^3 K_{ij}}{\sum_{j=1}^3 K_{kj}}$$

With an appropriate choice of channel position, which has been realized in the instrument,  $q_{12}$  and  $q_{32}$  can be made close to zero, and  $n_{2c}$  will be determined by the numerator of the expression for  $n_{2c}$ . Specific activity of an  $^{241}\text{Am}$  sample of mass  $m$  in measurements over  $\gamma$ -radiation of  $E=59.5$  keV ( $A_\gamma$ ) and specific activity of TUR of the Chernobyl origin ( $A_{\text{TUR}}$ ) calculated as described above will be equal to:  $A_\gamma = n_{2c} k_\gamma^{-1} m^{-1}$ ,  $[\text{Bq/kg}]$  and  $A_{\text{TUR}} = n_{2c} k_{\text{TUR}}^{-1} m^{-1} = A_\gamma \delta^{-1} \approx 2A_\gamma$ ,  $[\text{Bq/g}]$ , where  $k_\gamma = K_{22}$  and  $k_{\text{TUR}}$  are respective sensitivities,  $\delta \sim 0.5$  is the fractional coefficient of  $^{241}\text{Am}$  activity in the total  $\alpha$ -activity of TUR. The relationship (1.4) is put into the software of the instrument.

Alpha-radiation spectrum from a thin source, because of limited energy resolution of GSO detectors, appears as a rather narrow absorption peak with a poor resolution of the peaks of individual TUR. Amplification coefficient of a spectrometric amplifier in the  $\alpha$ -mode is set in such a way that the amplitude distribution peak of TUR  $\alpha$ -radia-

tion is within the limits of the 2<sup>nd</sup> channel. Amplitude boundaries and channel widths are not changed. For the  $\alpha$ -mode, the energy ranges of the working channels Nos.1,2 and 3 are respectively equal to 2...3 MeV, 3.9...8 MeV, 10.4...16.6 MeV. An open measurement cell is used. The GSO scintillator surface is open to  $\alpha$ -radiation. In the 1<sup>st</sup> channel, detection of  $\gamma$ - and  $\beta$ -radiation from noise-forming admixtures present in the sample is possible (though most of them are removed by radiochemical treatment). They are detected in this channel in the  $\alpha$ -mode because the so-called scintillation detection efficiency ratios  $\gamma/\alpha$  and  $\beta/\alpha$  are equal to  $\sim 2...3$ . Thus, the useful signal pulse counting rate  $n_c^\alpha$  in the second TUR  $\alpha$ -radiation channel is  $n_c^\alpha = n_{c+\beta}^\alpha - n_\beta^\alpha$ , [s<sup>-1</sup>].

The  $\alpha$ -particle flux density  $\Pi_\alpha$  from the source surface of area  $S_1$  is  $\Pi_\alpha = n_c^\alpha \cdot k_{\alpha n}^{-1} S_1^{-1}$  [ $\alpha$ -particles/cm<sup>2</sup> s], where  $k_{\alpha n}$  is the  $\alpha$ -channel sensitivity.

Activity  $A_\alpha$  measured over  $\alpha$ -radiation is  $A_\alpha = n_c^\alpha \cdot k_{\alpha A}^{-1}$  [Bq/sample], where  $K_{\alpha A}$  is the  $\alpha$ -channel sensitivity for  $\alpha$ -activity (which is valid for thin-layer sources).

Parameters  $q_{21}$ ,  $q_{13}$ ,  $q_{23}$ ,  $k_\gamma$ ,  $k_{\alpha n}$ ,  $k_{\alpha A}$ ,  $k_{TYP}$ ,  $\delta$  are determined by calibration. The first four ( $q_{21}$ ,  $q_{13}$ ,  $q_{23}$ ,  $k_\gamma$ ) are determined using bulky radionuclide  $\gamma$ -radiation sources of a specified density (sample imitants), the fifth and the sixth ( $k_{\alpha n}$ ,  $k_{\alpha A}$ ) — using a reference  $\alpha$ -radiation source. The last two ( $k_{TYP}$ ,  $\delta$ ) are corrected using radiochemical analysis data.

Thus, RK-AG-02 radiometer ensures high sensitivity in <sup>241</sup>Am detection, though  $\gamma$ -quanta emitted by <sup>241</sup>Am are of low energy and the accompanying <sup>137</sup>Cs background is high. This has been achieved by a whole complex of our new developments — the use of a modified windows method and the oxide scintillator GSO, account for self-absorption of  $\gamma$ -radiation in the sample, introduction of a stabilization system to the measurement circuit. We have obtained the minimum detectable activity of  $\sim 30$  Bq/kg with samples of 50 cm<sup>3</sup> volume and 40 min measurement time without outer protection. Using a standard stationary lead protection of 5 cm thickness, the minimum detectable activity was  $\sim 5$  Bq/kg. It should be also noted that our method ensures high accuracy ( $\sim 10$ – $15\%$ ) and reproducibility in routine measurements of specific activity of <sup>241</sup>Am and TUR, including the case of so-called “hot” particles in soil samples of Chernobyl origin and aerosol filters, without any radiochemical treatment.

### 8.3.6. Original features of RK-AG-02 radiometer

The structural design of RK-AG-02 radiometer [24] is based on the principle of instrumental construction of the measurement channels—windows (3 pcs.) on the basis of amplitude differential discriminators.

This ensures high detection efficiency of  $^{241}\text{Am}$  against strong  $^{137}\text{Cs}$  background. E.g., radiometers-spectrometers produced by Violinist, USA, which use an analog to digit converter in combination with programmed formation of the accumulation windows and data processing, because their response was not sufficiently fast, could not provide a satisfactory solution to the problem of  $^{241}\text{Am}$  detection on the accompanying  $^{137}\text{Cs}$  background in the Chernobyl exclusion zone.

The most substantial and original feature of the RK-AG-02 operation algorithm is simultaneous accounting for noises both from  $\gamma$ -radiation of  $^{137}\text{Cs}$  with  $E_x = 33$  keV (detection of the contribution from the photopeak of this line is carried out in a separate working window) and from continuous distribution of  $^{137}\text{Cs}$  and other radionuclides (detection of the Compton distribution is carried out in another separate working window). This peculiar feature of the RK-AG-02 operation algorithm allows reliable detection of very small  $^{241}\text{Am}$  activities (minimum detectable activity  $\sim 30$  Bq/kg or  $\sim 2$  Bq/sample at sample volume  $50\text{ cm}^3$ , measurement time  $\sim 20$  min without outer protection) on the background of very high loads from  $^{137}\text{Cs}$  ( $^{137}\text{Cs}$  activity in the sample can exceed the  $^{241}\text{Am}$  activity by 200–500 times and more) and other accompanying radionuclides. With a standard outer protection, the minimum detectable activity can be as low as  $\sim 5$  Bq/kg. The method of signal recording and processing used in the RK-AG-02 radiometer has been patented [25].

The method of  $^{241}\text{Am}$  detection using RK-AG-02 radiometer is an instrumental alternative to radiochemical methods, requiring substantially shorter measurement time — several hours or even tens of minutes, as compared with several days that are required by radiochemical methods.

A unique property of scintillation detectors based on gadolinium orthosilicate (GSO) as compared with alkali halide crystals like CsI(Tl) is the absence of an escape peak in the working range of  $^{241}\text{Am}$  detection. Moreover, GSO includes gadolinium, which has, at  $E = 50.24$  keV, a sharp rise in the absorption cross-section (so-called “K-jump”) [26], resulting in an increased  $^{241}\text{Am}$  detection efficiency as compared with

other scintillators [27]. This also contributes to high sensitivity and low level of minimum detectable  $^{241}\text{Am}$  activity shown by the RK-AG-02 radiometer.

Because oxide scintillators used in this radiometer are non-hygroscopic, RK-AG-02 can be used for direct recording of alpha-radiation by an open scintillator (free path of  $\alpha$ -particles of 5 MeV energy in air is  $\sim 5$  cm) with the aim of monitoring the surface contamination and detecting the presence of  $\alpha$ -emitters on the sample surface.

The portable radiometer RK-AG-02 is, in fact, a selective radiometer for the X-ray range. Therefore, accounting for rather low energies of the detected energies of  $\gamma$ -quanta ( $\sim 20$ – $150$  keV), relatively low light output of GSO scintillator and rather narrow energy windows of the differential discriminators, high requirements are put to the constituent units of the radiometer as for operation stability, noise characteristics etc.

To achieve high sensitivity and reliability in measurements of low  $^{241}\text{Am}$  activities with RK-AG-02 radiometer, many technical problems had to be solved. E.g., an analog system for stabilization of the amplification coefficient in the measurement circuit had to be developed (with a reference LED in the detector). The lower detection limit also depends upon electromagnetic compatibility of electronic units of the scintillation block.

### *8.3.7. Design features of the radiometer*

Alpha-gamma radiometer RK-AG-02M consists of the detection block (DB), data processing block (DPB), stabilization block (SB) and power supply module (PM) [24]. Preliminary processing of signals, formation of measurement channels, pulse counting in the channels, sampling from counters according to the pre-set algorithm are carried out in the preliminary signal processing module (PSPM). Storage of the processing data, calculation of counting rates, flux density and activity, visualization of the calculation results, control of PSPM regimes and input of working parameters is carried out by a built-in PC of a “hand-hold” type (CASSIOPEIA A-11A).

The radiometer comprises a passive protection (PP) — a vessel of a complex shape made of stainless steel with a device for loading of the measurement cells, as well as special three-dimensional reference sources of  $\gamma$ -radiation for calibration of the radiometer. There

are also special three-dimensional  $\gamma$ -radiation sources for tuning and determination of coefficients  $q_{21}$ ,  $q_{13}$ ,  $q_{23}$ ,  $k_\gamma$ ,  $k_{\alpha n}$ ,  $k_{\alpha A}$ ,  $k_{\text{TYP}}$ ,  $\delta$ . There is also a gating module (GM) for tuning of the differential discriminator windows and ensuring operation in the laboratory conditions in the multi-channel spectrometer mode in combination with an external analyzer. The whole instrument set is placed in a special container designed for both transportation and operation.

Data input, regime control, display of the results, etc. are ensured by the PC with software based on Windows CE 2.0 in combination with LCD.

In the  $\gamma$ -mode, the energy ranges of the differential channels Nos.1,2 and 3 are, respectively, 27...37 keV, 55...80 keV, 92...163 keV, and in  $\alpha$ -mode — 2...3 MeV, 3.9...8 MeV, 10.4...16.6 MeV. The amplitude equivalents of the channel energy ranges are, respectively, 380...730 mV, 970...1790 mV, 2290...4600 mV. These ranges can be controllably varied depending of individual characteristics of the PMT used.

Preliminary processing of spectrometric signals using three differential discriminators, including formation of the three windows, formation of three counting channels, pulse counting in the channels by the buffer counters, cyclic data sampling by the processor, etc., is carried out in the PSPM module. This module also includes a 8-digit microprocessor R80S31VN (an analog of Z80), buffer counters and an interface unit for PC data input from the detection block. The pulse counting in the three channels is made by a R82S54 type chip with three independent counters.

The DB electron subblock comprises a high-voltage transformer of the PMT power supply, linear spectrometric amplifier with the time constant of 2  $\mu$ s, and linear voltage stabilizers. Manual voltage control is possible within 1000...1600 V with appropriate indication, as well as remote control of the amplification coefficient ( $K=40$ ; 320) of the spectrometric amplifier in switching over the detection modes for  $\alpha$ - or  $\gamma$ -radiation.

For tuning of the working window limits in laboratory conditions, a special gating module is used, which allows visual observation of the energy spectrum detected in the windows No.1,2 and 3 using an external multi-channel spectrometer.

In the detector, a 5 mm thick GSO scintillator is used. The “pedestal” Compton level is compensated for by a new signal processing

algorithm. The detector design ensures its protection from light (a thin plastic membrane lid, which is also a reflector for the scintillator). The energy resolution of the detection block is (for  $^{241}\text{Am}$ ,  $E_\gamma = 59.537 \text{ keV}$ )  $\sim 28\%$ .

The device for sample loading serves also as a passive protection (stainless steel of 1 cm thickness). Its design allows activity measurements of the aerosol filters.

For tuning and calibration of the instrument, specially designed three-dimensional radionuclide sources of  $\gamma$ -radiation are used, based on a polymer binder of ion-exchange resins (material density  $\rho = 0.8 \text{ g/m}^3$ ) containing radionuclides  $^{241}\text{Am}$ ,  $^{137}\text{Cs}$  and  $^{22}\text{Na}$  of different activity. Sources are also used that imitate the  $^{241}\text{Am}$  and  $^{137}\text{Cs}$  activity ratio characteristic for the Chernobyl exclusion zone, as well as standard  $\alpha$ -radiation sources of 2G9 type ( $^{239}\text{Pu}$ ).

As GSO scintillator is not hygroscopic, one and the same detector can be alternately used for measurements of  $^{241}\text{Am}$   $\gamma$ -radiation ( $\gamma$ -radiation detection mode) and  $\alpha$ -radiation ( $\alpha$ -radiation detection mode) directly on the sample surface.

The loading unit of the scintillation block fully guarantees its protection from light. With the membrane lid open, the scintillator works as an efficient detector of  $\alpha$ -radiation. Light protection of the PMT is ensured by the the passive protection design. High voltage cut-off is envisaged. Thus, the detection block can be used for detection of either  $\gamma$ - or  $\alpha$ -излучения. The detector design and technology of its preparation have been patented [22, 27], as well as technical solutions used in preparation of GSO crystals [32, 33].

#### *8.3.8. Parameters and characteristics of RK-AG-02 radiometer units*

##### **Detection block:**

1. Scintillator material and dimensions — gadolinium silicate (GSO) single crystal,  $\varnothing 45 \times 5 \text{ mm}$ ;
2. Photoelectronic multiplier (PMT) — FEU-176;
3. Photocathode working area diameter — 45 mm;
4. Optimum PMT working voltage — 1050...1100 B;
5. Energy resolution ( $^{241}\text{Am}$ ) — 28...32%;
6. Amplification coefficient of spectrometric amplifier (software-controlled switchover):  $\gamma$  -mode — 320,  $\alpha$ -mode — 40;

7. Amplifier output signal — quasi-Gaussian, duration 3  $\mu$ s;
8. Amplifier integral non-linearity in the 0...5 V range — not more than 0.5%;
9. Output signal temperature instability — not more than 0.01% °C;
10. Maximum load under normal operation — 5,000 pulses/s;
11. Passive protection thickness (stainless steel) — 1 cm;
12. Overall dimensions: without passive protection —  $\varnothing 65 \times 345$  mm, with passive protection —  $125 \times 125 \times 510$  mm

#### **Data processing block:**

1. Amplitude equivalent of energy ranges for differential channels 1, 2 and 3, respectively: 0.4...0.7 V, 1...1.8 V, 2.3...4.6 V (tunable);
2. Timer operation frequency — 10 MHz.
3. Data displaying periodicity — 2.3 s;
4. LCD  $480 \times 240$  dots/0.24 dpi;
5. PC operation system: Windows CE 2.0;
6. RAM — 6 Mbyte.

### ***8.4. Dosimeters for detection of solar radiation***

Solar UV radiation is one of the most powerful factors affecting human health (see the reviews [44] and references therein). The International Commission on Radiation (CIE) has defined, judging from the photobiological point of view, the following specific ranges of UV solar radiation: from 315 to 400 nm (UVA), from 280 to 315 nm (UVB) and from 100 to 280 nm (UVC). Radiation in the UVB range is partially absorbed by the stratosphere ozone layer, while the UVC radiation is absorbed almost completely. Due to its ability to destroy DNA and other biological macromolecules, the UVB region is generally associated with skin cancer. This radiation causes formation of the cataract, affects the immune system of humans and animals, and even leads to the extinction of certain kinds of plants.

It is quite clear that potential risk related to UV solar radiation factors should be adequately estimated. For this purpose, convenient and reliable methods are required for measurements of UV radiation parameters and their monitoring.

By the present time, several types of UV radiation meters have been developed (see reviews [45,46] and references therein).

First of all, one should mention broadband spectral instruments used to measure the total energy of UV radiation. Thus, in Robertson-Berger broadband meters the spectral curve of the photoelectric sensitivity is close to the biological effective spectrum of UV radiation for erythema [47] (the Diffey curve). However, the use of such instruments is limited, because different biological processes have different effective spectra.

Secondly, there are laboratory stationary spectroradiometers, which can scan the entire UV spectrum in detail. The spectral data are weighted with respect to the effective spectrum for any biological process.

Thirdly, there are biological dosimeters, e.g., a solar dosimeter based on DNA [48], which directly determine the spectral density of the light energy falling onto the measurement surface with respect to the spectral density of photobiological efficiency.

Next, there are dosimeters based on calibrated sets of photochromic materials, which allow reconstruction of the real solar spectrum in UVA and UVB ranges [49].

Finally, in the recent years instruments have been developed that measure UV radiation parameters in certain narrow spectral bands cut out by light filters [49]. In the best meters of this type, UV radiation is being filtered using interference light filters [50]. Calculation of biologically active doses is carried out using the model solar spectrum at different polar angles and effective biological spectrum for erythema [47].

A disadvantage of all these types of UV radiation meters is that they are either large-sized stationary installations or “passive” instruments that measure the absorbed dose not accounting for dynamics of spectral-energetic parameters of UV radiation.

The existing portable UV meters, as a rule, do not account for the so-called “cosine factor” — a qualitative coefficient describing variation of the instrument readings as function of light incidence angle for a concrete design of the photoreceiver.

Therefore, to meet the most important practical requirements, two types of UV solar radiation meters are to be developed:

- a small-sized inexpensive “household” instrument, which would give an adequate response to UVA and UVB radiation, allowing to evaluate hazardous factors in the real time mode. Such an instrument will



found broad application in health resorts, on agricultural work sites etc, allowing to reduce the risk of UV radiation-induced illnesses;

- a portable professional instrument, which would make it possible to determine both spectral-energetic parameters of biologically active UV radiation in the real time mode and the integral dose of absorbed radiation in the given time period. Such an instrument is necessary for development of new efficient protection methods against hazardous factors of UV solar radiation.

STC RI has developed and produced experimental UV meters of both types, using original detectors based on zinc selenide crystals as UV radiation receivers. The multi-filter professional variant allows one to measure the intensity and integral dose accounting for the cosine factor, as well to reconstruct the UV radiation spectrum in the 280–400 nm range using a specially developed software.

#### 8.4.1. Detector

Unique possibilities of directed property variation offered by isovalently doped AIBVI compounds, and, in particular, by ZnSe(Te) [51,52], opened the way for their broad application in radiation instruments – detectors of  $\alpha$ -,  $\beta$ -, X-ray and  $\gamma$ -radiation [53]. Recent studies have shown that ZnSe(Te) crystals can be also used as components of “semiconductor-metal” structures with Schottky barrier that are photosensitive in the UV range [53–55]. Though many different types of UV detectors are known (e.g., based on GaAs, InP, Si, GaN, SiC, etc.), most of them have serious disadvantages — either highly complex way of production, or low sensitivity, poor reproducibility, low radiation stability, spectral sensitivity range not meeting the requirements of specific applications [56]. As problems of detection and quantitative evaluation of UV radiation effects upon materials and biological objects has been attiring more and more attention, development and studies of new types of UV detectors is of undeniable interest. In this paper, we describe properties of photoreceivers with the “metal-semiconductor” transition on the basis of *n*-type ZnSe crystals, and we also report our studies on how their properties are affected by bias voltage, temperature, substrate doping level, etc.

As substrates, we used zinc selenide crystals doped with Te and O. Concentration of free electrons  $n_0$  ( $n_0 = 10^{12}$ – $10^{18}$  cm<sup>-3</sup>) was determined both by the activator concentration and thermodynamic parameters of thermal pre-treatment of the crystals in Zn vapor [57]. These dop-

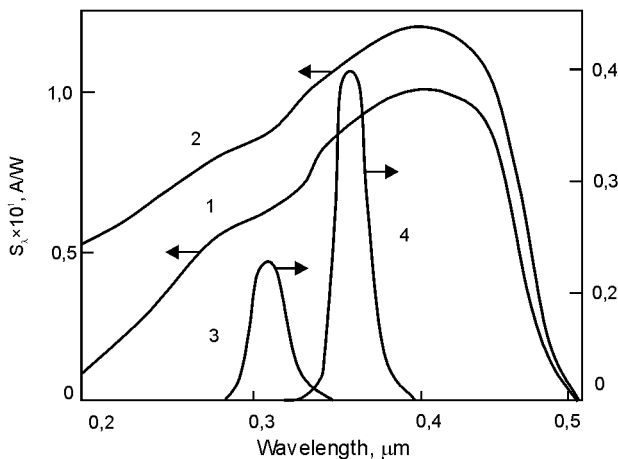


Fig.8.20. Short circuit current  $J_{sc}$  and idle voltage  $U_{oc}$  as functions of incident radiation  $P_o$  at 300 K. In Insert: loading characteristic of the photodiode  $n\text{-ZnSe}(\text{Te})\text{-Ni}$ .

ants create donor levels in  $\text{ZnSe}$  crystals, with activation energy of  $E_a < 0.05$  eV [52,57]. Semi-transparent barrier contacts were made of nickel and were characterized by high and uniform transmission in the UV range [54,55]. Ohmic indium contacts were applied onto the opposite side of the substrate. Effective area of the photoreceivers was  $0.01\text{--}0.1\text{ cm}^2$ . One should note very high radiation stability of the substrate material, which practically did not change its properties up to  $\gamma$ -radiation doses of  $10^8$  rad [52,57].

It has been shown [54,55] that the height of the Schottky barrier  $\phi_0$  for  $\text{Ni-ZnSe}$  depends upon the doping level of the substrate and increases from 1.2 to 2.0 eV when the concentration  $n_0$  is reduced from  $10^{17}$  to  $10^{15}\text{ cm}^{-3}$ . The dark current density  $j_0$  near  $T \cong 300\text{ K}$  was changed within the limits  $10^{-16}\text{--}10^{-23}\text{ A/cm}^2$ . The photosensitivity spectrum of the photoreceivers at the bias voltage  $U_S = 0\text{ V}$  is a broad band in the  $0.20\text{--}0.47\text{ }\mu\text{m}$  region (Fig.8.20). Typical values of the monochromatic current sensitivity  $S_\lambda$  at  $\lambda_{\text{max}} = 0.42\text{--}0.44\text{ }\mu\text{m}$  are  $0.1\text{--}0.15\text{ A/W}$ , which corresponds to quantum efficiency of  $0.3\text{--}0.4$  electron/quantum. The dynamic linearity range of the ampere-watt characteristic is not less than six orders of magnitude.

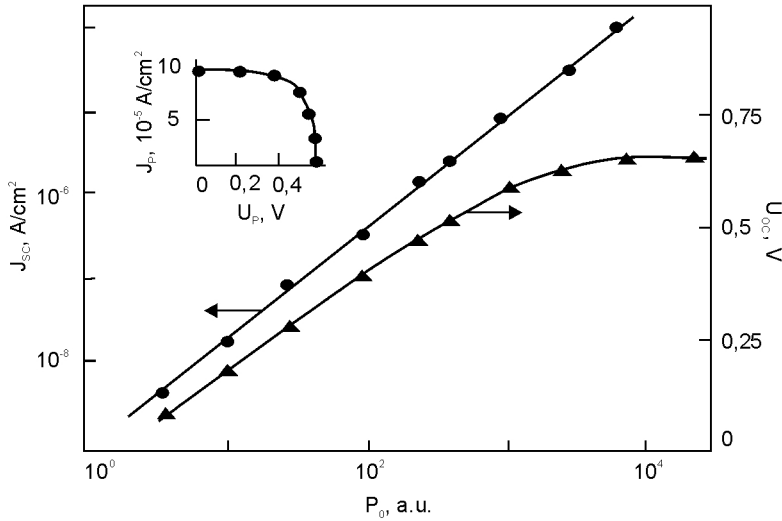


Fig.8.21. Photosensitivity  $S_\lambda$  spectra of the structure  $n\text{-ZnSe(Te)} - \text{Ni}$  at  $U_s = 0$  V (1) and 6 V (2) and  $T = 300$  K, and photosensitivity ranges of the photoreceivers with light filters in UVA (4) and UVB (3) rangers.

A typical loading characteristic for the  $n\text{-ZnSe(Te,O)}\text{-Ni}$  contact is shown in Fig.8.21. The filling factor  $ff$  of this characteristic is 0.9 ( $\varphi_0 = 1.2$  eV) and is decreased to 0.6 for samples with  $\varphi_0 = 2.0$  eV. As already noted, large  $\varphi_0$  is observed for contacts with lower carrier concentration in the substrate. This leads to an increase in sequential resistance of the photodiode and deviation of the loading curve from the rectangular shape, i.e., the  $ff$  value is reduced [50], which is to be accounted for in creation of Schottky barrier structures based on  $n\text{-ZnSe(Te,O)} - \text{Ni}$  for specific application fields. As  $j_0$  is low, the sensitivity threshold  $P_{min}$  in a unit frequency range  $\Delta f$  was estimated by the formula  $P_{min} = j_0 / \sqrt{\Delta f} \cdot S_\lambda$ , and, for the structures studied, was  $\leq 10\text{--}15 \text{ W cm}^{-2} \text{ Hz}^{-1/2}$ . Therefore, photodiodes with Schottky barriers can be used as highly sensitive photoreceivers of UV radiation.

Our studies on effects of preparation technology and other factors upon output parameters of the photoreceivers with Schottky barrier have shown the following. At 230–350 K their sensitivity at  $\lambda \leq 0.4 \mu\text{m}$  varies not more than by 0.1%/K, and the temperature shift of the long-wave edge of the photosensitivity spectrum is about

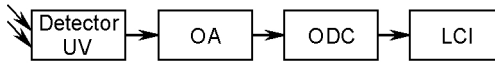


Fig.8.22. Block diagram of the household UV radiation dose rate meter: OA — operation amplifier; ADC — analog-to-digit converter; LCI — liquid crystal indicator.

$7 \cdot 10^{-4}$  eV/K, being close to the temperature variation coefficients for  $\varphi_0$  and  $E_g$  [54,55].

As it is seen from Fig.8.20, the photosensitivity spectrum of ZnSe-based Schottky diodes covers all biologically relevant ranges — UVA, UVB, UVC, — and remains “blind” at  $\lambda > 480$  nm, which makes the task of development of UV filters much easier. Basing on the  $n$ -ZnSe(Te,O)-Ni structures in combination with filters made of optical glass, selective photodetectors have been developed for UVA and UVB ranges, which were used in development of small-sized household and professional instruments.

As the most dangerous for human health is the UVB range, special attention was paid to achieve similarity between the transmission spectrum of the UVB filter and the spectral density  $D_\lambda$  of photobiological efficiency:  $D_\lambda = E_\lambda K_\lambda$ , where  $E_\lambda$  is the spectral density of the standard solar radiation, and  $K_\lambda$  is the standard biological action spectrum for erythema (the Diffey curve, approved by CIE in 1987).

In this case, the photodetector measures the photobiological activity (F) of UV radiation in the wavelength range from  $\lambda_1$  to  $\lambda_2$  :

$$F = \int_{\lambda_1}^{\lambda_2} D_\lambda d\lambda$$

#### 8.4.2. Household UV radiation dose meter

The instrument is designed for measurement of UVA and UVB radiation in  $\text{W/m}^2$ . Among the advantages of the instrument are its small size, high sensitivity in the range of UV radiation biological activity, and low energy consumption. The instrument comprises a UV radiation detector based on ZnSe, an analog-to-digit converter (ADC) in the form of a KR572PV5 microchip, and a liquid crystal indicator (LCI). The block design of the instrument is shown in Fig.8.22.

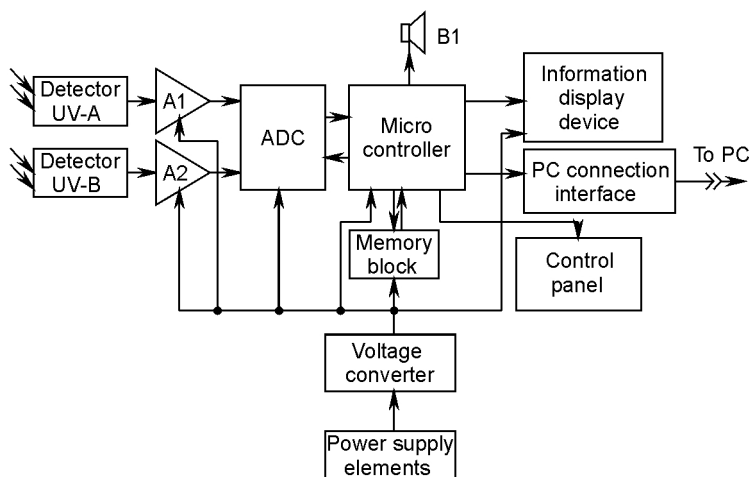


Fig.8.23. Block diagram of the professional UV radiation meter: A1, A2 — amplifiers-converters photocurrent-voltage; B1 — sound signal device; X1 — joint for connection of the instrument to the sequentail PC port.

The detector is designed for converting the UV radiation intensity into electric current. As shown above, its current sensitivity ( $S_X$ ) is monochromatic at wavelengths 310–360 nm (about 0.02 A/W), and its internal resistance is high. Accounting for these peculiar features, we used a stage circuit ensuring amplification of the detector current and its conversion into voltage. Specifically, we used a current amplifier based on an integral operation amplifier with microconsumption. From the amplifier output, the signal comes to the ADC input, is converted to a digital code and is displayed on LCD. The instrument uses a 3½ digit indicator directly conjugated with ADC. The instrument has two measurement ranges: 0–10 W/m<sup>2</sup>, 0–100 W/m<sup>2</sup>.

To weaken the influence of the cosine factor, the specially made Teflon diffusor was placed before the detector, which ensured, in addition, almost full independence of the readings upon azimuth values.

Effective biological spectrum for the erytheme, weighted with respect to the standard solar spectrum, is close to the transmission spectrum of light filters designed for UVB region. Because of this, the

developed household dosimeter with a Teflon diffusor allows measurements of the solar protection factor SPF — the ratio of photobiological efficiency of UV radiation in the wavelength range from  $\lambda_1$  to  $\lambda_2$  without a protecting material to the same photobiological efficiency after transmission of the solar light through the protective material:

$$SPF = \frac{\int_{\lambda_1}^{\lambda_2} D_{\lambda} d\lambda}{\int_{\lambda_1}^{\lambda_2} D_{\lambda} T_{\lambda} d\lambda}$$

where  $T_{\lambda}$  is transmission of the solar radiation protective material at the wavelength  $\lambda$ .

Thus, the proposed instrument can be also used for measurements of protective properties of various materials (tissues, cremes, etc.) in UVA and UVB ranges. The instrument receives power from a galvanic element of 9 V nominal voltage, the consumed current is 0.7 mA, time of continuous operation — 20 days. Overall dimensions of the instrument: 100×70×15 mm, weight — not more than 100 g.

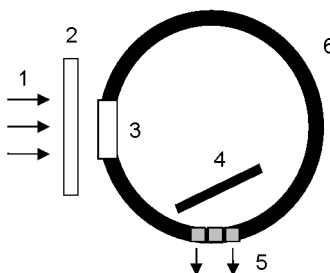
#### 8.4.3. Professional UV radiation meter

The professional UV radiation meter has been developed on the basis of modern microelectronics. It is designed for measurement of intensity and integral dose of UV radiation in UVA and UVB spectral ranges. The instrument allows to carry out routine measurements of UV radiation dose, information storage during a pre-set time period and its transfer to an external computer using an appropriate interface, and ensures sound indication when the pre-set UV radiation dose threshold is reached in each of its channels.

The UV radiation meter comprises: two detectors of UV radiation with sensitivity spectra corresponding to UVA and UVB spectral ranges; two identical amplifiers-converters; a two-channel ADC, microcontroller, memory block, control board, indicator device, voltage transformer, and an interface for connection with the computer. The block diagram of the instrument is shown in Fig.8.23.

UV radiation falling onto the detectors is converted into electric signals. The signals from detectors come to the inputs of amplifiers-

Fig.8.24. Scheme of the integrating sphere:  
 1 — source of UV radiation;  
 2 — tissue, creme, etc. (for measurement of SPF);  
 3 — teflon window (a diffuser of special shape);  
 4 — shielding from direct UV rays;  
 5 — set of UV detectors with light filters;  
 6 — the integrating sphere itself.



converters U1 and U2, made on the basis of operational amplifiers. The amplified signals come to the inputs of a two-channel ADC, where they are transformed into digital form and go to the microcontroller.

The microcontroller carries out further processing of the obtained information:

- multiplying of the digitized value of UV radiation intensity by appropriate coefficients to obtain intensity values in the standard measurement units ( $\text{W}/\text{m}^2$ );
- accumulation (summation) of the intensity values to obtain the value of the accumulated radiation dose;
- writing of the obtained information into the memory block after equal time intervals that can be pre-set by the user;
- comparison of the accumulated dose values with the pre-set threshold value, which is introduced beforehand into the controller memory; switching on of sound signalization if the threshold value is surpassed;
- information output to the display;
- sampling from the control board of the instrument;
- conversion of the information read out by the controller and its transfer to the memory block in the form required for the COM-port of the computer (RS-232) by means of an interface device, which is a part of the instrument.

The information display device (specifically, an intellectual two-line LCI) indicates the values of intensity and accumulated UV radiation dose simultaneously through two channels, in standard measurement units ( $\text{W}/\text{m}^2$  and  $\text{J}/\text{m}^2$ , respectively), and it also indicates the operation mode. For power supply, 3 V voltage is used, and the consumed current is  $\sim 20$  mA.

It would be interesting to broaden functional possibilities of the professional UV radiation meter. Recently, an assumption has been made that experimentally observed changes in diffuse reflection coefficient [58] and absorption coefficient [59] of human skin under UV irradiation are due to functioning of protection mechanisms against unfavorable effects of irradiation. In this connection, it is proposed to equip the developed professional instrument by an integrating photometric Ulbricht sphere (see Fig.8.24), which could be used for measurement of transmission and reflection coefficients of light-scattering objects, as well as (using a multi-filter system and calibrated detectors) for determination of spectral dependences of these coefficients by means of special computer processing (see [60]). The use of the Ulbricht sphere will also allow a more precise determination of SPF for different materials.

It follows from the theory of multiple reflections inside the Ulbricht sphere that illumination of the internal surface of the sphere is equal at all points and is expressed as

$$E = \left( \frac{F}{4\pi R^2} \times \frac{\rho}{1 - \rho} \right)$$

where  $F$  is the light flux entering the sphere,  $R$  is radius of the sphere, and  $\rho$  is reflection coefficient of the surface of the sphere. To obtain high values of  $E$ ,  $\rho$  should be sufficiently high. Therefore, internal surface of the sphere is covered with a layer of  $\text{BaSO}_4$ , for which the diffuse reflection coefficient is more than 95% in the UV range.

It would be also interesting to consider the use in a professional dosimeter of the Ulbricht sphere with multi-filter detectors for computer reconstruction of the entire biologically active solar UV spectrum basing on several experimental points. Taking this information into consideration will allow, in turn, more precise determination of SPF. Presently, the sphere and the computer software for reconstruction of the spectrum are in the course of development.

Thus, the following conclusions could be made on the basis of our studies:

- Experimental samples of photodetectors have been developed and produced on the basis of surface barrier Schottky photodiodes of



*n*-ZnSe(Te,O)-Ni, which are sensitive in the UV range and “blind” in the visible range of solar radiation.

- On the basis of said Schottky diodes, experimental samples have been developed and produced of the household and professional variants of the solar UV radiation meter in UVA and UVB ranges. In the instruments developed, the effects of the cosine factor have been minimized.
- The use of an integrating Ulbricht sphere in the professional variant of the instrument allows to substantially broaden its functional possibilities.

The main parameters and technical characteristics of a solar radiation dosimeter “Helios” based on ZnSe(Te) detectors are the following:

Power source:	DC cell (output voltage 9 V) or a solar element (in this case operation time is not limited).
Consumed current:	not more than 0.7 mA
Overall dimensions:	100×70×15 mm <sup>3</sup>
Weight:	not more than 100 g
Time of continuous operation of power elements	20 days

## REFERENCES

1. *Ivanov V.I.* Course of dosimetry. Moscow: Energoizdat, 1988
2. *Nirchl J.C.* Photodiode scintillation detector for radiation instrumentation // Nucl. Instrum. and Methods. – 1984. – **226**. – P.487–495.
3. *Goyot M., Ille B., Lebrun P. e.a.* // Nucl. Instrum. and Methods. – 1988. – **A263**, No.1. – P.180.
4. *Krasnokutskii R.N., Kurchaninov A.L., Tikhonov V.V. e.a.* // Pribory i Tekhn. Eksp. – 1988. – No.3. – P.129.
5. *Krasnokutskii R.N.* // Pribory i Tekhn. Eksp. – 1988. – No.5. – P.118.
6. *Horiuchi K., Sato T., Kobayashi E.* A high-sensitivity neutral dosimeter using the coherent demodulation technique // IEEE Trans.Nucl.Sci. – 1995. – **42**, No.6. – P.2203–2208.
7. *Ryzhikov V.D., Burachas S.F., Volkov V.G. e.a.* Neutron flux measurements using “scintillator-photodiode-preamplifier” system and new type scintillators // 5<sup>th</sup> Intern.Conf.Applic.Nucl.Techn. “Neutrons in Research and Industry”, 1996, Crete, Greece. – Abstracts.
8. *Schotanus P., Dorenbos P., Ryzhikov V.* Detection of CdS(Te) and ZnSe(Te) scintillation light with silicon photodiodes // IEEE Trans.Nucl.Sci. – 1992. – **39**. – P.546–550.
9. *Gunji S. e.a.* Nucl.Instr.and Meth., 1990. – **A295**. – P.401.
10. *Danshin E.A., Ryzhikov V.D. e.a.* Abstracts of Conference “Luminescent Detectors and Transformations of Ionizing Radiation” (LUMDETR’94), 1994, Tallinn, Estonia
11. *Mashchenko N.P., Murashko V.P.* Radiation effects and radiation protection of population in nuclear accidents in atomic power stations. – Kiev: Vyshcha shkola, 1992.
12. *Davins D.* Energy. Moscow: Energoatomizdat, 1985.
13. *Matveev L.V., Rudik A.P.* Nearly everything about a nuclear reactor. – Moscow: Energoatomizdat, 1990.
14. *Prister B.S., Loshchilov N.A., Nemets O.F., Poyarkov V.A.* Foundations of agricultural radiology. – Kiev: Urozhai, 1991.
15. *Ivanov E.A., Ramzina T.V., Khamyanov L.P. e.a.* Radioactive contamination of the environment by <sup>241</sup>Am due to the accident at Chernobyl nuclear power station // Atomnaya energiya. – 1994. – **77**, No.2. – P.140–145.
16. *Sukhoruchkin A.* Americium-241: nothing unexpected? // Vestnik Chernobylya (newspaper). – 1994. – No.1 (520). – P.1.

17. *Rovinski F.Ya., Yokhelson S.B., Yushkan E.I.* Methods of analysis of environment contamination. Toxic metals and radionuclides. – Moscow: Atomizdat, 1978.
18. *Nemets O.F., Gofman Yu.V.* Handbook on nuclear physics. – Kiev: Naukova Dumka, 1975.
19. *Burachas S.F., Pirogov E.M., Ryzhikov V.D. e.a.* Method for determination of americium-241 specific activity. Patent of Ukraine No.25382..
20. “Alpha-gamma-radiometer RK-AG-01”. Scientific and Technical Report of STC RI. Kharkov, 1996.
21. *Burachas S.F., Pirogov E.N., Ryzhikov V.D. e.a.* Alpha-gamma radiometer RK-AG-01 on the basis of scintillator GSO for routine monitoring of  $^{241}\text{Am}$  and other transuranic radionuclides. // *Pribery i tekhnika eksperimenta.* – 1997. – No.4. – P.121–123.
22. *Burachas S.F., Pirogov E.M., Ryzhikov V.D. e.a.* Device for detection of soft gamma- and alpha radiation. Patent of Ukraine No.15327.
23. *Ryzhikov V.D., Grinev B.V., Pirogov E.N., Lysetska O.K., Onishchenko G.M. e.a.* Calibration and measuring of Am-241 activity in Chernobyl environment samples of various density using a selective gamma- radiometer. 10th Symposium on Radiation Measurements & Applications, May 21–23, 2002. University of Michigan. Ann Arbor, Michigan. USA
24. *Ryzhikov V.D., Onishchenko G.M., Pirogov E.N. e.a.* Alpha-gamma radiometer-spectrometer RK-AG-02 – a compact instrument for routine monitoring of  $^{241}\text{Am}$  and other transuranic radionuclides in field and laboratory conditions // *Pribery i tekhnika eksperimenta.* – 2001. – No.3. – P.122.
25. *Burachas S.F., Pirogov E.N., Ryzhikov V.D. e.a.* Method for determination of americium-241 specific activity. Patent of Ukraine No.25484.
26. *Storm E., Israel Kh.* Interaction cross-sections of gamma-radiation. – Moscow: Atomizdat, 1973.
27. *Burachas S.F., Pirogov E.M., Ryzhikov V.D.* Scintillation block for detection of gamma-radiation and method for its fabrication. Patent of Ukraine No.24448.
28. *Ryzhikov V.D., Spasov V.G., Pirogov E.N., Onishchenko G.M. e.a.* The use of oxide scintillation crystals GSO in X-ray range instruments // Int.Conf. “Properties of excited states of atom nuclei and mechanisms of nuclear reactions”. 51th Meeting on nuclear spectroscopy and atom nucleus structure. Russia, Sarov, Sept.3–8, 2001.
29. *Babenko V.V., Kazimirov A.S., Rudyk A.F.* Problems in determination of low activities. Preprint AKP-2-98, Kiev, 1998.

30. *Gerfot L., Koch H., Hubner K.* Practical manual on radioactivity and radiochemistry. Moscow: Mir, 1984.
31. *Gol'din M.L.* Radiation measurement equipment in agricultural production. Moscow: Energoatomizdat, 1986.
32. *Burachas S.F., Pirogov E.M., Ryzhikov V.D. e.a.* Method of charge melting for complex oxide single crystals. Patent of Ukraine No.17930.
33. *Burachas S.F., Bondar V.G., Pirogov e.M. e.a.* Method for restoration of noble metal crucibles for crystal growth. Patent of Ukraine No.3395.
34. *Ryzhikov V.D., Burachas S.F., Piven' L.A., Pirogov E.N., Koval' A.F., Svishch V.M., Kirsanov S.P., Zheltonozhskii V.A., Tabachnyi L.Ya., Grinchuk I.R.* Scintillators BGO, GSO and radiation instruments based on them. Abstracts of International Conference on Inorganic Scintillators And Their Applications, September 22–25, 1997, Shanghai, China.
35. *Ryzhikov V.D., Burachas S.F., Piven' L.A., Pirogov E.N., Koval' A.F., Svishch V.M., Kirsanov S.P., Zheltonozhskii V.A., Bondar'kov M.D., Sadovnikov L.V., Tabachnyi L.Ya., Solomatin Yu.P., Grinchuk I.R.* The new alpha-gamma radiometer based on GSO scintillator for measurements of transuranic radionuclides activity. Abstracts of Nuclear Science Symposium, November 11–13, 1997, Albuquerque, New Mexico, USA.
36. *Ryzhikov V.D., Burachas S.F., Piven' L.A., Pirogov E.N., Koval' A.F., Khara G.I., Svishch V.M., Kirsanov S.P., Tabachnyi L.Ya., Solomatin Yu.P., Grinchuk I.R.* Advanced alpha-gamma radiometer-spectrometer based on GSO scintillator and PC HP Palmtop 320 LX for transuranic radionuclides activity monitoring. Abstracts of Symposium on Radiation Measurements and Applications, May 12–14, 1998, Ann Arbor, Michigan, USA.
37. *Ryzhikov V.D., Burachas S.F., Piven' L.A., Pirogov E.N., Koval' A.F., Khara G.I., Svishch V.M., Kirsanov S.P., Tabachnyi L.Ya., Polakov V.D., Grinchuk I.R.* Advanced radiometer based on PC HP Palmtop and GSO scintillator for transuranic radionuclides activity monitoring. Abstracts and Summaries for Nuclear Science Symposium-98, November 12–15, 1998, Toronto, Canada.
38. *Burachas S.F., Nagornaya L.L., Pirogov E.N., Ryzhikov V.D. e.a.* Spectrometric scintillation single crystals on the basis of complex oxides with high atomic number and instruments based on them // Int.Conf. on Nuclear Physics “50 years of nuclear shells”, April 21–24 1999, Dubna-St.Petersburg, P.177.
39. *Burachas S.F., Nagornaya L.L., Onishchenko G.M., Ryzhikov V.D. e.a.* Promising scintillation single crystals based on complex oxides with high atomic number // Int.Conf. “Perspective materials”, Oct.3–7, 1999, Kiev, Ukraine.

40. Ryzhikov V.D., Burachas S.F., Onishchenko G.M., Pirogov E.N., Svishch V.M., Kirsanov S.P., Tabachnyi L.Ya., Polakov V.D., Grinchuk I.R. Advanced alpha-gamma radiometer-spectrometer based on GSO scintillator and handheld PC. // Nuclear Science Symposium-99, October 14–16, 1999, Seattle, USA.
41. Atroshchenko L.V., Burachas S.F., Gal'chinet'skii L.P., Grinev B.V., Ryzhikov V.D., Starzhinskiy N.G. Scintillator crystals and detectors of ionizing radiations on their base. – Kiev: Naukova dumka, 1998. – 312 p.
42. Bondar'kov M.D., Burachas S.F., Zheltonozhskii V.A. e.a. // Pribory i tekhnika eksperimenta. – 1997. – No.4. – P.121.
43. Bondar'kov M.D., Burachas S.F., Zheltonozhskii V.A. e.a. // Pribory i tekhnika eksperimenta. – 1996. – No.3. – P.83.
44. Longstreth J., de Gruijl F.R., Kripke M.L., Abseck S., Arnold F., Slaper H.J., Velders G., Takizawa Y., van der Leun J.C. Health risks // J. Photochemistry and Photobiology, B: Biology – 1998.– **46**, No.1–3 – P. 20–39.
45. Driscoll M.H. Dosimetry methods for UV radiation // Protection Dosimetry. – 1997.– **72**, No.3–4.– P. 217–223
46. Bais A.F. Spectral solar UV measurements within SESAME. In: Advances in Solar Ultraviolet Spectroradiometry (ed. A.R.Webb), Luxembourg, EC, 1997. – P.173–182.
47. McKinlay A.F., Diffey B.L.. A reference action spectrum for ultraviolet induced erythema in human skin // CIE-Journal.– 1987.– **6**, No.1 . – P. 17–22.
48. Ishigaki Y., Takayama A., Yamashita S., Nikaido O. Development and characterization of a DNA solar dosimeter // J. Photochemistry and Photobiology, B: Biology.– 1999.– **50**, No.2–3.– P.184 – 188.
49. Parisi A.V., Wong J.C.F., Moore G.I. Assessment of the exposure to biologically effective UV radiation using dosimetric technique to evaluate the solar spectrum// Phys. Med. Biol.– 1997.– **42**, No. 1.– P. 77–88.
50. Richards D.L., Davies R.E., Boone J.L. A selective Pt-CdS photodiode to monitor erythema flux // J. Photochemistry and Photobiology, B: Biology.– 1998.– **47**, No.1.– P.22–30.
51. Ryzhikov V.D., Silin V.I., Starzhinskiy N.G. A new ZnSe(Te) scintillator: luminescence mechanism // Nucl. Traces Radiat. Meas. – 1993. – **2**, No.1. – P.53–55.
52. Atroshchenko L.V., Burachas S.F., Ryzhikov V.D. e.a. Scintillator crystals and detectors on their base. Kyiv: Naukova dumka, 1998.

53. *Baranyuk V.S., Makhniy V.P., Melnik V.V., Ryzhikov V.D.* Detectors of ionizing and ultraviolet radiation on the basis of broad-band compounds  $A^2B^6$  // Abstract Booklet of the First International Conference on Material Science of Chalcogenide and Diamond – Structure Semiconductors, Vol.1 – Chernivtsi, 1994.– P.22
54. *Makhniy V.P., Melnik V.V.* Photoelectric properties of contacts Ni-ZnSe // Fizika i tekhnika poluprovodnikov.– 1995.– **29**, No. 8.– P. 1468–1472.
55. *Makhniy V.P.* UV photoreceivers on the basis of zinc selenide // Zhurn. tekhn.fiziki.– 1998.– **68**, No.9.– P.123–125
56. *Rogalski A., Razeghi M.* Semiconductor ultraviolet photodetectors // Opto-Electr. Rev.– 1996.– 4.– P.13.
57. *Ryzhikov V.D.* Scintillation crystals of semiconductor compounds  $A^{II}B^{VI}$ : preparation, properties, application. – Moscow: NIITEKhIM, 1989.
58. *Cader A., Jankowski J.* Reflection of ultraviolet radiation from different skin types // Health Physics.– 1998.– **74**, No.2.
59. *de Gruijl F.R.* Health effects from solar ultraviolet radiation // Radiation Protection Dosimetry.– 1997.– **72**, No.3–4 .– P.177–196.
60. *Malakhov B.A.* The use of filters for measurement of spectral characteristics of low-intensity light sources // Pribory i tekhnika eksper.– 1983. – No.2. – P.172–173.

## CHAPTER 9

# INSTRUMENTS AND DETECTORS ON THE BASE OF SCINTILLATOR CRYSTALS FOR SECURITY AND CUSTOMS INSPECTION SYSTEMS

### *9.1. Introduction*

X-ray digital radiography is a rapidly expanding and one of the most important methods of modern non-destructive testing [1]. In this method, alongside with the use of luminescent screens with subsequent transformation of the image onto CCD-matrix, one of the main technical solutions is conversion of the penetrating X-ray radiation by a detector array of ‘scintillator-photodiode’ (S-PD) type with its subsequent amplification and digitalization of the signal.

Advantages of CCD devices are instant imaging of the whole object and high spatial resolution (3–5 line pairs per mm). Their disadvantage is a limited energy range, consequently, limited thickness of the inspected object, as well as higher costs, as compared with S-PD arrays.

In non-destructive testing systems using S-PD arrays it is possible to use scintillators of different atomic number, density and size, which allows operation in the energy range from 20 keV to 10 MeV, i.e., steel equivalent thickness is from 100 mm to 300 mm. The use of two-energy detection systems solves the problem of distinguishing between substances of similar density, but different effective atomic numbers. Both these qualities are not attainable for CCD-matrix.

Our task in developing this method consisted in the maximum use of its advantages. Specifically, we aimed at increased sensitivity and detecting ability due to optimization of parameters of the S-PD pair and an extensive use of the features of two-energy radiography. Transition to multi-energy radiography was envisaged for detection

of substances with close values of the effective atomic number. The resolution was to be increased due to modernization of the design and making smaller the detector aperture. And, finally, passing from two- to three-dimensional imaging was also essential.

The above-listed directions in the system improvement were the objectives of our studies.

## ***9.2. Experimental procedures***

Measurements of the detector sensitivity and light output of the crystals were carried out on a testing board using X-ray sources IRI ( $U_a=40\text{--}200$  kV,  $I_a=0.4\text{--}1.0$  mA, W anode) and REIS ( $U_a=5\text{--}45$  kV,  $I_a=5\text{--}50$  mA, Ag anode), RUP-350 ( $U_a=300$  kV,  $I_a=6$  mA) and an optical power meter “Kvarts-01”. Time characteristics were measured using a testing board designed for afterglow measurements [2].

To obtain shadow X-ray images, we used testing boards «Poliscan» (a 128-channel array of photodiode-based detectors) and «Photocell» (for 32- 64-, 128- and 1024-channel detectors based on PRD). Using the Photocell board, 60 2D images of a small object were obtained at different angles (with step  $6^\circ$ ), from which a 3D image was reconstructed.

For detection of X-ray radiation, we used detector arrays of types S-PD and scintillator-photoreceiving device (PRD). PRD includes an array of photodiodes (32, 64, 128 and 1024 channels), amplifier and commutator mounted on one silicon crystal.

We used standard scintillation crystals CsI(Tl),  $\text{CdWO}_4$  and an original scintillator  $\text{ZnSe}(\text{Te})$  developed by STC “Institute for Single Crystals” [2]. The photodiodes used were obtained from producers CCB Ritm, SPO Bit, Ukraine, and Hamamatsu, as well as PRD from SPO Bit, Kiev, Ukraine.

In our studies, we used experimental procedures traditional for scanning introscopy (Fig.9.1).

Scintillator plates of the following types were tested:

- Plates of discrete scintillation elements (DSE) — one element per channel;
- Continuous solid plates of a single crystal (SCP) — by the size of the photosensitive area of a multi-channel photoreceiver;
- Plates of dispersed scintillator (DSP) — made of tiny calibrated particles of  $\text{ZnSe}(\text{Te})$  crystals arranged into a monolayer and optical epoxy adhesive UP4-20-3M [3].



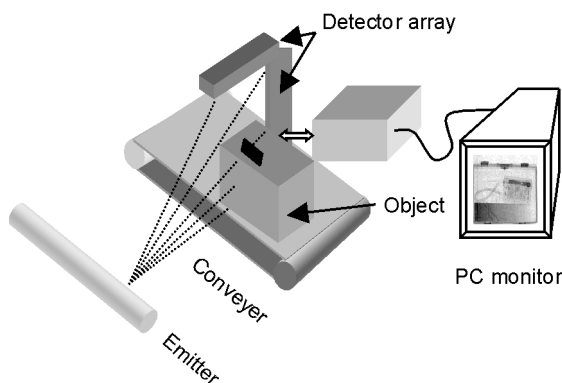


Fig.9.1. Digital radiograph with detector array.

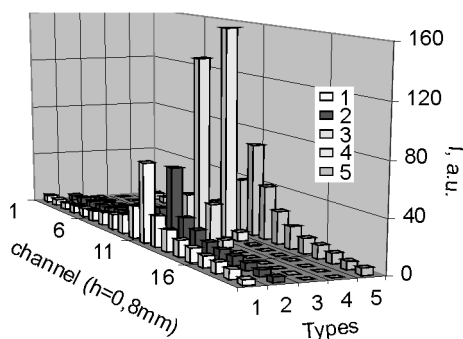


Fig.9.2. Mutual interference of neighboring channels for different scintillators and types of scintillation elements: 1 — single crystal plate ZnSe(Te) with  $h=0,8\text{ mm}$ ; 2 — single crystal plate ZnSe(Te) with  $h=0,6\text{mm}$ ; 3 — composite small-crystalline plate ZnSe(Te) (grain size  $0,4\text{ mm}$ ); 4 — individual single elements for each channel; 5 — single crystal plate CsI(Tl) with  $h=0,8\text{ mm}$ .

Comparative measurements have shown (Fig.9.2) that serious competition to DSE plates can come only from DSP.

Interference of neighboring channels was studied for DSP prepared from ZnSe(Te) grains of different size. It is obvious that with smaller grain size the interference of neighboring channels is reduced. However, the DSP light output is also dependent upon grain size and has maximum at the grain size  $\sim 0.5\text{ mm}$ .

The use of laws of geometrical optics, namely, placing the inspected object much closer to the source of sharp focus than to the detector array, allows one, using DSE with step 0.8 mm, to achieve detecting abilities of 10–15 mm (Fig.9.3, microchip).

Multi-energy approach is a new promising direction in the modern digital radiography. In the most common case, it is two-energy radiography. [3, 4].

As distinct from the conventional method, when the spatial structure of the object is reconstructed, in the multi-energy radiography we can reconstruct its substantial structure, effective atomic number, chemical (elemental) composition, molar concentrations of simple components, etc.

For determination of the effective atomic number and density of materials with unknown or variable composition, it is sufficient to use two-energy radiography. The effective atomic number  $Z_{\text{eff}}$  is unambiguously related to the ratio of radiographic reflexes measured at two different energies of radiation [3].

$$R = R_1/R_2 = \frac{\ln[V_0(E_1)/V(E_1)]}{\ln[V_0(E_2)/V(E_2)]} \quad (1)$$

( $V_0$  and  $V$  are the signals recorded by the detectors without and with the inspected object, respectively. A universal radiographic law is assumed to be valid:

$$Z_{\text{eff}} = [(aR + b)/(cR + d)]^{1/3} \quad (2)$$

The calibration constants are determined from measurements on objects of known composition. The error in  $Z_{\text{eff}}$  determination is proportional to the contrast sensitivity of the detectors

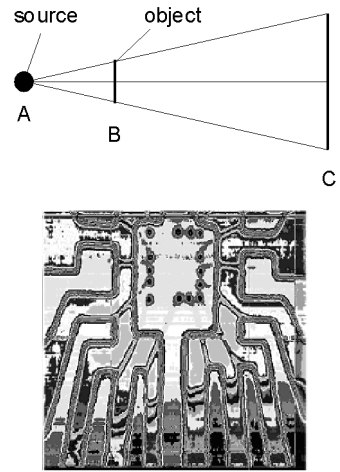


Fig.9.3. Experimental arrangement and microchip in plastic tank in x-ray view.

$$S_z = (\Delta Z / Z) \propto 2(\Delta d / d) \quad (3)$$

Estimates show that for introscopy systems with resolution to 4 lines/mm the effective atomic number can be reconstructed with accuracy of up to 95%. This is much better than 50% accuracy for the existing methods [3, 4].

### 9.3. Discussion

Results of our studies have shown that in S-PD detectors for digital radiography the most preferable scintillators for the high energy region are CWO (0.5–10 MeV), CsI(Tl) (0.08–0.5 MeV), while in the low-energy region (20–60 keV) ZnSe(Te) is unchallenged.

Accounting for a trend in the modern digital radiography (both in the inspection and medical instruments) to use two-energy detector arrays, the combination of ZnSe(Te) and CsI(Tl)/CWO results in a new quality of the detection system [5–7].

Effective atomic number  $Z$  of ZnSe is the same as of copper, which is usually used as a filter of the high-energy array. Therefore, if a detector with ZnSe(Te) as filter is placed before the high-energy array, this simplifies the design and improves technical characteristics of the detecting circuit as a whole [8].

A unique combination of properties characterizing the original scintillator ZnSe(Te) — high light output, fast response, radiation stability, rather low effective atomic number together with sufficiently high density — makes this material the best among known scintillators for the low-energy detector. By using a combination of crystals ZnSe(Te)/CsI(Tl) in the two-energy detector array, we have substantially improved the sensitivity of equipment designed for detection of organic inclusions (Fig.9.4).

Using a simplified model of the two-energy detector array and the spectrum of an X-ray tube with a tungsten anode (Fig.9.5), evaluation has been carried out of the signal ratio from high- and low-energy detectors (HED and LED) in the presence of an inspected object (which can be of different thickness and chemical composition). The other objective was to estimate reliability of the results obtained using a 12-digit ADC (noise of quantization).

Calculations were carried out for the following substances: Al, Cu, Fe, NaCl, H<sub>2</sub>O, C<sub>12</sub>H<sub>22</sub>O<sub>11</sub> (sugar). In our calculations, we used a

simplified model of the two-energy detector array — each detector was replaced by a ZnSe scintillator of 0.5 mm thickness (LED) and CsI scintillator of 4 mm thickness (HED). Filtration effects of LED were accounted for. As an output detector signal, we used the calculated light flux (in relative units) formed in the scintillator under X-ray irradiation.

The calculated data were then normalized. The initial data were calculated for different thickness  $l$  of the inspected object (in cm). However, more informative is the use of parameter  $cl$  ( $\text{g}/\text{cm}^2$ ) on the  $x$  axis, where  $\tilde{n}$  is the density of the inspected object. In such presentation, the calculated plots for one and the same substance (e.g., salt as crystals and as powder — difference in density) are identical, and comparison of substances with substantially different densities becomes more obvious. To evaluate signals in real radiographic systems, it is convenient to show the signal sum HED+LED along the X axis.

To determine possibilities of substance identification, we have considered different values derived from the initial calculated signals (sum 1–2, difference 2–1, ratios 1 to 2 and 2 to 1 (1 — LED, 2 — HED signal)). These plots, (sugar) and (iron) as function of  $cl$  ( $\text{g}/\text{cm}^2$ ), are presented in Fig.9.6.

For determination of the effective atomic number of a substance, it is possible to use, as a substance characteristic, the ratio of signals HED/LED from the high-energy detector (HED) and low-energy detector (LED), accounting for the total signal (HED+LED). (Fig.9.7a) allows to assess the substance identification possibility in a real digital radiography system (DRS). Ratios 2/1 are given for different substances

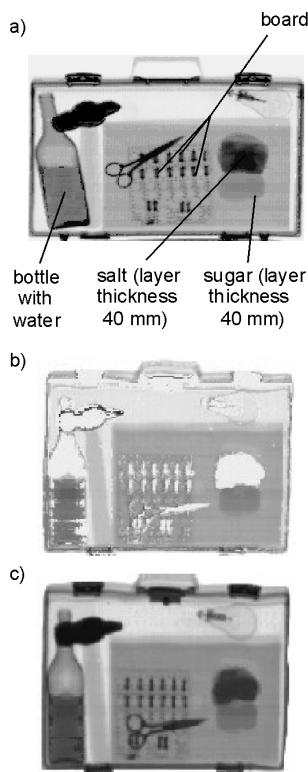


Fig.9.4. Object images obtained using the two-energy introscope: a) general shadow picture of the object; b) shadow picture with inorganic material singled out; c) shadow image with organic material singled out.

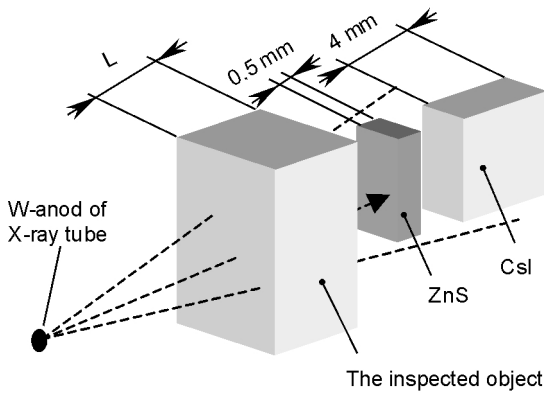


Fig.9.5. A model of the two-energy detector array and spectrum of the X-ray tube with a tungsten anode.

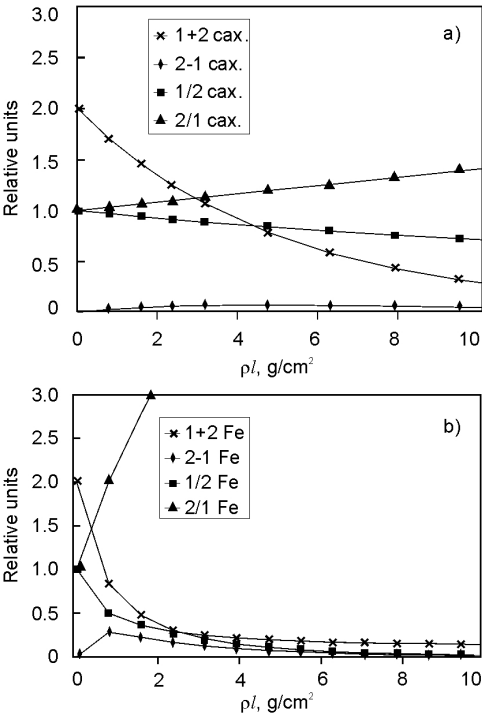


Fig.9.6. Ratios, differences and sum of normalized light flow for sugar (a) and iron (b) LED (1) and HED (2).

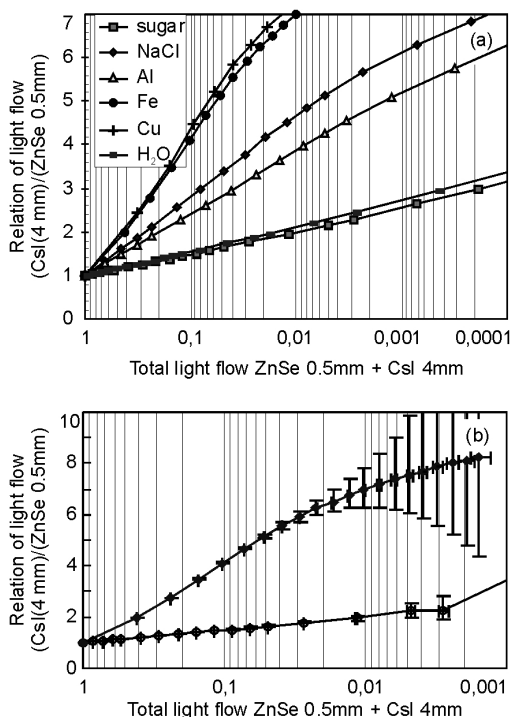


Fig.9.7. The Determination of the composition of substance by 2-energy method. Two scintillators — ZnSe (0,5mm) and CsI (4mm).

depending upon the signal (1–2) characterizing the fraction of X-ray radiation transmitted through the substance. Both these parameters can be easily calculated using DRS.

In using the linear amplifying circuit model, estimates of errors introduced by a 12-digit ADC show that with the total signal from two detectors less than 0.5% of the initial value, the identification errors is significantly increased (Fig.9.7b). Our calculations have allowed evaluation of possibilities of the two-energy method for substance determination in digital radiographic systems.

It can be used in inspection systems, including anti-terrorist activities, in technical diagnostics, medicine. An important point is combination of principles of multi-energeticity (reconstruction

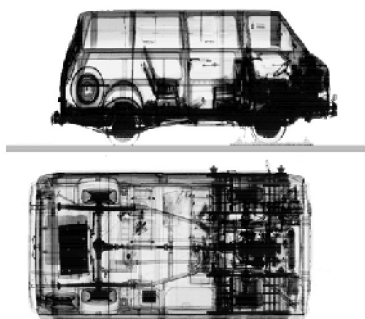


Fig.9.8. Image car in x-ray.

of substantial structure) and tomography (reconstruction of spatial structure). This allows creation of “multi-energy tomographs” — new instruments with unique possibilities in detection and diagnostics. This opens new prospects of broad application of the multi-energy approach in different fields of science and technology. It is essential that, to ensure reliable (close to 100%) detection of explosives and other forbidden substances and objects, chemical composition of the inspected objects

should be reconstructed.

As most explosives are of organic origin, it is necessary to reconstruct the chemical formulas of organic compounds. They are composed, as a rule, of 3 or 4 main elements. Therefore, detection of explosives requires 3- or even 4-energy radiography. We have obtained theoretical expressions for relative (molar) concentrations of simple chemical components of a complex compound or a mixture of substances. This means a possibility of reconstruction of the chemical formulas of inspected substances and objects [4].

For identification of organic compounds containing two, three or all four main elements (hydrogen, carbon, nitrogen and oxygen) it is sufficient to use 2-, 3- or 4-radiography. As a whole, it allows distinction of organic materials both from inorganics and from other organics, and, consequently, to detect explosives on the background of inorganics or organics. The expected accuracy of such monitoring is 80–95%.

When we used scintillator with different atomic number, density and thickness, we can control objects with size from several mm to several m (Fig.9.8).

Using the tomography principle, we can obtain 3D images of different objects, process them with an appropriate specially designed software and look at the object from different directions and from inside. In our opinion, this method, combined with multienergy possibilities is very promising for future developments of inspection systems.

### ***9.4. Conclusion***

Testing has been carried out of a wide class of objects with dimensions from mm to several meters with absorption in steel equivalent from several mm to 250 mm.

For different objects and different control objectives, different types of arrays and methods can be recommended.

The best spatial resolution is achieved by using methods of geometrical optics for photoreceivers with integrated electronics and dispersed scintillators.

The best detection of dangerous materials, especially explosives, is achieved by using multienergy methods, especially with scintillators of low density and atomic number, such as  $\text{ZnSe}(\text{Te})$  [6, 9].

Inspection of large objects was realized using scintillation detectors based on CWO or  $\text{CsI}(\text{Tl})$ .

Finally, a wide variety of inspection instruments based on digital radiography methods have been proposed, and installations that allowed a pioneering realization of 3D imaging have been developed.



## REFERENCES

1. *R.M. Harrison*, Digital radiography — a review of detector design // Nucl. Instr. and Meth. — 1991. — **A310**. — P.24–34.
2. *V.D. Ryzhikov, N.G. Starzhinskiy, L.P. Gal'chinetskii, D.N. Kozin, V.P. Sokhin, A.D. Opolonin, V.M. Svishch, E.K. Lisetskaya*, Scintillator-photodiode detecting systems for two-level X-ray inspection systems // 15th World Conference on Non-Destructive Testing, Rome (Italy), 15–21 October, 2000, Abstracts Book, P. 466.
3. *S.V. Naydenov, V.D. Ryzhikov*, Determining Chemical Compositions by Method of Multi-Energy Radiography // Technical Physics Letters. — 2002. — **28**, No.5. — P.357–360.
4. *S.V.Naydenov, V.D.Ryzhikov, C.Smith*, Direct reconstruction effective atomic number of materials by the method of multi-energy radiography. // NIM(B). — 2004. — **215**. — P.552–560.
5. The X-Ray Introscope System “Poliscan-4”, Prospects, [stcrl@isc.kharkov.com](mailto:stcrl@isc.kharkov.com)
6. *L.V.Atroshchenko, B.V.Grinev, V.D.Ryzhikov e.a. (Ed. Prof.V.D.Ryzhikov)*. Scintillator crystals and detectors of ionizing radiation on their base.- Kiev: Naukova Dumka. — 1988. — 322 pp.
7. *V.G.Volkov, B.V.Grinev, V.D.Ryzhikov e.a.* Small-crystalline detectors of ionizing radiation on the basis of ZnSe(Te) // Pribery i Tekhnika Eksp. (Moscow). — 1999. — No.6. — P.37–42.
8. Detection system for X-ray introscope. Patent of Ukraine, No. 2001053401 from 21.05.2001.
9. Heimann, Prospects, Germany, 2003, <http://www.heimannsystems.com>.

# CHAPTER 10

## A SIMPLE METHOD FOR THE CALCULATION OF PHOTON DOSE CONVERSION FACTORS IN NON-TISSUE PHANTOM AS LIKE THE PMMA SLAB

### *10.1. Introduction*

Two operational quantities,  $H_P(10)$  and  $H_S(0.07)$ , for individual monitoring are defined in the ICRU sphere (which is composed of 10.1% hydrogen, 11.1% carbon, 2.6% nitrogen, and 76.2% oxygen; density 1.0 g/cm<sup>3</sup>; diameter 30 cm) [5] and related to a specific point within human body. The ICRU sphere is used to model the human body; however, it is difficult to measure dose quantities near the surface.

Various types of phantoms have been used as an alternative to the ICRU sphere. The International Atomic Energy Agency (IAEA), for example, applied a 30 cm cube water phantom for an intercomparison of dosimeter performances in measuring operational quantities. It has been shown by some calculations and experiments [2] that the photon dose equivalent conversion factors for a 30 cm cube, a 30 cm × 30 cm × 15 cm slab of water, or ICRU tissue are about the same. However, the American National Standards Institute (ANSI), suggested a PMMA slab phantom (polymethyl methacrylate, 8.04% hydrogen, 59.98% carbon, and 31.96% oxygen; density 1.17 g/cm<sup>3</sup>; commercially called as Lucite™, Perspex™, Plexglas™) as a calibration phantom, and defined the dose conversion factor in terms of ICRU tissue kerma [1]. The International Commission on Radiation Units and Measurements (ICRU), also recommended 30 cm × 30 cm × 15 cm PMMA slab as a calibration phantom. Its mass is close to that of the ICRU sphere, and its backscatter characteristics are acceptably close to that of the human trunk for photon irradiation [6].

The photon intensity on the surface of the PMMA slab phantom is higher than that for a tissue equivalent slab [1].

The dose equivalent depends on the photon spectrum which is built up in the phantom. The photon spectrum at depths of 7 and 1,000 mg/ m<sup>2</sup> may be approximated by the backscattered photon spectrum on the surface of phantom. Previous workers [2] used these concepts to calculate the dose conversion factors in the PMMA slab phantom. Two calculation steps are required for obtaining the dose conversion factors at different depths in the PMMA slab. In the first step, dose conversion factors and backscatter factors must be obtained for the ICRU cube or slab phantom. The backscatter factor calculation in the PMMA slab phantom is calculated next. As two steps are required to obtain the dose conversion factors for the PMMA slab phantom, the method accepted by the ANSI or the ICRU is referred to as the indirect method in this work.

In this study, a direct method using MCNP4A (Monte Carlo N-Particle, Version 4A) [3] simulation code is used to directly calculate the ICRU tissue kerma in the PMMA slab phantom. The backscatter factors for the ICRU and PMMA slab phantom are no longer needed to obtain the dose conversion factors because the dose equivalent can be directly calculated by multiplying the built up fluence in the PMMA slab phantom by the virtual energy deposition in ICRU tissue.

### ***10.2 Computational model***

For the calculation using MCNP4A, the phantom is assumed to be a slab of ICRU tissue or of the PMMA material with front face area of 30 cm 30 cm and thickness of 15 cm. The elemental composition has been given in the previous section.

The following irradiation conditions were used in the calculations. The phantom is surrounded by vacuum. It is irradiated by unidirectional monoenergetic photon beams; the direction of the beams is normal to the front face of the slab. The geometry is shown in Fig.10.1.

For calculation of dose equivalent at the different depths, two tally discs are located at depths of 7 and 1,000 mg/cm<sup>2</sup>, respectively. The diameters of the tally discs are both 2.5 cm [2]. The thickness of the tally discs were designed so that the average dose equivalent at 7 and 1,000 mg/cm<sup>2</sup> depths in the PMMA slab phantom would be well characterized. The tally surface area for the backscatter

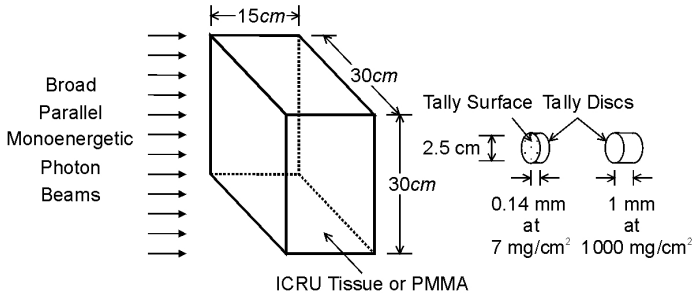


Fig.10.1. Problem Geometry for the ICRU Tissue or PMMA Slab Phantom.

factor calculation has a diameter of 2.5 cm and located on the front face of the phantom. Backscattered fluence across the tally surface was scored and used for the calculation of the backscatter factor. The fluence from the source and phantom were converted to ICRU tissue kerma.

In this calculation, no energy cut-off is used, and low energy photons are killed using the low energy photon attenuation coefficients. Photon interactions in the MCNP4A code are performed by MCNP photon library, MCPLIB which is based on evaluated data from Evaluated Nuclear Data Files (ENDF) [3]. In this study, the secondary electron and bremsstrahlung contributions are not considered, to facilitate comparison with previous works [1].

### 10.3 Indirect method

ANSI has accepted the indirect method for these calculations. The corrected conversion factors for incident photon spectra are calculated as follows.

$$C_x(d) = \frac{H(d)_{\text{spectrum}}}{K_a} \times \frac{\text{BSF}_{\text{ANSIslab}}}{\text{BSF}_{\text{ICRUtissuecube}}}, \quad (10.1)$$

where

$$\frac{H(d)_{\text{spectrum}}}{K_a} = \frac{\sum \frac{H(d,E)}{K_a} \Phi(E) \mu(E) \Delta E}{\sum \Phi(E) \mu(E) \Delta E}, \text{ where}$$

$\frac{H(d)_{\text{spectrum}}}{K_a}$  = dose conversion factor for incident photon spectrum

(Sv/Gy),

$H(d, E)$  = dose equivalent at depth  $d$  ( $10^{-1}$  g/cm<sup>2</sup>) for photon energy  $E$  (Sv), where  $d$  is 0.07 or 10,

$\Phi(E)$  = incident photon spectrum (photos/cm<sup>2</sup>/J),

$\mu(E)$  = mass energy absorption coefficient for air (cm<sup>2</sup>/kg),

$K_a$  = air kerma for incident photon spectrum (Gy),

$\text{BSF}_{\text{phantom}} = \frac{\int_0^{E_0} K_{\text{ICRU tissue}}^{\text{phantom}}(E) dE}{K_{\text{ICRU tissue}}(E_0)}$  = backscatter factor on the phantom surface,

$K_{\text{ICRU tissue}}^{\text{phantom}}(E) = E \Phi(E) \left[ \frac{\mu_{\text{tr}}(E)}{\rho} \right]_{\text{ICRU tissue}}$ , where

$K_{\text{ICRU tissue}}^{\text{phantom}}(E)$  = ICRU tissue kerma for photon energy  $E$  on the phantom surface (Gy),

$\left[ \frac{\mu_{\text{tr}}(E)}{\rho} \right]_{\text{ICRU tissue}}$  = mass energy transfer coefficient for ICRU tissue (cm<sup>2</sup>/kg),

$\Phi(E)$  = photon spectrum on the phantom (photos/cm<sup>2</sup>/J), and

$K_{\text{ICRU tissue}}(E_0)$  = ICRU tissue kerma for incident photon energy  $E_0$  (Gy).

The backscatter factor is defined as the ratio of kerma in the ICRU tissue at the surface of the phantom to the kerma for the same material at the same in space in the absence of the phantom. The fluence in the phantom is built up by the interactions of photons within the phantom substance.

If the incident photons are monoenergetic, the Eq.(10.1) can be written as the following.

$$C_x(d) = \frac{H(d)}{K_a} \times \frac{\text{BSF}_{\text{ANSI slab}}}{\text{BSF}_{\text{ICRU tissue cube}}}, \quad (10.2)$$

where

$K_a$  = air kerma for incident photon (Gy), and

$H(d)$  = dose equivalent at depth  $d$  ( $10^{-1}$  g/cm<sup>2</sup>) of ICRU slab (Sv).

In the indirect method, the dose conversion factors for the PMMA slab phantom are corrected from that for the ICRU tissue slab phantom through use of Eq.(10.2). This concept may be acceptable for many radiation protection purposes for photon irradiation with higher energies but may not be acceptable for lower energies. Thus, the indirect method accepted by ANSI cannot perform the unique calculation approach to obtain the dose conversion factors for PMMA slab phantom for all energies.

#### 10.4 Direct method

Two methods can be used in the MCNP code for the calculation of energy absorption in a small volume element. The first method is to use the F6 tally, which is a heating and energy deposition tally, estimated by

$$F6 = \frac{\rho_a}{\rho_g} \int_V \int_t \int_E h(E) \Phi(\mathbf{r}, E, t) dE dt \frac{dV}{V}, \quad (10.3)$$

where

$\rho_a$  = atom density (atoms/barn×cm),

$\rho_g$  = gram density (grams/cm<sup>3</sup>),

$\Phi(\mathbf{r}, E, T)$  = particle spectrum (particles/cm<sup>2</sup>/sec/MeV),

$V$  = volume of tally cell (cm<sup>3</sup>),

$h(E)$  = heating response of material (cm<sup>2</sup>×MeV)

=  $\sigma_T(E) h_{\text{avg}}(E)$ , and

$\sigma_T(E)$  = total photon cross section of photon energy  $E$  (cm<sup>2</sup>).

In MCNP4A, the heating number of photon is defined by

$$h_{\text{avg}}(E) = \sum_{i=1}^3 p_i(E) (E - \bar{E}_{\text{out}_i}), \quad (10.4)$$

where

$E$  = incident photon energy (MeV),

$p_i(E)$  = probability of reaction  $i$ ,

$\bar{E}_{\text{out}_i}$  = average exciting photon for reaction  $i$  (MeV),

$i = 1$  for incoherent (Compton) scattering with form factors,

$i = 2$  for pair production ( $\bar{E}_{\text{out}} = 1.022016 \text{ MeV} = 2m_0c^2$ ),

$i = 3$  for photoelectric effect.

All energy transferred to electrons is assumed to be deposited locally.

If the F6 tally is used to estimate energy deposition in small volume of the ICRU tissue slab phantom, the F6 tally gives an absorbed dose (equal to dose equivalent for photons), or a dose conversion factor directly, for the ICRU tissue slab phantom. However, the F6 tally used in the PMMA slab phantom does not give dose equivalent but kerma. The deposition of energy, the kerma in PMMA substance, is not dose equivalent because dose equivalent must be deposition of energy in tissue. Although dose equivalent is calculated by using the F6 tally in the ICRU slab phantom, the F6 tally cannot give the dose equivalent conversion factor in the PMMA slab phantom directly.

The other method, the combination of a track length estimate of cell flux and an energy-dependent multiplier, can give exactly the same results as the F6 tally. The track length estimate of cell flux is called as F4 in MCNP4A and estimated by

$$F4 = \int_V \int_t \int_E h(E) \Phi(\mathbf{r}, E, t) dE dt \frac{dV}{V}. \quad (10.5)$$

The F4 tally multiplied by  $\sigma_T h_{\text{avg}}(E) \rho_a / \rho_g$  is the F6 tally. Thus, any flux of the form  $\int \Phi(E) dE$  can be transformed into  $\int R(E) \Phi(E) dE$ , where  $R(E)$  is any combination of sums and products of energy-dependent quantities known to MCNP.

In this work, the energy-dependent quantity is the heating response of ICRU tissue composition instead of the heating response of the PMMA substance because it can convert the track length estimate of cell flux to corresponding quantity of ICRU tissue kerma or absorbed dose. If the heating response of ICRU tissue is multiplied by the fluence built up in a cell of the PMMA slab phantom, the result of the F4 tally will give the dose equivalent in the PMMA slab phantom. The dose conversion factor,  $\frac{P(d)}{K_a}$ , for the PMMA slab phantom is given as:

$$\frac{P(d)}{K_a} = C \frac{\int \Phi_{\text{PMMAslab}}(E) R(E) dE}{K_a}, \quad (10.6)$$

where

$$C = 1.60219 \cdot 10^{-10} \frac{\text{Gy}}{\text{MeV/g}}$$

×PMMA atom density (atoms/cm<sup>3</sup>)/PMMA gram density (grams/cm<sup>3</sup>),  
 $\Phi_{\text{PMMA slab}}$  = photon spectrum built in the PMMA slab phantom (photons/cm<sup>2</sup>/MeV),

$R(E)$  = heating response of ICRU tissue instead of PMMA (cm<sup>2</sup>×MeV)  
 $= \sigma_T(E)h_{\text{avg}}(E)$ , and

$K_a$  = air kerma for incident photon energy  $E_0$  (Gy).

The air kerma,  $K_a$ , is calculated by using MCNP photon library, MCPLIB.

### 10.5 Results

Calculations of the dose conversion factors for the PMMA slab phantom by the indirect and the direct methods were made. For comparison of dose conversion factors between the two methods, the backscatter factors in the ICRU tissue slab phantom and the PMMA slab phantom were calculated (Table 10.1). The dose conversion factor was obtained by Eq.(10.2) and it denoted as  $C_x(d)$ .  $\frac{P(d)}{K_a}$  denotes the dose conversion factor in the PMMA slab phantom obtained by the direct method.

Comparisons between  $C_x(d)$  and  $\frac{P(d)}{K_a}$  at  $d = 7$  and  $1,000 \text{ mg/cm}^2$  are shown in Fig.10.2 and 10.3, respectively. For low energy photons less than 100 keV and at the  $1000 \text{ mg/cm}^2$  depth, the dose conversion factors are considerably different. On the other hand, at the  $7 \text{ mg/cm}^2$  depth, the two methods give nearly the same results at most photon energies. Thus, the dose equivalent distributions are similar at shallow depths. At deeper levels, however, the dose equivalent changes considerably with depth. For low energy photons, the discrepancy between the results of the two methods is considerable. The percent difference between two methods is shown in more detail for low energy photons in Fig.10.4. If the incident photon energies are less than 100 keV, the kerma of backscatter photons is not proportional to the amount of energy deposition in deeper in the phantoms. The indirect method underestimates the dose equivalent at deep levels for low energy photons. For about 100 to 1,000 keV incident photons, the results of the direct method are somewhat higher than that of the indirect method.



Table 10.1. Comparison of Dose Conversion Factors by the Direct Method and Indirect Methods

Photon Energy (keV)	Kerma Factors from MCNP (pGy-cm <sup>2</sup> )		Conversion Factors for ICRU Tissue Slab (Sv/Gy)		Backscatter Factors (BSF)		Conversion Factors by Indirect Method (Sv/Gy)		Conversion Factors by Direct Method (Sv/Gy)	
	$\frac{K_a}{\Phi}$	$\frac{K_T}{\Phi}$	$\frac{H(0.07)}{K_a}$	$\frac{H(10)}{K_a}$	ICRU	PMMA	$C_x(0.07)$	$C_x(10)$	$\frac{P(0.07)}{K_a}$	$\frac{P(10)}{K_a}$
10	7.245	6.915	0.944	0.010	1.016	1.027	0.954	0.010	0.965	0.048
15	2.977	2.805	0.987	0.278	1.055	1.086	1.015	0.286	1.025	0.449
20	1.579	1.478	1.051	0.638	1.117	1.176	1.107	0.672	1.101	0.815
30	0.668	0.625	1.248	1.133	1.338	1.452	1.354	1.229	1.355	1.326
40	0.400	0.380	1.467	1.531	1.535	1.671	1.597	1.668	1.595	1.762
50	0.305	0.299	1.662	1.810	1.680	1.801	1.781	1.940	1.787	2.015
60	0.278	0.281	1.718	1.923	1.693	1.841	1.868	2.090	1.874	2.090
80	0.302	0.319	1.711	1.885	1.617	1.689	1.788	1.970	1.782	2.033
100	0.369	0.398	1.653	1.777	1.526	1.583	1.715	1.843	1.703	1.899
150	0.599	0.657	1.505	1.579	1.378	1.416	1.547	1.623	1.544	1.632
200	0.857	0.942	1.410	1.475	1.278	1.312	1.447	1.513	1.440	1.525
300	1.382	1.521	1.314	1.362	1.194	1.211	1.332	1.381	1.330	1.379
400	1.892	2.083	1.275	1.292	1.158	1.166	1.283	1.300	1.283	1.312
500	2.380	2.620	1.240	1.254	1.122	1.138	1.258	1.272	1.255	1.276
600	2.843	3.131	1.212	1.223	1.101	1.113	1.225	1.235	1.224	1.238
800	3.703	4.078	1.184	1.184	1.076	1.085	1.194	1.195	1.196	1.194
1000	4.480	4.934	1.166	1.164	1.060	1.067	1.174	1.171	1.174	1.172
1500	6.147	6.769	1.142	1.142	1.038	1.041	1.145	1.145	1.146	1.145
2000	7.557	8.316	1.133	1.120	1.030	1.034	1.137	1.124	1.137	1.125
3000	9.982	10.948	1.119	1.109	1.021	1.021	1.120	1.109	1.120	1.112
4000	12.146	13.264	1.111	1.098	1.017	1.018	1.112	1.099	1.113	1.101
5000	14.190	15.427	1.102	1.091	1.014	1.015	1.103	1.092	1.103	1.094
6000	16.100	17.432	1.099	1.086	1.014	1.015	1.100	1.088	1.100	1.088
8000	19.979	21.452	1.085	1.074	1.011	1.012	1.086	1.074	1.086	1.075
10000	24.141	25.712	1.076	1.065	1.011	1.011	1.076	1.065	1.076	1.066

## 10.6 Conclusions

The direct method is a simple method for obtaining the dose conversion factor in terms of ICRU tissue kerma for incident photons in the PMMA slab phantom. It can reduce computation time and en-

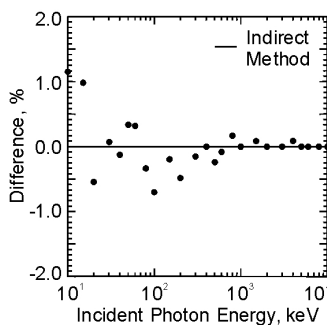


Fig.2. Percent Difference in Dose Conversion Factors between Direct and Indirect Method at a Depth of 7 mg/cm<sup>2</sup>.

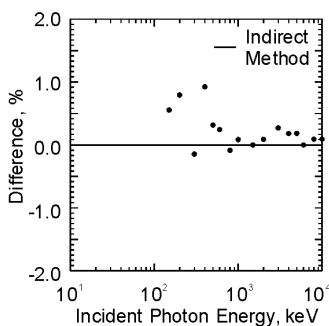


Fig.3. Percent Difference in Dose Conversion Factors between Direct and Indirect Method at a Depth of 1000 mg/cm<sup>2</sup>.

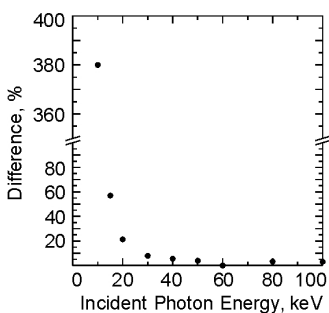


Fig.4. Percent Difference in Dose Conversion Factors between Direct and Indirect Method at a Depth of 1000 mg/cm<sup>2</sup> for Low Energy Photons.

hance its accuracy. Although the results of the two methods show the same value at certain energies, the indirect method appears to have additional statistical errors from the calculations of the backscatter factors. Furthermore, the indirect method does not present acceptable results for low energy photons.

The direct method may also be useful for calculating dose conversion factors in non-tissue material, and can save computation time for the calculation of directional dose conversion factor.

## REFERENCES

1. American National Standards Institute, American National Standard for Dosimetry – Personnel Dosimetry Performance – Criteria for Testing, ANSI N13.11 – 1993.
2. *Bartlett D.T., Dimbylow P.J., Francis T.M.*, Calculated Backscatter from Phantoms for Photon Dosimeter Calibration // Radiat. Prot. Dosim. – 1990. – **32**. – P.123.
3. *Briesmeister J.F.*, MCNP-A General Monte Carlo N-Particle Transport Code, Version 4A, LA-12625-M, Los Alamos National Laboratory – 1993.
4. *Grosswendt B.* Conversion Coefficients for Calibrating Individual Photon Dosimeters in terms of Dose Equivalents Defined in an ICRU Tissue Cube and PMMA Slabs // Radiat. Prot. Dosim. – 1990. – **32**. – P.219.
5. International Commission on Radiation Units and Measurements, Determination of Dose Equivalents Resulting for External Radiation Sources, ICRU Report 39 Bethesda, MD – 1985.
6. International Commission on Radiation Units and Measurements, Measurement of Dose Equivalents from External Photon and Electron Radiation, ICRU Report 47, Bethesda, MD – 1992.
7. *Will W.*, Measurement of Conversion Coefficients for Calibrating Individual Dosimeters with respect to the Operational Dose Quantities on the PMMA Slab Phantom // Radiat. Prot. Dosim. – 1991. – **37**. – P.79.

## CHAPTER 11

# DOSE EQUIVALENT PER UNIT FLUENCE NEAR THE SURFACE OF THE ICRU PHANTOM BY INCLUDING THE SECONDARY ELECTRON TRANSPORT FOR PHOTONS

### *11.1. Introduction*

Since the first introduction of operational quantities in ICRU Report 39 [1], some specified depths such as 10, 3, and 0.07 mm have been used for the definition of the operational quantities. For area monitoring, ambient dose equivalent,  $H^*(d)$ , and directional dose equivalent,  $H'(d, \Omega)$ , are defined in the ICRU sphere (a 30 cm diameter sphere made of ICRU tissue substitute). The recommended depth for penetrating radiation is 10 mm and for low-penetrating radiation is 0.07 mm. The ambient dose equivalent is defined at a depth along the principle axis of the ICRU sphere. The directional dose equivalent is at the same depth along a radius in a specified direction,  $\Omega$ . For individual monitoring, two operational quantities (individual dose equivalent, penetrating and individual dose equivalent, superficial) were simplified to personal dose equivalent,  $H_p(d)$ , in ICRU Reports 47 [2] and 51 [3]. As the personal dose equivalent is defined at a point in the human body, a conversion coefficient is used to change measurable quantity to operational quantity. Therefore, the conversion coefficient is a combination of measurable quantity on the human body and dose equivalent in the human body. Dose equivalent in an appropriate phantom has used for the definition of conversion coefficients instead of that in the human body. The ICRU sphere and the ICRU slab (a 30 cm  $\times$  30 cm  $\times$  15 cm slab made of ICRU tissue substitute) are appropriate phantoms. For strongly penetrating radiation, a depth of 10 mm is used as a recommended depth to monitor the protection quantities

such as effective dose equivalent,  $H_E$ , or effective dose,  $E$ . For weakly penetrating radiation, a depth of 0.07 and 3 mm is also recommended for skin and eye, respectively.

ICRP Publication 74 [4] summarized the method of calculating conversion coefficients and provided the recommended values. In the case of photon irradiation, the ICRP adapted the conversion coefficients performed by applying the kerma approximation. The kerma approximation is an assumption that all secondary electrons generating by photons are in equilibrium. Using this assumption, kinetic energy of the secondary electron can be transferred to the medium within the immediate region of photon interaction. Therefore, an absorbed dose is equal to the tissue kerma minus the bremsstrahlung losses. The dose equivalent at a point of interest is numerically equal to the absorbed dose because the radiation-weighting factor,  $w_R$ , for electrons and photons of all energy is 1.

Validations of the kerma approximation have been examined by previous researches [5,6]. Rogers [5] considered both photon and electron transports for calculating distributions of the dose equivalent. He used a 30 cm thick semi-infinite slab made of ICRU tissue substitute. EGS3 Monte Carlo electron-photon transport simulation package was used as a tool for the calculations. The results he obtained were in very close agreement with the results of the kerma approximation for photon energies up to 3 MeV. However, at higher photon energies than 3 MeV, the values at a depth of 10 mm were lower than the values of the kerma approximation. Ferrari and Pelliccioni [6] also performed a calculation for the ambient dose equivalent by the Monte Carlo method, using FLUKA code. Their results were very similar to those of Rogers for photon of all energy because both calculations accounted for the secondary electron transports and by placing the phantoms in a vacuum. They pointed out that the recommended dose equivalents were over-estimated at photon energies higher than 3 MeV. The over-estimation is caused by ignoring the secondary electron transport and placing the phantom in air under a condition of charged particles equilibrium.

As the energy of electron increases and location of electron is closer to the surface, the kerma approximation becomes invalid because the electron equilibrium is no longer complete. When the electron equilibrium at a depth of 10 mm is undeveloped, the closer point, especially

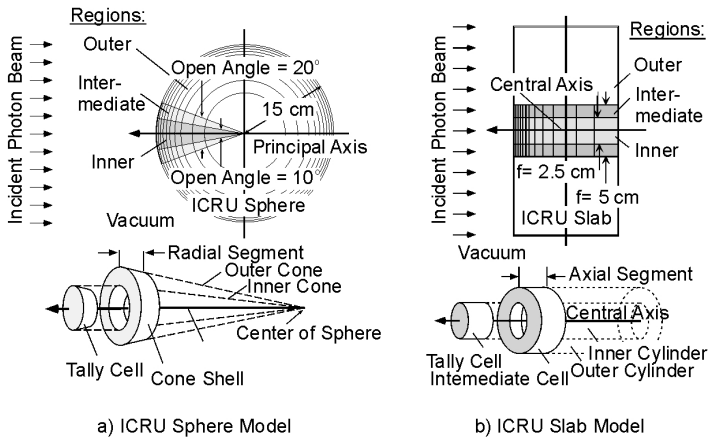


Fig.11.1. Computational Geometry and Tally Cell Arrangement of ICRU Model

at a depth of 3 and 0.07 mm, becomes increasingly incomplete. This paper presents that over-estimation by applying the kerma approximation exists not only at the depth of 10 mm but also at the depth of 3 and 0.07 mm. In order to accomplish this presentation, distributions of dose equivalent per unit fluence in the ICRU sphere and the ICRU slab were re-calculated by using MCNP code [7] and compared with values of references [4,5,6,8].

### 11.2. Computational method

Since the version 4A was released, the MCNP has been able to simulate electron transport as well as neutron and photon transports. The MCNP code provides a pulse height tally (F8) as one of the new features. It records energy deposited in a cell by photons and electrons. The deposited energy can be easily converted to dose or dose equivalent.

In order to calculate the dose equivalents for the ICRU sphere and the ICRU slab, the computational conditions were modeled as shown in Fig.11.1. The irradiation condition was assumed as a mono-energetic broad parallel photon beam in a vacuum. Ferrari and Pelliccioni discussed this condition [6]. Each phantom was divided into three regions to reduce the calculation time. In the model of the ICRU sphere, the outer region is outside the outer cone; the inner region is inside the inner

cone; and the intermediate region is between the two cones. The inner cone has an opening angle of  $10^\circ$  and its vortex is located at the center of the sphere. The vortex of the outer cone is also located at the vortex of the inner cone and has an opening angle of  $20^\circ$  so that it surrounds the inner cone. The inner cone was divided into radial segments that were used as tally cells. Similarly, in the model of the ICRU slab, the outer region is outside the outer cylinder; the inner region is inside the inner cylinder; and the intermediate region is between the two cylinders. The radius of the inner and outer cylinders is 2.5 and 5 cm, respectively. The inner cylinder was also divided into axial segments for the same purpose as the ICRU sphere model. Segments of both models are very thin at a depth of 0.07, 3, and 10 mm and the thickness is 0.06, 0.08, and 1.1 mm, respectively. The dose equivalent was averaged at a segment volume. In the outer region, the secondary electron with energy of 0.5 MeV is unable to reach the inner region because its range is shorter than the thickness of the intermediate region. All of its energy is transferred to the intermediate region due to region, it was dependent on multiple scattering and continuous slowing down. While an energy cut-off for an electron transport was fixed by 0.5 MeV in the outer energy of the incident photon in the inner and intermediate regions.

For photon energies up to 0.02 MeV, the energy cut-off in the inner region was 0.001 MeV and in the intermediate region was 0.01 MeV. The range of an electron of 0.01 MeV is shorter than one-tenth of the thickness of the thinnest tally cell, which is  $0.0004 \text{ g}\cdot\text{cm}^{-2}$ . Table 1 lists the maximum range of a recoil electron in the ICRU tissue substitute from Compton scattering. For photon energies between 0.03 and 0.2 MeV, 0.01 MeV was given as the energy cut-off in the inner and intermediate regions. An electron of 0.05 MeV cannot go further than 0.04 mm in the ICRU tissue substitute. For photon energy higher than 0.2 MeV, the energy cut-off for an electron transport was set at 0.05 MeV. When energy of an electron was below the energy cut-off, the electron transport was terminated and its energy was absorbed into the medium. The transport of a photon was terminated by the limitation of the cross section.

### **11.3. Results and discussions**

In the case of a unidirectional photon field, the directional dose equivalent on the principal axis of the ICRU sphere has the same

Table 11.1. Maximum Energy of Recoil Electron by Compton Scattering and Its Corresponding Range in the ICRU Tissue

Photon Energy (MeV)	Maximum Recoil Electron Energy (MeV)	Electron Range* (g·cm <sup>-2</sup> )
0.010	$3.766 \cdot 10^{-4}$	$1.663 \cdot 10^{-6}$
0.015	$8.318 \cdot 10^{-4}$	$3.672 \cdot 10^{-6}$
0.020	$1.452 \cdot 10^{-3}$	$8.649 \cdot 10^{-6}$
0.030	$3.152 \cdot 10^{-3}$	$3.381 \cdot 10^{-5}$
0.040	$5.415 \cdot 10^{-3}$	$8.671 \cdot 10^{-5}$
0.050	$8.183 \cdot 10^{-3}$	$1.785 \cdot 10^{-4}$
0.060	$1.141 \cdot 10^{-2}$	$3.208 \cdot 10^{-4}$
0.080	$1.908 \cdot 10^{-2}$	$7.964 \cdot 10^{-4}$
0.100	$2.813 \cdot 10^{-2}$	$1.584 \cdot 10^{-3}$
0.150	$5.549 \cdot 10^{-2}$	$5.234 \cdot 10^{-3}$
0.200	$8.782 \cdot 10^{-2}$	$1.159 \cdot 10^{-2}$
0.300	$1.620 \cdot 10^{-1}$	$3.229 \cdot 10^{-2}$
0.400	$2.441 \cdot 10^{-1}$	$6.201 \cdot 10^{-2}$
0.500	$3.309 \cdot 10^{-1}$	$9.854 \cdot 10^{-2}$
0.600	$4.208 \cdot 10^{-1}$	$1.399 \cdot 10^{-1}$
0.800	$6.063 \cdot 10^{-1}$	$2.320 \cdot 10^{-1}$
1.000	$7.965 \cdot 10^{-1}$	$3.316 \cdot 10^{-1}$
1.500	$1.282 \cdot 10^{-1}$	$5.940 \cdot 10^{-1}$
2.000	1.773	$8.620 \cdot 10^{-1}$
3.000	2.765	1.394
4.000	3.760	1.917
5.000	4.757	2.428
6.000	5.755	2.930
8.000	7.752	3.907
10.000	9.751	4.853

\* Taken from the output of the MCNP calculation

numerical value as the ambient dose equivalent. It is also the same value as the personal dose equivalent in the ICRU sphere.

The dose equivalent per unit photon fluence in the ICRU sphere was calculated by using the electron transport (refer to “With Electron Transport”) and the kerma approximation (refer to “No Electron Transport”). Both conversion coefficient distributions along the principal axis were plotted in Fig.11.2. for incident photons of various energies. When including the electron transport, relative standard deviations of conversion coefficients at a depth of 0.07 mm are in the range of 10 to



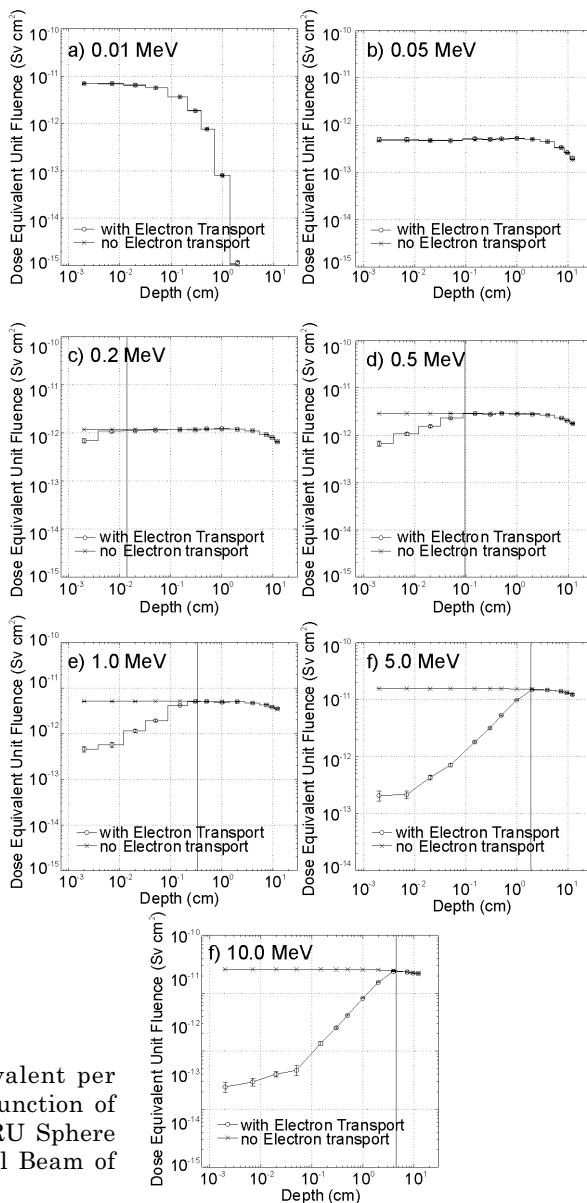


Fig.11.2. Dose Equivalent per Unit Fluence as a Function of the Depth in the ICRU Sphere Exposed to a Parallel Beam of Incident Photons.

15% at photon energies above 0.8 MeV. The relative standard deviations are plotted in figures when it is necessary. Statistical variances of calculations using the kerma approximation were less than 1% and not plotted. At photon energies up to 0.1 MeV, both distributions are coincident. In this photon energy range, it is seen that the transport of the secondary electron can be ignored. Although the maximum energy of a recoil electron from Compton scattering by photons of 0.2 MeV is about 0.088 MeV and the range of the recoil electron is  $0.012 \text{ g}\cdot\text{cm}^{-2}$ , the values at the depth of 0.07 mm are still similar. At photon energies higher than 0.2 MeV, discrepancies between results of the electron transport and the kerma approximation exist from the surface to the depth of the electron range as shown in Fig.11.2 (c–g). The vertical lines in the figures indicate the maximum range of the recoil electron in the ICRU tissue substitute. The kerma approximation is no longer valid at a depth less than the maximum electron range because the charged particles equilibrium is not established.

Conversion coefficients at a depth of 10 mm are summarized in Table 11.2 over the photon energy ranges from 0.01 to 10 MeV. The conversion coefficients with no electron transport correspond to the values of the ICRP Publication 74 due to the kerma approximation. The conversion coefficients with electron transport are comparable to the data of Ferrari and Pelliccioni. There are no significant differences between two data sets. The maximum difference is about 9.8% at photon energy of 0.08 MeV. The conversion coefficients at a depth of 10 mm are plotted in Fig.11.3a as a function of incident photon energy. All of the points overlap each other up to photon energies of 3 MeV. However, at photon energies higher than 3 MeV, there are great discrepancies between data points with electron transport and no electron transport. Over-estimations of conversion coefficients with no electron transport are observed at photon energies higher than 3 MeV. This result confirms the conclusion of Ferrari and Pelliccioni. It also enables MCNP code to be applied to the conversion coefficient calculation when the transport of the secondary electron is considered.

Conversion coefficients at a depth of 3 mm are summarized in Table 11.3. Because the ICRP Publication 74 does not present the data at a depth of 3 mm, the data of the ICRP Publication 51 [8] is used to compare the results with no electron transport. The differences between conversion coefficients are minute. At a depth of 3 mm in the ICRU

Table 11.2. Conversion Coefficients from Photon Fluence to Personal Dose Equivalent at a Depth of 10 mm in the ICRU Sphere.

Photon Energy (MeV)	Dose Equivalent per Unit Fluence (pSv-cm <sup>2</sup> )			
	With Electron Transport		No Electron Transport	
	This Work	Ferrari and Pelliccioni [6]	This Work	ICRP 74 [4]
0.010	0.080	0.082	0.080	0.061
0.015	0.856	0.84	0.842	0.83
0.020	1.029	1.04	1.014	1.05
0.030	0.748	0.81	0.758	0.81
0.040	0.606	0.61	0.589	0.64
0.050	0.525	0.51	0.514	0.55
0.060	0.479	0.51	0.489	0.51
0.080	0.510	0.56	0.527	0.53
0.100	0.615	0.62	0.614	0.61
0.150	0.881	0.87	0.894	0.89
0.200	1.212	1.23	1.200	1.20
0.300	1.789	1.81	1.797	1.80
0.400	2.282	2.36	2.359	2.38
0.500	2.796	2.78	2.887	2.93
0.600	3.256	3.46	3.388	3.44
0.800	4.190	4.29	4.299	4.38
1.000	4.891	5.18	5.124	5.20
1.500	6.828	6.92	6.899	6.90
2.000	8.217	8.25	8.400	8.60
3.000	10.60	10.4	10.99	11.1
4.000	10.63	10.7	13.26	13.4
5.000	9.811	10.4	15.40	15.5
6.000	9.630	9.57	17.39	17.6
8.000	8.558	9.10	21.36	21.6
10.000	8.199	8.76	25.56	25.6

Note:  $H_P(10) = H^*(10) = H'(10,0^\circ)$  in the ICRU sphere for parallel beam

sphere, reference data are not available to compare the conversion coefficients with electron transport. In Fig.11.3b, over-estimation at a depth of 3 mm appears at photon energies that are approximately higher than 1 MeV. In order to compare a trend of conversion coefficients as a function of incident photon energy, the data of Rogers was linearly interpolated between depths of 2 and 4 mm and listed in Table 11.3.

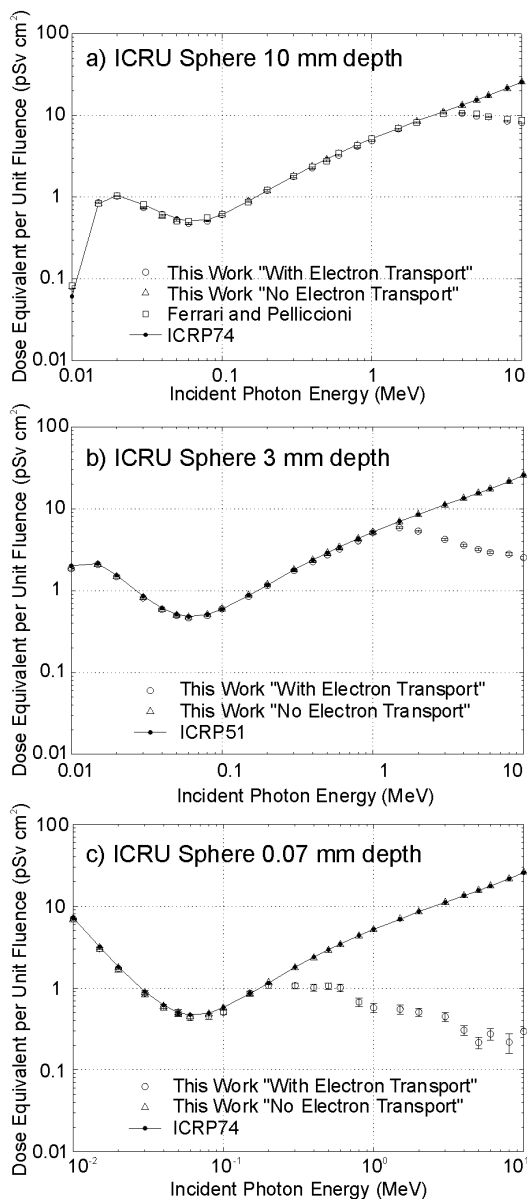


Fig.11.3. Comparison of a Dose Equivalent per Unit Fluence at Various Depth on the Principal Axis of the ICRU Sphere as a Function of Incident Photon Energy.

Table 11.3. Conversion Coefficients from Photon Fluence to Personal Dose Equivalent at a Depth of 3 mm in the ICRU Sphere

Photon Energy (MeV)	Dose Equivalent per Unit Fluence (pSv cm <sup>2</sup> )			
	With Electron Transport		No Electron Transport	
	This Work	Rogers <sup>[5]</sup> *	This Work	ICRP 51 <sup>[8]</sup>
0.010	1.853		1.877	2.01
0.015	2.087	2.14	2.088	2.14
0.020	1.484	1.51	1.474	1.54
0.030	0.812	0.854	0.822	0.859
0.040	0.592	0.626	0.591	0.610
0.050	0.498	0.527	0.501	0.512
0.060	0.464	0.532	0.473	0.483
0.080	0.495	0.578	0.509	0.511
0.100	0.598	0.658	0.596	0.594
0.150	0.849		0.880	0.872
0.200	1.151	1.31	1.188	1.16
0.300	1.754	1.96	1.791	1.80
0.400	2.256	2.53	2.361	2.37
0.500	2.732	2.97	2.893	2.90
0.600	3.218	3.37	3.395	3.41
0.800	4.052	4.14	4.323	4.34
1.000	5.124	4.59	5.161	5.18
1.500	5.871		6.954	6.99
2.000	5.339	4.50	8.481	8.48
3.000	4.217	3.62	11.08	11.2
4.000	3.596	3.08	13.38	13.4
5.000	3.188	2.79	15.54	15.5
6.000	2.931	2.57	17.53	17.5
8.000	2.791	2.32	21.53	21.5
10.000	2.536	2.24	25.78	25.7

\* These data were linearly interpolated between depths of 2 and 4 mm in the semi-finite ICRU slab.

Conversion coefficients at a depth of 0.07 mm are listed in Table 11.4 together with the data of the ICRP Publication 74. For a depth of 0.07 mm in the ICRU sphere, there is no reference data to compare conversion coefficients with electron transport. In Table 11.4, the results of this work and the data of the ICRP Publication 74 are very close when no electron transport is considered. At photon energies

Table 11.4. Conversion Coefficients from Photon Fluence to Personal Dose Equivalent at a Depth of 0.07 mm in the ICRU Sphere

Photon Energy (MeV)	Dose Equivalent per Unit Fluence (pSv·cm <sup>2</sup> )		
	With Electron Transport	No Electron Transport	
	This Work	This Work	ICRP 74 [4]
0.010	6.990	6.845	7.20
0.015	3.032	2.947	3.19
0.020	1.725	1.664	1.81
0.030	0.866	0.820	0.90
0.040	0.583	0.567	0.62
0.050	0.501	0.474	0.50
0.060	0.441	0.447	0.47
0.080	0.452	0.485	0.49
0.100	0.505	0.572	0.58
0.150	0.857	0.855	0.85
0.200	1.078	1.163	1.15
0.300	1.066	1.766	1.80
0.400	1.013	2.337	2.38
0.500	1.060	2.874	2.93
0.600	1.005	3.380	3.44
0.800	0.672	4.317	4.38
1.000	0.576	5.161	5.20
1.500	0.549	6.967	6.90
2.000	0.507	8.492	8.60
3.000	0.447	11.11	11.1
4.000	0.306	13.42	13.4
5.000	0.215	15.58	15.5
6.000	0.275	17.58	17.6
8.000	0.218	21.60	21.6
10.000	0.295	25.86	25.6

Note:  $H_P(0.07) = H'(0.07, 0^\circ)$  in the ICRU sphere for parallel beam

up to 0.2 MeV, the conversion coefficients with electron transport are indistinguishable from those with no electron transport. This shows that MCNP code is reliable when it is used to calculate the conversion coefficient at a depth of 0.07 mm with electron transport as well as with no electron transport. Fig.11.3c demonstrates that at photon energy higher than about 0.2 MeV, conversion coefficients of the ICRP Publication 74 are over-estimated due to the kerma approximation.

The distributions of conversion coefficients in the ICRU slab are similar to those in the ICRU sphere. Conversion coefficients at a depth of 10, 3, and 0.07 mm are shown in Tables 11.5 to 11.7 and are compared with published data [5,6] in Fig.11.4. At photon energy of 3, 1, and 0.2 MeV, the conversion coefficients with electron transport and no electron transport become noticeably different at a depth of 10, 3, and 0.07 mm, respectively. Fig.11.5. show the comparison between conversion coefficients with electron transport in the ICRU sphere and the ICRU slab. The values of the ICRU slab are slightly higher than the values of the ICRU sphere.

#### **11.4. Conclusions**

Conversion coefficients at a depth of 10, 3, and 0.07 mm were re-calculated using the kerma approximation and inclusion of the secondary electron transport. At photon energies lower than a specific energy, conversion coefficients with no electron transport compared to those with electron transport were over-estimated. At a depth of 10 mm, the over-estimation was seen at photon energies of 3 MeV as mentioned in the ICRP Publication 74. At a depth of 3 and 0.07 mm, the over-estimation was newly observed at photon energies higher than 1 and 0.2 MeV for the ICRU sphere and the ICRU slab, respectively. It demonstrated that the conversion coefficients recommended by the ICRP are questionable not only at a depth of 10 mm but also at a depth of 3 and 0.07 mm.

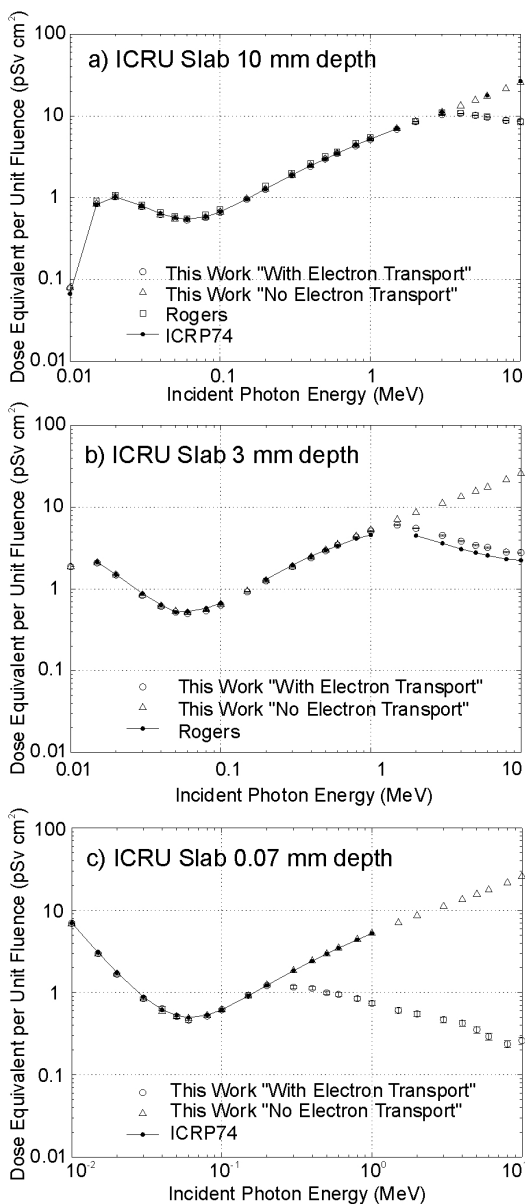


Fig.11.4. Comparison of a Dose Equivalent per Unit Fluence at Various Depths on the Central Axis of the ICRU Slab as a Function of Incident Photon Energy



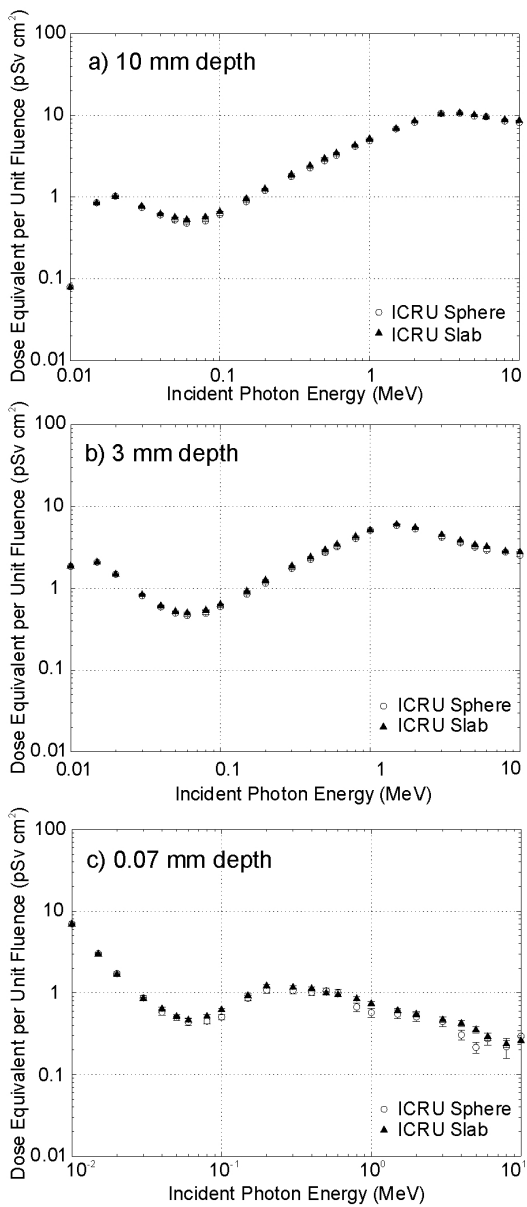


Fig.11.5. Comparison of a Dose Equivalent per Unit Fluence at Various Depths in the ICRU Sphere and the ICRU Slab as a Function of Incident Photon Energy

Table 11.5. Conversion Coefficients from Photon Fluence to Personal Dose Equivalent at a Depth of 10 mm in the ICRU Slab

Photon Energy (MeV)	Dose Equivalent per Unit Fluence (pSv·cm <sup>2</sup> )			
	With Electron Transport		No Electron Transport	
	This Work	Rogers [5]	This Work	ICRP 74 [4]
0.010	0.079		0.079	0.067
0.015	0.844	0.914	0.841	0.824
0.020	1.025	1.070	1.016	1.026
0.030	0.775	0.816	0.773	0.802
0.040	0.622	0.655	0.618	0.639
0.050	0.566	0.586	0.551	0.570
0.060	0.533	0.555	0.534	0.547
0.080	0.571	0.618	0.579	0.584
0.100	0.664	0.72	0.670	0.672
0.150	0.960		0.965	0.963
0.200	1.264	1.39	1.279	1.277
0.300	1.899	1.99	1.892	1.889
0.400	2.429	2.63	2.467	2.457
0.500	2.979	3.18	2.998	2.975
0.600	3.470	3.62	3.501	3.482
0.800	4.310	4.66	4.417	4.391
1.000	5.180	5.49	5.241	5.216
1.500	6.879		7.004	6.993
2.000	8.545	8.64	8.506	
3.000	10.42	11.0	11.07	11.125
4.000	10.77	10.9	13.35	
5.000	10.14	10.2	15.49	
6.000	9.625	9.77	17.46	17.855
8.000	8.839	8.82	21.43	
10.000	8.657	8.50	25.64	26.664

Note:  $H_P(10) = H'(10,0^\circ)$  in the ICRU slab for parallel beam

Table 11.6. Conversion Coefficients from Photon Fluence to Personal Dose Equivalent at a Depth of 3 mm in the ICRU Slab

Photon Energy (MeV)	Dose Equivalent per Unit Fluence (pSv-cm <sup>2</sup> )			
	With Electron Transport		No Electron Transport	
	This Work	Rogers [5]*	This Work	Nelson and Chilton [9]
0.010	1.875		1.880	1.84
0.015	2.091	2.14	2.088	2.09
0.020	1.482	1.51	1.477	1.51
0.030	0.836	0.88	0.842	0.897
0.040	0.611	0.64	0.617	0.636
0.050	0.523	0.52	0.535	0.555
0.060	0.501	0.53	0.513	0.538
0.080	0.542	0.58	0.556	0.591
0.100	0.636	0.67	0.647	0.689
0.150	0.923		0.941	
0.200	1.257	1.31	1.258	
0.300	1.879	1.96	1.875	
0.400	2.405	2.53	2.452	
0.500	2.945	2.97	2.993	
0.600	3.435	3.37	3.499	
0.800	4.313	4.14	4.430	
1.000	5.141	4.59	5.265	
1.500	6.043		7.053	
2.000	5.526	4.50	8.572	
3.000	4.510	3.62	11.16	
4.000	3.842	3.08	13.46	
5.000	3.418	2.79	15.61	
6.000	3.222	2.57	17.60	
8.000	2.827	2.32	21.60	
10.000	2.784	2.24	25.85	

\* These data were linearly interpolated between depths of 2 and 4 mm in the semi-finite ICRU slab.

Table 11.7. Conversion Coefficients from Photon Fluence to Personal Dose Equivalent at a Depth of 0.07 mm in the ICRU Slab

Photon Energy (MeV)	Dose Equivalent per Unit Fluence (pSv·cm <sup>2</sup> )		
	With Electron Transport	No Electron Transport	
	This Work	This Work	ICRP 74 [4]
0.010	6.943	6.850	7.036
0.015	2.983	2.952	3.061
0.020	1.675	1.671	1.756
0.030	0.849	0.834	0.887
0.040	0.636	0.591	0.619
0.050	0.513	0.506	0.527
0.060	0.463	0.484	0.496
0.080	0.516	0.525	0.532
0.100	0.619	0.617	0.619
0.150	0.927	0.911	0.909
0.200	1.216	1.228	1.226
0.300	1.168	1.843	1.844
0.400	1.127	2.421	2.419
0.500	0.993	2.966	2.961
0.600	0.949	3.475	3.465
0.800	0.844	4.408	4.387
1.000	0.739	5.250	5.243
1.500	0.608	7.049	
2.000	0.550	8.572	
3.000	0.469	11.18	
4.000	0.423	13.48	
5.000	0.353	15.65	
6.000	0.292	17.65	
8.000	0.237	21.66	
10.000	0.260	25.93	

Note:  $H_P(0.07) = H'(0.07, 0^\circ)$  in the ICRU slab for parallel beam

---

REFERENCES

1. International Commission on Radiation Units and Measurements. Determination of Dose Equivalents Resulting for External Radiation Sources. ICRU Report 39 (Bethesda, MD: ICRU Publications) 1985.
2. International Commission on Radiation Units and Measurements. Measurement of Dose Equivalents from External Photons and Electron Radiations. ICRU Report 47 (Bethesda, MD: ICRU Publications) 1992.
3. International Commission on Radiation Units and Measurements. Quantities and Units in Radiation Protection Dosimetry. ICRU Report 51 (Bethesda, MD: ICRU Publications) 1993.
4. International Commission on Radiological Protection. Conversion Coefficients for Use in Radiological Protection Against External Radiation. ICRP Publication 74 (Pergamon Press) 1997.
5. *Rogers D.W.O.* Fluence to Dose Equivalent Conversion Factors Calculated with EGS3 for Electrons from 100 keV to 20 GeV and Photons from 11 keV to 20 GeV. // Health Phys. – 1984. – **45**. – P.891–914.
6. *Ferrari A., Pelliccioni M.* On the Conversion Coefficients From Fluence to Ambient Dose Equivalent // Radiat. Prot. Dosim. – 1994. – **51**. – P.251–255.
7. *Briesmeister J. F.* (ed.), MCNP-A General Monte Carlo N-Particle Transport Code. Report LA-12625-M Version 4A (Los Alamos, NM: Radiation Shielding Information Center, Oak Ridge National Laboratory) 1993.
8. International Commission on Radiological Protection. Data for Use in Protection Against External Radiation. ICRP Publication 51 (Oxford: Pergamon Press) 1987.
9. *Nelson F. F., Chilton A. B.* Low-Energy Photon Dose Deposition in Tissue Slab and Spherical Phantoms. Report NUREG/CR-3425 (Washington, DC: US Nuclear Regulatory Commission) 1983.
10. *Williams G., Swanson W.P., Kragh P., Drexler, G.* Calculation and Analysis of Photon Dose Equivalent Distributions in the ICRU Sphere. Report GSF Bericht S-958 (Gesellschaft für Strahlen-und Umweltforschung mbH, Munchen) 1983.
11. *Dimbylow P.J., Francis T.H.* A Calculation of the Photon Depth Dose Distribution in the ICRU Sphere for a Broad Parallel Beam, a Point Sources and Isotropic Field. Report NRPB-R92 (London, England, HMSO) 1979.

12. *Grosswendt B., Hohlfeld K., Kramer H.M., Selbach H-J.* Conversion Factors for ICRU Dose Equivalent Quantities for the Calibration of Radiation Protection Dosimeters. Report PTB-DOS-11E (Physikalisch-Technische Bundesanstalt, Braunschweig) 1988.
13. *Wagner S.R. Grosswendt, B. Harvey J.R. Mill A.J. Selbach H-J., Siebert B.R.L.* Unified Conversion Function for New ICRU Operational Radiation Protection Quantities. // Radiat. Prot. Dosim. – 1985. – **12**. – P.231–235.
14. *Clark M.J. Chartier J.-L. Siebert B.R.L., Zankl M.* Comparison of Personal Dose Equivalent and Effective Dose. // Radiat. Prot. Dosim. – 1998. – **78**. – P.91–99.

**B.Grynyov  
V.Ryzhikov  
Jong Kyung Kim  
Moosung Jae**

**Scintillator Crystals,  
Radiation Detectors  
&  
Instruments on Their Base**

Translation into English  
Longin N.Lisetski

**Ukraine – Kharkiv – 2004**

Editor V.Ryzhikov  
Executive Editor E.V.Sherbina  
Illustrations D.Nalivaiko  
Computer making-up D.V.Tkachev

Sent to the printer's 20.01.2004. Signed for publication 25.06.2004  
Demy 60×84/16. Paper offset No.1. Font Century SchoolBook. Offset. print.  
Edition 500.